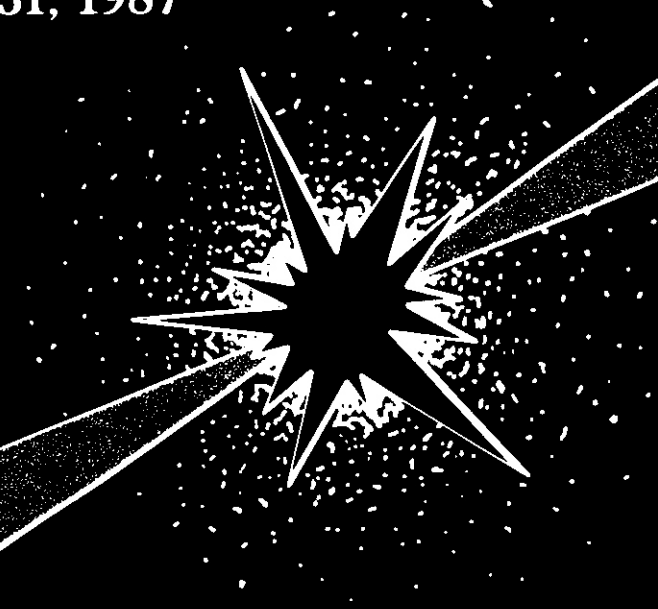
DOE/ER-0313/2

Fusion Reactor Materials

Semiannual Progress Report
for Period Ending
March 31, 1987



U. S. Department of Energy
Office of Fusion Energy

Printed in the United States of America Available from
National Technical Information Service
U.S. Department of Commerce
5285 Port Royal Road, Springfield, Virginia 22161
NTIS price codes— Printed Copy: A14 Microfiche A01

This report was prepared as an account of work sponsored by an agency of the United States Government Neither the United States Government nor any agency thereof, nor any of their employees, makes any warranty, express or implied. or assumes any legal liability or responsibility for the accuracy. completeness, or usefulness 01 any Information. apparatus, product. or process disclosed. or represents that its use would not infringe privately owned rights. Reference herein to any specific commercial product, process, or service by trade name, trademark, manufacturer. or otherwise. does not necessarily constitute or imply its endorsement, recommendation. or favoring by the United States Government or any agency thereof The views and opinions 01 authors expressed herein do not necessarily state or reflect those of the United States Government or any agency thereof

DOE/ER-0313/2
Oistribution
Categories
UC20, 20c

FUSION REACTOR MATERIALS SEMIANNUAL PROGRESS REPORT FOR THE PERIOD ENDING MARCH 31, 1987

Date Published: September 1937

Prepared for
DOE Office of Fusion Energy

Prepared by
OAK RIOGE NATIONAL LABORATORY
Oak Ridge, Tennessee 37831
operated by
MARTIN MARIETTA ENERGY SYSTEMS, INC.
for the
U.S. DEPARTMENT OF ENERGY
under Contract DE-AC05-840R21400

FOREWORD

This is the second in a series of semiannual technical progress reports on fusion reactor materials. This report combines research and development activities which were previously reported separately in the following technical progress reports:

- Alloy Development for Irradiation Performance
- Damage Analysis and Fundamental Studies
- Special Purpose Materials

These activities are concerned principally with the effects of the neutronic and chemical environment on the properties and performance of reactor materials; together they form one element of the overall materials program being conducted in support of the Magnetic Fusion Energy Program of the U.S. Department of Energy. The other major element of the program is concerned with the interactions between reactor materials and the plasma and is reported separately.

The Fusion Reactor Materials Program is a national effort involving several national laboratories, universities, and industries. The purpose of this series of reports is to provide a working technical record for the use of the program participants, and to provide a means of communicating the efforts of materials scientists to the rest of the fusion community, both nationally and worldwide.

This report has been compiled and edited under the guidance of A. F. Rowcliffe, Oak Ridge National Laboratory, and D. G. Doran, Battelle-Pacific Northwest Laboratory. Their efforts, the work of the publications staff in the Metals and Ceramics Division at ORNL, and the many persons who made technical contributions are gratefully acknowledged. T. C. Reuther, Reactor Technologies Branch, has responsibility within DOE for the programs reported on in this document.

G. M. Haas, Chief
Reactor Technologies Branch
Office of Fusion Energy

TABLE OF CONTENTS

FOREWORD iii

1. IRRADIATION FACILITIES, TEST MATRICES, AND EXPERIMENTAL METHODS 1

1.1 RTNS-II Irradiations and Operations (Lawrence Livermore National Laboratory) 3

Irradiations were performed on eighteen different experiments during this period. The joint research effort by U.S. and Japanese scientists who used the RTNS-II to test materials for future fusion reactors formally ended in March 1987. However, the last experiments at the RTNS-II Facility will end in late May, after which the Facility will be prepared for placement in storage. Over 450 experiments were performed during the five-year joint agreement involving 136 different researchers in 6 different countries.

1.2 Design and Fabrication of HFIR-MFE RE* Spectral Tailoring Irradiation Capsules (Oak Ridge National Laboratory and Midwest Technical, Inc.) 8

Design and fabrication of four HFIR-MFE-RB capsules (60, 200, 330, and 400°C) to accommodate specimens preirradiated in spectrally tailored experiments in the ORR are proceeding satisfactorily. The capsule designs are being standardized as much as possible and the fabrication drawings are being prepared on a computer-aided design (CAD) system to minimize overall long-term costs. Preparation of fabrication drawings for the capsule containment tube parts and 330°C capsule internal parts hes been completed, and fabrication of some parts has started. Fabrication drawings for the 60°C capsule are scheduled to be completed by May 1987, and for the 400 and 200°C capsules by August 1987. Operation of the 330 and 60°C capsules is scheduled to begin in April 1988, and the other two (400 and 200°C) in October 1989.*

A conventional temperature control gas gap between the test specimen holder and containment tube, although relatively small, was selected for the 330°C capsule design. Development efforts are in progress to test a larger particle-filled gap concept for possible use for temperature control in the 200°C capsule. In this concept, temperature would be controlled primarily by varying the inert gas pressure in an annular bed of coarselfine microspheres to change its thermal conductance.

1.3 The HFIR Instrumented (JP Type) Target Temperature Test (TTT) Capsule (Oak Ridge National Laboratory) 10

The JP-TTT capsule completed four out of five planned HFIR irradiation cycles on November 14, 1986. when the HFIR was shut down to resolve the reactor pressure vessel integrity issue. The capsule accumulated a total of 82.04 full power days (FPD) at 100 MW reactor power.

The thermal analysis was completed with the conclusion that the heat generation rate axial profile should be modified to match the JP DPA curve profile to reflect the steeper gradient observed outside the 300-mm centered about the horizontal midplane (HMP).

1.4 Operation of the U.S./Japan ORR Spectral Tailoring Experiments (Oak Ridge National Laboratory) 18

The ORR-MFE-63 and -7J experiments continued irradiation during this reporting period ending on March 31, 1987. The total accumulated irradiation time is 474.7 full power days (FPD) at 30 MW reactor power.

1.5 Status of U.S./Japan Collaborative Testing in HFIR and ORR (Oak Ridge National Laboratory and Japan Atomic Energy Research Institute, assigned to ORNL) 19

All eight Phase-I target capsules have been disassembled and specimen testing is proceeding. The two spectrally tailored capsules continue operation in the Oak Ridge Research Reactor (ORR). At the end of this fiscal year. they will be removed for interim examination and reinsertion into R B positions in the High Flux Isotope Reactor (HFIR).

1.6 Fusion Program Research Materials Inventory (Oak Ridge National Laboratory and McDonnell Douglas Astronautics Company – St. Louis Division) 22

A summary of materials in the Fusion Program Research Materials Inventory indicates the nominal diameter of rod or thickness of sheet for product forms of each alloy and also indicates by weight the amount of each alloy in larger sizes available for fabrication to produce other product forms as needed by the program. No material was added to the inventory during this reporting period.

2. DOSIMETRY, DAMAGE PARAMETERS AND ACTIVATION CALCULATIONS 25

2.1 Neutronics Analysis in Support of the U.S./Japan Spectral Tailoring Capsules (Oak Ridge National Laboratory) 27

Scale factors obtained from previous comparisons of the calculated and measured neutron fluences in the ORR-MFE-6J dosimetry capsule are being used to scale the neutron fluences obtained from ongoing three-dimensional neutronics calculations. As of March 23, 1987, this procedure yields 61.6 appm He (not including 2.0 appm He from ^{10}B) and 6.88 dpa for type 316 stainless steel in ORR-MFE-6J and 96.3 appm He and 7.92 dpa in ORR-MFE-7J.

2.2 Cross Section Measurements fur Long-lived Isotopes (Argonne National laboratory) 28

Neutron production cross sections have been measured near 14.8 MeV for reactions leading to long-lived isotopes in fusion reactor materials. Pure elements and separated isotopes were irradiated at the RTNS II to fluences up to 10^{18} n/cm^2. Undesired activities were chemically separated and the long-lived activities were measured using liquid scintillation and x-ray spectrometry. Results are reported for the reactions $^{56}Fe(n,2n)^{55}Fe$ (2.73 y), $^{64}Ni(n,2n)^{63}Ni$ (100y), $^{63}Cu(n,p)^{63}Ni$, and $^{60}Ni(n,2n)^{59}Ni$ (76,000 y).

2.3 Measurements for the JP2, JP6, JP7 U.S./Japanese Experiments in HFIR (Argonne National Laboratory) 33

Results are reported for the JP2, JP6, and JP7 U.S./Japan experiments that focus on the swelling, tensile, and fatigue properties of stainless steel. The JP2 experiment has the highest exposure reported for HFIR (57,501 MWD) producing 55.2 dpa and 3345 appm helium in 316 stainless steel.

2.4 Dosimetry and Damage Analysis for the Omega West Reactor (Argonne National Laboratory) . . . 36

Five experiments have been completed in the Omega West Reactor (LANL) for comparison with 14 MeV measurements at RTNS II (LLNL). The use of water rather then helium coolant on some of the runs appears to have produced a significant spectral shift. Neutron fluences and damage rates are reported for each experiment.

2.5 Dosimetry and Damage Analysis for HFIR-CTR-47/48 (Argonne National Laboratory) 40

Dosimetry measurements and damage calculations have been completed for the CTR47/48 experiments in HFIR (ORNL) to study impact properties of ferritic alloys (HT9, T9). These irradiations have the highest reported exposure in the PTP position (46,113 MWD) resulting in 47.2 dpa and 2643 appm Re in 316 stainless steel.

2.6 Activation Calculations (Westinghouse Hanford Company) 43

Improved evaluations of the reactions induced on 11 elements were processed into the REAC2 cross section library. Limitations of the presence of tungsten in soft spectrum are no longer a major concern.

3. MATERIALS ENGINEERING AND DESIGN REQUIREMENTS 45

No contributions received this period

4. FUNDAMENTAL MECHANICAL BEHAVIOR . 49

4.1 Analysis of the Effect of Internal Hydrogen on the Fatigue Crack Growth of HT-9 (Pacific Northwest Laboratory) 51

Evaluation of the frequency dependence of the hydrogen effect on fatigue crack growth of HT-9 showed an increasing crack growth rate with decreasing frequency or increasing cyclic period. This result coupled with the plateau observed for the fatigue crack growth of HT-9 with internal hydrogen has been used to evaluate the hydrogen contribution to fatigue crack growth using the superposition of static and cyclic crack growth processes.

5. RADIATION EFFECTS: MECHANISTIC STUDIES, THEORY AND MODELING 55

5.1 The Influence of Both Major and Minor Element Composition on Void Swelling in Simple Austenitic Steels (Hanford Engineering Development Laboratory and University of Missouri – Rolla) 57

Data on the neutron-induced swelling of simple Fe-Ni-Cr austenitic alloys are presented to show that there are three compositional regimes of swelling as a function of nickel content. The intermediate transition regime can be shifted to higher or lower nickel levels as a function of chromium content, various solutes, displacement rate, temperature and helium level. Such shifts can preclude the observation of either the lower or upper nickel regime. The lower nickel regime is also obscured in ion bombardment studies due to factors that are atypical of the neutron environment.

Data are also presented to show the influence of silicon and phosphorus on the neutron-induced swelling of Fe-25Ni-15Cr and to demonstrate that the separate influence of each of these elements is more complex than previously observed. Similar complex trends have also been seen in ion bombardment experiments but there are additional distortions relative to the neutron-induced behavior that arise from the interaction of these elements with point defect gradients.

A model is presented to show that the major effect of composition on swelling lies in its influence on void nucleation, operating primarily on the intermediate transition regime. Compostional variations thus is due to the effect of each element on the vacancy supersaturation via their effect on either the equilibrium vacancy concentration or the effective vacancy diffusion coefficient.

5.2 The Behavior of Solute Segregation and Void Formation in Fe-Cr-Ni and Fe-Cr-Mn Steels Ouring Electron Irradiation (Faculty of Engineering, Hokkaido University; Hanford Engineering Development Laboratory; and Beijing University of Iron and Steel Technology) . . 81

The relative swelling behavior of Fe-Cr-Mn and Fe-Cr-Ni alloys during electron irradiation is shown to be different from that observed in neutron irradiations. This difference appears to a consequence of the different diffusion behavior of nickel and manganese in response to the operation of the inverse Kirkendall effect. The vacancy gradients driving the diffusion in these experiments are generated not only by the foil surfaces and the electron-generated radial displacement gradient but also by high angle grain boundaries deliberately centered in the middle of the electron beam. This procedure allows the relative diffusional characteristics of each element to be observed by EDX measurements across the grain boundary. The influence of helium and minor solutes on swelling was also studied in these experiments and yielded no behavior atypical of that observed in neutron irradiation studies.

5.3 The Critical Radius for Void Nucleation in Neutron Irradiated Ferritic Alloy, HT-9 (Arizona State University and Westinghouse Hanford Company) 92

Experimental measurements of cavity formation of HT-9 following irradiation to 39 dpa at 300, 400, 500 and 600°C are used as a basis for examining the critical radius for void nucleation model as applied to ferritic alloys. Calculations demonstrate that the value for critical radius following irradiation at 400°C can be predicted, that values for critical radius at 500 and 600°C are in agreement with experiment but that values for critical radius at 300°C are below experimental values. Calculations are compared with those on a ferritic alloy following ion bombardment. Possible explanations are suggested.

5.4 Defect Production and Hardening in Neutron-Irradiated Copper (Oak Ridge National Laboratory) 103

The fraction of Frenkel defects that survive in isolated or clustered form during room temperature irradiation of copper has been measured as a function of fluence by a combination of TEM and electrical resistivity methods. The ratio of surviving to created defects decreased from I2 to 4.7% as the fluence of 14-MeV neutrons increased from 1×10^{20} to 2.9×10^{21} n/m^2. A comparison of the TEM and resistivity data with radiation hardening studies indicates that the barrier strength of loops (β) may also depend on fluence, at least at low fluences.

5.5 Computer Simulation of Ion Beam Mixing – Part I (University of Wisconsin) 109

Ion beam mixing, which is defined as the application of energetic heavy ion beam to induce materials interactions in thin-film composite sample or pre-implanted solids, has been received a great concern by many research groups. However, the complicated nature of mixing process makes it hard to predict the dynamic behavior of the materials during ion beam irradiation. Monte Carlo methods have been used to solve this problem and in this study, the accuracy of such a program was tested to calculate the ion range before further modification of the program.

6. DEVELOPMENT OF STRUCTURAL ALLOYS 115

6.1 Ferritic Stainless Steels 117

6.1.1 Charpy Impact Test Results of Ferritic Alloys From the HFIR-MFE-RB2 Test (Westinghouse Hanford Company) 119

Miniature Charpy specimens of XT-9 in base metal, weld metal and heat affected zone (HAZ) metal conditions, and 9Cr-1Mo in base metal and weld metal conditions have been tested following irradiation in HFIR-MFE-RB2 at 55°C to ≈10 dpa. All specimen conditions have degraded properties (both DBTT and USE) in comparison with specimens irradiated to lower dose. 9Cr-Mo degraded more than NT-9 and weld metal performed worse than base metal which performed worse than HAZ material. Property degradation was approximately linear as a function of dose, indicating that degradation response had not saturated by I0 dpa.

6.1.2 Charpy Impact Test Results for Low Activation Ferritic Alloys (Westinghouse Hanford Company) 123

Six low activation ferritic alloys have been tested following irradiation at 365°C to 10 dpa and compared with control specimens in order to assess the effect of irradiation on Charpy impact properties. It is found that alloys of composition Fe-2Cr-1.5V, Fe-12Cr-6Mn-1V and Fe-12Cr-6Mn-1W develop unacceptably large shifts in DBTT due to irradiation, Fe-9Cr-1V develops a small shift and Fe-9Cr-1W and Fe-7.5Cr-2W develop negligible shifts. There is little effect on USE in all cases. It appears that alloy development of low activation ferritic alloys should be concentrated in the Fe-7.5 to 9Cr range.

6.1.3 Tempering Effects on a 12 Cr Low Activation Steel (University of Wisconsin) 135

A martensitic steel similar to HT-9 has been designed to reduce activation levels following irradiation. Hardness tests, optical metallography and transmission electron microscopy are being used to determine the response of the steel to tempering.

6.1.4 Properties of Welded Low Activation Ferritic Alloys (Auburn University) . . . 139

Sound autogeneous welds can be produced readily in thin sheets of the low activation ferritic alloys patterned on 2-1/4 Cr-1Mo, 9 Cr-1Mo and 12 Cr-1Mo steels. The as-welded 2-If4 Cr and 9 Cr alloys show typical microstructures of banite and martensite respectively, while 12 Cr alloys show the duplex ferrite-martensite. Observations indicate that there is a tendency to form delta ferrite in both fusion and heat-affected zones if the concentration of vanadium is greater than I wt%. In addition, the strengthening effect caused by the addition of tungsten and tantalum is not significant. The mechanical results suggest that a post-weld heat treatment is recommended for both 9 Cr and 12 Cr low activation alloys to enhance impact properties.

6.1.5 The Development of Ferritic Steels for Fast Induced-Radioactivity Decay (Oak Ridge National Laboratory) 155

Tensile studies were made on eight heats of normalized-and-tempered chromium-tungsten steel that contained various levels of chromium, tungsten, vanadium, and tantalum. The strength and ductility of these steels were found to compare favorably with the properties of analogous chromium-molybdenum steels that are presently being considered as candidate structural materials for fusion reactor applications.

6.1.6 Postirradiation Tensile Behavior of Nickel-Doped Ferritic Steels (Oak Ridge National Laboratory) 166

Tensile specimens of normalized-and-tempered 9Cr-1MoVNb, 9CR-1MoVNb-2Ni, 12Cr-1MoVW, 12Cr-1MoVW-1Ni, and 12Cr-1MoVW-2Ni steels were irradiated in the HFIR at 300, 400, and 500°C to displacement-damage levels of up to ~11 dpa. The nickel was added to the ferritic steels to produce helium during irradiation in this mixed-spectrum reactor. Up to 103 appm He was produced in the steels with 2% Ni. Irradiation at 300 and 400°C caused an increase in strength of a11 the steels relative to the strength in both the normalized-and-tempered condition end after aging the normalized-and- tempered steel for a time period similar to that in the reactor. The strength increases were accompanied by a loss of ductility. At 500°C, there was little change in the strength properties of the steels. The results at 300 and 400°C indicate an effect of helium on the strength increases; no helium effect was apparent for the specimens irradiated at 500°C.

6.2 Austenitic Stainless Steels 175

6.2.1 The Development of Austenitic Stainless Steels for Fast Induced-Radioactivity Decay (Oak Ridge National Laboratory) 177

As part of an alloy-development program for a nickel-free stsinless steel, five Fe-Mn, thirteen Fe-Cr-Mn, and fifteen Fe-Cr-Mn-C alloys were examined to determine the austenite-stable region in the Fe-Cr-Mn-C system. After various heat treatments, optical and electron microscopy studies and magnetic measurements were used to assess the microstructural constituents present. The results indicate that the Schaeffler diagram, which was developed to predict the phases present in Fe-Cr-Ni-C stainless steels, cannot be directly applied to Fe-Cr-Mn-C steels. Manganese has a lower austenite-stabilizing capability against δ-ferrite formation then the Schaeffler diagram predicts by simply considering it half as effective as nickel. However, its stabilizing capability against martensite formation is higher than predicted by the diagram on the same basis. The new results can be used to empirically establish the austenite-stable composition region that should be suitable for alloying to develop a manganese-stabilized stainless steel.

6.2.2 Some Effects of Thermal-Mechanical Pre-Treatment and Alloy Compositional Variation on Swelling of Austenitic Stainless Steels Irradiated in HFIR (Oak Ridge National Laboratory) 192

A precision densitometer has recently been installed at ORNL for remote measurement of immersion density of irradiated transmission electron microscopy (TEM) disks. Some disks have been measured from the HFIR-JP1 and -JP3 experiments, irradiated at 300 and 400°C, respectively, to 34 dpa, and nearly all the disks have been measured from HFIR-JP7 and -JP8, irradiated at 500°C to 34 and 57 dpa, respectively. Very little swelling was measured in any of the disks irradiated at 300 and 400°C, but swelling was variable, end in many cases quite large, at 500°C. Only a few alloys appear to be swelling resistant. Of the Japanese alloys, the JPCA was the best, particularly when irradiated in the 20% cold worked (CW) condition. Swelling of the USPCA in the 25% CW (B3) condition was less than the 20% CW JPCA after 57 dpa at 500°C. An unusual decrease in swelling occurred with increased dose from 34 to 57 dpa. The U.S. alloys included many modifications of the PCA composition, but the most swelling-resistant alloys contained 0.03 to 0.07 wt % P.

6.2.3 Irradiation-Produced Precipitates in Austenitic Stainless Steels Irradiated in HFIR to 36 dpa at 600°C (Japan Atomic Energy Research Institute, assigned to Oak Ridge National Laboratory) 209

Four solution-annealed austenitic stainless steels (JPCA, low-carbon stainless steel with titanium, low carbon stainless steel with titanium and niobium, and J316) were irradiated in HFIR to 36 dpa. In JPCA, swelling was very low (0.2%) and the only phase present was MC uniformly distributed in the matrix. On the other hand, the other three alloys indicated a large amount of swelling (>1%), and coarse precipitates, (mainly G, Laves, sad η-phase) were observed in low concentration throughout the matrix.

6.2.4 Microstructural Change of JPCA Irradiated to 58 dpa at 300°C in HFIR (Japan Atomic Energy Research Institute, assigned to Oak Ridge National Laboratory) **217**

Characteristic microstructural features observed in JPCA irradiated at 300°C in HFIR are the formation of many fine bubbles and dislocation loops. Radiation produced MC-type precipitates were found after only 34 dpa irradiation. The present work revealed that bubbles and dislocation loops do not show noticeable change during the irradiation from 34 (helium content: 2470 appm) to 58 dpa [helium content: 4260 appm). On the other hand, the number density of MC-type precipitates decreased during the irradiation. The microchemical examination of the precipitates showed that the chromium content decreased and the nickel and silicon were enriched during irradiation.

6.2.5 Mechanical Properties and Fracture Behavior of 20% Cold-Worked 316 Stainless Steel Irradiated to Very High Neutron Exposures (Hanford Engineering Development Laboratory and General Electric Company) **221**

Stainless steels irradiated in EBR-II at temperatures in the range 380 to 500°C tend to exhibit saturation of mechanical properties at relatively low fluence levels. At fluences on the Order of I3 to 15 x 10^{22} n/cm² (E > 0.1), however, there is a rapid increase in hardness just after the onset of void swelling. The hardness increase is not attributed just to the voids themselves but rather to an indirect effect of voids on nickel depletion in the alloy matrix. The strong dependence of stacking fault energy on nickel and chromium content and particularly on deformation temperature combine to promote extensive stress-induced formation of ε-martensite at room temperature. This leads to a very brittle failure mode characterized as quasi-cleavage. At higher deformation temperatures it leads to a failure mode designated channel fracture.

6.3 Vanadium Alloys **247**

6.3.1 Charpy Impact Properties of V-15Cr-5Ti (Westinghouse Hanford Company) **249**

Impact tests have been completed on unirradiated one-third size Charpy specimens of V-15Cr-5Ti. The ductile-to-brittle transition temperature was unexpectedly high, on the order of 130°C. Irradiation of this alloy in FFTF-MOTA in lithium-filled TZM subcapsules has also been completed at 385, 420, 520, and 600°C, with damage levels ranging from 10 to 30 dpa. Impact tests on these specimens are now being planned.

6.3.2 Preparation and Fabrication of Vanadium Base Alloys (Argonne National Laboratory) . . **251**

Past reports detailed the design and startup of a fabrication process flowsheet. The planned fabrication methods were used to process a 13 Kg quantity of V-15Cr-5Ti alloy. Adopting the same approach, a 2.6 Kg dual lot of V-10Cr-5Ti alloy was consolidated, consumable arc melted, extruded and final rolled to customer specified shapes and sizes during this reporting period. The primary products were 0.035" and 0.020" sheet for tensile tests and 0.140" stock for charpy bar tests. Additions1 sheet and bar material has been fabricated from previously cast alloys of V-20Ti, V-7.5Cr-15Ti and V-3Ti-1Si.

In addition, this effort provides for correlation of complementary fabrication work on V-12Cr-5Ti and V-10Cr-10Ti alloys at Teledyne Wah Chang Albany.

6.3.3 Effect of Heat Treatment and Impurity Concentration on the Tensile Deformation of Unirradiated and Irradiated Vanadium Alloys (Argonne National Laboratory) 254

The effect of heat treatment and oxygen, nitrogen, carbon, and hydrogen impurities on the yield strength, ultimate tensile strength, ductility, and fracture mode for the V-15Cr-5Ti, V-12Cr-5Ti, V-15Ti-7.5Cr, V-20Ti, snd V-3Ti-1Si alloys was determined from tensile tests at 20°C. In the case of the V-Cr-Ti alloys in the fully recrystallized condition, the results showed that for the slloys to exhibit ductile fracture on tensile deformation at 20°C, they must be annealed in vacuum (rather than in argon-filled capsules) and contain 800-900 ppm oxygen. The V-20Ti and V-3Ti-1Si alloys, which contain 800-900 ppm oxygen, exhibited ductile fracture after a recrystallization anneal in vacuum as well as in argon-filled capsules. These results were interpreted as evidence that vanadium alloys containing chromium solute are more susceptible to hydrogen embrittlement. The yield strength of vanadium alloys, which were similarly annealed in vacuum and contained comparable oxygen concentration (800-900 ppm), increased with an increase of the combined titanium and chromium concentration. The total elongation of these alloys was not significantly altered by the change in alloy composition. On the basis of microstructures obtained from ion-irradiated alloys, it was concluded that the V-3Ti-1Si and V-20Ti alloys were not intrinsically more resistant to hardening and emhrittlement on neutron irradiation than the V-15Cr-5Ti slloy.

6.3.4 She Formation of Titanium Tritide in V-20Ti (Oak Ridge National Laboratory) 263

More than expected amounts of ^3He were measured in V-20Ti because of whet appeared to be the formation of titanium tritide during the tritium trick procedure. Slightly more ^3He was also measured in warm-worked V-20Ti and other vanadium alloy specimens compared to annealed ones – probably because the diffusion of tritium was assisted by the presence of dislocations. The high-helium contents caused substantial losses in ductility in annealed V-20Ti specimens but had little effect in warm-worked specimens. The formation of titanium tritide in high-titanium-content vanadium alloys should he investigated further.

6.4 Copper Alloys 269

No contributions received this period

6.5 Environmental Effects on Structural Alloys 273

6.5.1 Corrosion of Vanadium Alloys in Flowing Lithium (Argonne National Laboratory) 275

Corrosion data are presented for several vanadium alloys exposed to flowing lithium at 482 and 427°C. Metallographic evaluation of the exposed specimens is also presented. The influence of alloy composition and exposure conditions on the corrosion behavior of vanadium alloys is discussed.

6.5.2 Thermal Convection Loop Studies in Support of Mass Transport Modeling of Lithium/12Cr-1MoVW Steel Systems (University of California – Los Angeles and Oak Ridge National Laboratory) 281

The 12Cr-1MoVW material was obtained from GA Technologies fusion slloy stockpile in January 1987. The standard ORNL thermal convection loop and specimen string were substantially redesigned to minimize some of the Uncertainties typically sssociated with mass transfer model development in liquid metal corrosion loop systems and to simplify loop febrication. The experimental systems snd specimens were then fabricated, installed, and tested during the current reporting period. Experimental operation is expected to begin in April 1987.

6.5.3 Thermal Gradient Mass Transfer in Ferrous Alloy Pb-17 at. % Li Systems (Oak Ridge National Laboratory) 285

Scanning electron microscopy and sssociated energy dispersive x-ray analysis of type 316 stainless and 12Cr-1MoVW steels exposed to thermally convective Pb-17 at, % Li yielded quantitative information about changes in surface morphology and

composition as a result of mass transfer reactions. In the case of type 316 stainless steel, substantial preferential dissolution of nickel and chromium occurred at 500°C and led to the formation of a deep corrosion zone of irregular penetration. The extent and morphology of this corrosion zone was found to be sensitive to the starting microstructure of the steel. The 12Cr-1MoVW steel corroded uniformly with no change in its surface concentration. Mass transfer deposits in the type 316 stainless steel system differed depending on their position in the cold leg, where the temperature varied from 400 to 460°C. Depending on the temperature, the majority of the deposits were principally composed of iron, iron-nickel, or chromium.

7. SOLID EREEOING MATERIALS 295

7.1 Model of Tritium Transport in Ceramic Breeder Materials (Argonne National Laboratory) . . . 297

A computer model of tritium transport and release is being developed. The model considers diffusion through the solid and desorption from the solid surface. The model is based on a differential equation that predicts heat transfer in a solid sphere at constant heat generation and heat radiation at the surface. The tritium release over tine calculated with our model was compared with the measured release for samples of Li_2SiO_3 from the LISA-I experiment. Overall agreement between the model and experiment was good. Improvements in the model to enable handling of samples with large distribution of grain sizes are now being considered. It is also envisaged that the diffusion-desorption model will be combined with programs which calculate the effective rate constants at different oxygen potentials.

7.2 Adsorption, Solution, and Desorption Characteristics of the $LiAlO_2$-H_2O System (Argonne National Laboratory) 300

Isotherms are reported for adsorption of H_2O on $LiAlO_2$ at 500°C and for solubility of OH^- in $LiAlO_2$ also at 500°C. The kinetics of the water evolution process appears to be second order in hydroxide content. Calculations have indicated that for the solid phase there is a critical oxygen activity below which tritide is the dominant tritium species rather than tritons which prevail above the critical oxygen activity. These relationships have important implications for the design, performance, and interpretation of tritium release experiments.

7.3 Solid Breeder Materials Fabrication and Mechanical Properties (Argonne National Laboratory) 304

The fabrication of lithium oxide rings for the CRITIC-I experiment was completed and the rings transferred to Chalk River. Lithium zirconate, lithium aluminate and lithium silicate ceramic powders were sent to Hanford Engineering and Development Laboratory to be fabricated for FUBR-1B replacement capsules. Three papers were prepared for the American Ceramic Society Special Symposium on "Fabrication and Properties of Lithium Ceramics." Initial materials have been synthesized to fabricate test specimens for the measurement of mechanical properties of lithium orthosilicate. The paper describing the mechanical properties of lithium oxide was published in the Journal of Nuclear Materials.

8. CERAMICS 305

No contributions received this period.

9. SUPERCONDUCTING MAGNET MATERIALS 309

9.1 Irradiation Effects on Organic Insulators (National Bureau of Standards) 311

An integrated approach has been developed for rapid screening of the influence of component variables on the performance of electrical insulators required for superconducting magnets in magnetic fusion energy systems. It incorporates an efficient method for specimen production in the form of 3.2-mm (0,125-in) diameter rods. Test methods include short-beam shear, fracture strength (G_{Ic}), and strain-controlled torsion. Unreinforced (neat resin) and glass-fiber reinforced specimens having three types of epoxy matrices and one type of bismaleimide matrix have been produced and submitted to ORNL for irradiation in the LTNIF facility. However, the irradiation was not performed during the present reporting period due to startup delays on the LTNIF facility. Furthermore, NBS has been informed by ORNL personnel that the required irradiation cannot be performed on the type € glass-reinforced specimens due to the interaction between the high thermal neutron flux in the reactor and the boron element in this type of glass.

1. IRRADIATON FACILITIES, TEST MATRICES, AND EXPERIMENTAL METHODS

RTNS-II IRRADIATIONS AND OPERATIONS - D. W. Short and D. W. Heikkinen (Lawrence Livermore National Laboratory)

OBJECTIVE

The objectives of this work are operation of RTNS-II (a 14-MeV neutron source facility), mchine development, and support of the experimental program that utilizes this facility. Experimenter services include dosimetry, handling, scheduling, coordination, and reporting. RTNS-II is supported jointly by the U.S. and Japan and is dedicated to mterials research for the fusion power program. Its primry use is to aid in the development of models of high-energy neutron effects. Such models are needed in interpreting and projecting to the fusion environment, engineering data obtained in other spectra.

SUMMARY

Irradiations were performed on eighteen different experiments during this period.

The joint research effort by U.S. and Japanese scientists who used the RTNS-II Lo test naterials for future fusion reactors formally ended in March 1907. However, the last experiments at the RTNS-II Facility will end in late May, after which the Facility will be prepared for placement in storage. Over 450 experiments were performed during the five-year joint agreement involving 136 different researchers in 6 different countries.

PROGRAM

Title: RTNS-II operations (WZJ-16)
Principal Investigator: D. W. short
Affiliation: Lawrence Liverniore National Laboratory

RELEVANT DAF'S PROGRAM PLAN TASK/SUBTASK

TASK II.A.2,3,4.
TASK II.B.3,4
TASK II.C.1,2,6,11,18.

IRRADIATION

During this quarter, irradiations (both dedicated and add-on) were clone for the following people.

Experimenter	or A*	mple Irradiated
Y. Shimomura (Hiroshima) R. Oshima (Osaka) Y. Kitano (Hiroshima) M. Kiritani (Hokkaido) H. Yoshida (Kyoto) H. Matsui (Tohoku) H. Abe (Kyushu) M. Guinan (LLNL) P. Hahn (LLNL) J. Huang (LLNL)	P	Au,Cu,Ag,V,Ni,Al,Si,Mo,Ge,Nb_3Sn,Fe, Mn-Al,Fe-Mo,Fe-Si displacement cascade damage, size & structure analyzed with TEM irradiated at 20°K
H. Moriyama (Kyoto)	P	Li,Pb,Be,F,Cl,Br & I - tritium recovery
D. Kneff (Rockwell) L. Greenwood (ANL)	A	Li, O, F, N, Al_2O_3,MgO, Si_3N_4 & SiC dosimetry & cross sections.
F. Ciinard (LANL)/ H. Frost (LANL)/ N. Iwamoto (Osaka)	P	SiC & Al_2O_3 - Loss tangent & dielectric constant.
T. Iida (Osaka)	A	Fiber optics & photomultiplier tubes - neutron damage.
M. Singh/C. Wang (LLNL)	A	Semiconductors - neutron damage
T. Terai	P	Li_2O, Li_2BeF_4, $Li_{17}Pb_{83}$ - Tritium production
H. Abe (Kyushu)/M. Guinan (LLNL)	P	Dilute Fe alloys - resistivity

Experimenter	P or A*	Sample Irradiated
K. Sumita (Osaka)	P	Oil - gamma irradiation
M. Kiritani/A. Okada (Hokkaido) M. Kiritani/T. Yoshiie (Hokkaido) M. Taniwaki (Hokkaido)	P	Metals & Ceramics - microstructures TEM, tensile - room temperature
M. Kiritani/A. Okada (Hokkaido) cont'd. K. Abe (Tohoku) H. Kayano (Tohoku) H. Kawanishi (Tokyo) M. Kiritani/H. Saka (Hokkaido/Nagoya) H. Yoshida (Kyoto) H. Mori (Osaka) R. Oshima (Osaka) M. Hirata (Osaka) Y. Shimomura (Hiroshima) N. Yoshida (Kyushu) C. Kinoshita (Kyushu) H. Heinisch (HEDL)		
M. Kiritani/A. Okada (Hokkaido) M. Kiritani/T. Yoshiie (Hokkaido) M. Taniwaki (Hokkaido) K. Abe (Tohoku) H. Kayano (Tohoku) H. Kawanishi (Tokyo) M. Kiritani/H. Saka (Hokkaido/Nagoya) H. Yoshida (Kyoto) H. Mori (Osaka) R. Oshima (Osaka) M. Hirata (Osaka) Y. Shimomura (Hiroshima) N. Yoshiiia (Kyushu) C. Kinoshita (Kyushu) H. Heinisch (Hedl)	P	Metals & Ceramics - microstructures TEM, tensile - 150° C / 350° C
C. Violet (LLNL)	A	Nd-Fe-B magnets - magnetic properties
K. Abe (Tohoku)	A	Kapton - tensile strength
C. Wang (LLNL)	A	Semiconductors - response & sensitivity
E. Franco (ARACOR)	P	Sic - x-ray diffraction
J. Kelly (Sandia)	A	GaAs - conductivity & carrier density
J. McDonald (PNL)	P	Plastic calorimetric detector - neutron kerma
R. Hopper (LLNL)	A	Carbon foam - radiation

* P = primry, A = add-on

RTNS-II STATUS - D. W. SHORT AND D. W. HEIKKINEN

The RTNS-II facility was constructed by Lawrence Livermore National Laboratory for DOE'S Office of Fusion Energy. It was built to provide a national center for the study of the effects of 14-MeV neutrons on mterials of interest to the fusion energy program. *The* facility contains two identical deuteron beam accelerators and rotating targets containing titanium tritide coatings. These two systems provide to laboratory experimenters the most intense sources of fusion neutrons in the world.

RTNS-II began producing neutrons in 1978 and was ready for regulary scheduled irradiations in 1979. Initial operation achieved a neutron source strength of 1.0 E t 13 n/s. In 1982, the government of Japan, through the Ministry of Education, Culture, and Science (Monbusho), joined in the support and utilization of the RTNS-II facility. As a result of this increased support, the second *neutron source* was activated and began irradiations in July 1983. The operations schedule was expanded from 10 neutrvn generating shifts every five days to approxinwtely 20 shifts every five days.

Improvements to the accelerator and target systems have teen made which increased neutron production and source strength. Other improvements have teen made to increase the reliability of high-risk components and to improve control and nwnitoring of various neutron source functions. During the last three years several buildings were added to RTNS-II: an office complex to house staff and visiting experimenters and a naterials laboratory for post-irradiation studies by Japanese experimenters.

The facility normally operates 24 hours per day, five days per week. Maintenance activities are required to support the operation of the neutron sources **and** usually occur during the day shift. Examples of these activities include target assembly, vacuum system service, experimental assembly and disassembly, target chiller service, tritium scrubber service, irradiated sample investigations, and contamination control activities.

Since the start of the RTNS-II Collaboration Project, the facility has produced about 8.1 E + 20 neutrons. Each year there has teen an increase in the number of hours that the facility produced neutrons until funding was reduced in 1986 and one source was put on standby. The number of hours increased gradually until calendar year 1985 when there was a **74** percent increase due partly to the experience of the RTNS-II staff and partly to excellent preparation by the experimenters. This is clearly shown by looking at the cumulative number of neutrons generated for each year as shown in Figure **1.**

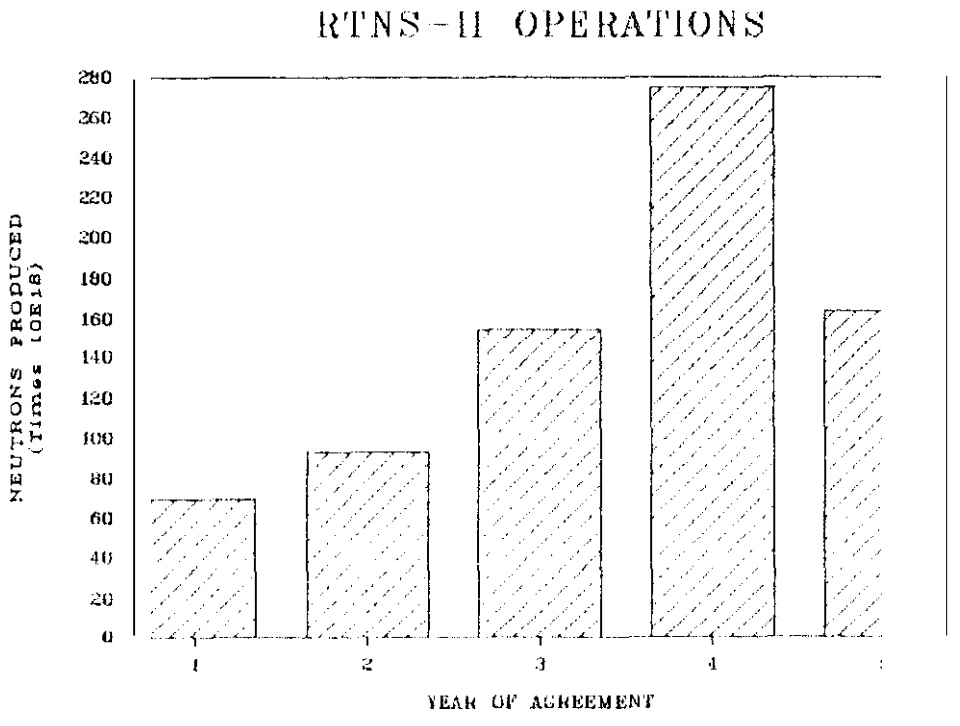


Figure **1.** Yearly generation of neutrons at RTNS-II,

Figure 2 illustrates the variation in average operational availability for the two neutron sources. (The operational availability **is** the percent of tine that a neutron source operates when **it is** scheduled to operate.) **It** took the staff several years to experience failures, learn about how to repair the systems quickly, and provide ways to increase the reliability. Since early 1985, the average availability has consistently teen greater than 80 percent except for the last **few** nnnths of 1986 when one source was reactivated after several months in standby.

A quantitative measure used to asses how well the project **has** performed **is** the productivity factor, defined as the number of neutrons generated per mchine hour per FTE assigned. This factor appropriately excludes experimenter's delays which affect the total number of neutrons produced in any given tine. (In many cases experimenter equipment was redesigned and modified to lessen delays and to make the experiment successful.) Figure **3** shows the marked improvement in productivity during the joint agreement.

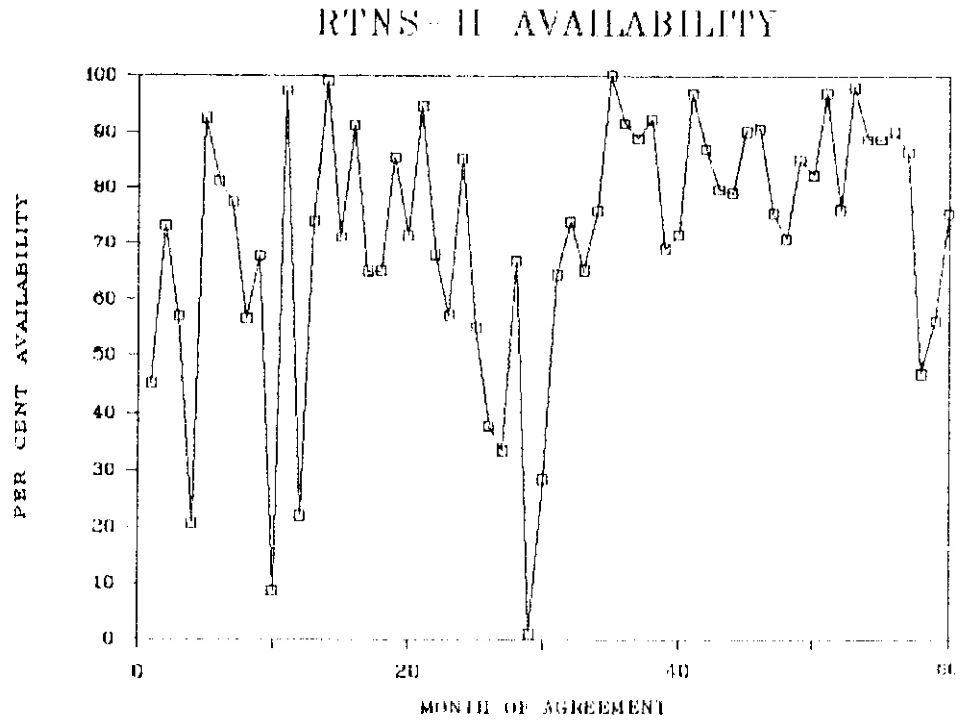


Figure 2. Average mchine availability has remained consistently high.

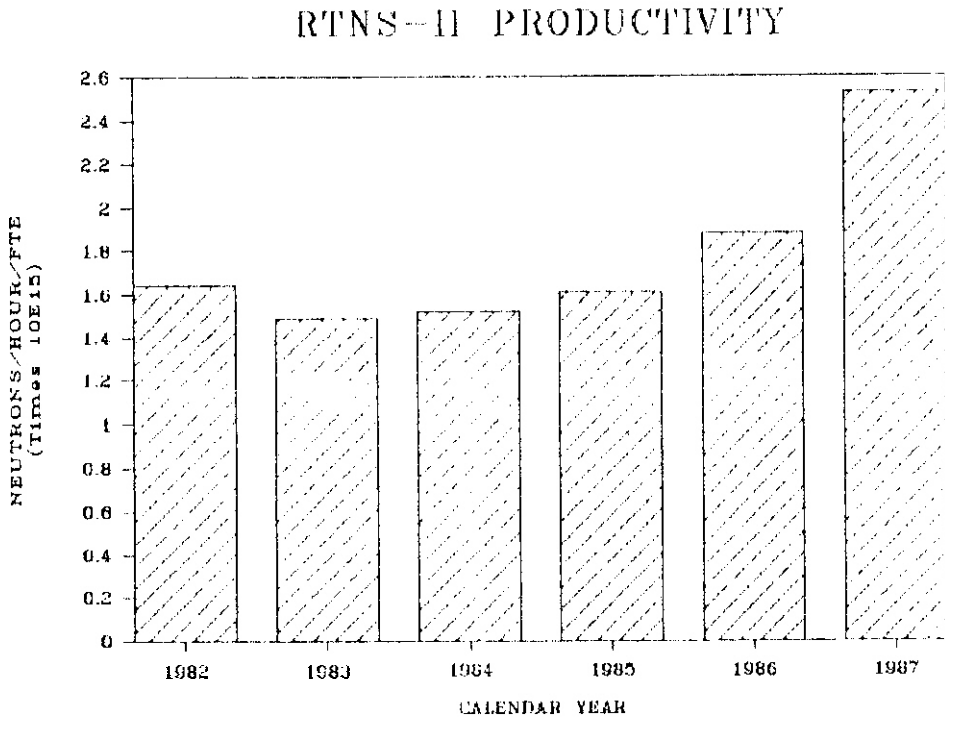


Figure 3. Average productivity factor shows a **mrked** improvement

The primary source of radiation exposure has always been activated mterials (targets, hub assemblies, experimenter's equipment, etc.). Since the beginning of the U.S./Japan Agreement, there has been a

significant increase in the annual number of neutrons produced. During the same period there has been a 49 percent decrease in the average annual radiation dose for Facility staff members. See Figure 4 for the yearly average radiation doses for the RTNS-II staff. The average dose was 21 percent lower in 1985 than in 1984 and 22 percent lower in 1986 than in 1985. If one looks at the risk involved in producing neutrons, the result is a 78 percent decrease in dose received per neutron generated. Since the first year of the Agreement, the dose per neutron generated has decreased by more than a factor of 4.5.

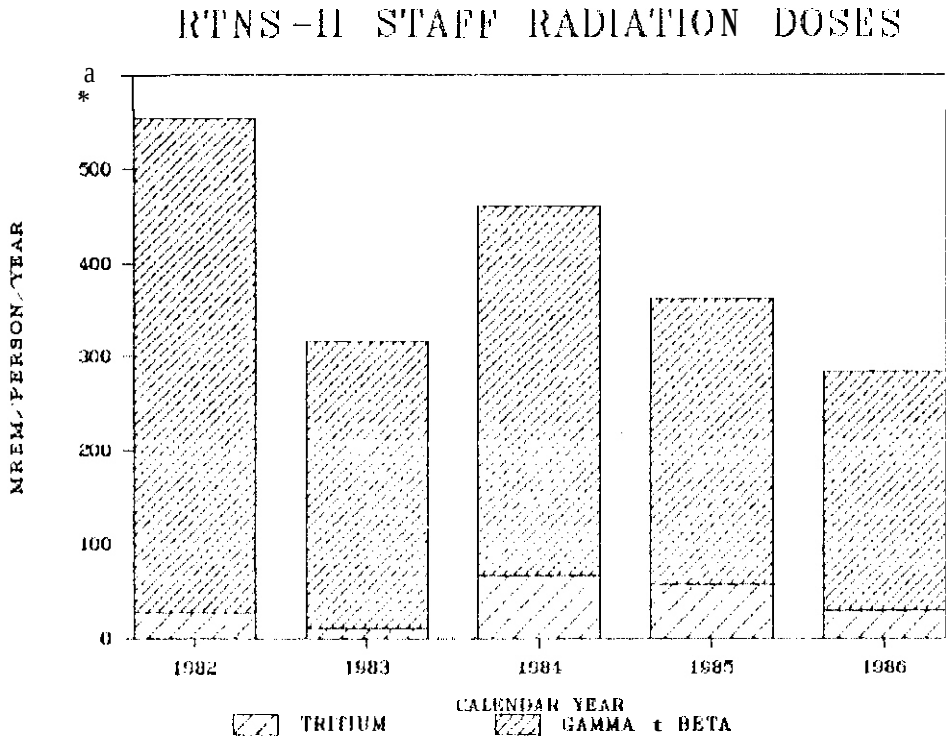


Figure 4. Staff radiation doses have decreased significantly.

DESIGN AND FABRICATION OF HFIK-MFE RB* SPECTRAL TAILORING IRRADIATION CAPSULES - A. W. Longest (Oak Ridge National Laboratory), J. E. Corum (Midwest Technical, Inc.), and K. R. Thoms (Oak Ridge National Laboratory)

OBJECTIVE

The objective of this work is to design and fabricate irradiation capsules for operation in the HFIK RB* positions. Japanese and U.S. speciinens are to he transferred to RR* positions following irradiation to ~10 dpa at temperatures of 60. 200, 330, and 400°C in ORR experiments ORR-MFE-6J and -7J.

SUMMARY

Design and fabrication of four HFIR-MFE-RB* capsules (60, 200, 330, and 400°C) to accommodate specimens preirradiated in spectrally tailored experiments in the ORR are proceeding satisfactorily. The capsule designs are being standardized as much as possible and the fabrication drawings are being prepared on a computer-aided design (CAD) system to minimize overall long-term costs. Preparation of fabrication drawings for the capsule containment tube parts and 330°C capsule internal parts has been completed, and fabrication of some parts has started. Fabrication drawings for the 60°C capsule are scheduled to he completed by May 1987, and for the 400 and 200°C capsules by August 1987. Operation of the 330 and 60°C capsules is scheduled to begin in April 1988, and the other two (400 and 200°C) in October 1989.

A conventional temperature control gas gap between the test specimen holder and containment tube, although relatively small, was selected for the 330°C capsule design. Development efforts are in progress to test a larger particle-filled gap concept for possible use for temperature control in the 200°C capsule. In this concept, temperature would **he** controlled primarily by varying the inert gas pressure **in** an annular bed of coarse/fine microspheres to change its thermal conductance.

PROGRESS AND STATUS

Introduction

The design and fabrication of four spectral-tailored capsules to accommodate the HFIR-MFE spectral tailoring specimens' that are being preirradiated in the ORR experiments ORR-MFE-6J and -75 are in progress. The capsules are being designed for insertion into any of the eight large-diameter holes (46 mm) of the new removable beryllium (RB*) facility that is scheduled to he installed in the HFIK in June 1987. These experiments will irradiate the Japanese and U.S. material speciinens at temperatures of 60, 200, 330, and 400°C to match their irrddiation temperatures in the OUR.

The extended shutdown of the HFIK (while the pressure vessel integrity problem is being resolved) has impacted the HFIK-MFE RB* capsule irradiation program described in the last report[2] in several ways. A decision to extend irradiation of the test speciinens in the OUR from the original target exposure level of ~5 to ~10 dpa reduced by four the number of irradiations required in the HFIK and chdnged the Schedules for the remaining irradiations. **In** addition, both the HFIR startup date and power level are uncertain at this time. Assuming that the reactor will be operating by early 1988 at 80 MW, the 330 and 60°C HFIK-MFE RB* capsules should begin an 18-month irradiation period in April 1988, and the other two (400 and 200°C) in October 1989. After these 18-month irradiations to ~20 dpa, the test specimens are to he removed, examined, and a portion reencapsulated for irradiation to ~30 dpa.

Facility description

The HFIK RB* capsule irradiation facility will allow spectral tailoring of the neutron flux by placement of appropriate neutron absorber shields around the in-core section of the capsule. Hafnium shields (42.2-mm-ID, 4.2-mm-thick) will he used for the present U.S./Japan collaborative MFE materials testing program to tailor the neutron spectrum to closely match (within ±20%) the helium production/atom displacement ratio (14 ppm He/dpa) expected in a fusion reactor first wall. Other features of the new RB* capsule irradiation facility which have been incorporated into the capsule designs include: (1) straight access into any of the eight 46-mm-diam positions, (2) peak unperturbed therinal and fast neutron flux levels of approximately 1.5×10^{15} and 5.0×10^{14} (>0.11 MeV) neutrons/cm^2·s, respectively, at *100* MW HFIR power, (3) peak unperturbed gamma heating rdte of approximately 18 W/g at 100 MW HFIR power, (4) standard capsule and lead tuhe design, (5) containment tube design parameters of 6.9 MPa (1000 psi) external pressure differential at 93°C (200°F), and (6) 180° capsule rotation at the end of each reactor cycle to provide uniform exposure to all specimens at a given elevation.

Capsule design

The HFIK-MFE RB* capsule containment tube (38.1-mm OD) will be made of 6061-T6 aluminum in the in-core region and type 304L stainless steel in the upper region. The upper and lower sections of the containment tube will be joined by a special aluminum-to-stainless steel transition tube. An oxide dispersion strengthened aluminum alloy containing 6 to R wt% Al_2O_3 has been selected for the speciinen holder in the higher temperature capsules to provide adequate strength and diinensional stability under the planned irradiation conditions; this alloy also meets requirements of high thermal conductivity (close to that of aluminum) dnd reasonably low density (2.74 g/cm^3). With the exception of the 60°C capsule, where the test speciinens wili be in direct contact with the reactor cooling water, the speciinen teinperatures (monitored by 21 thermocouples) will he controlled by varying the therinal conductance of a small gas gap region between the speciinen holder and the Containment tube. The axial temperature gradients, caused by curvature in the gamma heating rate profile, and end heat losses will he minimized by stepping the gas gap thickness and placing stainless steel spacers at the top and bottom ends of the speciinen holder.

The 200°C capsule presents a special design problem because it is difficult to remove the large dmount of gamma heat generated in the capsule while, at the same time, controlling the operating temperature at 200°C. An aluminum alloy specimen holder with a conventional temperature control gas gap would be a risky design for this capsule hecause the required gas gap would be too small to predict its operating thermal conductance with sufficient accuracy. Various other possible designs have been considered, one of which is the use of very low density material for the speciinen holder, such as 10% dense Duocel* aluminuin, which would generate less heat and permit use of a larger gas gap. Duocel aluminum may have ddequate thermal conductance, hut it needs to he tested to determine its diinensional stability under the planned irradiation conditions. A test piece of Duocel aluminum will be included in the 330°C capsule at a location above the MFE speciinen holder where its temperature will he in the vicinity of 200°C.

Also under investigation as a possible design concept for the 200°C capsule is the use of a relatively large temperature control gas gap (*–0.16* mm) filled with a binary (coarse/fine) mixture of SiC coated carbon microspheres. In this concept, temperature would be controlled primarily by varying the inert gas pressure (and hence the mean free path of the gas molecules) in the particle bed to change its therinal conductance. An apparatus for development testing of this design concept has been completed and first baseline results using a large bed of 500-μm Al_2O_3 particles have been obtained.

A backup design concept for the 200°C capsule is to utilize electrical heaters for temperature control. In this approach, gas gap thicknesses would be reduced to the minimum needed for assembly in the hot cell so that the capsule would operate below 200°C under the condition of no heater power. Disadvantages of this design concept, in addition to the added cost of heaters, are the additional temperature gradients induced by the electrical heaters and the possibility that high hedter power may be required because of the uncertainties in small-gap thermal conductances and in the gamma heating rate in the new facility.

Because this is the first of a series of KB* irradiation capsules, the capsule designs are being standardized as much as possible, and fabrication drawings are being prepared on a computer-aided design (CAD) system to minimize overall long-terin cost.

Capsule fabrication

An order has been placed for the special aluminum-to-stainless steel transition tube assemblies which will be used to join the aluminum in-core section of the capsule containment tube to the stainless steel iupper section. Fabrication of the remainder of the capsule containment tube parts, upper junction box, hafnium sleeves, and 330°C capsule internal parts will be started in April 1987.

FUTURE WORK

Design and preparation of fabrication drawings for the first four HFIK-MFC RB* capsules are scheduled to he completed by August 1987. Preparation of fabrication drawings for later reencapsulation of MFE specimens will be an intermittent effort. Fabrication of parts for the first four HFIR-MFE KB* capsules will continue into 1988.

*Manufactured by Energy Research and Generation, Inc., Oakland, California.

REFEKENCES

1. J. L. Scott, L. K. Mansur, M. L. Grossbeck, E. H. Lee, K. Farrell, L. L. Horton, A. F. Rowcliffe, and M. P. Tanaka, pp. 12-20 in ADIP Semiannu. Prog. Rep., March 31, 1985, DOE/ER-0045/14, U.S. DOE, Office of Fusion Energy.

2. A. W. Longest, J. E. Corum, and K. R. Thorns, "Design of the HFIR Spectral Tailoring Experiments in the HFIR RE* Capsule Irradiation Facility," Fusion Reactor Materials Semiannu. Prog. Rep. Sept. 30, 1986. DOE-ER-0313/1, U.S. DOE, Office of Fusion Energy.

THE HFIR INSTRUMENTEU (JP TYPE) TARGET TEMPERATURE TEST (TTT) CAPSULE — I. I. Siman-Tov (Oak Ridge National Laboratory)

OBJECTIVE

The primary objective of this experiment is to determine the temperatures in the JP series capsules by placing an instrumented JP mockup experiment in the modified HFIR instrumented target facility. A secondary objective is to determine the nuclear heating rate in stainless steel as a function of axial core position and time in a HFIR cycle.

SUMMARY

The JP-TTT capsule completed four out of five planned HFIR irradiation cycles on November 14, 1986, when the HFIK was shut down to resolve the reactor pressure vessel integrity issue. The capsule accumulated a total of 82.04 full power days (FPD) at 100 MW reactor power.

The thermal analysis was completed with the conclusion that the heat generation rate axial profile should be modified to match the JP DPA curve profile to reflect the steeper gradient observed outside the 300-mm centered about the horizontal midplane (HMP).

PROGRESS AND STATUS

Experiinent operation

Earlier details concerning the TTT experiinent have been previously described.[1-6] The TTT capsule completed four irradiation cycles, for a total of 82.04 FPD at 100 MW reactor power, before the HFIR was shut down on November 14, 1986. to resolve the reactor pressure vessel integrity issue. The capsule will complete the planned irradiation when the HFIR renews operation. The capsule was moved from the E-3 to the E-6 position for cycle IV and will be returned to position E-3 for the fifth cycle.

Figure 1 shows the specimen and thermocouple (TE) final configuration. Table 1 presents the temperature history for the four cycles at the center of the specimens. The temperatures in all positions except for G-1 are within 15% of the predicted values. Figures 2 and 3 present the temperature distribution during cycles III and IV, respectively. The top gamma susceptor (G-1) continued to run at low temperature. It should be noted that all of the temperatures continued rising steadily during all of the third cycle and started out higher in the fourth cycle, contrary to the usual behavior where the temperatures vary directly with the flux as dictated by the control plate movements (see cycles I and II). Figures 4 and 5 show the temperature of the regions above and below the HMP with the minimum and maximum temperature variation for these two cycles. It was noted that in general the lower half had larger temperature increases than the upper half. Since all thermocouples measured varying degrees of change, the observed temperature variation is not expected to be a drift in the thermocouple properties. A possible cause may be the relaxation of the magneformed housing tube since magneforming was performed over all the specimen positions and skipped over the gamma susceptor position.

Therinal analysis

The thermal analysis based on as-built TE axial positions and control gas-gap dimensions was completed. The original plan to use the radial temperature gradient in the gamma susceptors for the determination of nuclear heat rates in stainless steel had to be abandoned because the measured gradients did not yield sensible results. The surface thermocouples (like the others) were located in a thermocouple array tube (TCAT) and did not make direct contact with the surface of the gamma susceptor. Furtherinore, the surface TCAT was located in the steep temperature-gradient region of the control gas gap making it very sensitive to slight radial position variation. As a result, temperature gradients were too high as well as inconsistent with the axial flux profile in the HFIR target region. On the other hand, the center-line TCATs were in a practically isothermal region and consequently were used in a parametric study to determine the heat generation rate in the stainless steel.

Generally, temperatures remained within a ±15% band about the requested design temperature. One major discrepancy between predicted and experiinental temperatures occurred in the top gamma susceptor. Although there is no symmetric measurement at the bottom of the capsule, it was concluded that this was a true indication of the heat generation rate in this position, since both independent thermocouples, TE-101 and TE-102, read within less than 3°C of each other. This fact also indicates that there are no significant

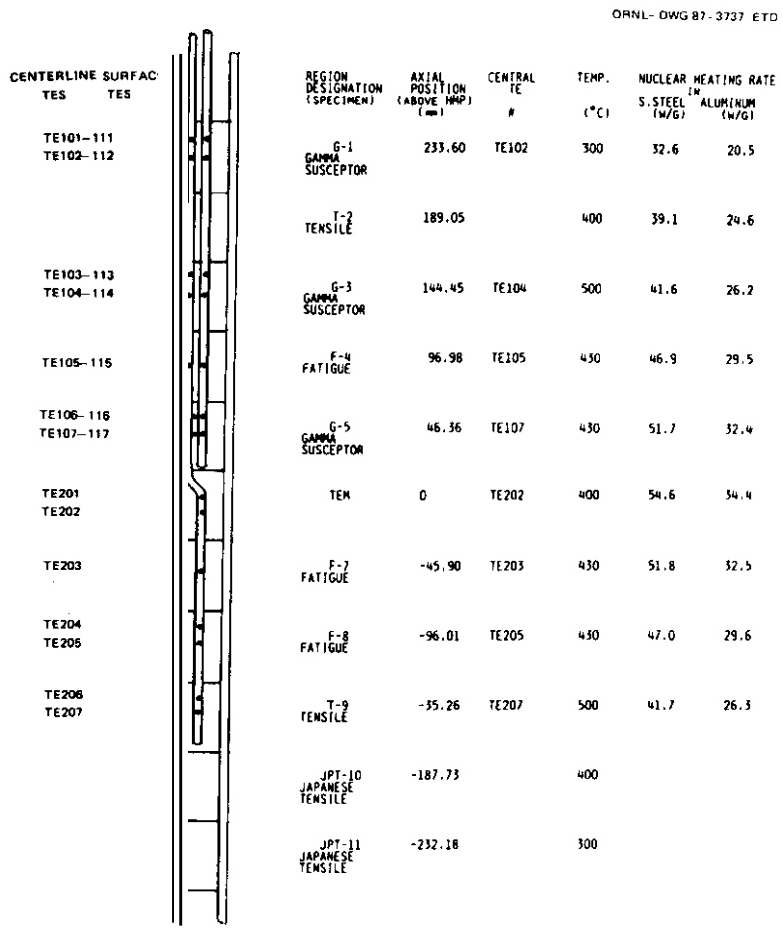
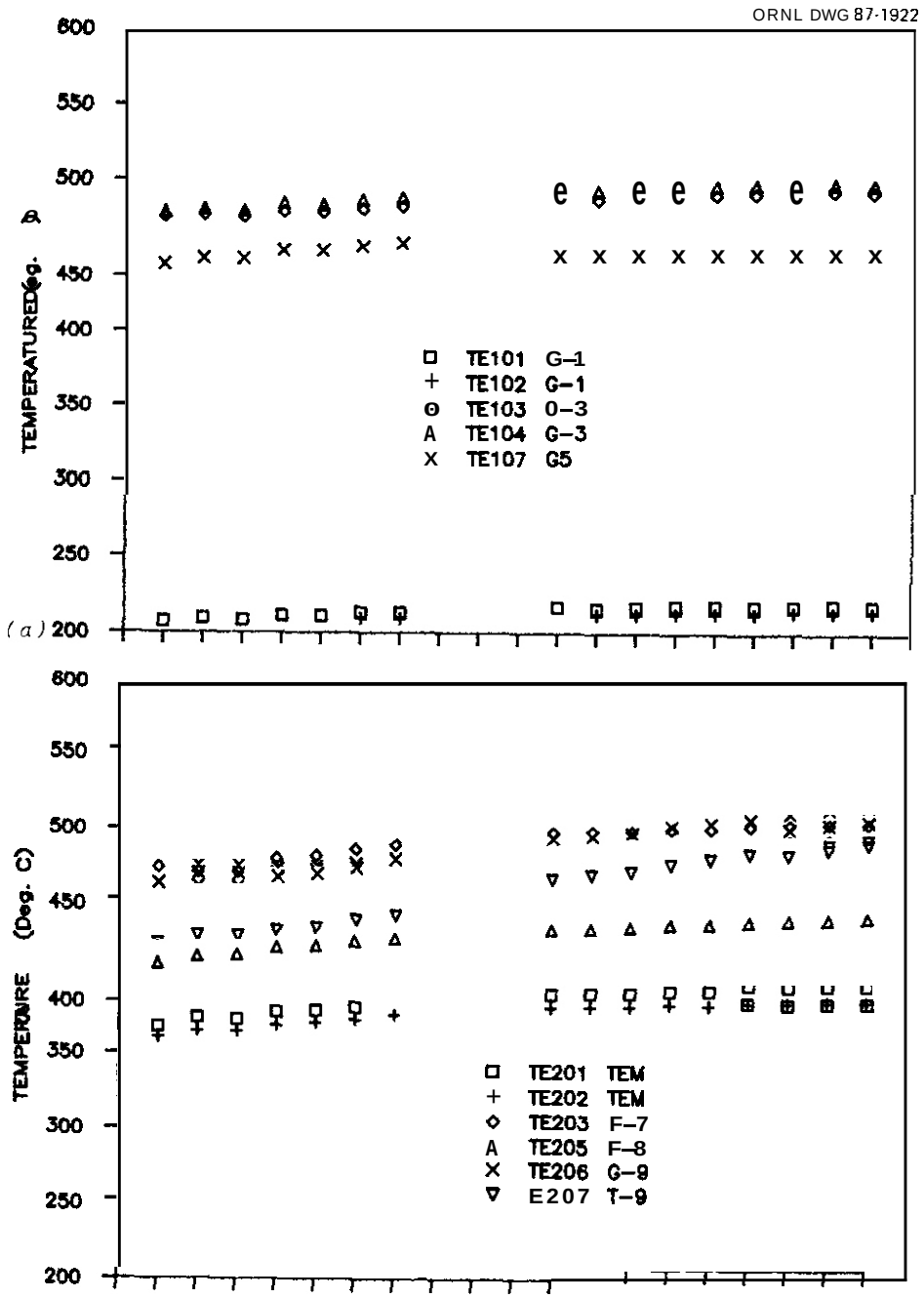


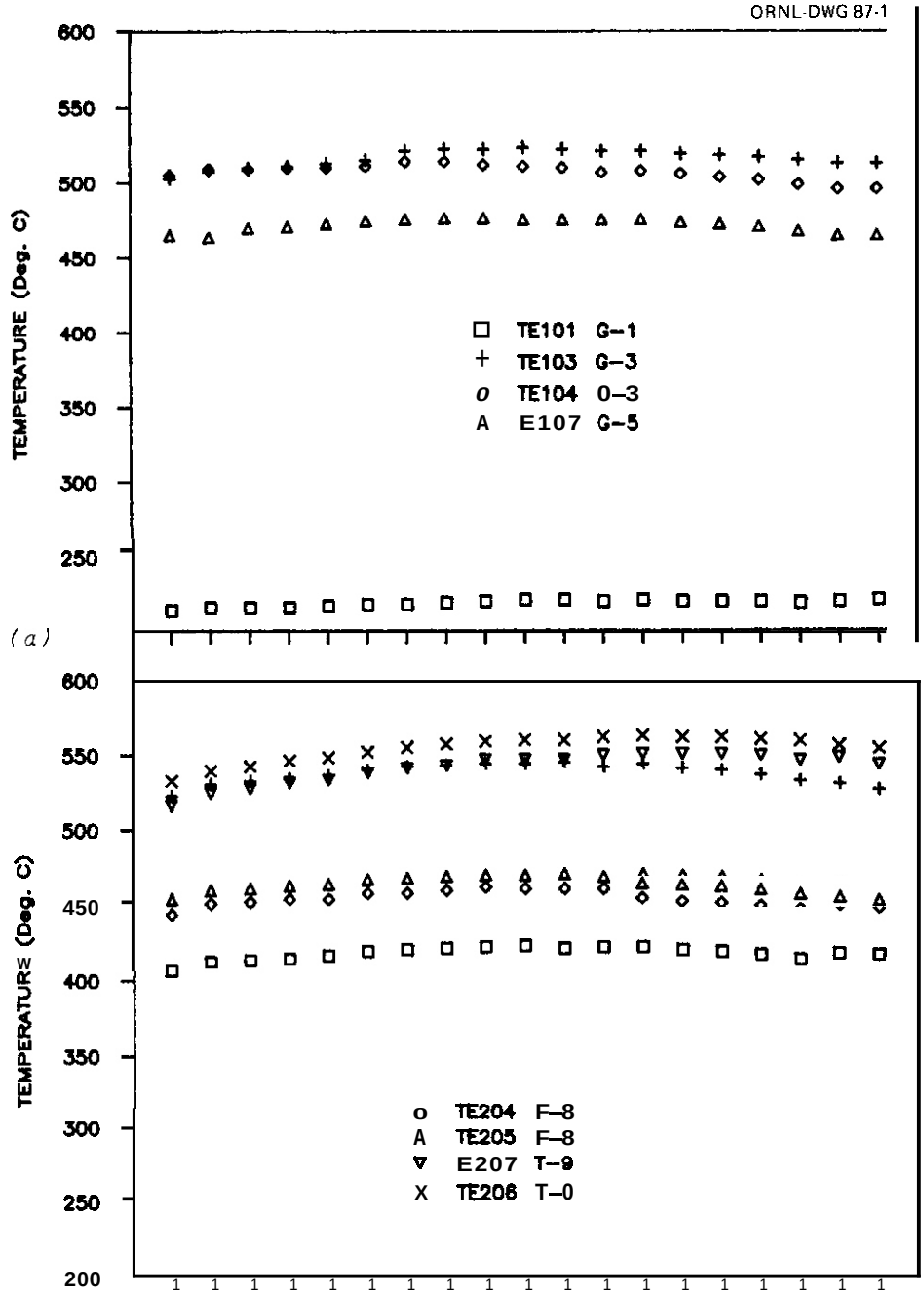
Fig. 1. Target temperature test (TTT) experiment configuration with associated parameters.

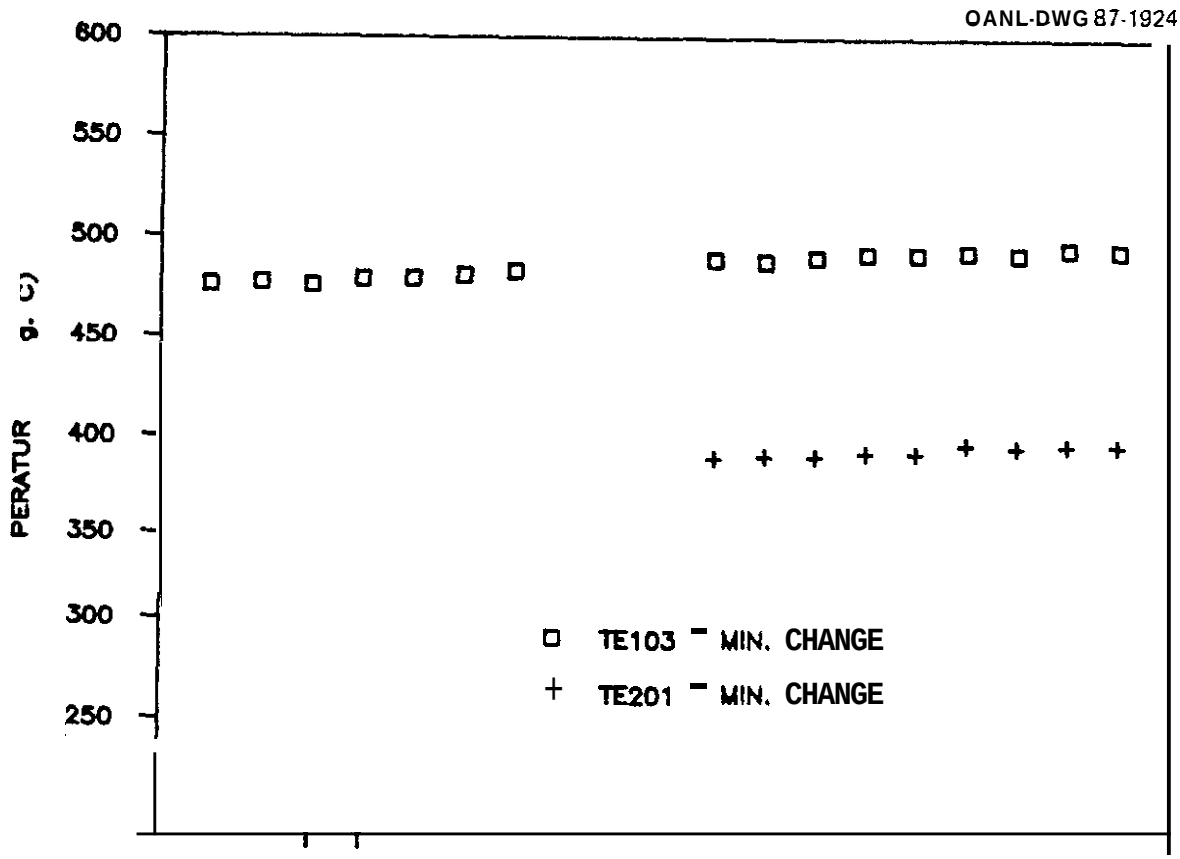
Table 1. Temperature history of the TTT specimens for cycles I through IV

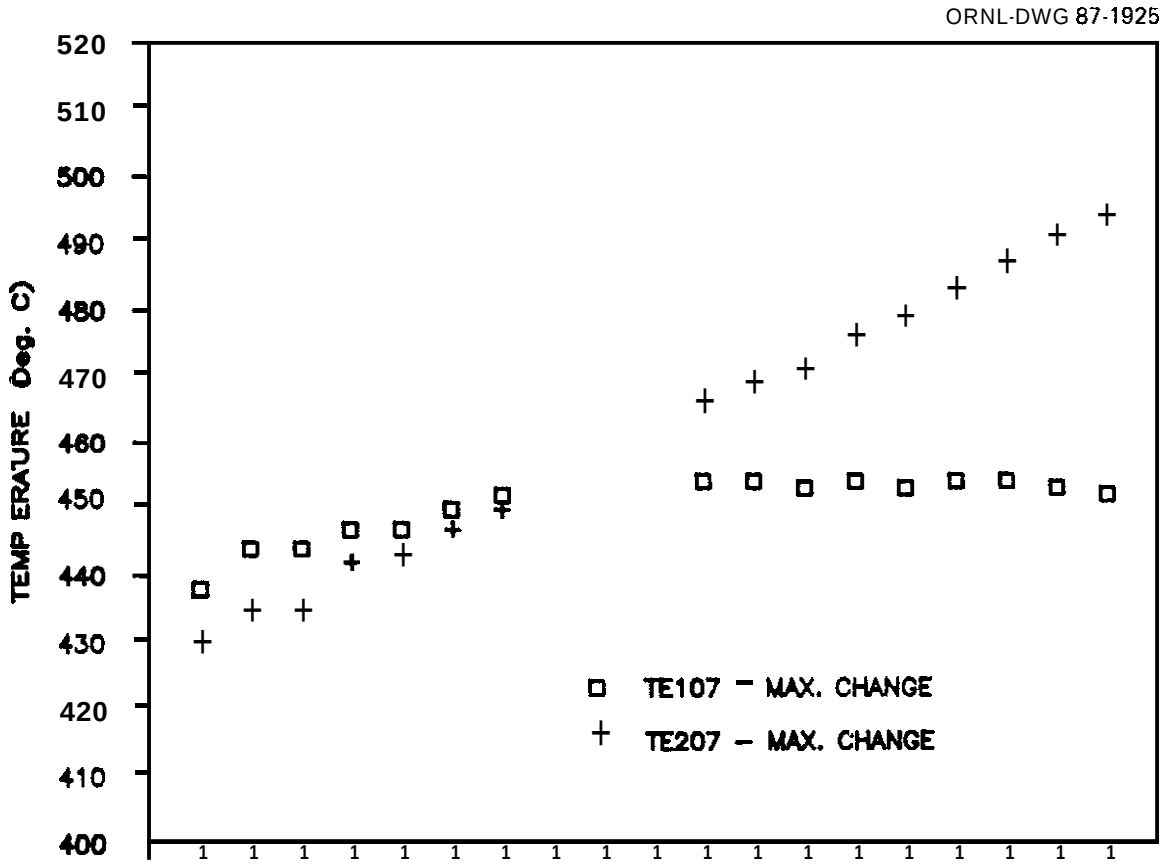
Specimen TE No.	G-1 TE-102 (°C)	G-3 TE-104 (°C)	F-4 TE-105 (°C)	G-5 TE-107 (°C)	TEM TE-202 (°C)	F-7 TE-204 (°C)	F-8 TE-205 (°C)	T-9 TE-207 (°C)
Desian Temperature	300	500	430	430	400	430	430	500
−15%	255	425	366	366	340	366	366	425
+15%	345	575	495	495	460	495	495	575
Cycle 1								
Average	205	500	433	449	356	471	419	444
Minimum	204	495	416	429	340	456	405	438
Maximum	207	509	441	456	363	417	426	450
Cycle 2								
Average	204	483	431	441	358	467	418	440
Minimum	199	475	424	434	349	456	406	427
Maximum	206	488	436	447	362	471	422	446
Cycle 3								
Average	212[a]	491	457[a]	450	377	491	430	461
Minimum	209	479		438	361	468	410	429
Maximum	213	500		454	386	504	443	493
Cycle 4								
Average	TE failed	507	TE failed	472	418	538	466	542
Minimum		496		464	407	523	454	517
Maximum	514			417	424	546	471	552

[a]Thermocouple failed during this cycle.


ORNL DWG 87-1922
TEMPERATURE (Deg. C)
600
550
500
450
400
350
300
250
200
(a)
TE101 G-1
TE102 G-1
TE103 0-3
TE104 G-3
TE107 G5
TE201 TEM
TE202 TEM
TE203 F-7
TE205 F-8
TE206 G-9
E207 T-9


ORNL-DWG 87-1
TEMPERATURE (Deg. C)
600
550
500
450
400
350
300
250
TE101 G-1
TE103 G-3
TE104 0-3
E107 G-5
(a)
TEMPERATURE (Deg. C)
600
550
500
450
400
350
300
250
200
TE204 F-8
TE205 F-8
E207 T-9
TE206 T-0


ORNL-DWG 87-1924
600
550
500
450
400
350
300
250
PERATUR
TE103 - MIN. CHANGE
TE201 - MIN. CHANGE


ORNL-DWG 87-1925
520
510
500
490
480
470
460
450
440
430
420
410
400
TEMP ERATURE (Deg. C)
TE107 - MAX. CHANGE
TE207 - MAX. CHANGE

axial heat flows at this location which would distort the evaluation of the heat generation rate there. Other neutron flux-related parameters were reviewed to help explain the lower heat generation rate for the top position. The JP-3 dpa also show a dropoff to 48% of their HMP values as compared with a dropoff to 58% of the design heat generation rate HMP value. A comparison between the historic design heat generation rate profile in stainless steel, the one based on the dpa profile, and the experimentally obtained values from the gamma susceptors, is presented in Fig. 6. (It was noted that the helium production rate also showed a dropoff to 48% of its HMP rate although it is not in general linearly proportional to fast flux or fluence.)

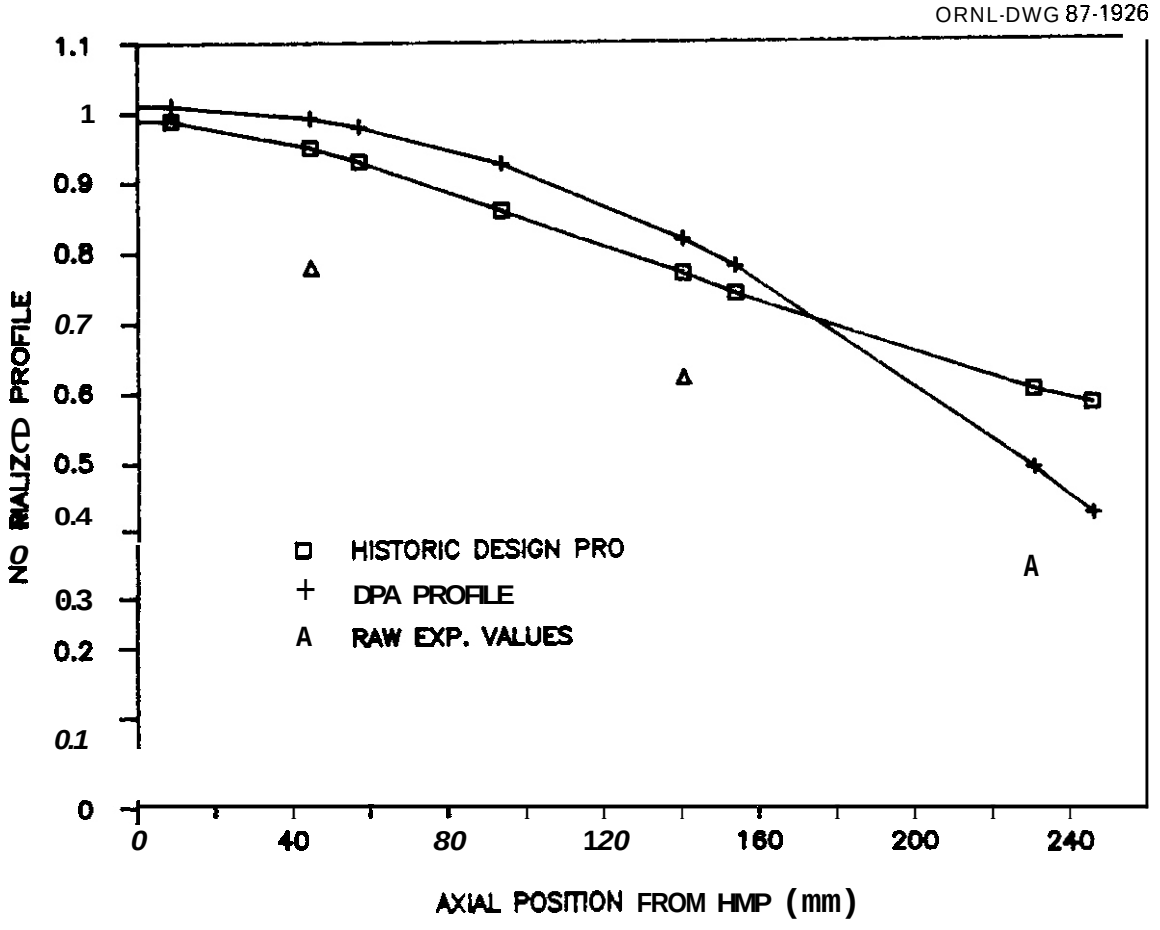


Fig. 6. Comparison of design and TTT experiment heat generation rates with normalized JP-3 dpa values.

CONCLUSIONS

The overall nuclear heating study based on the TTT experiment and other JP-3 related parameters indicates that the heat generation rate profile closely matches the dpa profile in the HFIR target region. It is therefore recommended that the following polynomial, with the associated constants for stainless steel and aluminum, be used for the gamma heating rates in the target facility:

$$q = A\,[0.99768 - (2.43933 \times 10^{-4})\,Z - (1.06640 \times 10^{-5})\,Z^2] \quad ,$$

where

q = heat generation rate in w/g,
Z = distance from the HMP in mm,
A = 54.6 w/g for stainless steel,
= 34.4 w/g for aluminum.

FUTURE WORK

The TTT experiment will complete the fifth HFIR irradiation cycle when the HFIR resumes operation. It will be returned to the E-3 target position for the final cycle. A thorough checkout of the thermocouples at the end of the experiment will aid in determining whether any fluence or damage flux-related changes in properties took place. It is recommended that accurate PIE dimensional measurements of the components directly affecting the thermal resistance he made. This may shed more light on reasons for the temperature increases observed during the third and fourth cycles. The TTT experiment report will he completed when all the data from the experiment as well as the PIE measurements will he available. An interim report is in the publication process.

REFERENCES

1. A. F. Rowcliffe, M. L. Grossbeck, and S. Jitsukawa, "The U.S./Japan Collaborative Testing Program in HFIR and ORR," pp. 38-43 in ADIP Semiannu. Prog. Rep., March 31, 1984, DOE/ER-0045/12, U.S. DOE, Office of Fusion Energy.

2. A. F. Rowcliffe et al., "The U.S./Japan Collaborative Testing Progrdin in HFIK and ORR: Speciinen Matrices for HFIR Irradiation," pp. 61-62 in ADIP Semiannu. Prog. Rep., Sept. 30, 1984, DOE/ER-0045/13, U.S. DOE, Office of Fusion Energy.

3. J. L. Scott and M. P. Tanaka, "Preparation for Postirradiation Examination of U.S./Japan HFIR Capsules," pp. 10–11 in ADIP Semiannu. Prog. Rep., March 31, 1985, DOE/ER-0045/14, U.S. DOE, Office of Fusion Energy.

4. J. L. Scott, M. L. Grossbeck, and M. P. Tanaka, "Phase I HFIR Capsules — Irradiation and Post-irradiation Examination," pp. 18-21 in ADIP Semiannu. Prog. Rep., Sept. 30, 1985, DOE/ER-0045/15, U.S. DOE, Office of Fusion Energy.

5. I. I. Siman-Tov, "Design of the HFIR (JP Type) Instrumented Target Capsule," pp. 9–10 in ADIP Semiannu. Prog. Rep., March 31, 1986, DOE/ER-0045/16, U.S. DOE, Office of Fusion Energy.

6. I. I. Siman-Tov, Fusion Reactor Materials Semiann. Prog. Rep. Sept. 30, DOE/ER-0313/1.

OPERATION OF THE U.S./JAPAN ORR SPECTRAL TAILORING EXPERIMENTS — I. I. Siman-Tov (Oak Ridge National Laboratory)

OBJECTIVE

The experiments in the U.S./Japan collaborative testing program in the ORR contain austenitic stainless steel alloys for possible use as first-wall and blanket structural materials in fusion reactors. These alloys will be irradiated with mixed-spectrum neutrons and with spectral tailoring to achieve the helium-to-displacement-per-atom (He/dpa) ratios predicted for fusion services.

SUMMARY

The ORR-MFE-6J and -7J experiments continued irradiation during this reporting period ending on March 31, 1987. The total accumulated irradiation time is 474.7 full power days (FPU) at 30 MW reactor power.

PROGRESS AND STATUS

The details of the U.S./Japan collaborative irradiation program have been described previously. [-6]

MFE-6J and -7J were not removed from the ORR in December of 1986 as stated in the last semiannual. This change was the result of the extended shutdown of the HFIR which is undergoing extensive analysis of its pressure vessel integrity.

ORR-MFE-6J — The experiment continued routine operation with typical temperatures ranging between 175 and 200°C in the 200°C region. The total accumulated irradiation time through March 31, 1987, is 414.7 FPD at 30 MW.

ORR-MFE-7J — The experiment continued routine operation with a maximum temperature of 330°C in the top region and an average of 400°C (at TE-5) in the bottom region. On December 6, 1986, the irradiation spectrum was hardened by replacing the hollow aluminum core piece with the solid one. The total accumulated irradiation time up to that point was 389.5 FPD at 30 MW reactor power. The total accumulated irradiation time through March 31, 1987, is 474.7 FPD at 30 MW.

FUTURE WORK

Both experiments will continue to be irradiated in the ORR through September 1987.

REFERENCES

1. J. A. Conlin and J. W. Woods, "Irradiation Experiments for the U.S./Japan Collaborative Testing Program in HFIR and ORR," p. 37 in ADIP Semiannu. Prog. Rep., March 31, 1984, DOE/ER-0045/12, U.S. DOE, Office of Fusion Energy.

2. J. A. Conlin and J. W. Woods, "Irradiation Experiments for the U.S./Japan Collaborative Testing Program in HFIR and ORR," pp. 66–67 in ADIP Semiannu. Prog. Rep., Sept. 30, 1984, DOE/ER-0045/13, U.S. DOE, Office of Fusion Energy.

3. I. I. Siman-Tov, J. A. Conlin and J. W. Woods, "Irradiation Experiments for the U.S./Japan Collaborative Testing Program in HFIR and ORR," p. 6 in ADIP Semiannu. Prog. Rep., March 31, 1985, DOE/ER-0045/14, U.S. DOE, Office of Fusion Energy.

4. I. I. Siman-Tov, "Assembly and Operation of the U.S./Japan Spectral Tailoring Experiments," p. 41 in ADIP Semiannu. Prog. Rep., Sept. 30, 1985, DOE/ER-0045/15, U.S. DOE, Office of Fusion Energy.

5. I. I. Siman-Tov, Fusion Reactor Materials Semiannu. Prog. Rep. Sept. 30, 1986, DOE-ER-0313/1, U.S. DOE, Office of Fusion Energy.

STATUS OF U.S./JAPAN COLLABORATIVE TESTING IN HFIR AND ORR — J. L. Scott (Oak Ridge National Laboratory) and S. Hamada (Japan Atomic Energy Research Institute, assigned to ORNL)

OBJECTIVE

The objective of this program is to determine the response of U.S. and Japanese austenitic stainless steels to the combined effects of displacement damage and helium generation at temperatures in the range of 65 to 600°C. Since a basic understanding is sought in addition to an engineering data base, many advanced alloys and model alloys are included in the program.

SUMMARY

All eight Phase-I target capsules have been disassembled and specimen testing is proceeding. The two spectrally tailored capsules continue operation in the flak Ridge Research Reactor (ORR). At the end of this fiscal year, they will he removed for interim exainination and reinsertion into RB* positions in the High Flux Isotope Reactor (HFIR).

PROGRESS AND STATUS

The program of U.S./Japan collaborative testing in HFIR and ORR consists of HFIK target capsules to be irradiated to levels of ahout 30, 50, and 100 dpa. In addition, spectrally tailored capsules are to he irradiated to 30 dpa with incremental removal and testing at about 10 and 20 dpa. During the next reencapsulation the spectrally tailored capsules will be transferred from the ORR to RQ* positions in HFIR. The collaborative test matrix and results to date have been presented previously.[1-7]

HFIK Irradiation Experiinents and Postirradiation Examination

All eight Phase-I target capsules have been disassembled and specimen testing is proceeding. Emphasis has been placed on disk density measurements. Results are presented elsewhere in this report.[8]

The Phase-It target capsules are now being designed and specimen preparation is under way. The objective of the Japanese side is to study the response of welds under the same conditions as the specimens in the Phase-I capsules. In contrast, the U.S. side now plans to study the response of isotopically tailored alloys and ferritic steels to the fusion neutron environment. Minor modifications to the test matrix are still being made, and the finai test matrix will be given in the next semiannual progress report.

Spectrally Tailored Experiments

The spectrally tailored experiments are experiencing scheduling difficulties because of the unexpected shutdown of HFIR on November 14, 1986. Charpy tests of surveillance specimens from the pressure vessel and vessel nozzle materials showed unexpected embrittlement caused by irradiation damage. The eariiest time that HFIR can restart now appears to be September 1987. As a result of the HFIR problem, the schedule for the spectrally tailored capsules has been changed. Present plans call for the ORR-MFE-6J and -7J capsules to remain in ORR throughout fiscal year 1987 and the specimens are expected to achieve damage levels of 8 to 10 dpa. These capsules will then be disassembled and some of the specimens will be removed for testing. The capsules will then be reconstituted and inserted in the HFIR RB* positions for an additional 10 dpa of exposure.

CONCLUSIONS

The U.S./Japan collaborative program of testing of first wall and blanket structural materials with mixed-spectrum fission reactors has been very successful to date. Some difficulties are being encountered as a result of the unexpected shutdown of HFIR; however, these difficulties should be resolved soon.

REFERENCES

1. A. F. Rowcliffe, M. L. Grossheck, and S. Jitsukawa, "The U.S./Japan Collaborative Testing Program in HFIR and ORR: Irradiation Matrices for HFIR Irradiation," pp. 38–43 in ADIP Semiannu. Prog. Rep. March 31, 1984, DOE/ER-0045/12, U.S. DOE, Office of Fusion Energy.

2. A. F. Rowcliffe, M. L. Grossheck, M. Tanaka, and S. Jitsukawa, "The U.S./Japan Collaborative Testing Program in HFIR and ORR: Speciinen Matrices for HFIR Irradiation," pp. 61-62 in ADIP Semiannu. Prog. Rep. Sept. 30, 1984, DOE/ER-0045/13, U.S. DOE, Office of Fusion Energy.

3. J. L. Scott and M. P. Tanaka, "Preparation for Postirradiation examination of U.S./Japan HFIK Capsules," pp. 10–11 in ADIP Semiannu. Prog. Rep. March 31, 1985, DOE/ER-0045/14, U.S. DOE, Dffice of Fusion Energy.

4. J. L. Scott, M. L. Grossbeck, and M. P. Tanaka, "Phase I HFIR Capsules – Irradiation and Post-irradiation Examination," pp. 18–21 in ADIP Semiannu. Prog. Rep. Sept. 30, 1985, DOE/ER-0045/15, U.S. DOE, Office of Fusion Energy.

5. J. L Scott et al., "Description of the U.S./Japan Spectral Tailoring Experiinent in ORR," pp. 22–40 in ADIP Semiannu. Prog. Rep. Sept. 30, 1985, DOE/ER-0045/15, U.S. DOE, Office of Fusion Energy.

6. J. L. Scott and M. P. Tanaka, "Status of U.S./Japan Collaborative Testing in HFIR and ORR," pp. 4–7 in ADIP Semiannu. Prog. Rep. March 31, 1986, DOE/ER-0045/16, U.S. DOE, Office of Fusion Energy.

7. J. L. Scott and M. P. Tanaka, "Status of U.S./Japan Collaborative Testing in HFIK and OUR," Fusion Reactor Materials Semiannu. Prog. Rep. Sept. 30, 1986, DOE-ER-0313/I, U.S. OOE, Office of Fusion Energy.

8. P. J. Maziasz, J. L. Scott, L. J. Turner, S. Hamada, M. P. Tanaka, "Some Effects of Thermal-Mechanical Pre-Treatment and Alloy Compositional Variation on Swelling of Austenitic Stainless Steels Irradiated in HFIR," pp. 192-208 in Fusion Reactor Materials Semiannual Progress Report March 31, 1987, DOE/ER-0313/12, U.S. DOE, Office of Fusion Energy.

FUSION PROGRAM RESEARCH MATERIALS INVENTORY — T. K. Roche (Oak Ridge National Laboratory) and J. W. Davis (McDonnell Douglas Astronautics Company — St. Louis Division)

OBJECTIVE

Oak Ridge National Laboratory maintains a central inventory of research materials to provide a common supply of materials for the Fusion Reactor Materials program. This minimizes unintended material variations and provides for economy in procurement and for centralized record-keeping. Initially, this inventory is to focus on materials related to first-wall and structural applications and related research, but various special-purpose materials may be added in the future.

The use of materials from this inventory that is coordinated with or otherwise related technically to the Fusion Reactor Materials program of the Department of Energy is encouraged.

PROGRESS AND STATUS

Materials requests shall be directed to the Fusion Program Research Materials Inventory at ORNL (Attention: T. K. Roche). Materials will be released directly if (a) the material is to be used for programs funded by the Office of Fusion Energy, with goals consistent with the approved Materials Program Plans of the Materials and Radiations Effects Branch, and (b) the requested amount of material is available without compromising other intended uses.

Materials requests that do not satisfy both (a) and (b) will be discussed with the staff of the Reactor Technologies Branch, Office of Fusion Energy, for agreement on action.

Records

Chemistry and materials preparation records are maintained for all inventory materials. All materials supplied to program users will be accompanied by summary characterization information.

Summary of Current Inventory and Material Movement During Period October 1, 1986, through March 31, 1987

A condensed, qualitative description of the content of materials in the Fusion Program Research Materials Inventory is given in Table 1. This table indicates the nominal diameter of rod or thickness of sheet for product forms of each alloy and also indicates by weight the amount of each alloy in larger sizes available for fabrication to produce other product forms as needed by the program. No materials was added to or distributed from the inventory during this reporting period.

Alloy compositions and more detail on the alloys and their procurement and/or fabrication are given in this and earlier ADIP progress reports.

Table 1. Summary status of materials available in the Fusion Program Research Materials Inventory

Alloy	Product Form: Ingot or bar[a] weight (kg)	Rod diameter (mm)	Thickness, mm: Sheet	Thickness, mm: Thin-wall tubing wall
Path A Alloys				
Type 316 SS	900	16, 7.2	13, 7.9	0.25
Path A PCA[b]	490	12	13	0.25
USSR Cr-Mn steel[c]		10.5	2.6	
NONMAGNE 30[d]		18.5	10	
Path B Alloys				
PE-16	140	16, 7.1	13, 1.6	0.25
B-1	180			
B-2	180			
B-3	180			
B-4	180			
B-6	180			
Path D Alloys				
LRO-37[e]			3.3, 1.6, 0.8	

Alloy	Product Form: Ingot or bar[a] weight (kg)	Rod diameter (mm)	Thickness, mm: Sheet	Thickness, mm: Thin-wall tubing wall
Path C Alloys				
Ti-64			2.5, 0.76	
Ti-62428	63		6.3, 3.2, 0.76	
Ti-5621s			2.5, 0.76	
Ti-38644			0.76, 0.25	
Nb-1%Zr		6.3	2.5, 1.5, 0.76	
Nb-5%Mo-1%Zr		6.3	2.5, 1.5, 0.76	
V-20%Ti		6.3	2.5. 1.5, 0.76	
V-15%Cr-5%Ti		6.3	2.5, 1.5, 0.76	
VANSTAR-7		6.3	2.5. 1.5, 0.76	

Table 1 (contd.)

Alloy	Product Form			
	Ingot or bar[a] weight (kg)	Rod diameter (mm)	Thickness, mm	
			Sheet	Thin-wall tubing wall thickness
Path E Alloys				
HT9 (AOD fusion heat)[f]	3400		***28.5,*** 15.8, 9.5, 3.1	
HT9 (AOD/ESR fusion heat)	7000	**25,** 50, 75	**28.5,** 15.8, 9.5, **3.1**	
HT9			3.1	
HT9 + *1%* Ni			4.5, 18	
HT9 + *2%* Ni			4.5, 18	
HT9 + *2%* Ni + Cr adjusted			4.5, 18	
T-9 modified[g]			4.5, 18	
T-9 modified + *2%* Ni			4.5, 18	
T-9 modified + *2%* Ni + Cr adjusted			4.5, 18	
2.25Cr-1Mo			[h]	

[a]Greater than **25** mm, minimum dimension

[b]Prime candidate alloy

[c]Rod and sheet of a USSR stainless steel supplied under the U.S./USSR Fusion Reactor Materials Exchange Program.

[d]NONMAGNE 30 is an austenitic steel with base composition Fe-14%Mn-2%Ni-2%Cr. It was supplied to the inventory by the Japanese Atomic Energy Research Institute.

[e]LRO-37 is the ordered alloy $(Fe,Ni)_3(V,Ti)$ with composition Fe-39.4%Ni-22.4%V-0.43%Ti.

[f]Alloy 12Cr-1MoVW with composition equivalent to Sandvik allay HT9

[g]T-9 modified is the alloy 9Cr-1MoVNb

[h]Material is thick-wall pipe, rerolled as necessary to produce sheet or rod.

2. DOSIMETRY, DAMAGE PARAMETERS AND ACTIVATION CALCULATIONS

NEUTRONICS ANALYSIS IN SUPPORT OF THE U.S./JAPAN SPECTRAL TAILORING CAPSULES — R. A. Lillie (Oak Ridge National Laboratory)

OBJECTIVE

The objective of this work is to provide the neutronic design for materials irradiation experiments ir both the Oak Ridge Research Reactor (ORR) and High Flux Isotope Reactor (HFIR). Spectral tailoring to control the fast and thermal fluxes is required to provide the desired displacement and helium production rates in alloys containing nickel.

SUMMARY

Scale factors obtained from previous comparisons' of the calculated and measured neutron fluences in the ORR-MFE-6J dosimetry capsule are being used to scale the neutron fluences obtained from ongoing three-dimensional neutronics calculations. As of March 23, 1987, this procedure yields 61.6 appm He (not including 2.0 appm He from ^{10}B) and 6.88 dpa for type 316 stainless steel in ORR-MFE-6J and 96.3 appm He and 7.92 dpa in OUR-MFE-7J.

PROGRESS AND STATUS

The operating and current calculated data based on the scaling factors are summarized in Table 1 for the ORR-MFE-6J and -7J experiments. Both experimental capsules have been exposed to 339,877.2 MWh as of March 23, 1987. On December 8, 1986, the water-cooled aluminum core piece in the ORR-MFE-7J experiment was replaced with a solid aluminum core piece. At the time of replacement, the ORR-MFE-7J experiment had been exposed to 280,639.8 MWh and had obtained 76.0 appm He and 6.30 dpa. Before the insertion of the solid aluminum core piece, the average dpa rate in the ORR-MFE-7J type 316 stainless steel specimens had been 5.91 dpa per full power year. After insertion of the solid aluminum core piece, the average dpa rate has increased to 7.16 dpa per full power year. The current average dpa rate in the ORR-MFE-6J experiment is 5.32 dpa per full power year and the projected insertion date for its solid aluminum core piece is still September 30, 1987.

Table 1. Operating and Calculated Data for the ORR-MFE-6J and -7J Experimental Capsules as of March 23, 1987

	ORR-MFE-6J	ORR-MFE-7J
Insertion date	6-28-85	6-28-85
Exposure, MWh	339,877.2	339,877.2
Equivalent full power days[a]	472.0	472.0
Thermal fluence, n/m^2	7.29×10^{25}	9.43×10^{25}
Total fluence, nm^2	2.44×10^{26}	2.97×10^{26}
dpa[c]	6.88	7.92
Direct helium, appm[b]	5.39	6.17
Two-step helium, appm[b]	56.2	90.1
Total helium, appm[b]	61.6	96.3

[a]Full power for the ORR is 30 MW.
[b]Helium and dpa values are for type 316 stainless steel.

FUTURE WORK

The three-dimensional neutronics calculations that monitor the radiation environment of the ORR-MFE-6J and -7J experiments will continue with each ORR cycle. The scale factors used to scale the calculated fluences will be updated as new experimental data become available.

REFERENCE

1. R. A. Lillie, "Neutronics Analysis in Suooort of U.S./Japan Soectral Tailoring Caosules." Fusion Reactor Materials Semiannu. Prog. Rep. Sept. 30, 1986, DOE-ER-0313/1, U.S. DOE, Office of Fusion Energy.

CROSS SECTION MEASUREMENTS FOR LONG-LIVED ISOTOPES, L. R. Greenwood and J. L. Bowers (Argonne National Laboratory)

OBJECTIVE

To measure 14 MeV neutron production cross sections for reactions leading to long-lived isotopes in fusion materials.

SUMMARY

Neutron production cross sections have been measured near 14.8 MeV for reactions leading to long-lived isotopes in fusion reactor materials. Pure elements and separated isotopes were irradiated at the RTNS II to fluences up to 10^{18} n/cm^2. Undesired activities were chemically separated and the long-lived activities were measured using liquid scintillation and x-ray spectrometry. Results are reported for the reactions ^{56}Fe(n,2n)^{55}Fe (2.73 y), ^{64}Ni(n,2n)^{63}Ni (100 y), ^{63}Cu(n,p)^{63}Ni, and ^{60}Ni(n,2n)^{59}Ni (76,000 y).

PROGRESS AND STATUS

The production of long-lived isotopes in fusion materials is of concern due to waste disposal restrictions. Previously we have reported data for the ^{27}Al(n,2n)^{26}Al 1720,000 y),[1] ^{94}Mo(n,,p)^{94}Nb (20,300 y), and ^{92}Mo(n,x)^{91}Nb (700 y) reactions.? In this study, we have measured the production of radioisotopes 'which decay by electron capture or beta decay using liquid scintillation counting and radiochemistry to separate undesired activities. Results are reported near 14.8 MeV for ^{55}Fe, ^{63}Ni, and ^{59}Ni.

The samples consisted of the pure elements Fe and Cu, and separated isotopes of ^{56}Fe, ^{60}Ni, and ^{64}Ni, obtained from Oak Ridge National Laboratory. The separated isotopes of Fe, and *Ni*, were powdered metals packed in thin aluminum tubing measuring 1.5-2.0 mm o.d. by 10-14 mm long. The natural le and Cu metal samples were pressed into discs measuring 3 mm o.d. by 1 ma thickness. All samples were packaged for irradiation with thin (0.02 mm) Fe and Nb dosimetry foils in thin (0.01 mm) Al wrapping.

The activities were produced during several separate 14 MeV neutron irradiations to high fluences (10^{17}-10^{18} n/cm^2) at the Rotating Target Neutron Source II at Lawrence Livermore National Laboratory.[2] Iron and niobium dosimetry foils were included with each sample to determine the actual neutron fluence at each sample location using the well-known ^{54}Fe(n,p)^{54}Mn and ^{93}Nb(n,2n)^{92}Nb reactions. A neutron fluence map was then produced far each irradiation; more detailed results have been published previously.[3]

The analysis of *each* sample begins with gamma spectroscopy to determine the presence of other stronger activities. Based on these results, radiochemical separations are planned in order to separate as many undesired activities is possible. Gamma spectroscopy is used to determine the degree of separation and to establish the residual activities which were not removed. The purified sample is then counted by liquid scintillation spectroscopy. The scintillation energy spectrum is recorded and analyzed to separate the desired activity from the residual contaminants. Standards are used where possible to determine the desired spectral response and *to* establish the instrumental efficiency. This technique has been successful in resolving many of the desired long-liveti activities. Details of the chemical and spectral separations are given below for each isotope.

Standard solutions of ^{55}Fe and ^{63}Ni were obtained from Amersham International. Liquid Scintillation samples were prepared for each reaction product depending an the expected count rate and dissolution required. Natural Fe, Ni, or Cu was added to the solutions to match the weight of the irradiated material. Hence, the quenching factors were identical for the standard and unknown activities, as confirmed by comparison of the energy spectra. In the case of ^{59}Ni, the spectrum was assumed to be similar to that of ^{55}Fe since the x-rays and conversion electrons only differ in. energy by about 1 keV. The ^{55}Fe standard activity was 12.51 μCi/g ±4.3% and the ^{63}Ni standard was 13.02 μCi/g ±2.5%. The ^{59}Ni x-rays were counted using a thin, intrinsic Ge detector which was calibrated using ^{54}Mn, ^{55}Fe, ^{137}Cs, and ^{241}Am standards.

Standard ion-exchange chemistry was used to remove a11 of the undesired activities in the samples.[5,6] The degree of separation was readily confirmed by gamma and x-ray spectrometry. The liquid scintillation spectra were then compared in detail to spectra obtained from the similarly prepared standard solutions.

^{55}Fe has a halflife of 2.73±.03 y and decays by electron capture producing Auger electrons and x-rays near 6 keV.[4] ^{55}Fe was produced by the ^{56}Fe(n,2n) reaction from natural Fe and isotopically separated ^{56}Fe(99.87%). The principal unwanted activities in the samples 'were ^{51}Cr, ^{54}Mn, ^{57}Co, and ^{58}Co. The first two 'were produced by reactions on ^{54}Fe, principally in the natural Fe target whereas the Co activities were observed from Co and Ni impurities in the ^{56}Fe samples.

Figure 1 shows the liquid scintillation Spectra far ^{55}Fe both from our samples and the standard solution. The data are given in Table I. As can he seen, our results far the ^{56}Fe(n,2n)^{55}Fe cross sections near 14.8 MeV have a standard deviation of only 2.68.

^{63}Ni has a halflife of 100.1±2.1 y and decays by β- emission with an end-point energy of 66 keV (average energy = 17 keV). ^{63}Ni was produced by the ^{64}Ni(n,2n) and ^{63}Cu(n,p) reactions. The ^{64}Ni was enriched to 93.57% and the copper had the natural abundance of 69.17% for ^{63}Cu. The ^{64}Ni samples contained undesirable activities of ^{54}Mn, ^{57}Co, ^{58}Co, and ^{60}Co, whereas the Cu samples contained mainly ^{60}Co.

In both cases, no residual activities were detected by gamma spectroscopy. Samples were prepared from the ion-exchange column wash and all of the unwanted activities could be accounted for within a few percent. Figure 2 shows the liquid scintillation spectra for each case, both before and after chemical separations, as well as the spectra from the standard solutions. As can be seen, the spectra from the separated materials closely match that of the standards. The neutron cross section data for each sample are listed in Table I. Again we note that the Scatter in the data is only 1.5% far both the Ni and Cu samples.

^{59}Ni has a halflife of 7.6 x 10^4 y and decays by electron capture emitting about 6 keV Auger electrons and 7 keV x-rays [4]. ^{59}Ni was produced from the ^{60}Ni(n,2n) reaction using separated isotopes of ^{60}Ni (99.81%). The principal unwanted activities were ^{54}Mn, ^{57}Co, ^{58}Co, and ^{60}Co. Unfortunately, we were not able to sufficiently separate ^{54}Mn from ^{59}Ni. Consequently, we decided to concentrate on counting the 7 keV x-rays from the decay of ^{59}Ni which have an intensity of 33.1±1.7%.[4] Samples were prepared from the purified Ni elutant by evaporating several milligrams of Ni onto an aluminum counting plate. Net corrections on the order of 10% were applied for self-absorption and scattering. In this case ^{63}Ni does not interfere since the β- decay produces no Co x-rays. Data are listed in Table I. Uncertainties are larger for this reaction due to poorer counting statistics and the large (17%) uncertainty in the halflife.[4]

All of the measured neutron cross sections are summarized in Table II, where they are also compared with previous data. In the Case of the ^{56}Fe(n,2n)^{55}Fe reaction, our data are seen to agree quite well with previous data by Wenusch,[7] Frehaut,[8] Molla,[9] and Kozyr.[10] The measurement by Joensson et al.[11] is clearly much lower. In the case of the ^{63}Cu(n,p)^{63}Ni reaction, our measured cross section is lower than previous measurements. However, most of these cross sections are measurements of the total proton production which includes other possible reactions and hence are expected to be larger than our measurement. The measurement by Molla et al.,[9] is directly comparable to ours since they measured the β- activity from ^{63}Ni. However, their value has a relatively large uncertainty (40%) compared to our measurement (6.7%). No previous data were found for the ^{60}Ni(n,2n)^{59}Ni or ^{64}Ni(n,2n)^{63}Ni reactions.

FUTURE WORK

The measured neutron cross sections can be used to calculate the production of these long-lived activities in fusion reactor materials. Such calculations are needed to estimate radioactivity levels around fusion reactors and to determine the residual activities in waste materials. These techniques of chemical separations and liquid scintillation spectral analysis, backed by gamma and x-ray spectroscopy, have proven to be quite successful in the measurement of weak, long-lived activities, and we plan to study other such reactions in the future. Measurements are now in progress for the reactions ^{14}N(n,p)^{14}C (5700 y), ^{94}Mo(n,2n)^{93}Mo (3500 y), ^{94}Zr(n,2n)^{93}Zr (1.5×10^6 y), and ^{93}Nb(n,n')^{93}Nb (13.6 y).

REFERENCES

1. R. K. Smither and L. R. Greenwood. J. Nucl. Mater. 122, 1071-1077 (1984).

2. L. R. Greenwood, D. G. Doran. and H. L. Heinisch, Phys. Rev. 34C,76-80 (1987).

3. D. W. Kneff. B. M. Oliver, H. Farrar IV, and L. R. Greenwood, Nucl. Sci. Eng. 92, 491-524 (1986).

4. E. Browne and H. B. Firestone, Table of Radioactive Isotopes, V. S. Shirley, Ed., John Wiley, New York (1986).

5. J. M. Nielsen, The Radiochemistry of Iron, NAS-NS3017, lb (1960).

6. L. J. Kirby, The Radiochemistry of Nickel. NAS-NS3051, 22 (1961).

7. R. Wenusch and H. Vonach, Oesterr. Sci. Acad. 99, 1 (1962).

8. J. Frehaut, A. Bertin, R. Bois, and J. Jary, Symp. on Neutron Cross Sections from 10-50 MeV, BNL/NCS-51245, 399 (1980).

9. N. I. Molla and S. M. Qaim, Nucl. Phys. 283A, 269 (1977)

10. Yu E. Kozyr and G. A. Prokopets, Sov. Nucl. Phy. 27, 329 (1978).

11. B. Joensson. K. Nyberg, and I. Bergqvist, Arkiv for Fysik 39, 295 (1969).

TABLE I

Results for $^{56}Fe(n,2n)^{55}Fe$

Sample	Energy[a] MeV	Fluence $10^{17}n/cm^2$	At. Ratio 10^{-8}	σ mb[b]
^{56}Fe-1	14.83	1.88	8.58	456.
^{56}Fe-2	14.82	1.61	7.34	456.
^{56}Fe-3	14.85	1.31	5.86	448.
Fe-1	14.68	10.30	48.6	472.
Fe-2	14.81	4.53	19.9	440.

Results for $^{63}Cu(n,p)^{63}Ni$

Sample	Energy[a] MeV	Fluence $10^{17}n/cm^2$	At. Ratio 10^{-8}	σ mb[c]
Cu-1	14.65	1.17	6.40	54.7
cu-2	14.65	1.14	6.16	54.0
cu-3	14.82	0.462	2.45	53.0

Results for $^{64}Ni(n,2n)^{63}Ni$

Sample	Energy[a] MeV	Fluence $10^{17}n/cm^2$	**At.** Ratio 10^{-7}	σ mb[c]
^{64}Ni-1	14.85	1.96	1.90	967.
^{64}Ni-2	14.83	1.65	1.57	948.

Results for $^{60}Ni(n,2n)^{59}Ni$

Sample	Energy[a] MeV	Fluence $10^{17}n/cm^2$	At. Ratio 10^{-8}	σ mb[d]
^{60}Ni-1	14.81	1.26	1.57	124±9
^{60}Ni-2	14.83	1.78	1.73	97±6
^{60}Ni-3	14.82	1.34	0.95	84±9

[a]Mean energy; width ≈0.5 MeV

[b]Uncert.: Stat. 1%, eff. 3%, std. 5%, $T_{1/2}$ 1.1%, fluence 5%, net 7.8%

[c]Uncert.: Stat. 1%, eff. 3%, std. 2.5%, $T_{1/2}$ 2.0%, fluence 5%, net 6.7%

[d]Uncert.: Stat. above, eff. 4%, $T_{1/2}$ 17%, fluence 5%, net 19-23%

TABLE II.

Summary and Comparison of Results with Previous Data

Reaction	Present E,	Present σ,mb	Previous E,	Previous σ,mb	Ref.
$^{56}Fe(n,2n)^{55}Fe$	14.8	454±35	14.0	440±90	7
			14.3	410±33	8
			14.7	440±40	9
			14.6	480±50	10
			15.1	190±40	11
$^{63}Cu(n,p)^{63}Ni$	14.7	54±4	14.7	125±50	9
$^{63}Cu(n,px)^{a}$			14.0	105±9	12
			14.1	149±30	13
$^{64}Ni(n,2n)^{63}Ni$	14.8	958±64		none	
$^{60}Ni(n,2n)^{59}Ni$	14.8	104±25		none	

[a]Total proton yield from ^{63}Cu includes other reactions

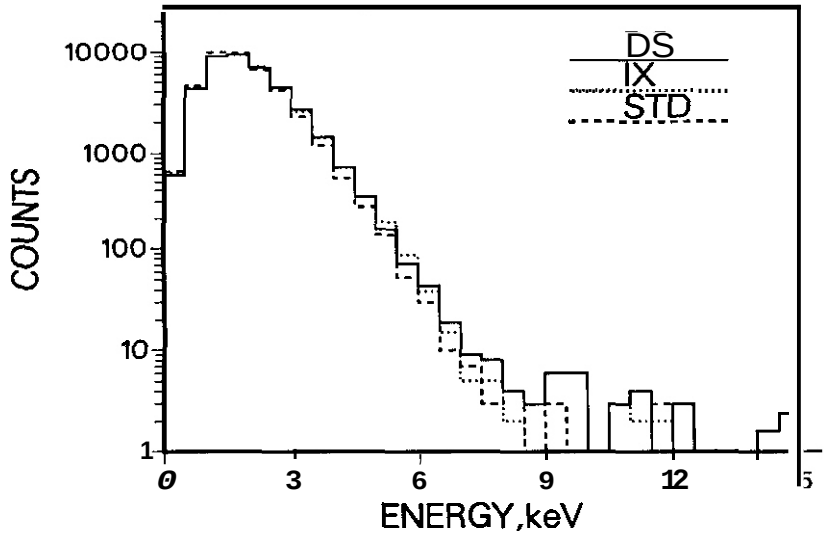


Fig. 1. Liquid scintillation spectra for ^{55}Fe from the $^{56}Fe(n,2n)$ reaction: The initlal dissolution (US); the ion-exchanged solution (IX); and the ^{55}Fe standard (STD).

12. D. L. Allan, Nucl. Phys. 24, 274 (1961).

13. R. S. Storey, Proc. Phys. Soc. 75, 526 (1960).

PUBLICATIONS

1. D. L. Sowers and L. R. Greenwood, Analysis of Long-Lived Isotopes by Liquid Scintillation Spectrometry, Proc. Int. Con?. on Methods and Applications of Radioanalytical Chemistry. Kona, Hawaii, April 5-10, 1987, to be published.

2. L. R. Greenwood, D. G. Doran, and H. L. Heinisch, Production of ^{91}Nb, ^{94}Nb, and ^{95}Nb from Mo by 14.5-14.8 MeV Neutrons, Phys. Rev. 35C, 76-80 (1987).

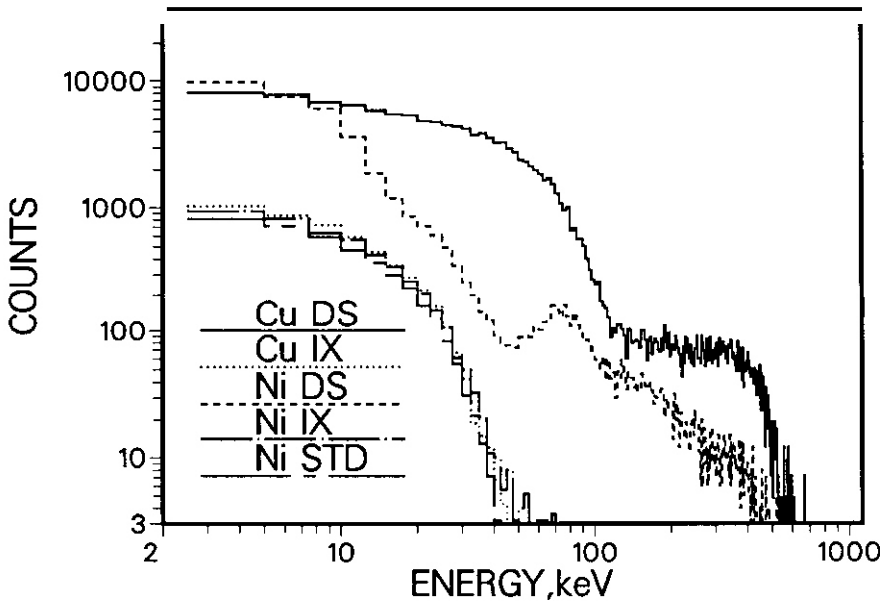


Fig. 2. Liquid scintillation spectra for ^{63}Ni from the ^{63}Cu(n,p) and ^{64}Ni(n,2n) reactions: The initial dissolutions (DS); ion-exchange products (IX); and ^{63}Ni standard (STD).

MEASUREMENTS FOR THE JP2, JP6, JP7 US/JAPANESE EXPERIMENTS IN HFIK - L. R. Greenwood (Argonne National Laboratory)

OBJECTIVE

To Characterize neutron irradiation facilities in terms of neutron **fluence.** spectra, and damage parameters.

SUMMARY

Results **are** reported for the JP2,JP6, and JP7 US/Japan experiments that focus on the swelling. tensile, and fatigue properties **of** stainless steel. The JP2 experiment has the highest exposure reported for HFIR (57,507 MWD) producing 55.2 dpa and 3345 appm helium in 316 stainless steel.

PROGRESS AND STATUS

Results are reported for the JP2, JP6, and JP7 U.S./Japanese experiments in HFIR to study swelling, tensile, and fatigue properties of stainless steel at 300-600°C. These three irradiations were conducted in the target position, as follows:

Experiment	Dates	Exposure
JP2	01/04/84 - 12/17/85	57,507 MWD
JP6	09/11/84 - 11/14/85	34,677 MWD
JP7	10/05/84 - 12/17/85	34,652 MWD

Results for the JP1 and JP3 experiments were reported previously.'

The JP2 experiment has the highest exposure yet reported in HFIR. Burnup corrections are quite severe. However, these corrections appear to be in good agreement (35%) for all five of the JP experiments, and we estimate that activities are accurate to 33%.

Dosimeters were located at six vertical locations in the JP2 and JP6 experiments and at three heights in JP7. One of the dosimeters **was** lost during disassembly at ORNL. The remaining 14 capsules were gamma counted at Argonne. Each capsule contained **Fe**, 0.1% Co-Al, and 80.2% Mn-Cu wires. The corrected activities are listed in Table I. Since runs JP6 and JP7 have nearly identical exposures, fluence and damage rates are reported jointly.

The vertical **flux** gradients were fit to **a** polynominal equation and the **average** results are given below:

$$f(z) = f(0)(1 + bz + cz^2), \quad z = \text{height in cm} \qquad (1)$$

For the threshold reactions the parameters **are** $b = 0.361 \times 10^{-3}$ and $c = -1.007 \times 10^{-3}$ in good agreement with parameters determined for the PTP position.[1] However, the thermal reactions have **a** flatter dependence with $b = 1.24 \times 10^{-3}$ and $c = -0.756 \times 10^{-3}$. Equation (2), with the fast parameters b and c, can be used to determine fluence or damage rates at any height in the assembly.

The neutron energy spectra were adjusted with the STAY'SL computer code using the midplate activities determined from the gradient data. The resultant neutron fluence values are given in Table II. The spectral adjustments were Small (<10%) and the spectrum is essentially the same as reported previously in the PTP position.'

Damage parameters were calculated with the SPECCER computer code[2] and the results are listed in Table III. Thermal effects for Ni and Cu are included **as** discussed in recent publications.[3,4] Far the very high exposure in the JP2 experiment, the thermal effect in Cu produces 9.6 times more helium than the fast reactions. For Ni, the thermal effect produces about 0.25 at. % helium resulting in 3345 appm in 316 stainless steel. The helium-to-dpa ratio is about 61:1 at midplane in JP2. Since these effects are not linear with the fluence, helium and damage gradients for 316 Stainless Steel **are** listed separately in Table IV.

FUTURE WORK

Samples have been gamma counted from the JP4, JP5, and JP8 experiments and analysis is now in progress.

REFERENCES

1. L. R. Greenwood, Damage Anal. and Fund. Studies Quarterly Prog. Rep., DOE/0046/24, pp. 5-9 (Feb. 1986).

2. L. R. Greenwood and R. K. Smither, ANL/FPP/TM-197, January 1985.

3. L. R. Greenwood, D. W. Kneff, and R. P. Skowranski, J. Nucl. Mater. 122-123, 1003-1010 (1984).

4. D. W. Kneff, L. R. Greenwood, B. M. Oliver, R. P. Skowranski, and E. L. Callis, Rad. Eff. 92-96, 53-56 (1986).

Table I.
Measured Activities for HFIR-JP2, JP6, JP7
Values (at/at-s) at 100 MW; ±3% accuracy

Height, cm	$^{58}Fe(n,\gamma)^{59}Fe$			$^{59}Co(n,\gamma)^{60}Co$		
	JP2	JP6	JP7	JP2	JP6	JP7
	(x 10^{-9})			(x 10^{-8})		
25.4	1.23	1.15		3.64	3.68	
16.5	1.79	1.70	1.84	5.36	5.71	5.80
7.1	2.20	2.15		6.25	6.65	
2.1	2.36	2.23	2.36	6.33	6.50	6.51
-12.1	2.02	1.91		5.48	5.81	
-21.0	1.39	1.35		4.39	4.48	
	$^{54}Fe(n,p)^{54}Mn$			$^{55}Mn(n,2n)^{54}Mn$		
	JP2	JP6	JP7	JP2	JP6	JP7
	(x 10^{-9})			(x 10^{-8})		
25.4	2.59	2.27	-	0.782	0.708	-
16.5	5.21	5.21	5.40	1.51	1.35	1.53
7.1	6.75	6.80		1.97	1.92	-
2.1	6.99	7.07	6.95	2.10	2.06	2.10
-12.1	5.93	5.89	-	1.72	1.81	-
-21.0	3.91	3.88	-	1.17	1.16	-

Table II.
Neutron Fluences **for HFIR-JP2, JP6, JP7**
Values are accurate to ±10%
Fluence x 10^{22} n/cm^2

Energy	JP2	JP6, JP7
Total	24.66	14.80
Thermal ((0.5 eV)	10.09	6.09
0.5 eV-0.11 MeV	7.97	4.77
>0.11 MeV	6.59	3.95
>1 MeV	3.35	*2.02*

Table III.
Damage Parameters for HFIR-JP2, 6, 7
Values at midplane: for gradients, use Eq. (1)

Element		JP2		JP6, JP7	
		He, appm	DPA	He, appm	DPA
Al		41.9	86.4	25.2	51.8
Ti		27.9	54.8	16.9	33.0
V		1.41	61.4	0.85	36.9
Cr		9.61	54.1	5.78	32.5
Mn[a]		8.48	59.6	5.10	35.8
Fe		17.07	47.9	10.28	28.8
Co[a]		8.40	60.1	5.05	36.1
Ni	Fast	226.0	51.5	137.0	31.0
	^{59}Ni	25,402.0	44.8	15,015.0	26.5
	Total	25,628.0	96.3	15,152.0	57.5
Cu	Fast	12.4	46.7	7.4	28.1
	^{65}Zn	119.2	0.2	38.3	0.1
	Total	131.6	46.9	45.7	28.2
Nb		3.12	46.3	1.88	27.8
Mo		-	34.5	-	20.7
316SS[b]		3345.0	55.2	1978.0	33.1

[a] Thermal self-shielding important for Mn, Co.
[b] 316SS: Fe (0.645), Ni (0.13). Cr (0.18), Mn (0.019), Mo (0.026).

Table IV.
Damage Gradients for HFIR-JP2, JP6, JP7
DPA includes thermal effect from ^{59}Ni.
Helium includes ^{59}Ni and fast reactions

Height, cm	JP2		JP6, JP7	
	He, appm	DPA	He, appm	OPA
0	3345	55.2	1978	33.1
3	3316	54.7	1957	32.8
6	3229	53.3	1897	31.9
9	3082	50.8	1796	30.4
12	2873	47.3	1653	28.3
15	2592	42.7	1464	25.5
18	2242	37.2	1234	22.2
21	1811	30.7	961	18.2
24	1293	23.1	650	13.7

DOSIMETRY AND DAMAGE ANALYSIS FOR THE OMEGA WEST REACTOR, L. R. Greenwood (Argonne National Laboratory)

OBJECTIVE

To characterize neutron irradiation facilities in terms of neutron fluence, spectra, and damage parameters.

SUMMARY

Five experiments have been completed in the Omega West Reactor (LANL) for comparison with 14 MeV measurements at RTNS II (LLNL). The use of water rather than helium coolant on some of the runs appears to have produced a significant spectral shift. Neutron fluences and damage rates are reported for each experiment.

PROGRESS AND STATUS

Dosimetry measurements and damage calculations have been completed for five irradiations in the Omega West Reactor at Los Alamos National Laboratory. The irradiations were conducted by Howard Heinisch (Hanford Engineering Development Laboratory) and are part of a series of fission-fusion comparisons with experiments at the 14 MeV Rotating Target Neutron Source II at Lawrence Livermore National Laboratory. The irradiations were conducted between October 13, 1985 and March 18, 1986, at temperatures between 90-280°C. The exposure parameters were as follows:

Irradiation	Dates	Exposure, FPH
4	10/23/85 - 12/13/85	199.4
5	01/21/86 - 02/05/86	79.3
6	01/10/86 - 01/16/86	23.8
	01/17/86 - 01/17/86	6.9
4	02/10/86 - 03/18/86	195.8

Similar experiments (No. 1-3) and spectral measurements were reported previously.[1,2]

Dosimetry capsules containing Fe, Co, Ti, and Ni wires were included with each irradiation. These wires were gamma counted at Argonne and the resulting activities are listed in Table I. The neutron energy spectrum determined in the spectral measurement[2] was then adjusted using the measured activities with the STAY'SL computer code. The resulting neutron flux and fluence values are listed in Tables II and III. Examination of the data indicates a spectral shift between runs 1-4 and runs 5-8. The thermal activities are about 30% higher in runs 1-4 whereas the fast reaction activities are about 20% lower. This difference is apparently due to a change in the cooling medium from helium (runs 1-4) to water (runs 5-8). The spectral measurements were also conducted with a helium coolant; hence, we do not have the optimal input spectrum for the water-cooled experiments. The differences in the adjusted neutron energy spectra are shown in Figs. 1 and 2.

Closer examination of the values in Tables I-III indicates small (10%) differences from run-to-run even with the same coolant material. In particular, the fluxes for runs 7 and 8 are about 3% and 10% higher than runs 5 and 6. These differences may be due to inaccuracies in the reactor power histories since we normalized data from nominal average power levels to 8 MW full power. Further measurements would be needed to resolve these small differences.

Damage calculations were performed with the SPECTER computer code[3] and the results are listed in Table IV. Values for runs 1-4 scale with the exposure level; however, the values for runs 5-8 are about 20% lower due to the spectral shift with the water coolant.

FUTURE WORK

Further measurements are planned in the Omega West Reactor.

REFERENCES

1. L. R. Greenwood, Damage Anal. and Fund. Studies Quarterly Prog. Rep. DOE/ER-0046/25, pp. 5-7 (May 1986).

2. L. R. Greenwood, Damage Anal. and Fund. Studies Quarterly Prog. Rep. DOE/ER-0046/4, pp. 15-20 (Feb. 1981).

3. L. R. Greenwood and R. K. Smither, ANL/FPP-TM-197, January 1985.

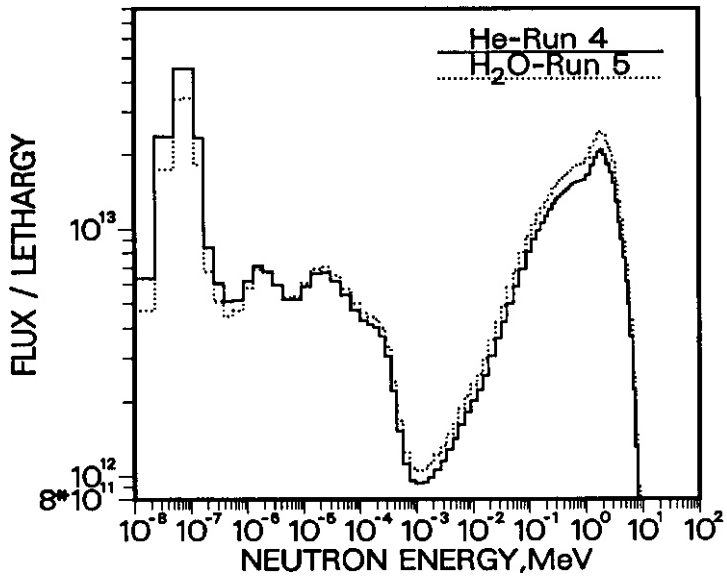


Fig. 1. Comparison of Water and Helium Cooled Neutron Spectra Measured in Omega West Reactor.

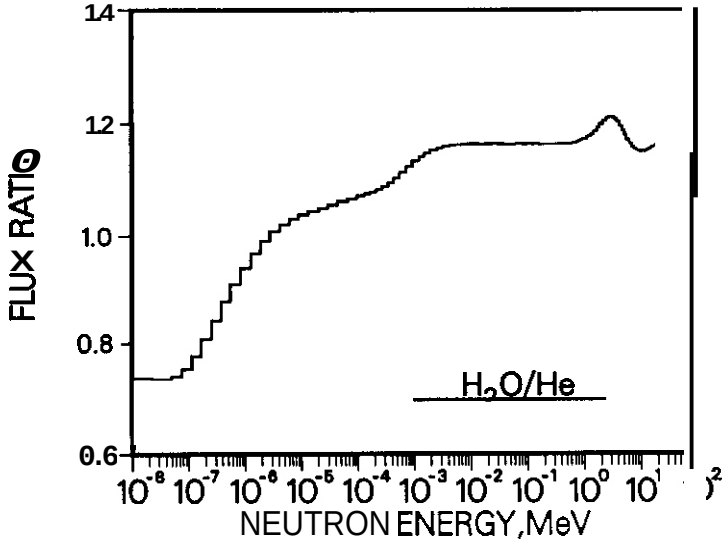


Fig. 2. Ratio of Water/Helium Cooled Spectra in the Omega West Reactor.

Table I.
Activity Measurements for Omega West Reactor
(Activity in atom/atom-s, ±2%, 8 MW)

Reaction		4	5	6	7	8
$^{58}Fe(n,\gamma)^{59}Fe$	(10^{-11})	7.12	5.43	5.54	5.67	6.46
$^{59}Co(n,\gamma)^{60}Co$	(10^{-9})	2.33	1.84	1.85	1.87	2.09
$^{54}Fe(n,p)^{54}Mn$	(10^{-12})	2.88	3.43	3.50	3.53	3.63
$^{58}Ni(n,p)^{58}Co$	(10^{-12})	3.62	4.46	4.13	4.63	4.75
$Ti(n,x)^{46}Sc$	(10^{-13})	3.88	4.38	4.61	4.56	4.80

Table II.
Neutron Fluxes for Omega West Reactor
(Flux x 10^{13} n/cm^2-s, 8 MW, ±10%)

Energy, MeV	4	5	6	7	8
Thermal <0.5 eV	7.84	5.93	5.99	6.07	6.88
0.5 eV - 0.1	5.03	5.33	5.30	5.28	5.69
>0.1	5.66	6.66	6.62	6.74	7.14
>1.0	2.80	3.33	3.31	3.40	3.55
Total	18.53	17.92	17.91	18.09	19.70

Table III.
Neutron Fluences for Omega West Reactor
(Fluence x10^{19} n/cm^2, ±10%)

Energy, MeV	4	5	6	7	8
Thermal <0.5 eV	5.63	1.69	0.513	0.151	4.85
0.5 eV - 0.1	3.61	1.52	0.454	0.131	4.01
>0.1	4.06	1.89	0.567	0.167	5.03
>1.0	2.01	0.947	0.284	0.084	2.50
Total	13.30	5.10	1.54	0.449	13.89

Table IV.
Damage Parameters for Omega West Reactor
(dpa $x10^{-3}$, He in appb)

	Run 4		Run 5		Run 6		Run 7		Run 8	
Element	dpa	He	dpa	HE	dpa	HE	dpa	He	dpa	He
Al	52.1	17.3	24.4	7.90	7.30	2.43	2.16	0.71	64.6	21.2
Ti	31.6	15.9	14.7	7.46	4.41	2.26	1.31	0.67	39.0	19.7
V	35.7	0.60	16.6	0.27	4.98	0.08	1.48	0.02	44.0	0.73
Cr	32.2	4.51	15.0	2.09	4.50	0.64	1.33	0.19	39.8	5.56
Fe	28.4	7.91	13.3	3.64	3.99	1.12	1.18	0.33	35.2	9.72
Ni	30.2	122.	14.0	56.8	4.21	17.3	1.25	5.10	37.2	151.
Cu	27.6	6.61	12.8	3.03	3.85	0.93	1.14	0.27	34.1	8.10
Nb	27.7	1.51	13.0	0.70	3.90	0.21	1.15	0.06	34.4	1.86

DOSIMETRY AND DAMAGE ANALYSIS FOR HFIR-CTR-47/48 - L. R. Greenwood (Argonne National Laboratory)

OBJECTIVE

To characterize neutron irradiation facilities in terms of neutron fluence and spectra as well as damage parameters.

SUMMARY

Dosimetry measurements and damage calculations have been completed for the CTR47/48 experiments in HFIR (ORNL) to study impact properties of ferritic alloys (HT9, T9). These irradiations have the highest reported exposure in the PTP position (46,113 MWD) resulting in 47.2 dpa and 2643 appm He in 316 Stainless steel.

PROGRESS AND STATUS

Dosimetry and damage calculations have been completed for the CTR47/48 experiments in the High Flux isotopes Reactor (HFIR) it Oak Ridge National Laboratory. These experiments were designed to study the impact properties of miniature Charpy V-Notch specimens of HT-9 and other alloys at 300-400°C. The samples were irradiated in the PTP position of HFIR from May 28, 1983 to February 24, 1985, for a net exposure of 46,113 MWD which is the highest exposure which we have reported. Other experiments in this series including CTR 30-46 have been reported previously.[1]

Dosimetry capsules containing Fe, 0.1% Co-Al, Ti, and 80% Mn-Cu wires were placed at five vertical locations in each assembly. One of the ten capsules was lost during disassembly; the other nine 'were gama counted at Argonne, and the resulting activities are listed in Table I. Due to the extremely high exposure of these samples, burnup corrections are quite large for all of the measured reactions. In particular, the raw activities for the $^{59}Co(n,\gamma)^{60}Co$ reaction at midplane are actually lower than in shorter experiments due to the fact that about 93% of the original ^{59}Co has been consumed, and hence, ^{60}Co is decaying faster than it is being produced. Burnup corrections were consequently about 50-706 for this reaction. For the threshold reactions, the corrections were about 30-40%. As discussed in previous reports,[1] the burnup cross section for ^{54}Mn is uncertain; however, the value of 14.6 b which we deduced previously, appears to fit the data quite well. In other words, our corrected activities agree quite well with previous experiments in the PT? position. Consequently, we are confident that the corrections are reliable and that the uncertainty in the activities is only about 3% above the usual 1-1.5% from counting statistics.

The activities in Table I can be used to determlne the vertical flux gradients. Data for both experiments is in good agreement with the parameters determined previously:[1]

$$f(z) = f(0)(1 + bz + cz^2),\ b = 5.02\times10^{-4},\ c = 1.00\times10^{-3},\ z = \text{height, cm} \quad (1)$$

Equation (1) can be used to describe flux gradients for any of the neutron fluence or damage parameters listed later by substituting the midplane value for f(0).

The neutron energy spectrum determined previously for the PTP position was then adjusted using the measured activities with the STAY'SL computer code. The resulting neutron fluence values are listed in Table II. The fluences and neutron energy spectrum are in good agreement with previous data. Damage calculations 'were performed with the SPECTER computer code[2] and the results are listed in Table III. These damage levels are the highest which we have yet reported for HFIR. The thermally-generated helium for Ni and Cu are included in the table using previously published procedures.[3,4] As can be seen, the recently discovered effect in Cu produces about 7 times more helium than fast neutron reactions: however, the extra damage effect is minimal (0.14 dpa). In the Ni case, the extra damage is nearly equal to the fast neutron damage. Since the helium and extra damage in nickel do not scale linearly with the exposure, Eq. 1 cannot be used in this case. Hence, damage gradients for stainless steel are listed separately in Table IV.

FUTURE WORK

Analysis i3 in progress for the MFE4A/4B spectral tailoring experiments in HFIR.

REFERENCES

1. L. R. Greenwood, Alloy Development for Irradiation Performance Semiannual Progress Reports, DOE/ER-0045/14, pp. 22-26 (March 1985); DOE/ER-0045/13, pp. 13-11 (Sept. 1984); and DOE/ER-0045/11, pp. 30-37, (Sept. 1983).

2. L. R. Greenwood and R. K. Smither, ANL/FPP/TM-197, January 1985.

3. L. R. Greenwood, D. W. Kneff, and R. P. Skowronski, J. Nucl. Mater. 122-123, pp. 1003-1010 (1984).

4. D. W. Kneff, L. R. Greenwood. B. M. Oliver, R. P. Skowronski. and E. L. Callis, Rad. Eff. 92-96, pp. 53-56 (1986).

PUBLICATIONS

1. L. R. Greenwood, J. Nucl. Mater., 141-143, 654 (1986).

2. W. A. Coghlan. F. W. Clinard, N. Itch, and L. R. Greenwood, J. Nucl. Mater. 141-143, 382 (1986).

Table I.
Measured Activities for HFIR-CTR47/48
Values (at/at-S) at 100 MW; ±3% accuracy

Height, cm	$^{59}Co(n,\gamma)^{60}Co$ (x 10-8)		$^{54}Fe(n,p)^{54}Mn$ (x 10^{-11})		$^{55}Mn(n,2n)^{54}Mn$ (x 10^{-13})	
	47	48	47	48	47	48
21.9	3.74	3.66	3.90	4.01	1.20	1.21
12.7	5.69	-	6.66	-	1.94	-
0.0	6.85	6.80	7.81	7.84	2.30	2.47
-12.7	5.58	5.62	6.51	6.45	1.86	1.93
-21.9	3.51	3.57	3.74	3.78	1.13	1.15

Table II.
Neutmn Fluxes/Fluences for HFIR CTR 47/48
46, 113 MWD (100 MW); ±10%

Energy	Flux ($*10^{15}$ n/cm^2-s)	Fluence ($*10^{22}$ n/cm^2)
Total	5.09	20.28
Th (<0.5 eV)	1.99	7.93
0.5 eV-0.11 MeV	1.69	6.72
>0.11 MeV	1.41	5.63

Table III.
Damage Parameters - HFIR CTR 47/48
Values at midplane: for gradients, use Eq. (1)

Element		dpa	He, appm
Al		74.3	36.9
Ti		47.3	24.6
V		52.9	1.24
Cr		46.8	8.47
Mn[a]		51.1	7.47
Fe		41.4	15.1
Co[a]		51.1	7.40
Ni	Fast	44.4	200.0
	^{59}Ni	35.3	20,041.0
	Total	79.7	20,241.0
Cu	Fast	40.3	10.9
	^{65}Zn	0.14	71.1
	Total	40.4	82.0
Nb		40.0	2.76
Mo		29.7	-
316SS[b]		47.2	2643.0

[a] Thermal self-shielding important for Mn, Co specimens.
[b] 316SS: Fe (0.645), Ni (0.13), Cr (0.18), Mn (0.019), Mo (0.026).

Table IV.
Damage Gradients for 316SS - CTR 47/48
Helium includes ^{59}Ni and fast reactions
DPA includes extra thermal effect (He/567)

Height, cm	He, appm	DPA
0	2643	47.2
3	2618	46.8
6	2544	45.5
9	2420	43.4
12	2242	40.4
15	2007	36.5
18	1716	31.7
21	1364	26.1
24	949	19.6

ACTIVATION CALCULATIONS - F. M. Mann (Westinghouse Hanford Company)

OBJECTIVE

The objective of this work is to calculate with reasonably accuracy and completeness the activation that elements in fusion reactors will experience.

SUMMARY

Improved evaluations of the reactions induced on 11 elements were processed into the REAC2 cross section library. Limitations of the presence of tungsten in soft spectrum are no longer a major concern.

PROGRESS AND STATUS

Introduction

The accuracy of the calculation of the transmutation of elements and the production of radioactive nuclides in large part depends on the accuracy of the nuclear data used. The philosophy of the REAC2 cross section library is to provide accuracy commiserate with the need and cost of the data. Therefore in the first release of the REAC2 cross section library[1] for many nuclei, systematic and estimated cross section values were used. However, for certain reaction paths (such as W leading to Ir) improvements were needed.

Results

For 11 nuclides (Nb93, Cs133, Nd148, Eu151, Eu153, W182, W183, W184, W186, Re185, and Re187), the ENDF/B-V[2] (n,gamma) reaction evaluations were processed using the NJOY Nuclear Data Processing System3 were processed into a 620 group structure. These cross sections plus any other reactions for those elements appearing in ENDF/B-V (see Table 1) were then processed into the default 63 group structure of REAC2.[4]

Because of their importance in determining the reaction path, the isomeric state branching of Eu151(n,gamma) and Ir191(n,gamma) were calculated with the HAUSER*5.[5] These calculations which agree well with the extremely limited experimental data were then processed in the same manner as the other cross sections.

Discussion

Previous calculations6 had shown that in very soft spectrum that tungsten could be limited at very high fluences by the production of Ir192*. The calculations were rerun with the new cross section set and the limitations due to Ir-192* have disappeared. Much of the reduction is due to a better estimate of the Ir191 (n,gamma) isomeric state branching ratio; however, some of the reduction remains unexplained.

However, tungsten is still limited at around the percent level due to other nuclide production (Hf-178* and Re-186*). Assuming a 6 year irradiation (approximately 20 MW year/meter*2) and a disposal limit of 100 Curies/meter*2 (a value typical of NRC regulations[7] for non gama emitting decays), then (see Table I) the concentration at the first wall position in STARFIRE[8] (a water-cooled design) would be limited to about .5% and in MARS9 (a liquid metal design) to about 0.2% in order to be buried as a Class C material in a near surface disposal site.

CONCLUSIONS

The REAC2 cross section library has been improved with the result that new calculations show that the limitation on W is no longer a major concern.

REFERENCES

1. F. M. Mann, "Cross Sections for Reduced Activation Studies", DAFS Quarterly Progress Report, February 1985, DOE/ER-0046/20, (1985) 18.

2. R. Kinsey, Compiler, "ENDF/B Summary Documentation (ENDF-201)," 3rd Edition (ENDF/B-V), BNL-NCS-17541, Brookhaven National Laboratory (1979). Version V.2 was released in 1982-3.

3. R. E. MacFarlane, D. W. Muir, and R. M. Eoicourt, "The NJOY Nuclear Data Processing System, Volume 1: User's Manual," LA-9303-M, Vol. 1 (ENDF-324), Los Alamos National Laboratory, 1982.

4. REAC2 is an outgrowth of REAC, which is documented in F. M. Mann, "Transmutation of Alloys in MFE

Facilities as Calculated by REAC [A Computer Code System for Activation and Transmutation," HEOL-TME 81-37, Hanford Engineering Oevelopment Laboratory, 1982.

5. F. M. Mann, "HAUSER*5, A Computer Code to Calculate Nuclear Cross Sections," HEOL-TME 78-83, Hanford Engineering Oevelopment Laboratory, 1919.

6. F. M. Mann, "Activation Calculations Using an Expanded Nuclear Data Base", OAFS Quarterly Progress Report, February 1986, DOE/ER-0046/24, (1985) 30.

7. Final Environmental Impact Statement *on* 10 CFR Part 61, "Licensing Requirements for Land Disposal of Radioactive Waste", NUREG-0945. Vol. 3, Appendix F, U.S. Nuclear Regulatory Commission, 1982.

8. "STARFIRE - A Commercial Tokomak Fusion Power Plant Study", ANLIFPP-80-1, Argonne National Laboratory, 1980.

9. B. G. Logan, et al, "Mirror Advanced Reactor Study (MARS)", UCRL-53480, Lawrence Livermore National Laboratory, 1984.

Table 1
Activation in Tungsten
6 Year irradiation, 3000 day Cooling

		STARFIRE		MARS	
Product	Disposal Limits (Curies/cm**3)	Decay Rate (Curies/cm**3)	Ratio	Oecay Rate (Curies/cm**3)	Ratio
T	•	1.23e-2	*	1.46e-2	*
Hf 178*	1.0e-4 a]	9.87e-3	0.010	4.94e-2	0.002
Ta 179	*	2.18e-2	*	9.48e-2	*
Re 184*		2.75e-2		3.07e-5	
Re 186*	1.0e-4 a]	1.10e-2	0.009	1.35e-3	0.074

* short half-live, no limit on Class C burial
a) no NRC limit, but 1.0e-4 typical of values for non gamma emitting nuclei

3. MATERIALS ENGINEERING AND DESIGN REQUIREMENTS

No contributions received this period.

4. FUNDAMENTAL MECHANICAL BEHAVIOR

ANALYSIS OF THE EFFECT OF INTERNAL HYDROGEN ON THE FATIGUE CRACK GROWTH OF HT-9 -- R. H. Jones (Pacific Northwest Laboratory)

OBJECTIVE

Internal hydrogen was shown in a previous report (1) to greatly accelerate the fatigue crack growth of HT-9. As part of an on-going evaluation of environmental effects on the crack growth of fusion reactor materials, further analysis of the effect of hydrogen on the fatigue crack growth of HT-9 has been carried out. The objective of this study is to develop the mechanism and modeling capability to predict environmental effects on subcritical crack growth of fusion reactor materials.

SUMMARY

Evaluation of the frequency dependence of the hydrogen effect on fatigue crack growth of HT-9 showed an increasing crack growth rate with decreasing frequency or increasing cyclic period. This result coupled with the plateau observed for the fatigue crack growth of HT-9 with internal hydrogen has been used to evaluate the hydrogen contribution to fatigue crack growth using the superposition of static and cyclic crack growth processes.

PROGRESS AND STATUS

Background

Structural materials in fusion reactors will be subjected to static and cyclic loading conditions and the presence of hydrogen in these systems is unavoidable. Hydrogen will be present in fusion reactor materials from direct injection from the plasma, tritium gas in the breeding blanket, nuclear (n,p) reactions and cathodic reduction for water cooled reactors. Hydrogen has been shown to induce cracking in a wide variety of materials including ferritic steels, austenitic stainless steels, nickel-based alloys and aluminum alloys. The collection of hydrogen at particle-matrix interfaces, grain boundaries or other defects ahead of the crack tip is thought to be a key step in hydrogen induced subcritical crack growth.

Some key parameters in hydrogen induced crack growth include temperature, loading mode and hydrogen activity. Experiments and analysis are in progress to determine the temperature dependence of hydrogen induced crack growth while previous work in this program (1) has shown that hydrogen affects the cyclic crack growth behavior of HT-9. Esaklul and Gerberich (2) and Pao, Wei and Wei (3) have shown that hydrogen can reduce the fatigue crack threshold stress intensity and increase the crack growth rates in the stage I and II crack growth regime of ferritic steels.

It was also shown in a previous study (4) in this program that external cathodic hydrogen caused subcritical crack growth in static load conditions. Tests were performed at the open circuit potential and -600 mV in IN H_2SO_4 at 25°C as shown in Figure 1. These results are generally consistent with those produced in gaseous hydrogen where the crack growth-stress intensity threshold increases and the crack growth rate in stage II decreases with decreasing hydrogen activity. This comparison is made in Figure 1a and 1b where the hydrogen activity at open circuit conditions is less fhan at -600 mV. A threshold stress intensity of 20 to 30 $MPa\sqrt{m}$ and a stage II crack growth rate of $5x10^{-6}$ mm/s is indicated by the data given in Figure 1. A fracture toughness of 100 to 110 $MPa\sqrt{m}$ is also suggested by the increasing crack growth rate in stage III. A fracture mode of about 30% intergranular and the remainder quasi-cleavage accompanied the subcritical growth process.

Hydrogen was shown to increase the fatigue crack growth rate of HT-9 as reported previously (1). In these tests, hydrogen was introduced into the steel by cathodic charging prior to fatigue crack growth testing. Tests were performed at 0.2, 1, and 5 Hz with hydrogen causing an enhancement at each frequency. The fatigue crack growth data showed some variability from the loss of hydrogen during the low frequency tests and perhaps from variations in hydrogen charging. The maximum effect observed in the reported results has been taken to represent the hydrogen effect on fatigue crack growth. It is possible that further testing would produce a hydrogen enhanced crack growth rate greater than that observed but in the absence of further data the extent of the hydrogen enhancement was taken from the available data. The effect of hydrogen on the fatigue crack growth rate of HT-9 tested at a frequency of 5 Hz and an R ratio of 0.5 is shown in Figure 2 where it can be seen that hydrogen caused the fatigue crack growth rate to exceed the air test at ΔK values less than about $16 MPa\sqrt{m}$. The hydrogen effect had a stress intensity threshold of about 9 $MPa\sqrt{m}$ while there was no clear evidence of a threshold in the air test results.

Analysis

The kinetics of hydrogen induced crack growth of materials is thought to result from the collection of a critical concentration of hydrogen ahead of the crack *(5)*. Crack extension is thought to occur by a rapid crack jump through this embrittled region. The depth at which the critical hydrogen concentration must be

exceeded varies for internal and external hydrogen with estimates of about 100 μm for internal hydrogen and 500 A for external hydrogen. In both cases. the crack growth rate is a function of the hydrogen diffusion time. The driving force for hydrogen to collect at the-crack tip is the hydrostatic stress at the tip as expressed by Equation 1 below:

$$C(x) = C_o \exp \sigma(x) \bar{V}_H / 3RT \quad (1)$$

where C_o is the initial concentration, $\sigma(x)$ is the stress tensor normal to the crack growth direction and $\bar{V}_H$ is the partial molar volume of hydrogen in the metal. In a cyclic load test such as the fatigue crack growth test, the stress is varying with time such that the amount of time above some threshold stress increases with decreasing test frequency. Therefore, it is expected that the crack growth rate per cycle should increase with increasing cycle period or with decreasing frequency.

An increase in the hydrogen contribution to the crack gruwth rate with decreasing test frequency was observed for the HT-9 as shown in Figure 3. The value for A da/dN was obtained as shown in Figure 2 for each of the test frequencies and for the maximum hydrogen enhancement for each test condition. As mentioned previously, the test results showed some variability but the maximum effect was used for this analysis. A clear increase in the hydrogen enhanced crack growth rate for decreasinq frequency is shown in Figure 3 but the effect appears to be saturating at test frequencies less than 0.2 Hz. This saturation may be occurring because static load conditions are approached as the test frequency decreases or because there was hydrogen loss from the crack tip region at low frequencies. There was some experimental evidence that hydrogen loss from the crack tip occurred at a test frequency of 0.2 Hz as the percentage of intergranular fracture increased with decreasing ΔK and crack growth rate at test frequencies of 1 and 5 Hz but decreased at 0.2 Hz.

The frequency dependence observed for the hydrogen enhanced cyclic crack growth rate suggests that the fatigue crack growth rate curve for hydrogen charged material results from a superposition between the cyclic crack growth rate and static hydrogen induced subcritical crack growth. The following superposition model for corrosion fatigue can be used for the hydrogen cast:

$$(da/dN) = (da/dN)_m + (da/dN)_s + (da/dN)_{cf} \quad (2)$$

where $(da/dN)_m$ is the fatigue crack growth from purely mechanical fracture processts in the absence of any environmental effect, $(da/dN)_s$ is from the environment induced static load crack growth and $(da/dN)_{cf}$ is the environmental effect on the cyclic load crack growth rate. For hydrogen induced crack growth in HT-9, $(da/dN)_m$ can be obtained from the fatigue crack growth rate in air. Figure 4. at the ΔK of interest while $(da/dN)_s$ can be obtained from the static load subcritical crack growth rate, Figure 1b, and the relationship $da/dN = C\,(da/dt) / f$ where C is a correlation coefficient, da/dt is the static load crack growth rate and f is the cyclic load test frequency. Assuming that hydrogen does not affect the cyclic crack growth behavior of HT-9, the value of C is equal to $[(da/dN) - (da/dN)_m]f/(da/dt)$. At a ΔK value of 12.5 MPa$\sqrt{m}$, the value of C is equal to 22 so that Equation 2 can be rewritten:

$$(da/dN) = (da/dN)_m + 22\,(da/dt) / f \quad (3)$$

Equation 3 is accurate to within a factor of two for hydrogen induced fatigue crack growth rates in the threshold and plateau region of Figure 2, AK values of 10-13 MPa$\sqrt{m}$, but is inadequate to describe the entire hydrogen induced curve. This breakdowri in the model results from the variability in C over the ΔK range of interest, 22 was determined for a AK of 12.5 MPa$\sqrt{m}$, and the mismatch in the stress intensity at which the hydrogen plateau occurs in the static and cyclic load tests. In the static tests, Figure 1, the plateau region occurred at stress intensity values of 30 to 60 MPa$\sqrt{m}$, while for the cyclic load tests the plateau occurred at AK values of about 10 to 14 MPa$\sqrt{m}$. The static load and cyclic load values can be compared using Equation 4 below and assuming the K_{max} is equivalent to the static load stress intensity:

$$AK = (1-R)K_{max} \quad (4)$$

where R is the load ratio, P_{min}/P_{max} and K_{max} is the maximum stress intensity during the cyclic load test. The data in Figure 2 was obtained at an R of 0.5; therefore, the static stress intensity values should be a factor of 2 greater than the AK values. This correlation suggests that the plateau in cyclic load tests correspond to a static stress intensity of 20 to 28 MPa$\sqrt{m}$ which is considerably less than the range determined in the static load tests. It is well established that the threshold stress intensity in corrosion fatigue occurs at substantially lower values than the threshold stress intensity in stress corrosion (static loads). This shift in the threshold stress intensity results from the cyclic loads producing a dynamically strained crack tip which maintains an active corrosion reaction. Stirring action of the opening and closing crack on the crack tip solution may also contribute to maintaining a high corrosion rate at the crack tip. These processes would not seem to be important for hydrogen induced cracking frum internal hydrogen, although they could be important for external hydrogen. In the present case, the comparison is needed between static and cyclic load crack growth thresholds for internal hydrogen; however, this type of data is not available primarily because the complication of crack closure effects have obscured the data on hydrogen effects on cyclic crack growth.

It is conceivable that hydrogen alters the cyclic load crack growth rate which would result in the $(da/dN)_{cf}$ term being a non-zero value. Kimura and Birnbaum *(6)* have proposed that hydrogen enhances slip in iron which could enhance the alternating slip crack growth process during cyclic load crack growth. Evidence for a clear change in the striation spacing or cycles per striation was not obtained for HT-9 where the striation spacing was about 0.17 μm for both the hydrogen charged and uncharged materials; however, a statistically relevant analysis was not undertaken. A non-zero $(da/dN)_c$ term could account for some of the differences between Equation 3 and the measured hydrogen induced cyclic load crack growth rate results; however, more evaluation is needed before such a conclusion can be reached.

FUTURE WORK

Both the static and cyclic hydrogen induced crack growth measurements in HT-9 were made at 25°C; however, the crack growth rates at fusion relevant temperatures are needed. Estimates of the crack growth rates as a function of temperature have been made but comparison to experiment is complicated by the lack of reliable elevated temperature hydrogen induced crack growth rate data. Crack growth rate measurements in elevated temperature aqueous solutions are in progress. These tests offer the potential of eliminating the hydrogen loss problem that occurs for hydrogen charged samples. Tests in hydrogen gas at elevated temperatures would also solve this problem but the experimental capability is not readily available. If temperature dependent hydrogen induced crack growth data is obtained, the data will be used to assess existing models for the temperature dependence of static and cyclic load crack growth rates in hydrogen.

REFERENCES

1. G. F. Rodkey and R. H. Jones, "Effect of Internal Hydrogen on the Fatigue Crack Growth of HT-9", in the First Semiannual Progress Report on Fusion Reactor Materials.
2. K. A. Esaklul and W. W. Gerberich. in 16th ASTM Fracture Mechanics Conference, held August 1983, Battelle Memorial Institute, Columbus, OH, 1983.
3. P. S. Pao. W. Wei and R. P. Wei, p. 565, in Environment Sensitive Fracture of Engineering Materials, Z. A. Foroulis, ed., TMS-AIME, Warrendale, PA, 1979.
4. R. H. Jones, Metall. Trans. 17A, 1229, (1986).
5. W. W. Gerberich, T. Livne and X. Chen, p. 243, in Proc. of Symposium on Modeling Environmental Effects on Crack Growth Processes, R. H. Jones and W. W. Gerberich, eds., TMS-AIME, Warrendale, PA, 1986.
6. A. Kimura and H. K. Birnbaum, Scripta Met. 21, 53, (1987).

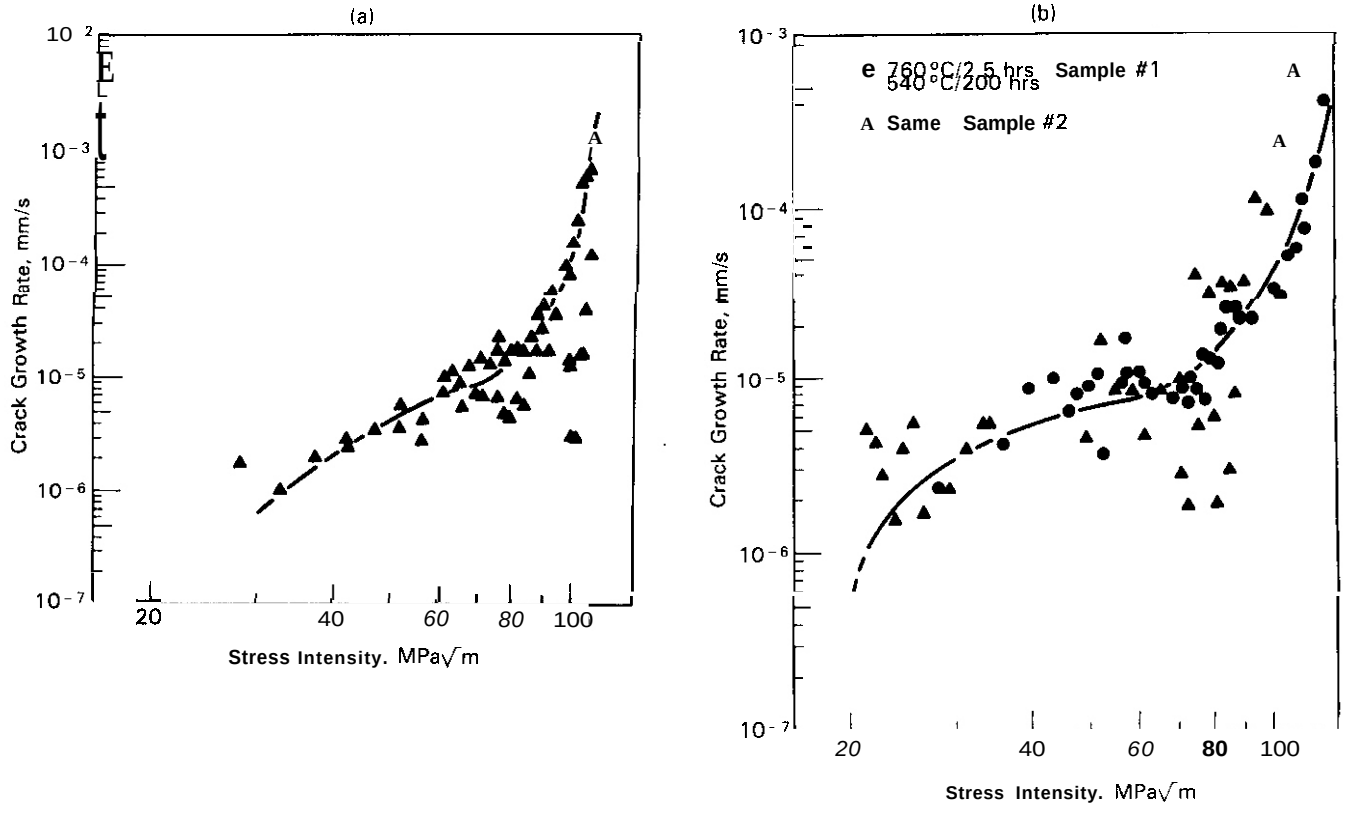


Fig. 1. Hydrogen induced subcritical crack growth rate curves for HT-9, a) heat treated at 760°C/2.5 h and tested in 1 N H_2SO_4 at -0.44 V (SCE), open circuit, b) heat treated at 760°C plus 540°C and tested in 1 N H_2SO_4 at -0.6 V (SCE).

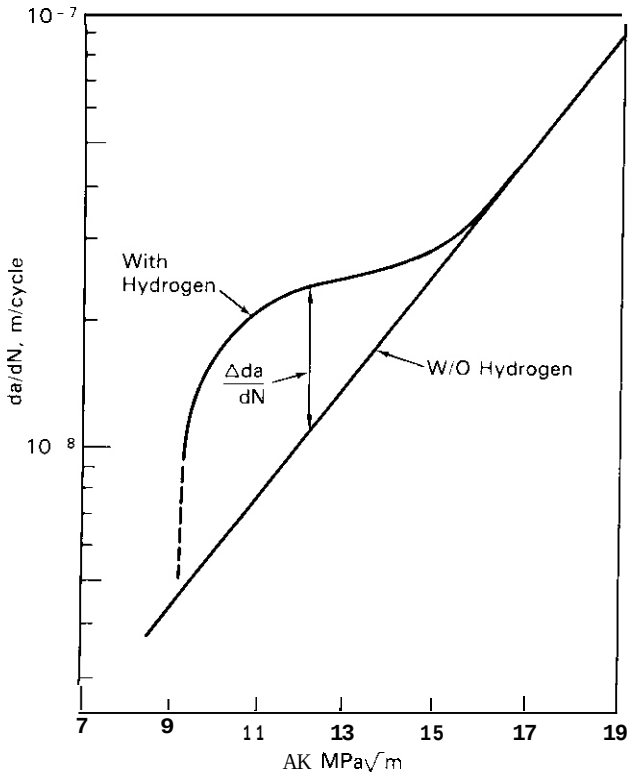


Fig. 2. Fatigue crack growth behavior of HT-9 tested at 5 Hz R=0.5 with and without hydrogen.

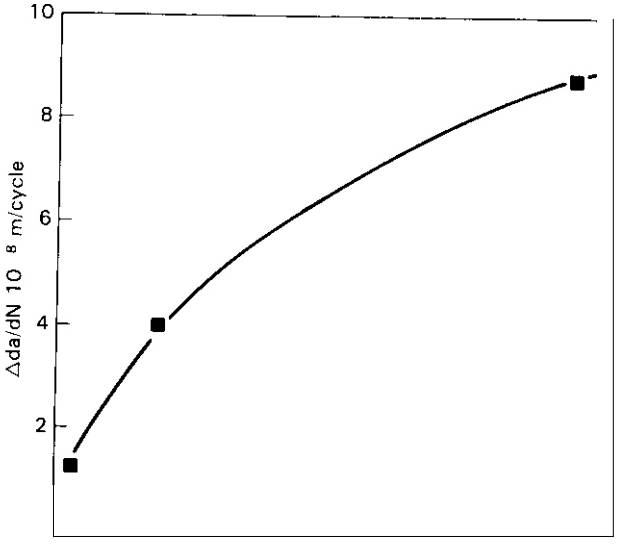


Fig. 3. Hydrogen induced increase in the fatigue crack-growth rate of HT-9 versus inverse frequency.

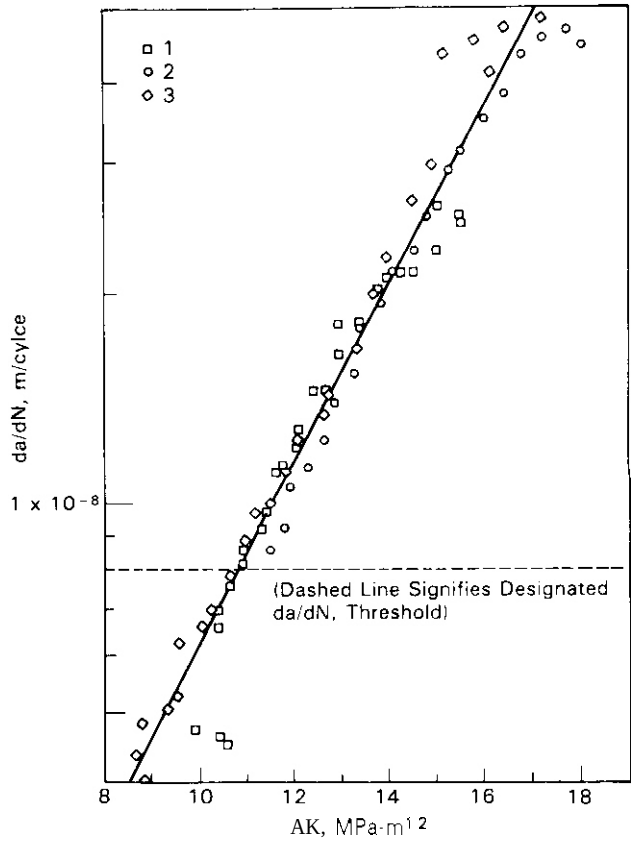


Fig. 4. Fatigue crack growth rate of HT-9 tested in air at 5 Hz and R=0.5.

5. RADIATION EFFECTS: MECHANISTIC STUDIES, THEORY AND MODELING

THE INFLUENCE OF BOTH MAJOR AND MINOR ELEMENT COMPOSITION ON VOID SWELLING IN SIMPLE AUSTENITIC STEELS -

F. A. Garner (Hanford Engineering Development Laboratory)
Arvind S. Kumar (University of Missouri-Rolla)

OBJECTIVE

The object of this effort is to determine the mechanisms by which the microstructural evolution of irradiated austenitic alloys respond to differences in composition or radiation variables.

SUMMARY

Data on the neutron-induced swelling of simple Fe-Ni-Cr austenitic alloys are presented to show that there are three compositional regimes of swelling as a function of nickel content. The intermediate transition regime can he shifted to higher or lower nickel levels as a function of chromium content, various solutes, displacement rate, temperature and helium level. Such shifts can preclude the observation of either the lower or upper nickel regime. The lower nickel regime is also obscured in ion bombardment studies due to factors that are atypical of the neutron environment.

Data are also presented to show the influence of silicon and phosphorus on the neutron-induced swelling of Fe-25Ni-15Cr and to demonstrate that the separate influence of each of these elements is more complex than previously observed. Similar complex trends have also been seen in ion bombardment experiments but there are additional distortions relative to the neutron-induced behavior that arise from the interaction of these elements with point defect gradients.

A model is presented to show that the major effect of composition on swelling lies in its influence on void nucleation, operating primarily on the intermediate transition regime. Compositional variations thus appear as a "temperature shift" analogous to that associated with changes in displacement rate. This shift is due to the effect of each element on the vacancy supersaturation via their effect on either the equilibrium vacancy concentration or the effective vacancy diffusion coefficient.

PROGRESS AND STATUS

Introduction

The radiation-induced swelling of Fe-Ni-Cr austenitic alloys For both fast reactor and fusion reactor applications has been the subject of many investigations too numerous to list. While the majority of these studies have focused on steels of technological relevance, some have addressed the compositional dependence of relatively solute-free binary Fe-Ni and ternary Fe-Ni-Cr alloys. Others have addressed the influence of single solute elements for a given base composition. The majority of both types of investigations involved the use of charged particle irradiation at displacement rates which were orders of magnitude greater than that of typical neutron environments.

The radiation damage community has become increasingly aware, however, that the use of charged particle simulation techniques often distorts the swelling behavior relative to that produced by the neutron environment. This distortion arises not only from the increased displacement rate but from the combined influence of displacement gradients, the inverse Kirkendall effect, stresses arising from differential swelling, surface influence and the action of the injected interstitial. All of these can combine to alter or even mask the influence of a given elemental species, many of which act synergistically.

The full understanding of the influence of both material and environmental variables on swelling requires comparative irradiations using both neutrons and charged particles. It also requires that the most definitive experiments involve the use of single-variable comparisons designed to isolate the individual contributions without the complication of significant synergisms.

Therefore, the first objective of this paper is to provide single-variable data sets on the compositional dependence of neutron-induced swelling and to make comparisons with comparable charged particle irradiation data. The second objective is to propose mechanisms which account for the observed features of the data. This paper concentrates on the dependence of swelling on nickel, chromium, silicon and phosphorus, each varied separately.

Experimental Details

The majority of the neutron data presented in this paper were derived from two experiments. These were the AAVII experiment' on the influence of nickel and chromium and the AAIX experiment which addressed nickel and chromium effects in addition to the influence of residual elements on the swelling of Fe-25Ni-15Cr.* The irradiation vehicles for AAVII and AAIX were identical and were placed in Row 2 of the Experimental Breeder Reactor II (EBR-II) at displacement rates which ranged from 0.6 to 1.1 x 10^{-6} dpa/sec.

Tne specimens at each of eight nominal irradiation temperatures between 400 and 650°C were irradiated in stainless steel subcapsules containing static sodium. The temperatures drifted somewhat during irradiation and varied ±5°C at 400°C and ±15°C at 650°C. The compositions of each alloy are given in Tables 1 and 2. Whereas The AAVII specimens were in the form of transmission electron microscopy disks (3 mm diameter by 0.25 mm thick) the AAIX specimens were in the form of rods (3 mm diameter by 12.7 mm long) with both specimen types in the solution annealed condition (1030°C/0.5 hr/air cool). The AAIX experiment involved only one round of irradiation to neutron fluences of $\leq 2.9 \times 10^{22}$ n/cm^2 (E > 0.1 MeV) while the AAVII experiment involved successive rounds of irradiation, removal from the subcapsule, measurement and reincapsulation, proceeding to fluences as high as 2.2×10^{23} n/cm^2 (E > 0.1 MeV). Some aspects of the AAVII data have been presented in an earlier paper.[1] Tne neutron spectrum in the EBR-II reactor produces approximately 5 dpa for each 1.0×10^{22} n/cm^2 (E > 0.1 MeV).

The radiation-induced changes in density in these studies range from densifications of <1% to ~70% swelling and were measured using an automated immersion density technique accurate to ±0.16% swelling. Data were retrieved from most but not all combinations of alloy, temperature and neutron fluence, a factor which in some cases can lead to misleading trends unless the data are viewed in their entirety. The results of the

Table 1. Composition* of the simple iron-nickel-chromium alloys employed in the AAVII and AAIX experiments

Designation	Fe	Ni	Cr	C	O	N
E18	3al+	12.1	15.1	0.005	0.016	0.0024
E90	Bal	15.7	15.6	0.013	---	---
E39	3al	20.3	7.5	0.004	0.016	0.0014
E26	Bal	20.1	11.8	0.002	0.016	0.0019
E19	3al	19.4	14.9	0.003	0.018	0.0015
E27	Bal	24.7	10.2	<0.001	0.012	0.0017
E20	Bal	21.3	15.3	0.003	0.014	0.0024
E33	Bal	25.8	14.8	0.005	0.023	0.0023
E21	Bal	29.6	15.3	0.004	0.017	0.0020
E37	Bal	35.5	7.5	0.002	0.016	0.0013
E22	Bal	34.5	15.1	0.003	0.017	0.0021
E38	Bal	35.2	20.0	0.004	0.017	0.0010
E25	Bal	35.1	21.7	0.004	0.015	0.0020
E23	Bal	45.3	15.0	0.002	0.014	0.0017
E24	Bal	75.1	14.6	0.001	0.0077	0.0011

*Weight percent
+Bal = balance, Si ≤ 0.02, P ≤0.005 for all alloys

Table 2. Composition* of residual element series alloys employed in the AAIX experiment

Designation	Fe	Ni	Cr	C	O	N	Residual Element
E103	Bal+	24.1	14.7	0.004	0.013	0.0019	0.013 P
E104	Bal	25.0	15.2	0.001	0.014	0.0018	0.055 P
E105	Bal	24.7	15.3	0.002	0.016	0.0019	0.10 P
E87	Bal	25.0	15.3	0.009	0.014	0.0022	0.14 Si
E30	Bal	25.2	15.7	0.006	0.008	0.0017	0.39 Si
E31	Bal	25.5	15.5	0.009	0.007	0.0020	0.70 Si
E88	Bal	25.10	15.2	0.008	0.010	0.0025	0.90 Si

*Weight percent
+Bal = balance

AAVII and AAIX experiments are also compared with those of two other neutron irradiation experiments in EBR-II designated AAXI* and AD-1**. The experimental details of these are published elsewhere.[1,2]

Results

The displacement rates varied over a factor of approximately two from the middle of the EBR-II core to the positions of the outermost subcapsules and each subcapsule was subject to unique minor thermal variations.

Thus single-variable comparisons of temperature dependence for a given composition cannot be made without introducing differences in displacement rate, dpa level and capsule thermal history. True single-variable comparisons of the influence of nickel and chromium can only be made within a given subcapsule at a specific neutron exposure. For each of the residual element series of alloys one must also factor out the possible influence of relatively small variations in nickel and chromium. Therefore the influence of the major solvent atoms will be examined prior to consideration of the minor solute influence. However, as we shall see later, the impact of some variables such as displacement rate and minor solvent differences is small enough to ignore.

Fig. 1 demonstrates that increases in nickel at ~15% chromium lead to a complex behavior involving three separate regimes. At the higher irradiation temperatures only two regimes are seen, one in which nickel additions lead to a reduction of swelling and another higher nickel regime where swelling increases with increasing nickel level. At lower irradiation temperatures, however, another regime appears at lower nickel levels to produce a plateau of composition-independent swelling. As shown in Fig. 1b, this plateau can be overlooked when there are gaps in the data matrix. As the irradiation temperature increases the transition regime between the low nickel and high nickel regimes shifts toward lower nickel levels and the plateau eventually disappears.

The range of chromium variation examined in the AAVII experiment was not as extensive as that of nickel and was studied only at *20, 25* and 35% nickel. Fig. *2* shows that at 20% nickel there appears to be a similar plateau with chromium content at low temperatures. This plateau disappears as the temperature is raised or as the nickel level is increased to *25%.* As shown in Fig. 3 the plateau is not visible at any temperature when the nickel level is increased to 35%.

Whereas increases in nickel tend to strongly decrease swelling for iron-rich alloys, chromium acts to increase swelling. These opposing trends are confirmed by the results of another experiment designated AD-1 in which five of these alloys were irradiated in the form of tensile specimens.[2] Fig. 4 shows a comparison of the AD-1 and AAVII data. Although the temperatures and fluences of the two experiments are not identical, the results are quite compatible, particularly when viewed in their entirety or when plotted vs. neutron fluence for a given composition, as shown in Fig. *5* for Fe-25Ni-15Cr. The plateau regime is not visible in either the AD-1 data or the partial set of AAVII data shown in Fig. 4 because only nickel levels greater than *25%* were included in AD-1. Fig. *5* also includes some limited swelling data for Fe-25Ni-15Cr irradiated in the AAXI experiment,[3] which also utilized disk specimens. Once again there is excellent agreement in spite of the fact that the neutron fluences and irradiation temperatures of AAXI did not match those of the other experiments.

Fig. *5* also shows that at any given fluence level there must be a temperature regime over which there is a temperature-independent plateau in the swelling of Fe-25Ni-15Cr since all data below 510°C falls on a single line with neutron fluence. Similar plateaus with varying ranges of temperature were observed for most alloys in the AAVII experiment.[1] Figs. *5* through 7 demonstrate that the primary influence of composition and temperature resides in the duration of the transient regime of swelling and that the post-transient steady-state swelling rate appears to be ~1%/dpa, independent of the temperature, composition and displacement rate (over the narrow range studied). Similar curves for the other alloys in AAVII can be found in reference 1. Since there do not appear to be strong effects of displacement rate on either the transient or steady-state regimes of these alloys, comparisons of compositional influence can be made between data from various subcapsules, at least for the simple alloys used in the AAXII experiment. Displacement rate effects on the transient regime of swelling are known to be quite strong in solute-modified alloys, however[4,5] so comparison of data between subcapsules was not attempted for the AAIX experiment.

Residual Element Effects

Fig. 8 shows that the effect of silicon observed in AAIX is also complex. Silicon additions first cause a sharp increase in swelling followed by a decrease thereafter. No data are shown for irradiation at 593 and 649°C since swelling at all silicon levels is <0.10%, within the uncertainty of the measurement technique. The first sharp increase in swelling with silicon has not previously been reported for neutron irradiation.

*The AA series of experiments were conducted by the U.S. Breeder Reactor Program of the U.S. Department of Energy.

**The AD-1 experiment was conducted by the U.S. Fusion Materials Program of the U.S. Department of Energy.

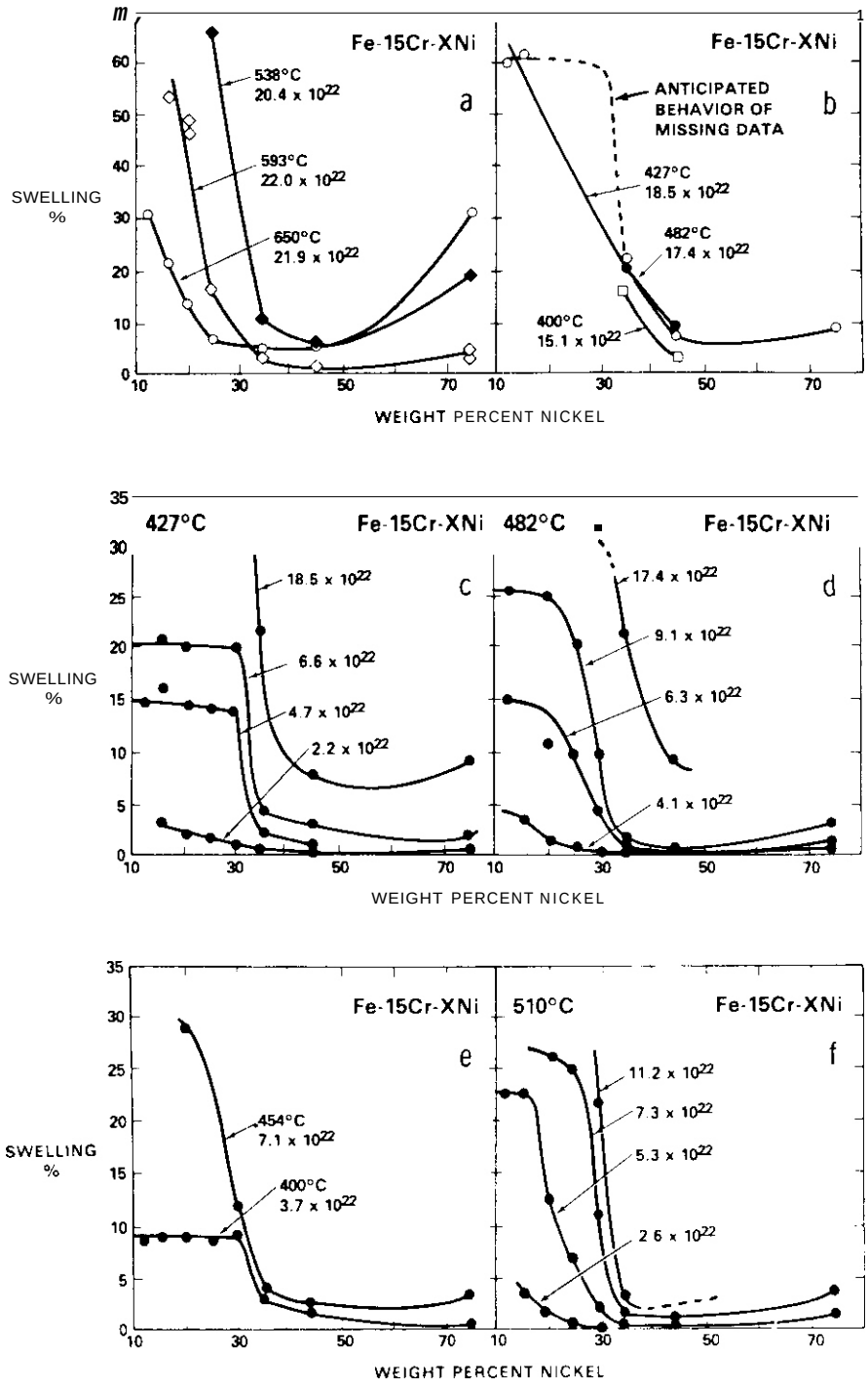


Fig. 1. The nickel dependence of simple Fe-15Cr-XNi alloys irradiated in the AAVII and AAIX experiments in EBR-II. Lines are drawn only through data points sharing a common environmental history. Note that at 427°C the gap in the data of 1b at intermediate nickel levels may obscure a plateau such as those seen at lower fluence in 1c.

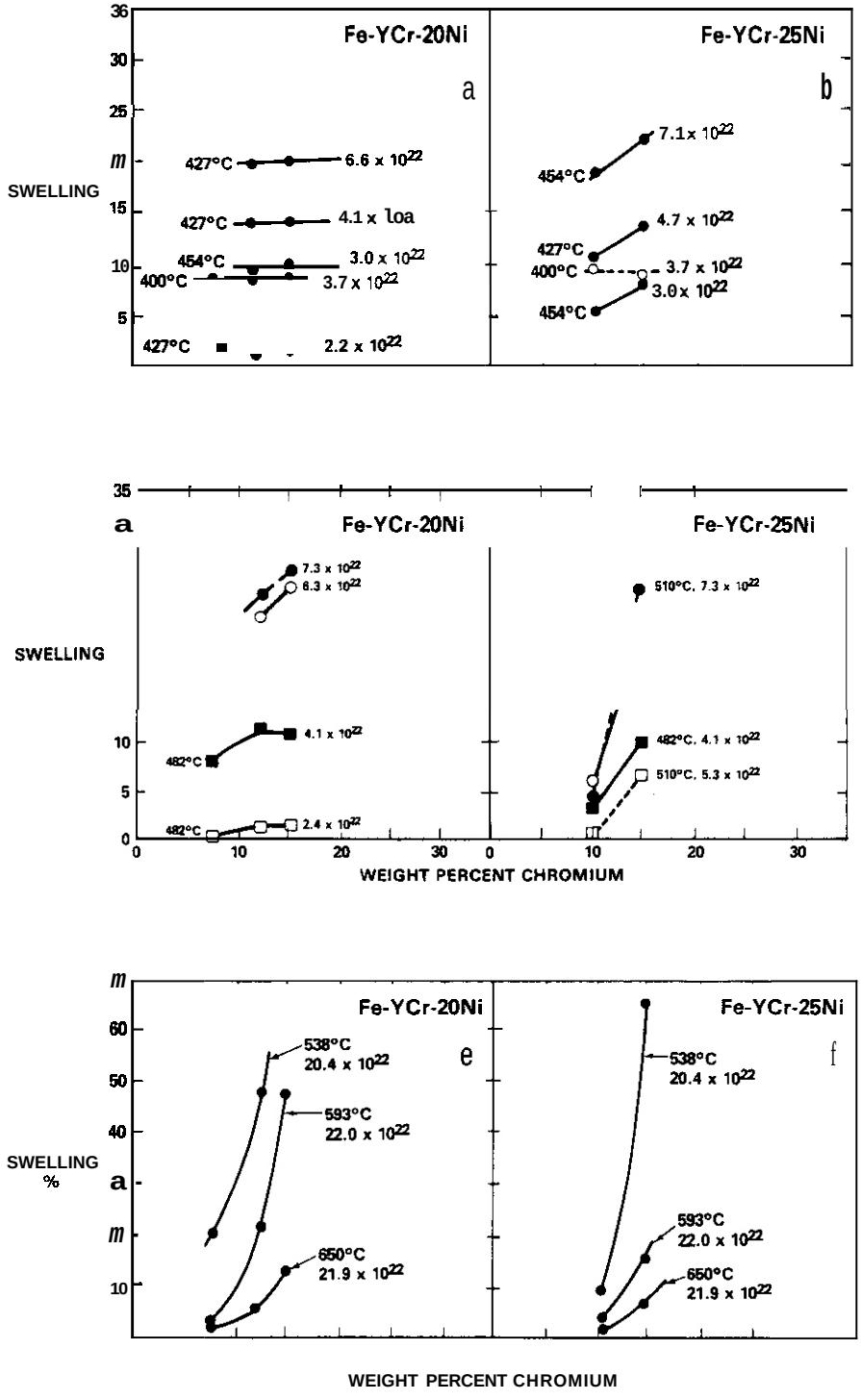


Fig. 2. The dependence of neutron-induced swelling on chromium content for Fe-Cr-Ni alloys containing 20 and 25% nickel.

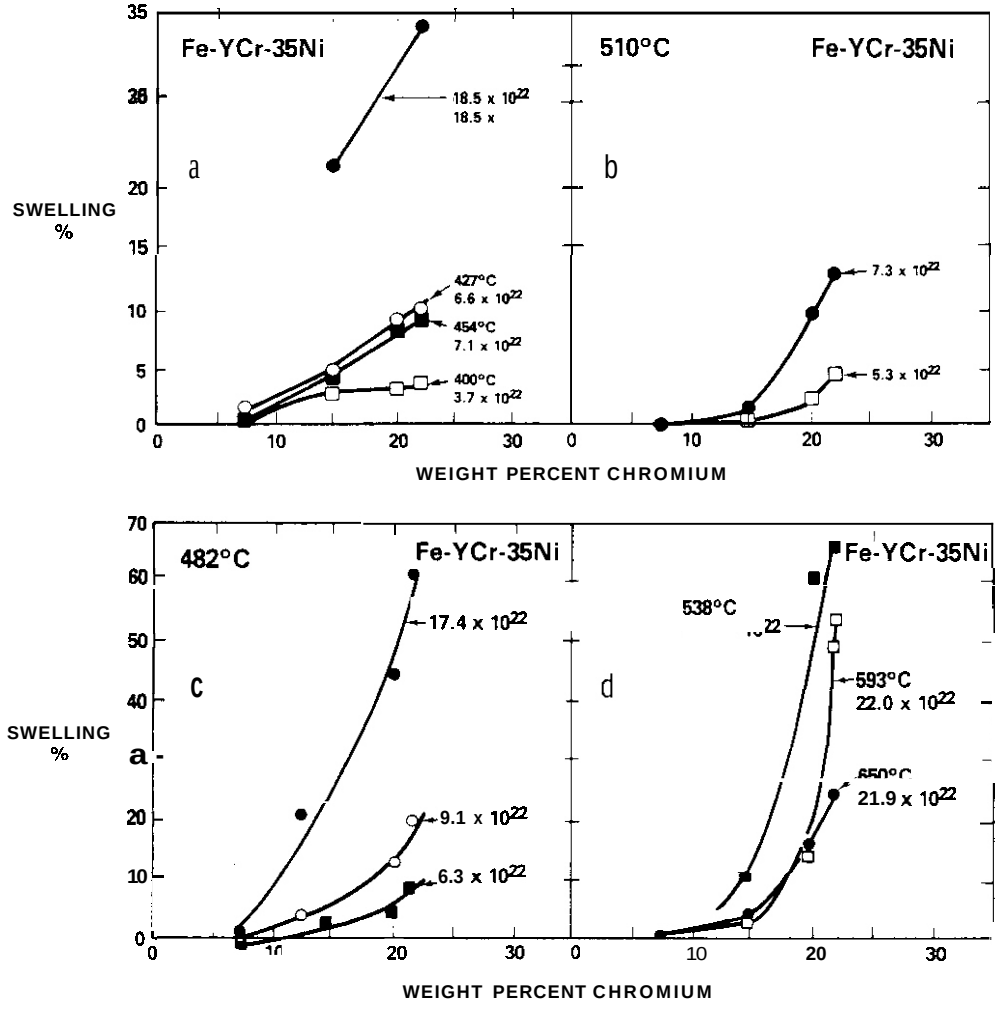


Fig. 3. The dependence of neutron-induced swelling on chromium content for Fe-Cr-Ni alloys containing 35% nickel

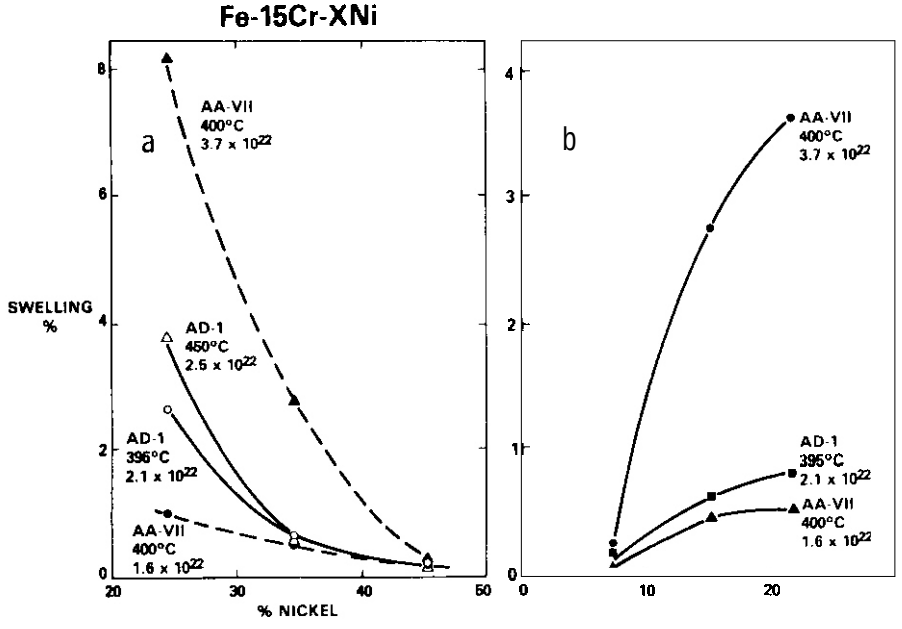


Fig. 4. Comparison of swelling of Fe-Ni-Cr alloys irradiated in the AAVII and AD-1 experiments,',' showing consistency of swelling trends with temperature, fluence and composition. The alloys in (a) are at 15% chromium and those in (b) are at 35% nickel.

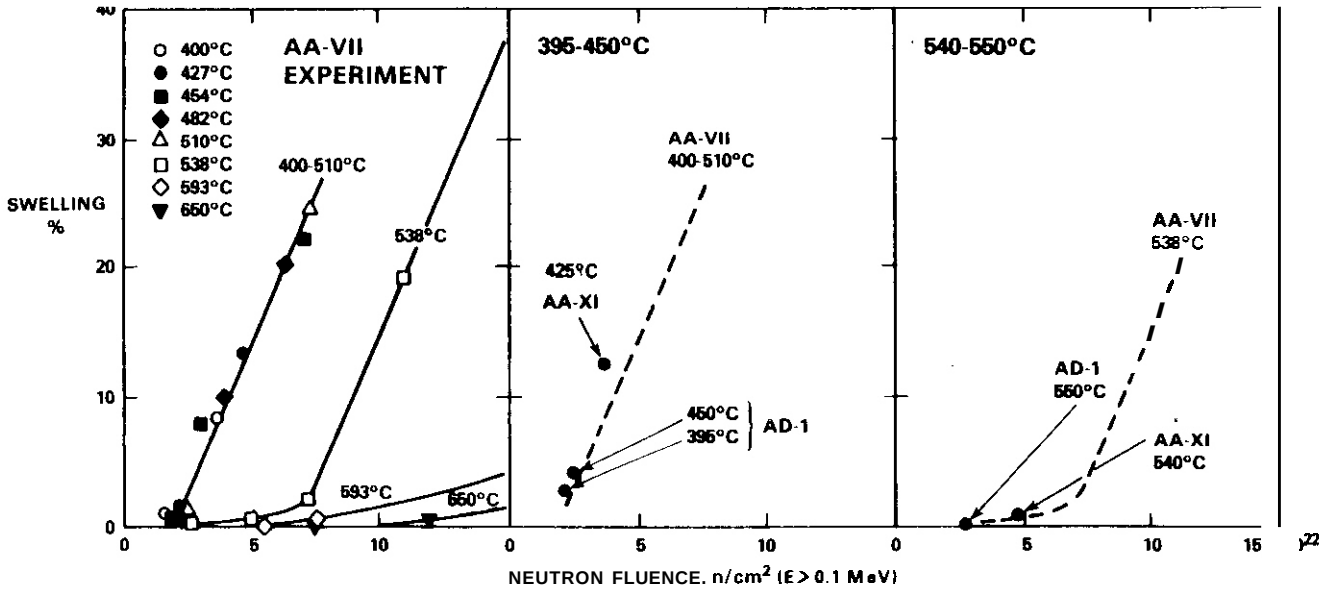


fig. 5. Comparison of Fe-25Ni-15Cr swelling behavior in three separate EBR-II irradiations experiments. Note that the five lowest irradiation temperatures of AAVII produce the same swelling behavior with fluence, suggesting that a plateau with temperature also exists.

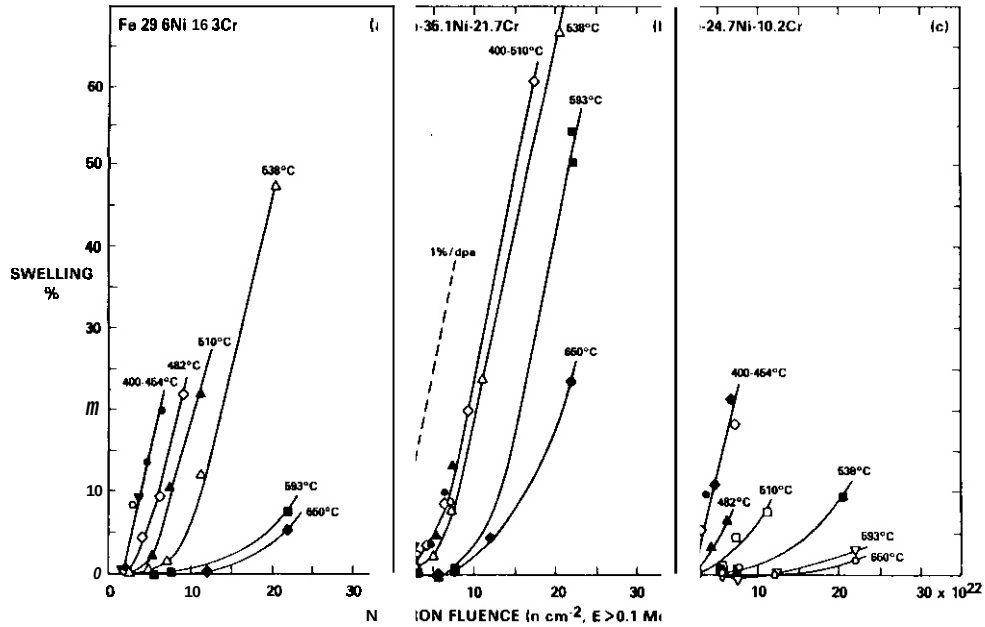


Fig. 6. Swelling of various Fe-Cr-Ni alloys, showing temperature-independent regime of swelling at relatively low temperatures, followed by a progressive extension of the transient regime with increased temoerature.

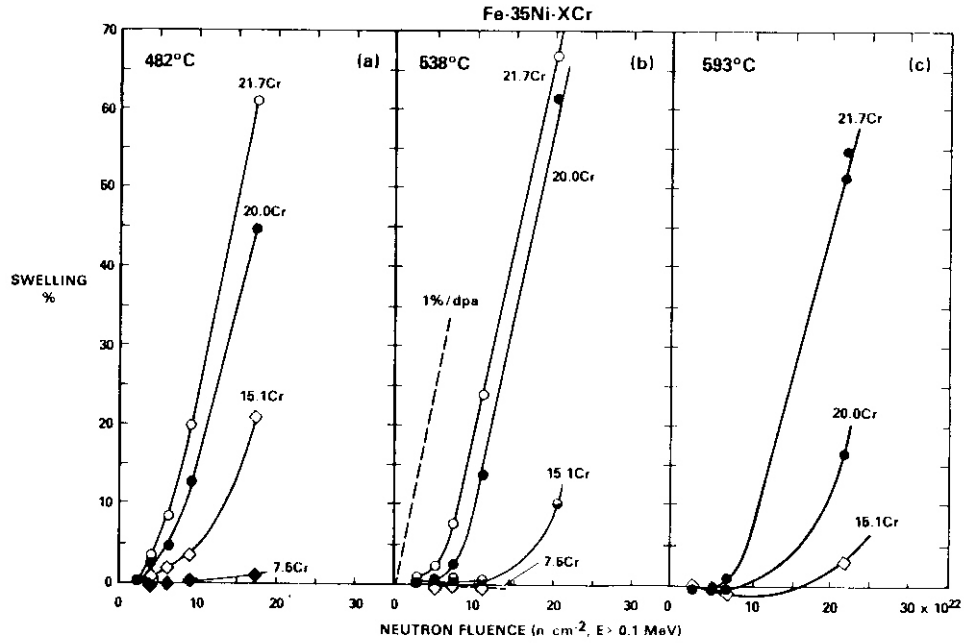


Fig. 7. Swelling of Fe-35Ni-XCr at three temperatures, showing that decreases in chromium cause an extension of the transient regime analogous to that caused by increases in temperature. Increases in nickel also lead to the same behavior.[1]

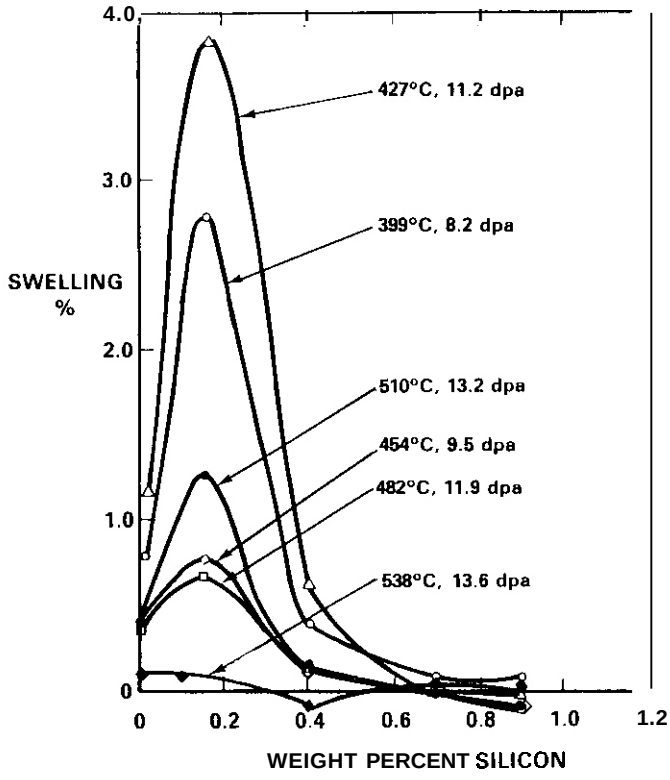


Fig. 8. Influence of silicon on neutron-induced swelling of Fe-25Ni-15Cr at various combinations of temperature and neutron fluence.

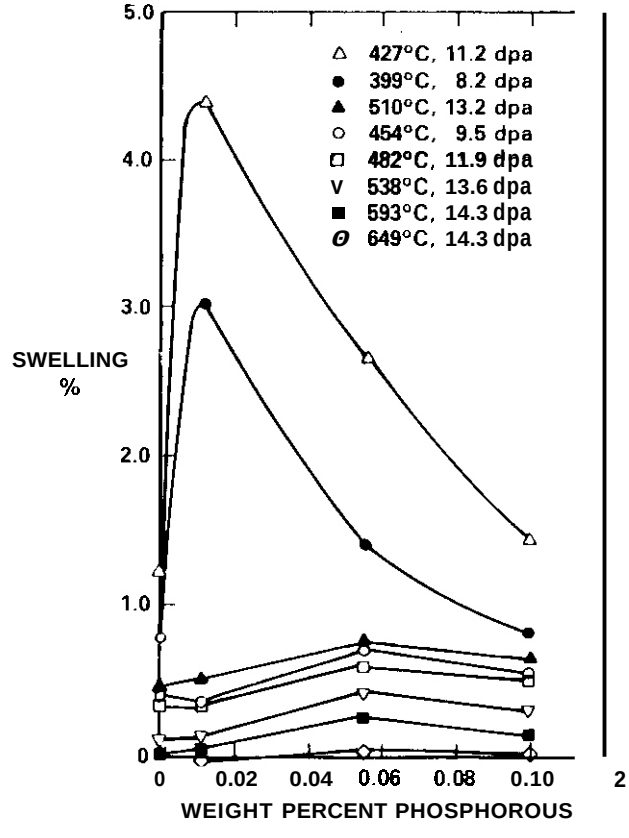


Fig. 9. Influence of phosphorus on neutron-induced swelling of Fe-25Ni-15Cr at various combinations of temperature and neutron fluence.

Fig. 9 shows that a similar sharp increase in swelling of Fe-25Ni-15Cr occurs at relatively low temperatures when phosphorus is first increased. This behavior also has not been reported previously for neutron irradiation. A reduction in swelling ensues with increasing phosphorus levels, however, similar to the behavior observed with silicon additions. At higher temperatures the swelling is lower as one would expect from reference 1 and does not show the complex behavior seen at 399 and 427°C. The swelling at a given phosphorus level decreases with increasing temperature and increases with increasing fluence as would be expected. However, the possibility exists that a portion of the observed decrease in density in the phosphorus-bearing alloys at these high temperatures may not be due only to void swelling but may be the result of phase instabilities associated with precipitation of a-phase and phosphides.',' Phosphorus is known to decrease neutron-induced swelling at higher temperatures in a variety of solute-modified AISI 316 steels by extending the duration of the transient regime that precedes the onset of steady-state swelling.[6,8]

Discussion

Possible Synergisms

While the separate effects of nickel and chromium are easily demonstrated, there are minor variations of these two elements within each of the series of residual element (solute-modified) alloys. To insure that the trends seen in the phosphorus or silicon series are not an artifact of these solvent differences, the swelling behavior of two ternary alloys spanning the greatest compositional gap and the greatest potential swelling difference were compared, as shown in Fig. 10. Note that this largest possible difference in swelling is inadequate to account for any of the features shown in Figs. 7 and 8. For instance, the 0.2% difference in swelling at both 399 and 427°C due to differences in chromium and nickel is much smaller than the 2 to 3% differences attributed to low levels of phosphorus and silicon.

While the small differences in nickel and chromium do not mask the effects of silicon and phosphorus we must conclude that small unmeasured differences in silicon and/or phosphorus could easily obscure the underlying solvent element behavior in other experiments, particularly at low levels of solute.

Ion Bombardment Results: Nickel and Chromium

The Fe-Ni-Cr studies of Johnston and coworker~~,and Bates and Johnston" utilized 5 MeV Ni^{+} ions and were conducted at 575, 625, 675 and 725°C with peak swelling at 117 dpa attained at 675°C. These studies demonstrated some of the features observed in the neutron data, namely the opposing effects of chromium and nickel additions and the minimum in swelling at intermediate nickel levels. These studies also demonstrated that the primary effect of increased nickel in iron-rich alloys was to prolong the duration of the transient regime that precedes steady-state swelling, a conclusion also in agreement with the results of the neutron studies.

However, these and other ion studies did not forecast the emergence of the plateaus with variation of either nickel, chromium or temperature that were observed in the neutron data. Ion studies also did not predict a steady-state swelling rate that was insensitive to temperature and other variables. These deficiencies are thought to be primarily the consequence of the tradeoffs involved in the simulation technique. These involve the strong temperature-dependent influence of the injected interstitial and the specimen surface.[12-16] The steep displacement gradients inherent in both ion and electron irradiations also lead to a significant depletion of nickel in the region where the peak displacement level occurs,[17-20] causing an additional temperature-dependent distortion of the swelling behavior relative to that of neutron irradiation. Consequently, as shown in Figs. 11 and 12, the ion-induced swelling of Fe-Ni-Cr alloys at all compositions studied was found to be Peaked with temoerature., and does not exhibit a plateau behavior under any conditions. A similar type of behavior was observed by Gessel and Rowcliffe" 'in ion irradiations of Fe-20Ni-7.5Cr and in Fe-12Ni-20Cr by Sethi and Okamoto.[18]

Ion Bombardment: Solute Effects

No comparable ion studies have been conducted at the 25% nickel level employed in the neutron experiments. However, comparable data are available for Fe-20Ni-15Cr[11] and Fe-20Ni-7.5Cr[21] as a function of silicon. Limited data on phosphorus effects are available for Fe-20Ni-15Cr[11] and Fe-15Ni-13.7Cr.[22]

Figs. 12 and 13 show that above 600°C silicon always acts to reduce swelling, but at 575°C silicon additions first increase and then decrease swelling, similar to the behavior observed at temperatures below 500°C in the neutron studies of Fig. 8. Fig. 13 also shows that the swelling behavior of the Fe-20Ni-15Cr alloy at 575°C is mirrored in the void density behavior, suggesting that the possibly complex role or roles played by silicon affect primarily the void nucleation process. Sethi and Okamoto also observed that silicon increased the swelling of Fe-12Ni-20Cr below 575°C and decreased swelling above 575°C, with the primary influence reflected in the void density.[18]

As shown in Fig. 14 the swelling of Fe-20Ni-15Cr at 675°C actually increases with the addition of 0.05 wt% phosphorus." If the ion data for Fe-15Ni-13.7Cr in Fig. 14 are normalized to the same dpa level," one would also conclude that the addition of 0.05% phosphorus prohably increased the swelling somewhat. These

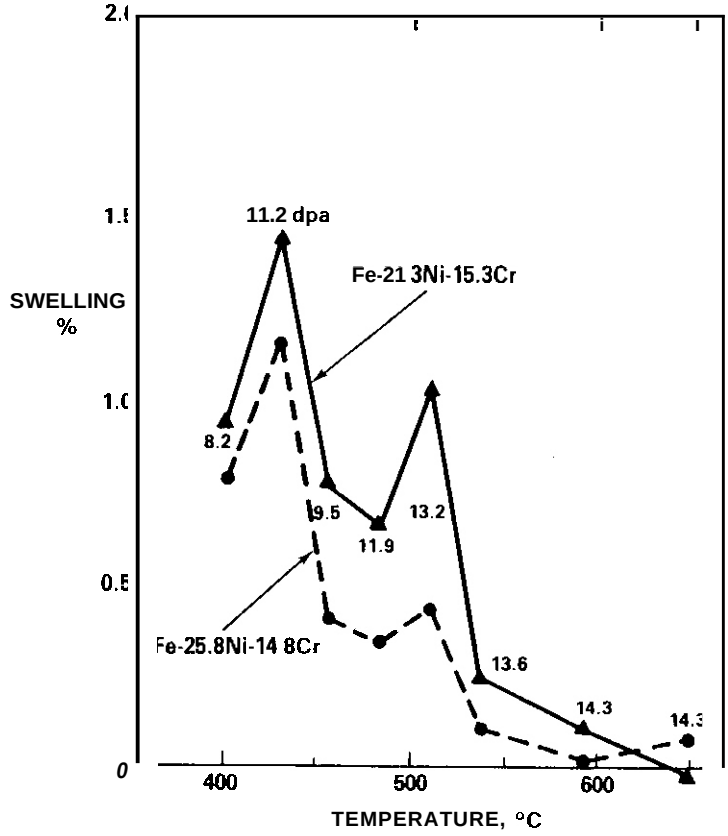


Fig. 10. Effect of relatively minor variations in nickel and chromium on the swelling of Fe-Ni-Cr alloys. These two alloys (E20 and E33) were chosen to span the maximum variation seen in the residual element alloy series. The displacement level for each irradiation temperature is shown beside the individual pairs of data.

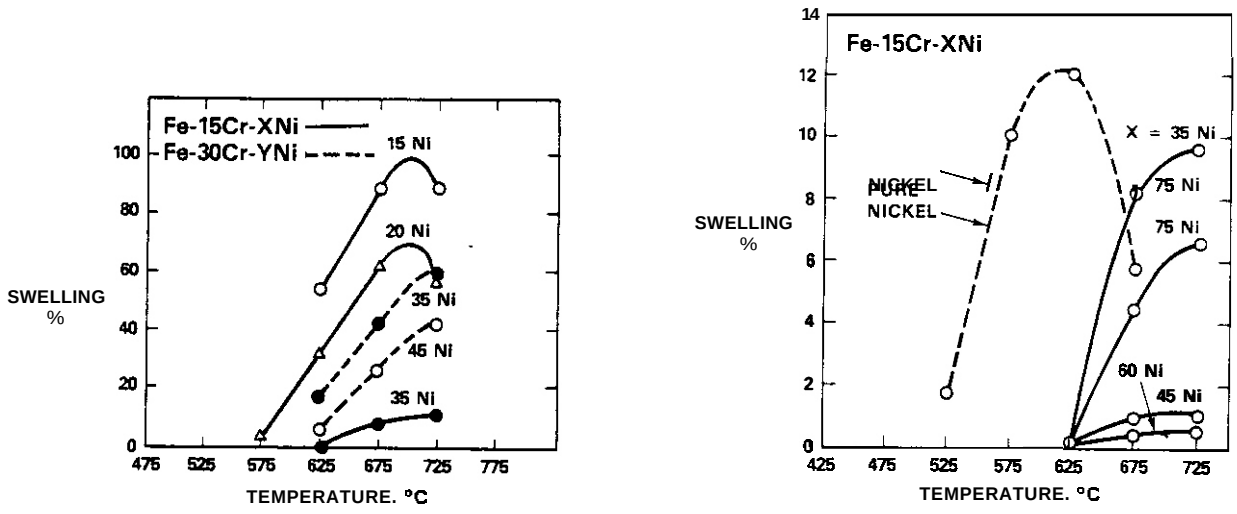


Fig. 11. Effect of temperature, nickel and chromium content on ion-induced swelling of Fe-Ni-Cr alloys at 117 dpa,[8] showing peaked swelling with temperature. There is an absence of swelling plateaus with either composition or temperature.

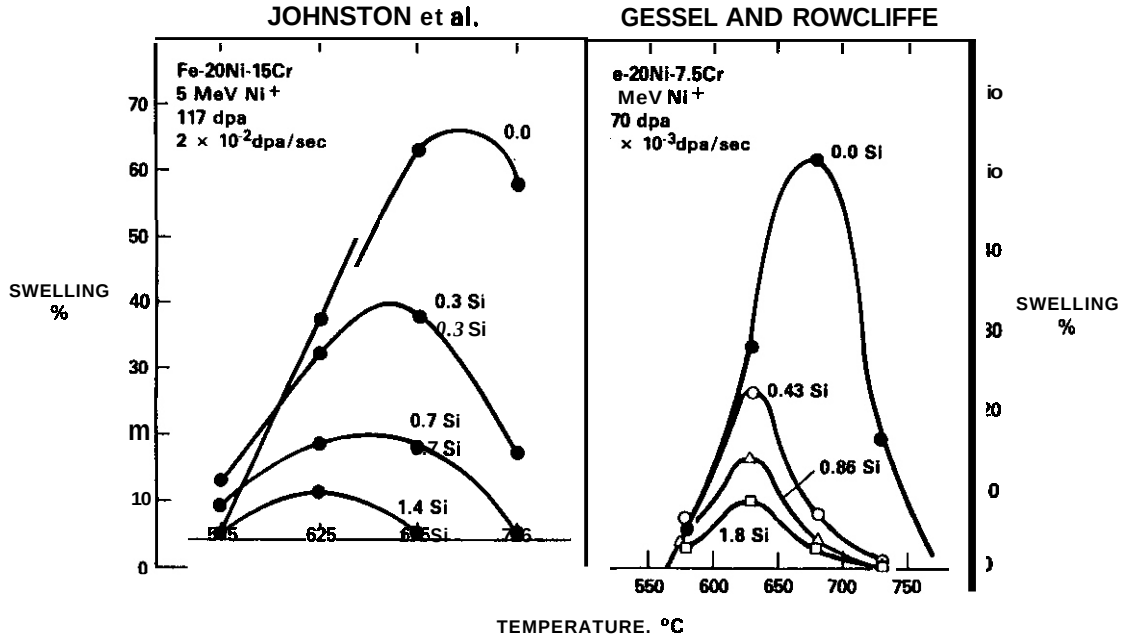


Fig. 12. Influence of silicon on ion-induced swelling of Fe-Ni-Cr alloys.[9,11,21]

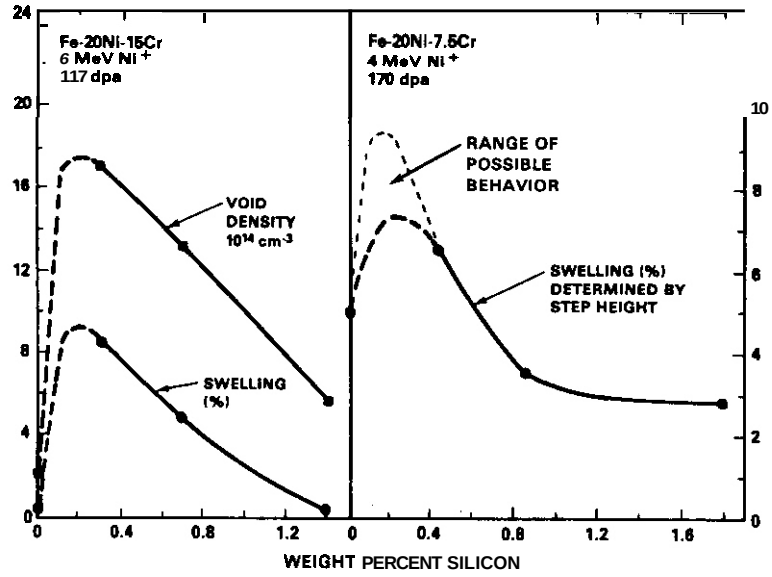


Fig. 13. Influence of silicon on ion-induced swelling (replotted from Fig. 12) and void density. The void density data are previously unpublished and were supplied by T. Lauritzen of General Electric Company.

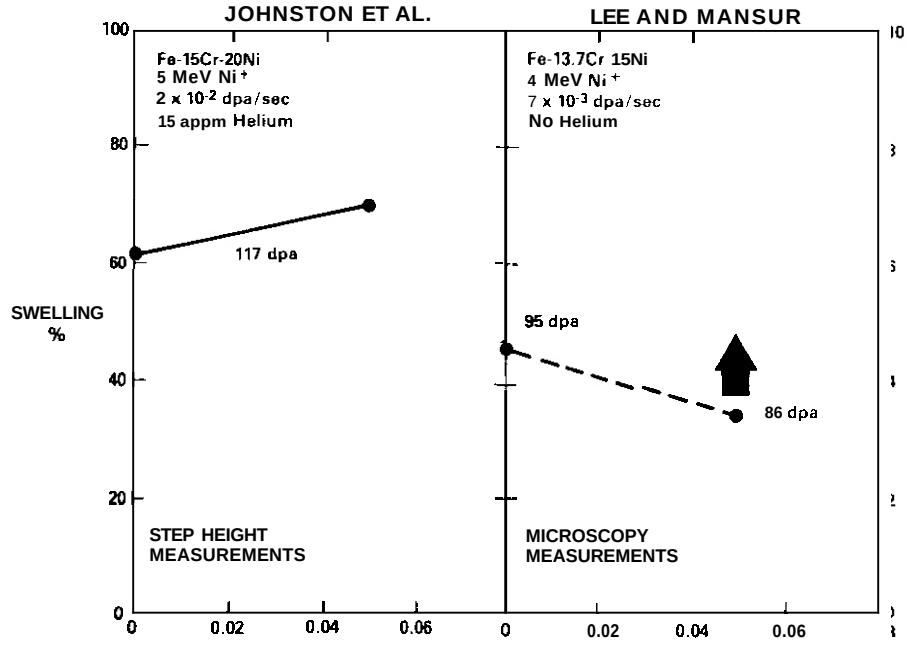


Fig. 14. Influence of phosphorus on ion-induced swelling of Fe-Ni-Cr alloys.[11,22] The arrow indicates expected movement if the 86 dpa datum is normalized to the 95 dpa datum.

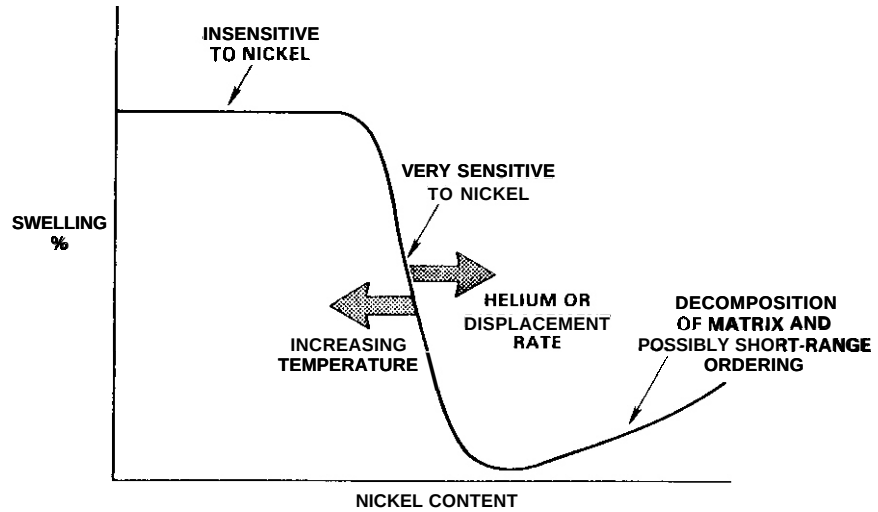


Fig. 15. Schematic behavior of the three regimes of the composition dependence of Fe-Ni-Cr austenitic alloys. The influence of other radiation variables on the relative location of the intermediate regime is also shown.

data, though not as complete as those of the silicon studies, could be consistent with the trend of the neutron data shown in Fig. 9 if a swelling peak existed between 0 and 0.05% phosphorus. This proposal could easily be examined by additional ion experiments conducted at intermediate phosphorus levels.

A Nickel-Eased Model

There are two ways to visualize the results of these studies, both of which are based on the same principles. First, consider the following scenario in which a series of side-by-side irradiations are conducted on a set of Fe-Ni-Cr alloys, some modified with various solutes. If the fluence attained is sufficient to place all alloys well above the minimum incubation period,[4,23,24] one would expect the solute-free binary Fe-Ni alloys at a given temperature and fluence to exhibit the three regime behavior shown in Fig. 15. The composition-insensitive regime at low nickel would be separated from the high nickel regime by an intermediate transient regime representing the proposed influence of nickel on void nucleation via its effect in increasing D_V^{eff}, the effective vacancy diffusion coefficient.[23,25] The dependence of both swelling and void density of simple ternary alloys with nickel content has been demonstrated in several other papers.[2,26,27]

Garner and Wolfer have provided a rate-theory model that explains how the post-transient swelling rate can be independent of material and environmental variables.[**] Several recent studies have shown that a factor of two increase in vacancy diffusivity can cause an extension of the transient regime of swelling and thus cause the sharp drop in void density and swelling associated with an increase in the nickel level from 15 to 35%.[25,26] The increased diffusivity arises from the compositional dependence of D_V^0, the pre-exponential diffusion coefficient, rather than that of the activation energies for vacancy formation or migration.[25,28-30]

On the basis of diffusivity increases alone one would except an increased difficulty of void nucleation to persist until ~75% nickel. However, above 40% nickel the alloy begins to decompose during irradiation into relatively large micro-volumes of nickel-poor chromium-rich regions (which nucleate voids more easily), separated by comparable volumes of nickel-rich chromium-poor regions.[27,31-33] This tendency toward decomposition is thought to be the consequence of an inherent but extremely sluggish tendency of Fe-Ni-Cr alloys in the invar compositional range to decompose in a spinodal-like manner.[31-34] The decomposition is accelerated primarily by radiation-enhanced diffusion and secondarily by the segregation of nickel at radiation-produced microstructural sinks.

At the relatively high temperatures characteristic of the ion irradiation studies[9,10] the interaction of composition-dependent changes in diffusivity and the ion-induced spinodal-like decomposition[27,32] lead to iso-swelling contours that are remarkably similar to measured interdiffusion coefficients for Fe-Ni-Cr alloys as shown in Fig. 16.

Another important point to recognize is that the intermediate transient regime will shift up or down-scale in nickel content with any variable that affects void nucleation. This shift can be large enough to erase either the low nickel plateau or the high nickel upswing in swelling. Fig. la, for instance, demonstrates the complete erasure of the plateau regime at higher irradiation temperatures. Rotman and Oimitrov note that the strong influence of nickel to reduce the swelling of electron irradiated Fe-Ni-Cr alloys disappeared when 70 appm of helium were preinjected,[35] thus demonstrating the shift of the intermediate regime to higher nickel levels. Thus only the plateau regime was observed after helium additions, erasing even the intermediate nickel regime in this experiment.

Rotman and coworkers also note that their results are strongly influenced by the radial (and axial) redistribution of nickel induced in the irradiated volume by the steep displacement gradients.[20] Similar beam-induced distortions in the response of swelling of Fe-Ni-Cr alloys to nickel content have been observed by Walters[36] and Muroga and coworkers.[19] Compositional redistributions have also been observed in proton and heavy ion irradiations.[17,18,37,38].

Since there are essentially no displacement gradients in neutron irradiations the bulk composition is unchanged, but we would still expect the intermediate transient regime to shift to higher nickel contents with increases in displacement rate and/or helium level since both facilitate void nucleation.[26] Increases in chromium level also shift the intermediate regime toward higher nickels due to chromium's role in decreasing the effective vacancy diffusion coefficient.[25]

The Role of Solute Elements in the Nickel-Based Model

For many common solute elements, however, the intermediate regime is shifted toward lower nickel levels, via their often very strong effects on the effective vacancy diffusion coefficient[25,39,40] and/or the vacancy formation energy.[6,8]. Silicon is thought to operate primarily by the former mechanism and phosphorus by the latter. In effect, large increases in nickel, moderate increases in silicon and small increases in phosphorus all lead to reduced void nucleation rates via their effect on reducing the vacancy supersaturation, particularly at temperatures where void nucleation in the base ternary alloy is becoming increasingly more difficult.

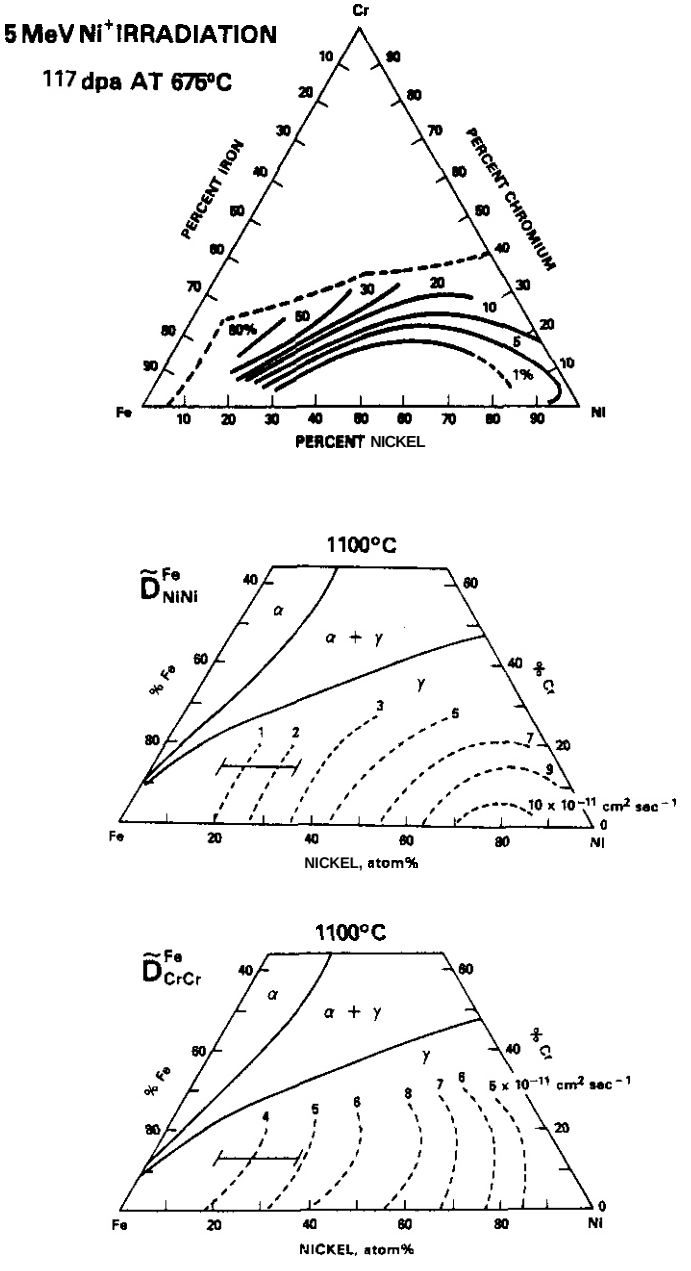


Fig. 16. Comparison of the iso-swelling contours constructed by Johnston and coworkers[5] and the inter-diffusion coefficients of Ouh and Dayananda.[**] Note that increasing the nickel content from 15 to 35% at 15% chromium yields a 28% increase in D^{Fe}_{CrCr} and ~300% increase in D^{Fe}_{NiNi}, corresponding to roughly a factor of two increase in the effective vacancy diffusion coefficient D^{eff}_{V}.

A Temperature-Based Model

We noted earlier that there were two ways to visualize the effects of composition on swelling. The effects of various elements and environmental variables on swelling can be better visualized in terms of the temperature dependence of void nucleation. As schematically shown in Fig. 17, calculations of void nucleation typically show one "low temperature" plateau regime in which the nucleation rate is insensitive to temperature and another "high temperature" regime in which the nucleation rate falls orders of magnitude over a relatively small range of increasing temperature.[8,39,40] If one visualizes the nucleation behavior in terms of r_c^*, the critical radius for bubble-to-void conversion, one sees a low temperature plateau regime followed by a sharp increase in r_c^* above a temperature which is dependent on a variety of factors such as D_v, displacement rate and helium content.[26,41]

The swelling plateau and the subsequent decline in swelling with temperature observed in neutron irradiations of Fe-Ni-Cr alloys are thought to represent the consequences of these two regimes of void nucleation. During charged particle irradiation each of these regimes is distorted (relative to the neutron-induced behavior) but one sometimes sees void density profiles similar to that of Fig. 17, providing that voids nucleate without too much difficulty at lower temperatures and that the helium levels are sufficient to facilitate void nucleation but not large enough to dominate the nucleation behavior. An example of such behavior is shown in Fig. 18.

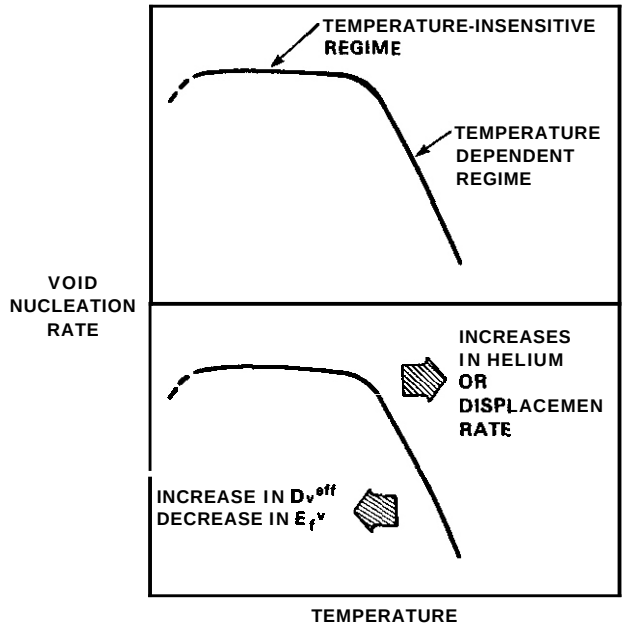


Fig. 17. Schematic representation of the two major temperature regimes of void nucleation in simple Fe-Cr-Ni alloys. The influence of some important variables on the shift of the "high temperature" regime is also shown. D_v^{eff} is the effective vacancy diffusion coefficient and E_f^v is the vacancy formation energy.

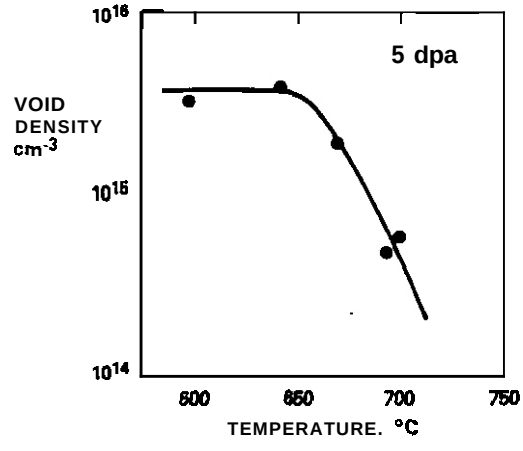


Fig. 18. Void densities observed in 1.0 MeV electron irradiation of FE-25Ni-15Cr containing 6 appm preinjected helium, showing low-temperature plateau of void density.(Unpublished data of R. W. Powell and F. A. Garner,Westinghouse Hanford Company.)

Fig. 19 demonstrates the proposed relationship between the observed duration of the transient regime of swelling and the void nucleation rate as a function of temperature and nickel content. Note that increases in nickel content represent a shift of the "high-temperature regime" toward lower temperatures. This is analogous to the "temperature shift" associated with changes in displacement rate.[7] In effect an increase in nickel level produces the same effect as does an increase in temperature. This is exactly what one would expect if nickel additions lead to an increase in the vacancy diffusivity. Fig. 20 shows that exactly this kind of behavior was observed by Hishinuma in the void density of a series of electron irradiated Fe-17.1Cr-XNi alloys.[42,43]

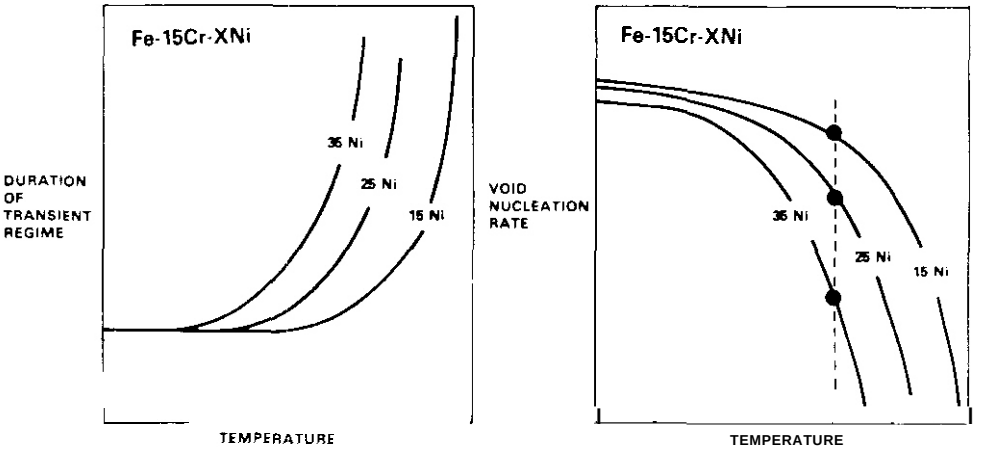


Fig. 19. Schematic representation of the composition dependence of the transient regime of swelling (from ref. 1) and the void nucleation rate. Note that increases in nickel are similar to increases in temperature in that both act to decrease void nucleation sharply in the "high temperature" regime.

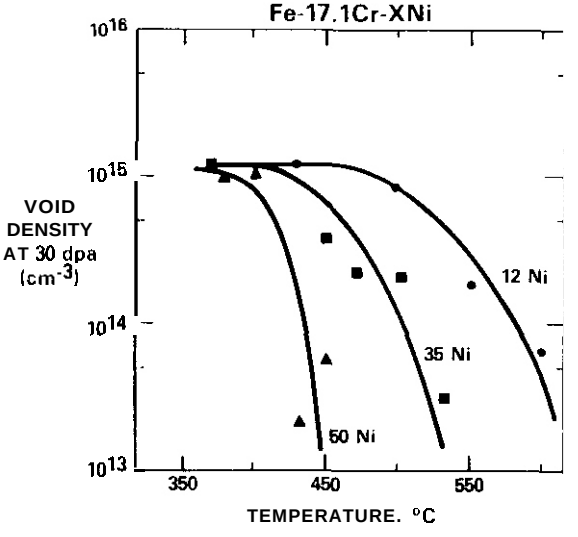


Fig. 20. Effect of nickel on void density in Fe-17.1Cr-XNi alloys irradiated with 1.0 MeV electrons to 30 dpa, as observed by Hishinuma.[43] Note shift of "high temperature" regime toward lower temperatures with increasing nickel content.

The interaction between beam-induced nickel redistribution and the influence of surfaces and higher displacement rates apparently tends to suppress the high nickel regime of swelling in electron irradiation. The studies of Rotman,[20] Walters,[36] Hishinuma[42,43] and Levy[44] do not show an increase in swelling above some nickel level. However, none of these studies exceeded nickel levels of 75, 60, 50 and 50% respectively. Note in Fig. 1 that the upswing in neutron-induced swelling often does not occur until well above 50-60% nickel. In a study by Korenko employing nickel levels of 20, 25, 35 and 85%, an upswing was observed, however, as shown in Fig. 21.

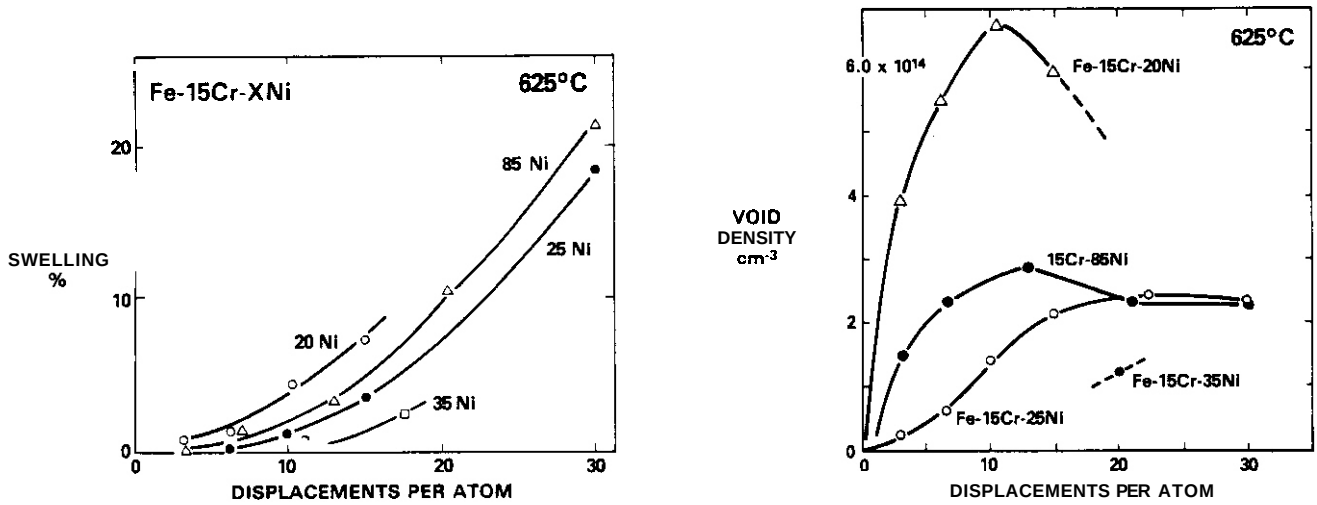


Fig. 21. Effect of nickel content on the swelling induced by 1.0 MeV electrons in annealed Fe-15Cr-XNi alloys at 625°C. (Unpublished data courtesy of M. K. Korenko, Westinghouse Hanford Company). Note that the primary influence of nickel resides in the duration of the transient regime via its effect on void nucleation.

Solute Effects in the Temperature-Based Model

Silicon is much more effective per atom than nickel in causing D_V to increase and thereby reducing void nucleation.[25,39,40] At any given temperature void nucleation is delayed by silicon additions,[9,45-47] but the downward shift of the "high temperature" regime is best demonstrated by studies conducted at more than one temperature, as shown in Figs. 22 and 23. Note that small increases in silicon exert their strongest influence at high temperature as predicted in earlier papers,[25,39,40] and that increases in silicon have the same effect as increases in temperature. In both cases there is a comparable increase in vacancy diffusivity.

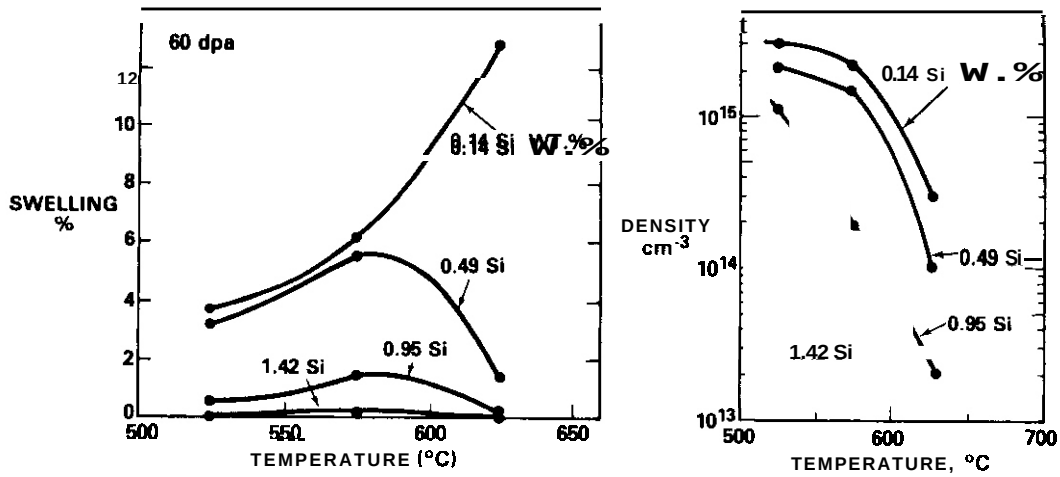


Fig. 22. (a) Effect of silicon on the swelling of 20% cold-worked Fe-12Cr-15Ni irradiated with 46.5 Mev Ni^+ ions to 60 dpa, as observed by Mazey, Harries and Hudson.[*] (b) The "high-temperature" regime of void density is shifted toward lower temperatures by silicon additions.

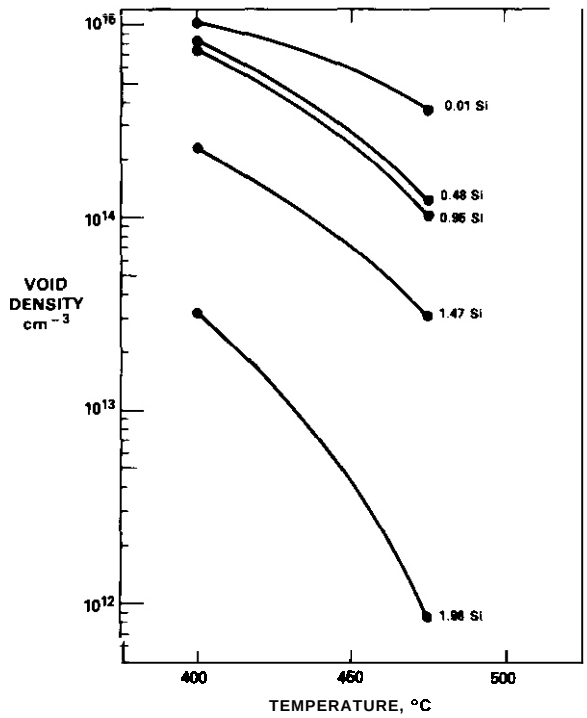


Fig. 23. Effect of silicon on void density in annealed AISI 316 during neutron irradiation as observed by Brager and Garner.[46]

It should be noted that in neutron irradiations it is possible with silicon additions to see more than two regimes of swelling. Brager and Garner[46] have shown that for alloys with relatively low nickel Content and relatively high silicon levels, the co-precipitation of nickel and silicon can cause a third regime of increased swelling arising from the removal of these elements from solution. If the silicon levels are very high, the removal of nickel can also lead to ferrite formation and the rate of swelling will decrease. Thus four regimes of swelling are possible in silicon-doped alloys.

An additional consideration for simulation studies is that silicon changes the rate of heam-induced nickel redistribution in ion irradiation studies,[**] leading to a synergism not operating in the neutron irradiation studies.

Whereas nickel and silicon increase the pre-exponential term D_V^0 of the vacancy diffusion coefficient and thereby reduce the concentration C_V of vacancies during irradiation, phosphorus is thought to strongly increase C_{VO}, the equilibrium concentration of thermal vacancies.[6,8] A change in nickel level thus exerts roughly the same percentage increase in vacancy diffusivity (and decrease in vacancy super-saturation C_V/C_{VO}) at all temperatures and displacement rates. Silicon behaves in a similar manner, but is more effective than nickel on a per-atom basis. Phosphorus, however, exerts an even stronger influence per atom, hut operates primarily on the thermal vacancy concentration. Thus the supersaturation of vacancies is reduced by phosphorus from the "bottom rather than the top." This is the consequence of the very large binding energy (0.4 eV) of phosphorus with vacancies, as measured in Fe-14Ni-18Cr by position annihilation.[48,49] In effect this represents a very large decrease in the vacancy formation energy.

The influence of phosphorus increases only until its solubility limit is reached,[50] however, and its solubility limit in Fe-Ni alloys falls strongly as a function of declining temperature.' In one respect, however, the influence of phosphorus is quite different from that of silicon and nickel. Below the solubility limit the effect is roughly proportional to the percentage of solubility and not the total phosphorus level. Therefore, a given level of phosphorus can exert different effects on the vacancy supersaturation at different temperatures. The maximum effect of phosphorus at any temperature is to reduce the supersaturation by almost exactly an order of magnitude, due to a corresponding increase in diffusivity measured at a variety of temperatures, including those of the void temperature regime.[50,51]

AS shown in Fig. 24, Dean and Goldstein[51] used the STEM microanalysis technique to measure at relatively low temperatures the increased diffusivity of Fe-Ni binaries due to phosphorus. As shown in Fig. 25 much larger amounts of phosphorus are necessary to increase the diffusivity at higher temperature but the maximum influence is still limited to approximately one order of magnitude.

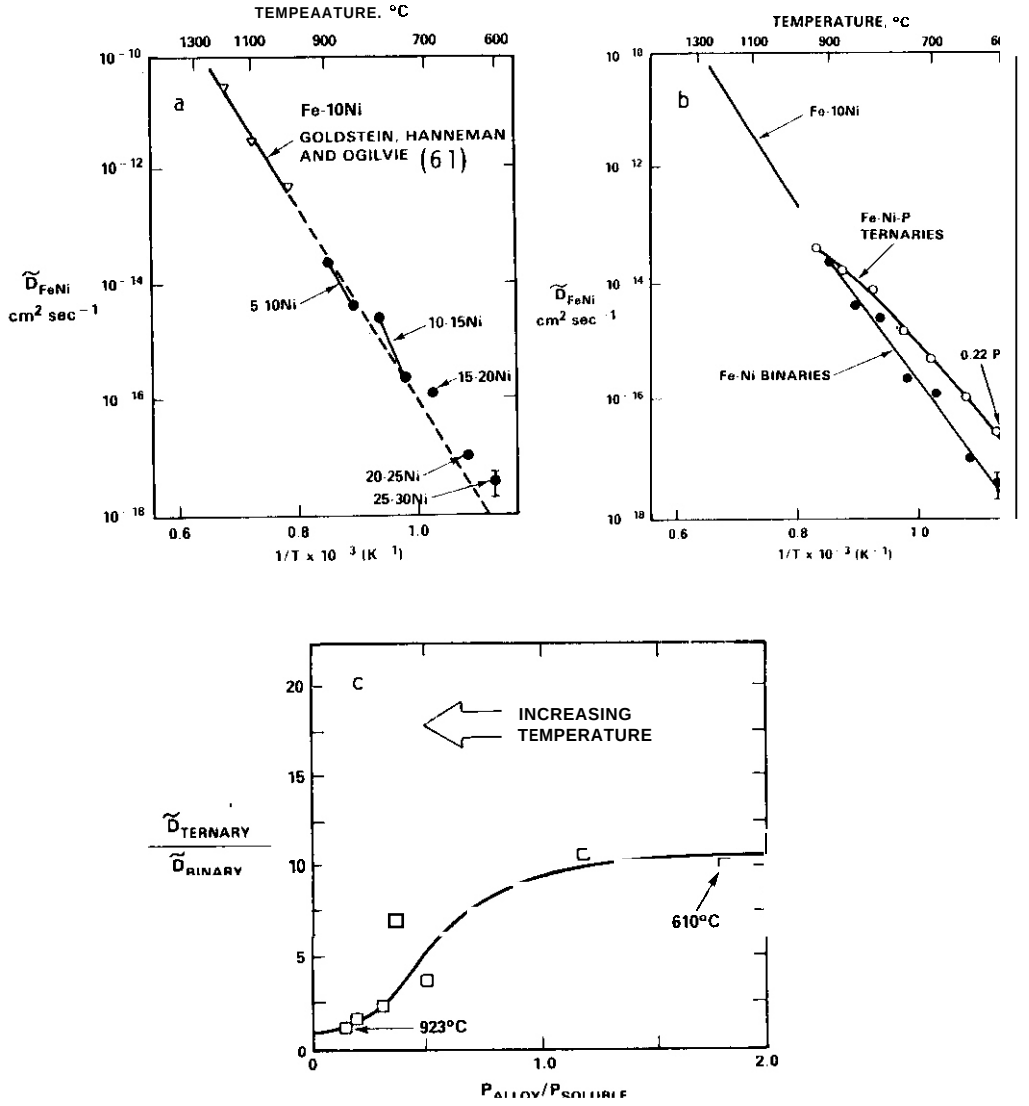


Fig. 24. Measurements of the interdiffusion coefficients of (a) Fe-Ni and (b) Fe-Ni-P alloys by Dean and Goldstein.[50] As shown in (b) all ternary alloys except two (25 and 30 Ni) contained 0.15 ± 0.03 wt% P. (c) The increase in diffusivity by phosphorus is related to the percentage solubility at a given temperature and does not exceed a factor of ten.

The primary influence of phosphorus in this model is thus directed toward its role while in solution. Eventually much of the phosphorus will be removed by precipitation which will hasten the end of the transient regime of swelling. The action of phosphide precipitates is considered in this model to be secondary, with the exception that phosphorus additions have been found to delay the removal of nickel and silicon from solution and into precipitates.' These elements (especially silicon) have already been shown to have a large effect on void nucleation while in solution.

In a recent paper Itoh and coworkers[52] have shown in a variety of neutron-irradiated 316 stainless steels that phosphorus exerts its major influence while in solution and not after precipitation. Phosphorus in solution was found by Itoh to retard the recovery of dislocations in cold-worked steels and the development of γ' and G-phase precipitates. These precipitates form by concentrating nickel and silicon from the matrix. This delay in microchemical evolution of the matrix occurs despite the fact that the phosphide phase is in itself rich in nickel and silicon as observed by Itoh and coworkers,[52] Lee and coworkers[53] and Yang.[54] However, the amount of phosphide formed and its associated removal of nickel and silicon is

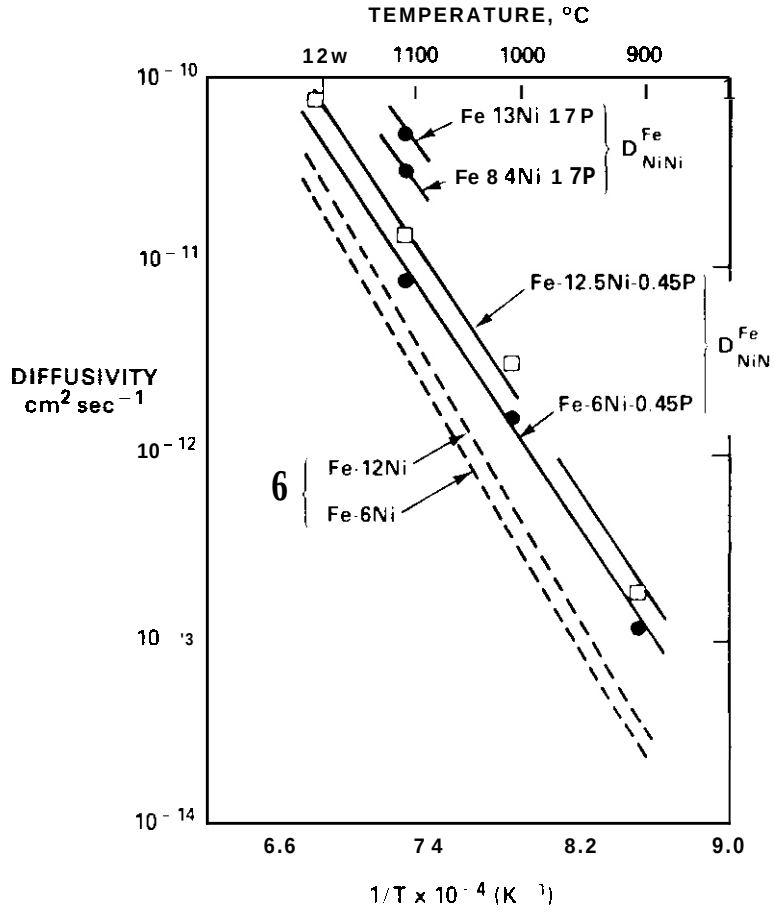


Fig. 25. The combined effect of nickel and phosphorus level on the diffusivity of Fe-Ni binary alloys at high temperatures, as measured by Heyward and Goldstein.[51]

limited by the small amount of phosphorus available. Itoh and coworkers did not address the nature of the interaction of phosphorus and vacancies but cited the model of Garner and Brager[8] as a possible explanation.

The studies and theories of Lee, Mansur and their coworkers[22,55-56] do not recognize a role for phosphorus while in solution but are directed primarily toward its role as a precipitate-former. The precipitates are postulated to increase the sink density for point defects and serve as nucleation sites for stable helium bubbles which are too small to easily grow into voids. These proposed roles are not necessarily in conflict with the model proposed in this paper and both kinds of mechanisms may be operating. Precipitate-based models would be most important in situations where large amounts of helium are produced. However, all of the alloys used in the neutron and various ion studies cited in this paper contained very large amounts of gas (O_2, N_2).

Fig. 26 illustrates the impact of the temperature and solubility considerations on the comparison of the neutron and ion studies of phosphorus effects. (We must assume in this analysis that the solubility of phosphorus is not strongly affected by the presence of 15% chromium, since data are available only for the Fe-Ni-P system'.) As shown in Fig. 26, in the neutron study the Fe-15Cr-25Ni-0.013P alloy is undersaturated at all irradiation temperatures, the Fe-15Cr-25Ni-0.055P alloy is undersaturated only above ~500°C and the Fe-15-25Ni-0.10P alloy is undersaturated only above ~600°C. Thus the maximum effect of phosphorus on vacancy supersaturation is maintained throughout much of the experimental matrix of the neutron study as shown in Fig. 26b. At this point we cannot factor into the analysis the possible effects of radiation-induced segregration on solubility of phosphrous.

The ion experiments shown in Fig. 14 were conducted at 675°C and 0.055 wt.% phosphorus. As shown in Fig. 26a this is a condition which represents only 25% of the solubility limit, illustrating another possible shortcoming of charged particle studies which are traditionally conducted at very high displacement rates. These studies require irradiation temperatures which must be higher by 100-150°C to account for the well-known "temperature-shift" effect.'' In effect, the temperature shift guarantees that the role of phosphorus in ion irradiations will be strongly reduced relative to that of typical neutron irradiations.

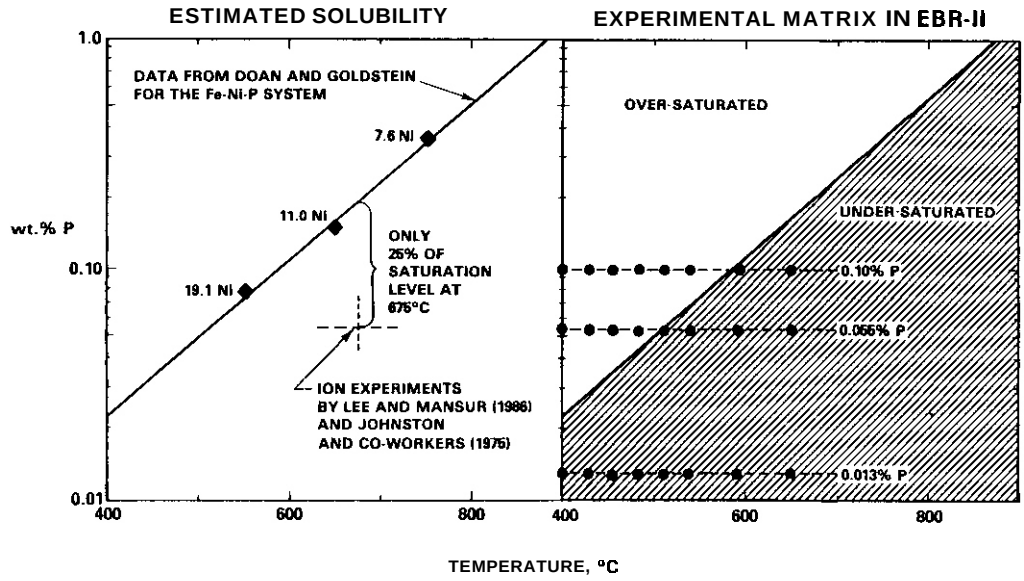


Fig. 26. Solubility-based analysis of phosphorus effects on vacancy concentrations in Fe-Ni-P alloys. The solubility vs. temperature curve is plotted from the points where the four phase fields meet (γ, $\gamma + \alpha$, $\gamma + \alpha$ + phosphide, γ + phosphide) as described by Doan and Goldstein.' The nickel level for each four-phase point is shown, but the solubility of phosphorus in the γ phase does not change very much with increasing nickel level.

It is doubtful, however, that this is the only shortcoming of such an experiment. The strong binding of phosphorus with vacancies will most likely cause it to couple with the large gradients in vacancy concentration associated with the use of 4.0 and 5.0 MeV Ni^+ ions as well as the additional strong influence of the surface at 675°C. The latter effect has been shown analytically to be very large at temperatures of 625°C and above by Bullough and Haynes[58] and by the analysis of denuded zone data by Garner and Laidler.[58]

There is a large amount of evidence that shows that such coupling will lead to rapid depletion of elements which bind with vacancies or interstitials.[59,60] Due to the particularly strong binding of phosphorus with vacancies, much of the phosphorus in the ion-bombarded Fe-Ni-Cr alloys may be depleted in the peak damage region before it can exert its full influence on void nucleation. This might give the erroneous impression that phosphorus has very little effect, even less than anticipated at the 25% solubility level.

An Unresolved

When phosphorus or silicon were added to alloys already containing other solutes, the large increase in swelling at low temperatures with small addition of either solute was not observed in any earlier study. Thus relatively pure alloys experience somewhat more difficulty than slightly impure alloys in nucleating voids, but only at the lower temperature range of void nucleation. This phenomenon occurred in both neutron and ion irradiation studies and therefore is not an artifact of the simulation technique. Precipitation also does not appear to be involved at these low solute levels. Perhaps it may be related to the evolution of Frank Loops and dislocations, but it cannot be described by the diffusivity-related model advanced in this paper. The resolution of this issue will require irradiations to be conducted to displacement levels where the first voids just begin to appear, followed by microscopy examination to observe the effects of solutes on dislocation and loop microstructure.

CONCLUSIONS

Although the results of charged particle irradiation studies are subject to a number of factors that distort the compositional and environmental dependence of void swelling, there is agreement with some of the major conclusions drawn from neutron irradiation studies, particularly when these studies are conducted on very simple alloys that minimize the number of synergisms operating. In general the trends revealed by neutron irradiation are more complex, exhibiting additional regimes of behavior not seen in the charged particle studies.

It was shown that the swelling behavior of Fe-Ni-Cr alloys can be characterized by three regimes involving different levels of difficulty in void nucleation. These various regimes can be shifted with respect to each other by both environmental factors such as helium, displacement rate, temperature and by compositional factors which primarily affect the rate of void nucleatinn. Two of these compositional factors are the influence of composition on the effective vacancy diffusion coefficient and the vacancy formation energy while the third involves the tendency of alloys in the intermediate nickel range to decompose in a spinodal-like fashion. The latter facilitates the nucleation of voids in microvolumes of lower nickel and higher chromium content.

The effects of variations in solvent composition and solute additions can also be visualized in terms of a "temperature shift" that is directly analogous to that associated with changes in displacement rate.

FUTURE WORK

This effort will continue as more data are collected from various irradiation experiments conducted in EBR-II and FFTF.

REFEKENCES

1. F. A. Garner and H. R. Brager, pp. 187-201 in ***Effects of Radiation on Materials: Twelfth International symposium, ASTM STP 870***, F. A. Garner and J. S. Perrin, Eds., American Society for Testing and Materials, Philadelphia, PA, 1985.

2. H. R. Brager, F. A. Garner and M. L. Hamilton, *Journal* of ***Nuclear Materials***, Vols. 133 and 134, pp. 594-598 (1985).

3. F. A. Garner and H. R. Braqer, pp. 62-65 in ***Damage Analysis and Fundamental Studies Quarterly Progress*** *Report, DOE/ER-0046/19*, U. S. Department of Energy, November 1984.

4. F. A. Garner, ***Journal*** of ***Nuclear Materials,*** Vols. 122 and 123, pp. 459-471 (1984).

5. D. L. Porter and F. A. Garner, pp. 212-220 in ***Effects*** of ***Radiation on Materials: Twelfth International symposium, ASTM STP 870***, F. A. Garner and J. S. Perrin, Eds., American Society for Testing and Materials, Philadelphia, PA, 1985.

6. F. A. Garner, "The Influence of Phosphorus on the Neutron or Ion-Induced Swelling of Fe-Ni-Cr Alloys," ***Fusion structural Materials semiannual Progress Report,*** U. S. Department of Energy, December 1986, in press.

7. A. S. Doan, Jr., and J. I. Goldstein, ***Metallurgical Transactions,*** Vol. 1, pp. 1759-1767 (1970).

8. F. A. Garner and H. R. Brager, *Journal* ***of*** *Nuclear* ***Materials,*** Vols. 133 and 134, pp. 511-514 (1985)

9. W. G. Johnston, T. Lauritzen, J. H. Rosolowski and A. M. Turkalo, pp. 227-266 in ***Radiation Damage in Metals,*** American Society of Metals, Cleveland, OH, 1976.

10. W. G. Johnston, J. H. Rosolowski, A. M. Turkalo and T. Lauritzen, *Journal* ***of Nuclear Materials,*** Vol. 54, pp. 24-40 (1974).

11. J. F. Bates and W. G. Johnston, pp. 625-644 in ***Proceedings, AIME International Conference on Radiation Effects in Breeder*** *Reactor* ***structural Materials,*** Scottsdale, AZ, American Institute of Mining, Metallurgical and Petroleum Engineers, June 1977.

12. F. A. Garner and J. J. Laidler, pp. 177-240 in ***Proceedings,*** *Workshop* ***on correlation of Neutron and Charged Particle Damage***, CONF-760673, Oak Ridge National Laboratory, Oak Ridge, TN, 8-10 June 1976.

13. F. A. Garner, ***Journal of Nuclear Materials,*** Vol. 117, pp. 177-197 (1983).

14. D. L. Plumton, H. Attaya and W. G. Wolfer, *Journal* ***of*** *Nuclear* ***Materials,*** Vols. 122 and 123, pp. 650-653 (1984).

15. B. Badger, Jr., D. L. Plumton, S. 3. Zinkle, R. L. Sindelar, G. L. Kulcinsky, R. A. Dodd and W. G. Wolfer, pp. 297-316 in ***Effects*** of ***Radiation on Materials: Twelfth International symposium ASTM STP 870,*** F. A. Garner and J. S. Perrin, Eds., American Society for Testing and Materials, Philadelphia, PA, 1985.

16. A. S. Kumar and F. A. Garner, ibid, pp. 493-506

17. W. G. Johnston, W. G. Morris and A. M. Turkalo, pp. 421-430 in ***Proceedings, AIME International conference on Radiation Effects in Breeder Reactor structural Materials,*** Scottsdale, AZ, American Institute of Mining, Metallurgical and Petroleum Engineers, June 1977.

18. V. K. Sethi and P. R. Okamoto, pp. 109-121 in ***Phase Stability During Irradiation,*** J. R. Holland, L. K. Mansur and D. I. Potter, Eds., The Metallurgical Society of AIME, Warrendale, PA, 1981.

19. T. Muroga, H. Murakami, N. Yoshida and K. Kitajima, "The Impact of Nonequilibrium Solute Segregation on HVEM Irradiation Studies," presented at ***International Symposium on Behavior of Lattice Imperfections in Materials,*** Osaka University, Japan, November 18-20, 1985.

20. F. Rotman, D. Gilbon, H. Lorent and O. Dimitrov, in ***Proceedings, International conference on vacancies and Interstitials in Metals and Alloys,*** Berlin, Germany, September 14-19, 1986, in press.

21. G. R. Gessel and A. F. Rowcliffe, pp. 431-442 in ***Proceedings, AIME International Conference on Radiation Effects in Breeder Reactor Structural Materials,*** Scottsdale, AZ, American Institute of Mining, Metallurgical and Petroleum Engineers, June 1977.

22. E. H. Lee and L. K. Mansur, ***Journal of Nuclear Materials,*** Vols. 141-143, pp. 695-702 (1986).

23. F. A. Garner and W. G. Wolfer, *Journal* ***of Nuclear Materials,*** Vols. 122 and 123, pp. 201-206 (1984)

24. F. A. Garner, *Journal* ***of Nuclear Materials,*** Vols. 133 and 134, pp. 113-118 (1985).

25. 8. Esmailzadeh and A. S. Kumar, pp. 468-480 in ***Effects of Radiation on Materials: Twelfth International Symposium,*** *ASTM STP 870,* F. A. Garner and J. S. Perrin, Eds., American Society For Testing and Materials, Philadelphia, PA, 1985.

26. W. A. Coghlan and F. A. Garner, "Effect of Nickel Content on the Minimum Critical Radius In Ternary Austenitic Alloys." to be published in ***Radiation-Induced Changes in Microstructures.,*** ASTM STP 955. F. A. Garner, N. H. Packan' and A. S. Kumar, Eds., American Society for Testing and Materials, Philadelphia, PA, 1987.

27. R. A. Dodd, F. A. Garner, J.-J. Kai, T. Lauritzen and W. G. Johnston, "Spinodal-Like Decomposition and Swelling Induced by Ion Irradiation in Simple ie-Ni and Fe-Ni-Cr Alloys," ibid.

28. S. J. Rothman, L. J. Nowicki and G. E. Murch, ***Journal of Physics F: Metal Physics,*** Vol. 10, pp. 383-398 (1980).

29. B. Million, J. Ruzickova, J. Velisek and J. Vrestal, Materials Science and Engineering, Vol. 50, pp. 43-52 (1981).

30. J. G. Duh and M. A. Dayananda, ***Diffusion and Defect Data,*** Vol. 39, 1, (1985).

31. H. R. Brager and F. A. Garner, pp. 139-150 in ***Effects of Radiation on Materials: Twelfth International symposium,*** ASTM STP 870, F. A. Garner and J. S. Perrin, Eds., American Society for Testing and Materials, Philadelphia, PA, 1985.

32. F. A. Garner, H. R. Brager, R. A. Dodd and T. Lauritzen, ***Nuclear Instruments and Methods in Physics Research,*** Vol. 616, pp. 244-250 (1986).

33. F. A. Garner, H. R. Brager and J. M. McCarthy, "Neutron-Induced Spinodal-Like Decomposition of Fe-Ni and Fe-Ni-Cr Alloys," to be published in ref. 26.

34. K. C. Russell and F. A. Garner, "An Unexpected Phase Transformation in ie-Ni Invar Alloys," presented at 116th Annual Meeting of the Metallurgical Society of AIME in Denver, CO, February 24, 1987.

35. F. Rotman and O. Dimitrov, "Void Swelling in Electron-Irradiated Fe-Cr-Ni Model Alloys," to be published in ref. 26.

36. G. P. Walters, ***Journal of Nuclear Materials,*** Vol. 136, pp. 263-279 (1985).

37. A. D. Marwick, R. C. Pillar and M. E. Horten, pp. 11-15 in ***Dimensional Stability and Mechanical Behavior of Irradiated Metals and Alloys,*** Vol. 2, British Nuclear Energy Society, London, 1984.

38. T. Kimoto and H. Shiraishi, "Compositional Redistribution in Fe-Ni-Cr Alloys Under Proton Irradiation," to be published in ref. 26.

39. F. A. Garner and W. G. Wolfer, ***Journal of Nuclear Materials,*** Vol. 102, pp. 141-150 (1981).

40. 8. Esmailzadeh, A. S. Kumar and F. A. Garner, *Journal of Nuclear Materials*, Vols. 133 and 134, pp. 590-593 (1985).

41. W. A. Coghlan and L. K. Mansur, *Journal of Nuclear Materials,* Vols. 122 and 123, pp. 495-501 (1984).

42. A. Hishinuma, Y. Katano and K. Shiraishi, *Journal of Nuclear Materials,* Vols. 103 and 104, pp. 1063-1068 (1981).

43. A. Hishinuma, "Electron-Induced 'Void Swelling in Fe-Cr-Ni Ternary Austenitic Alloys," JAERI-memo 58-001, (in Japanese) Tokai Research Establishment, Japan, 1983.

44. V. Levy, N. Aram, L. Le Naour. G. Didout and J. Delaplace, pp. 709-725 in *Proceedings of AIME International Conference on Radiation Effects In Breeder Reactor Structural Materials,* Scottsdale, AZ, American Institute of Mining, Metallurgical and Petroleum Engineers, June 1977.

45. B. N. Singh, T. Leffers, M. J. Makin, G. P. Walters and A. J. E. Foreman, *Journal of Nuclear Materials,* Vols. 103 and 104, pp. 1041-1046 (1981).

46. H. R. Brager and F. A. Garner, pp. 219-235 in *Phase Stability During Irradiation,* J. R. Holland, L. K. Mansur and D. I. Potter, Eds., The Metallurgical Society of AIME, Warrendale, PA, 1981.

47. D. J. Mazey, D. R. Harries and J. A. Hudson, pp. 61-67 in *Proceedings of International Conference on Irradiation Behavior of Metallic Materials for Fast Reactor Core Components,* Corsica, France, June 1979.

48. A. Azarian and K. Kheloufi, *Journal of Nuclear Materials,* Vol. 97, pp. 25-26 (1981).

49. A. Azarian, "Contribution a 1'Etude des Defauts Ponctuels dans les Aciers Inoxydahles," CEA-R-4617, Doctoral Thesis, University of Paris, 1974.

50. O. C. Dean and J. I. Goldstein, *Metallurgical Transactions,* Vol. 17A, pp. 1131-1138 (1986).

51. T. R. Heyward and J. I. Goldstein, *Metallurgical Transactions,* Vol. 4, pp. 2335-2342 (1973).

52. M. Itoh, S. Onose and S. Yuhara, "Void Swelling and Microstructural Change in Neutron Irradiated Type 316 Stainless Steel," to he published in ref. 26.

53. E. H. Lee, P. J. Maziasz and A. F. Rowcliffe, pp. 191-218 in *Phase Stablity During Irradiation*, J. R. Holland, L. K. Mansur and D. I. Potter, Eds., The Metallurgical Society of AIME, Warrendale, PA, 1981.

54. W. J. S. Yang, "Precipitate Evolution in 316-Type Stainless Steels Irradiated in EBR-II," to he published in ref. 26.

55. E. H. Lee, L. K. Mansur and A. F. Rowcliffe, *Journal of Nuclear Materials,* Vols. 122 and 123, pp. 299-304 (1984).

56. L. K. Mansur, M. H. Haynes and E. H. Lee, pp. 359-382 in *Phase Stablity During Irradiation,* J. R. Holland, L. K. Mansur and D. I. Potter, Eds., The Metallurgical Society of AIME, Warrendale, PA, 1981.

57. A. D. Brailsford and L. K. Mansur, Journal of Nuclear Materials, Vols. 103 and 104, pp. 1403-1408 (1981).

58. R. Bullough and M. H. Haynes, Journal of Nuclear Materials, Vol. 68, pp. 286 (1977).

59. N. Q. Lam, *Journal of Nuclear Materials,* Vol. 117, pp. 106-112 (1983).

60. N. Q. Lam and P. R. Okamoto, pp. 430-449 in *Effects of Radiation on Materials: Twelfth International Symposium, ASTM STP 870,* F. A. Garner and J. S. Perrin, Eds., American Society for Testing and Materials, Philadelphia, PA, 1985.

61. J. I. Goldstein, R. E. Hanneman and R. E. Ogilvie, *Transactions TMS-AIME*, Vol. 233, pp. 812-820 (1965).

THE BEHAVIOR OF SOLUTE SEGREGATION AND VOID FORMATION IN Fe-Cr-Ni AND Fe-Cr-Mn STEELS DURING ELECTRON IRRADIATION

H. Takahashi+, F. A. Garner*, H. Itoh+, B. Hu** and S. Ohnuki+

+Faculty of Engineering, Hokkaido University, Sapporo 060, Japan
*Hanford Engineering Development Laboratory, Richland, WA 99352, USA
**Beijing University of Iron and Steel Technology, Beijing, China

OBJECTIVE

The object of this effort is to determine the mechanisms by which the microstructural evolution of irradiated austenitic alloys respond to differences in composition or radiation variables.

SUMMARY

The relative swelling behavior of Fe-Cr-Mn and Fe-Cr-Ni alloys during electron irradiation is shown to be different from that observed in neutron irradiations. This difference appears to a consequence of the different diffusion behavior of nickel and manganese in response to the operation of the inverse Kirkendall effect. The vacancy gradients driving the diffusion in these experiments are generated not only by the foil surfaces and the electron-generated radial displacement gradient but also by high angle grain boundaries deliberately centered in the middle of the electron beam. This procedure allows the relative diffusional characteristics of each element to be observed by EDX measurements across the grain boundary. The influence of helium and minor solutes on swelling was also studied in these experiments and yielded no behavior atypical of that observed in neutron irradiation studies.

PROGRESS AND STATUS

Introduction

Current studies on fusion reactor structural materials are largely directed toward solute-modified 316 stainless steels and ferritic steels.[1] Recent attention has also been focused on a new objective of reducing the level of long-lived radioactivity of reactor components for eventual disposal or recycle.[1] One approach to reducing long term radioactivity is to replace nickel with manganese in iron-based steels.[3-9]

Charged particle irradiation of manganese stabilized austenitic steels show that manganese substitution is not expected to preclude either swelling or phase instabilities.[*-'] Other neutron irradiation studies have confirmed this conclusion for alloys with partial or total substitution of manganese for While there are many common features of irradiation behavior in the Fe-Cr-Mn and Fe-Cr-Ni systems there are some significant differences.[12,13] In the Fe-Cr-Mn system swelling is less dependent on composition but these alloys are prone to a greater degree of phase instability. This latter difference is due to the fact that iron segregates to microstructural sinks in Fe-Cr-Mn alloys while nickel segregates in Fe-Cr-Ni alloys. Segregation *of* iron often leads *to* the formation of ferrite.

Electron irradiation studies are now in progress to define the compositional response of microstructural and microchemical evolution in the Fe-Cr-Mn-Ni system. Some results have been reported earlier on Fe-17Cr-19Mn-XNi alloys where X = 0.03, 1.5, 4.5 and 5.9.[1] One feature of these studies has been the irradiation of regions which straddle a high angle grain boundary. Such boundaries serve as strong sinks for radiation-induced point defects. Post-irradiation examination of the elemental profiles that develop near these boundaries supply information on the role of each element in the diffusional processes which control swelling, irradiation creep and phase stability.

This irradiation technique has now been extended to three other steels. One is Fe-15Cr-30Ni, another is Fe-15Cr-20Mn and the third is Fe-15Cr-15Mn with significant additions of C, N, W, V, Si and P. This latter alloy is more representative of a typical commercial alloy.[3]

Experimental Procedures

The compositions of the alloys are given in Table 1. Sheet material was cold-rolled to 0.12 mm thickness and punched to yield microscopy disks of 3 mm diameter. The disks were annealed at 1300K for 30 minutes in evacuated silica capsules and then electropolished at room temperature using a 1 to 19 mixture of $HCLO_4$ and CH_3COOH.

Table 1. Compositional analysis of alloys (wt%)

Alloy Designation		Fe	Ni	Cr	Mn	C	O	N	W	V	Si	P
E21	Fe-15Cr-30Ni	Bal	29.6	15.3	--	0.004	0.017	0.002	-			
R70	Fe-15Cr-20Mn	65	-	15	20		-			-		
988	Fe-15Cr-15Mn(W,V)	Bal	*0.5*	15	15	0.30		0.30	2.0	2.0	0.4	0.05

Electron irradiation at 1.3 MeV was performed in the Hokkaido University H-1300 HVEM using a beam 1.5 μm in diameter with a peak intensity of 4 x 10^{-3} dpa/sec and an average displacement rate of 2 x 10^{-3} dpa/sec. Using the procedure outlined in reference 14, the beam-induced temperature rise is calculated to be 15°C or less. Typical thicknesses of the foil in the irradiated areas were 800 to 1000 nm. For segregation studies the beam was centered on a high angle grain boundary with the beam most often parallel to the <110> direction of one grain. The angle between the specimen normal and the electron beam was usually less than 20°. Some specimens were also simultaneously irradiated with 300 KeV helium ions using an accelerator arrangement described elsewhere.[15]

The post-irradiation composition analyses were performed using a 200 KV TEM/STEM electron microscope equipped with an energy dispersive X-ray spectrometer (EDX). The composition at any point was determined using the relative intensities of the K_α X-rays. The individual measurements of composition represent an average composition through the foil thickness and therefore do not supply information on the influence of foil surfaces on composition. The swelling was measured in a region which was about 100 to 200 nm from the grain boundary.

Results

The microstructural evolution during irradiation varied strongly with alloy composition and irradiation temperature. Figures 1 and 2 show micrographs of void swelling behavior at two different temperatures. Voids form after only 2 dpa in the Fe-15Cr-30Ni alloy and a void depleted zone forms along the grain boundary. Voids formed at all five temperatures investigated in the range 573 to 773K. The void number density saturated quickly at each temperature, reaching 1 x 10^{22} m^{-3} at 623K and 5 x 10^{21} m^{-3} at 773K.

In the Fe-Cr-Mn alloys voids formed in significant numbers only in the range 623-723K, and were at lower densities than observed in Fe-15Cr-30Ni. The swelling behavior vs. displacement dose for the nickel and manganese-stabilized alloys is shown in Figures 3 and 4. Note in Figure 4 that the addition of solutes and reduction of the manganese level delays the onset of swelling somewhat, but the differences are not very large and appear to reflect only an extension of the incubation period.

Figures 5a and 5b show that nickel indeed segregates at grain boundaries in Fe-15Cr-30Ni and is depleted in the immediate vicinity of the boundary. Chromium and iron exhibit the opposite behavior. If one subtracts the mean matrix composition from that at the grain boundary, it is seen in Figure 6 that the amount of segregation is strongly dependent on temperature, a characteristic behavior of the inverse Kirkendall phenomenon.

The composition profiles for Fe-15Cr-20Mn are shown in Figure 7 and clearly show at the lower two temperatures a depletion of manganese at the boundary and a subsequent enrichment of iron. The situation at the two higher temperatures is not very clear and the manganese levels appears to fluctuate, indicating that other Processes may be involved. One possibility is the sublimation of manganese, which at the irradiation temperature has a very high vapor pressure,

Figures 8 and 9 indicate that the addition of solute and a reduction of manganese content from 20 to 15% leads to a substantial reduction in segregation regardless of the irradiation temperature. This reduction is probably related to the presence of the solutes rather than the difference in manganese content since neutron irradiation studies show that swelling is not very sensitive to manganese content.[11]

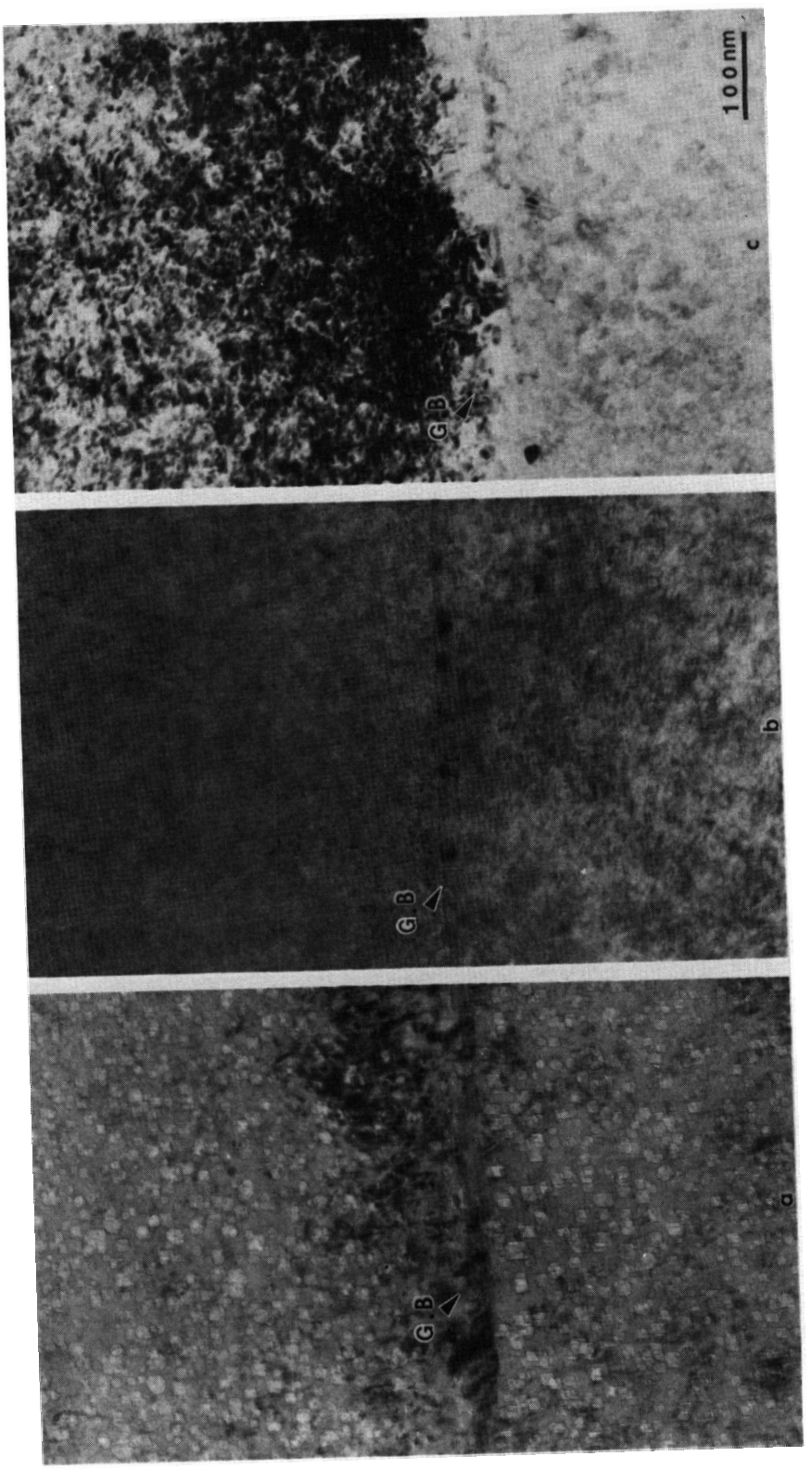


Fig. 1. Damage structures after electron irradiation at 623 K; (a) 12 dpa, Fe-15Cr-30Ni, (b) 12 dpa, Fe-15Cr-20Mn, (c) 15 dpa, Fe-15Cr-15Mn (W,V).

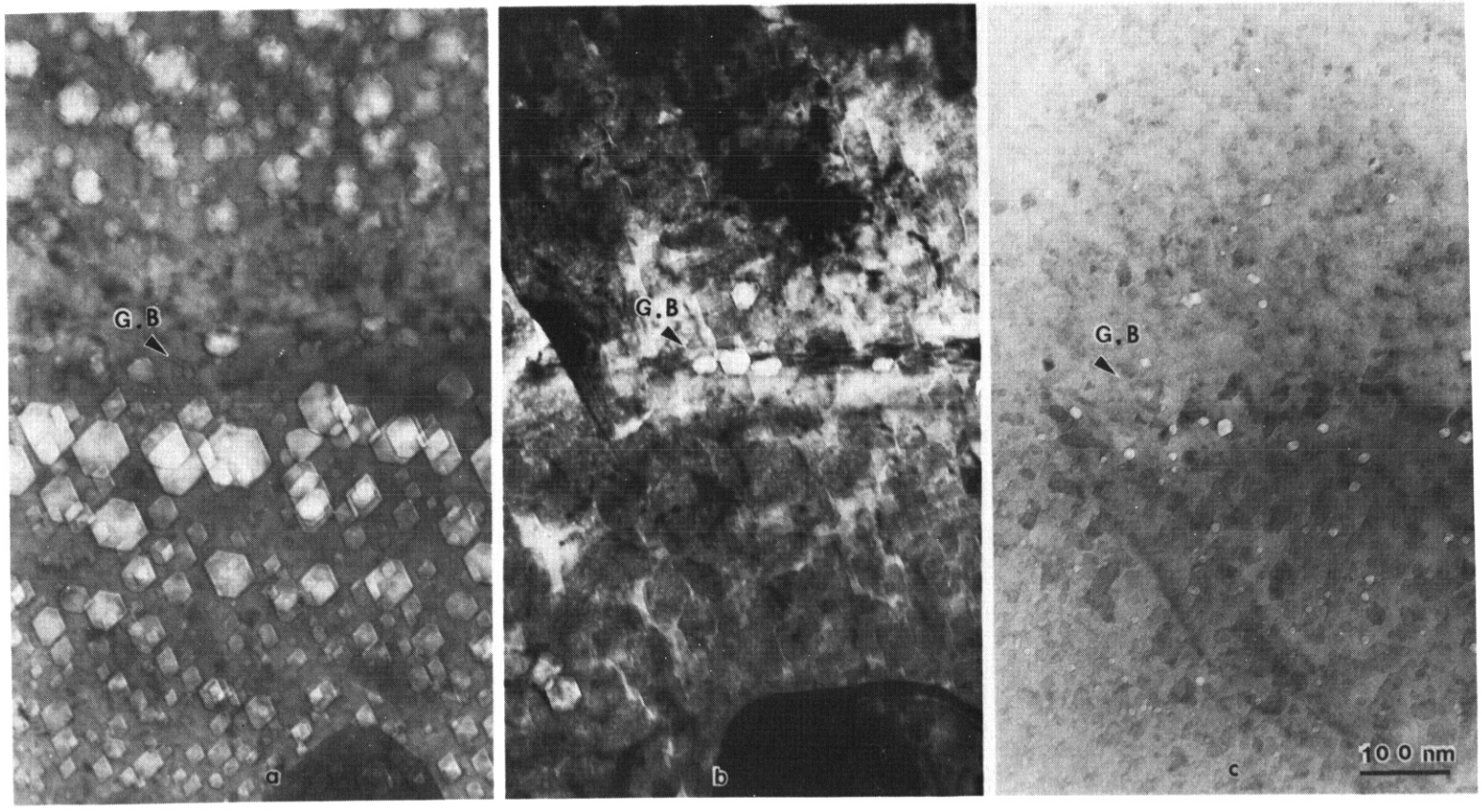


Fig. 2. Damage structures after ion at 723 K; (a) 15 dpa, Fe-15Cr-30Ni, (b) 16 dpa, Fe-15Cr-20Mn, (c) 10 dpa, Fe-15Cr-15Mn (W,V).

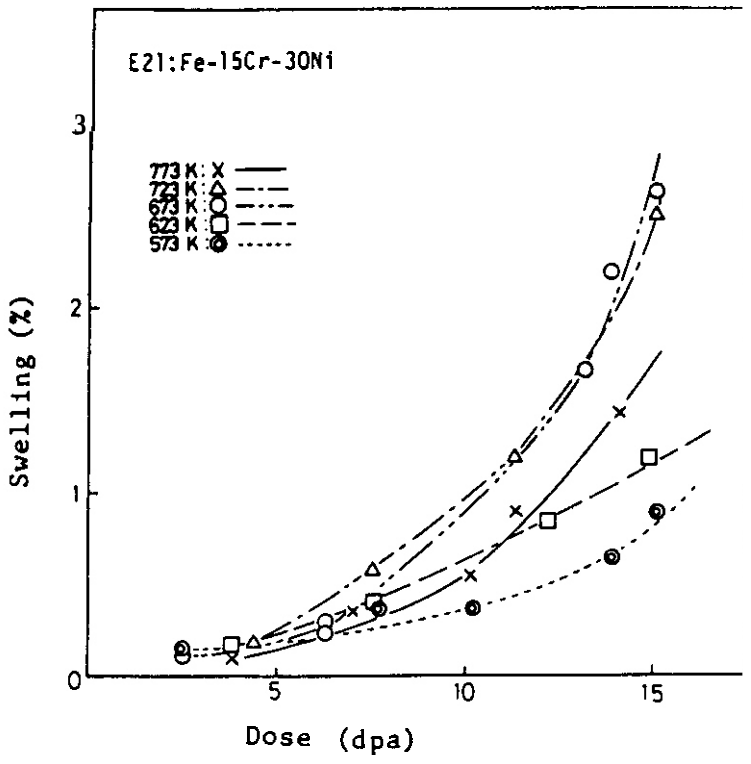


Fig. 3. Dose dependence of swelling for the Fe-15Cr-30Ni alloy at various temperatures.

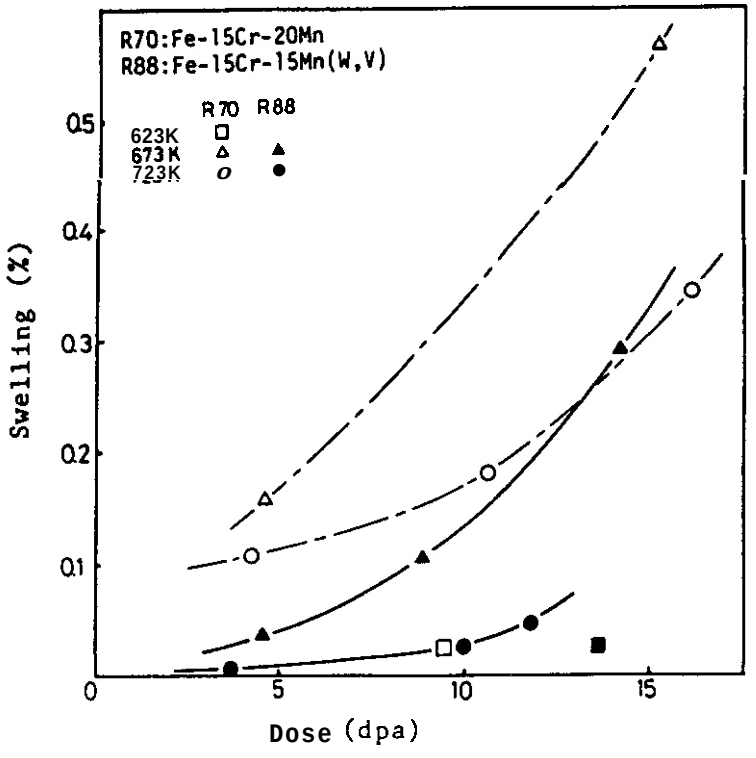


Fig. 4. Dose dependence of swelling for the 15Cr-20Mn and Fe-15Cr-15Mn (W,V) alloys at various temperatures.

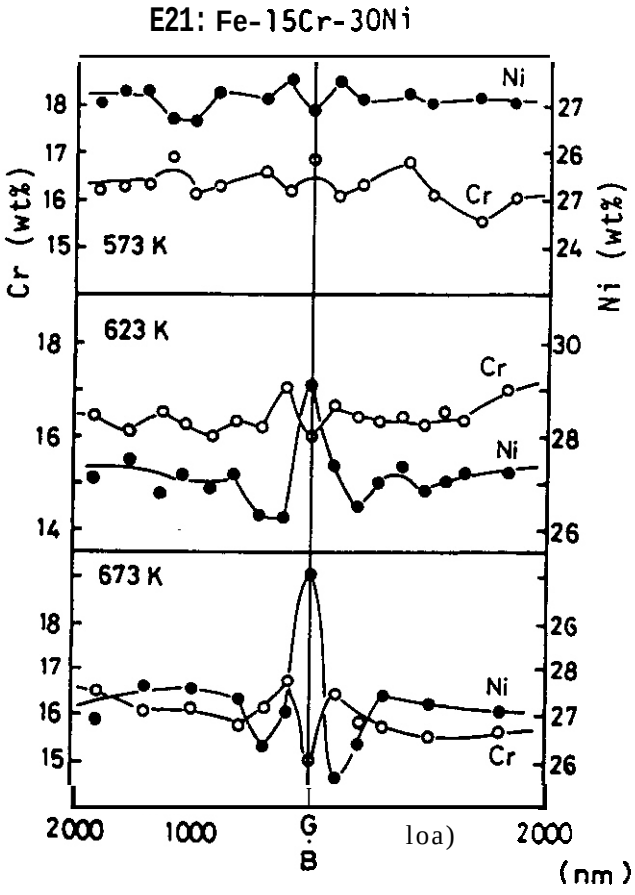


Fig. 5a. The profiles of nickel and chromium concentration as a function of distance from grain boundary (G.B) for Fe-15Cr-30Ni electron-irradiated to 15 dpa at 573-673 K.

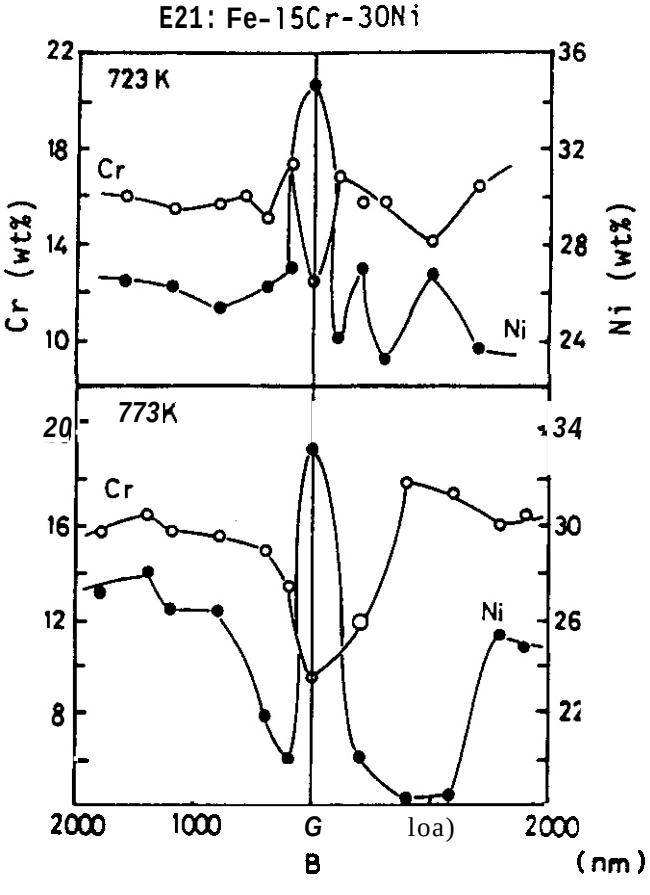


Fig. 5b. The profiles of nickel and chromium concentration as a function of distance from grain boundary (G.B) for Fe-15Cr-30Ni electron-irradiated to 15 dpa at 723-773 K.

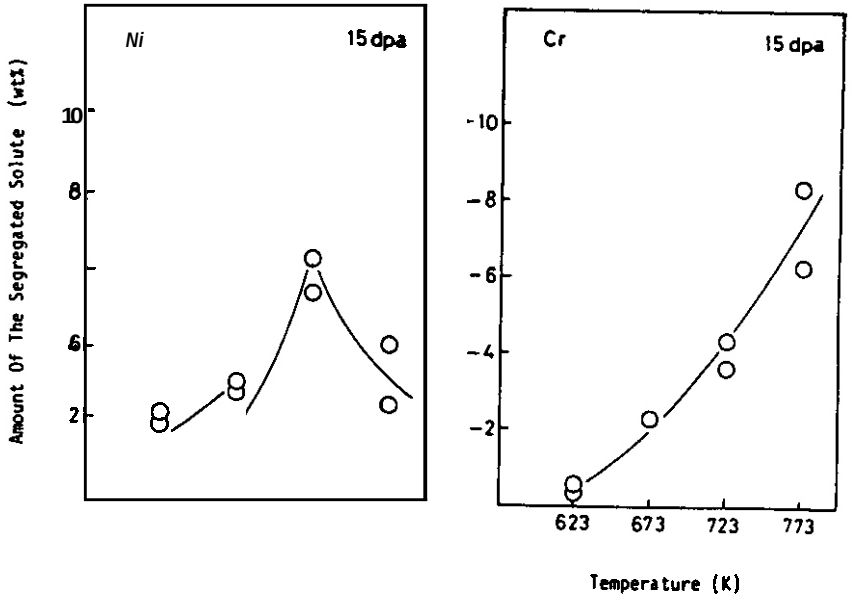


Fig. 6. Temperature dependence of amou.t of segregation for Fe-15Cr-30Ni electron-irradiated to 15 dpa.

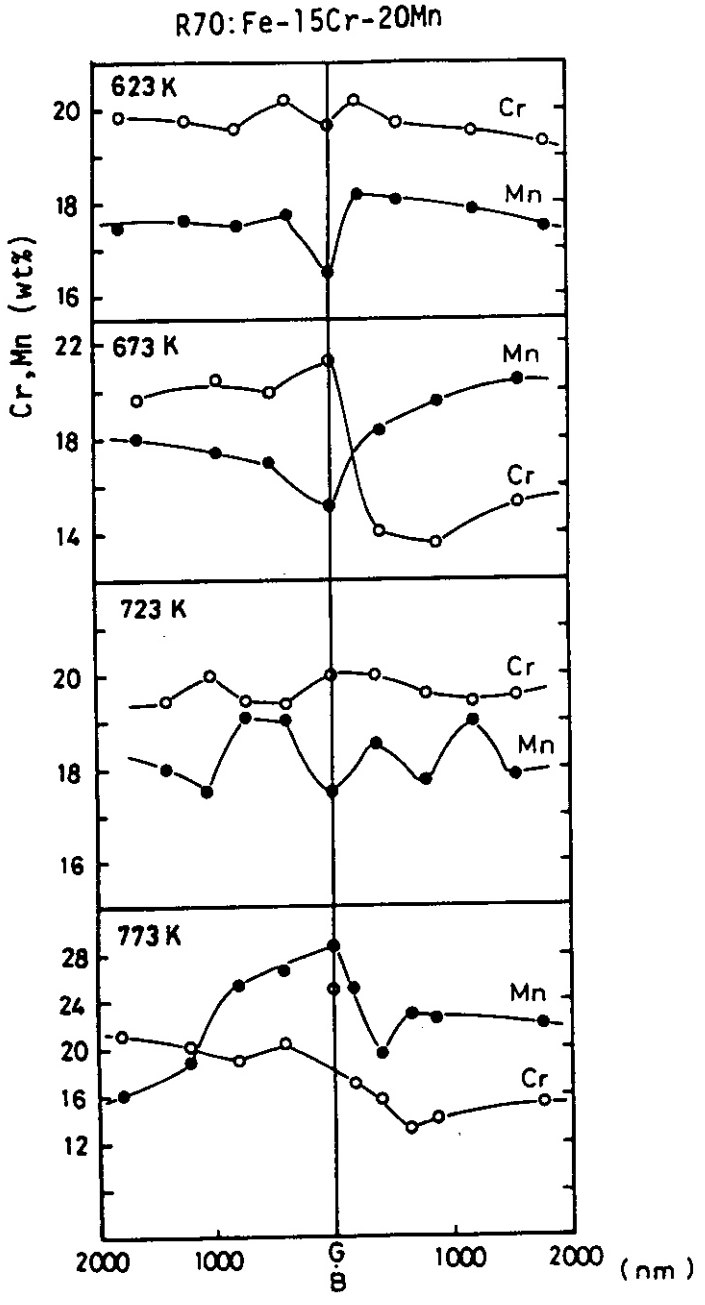


Fig. 7. The profiles of chromium and manganese concentration as a function of distance from grain boundary (G.B) for Fe-15Cr-20Mn electron-irradiated to 15 dpa at 623-773 K.

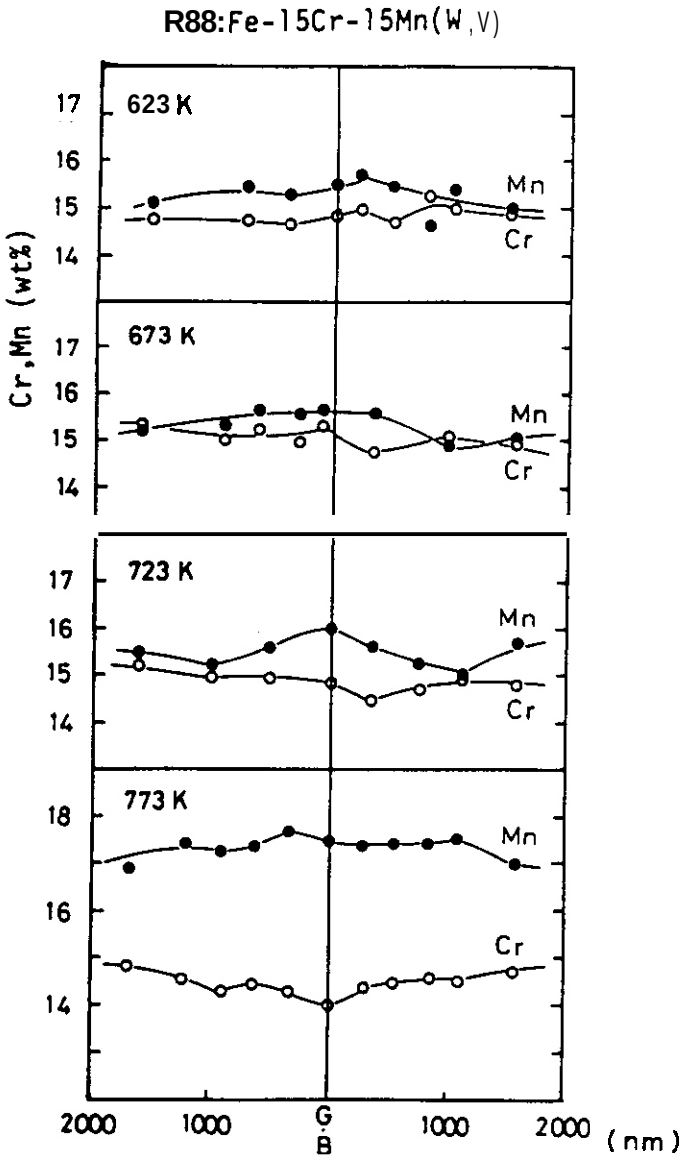


Fig. 8a. The profiles of chromium and manganese concentration as a function of distance from grain boundary (G.8) for Fe-15Cr-15Mn (W,V) electron-irradiated to 15 dpa at 623-773 K.

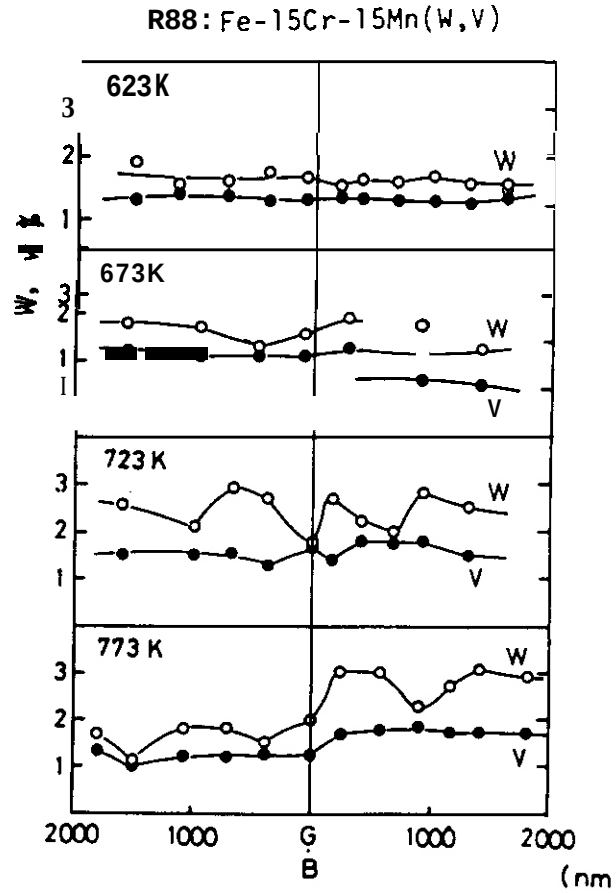


Fig. 8b. The profiles of alloying element (W,V) concentration as a function of distance from grain boundary (G.B) for Fe-15Cr-15Mn (W,V) electron-irradiated at 623-773 K.

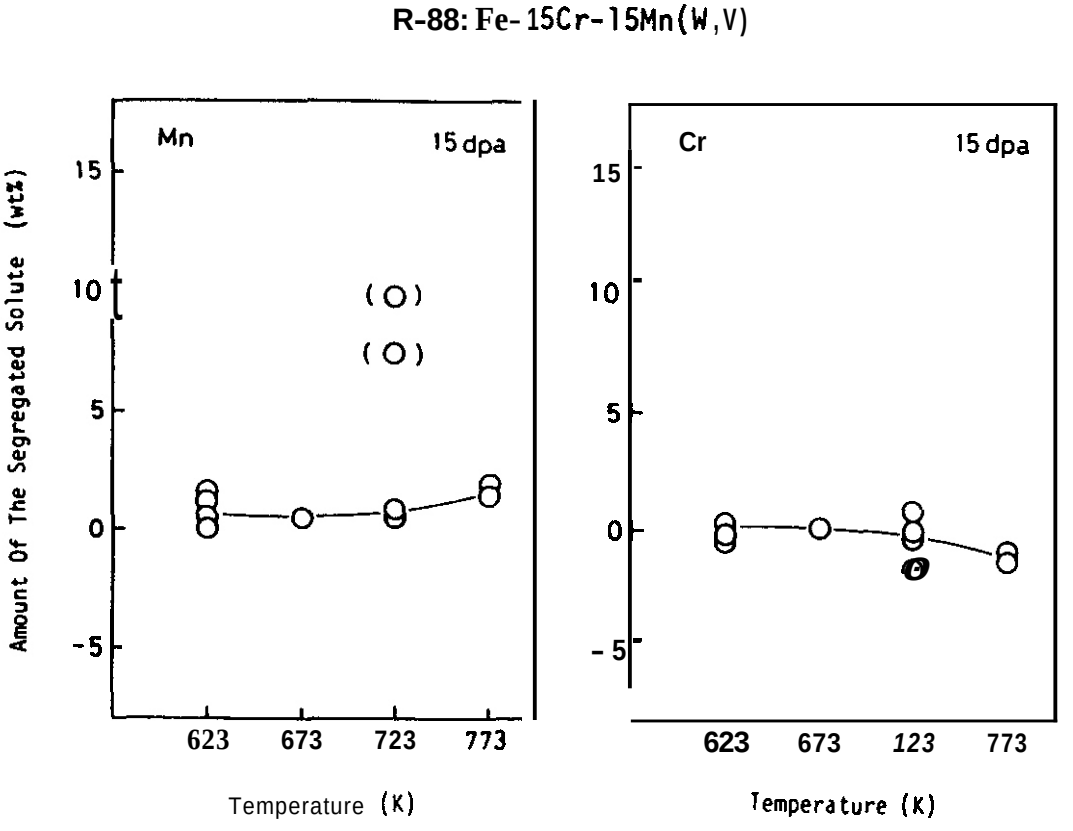


Fig. 9. Temperature dependence of amount of segregation for Fe-15Cr-15Mn (W,V) electron-irradiated to 15 dpa.

When dual ion irradiation was performed at a rate of about 5 appm/dpa the void swelling at 673K was 0.84% at 5.4 dpa, an increase of a factor of about five compared to irradiation without helium. Small bubble-like cavities also formed on the grain boundary. Helium obviously promotes the formation of both bubbles and cavities during electron irradiation of Fe-Cr-Mn alloys. This is in agreement with the results of other studies.[5,15]

Discussion

The higher swelling of Fe-15Cr-30Ni compared to that of Fe-15Cr-20Mn during electron irradiation was initially somewhat surprising. Based on neutron irradiation studies of these two alloys[11-13,16] one would expect the opposite to be true. However, it is important to recognize that there are some substantial differences in the various processes involved in the two different kinds of experiment.

The neutron irradiation case is representative of true bulk behavior unmodified by any large scale changes in composition. However, these electron irradiation studies were conducted in a manner where substantial changes in composition occurred within the region where the swelling was measured. These changes are much larger than indicated in Figures 5 through 7.

Superimposed on the influence of the grain boundary on segregation is the equally strong influence of two foil surfaces. Thus in the center of the foil the nickel level is much lower than that indicated by the EDX measurement. Nickel not only flows toward the grain boundaries and foil surfaces but also flows down the electron-generated displacement gradient and out of the irradiated area in the radial direction.[17-19] These flows are a consequence of the inverse Kirkendall effect in which the slowest diffusing element migrates by default toward the bottom of vacancy gradients. As described elsewhere this and other factors inherent in charged particle studies act to distort the compositional dependence of swelling relative to that of neutron-irradiated materials.[20] In this case the actual nickel concentration in the measured area is very low and the chromium level is increased. Based on the results of neutron studies we would expect swelling to be accelerated for such changes.

The differences in diffusivity of manganese, iron and chromium are not as large as those of nickel, iron and chromium.[21] Thus the rate of segregation is slower in Fe-Cr-Mn alloys. Based on the compositional profiles, one would expect manganese to slowly flow into the area where voids are measured. These

experiments were conducted to low enough dpa levels that the effect of segregation on swelling of Fe-15Cr-20Mn was therefore not as pronounced as that of Fe-15Cr-30Ni. However, there is some concern that at higher temperatures the volatility of manganese may also be affecting the results of this study.

The electron-induced segregation profiles confirm that manganese and nickel flow in opposite directions along a vacancy gradient, as earlier observed in neutron studies.[20] This implies that manganese, unlike nickel, is not the slowest diffusing element in the alloy. Oikawa has indeed shown in iron-rich austenite that both manganese and chromium have similar diffusivities but diffuse faster than iron.[21] As discussed in references 20 and 22, while nickel diffuses slower than iron, increases in nickel lead to an increase in the diffusivities of all elements in the alloy. The different influence of each element on diffusion leads to substantially different levels of segregation in response to the inverse Kirkendall effect and significantly different rates of void nucleation in response to the compositional influence on vacancy supersaturation.[20,22]

CONCLUSIONS

The irradiation of Fe-Cr-Ni and Fe-Cr-Mn alloys with electrons yields swelling behaviors that are different from that produced with neutrons. These differences are largely the result of compositional changes resulting from the operation of the inverse Kirkendall effect. Nickel and manganese are shown to flow in opposite directions along vacancy gradients generated at grain boundaries, hence also at foil surfaces and along the radial displacement gradients inherent in electron irradiation studies. The results of this and other published studies show that swelling of alloys in the Fe-Cr-Mn-Ni system is also sensitive to the addition of solute elements and the presence of helium gas.

FUTURE WORK

This effort will continue as more data are collected from various irradiation experiments conducted in EBR-II, FFTF and in the HVEM.

REFERENCES

1. D. R. Harries, Proceedings, pp. 141-155 in Topical Conference on Ferritic Alloys for Use in Nuclear Energy Technologies, J. W. Davis and D. J. Michel, Eds., American Institute of Mining, Metallurgical, and Petroleum Engineers, 1983.

2. Report of the DOE Panel on Low Activation Materials for Fusion Applications, Center for Plasma Physics and Fusion Engineering, Univ. of California, Los Angeles, 1983.

3. H. R. Brager, F. A. Garner, D. S. Gelles, and M. L. Hamilton, Journal of Nuclear Materials, Vols. 133 and 134, pp. 907-911, 1985.

4. H. Takahashi, T. Takeyama, K. Tanikawa, and R. Miura, Journal of Nuclear Materials, Vols. 133 & 134, pp. 566-570, 1985.

5. M. Snykers, and E. Ruedl, Journal of Nuclear Materials, Vols. 103 & 104, pp. 1075-1078, 1981.

6. D. J. Mazey, J. A. Hudson, and J. M. Titchmarsh, Journal of Nuclear Materials, Vol. 107, p. 2, 1982.

7. R. M. Boothby, D. R. Harries, and T. M. Williams, Journal of Nuclear Materials, Vol. 115, p. 16, 1983.

8. R. L. Kleuh, and E. E. Bloom, pp. 73-85 in Optimizing Materials for Nuclear Applications, F. A. Garner, D. S. Gelles and F. W. Wiffen, Eds.; TMS-AIME, Warrendale, PA, 1985.

9. A. H. Bott, F. B. Pickering, and G. J. Butterworth, Journal of Nuclear Materials, Vols. 141-143, pp. 1088-1096, 1986.

10. D. S. Gelles, and F. A. Garner, Journal of Nuclear Materials, Vols. 133 & 134, pp. 521-524, 1985.

11. F. A. Garner, and H. R. Brager, "Neutron-Induced Swelling of Fe-Mn and Fe-Cr-Mn Austenitic Alloys," HEDL-SA-3437, Hanford Engineering Development Laboratory, May 1986, also to be published in ASTM STP 955, Radiation-Induced Change in Microstructure, in press.

12. F. A. Garner, H R. Brager, O. S. Gelles, and J. M. McCarthy, accepted for publication in Journal of Nuclear Materials.

13. F. A. Garner and H. R. Brager, pp. 87-109 in Optimizing Materials for Nuclear Applications, F. A. Garner, D. S. Gelles and F. W. Wiffen, Eds.; TMS-AIME, Warrendale, PA, 1985.

14. F. A. Garner, L. E. Thomas, and D. S. Gelles, in Experimental Methods for Charged Particle Irradiations, CDNF-750947, D. Kramer, Ed.; Gatlinburg, TN, pp. 51-81, 1975.

15. T. Takeyama, S. Dhnuki, and H. Takahashi, Journal of Nuclear Materials, Vols. 133 & 134, pp. 571-574, 1985.

16. F. A. Garner and H. R. Brager, pp. 187-201 in Effect of Radiation on Materials: Twelfth Conference, ASTM STP 870, F. A. Garner and J. S. Perrin, Eds., American Society for Testing and Materials, Philadelphia, PA, 1985.

17. F. Rotman, D. Gilbon, H. Lorent, and O. Dimitrov, in Proceedings International Conference on Vacancies and Interstitials in Metals and Alloys, Berlin, Germany, September 14-19, 1986, in press.

18. T. Muroga, H. Murakami, N. Yoshida, and K. Kitajima, "The Impact of Nonequilibrium Solute Segregation on HVEM Irradiation Studies," presented at International Symposium on Behavior of Lattice Imperfections in Materials, Osaka University, Japan, November 18-20, 1985.

19. G. P. Walters, Journal of Nuclear Materials, Vol. 136, pp. 263-279, 1985.

20. F. A. Garner and A. S. Kumar, "The Influence of Both Major and Minor Element Composition on Void Swelling In Single Austenitic Steels," in this publication.

21. H. Oikawa, Technical Reports of Tohoku University, Vol. 47, No. 2, p. 215, 1982.

22. W. A. Coghlan and F. A. Garner, "Effect of Nickel Content on the Minimum Critical Radius In Ternary Austenitic Alloys," HEDL-SA-3436, Hanford Engineering Development Laboratory, October 1986; also to be published in ASTM STP 955, Radiation-Induced Changes in Microstructure, in press.

THE CRITICAL RADIUS FOR VOID NUCLEATION IN NEUTRON IRRADIATED FERRITIC ALLOY, HT-9 - W. A. Coghlan (Arizona State University] and D. S. Gelles (Westinghouse Hanford Company)

OBJECTIVE

The objective of this work is to provide guidance on the applicability of martensitic steels for fusion reactor structural materials.

SUMMARY

Experimental measurements of cavity formation in HT-9 following irradiation to 39 dpa at 300, 400, 500 and 600°C are used as a basis for examining the critical radius for void nucleation model as applied to ferritic alloys. Calculations demonstrate that the value for critical radius following irradiation at 400°C can be predicted, that values for critical radius at 500 and 600°C are in agreement with experiment but that values for critical radius at 300°C are below experimental values. Calculations are compared with those on a ferritic alloy following ion bombardment. Possible explanations are suggested.

PROGRESS AND STATUS

Introduction

Ferritic and martensitic alloys are being considered for both fusion and fission applications. These alloys have shown surprising resistance to irradiation damage. The early results showed very little swelling and creep;[1-4] however, more recent experiments[5,6] have shown a dependence of swelling on helium generation rate. although at a much lower rate and at a higher fluence than in austenitic alloys. This resistance is thought to be due to both difficulty in nucleating voids and in a lower steady state swelling rate after they form. The purpose of the present work is to explore some of the reasons for this resistance. We have compared calculated critical radii for void nucleation with those measured after neutron irradiation to determine the physical parameters necessary to the calculation. The critical radius is defined as the cavity radius required for bias driven growth.

In the present experiment, samples of alloy HT-9 were irradiated in the High Flux Isotope Reactor (HFIR) at the Oak Ridge National Laboratory. HT-9 is a martensitic steel made by Sandvik that contains 12% Cr, 1%Mo, 0.2% C, 0.5% Ni, 0.5% Mn, 0.5% W, and 0.3% V. The presence of the Ni produces significant helium under HFIR irradiation. Because the helium is produced by a two-step reaction, the Heldpa ratio rises rapidly over the first 10-20 dpa. After 39 dpa, 115 appm He^7 is produced in HT-9. This compares to 3 appm He for the same neutron dose in the Fast Flux Test Facility (FFTF). For comparison, more than 400 appm helium is expected for the same dose in the first wall of a fusion reactor.7

The critical radius calculation is based on the model developed at Oak Ridge National Laboratory.[8,9] Recently this work was extended to ferritic Fe-10%Cr alloys following ion irradiation[10] and the parameters chosen for the present study were based on this work.

The report begins with a description of the unimodal and bimodal cavity distributions found in samples irradiated in HFIR. We then present a summary of the model used to calculate the critical radii and present calculated results based on a fit to the experimental data. Finally we predict the behavior of these alloys under fusion irradiation conditions based on the model.

Experimental measurement of bubbles and voids

Specimens examined in this experiment were transmission electron microscopy disks of heat 91354 irradiated at 300, 400, 500, and 600°C in the HFIR-CTR-30 experiment. The heat treat conditions were 40% CW + 1038°C/5 minlair cool (AC) + 760°C/0.5hr/AC.[6] The samples were irradiated to 39 dpa (8×10^{26} n/m^2, E > 0.1 MeV). The experimental procedures in the present study were identical to those described previously.[10] The precipitate structures were described previously.6 We are primarily concerned with the cavity and dislocation structures in the present study.

Unimodal cavity distributions typical of bubbles were seen at 300, 500, and 600°C. The specimens irradiated at 400°C were found to contain a low density, nonuniform distribution of faceted cavities typical of voids and a higher density of smaller spherical cavities. These smaller cavities, which are expected to be helium bubbles, were most prominent at the grain boundaries but were also seen throughout the grains. These differences can be seen in the high magnification pictures shown in Fig. 1. The largest cavity radii for the 300, 500, and 600°C irradiations are 0.8, 2, and 5nm, respectively. The bimodal distribution found for the sample irradiated at 400°C is shown in Fig. 2. The largest bubbles not associated with grain boundaries appear to have a radius of 1.25 nm. This value we believe is the critical radius for void nucleation at 400°C.

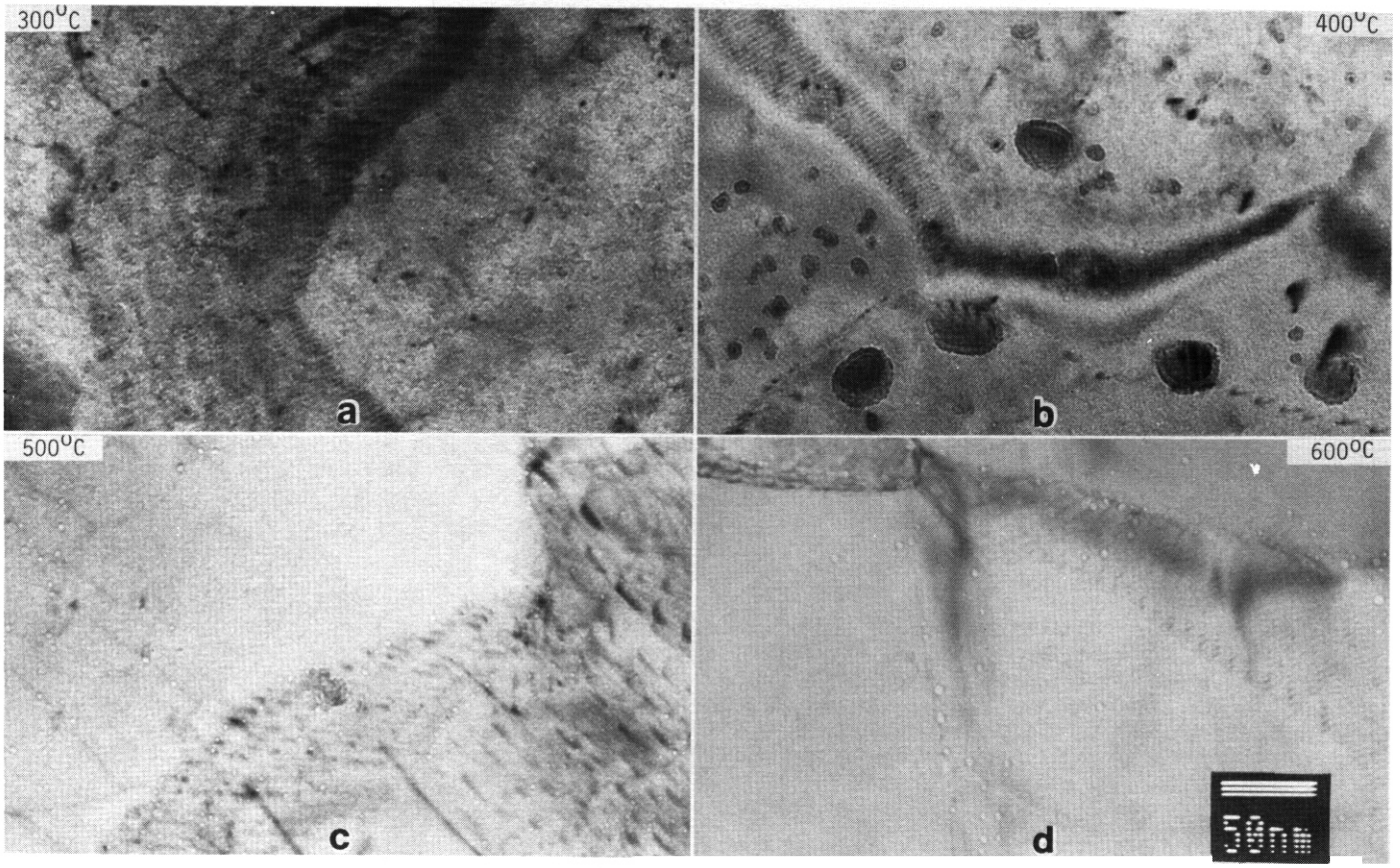


Fig. 1. Microstructures at high magnification for HT-9 specimens irradiated in HFIR-CTR-30 showing bubble structure.

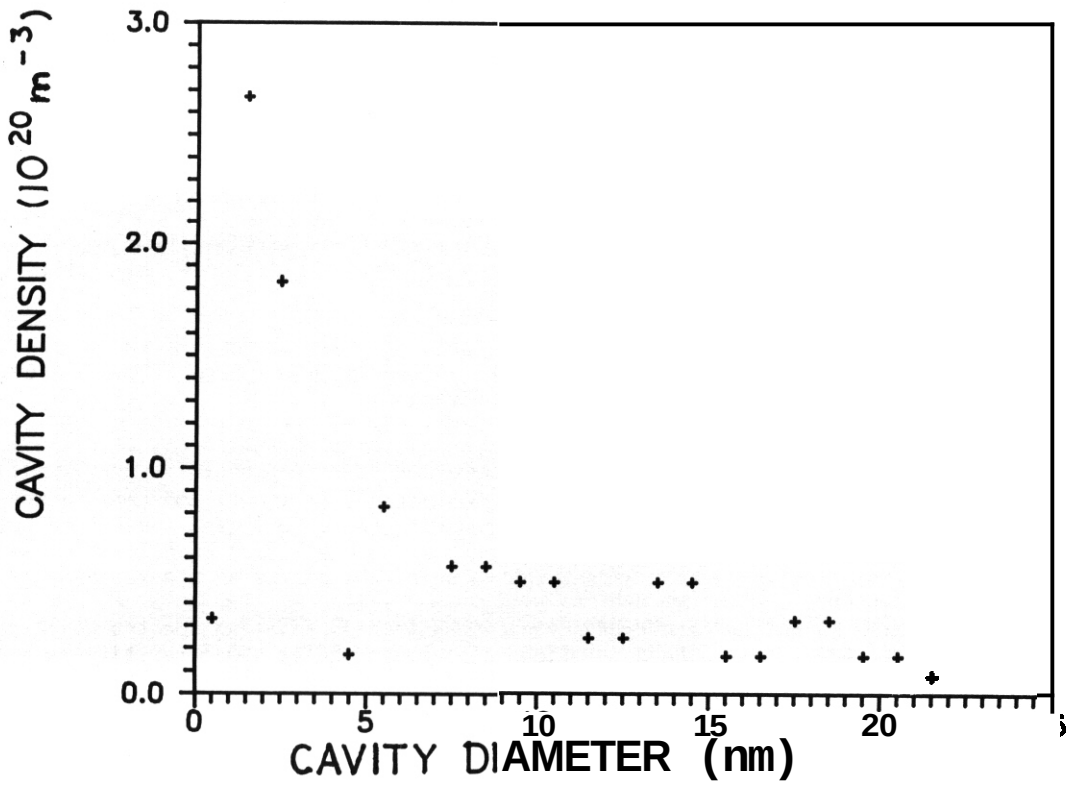


Fig. 2. Histogram showing the bimodal cavity distribution for HT-9 irradiated to 39 dpa in HFIR at 400°C.

The dislocation structures also show differences which are illustrated in Fig. 3. The samples irradiated at 300 and 400°C show a mixture of network dislocations and dislocation loops, primarily of the type a<100>. At 300°C the largest loops are 13 nm in diameter while at 400°C they have increased to as large as 33 nm diameter. For samples irradiated at 500 and 600°C the dislocations are found primarily in subgrain boundaries with few dislocations within the subgrains. The total dislocation density is estimated to be 5 x 10^{14} m^{-2} for the sample irradiated at 400°C. The dislocation density is considerably lower for samples irradiated at the higher temperature.

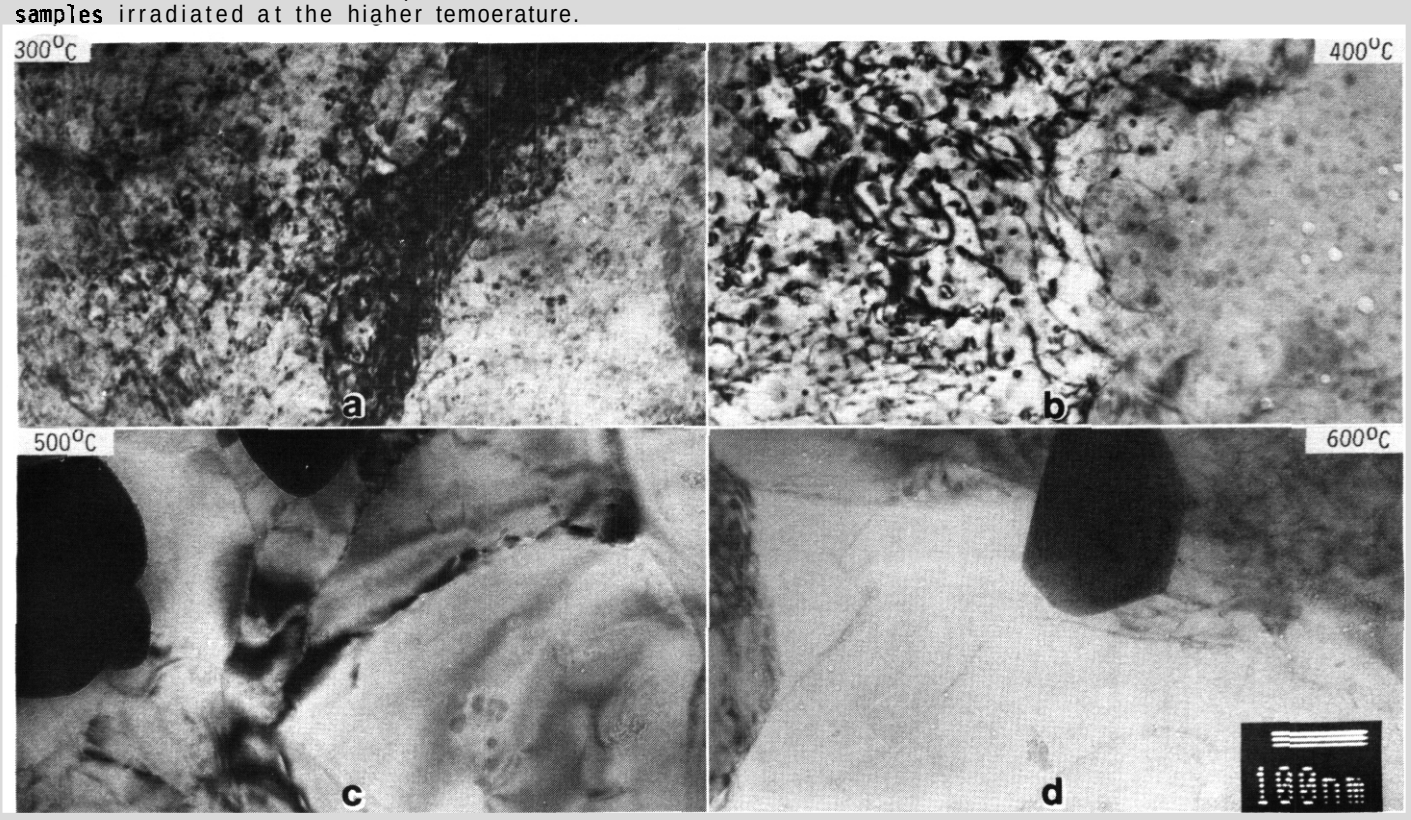


Fig. 3. Microstructures of HT-9 specimens irradiated in HFIR to 39 dpa showing dislocation structures.

Calculation procedures

Critical radii for void nucleation from bubbles containing helium gas (as described by the van der Uaals equation) have been presented recently[8,9] and only a summary of the equations used for these calculations will be presented here. A much more compact form for the equations will be given here than appears in the cited references. This equivalent form was derived by Trinkaus and Mansur[11] and greatly simplifies their use.

In the absence of radiation, a material is assumed to contain a thermal equilibrium concentration of vacancies and no interstitials. The formation energy of the latter is too high to allow an appreciable equilibrium concentration. The equilibrium concentration of vacancies is

$$C_v^o = \Omega^{-1} \exp(S_v^f/k) \exp(-E_v^f/kT) \quad (1)$$

The terms S_v^f, k, and T are the vacancy formation entropy, Boltzmann's constant, and temperature, respectively. The remaining expressions are given in Table 1 along with the values used for the calculations which follow. We have assumed a value of zero for the entropy which simplifies Eq. (1) and does not change the general results calculated. It would only affect the value of the diffusion pre-exponential.

The model will be used to calculate results for various neutron irradiation spectra which may show different defect survival fractions, f_c. The generation rates of vacancies and interstitials are

$$G = f_c G + G_T, \text{ and} \quad (2)$$

$$G_i = f_c G \quad (3)$$

where G is the generation rate of Frenkel pairs, G_T is the thermal production of vacancies, and f_c is the fraction that survive immediate recombination.

Table 1. Parameters used for calculations

	Value	Units
Vacancy motion energy, E_v^m	0.7	eV
Vacancy formation energy, E_v^f	1.9	eV
Self Diffusion Energy, Q	2.6	eV
Vacancy pre-exponential, D_v^o	1.9×10^{-4}	m^2/s
Interstitial motion energy, E_i^m	0.26	eV
Interstitial pre-exponential, D_i^o	1.0×10^{-6}	m^2/s
Recombination radius, r_o	0.344	nm
Cascade efficiency, f_c	0.3	
Lattice parameter, a_o	0.35	nm
Atomic volume, Ω	1.07×10^{-29}	m3
Defect production, G	1.0×10^{-6}	dpa/s
Dislocation density, L	5×10^{14}	m^{-2}

The defects that are produced accumulate in the sample or annihilate by recombination or diffuse to dislocations. The recombination coefficient is

$$R = 4\pi r_o (D_v + D_i)/\Omega \tag{4}$$

and the loss rate of defects to dislocations is

$$K_{v,i} = L D_{v,i} Z^d_{v,i}$$

where the v,i subscript implies either vacancy or interstitial and Z^d is the dislocation sink efficiency. All other parameters are defined in Table 1.

With the above definitions, the steady-state vacancy and interstitial concentrations can be found algebraically and are given in Eqs. (6) and (7).

$$C_v = \frac{[K_i K_v + R(G_i - G_v)]}{2RK_v}\left[\left(1 + \frac{4RG_v K_i K_v}{[K_i K_v + R(G_i - G_v)]^2}\right)^{1/2} - 1\right] \tag{6}$$

$$C_i = \frac{[K_i K_v + R(G_v - G_i)]}{2RK_i}\left[\left(1 + \frac{4RG_i K_i K_v}{[K_i K_v + R(G_v - G_i)]^2}\right)^{1/2} - 1\right] \tag{7}$$

If the dominant sink is the dislocation network, the bulk of the thermally produced defects will be emitted by dislocations and the thermal vacancy production will be

$$G_T = Z^d_v L D_v C^o_v \tag{8}$$

Using the above defect concentrations the minimum critical radius is

$$r^*_c = \frac{4\gamma}{3f}\,\frac{3}{2}\,\frac{1+\delta}{2+\delta} \tag{9}$$

where $\delta = \sqrt{(1+3Bf/kT)}$

$f = kT \ln [(1-Z)C_v/C^o_v + Z]/\Omega$

$Z = Z^c_v Z^d_i / Z^c_i Z^d_v$

and the van der Waals constant, B, according to reference 12 is

$$B = 6.65 \times 10^{-27}[4.5 \times 10^{-4} + 5.42/(1890 + T)].$$

In our calculations all the sink efficiencies are chosen to be equal to 1 except for Z_i^d which is used as an adjustable parameter. The bias, which reflects the excess vacancy flux to a neutral sink such as a void, equals Z-1 for the dislocation dominated case.

Calculation of the critical radii in HT-9

Fig. 4 shows the minimum of critical radius as a function of irradiation temperature calculated for several values of surface energy (γ): 0.4, 1.2 and 2.4 J/m^2. Minimum critical radius values are between 0.1 and 0.6 nm at 300°C, 0.3 and 3.0 nm at 400°C, 40 and 300 nm at 500°C and 4000 and 30000 nm at 600°C. Stars designate the experimentally determined maximum bubble radii. The adjustable parameters used to generate these results have been chosen to ensure that the critical radius has been exceeded at 400°C but not at 500 or 600°C. The curve defining minimum critical radius fits the 400°C neutron data best for a surface energy of 1.2 J/m^2 but at 300°C all curves are below the deduced minimum critical radius.

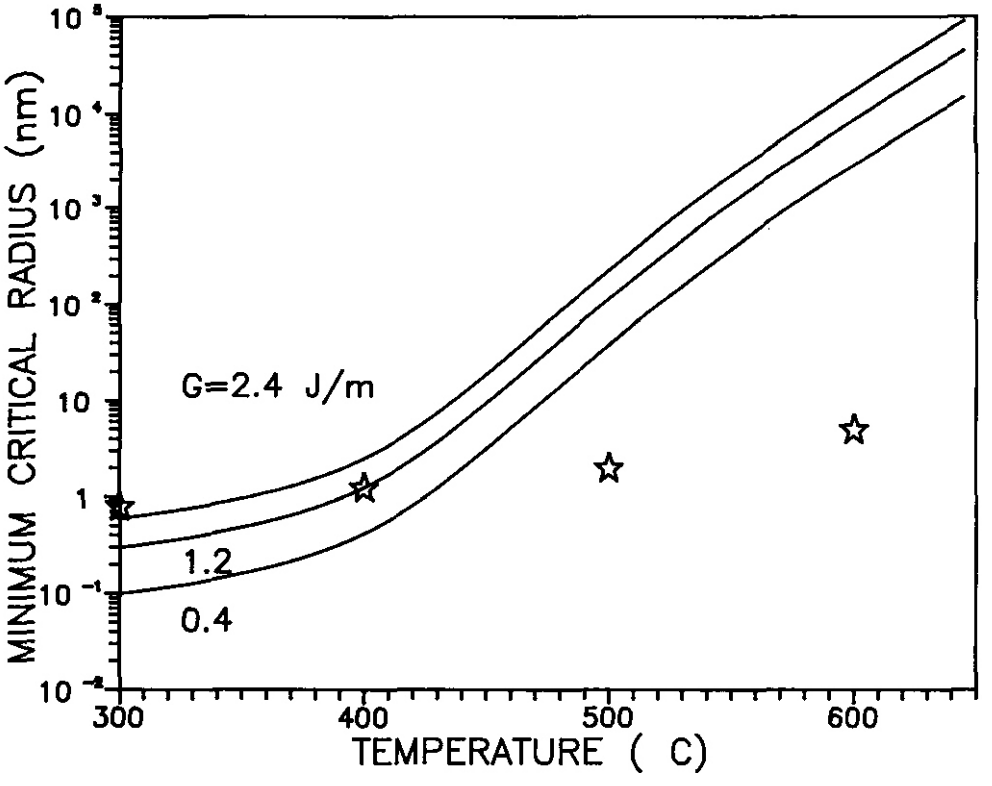


Fig. 4. Minimum critical radius versus temperature for several values of surface energy. The stars at 300, 500, and 600°C are experimentally determined maximum cavity radii. The star at 400°C is the minimum critical radius found there.

The effect of the self-diffusion activation energy, Q, on the minimum critical radius can be significant, and increases in Q bring the critical radius predictions into closer agreement with experiment. Fig. 5 has been prepared to show this effect. The values used for Q varied from 2.6 eV, the generally accepted value, to 3.0 eV. Higher values for Q appear to give more reasonable estimates for the minimum critical radius at 300°C.

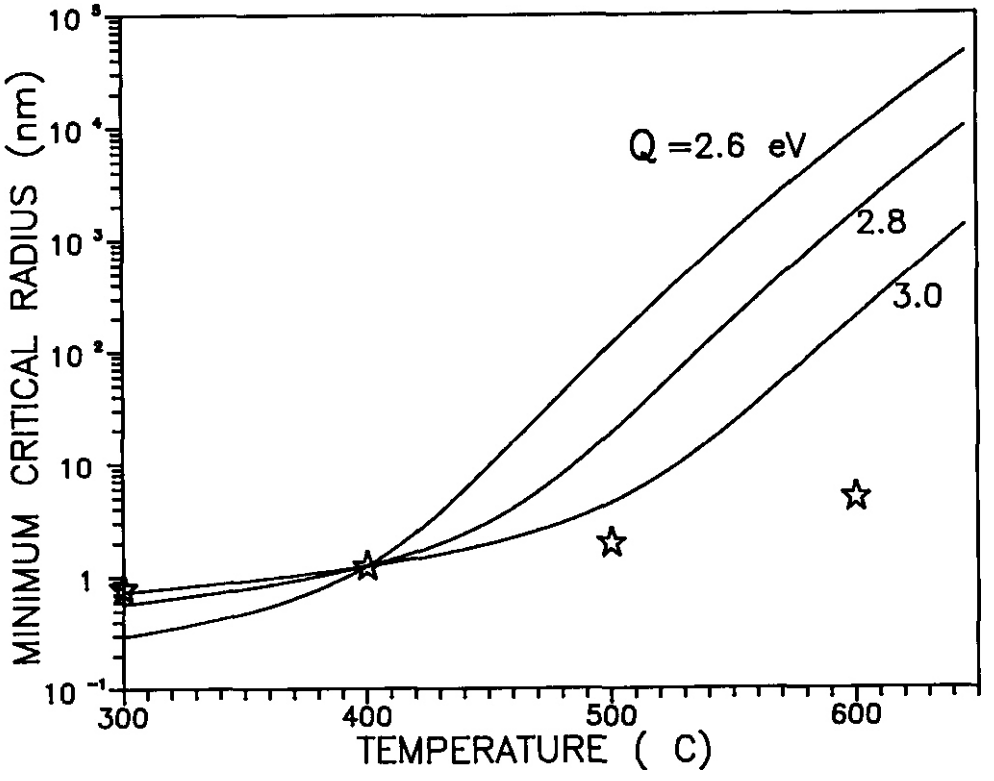


Fig. 5. Minimum critical radius versus temperature for several values of self-diffusion activation energy. The stars at 300, 500, and 600°C are experimentally determined average cavity radii. The star at 400°C is the minimum critical radius found there.

Fig. 6 shows the effect of large changes in the sink efficiency ratio, Z, on the minimum critical radius. Z is allowed to vary from 1.001 to 2.0 but only at very high values of Z are reasonable values obtained for critical radius at 300°C.

The effect of dislocation density on minimum critical radius is shown in Fig. 7. The sink strength is varied from $2x10^{13}$ to $5x10^{14}$ m^{-2} and is expected to be primarily due to the presence of dislocations, and the critical radius depends linearly on dislocation density.[13] The dislocation density is known to vary with irradiation temperature[13] approximately in the fashion shown in Fig. 8. The effect of a variable dislocation density on minimum critical radius can be computed based on Fig. 8. This result is shown in Fig. 9 and is compared with a fixed dislocation density value of $5x10^{14}$ m^{-2}. The effect of this variation is very pronounced although the observed cavities are still subcritical. At 500°C, the critical radius is reduced by an order of magnitude which would reduce the required helium atoms by nearly three orders of magnitude. Still, HT-9 would be very resistant to void swelling.

An alternate way of describing critical radius is in terms of the number of gas atoms per cavity. Fig. 10 provides this alternate representation of the data in Fig. 9. Fig. 10 shows that at 300°C, a cavity must contain 10 gas atoms to begin to grow as a void. At 400°C, two hundred gas atoms are needed and at 500°C, 10^5 gas atoms are required.

Discussion

In order to predict the swelling response of ferritic alloys in a fusion environment, the effect of He/dpa ratio must be taken into account. It is very difficult to attain a realistic He/dpa ratio experimentally, and therefore, theoretical estimates for swelling response are valuable. According to the critical cavity model, the major consequence of increases in He/dpa is expected to be in the accumulation of helium in bubbles and the promotion of bubbles beyond the critical cavity radius. An increase in he/dpa

should (as a first approximation) correspond directly to an increased accumulation of helium atoms in voids. The present effort is intended to provide a basis for extrapolation of observed swelling behavior in HFIR to that in a fusion environment, which corresponds to a four fold increase in Heldpa and therefore a four fold increase in helium accumulation at bubbles. With all other things remaining the same, one can then conclude that cavities in HT-9 should reach critical size four times faster in a fusion environment than in HFIR.

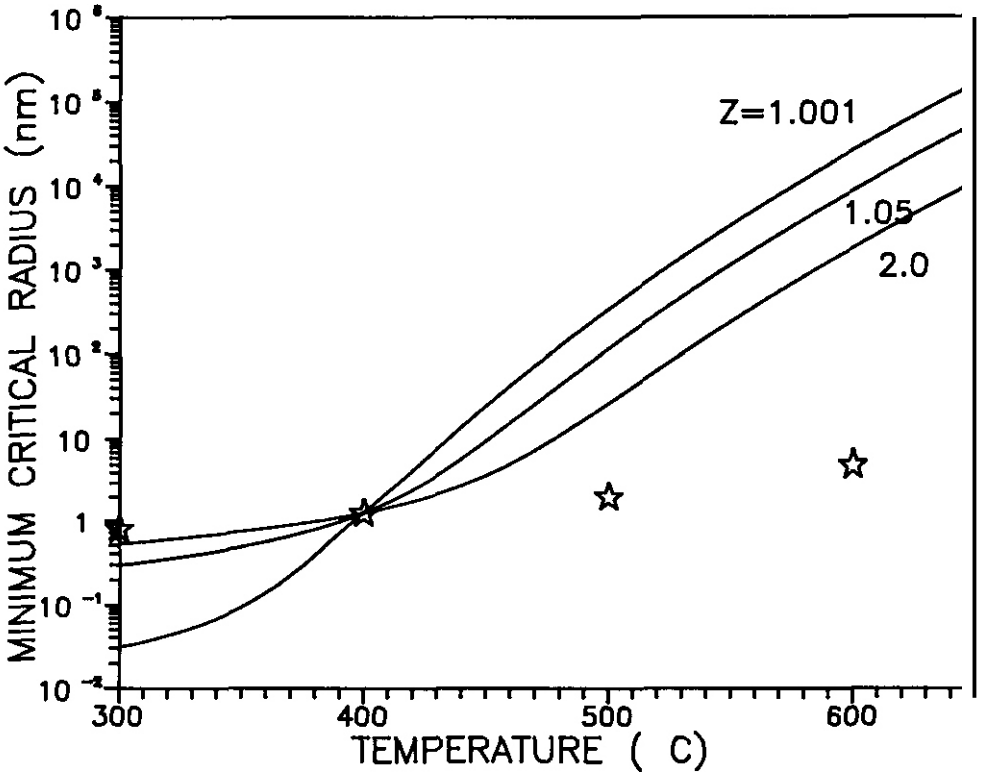


Fig. 6. Minimum critical radius versus temperature for several values of the sink efficiency ratio, Z. The stars at 300, 500, and 600°C are experimentally determined average cavity radii. The star at 400°C is the minimum critical radius found there.

Only two papers have addressed the question of critical cavity behavior in ferritic alloys: Horton and Mansur[10] and the present work. Therefore, they must provide a basis for accessing the validity of the concept and extrapolation of observed behavior to a fusion environment.

Horton and Mansur analyzed the case of ion bombardment of Fe-10Cr at 527°C, using parameters similar to the present study except that the displacement rate was 8×10^{-3} dpa/s, the point defect survival fraction was 0.5 and the dislocation density was 10^{13} m^{-2}. When traditional values for physical constants were used [surface energy = 1 J/m^2, vacancy formation entropy = 1.5k, bias = 0.05, energy for self diffusion = 2.6 eV and vacancy migration energy = 1.2 eV), extremely high values were calculated for minimum critical radius. In order to obtain reasonable values for critical radius while holding the energy for self diffusion constant, the bias had to be set at 0.2, the surface energy greater than 1 J/m^2 and the vacancy formation entropy equal to or less than k. Alternately, higher values of the energy for self diffusion provided reasonable values for minimum critical radius without adjustment of surface energy or vacancy formation energy. A check of the effect of the bias parameter on observed cavity growth showed a best fit for values less than or equal to 0.2. This was in agreement with bias values suggested by Sniegowski and Wolfer[14] of between 0.20 and 0.28 for cavity radii of 2 to 50 nm, respectively. However, Horton and Mansur note that the use of a lower value for the defect survival fraction, such as 0.2 made the calculation of critical radius much more difficult but gave more reasonable estimates for void growth behavior.

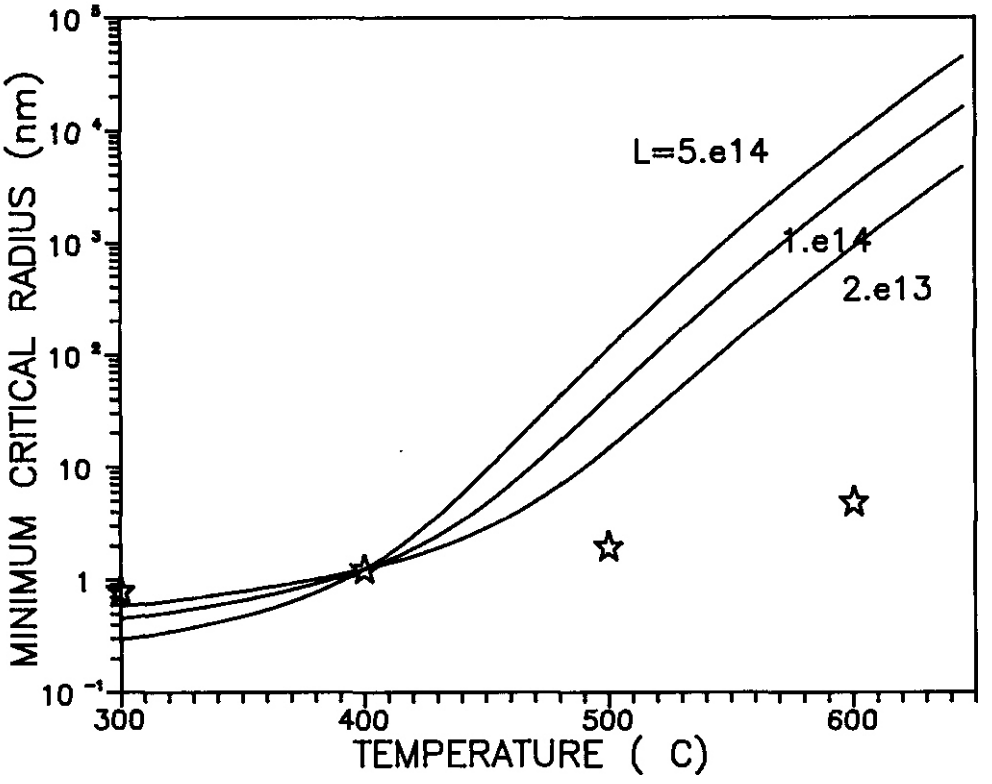


Fig. 7. Minimum critical radius versus temperature for several values of sink strength. The stars at 300, 500, and 600°C are experimentally determined average cavity radii. The star at 400°C is the minimum critical radius found there.

The present calculations indicate that a critical cavity radius at 400°C can be attained for a neutron environment using reasonable values for physical parameters. Based on these values, predictions for higher temperatures are reasonable, but predictions at 300°C do not agree with experiment. One possibility is that the cavities at 300°C have exceeded the critical radius and are growing as voids. However, the growth rate at this temperature is slow. The predictions come closer when more reasonable values are used for the dislocation density as a function of temperature. As with the Horton and Mansur calculations, best agreement is obtained when higher values of the energy for self diffusion are used. Changing the bias from 0.05 to 1.0 (Z from 1.05 to 2.00) increased the minimum critical radius at 300°C by only a factor of two. Increasing the value of the surface energy improved predictions at 300°C but degraded the prediction at 400°C. However, variations in the value of the enthalpy for vacancy migration were found to make only minor differences and those differences were similar at all temperatures so that compensating changes were also required. Therefore, variations in the enthalpy for vacancy migration were not discussed.

The difficulties which arise in predicting minimum critical cavity size may be experimental. In general, bubbles form in association with dislocations. This can be clearly seen in Fig. 1 which shows bubbles on grain boundaries connected to grain boundary dislocations. Bubbles probably form on dislocations by a solute drag mechanism, but once there, they are not exposed to the same point defect concentration gradients as bubbles which are not connected to dislocations. Therefore, measurements of critical bubble sizes may have *to* be made for bubbles not connected *to* dislocations.

An alternate method for the onset of bias driven cavity growth can be envisioned based on decoupling of bubbles from dislocations. Oecoupling would be expected if bubbles could not keep up with moving dislocations. This would be more likely to occur as bubbles grew in size. Therefore, a corollary to the critical radius model could require decoupling and the decoupling process may occur only after the bubble has grown larger than the critical size. Then the onset of bias driven growth would be initiated by a decoupling event.

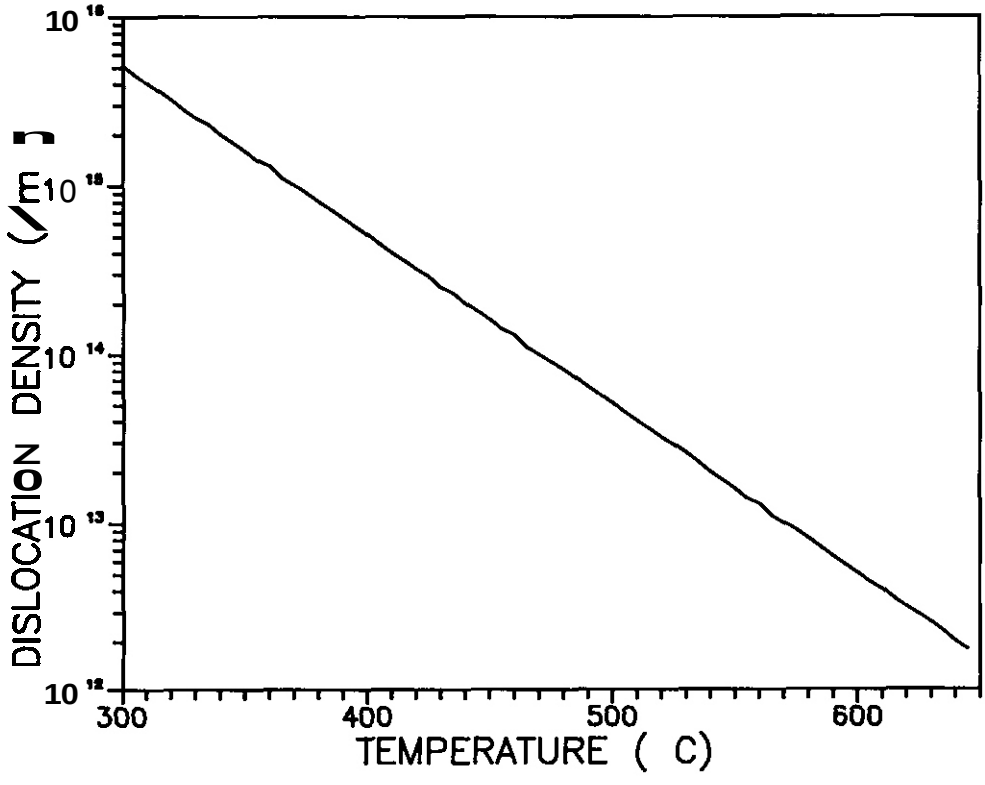


Fig. 8. Estimated dislocation density versus temperature for HT-9 irradiated in HFIR.

CONCLUSIONS

Calculations have shown that the critical radius model for bias driven void growth as applied to ferritic alloys can successfully predict behavior observed in HT-9 following irradiation in HFIR to 39 dpa at 400, 500 and 600°C using reasonable values for physical parameters. Predictions at 300°C underpredict observed response. Reasonable agreement can be obtained if a higher value is used for the energy of self diffusion.

FUTURE WORK

This effort will be continued when experimental results warrant it.

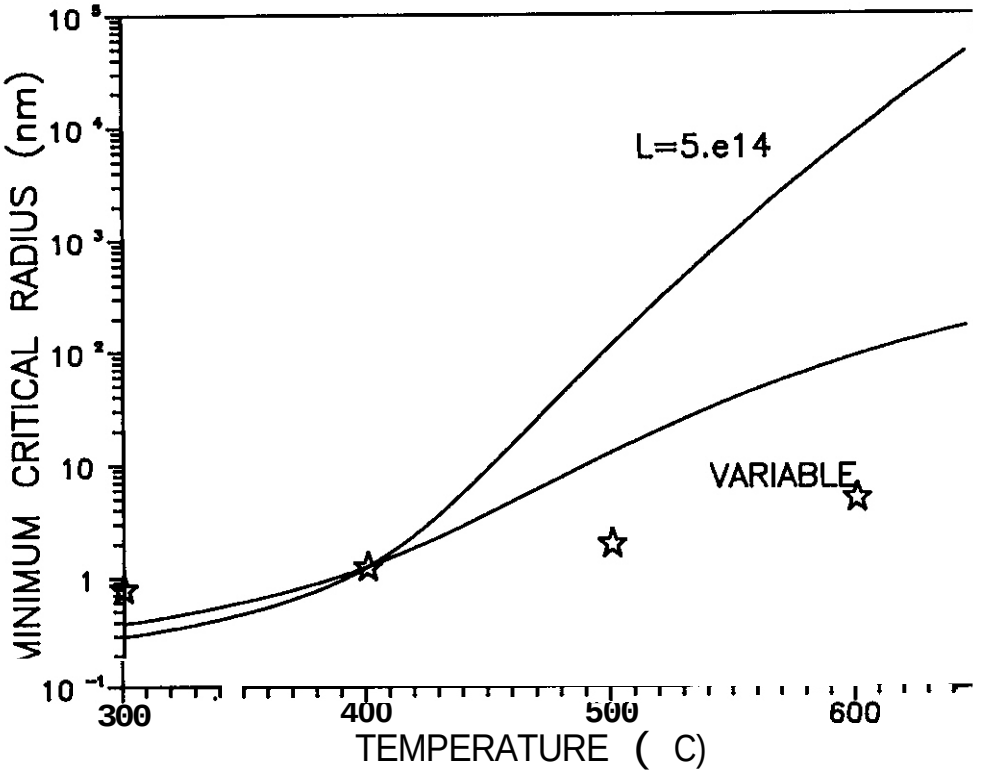


Fig. 9. Minimum critical radius versus temperature calculated for constant dislocation density and the temperature dependent dislocation density shown in Fig. 8. The stars at 300. 500, and 600°C are experimentally determined average cavity radii. The star at 400°C is the minimum critical radius found there.

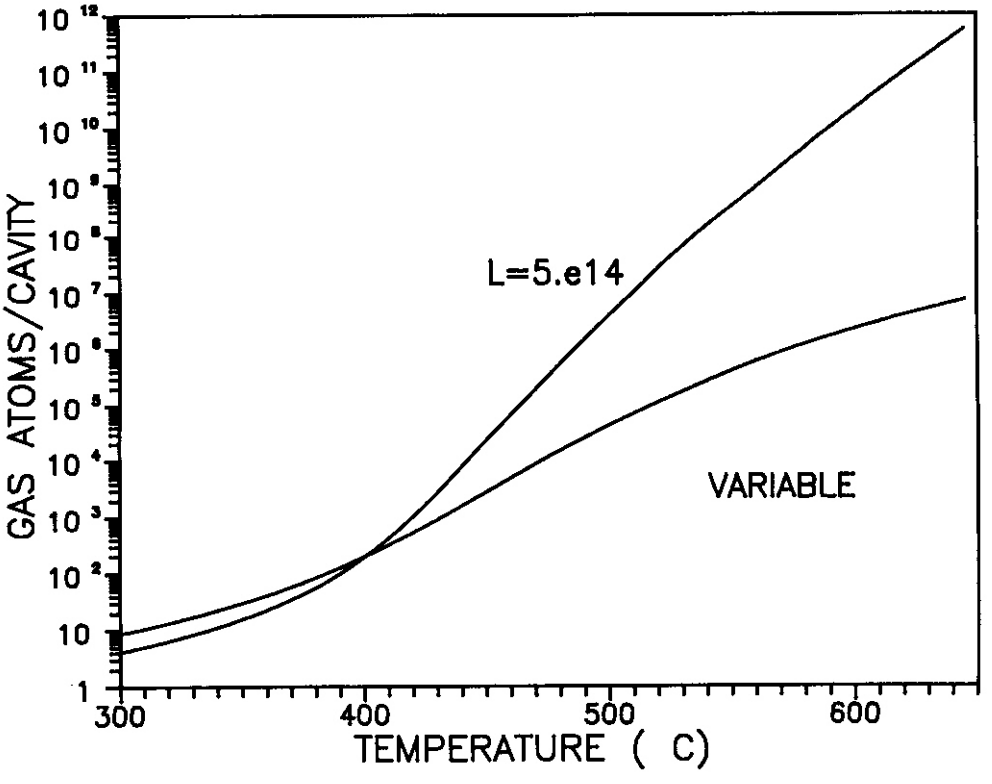


Fig. 10. The critical number of helium atoms required for the minimum critical radii plotted in Fig. 9.

REFERENCES

1. W. Vandermeulen. A. De Bremaecker, S. de Burbure, J.J. Huet, and Ph. Van Asbroeck, Proceedings of Irradiation Behaviour of Metallic Materials for Fast Reactor Core Components, Ajaccio, Corse, France, 1, (1979).

2. J. J. Huet, A. De Bremaecker. M. Snykers, Ph. Van Asbroeck, and W. Vandermeulen, IBID Reference 1, 5.

3. J. Erler, A. Maillard, J. Lehmann, and J. M. Dupouy, IBID Reference 1, 11

4. D. S. Gelles and L. E. Thomas, in Proceedings of Topical Conference on Ferritic Alloys for Use in Nuclear Energy Technologies, Ed. J. W. Davis and D. J. Michel, The Metallurgical Society of AIME, Warrendale, PA, 559 (1984).

5. J. M. Vitek and R. L. Klueh, in Alloy Development for Irradiation Performance Semiannual Progress Report for Period Ending September 30, 1983, DOE/ER-0045/11, Oak Ridge National Laboratory, Oak Ridge, TN, 108 (1984).

6. D. S. Gelles, IBID Reference 5 for Period Ending March 31, 1985, DOE/ER-0045/14, Oak Ridge National Laboratory, Oak Ridge, TN, 129 (1984).

7. L. R. Greenwood, in Damage Analysis and Fundamental Studies quarterly Progress Report for Period Ending December 31, 1981, DOE/ER-0046/8, U.S. Dept. of Energy, Washington DC., 5.

8. L. K. Mansur and W. A. Coghlan, J. Nucl. Mat. 119, 1-25 (1983).

9. W. A. Coghlan and L. K. Mansur, in Effects of Radiation on Materials: Twelfth International Symposium, ASTM STP 870, F. A. Garner and J. S. Perrin. Eds., American Society for Testing Materials, Philadelphia, 481 (1985).

10. L. L Horton and L. K. Mansur, IBID Reference 9, 344-362.

11. L. K. Mansur, E. H. Lee, P. J. Magiasz and A. P. Rowcliffe, J. Nucl. Mat., 141-143 633 (1986).

12. N. V. Tsederberg, V. N. Popov, and N. A. Morozova, "Thermodynamic and Thermophysical Properties of Helium," Israel Program for Scientific Translations, Keter Press, Jerusalem, 18-19 (1971).

13. D. S. Gelles, "Evaluation of Ferritic Alloy Fe-2 1/4 Cr-1Mo after Neutron Irradiation -- Microstructural Oevelopment," Submitted to Thirteenth ASTM International Symposium on the Effects of Radiation on Materials, Seattle, WA (June 1986).

14. J. J. Sniegowski and W. G. Wolfer, IBID Reference 4, 579-586.

DEFECT PROOUCTION AND HARDENING IN NEUTRON-IRRADIATED COPPER — S. J. Zinkle (Oak Ridge National Laboratory)

OBJECTIVE

The objective of this study is to determine the fraction of point defects that survive recombination events during neutron irradiation of copper, and to evaluate their subsequent effect on macroscopic material properties.

SUMMARY

The fraction of Frenkel defects that survive in isolated or clustered form during room temperature irradiation of copper has been measured as a function of fluence by a combination of TEM and electrical resistivity methods. The ratio of surviving to created defects decreased from 12 to 4.7% as the fluence of 14-MeV neutrons increased from 1×10^{20} to 2.9×10^{21} n/m^2. A comparison of the TEM and resistivity data with radiation hardening studies indicates that the barrier strength of loops (β) may also depend on fluence, at least at low fluences.

PROGRESS AND STATUS

Introduction

The number of point defects that are produced and retained as a result of an energetic displacement cascade is of fundamental importance to radiation effects studies. In-cascade recombination events and subsequent correlated recombination of Frenkel pairs reduces the number of point defects that survive an isolated displacement cascade to a fraction of the number that were initially created. Studies on copper and gold irradiated with neutrons at temperatures above recovery Stage II have found that the fraction of defects surviving correlated recombination in isolated or clustered form is $\varepsilon \approx 0.15$ (refs. 1–3). The parameter ε is independent of fluence since it refers to noninteracting displacement cascades and represents the maximum fraction of point defects that survive at irradiation temperatures where at least one of the defect types is mobile.

On the other hand, the number of Frenkel defects that ultimately survive the displacement event depends on the number of surrounding sinks and defect clusters that are present during the irradiation (interacting cascade effects). Long-range uncorrelated recombination of point defects at distant displacement cascades causes the number of surviving defects to increase at a rate that is less than linear with fluence.' When coupled with appropriate radiation damage models, measurements of ε and the surviving defect fraction η provide significant insight into the basic mechanisms of point defect production, migration, and clustering. The purpose of this paper is to determine the value of η as a function of fluence for 14-MeV neutron-irradiated copper.

Experimental procedures

Annealed pure copper foils were irradiated at room temperature with 14-MeV neutrons using the RTNS-II facility at the Lawrence Livermore National Laboratory. TEM disks and an electrical resistivity foil were irradiated to fluence levels between 1×10^{20} and 3×10^{21} n/m^2. Four resistivity measurements were made by interrupting the irradiation and immersing the sample assembly in liquid helium. Four fluence levels were obtained for the TEM disks by placing the disks at different distances from the neutron source. Vickers hardness measurements (10-g load) and electron microscopy were performed on the TEM disks following the irradiation. Further details of the experimental procedure are given elsewhere.[4,5]

Results

Tables 1 and 2 summarize the experimental measurements on defect cluster density and size,' microhardness change,[6] and electrical resistivity changes obtained from this investigation. The two tables also give yield strength data obtained by Mitchell' for copper irradiated with 14-MeV neutrons at room temperature. As reported elsewhere,[4] the defect cluster size was essentially independent of fluence in irradiated copper and copper alloys over the fluence range examined in this study. The cluster number density and electrical resistivity increase was less than linear with fluence.

The total concentration of surviving point defects (N_D) contained in visible clusters of density N may be calculated assuming that the clusters are circular dislocation loops.

Table 1. Experimental parameters for irradiated copper at the four fluence levels achieved by the TEM disks. The yield strength data are from Mitchell[1]

Fluence, n/m^2	1.4×10^{20}	4.3×10^{20}	1.07×10^{21}	1.85×10^{21}
Cluster density, $10^{22}/m^3$	0.62	1.2	3.3	4.4
Mean size, nm	3.25	2.91	2.92	2.85
ΔVHN	0	1.9	12.2	21.5
$\Delta\sigma_y$, MPa	8	18	48	68

Table 2. Experimental parameters for irradiated copper at the four fluence levels achieved by the resistivity foil. The yield strength data are from Mitchell[1]

Fluence, n/m^2	0.98×10^{20}	3.03×10^{20}	9.8×10^{20}	2.93×10^{21}
$\Delta\rho$, 10^{-11} n-m	0.685	1.976	4.051	8.568
$\Delta\sigma$, MPa	5	10	46	87

$$N_D = \pi \langle d^2 \rangle b N/4 \quad , \tag{1}$$

where $\langle d^2 \rangle$ is the mean square diameter and $b = a_0/\sqrt{3}$ is the Burgers vector of the loop. The cumulative production of point defects is directly proportional to the fluence ϕt,

$$N_D = 2 \sigma_d \phi t \quad , \tag{2}$$

where the displacement cross section for 14-MeV neutrons in copper is σ_d = 3690 barns according to Doran and Graves.[8] The factor of 2 in the equation is due to the creation of two point defects (vacancy and interstitial) for each displaced atom.

Table 3 gives the atomic fraction of surviving point defects [Eq. (1)] and the ratio of surviving to created point defects (η) as determined from TEM measurements. The values for the mean square diameters used in the calculations are given in ref. 5. In order to estimate the possible error due to the neglect of small loops that are invisible in TEM, the visible size distributions at large sizes were fitted to exponential equations which were then extrapolated down to small sizes.[5] The values for the point defect concentration and η using the exponential fit size distributions are also given in Table 3. The observed and exponential fit values should represent[5] the lower and upper bound to the actual value of η.

Table 3. Concentration of surviving point defects as determined from TEM measurements

Fluence (n/m^2)	Point defect concentration (10^{-5}/atom)		Surviving defect fraction (%)	
	Observed	Exponential fit	Observed	Exponential fit
1.4×10^{20}	1.34	1.44	12.9	13.8
4.3×10^{20}	2.14	2.46	6.8	7.8
1.07×10^{21}	5.26	5.42	6.7	6.9
1.85×10^{21}	7.64	7.72	5.6	5.6

A recent study has found that the electrical resistivity change ($\Delta\rho$) is directly proportional to the number of point defects even if the point defects are contained in small dislocation loops.[5] The atomic fraction of surviving point defects in isolated or clustered form is given by

$$N_D = 2 \Delta\rho/\rho_{FP} \quad ,$$

where $\rho_{FP} \sim 1.7$ $\mu\Omega$-m for copper irradiated with neutrons at room temperature. Table 4 gives the fluence-dependent concentration of surviving point defects as determined from Eq. (3).

The radiation strengthening due to dispersed barriers such as dislocation loops is generally given as[9]

Table 4. Concentration of surviving point defects as determined from resistivity measurements

Fiuence (n/m^2)	Point defect concentration (10^{-5}/atom)	Surviving defect fraction (%)
0.98×10^{20}	0.81	11.1
3.03×10^{20}	2.32	10.4
9.8×10^{20}	4.77	6.6
2.93×10^{21}	10.08	4.7

$$\Delta\tau = \frac{\mu b}{\beta}\sqrt{N\langle d\rangle}\ , \qquad (4)$$

where μ is the shear modulus (46 GPa for copper), $b = a_0/\sqrt{2}$ is the line dislocation Burgers vector, $\langle d\rangle$ is the mean loop diameter, and β is a constant related to the strength of the barrier. Weak barriers such as vacancy clusters are sometimes modeled with a slightly different equation9

$$\Delta\tau = \frac{\mu b}{\beta'}\langle d\rangle N^{2/3}\ , \qquad (5)$$

where 5' is another barrier strength constant. Application of the von Mises criterion between shear stress $\Delta\tau$ and yield strength $\Delta\sigma_y = 43\ \Delta\tau$ produces a relationship between hardening and loop density that could be used to calculate surviving point defect concentrations. However, it is of greater interest to use the TEM, resistivity, and radiation hardening data to determine the barrier strength constant β since this parameter is not generally known with good accuracy.

The value of β was determined at eight fluence levels (4 TEM, 4 resistivity) as follows: Eq. (4) and the von Mises criterion were used in combination with the observed and exponential fit TEM data to directly calcuiate 5 from Mitchell's[7] yield strength data (Table 1). Second, the resistivity results (Table 4) were used along with Eqs. (1) and (3) and a mean square cluster diameter of $\langle d^2\rangle = 8.7\ nm^2$ (determined from TEM[5]) to produce a caiculated vaiue of β at four different fluences. The results of these calculations are shown in Fig. 1. The calculated value of β decreases steadily from 16 to 3 as the neutron fluence increases from 1×10^{20} to $3 \times 10^{21}\ n/m^2$, which suggests that widely separated clusters (low densities) are not very effective at strengthening the metal. An even stronger fluence dependence for 6 was found when the microhardness data in Table 1 was substituted for the yield strength data. The barrier strength was also found to be fluence-dependent when Eq. (5) was used to model the radiation strengthening, although the fluence dependence was not quite as strong.

The fraction of point defects that survive correlated recombination in copper is $\varepsilon \simeq 0.15$, independent of fluence.[1-3] The fiuence dependence of the surviving defect fraction, η, is due to uncorreiated recombination of point defects at distant cascades. According to Simons,[10] the freely migrating defects in copper are predominantly (4:1) interstitial for neutron and other cascade-producing irradiations. Long-range migration of interstitials to existing distant cascades can therefore cause shrinkage and eventual annihilation of vacancy clusters *in* these regions. The probability of an interstitial encountering a vacancy cluster (as opposed to another interstitial) increases as the vacancy cluster density increases.

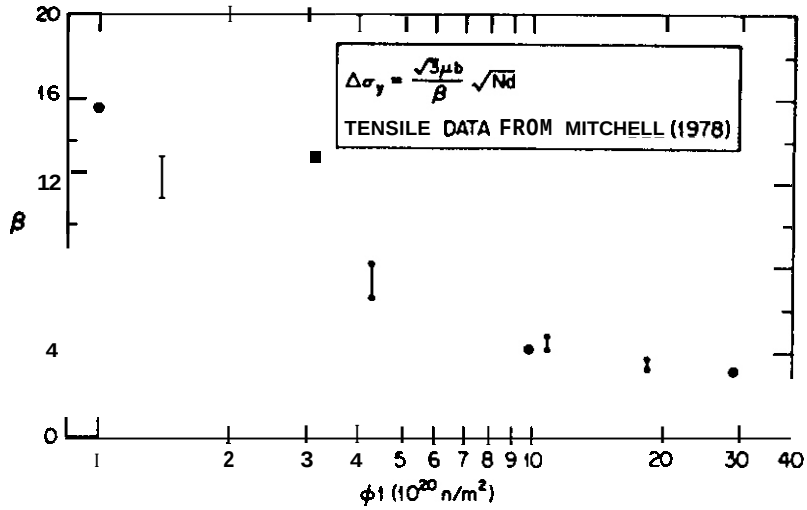


Fig. 1. Barrier strength of loops in neutron-irradiated copper. The vertical lines represent the bounds on β as determined from the observed and exponential fit TEM data. The filled circles represent the resistivity measurements.

This leads to a steady decrease in η with increasing fluence. Figure 2 shows the combined estimates of the surviving defect fraction from the TEM and resistivity analyses plotted as a function of fluence. Both analyses indicate that η decreases from ~12 to 4.7% as the fluence increases from 1×10^{20} to 3×10^{21} n/m^2. These calculations give a lower bound for the fraction of point defects that survive correlated recombination of $\varepsilon \geq 12\%$, since the maximum value of η (at $\phi t = 0$) is equal to ε.

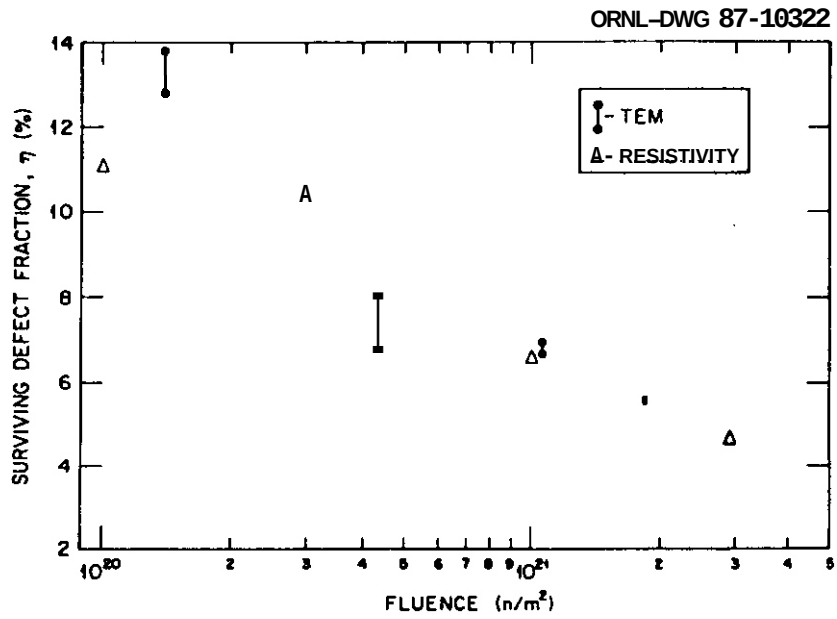


Fig. 2. Ratio of surviving to created defects in neutron-irradiated copper.

Discussion

Previous damage efficiency measurements in the literature have centered on the athermal recombination of close pairs[11,12] and on the fraction of freely migrating defects.[1,13,14] These parameters are of great importance for theoretical modeling of radiation damage in metals. The freely migrating defect fraction (f) is related to the fraction of point defects that survive correlated recombination (ε), the difference being that f does not include point defects that cluster during the cascade quench. The parameters ε and η are important from both a fundamental and a practical point of view. They represent the fraction of point defects that are available to produce microstructural changes in the metal during irradiation. The quantitative value of η derived in this study is only valid for irradiation conditions where recombination is the dominant sink term. A different fluence-dependent relationship for η holds for other irradiation conditions (e.g., the void swelling regime). The parameter η provides a measure of the amount of point defect migration and long-range interaction at a given irradiation condition.

Most previous studies that have measured surviving defect fractions have failed to investigate any possible fluence dependence of η. Kiritani et al.[13] have found that $\eta \simeq 4.5\%$ for gold irradiated with 14-MeV neutrons to a fluence of 4×10^{21} n/m^2, which is in good agreement with the value for copper in Fig. 2. Brager et al.[15] estimated that $\eta > 9.7\%$ for 14-MeV neutron irradiated copper over the fluence range of 8×10^{20} to 7×10^{21} n/m^2, which is higher than the present results. Data by Larson[16] indicate that η decreased steadily from 16 to 9% in copper irradiated at 43°C as the fission neutron fluence increased from 1.0 to 10.8 $\times 10^{22}$ n/m^2 ($E > 0.6$ MeV).

The barrier strength of dislocation loops, β, has been measured[17] or calculated[9] to be ~2 to 4 according to various authors. Figure 1 indicates that β is not constant over the fluence range of 1×10^{20} to 3×10^{21} n/m^2, but instead decreases with increasing fluence. One immediate note of caution to this observation is that the cluster density and yield strength change results for Fig. 1 were obtained in different irradiation experiments using copper of different purity levels. The copper used by Mitchell7 contained ~500 ppm of substitutional impurities compared to 25 ppm in the present case. This could, in principle, affect the measured change in strength due to short-range obstacles, since the strength increment due to short-range obstacles is not directly additive.[18] However, the impurities contained in Mitchell's copper produce <1 MPa of solid solution strengthening according to refs. 19 and 20. This should have a

negligible effect on the measured radiation hardening increment even at low fluences. The effect of interstitial impurities on the short-range obstacle strength is not known since they were not measured by Mitchell. Impurities can also influence the size and density of defect clusters produced during neutron irradiation.21 Electron microscopy measurements reported by Mitchell[7] are similar to those found in the present study. Mitchell found a cluster density of $3 \times 10^{22}/m^3$ and a mean diameter of ≅3 nm following irradiation to 1.3×10^{21} n/m². This produces $\beta \approx 4$ using his yield strength data, in agreement with Fig. 1.

There are some indications in the literature that Eq. (4) with β = constant does not hold over an extended range of loop densities. Makin and coworkers[17] found that $\Delta\sigma_y$ was not proportional to $\sqrt{N<d>}$ for loops of diameter <5 nm. Studies on obstacle-controlled yield strength[22] have found that the relation between strength increment and obstacle concentration is much more complex than given by Eq. (4). This complex behavior is observed even for weak short-range obstacles such as vacancy clusters and solute atoms. For example, three distinct hardening regimes have been identified in solution hardening in which the yield stress dependence on concentration varies from $C^{1/2}$ to C to $C^{2/3}$, respectively.[23] From the preceding discussion it appears plausible that p may not be constant over an extended fluence regime since the concentration dependence of the loop hardening may be changing. However, this possibility needs to be verified with carefully performed experiments that use a combination of TEM and yield strength measurements on identical specimens over an extended fluence range. The present results (Fig. 1) suggest that low densities of loops are relatively inefficient at producing an increase in strength, compared to Eq. (4). A constant barrier strength over the fluence range 1×10^{20} to 3×10^{21} n/m² is obtained by assuming $\Delta\sigma_y \sim N$.

CONCLUSIONS

Estimates of the surviving defect fraction (η) for a room temperature irradiation obtained from TEM and electrical resistivity measurements are in good agreement with each other. The value of η in copper decreased from 12% to 4.7% as the neutron fluence increased from 1×10^{20} to 2.9×10^{21} n/m². The low-fluence value of η provides a lower bound for the fraction of point defects that escape correlated recombination of $\epsilon \geq 12\%$.

Measurements of the barrier strength of loops in irradiated copper based on the dispersed barrier hardening model suggest that β is not constant at low neutron fluences. It is possible that a different hardening model is needed to describe the results. This possibility needs to be studied further with carefully performed experiments.

ACKNOWLEDGMENTS

Part of this work was performed while the author was under appointment to the Magnetic Fusion Energy Technology fellowship program. The author would like to thank M. W. Guinan for his assistance with the irradiations, and Frances Scarboro for manuscript preparation.

REFERENCES

1. U. Theis and H. Wollenberger, J. Nucl. Mater. 88, 121 (1980).

2. S. J. Zinkle and G. L. Kulcinski, J. Nucl. Mater. 122&123, 449 (1984).

3. M. Kiritani, T. Yoshiie, and S. Kojima, J. Nucl. Mater. 141&143, 625 (1986).

4. S. J. Zinkle, "Microstructure and Properties of Copper Alloys Following 14-MeV Neutron Irradiation," submitted to Journal of Nuclear Materials. (Preliminary results of this paper are given in S. J. Zinkle, Fusion Reactor Materials Semiann. Prog. Rep. Sept. 30, 1986, DOE-ER-0313/1).

5. S. J. Zinkle, "Electrical Resistivity of Small Dislocation Loops in Irradiated Copper," submitted to J. Phys. F. (1987).

6. S. J. Zinkle and G. L. Kulcinski, p. 141 in The Use of Small-Scale Specimens for Testing Irradiated Material, eds., W. R. Corwin and G. E. Lucas, Albuquerque, NM, Sept. 1983, ASTM-STP 888 (1986).

7. J. B. Mitchell, Lawrence Livermore Laboratory Report, UCRL-52388 (January 1978); also J. B. Mitchell et al., p. 172 in Radiation Effects and Tritium Technology for Fusion Reactors, Vol. II, eds., J. S. Watson and F. W. Wiffen, Gatlinburg, TN (1975).

8. D. G. Doran and N. J. Graves, Displacement Cross-Sections and PKA Spectra: Tables and Applications, HEDL-TME 76-70 (December 1976).

9. A. L. Bement, Jr., p. 693 in 2nd Int. Conf. on Strength of Metals and Alloys, ASM, 1970.

10. R. L. Simons, J. Nucl. Mater. 141&143, 665 (1986).

11. R. S. Averback et al., Phys. Rev. B 18, 4156 (1978).

12. J. H. Kinney, M. W. Guinan, and Z. A. Munir, J. Nucl. Mater. 122&123, 1028 (1984).

13. T. H. Blewitt, A. C. Klank, T. Scott, and W. Weber, p. 757 in Radiation-Induced Voids in Metals, eds., J. W. Corbett and L. C. Ianniello, Albany, NY, (US AEC CONF-710601, 1972).

14. L. E. Rehn, P. R. Okamoto, and R. S. Averback, Phys. Rev. B 30, 3073 (1984).

15. H. R. Brager, F. A. Garner, and N. F. Panayotou, J. Nucl. Mater. 103&104, 995 (1981).

16. 8. C. Larson, J. Appl. Crystallogr. 8, 150 (1975).

17. M. J. Makin, F. J. Minter, and S. A Manthorpe, Phil. Mag. 13, 729 (1966).

18. N M. Ghoniem, J. Alhajji, and F. A. Garner, p. 1054 in Effects of Radiation on Materials: 11th Conf., ASTM-STP 782, eds., H. R. Brager and J. S. Perrin (ASTM, 1982).

19. B. Smola, Czech. J. Phys. B 31, 447 (1981).

20. H. Wendt and R. Wagner, Acta Met. 30, 1561 (1982).

21. N. Yoshida et al., J. Nucl. Mater. 133&134, 405 (1985).

22. U. F. Kocks, Mat. Sci. Engr. 27, 291 (1977).

23. T. Suzuki, Japan J. Appl. Phys. 20, 449 (1981).

COMPUTER SIMULATION OF ION BEAM MIXING - PART I -- S. Han and G.L. Kulcinski (University of Wisconsin)

OBJECTIVE

The objective of this work is to develop a computer program that can simulate the ion beam mixing, which is a technique used for surface modification of materials to enable them to withstand high heat and aggressive environments.

SUMMARY

Ion beam mixing, which is defined as the application of eneryetic heavy ion beam to induce materials interactions in thin-film composite sample or pre-implanted solids, has been received a great concern by many research groups.[1,2,3,4,5,6,7] However, the complicated nature of mixing process makes it hard to predict the dynamic behavior of the materials during ion beam irradiation. Monte Carlo methods have been used to solvethis problem and in this study, the accuracy of such a program was tested to calculate the ion range before further modification of the program.

PROGRESS AND STATUS

Introduction

A Monte Carlo program has been developed to calculate the ion and defect distribution from ion beam irradiation of multilayer-multicomponent target. The adequate assessment of the scattering angles and the use of recently formulated electronic stopping cross section greatly enhanced the accuracy of the program compared with the existing experimental data.

Description of Model

1. Scattering angle evaluation

The scattering angle in the center-of-mass system between two charged particles under the influence of screened Coulomb potential is expressed as

$$\theta = \pi - 2b \int_0^{z_0} \frac{dz}{\sqrt{1 - \frac{z}{\varepsilon}\Phi\left(\frac{1}{z}\right) - b^2 z^2}} \tag{1}$$

where z_0 is the root of the equation:

$$1 - \frac{z}{\varepsilon}\Phi\left(\frac{1}{z}\right) - b^2 z^2 = 0 \tag{2}$$

and b is the reduced impact parameter, ε is the reduced energy, and Φ is the screening function, Furthermore, ε and b are expressed respectively as

$$\varepsilon = \frac{a}{Z_1 Z_2 e^2} \frac{M_2}{M_1 + M_2} E_{10}$$
$$b = \frac{p}{a} \tag{3}$$

where p is the impact parameter and a is the screening radius. Since θ is only a function of ε and b for a given interatomic potential e.g. Thomas-Fermi, Moliere, or Universal potential, it can be tabulated before the actual runs of the program. The relative error for calculating the scattering angle using the linear interpolation of such a tabular approach was estimated to be 0.1% on the average and 3% at the maximum. At high energy ($\varepsilon > 10^3$), the simple Coulomb potential is used to give the analytic expression of the scattering angle as

$$\theta_{Coul} = 2 \tan^{-1}\left(\frac{1}{2\varepsilon b}\right) . \tag{4}$$

2. Electronic stopping

Recent semiempirical formula by Zigler et al.[8] is used to calculate the electronic stopping cross section, which uses the scaling of the proton stopping power with eight fitting coefficients.

3. Electronic straggling

For high energy light ions in heavy medium, electronic straggling effect has been considered, which results in the spreading of the energy loss around the mean value. Bonderup and Hvelplund's model[9] based on the free electron gas calculation is used to evaluate the amount of straggling, which is expressed as

$$1 + \left(\frac{1}{5}\left(\frac{v_F}{v}\right)^2 + \frac{\hbar\omega_0}{2mv^2}\right) \ln\left(\frac{v}{v_F}\right)^2 \Big/ \left(1 + 13\chi^2\right)^{-0.5}\left(\frac{v}{v_F}\right)^2 \qquad (5)$$

where Ω_B^2 is Bohr straggling,[10] v_F and ω_0 are the Fermi velocity and plasma frequency of the target respectively, and χ is $e^2/\pi\hbar v_F$. Moreover, Ω_B^2 is expressed as

$$\Omega_B^2 = 4\pi Z_1^2 Z_2 e^4 \left(\frac{1 - 0.5\beta^2}{1 - \frac{2}{E}}\right) N\Delta x \qquad (6)$$

where β is the relativity factor (v/c) and N is the target atomic density.

4. Path length extension

To accelerate the calculation at high energy, the path length for next collision is extended in such a way that small scattering angle collisions and consequently small energy transfers, are neglected. With this, the calculation time can be reduced by 2 orders of magnitude at high energy for light ions.

Results and Discussion

For the low energy heavy ion, nuclear stopping process dominates the electronic stopping and for high energy light ions, vice versa. Hence, heavy ion range data have been chosen to check the accuracy of nuclear stopping and high energy light ion for electronic stopping.

Figure 1 shows the projected range and relative straggling of heavy ions into Si in reduced energy units.[11,12,13,14,15] The model prediction from this study is denoted with three lines for Moliere, Kr-C, and Universal potentials. It can be seen that the use of Universal potential reproduces the experimental data best and the relative straggling is almost independent of the choice of potentials. Figure 2 shows the projected range of N^{14} into Ni at various ion energies.[16] The calculation results are about 5% lower than the experiment. In Figure 3, the effect of electronic straggling is checked for 10 MeV He into Bi. The inclusion of electronic straggling results in the increase of the standard deviation by 11%. Figure 4 shows the ion and defect distribution for the case of multilayer-multicomponent target, 200 keV B^{11} into 2000 Å W film on SiO_2 substrate, which is a typical arrangement in ion beam mixing. There appear two ion concentration peaks, one in the W layer and the other in the SiO_2 substrate. However, the defect distribution shows only one peak in the first layer.

CONCLUSION

A Monte Carlo program to calculate the ion and damage distribution from ion beam irradiation on solid has been developed, which adopts the newly suggested interatomic potential and electronic stopping cross sections. In addition, the electronic straggling effect has been also taken into account for high energy light ions. This program can predict the ion range within the error of 10% with the capability to deal with multilayer-multicomponent target.

FUTURE WORK

The program will be modified to solve the ion beam mixing problem. The first step is the inclusion of a variable, time. The atomic relocation of the target should be profiled as a function of time. This step will enable us to simulate the collisional mixing process. Up to this stage atomic collision is the only driving force for the atomic motion in solids. Finally, the variable, temperature will be added to include

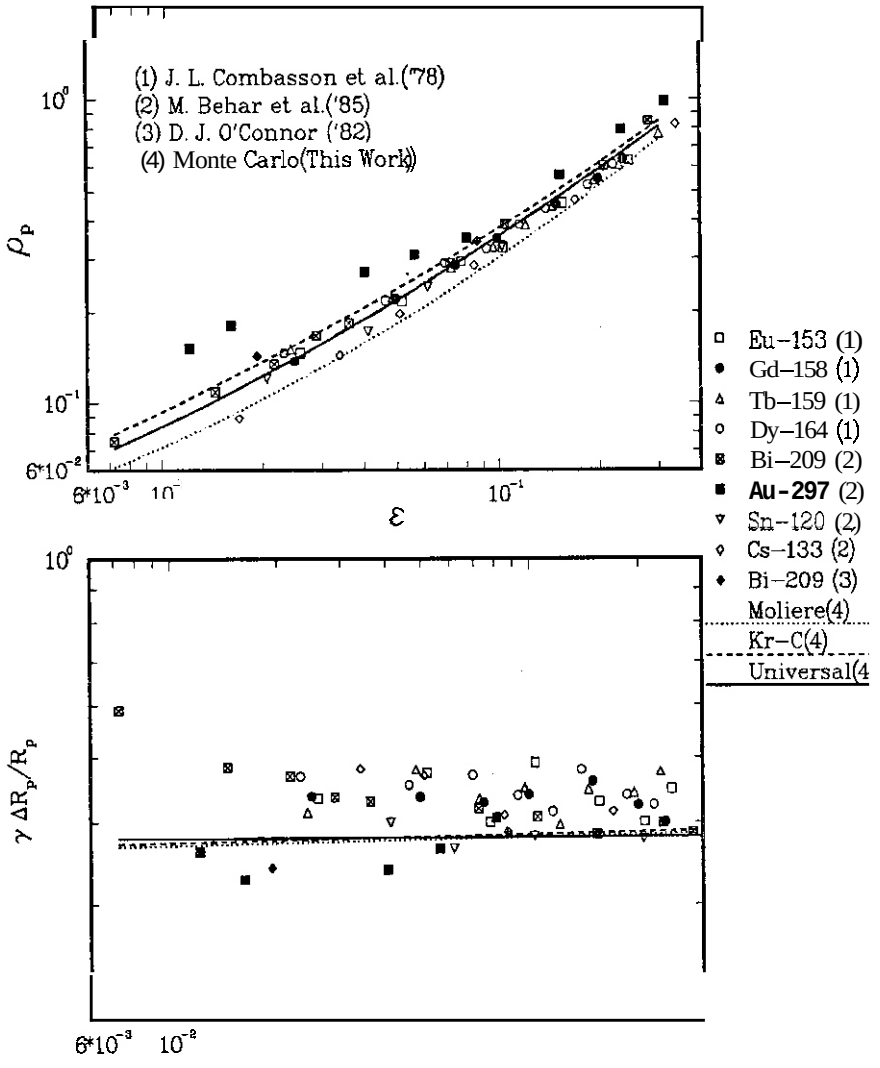


Figure 1. **Projected Range and Straggling** of **Heavy Ions on Si**

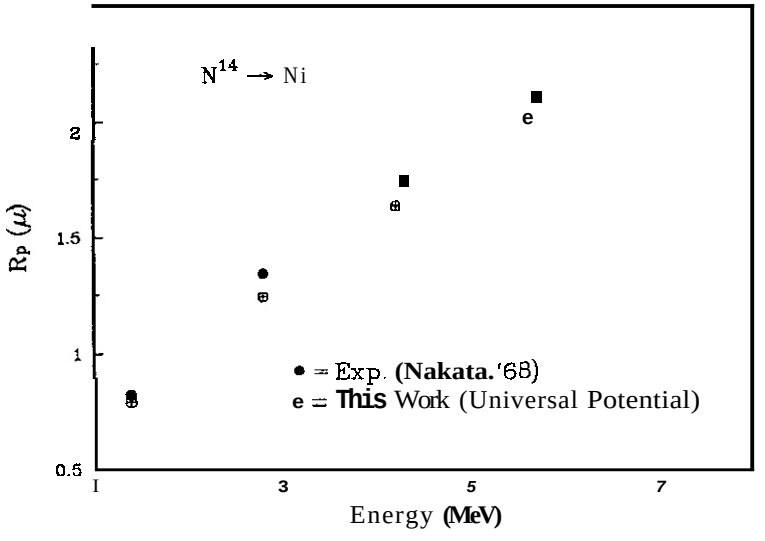


Figure 2. **Projected Range** of N^{14} into **Ni**

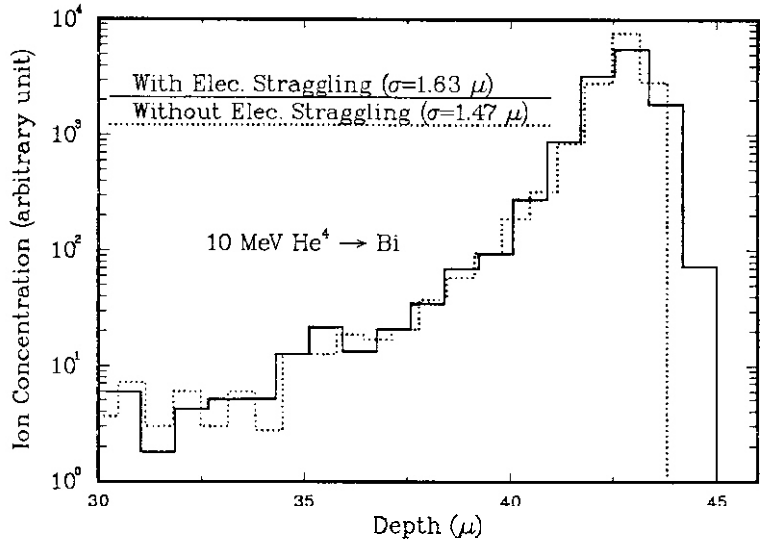


Figure 3. Ion Distribution for 10 MeV He^4 into Bi

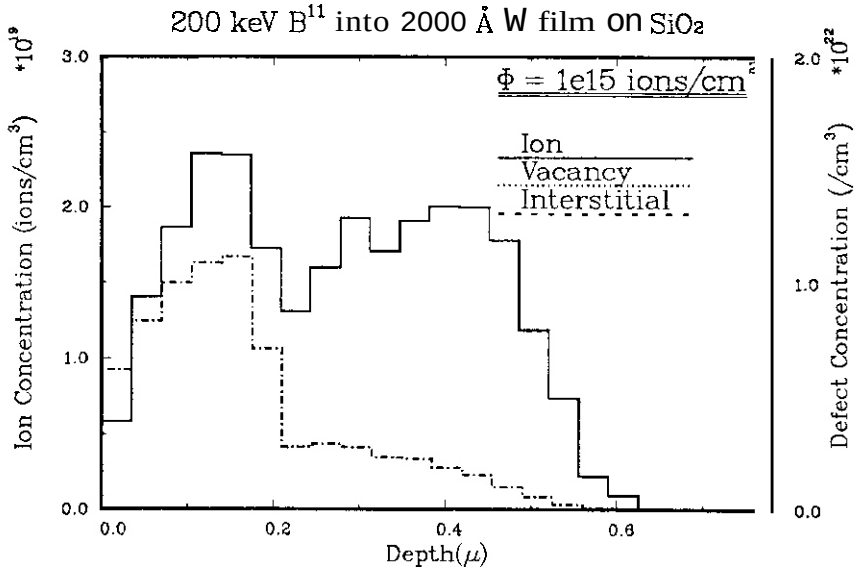


Figure 4. Ion and Defect Distribution

thermodynamic driving forces. In this stage, the defect configuration in the solids will be incorporated in the name of diffusional mixing along with the rapid quenching effect and spike effect to the usual collisional mixing process.

REFERENCES

1. J.W. Mayer, S.S. Lau, B.Y. Tsaur, J.M. Poate and J.K. Hirvonen, "Ion Implantation Metallurgy," (C.M. Preecy and J.K. Hirvonen, eds.), p. 37, *The Metallurgical Society of AIME* (1980).

2. J.W. Mayer, B.Y. Tsaur, S.S. Lau and L.S. Hung, *Nucl. Instr. and Meth.* 182/183, 1 (1981).

3. B.Y. Tsaur and J.W. Mayer, *Appl. Phys. Lett.* 37, 389 (1980).

4. B.Y. Tsaur, S.S. Lau and J.W. Mayer, *Appl. Phys. Lett.* 36, 823 (1980).

5. B.Y. Tsaur, J.W. Mayer, J.F. Graczyk and K.N. Tu, *J. Appl. Phys.* 51, 5334 (1980).

6. B.Y. Tsaur, J.W. Mayer and K.N. Tu, *J. Appt. Phys.* 51, 5326 (1980).

7. B.Y. Tsaur, S.S. Lau, L.S. Hung, and J.W. Mayer, *Nucl. Instr. and Meth.* 182/183, 67 (1981).

8. J.F. Zigler, J.P. Biersack, U. Littmark, "Stopping and Range of Ions in Solids," (Pergamon Press, New York, 1985) Vol. 1.

9. E. Bonderup and P. Hvelplund, *Phys. Rev.* A 4, 562 (1971).

10. N Bohr, *K. Dan. Vidensk. Selsk., Mat. Fys. Medd.* 18, No. 8 (1948).

11. J.L. Combasson, B.W. Farmery, D. McCulloch, G.W. Neilson and M.W. Thompson, *Rad. Effect* 36, 149 (1978).

12. D.J. O'Connor, *Nucl. Instr. and Meth.* 196, 493 (1982).

13. M. Behar et al., *Nucl. Instr. and Meth.* B6, 453 (1985).

14. M. Behar et al., *Rad. Effect* 90, 103 (1985).

15. O. Fink and J.P. Biersack, *Nucl. Instr. and Meth.* B15, 71 (1986).

16. H. Nakata, *Can. J. Phys.* 46, 2765 (1968).

6. DEVELOPMENT OF STRUCTURAL ALLOYS



6.1 Ferritic Stainless Steels

CHARPY IMPACT TEST RESULTS OF FERRITIC ALLOYS FROM THE HFIR-MFE-RBZ TEST - W. L. Hu and D. S. Gelles (Westinghouse Hanford Company)

OBJECTIVE

The objective of this work is to determine the effect of low temperature irradiation in HFIR on the properties of Path E alloys in order to determine the applicability of these alloys as first wall materials.

SUMMARY

Miniature Charpy specimens of HT-9 in base metal, weld metal and heat affected zone (HAZ) metal conditions, and 9Cr-1Mo in base metal and weld metal conditions have been tested following irradiation in HFIR-MFE-R82 at 55°C to ≈10 dpa. All specimen conditions have degraded properties (both DBTT and USE) in comparison with specimens irradiated to lower dose. 9Cr-Mo degraded more than HT-9 and weld metal performed worse than base metal which performed worse than HAZ material. Property degradation was approximately linear as a function of dose, indicating that degradation response had not saturated by 10 dpa.

PROGRESS AND STATUS

Introduction

In a previous report,[1] results were presented for miniature Charpy impact tests on ferritic alloy specimens irradiated in the HFIR-MFE-R81 test. That specimen matrix included HT-9 base metal and weld metal (heat 91353). and 9Cr-1Mo base metal and weld metal (heat 30176). The present effort involves the second test in that series known as the HFIR-MFE-R82 test which was irradiated to twice the dose reached in the R81 test and included specimens of HT-9 base and weld metal, and 9Cr-1Mo base and weld metal as well as HT-9 heat affected zone material. The purpose of the test series was to determine the effect of low temperature irradiation (≈ 50°C), on the mechanical properties of martensitic stainless steels.

Experimental procedures

The HFIR-MFE-R82 test was fabricated identically to the HFIR-MFE-RBI test[2,3] except that a six specimen matrix of HT-9 heat affected zone (HAZ) metal specimens was included and the matrix of HT-9 weld metal specimens was reduced to two and the matrix of 9Cr-1Mo specimens was reduced to four. The irradiation vehicle was irradiated for 22 cycles, double the dose of HFIR-MFE-R81 and was designed to operate at 50°C. Flux monitors were included and the results for the monitors have been analyzed and procedures given to provide dose determinations.4 The irradiation temperature was 55°C.[5]

The Charpy specimen test matrix is included in Table 1 along with test temperatures and fluence estimates as calculated from Reference 4. Helium production estimates are as follows:[4] for HT-9 at core centerline in R81, 20 appm He and in R82, 52 appm He whereas for 9Cr-1Mo in R81, 6 appm He and in R82, 12 appm He. Charpy testing procedures were as previously described.[6]

Results

The instrumented Charpy test results on HFIR-MFE-R82 specimens are included in Table 1 along with results from R81. Table 1 also provides updated estimates for R81 specimen doses as calculated based on reanalysis of available data from Reference 4. The results of Table 1 have been plotted in Fig. 1 which shows the R81 results as solid curves and the R82 results as dashed curves. Arrows have been included to show the effect of increased dose on the various specimen conditions. Figure 1 demonstrates that increased dose at 55°C in HFIR results in further shifts in the ductile-brittle transition temperature (DBTT) and decreases in the upper shelf energy (USE) for all conditions examined. Both HT-9 and 9Cr-1Mo are affected but the effect is somewhat greater in 9Cr-1Mo. Also, weld metal is more affected than is base metal in both cases but HAZ material in HT-9 is less affected than weld metal or base metal.

The OBTT and USE results are summarized in Table 2. The OBTT is 50 to 80°C for HT-9 conditions but is between 110 and 125°C for 9Cr-1Mo conditions following irradiation at 55°C to 10 dpa. The effect of increasing fluence on shift in DBTT for base metal specimens is plotted in Fig. 2. Figure 2 clearly shows that shift in OBTT continues to increase with increasing fluence in both HT-9 and 9Cr-1Mo in almost a linear fashion.

Discussion

When Charpy impact test results from R81 were first available, the higher degradation of properties in 9Cr-1Mo specimens in comparison HT-9 was unexpected. Not only did it not conform with behavior at higher temperatures, but also it could not have occurred as a result of a helium effect because more helium was

Table 1. Charpy specimen conditions irradiated in the HFIR-MFE-RBI and -RB2 experiments at 55°C with test results

Material	Specimen	Fluence* (dpa)	Test Temp. (°C)	P_{max} (kn)	E_{total} (J)	Normalized E_{total} (J/cm^2)
Hi-9 Base Metal (Ht 91353)	AA01	5.6	27	2.34	1.99	17.15
	02	5.6	50	2.34	5.03	45.44
	05	5.6	80	2.38	6.80	59.68
	14	5.6	110	2.60	5.48	47.99
	18	5.6	NT			
	19	5.6	NT			
	AA12	11.6	22	1.24	0.78	6.66
	15	11.6	50	1.90	1.41	11.89
	20	11.6	60	1.74	1.41	11.45
	06	11.6	75	1.85	3.94	34.25
	16	11.7	100	2.17	4.24	33.66
	13	11.7	150	2.14	4.04	32.74
HT-9 Weld Metal	AK00	5.6	34	1.60	1.25	10.43
	03	5.6	65	2.71	4.43	38.25
	08	5.6	80	2.62	7.01	56.81
	09	5.6	NT			
	AK04	11.4	21	1.05	0.38	3.11
	02	11.4	75	1.59	1.31	11.04
HT-9 HAZ	AL06	11.0	22	1.85	1.06	8.66
	01	10.5	50	1.73	2.48	20.78
	03	11.0	75	2.06	3.69	29.87
	02	11.4	100	2.02	5.03	42.19
	05	10.5	150	1.95	4.81	39.58
	04	11.4	NT			
9Cr-1Mo Rase Metal (Ht 30176)	FA03	5.5	34	1.22	0.51	4.46
	17	5.5	50	1.72	2.12	16.88
	05	5.5	70	1.64	1.86	17.47
	09	5.5	100	2.08	5.35	46.65
	11	5.5	120	1.74	5.11	45.05
	27	5.5	85	2.66	7.52	58.95
	FA20	10.9	75	0.88	0.58	5.04
	12	9.7	100	1.18	1.31	11.32
	14	10.9	125	1.80	4.85	38.72
	07	9.1	150	1.57	3.65	31.12
9Cr-1Mo Weld Metal	FJ04	5.4	65	2.29	1.54	12.85
	05	5.4	85	1.91	2.04	17.32
	06	5.4	140	2.29	7.29	60.18
	07	5.4	105	2.45	5.15	47.99
	FJ09	10.4	50	0.60	0.09	0.72
	02	10.4	100	1.22	0.51	4.35
	03	9.7	150	1.64	3.49	29.65
	OR	9.7	175	1.25	1.38	11.59

* Calculated from Reference 4
NT = not tested

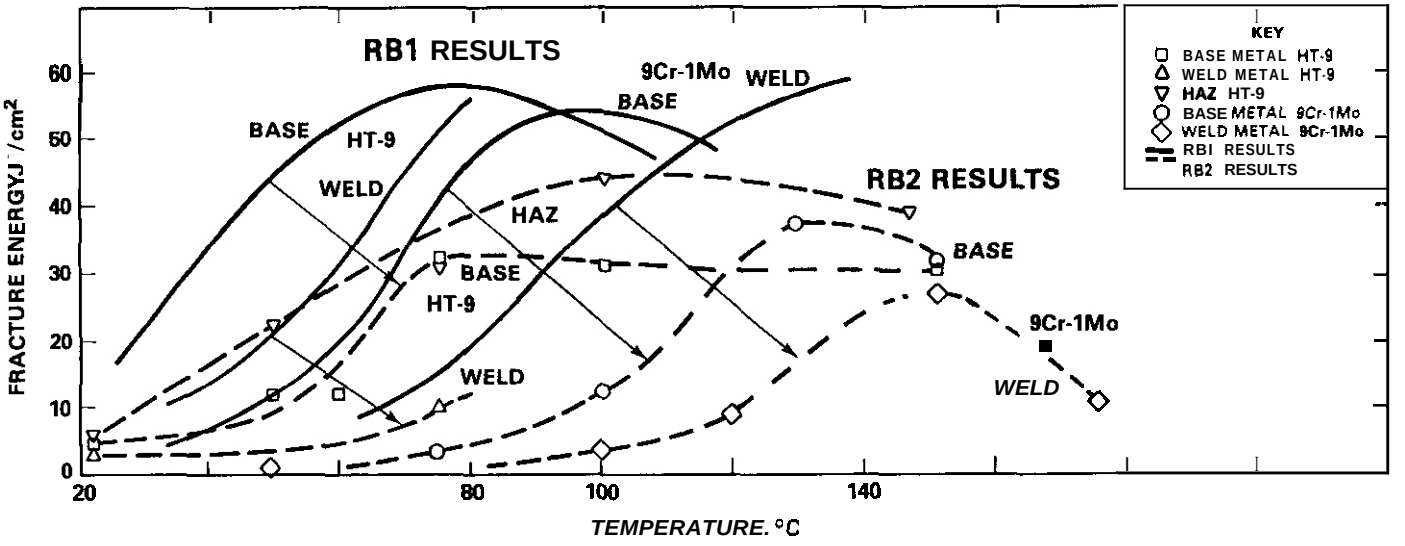


Fig. 1. Results of miniature charpy impact tests of HT-9 and 9Cr-1Mo specimens irradiated in the HFIR-MFE-RB1 and -RB2 tests showing normalized fracture energy as a function of test temperature.

Table 2. Summary of half sized Charpy specimen DBTT behavior for HT-9 and 9Cr-1Mo in HFIR-MFE-RB1 and RB2

		Unirradiated		RB1			RB2		
Alloy	Condition	OBTT	USE	DBTT	USE	DPA	DBTT	USE	DPA
		(°C)	(J/cm²)	(°C)	(J/cm²)		(°C)	(J/cm²)	
HT-9 11.6	BASE METAL	5	47	35	57	5.6	60	32	
	WELD METAL			60	>60	5.6	>80		11.4
	HAZ						50	45	11.0
9Cr-1Mo	BASE METAL	-25	80	65	52	5.5	110	38	10.3
	WELD METAL			90	60	5.4	125	27	10.0

generated in HT-9 than in 9Cr-1Mo. The behavior of specimens irradiated in the RB2 test directly match those from the RB1 test except that the effects are larger presumably due to higher accumulated dose. Therefore, the observed behavior must be ascribed to effects of irradiation at low temperature.

However, the mechanism which is causing this unexpected phenomenon is still not understood. The observation that heat treatment affects the magnitude of the DBTT shift suggests that carbide precipitation strengthening plays a role in the degradation process at low irradiation temperatures. The fact that the overaged condition (HAZ) provides the best properties suggests that either a segregation phenomena involving carbon solute in solution controls or that crack nucleation is encouraged at carbide precipitate sites by low temperature irradiation.

A major issue addressed by the HFIR mechanical properties irradiation test program is to determine at which irradiation temperature the property degradation is greatest. Dbserved shifts in DBTT for 9Cr-1Mo of greater than 100°C represent the highest shifts found for the alloy. (The largest observed shift for HT-9 was at an irradiation temperature of 390°C.) Figure 2 indicates that as a function of dose, the shift in DBTT is not saturating at 10 dpa. Irradiation to higher fluence can be expected to result in still higher values for DBTT. Therefore, the RB2 results demonstrate that higher dose experiments at 50°C are needed.

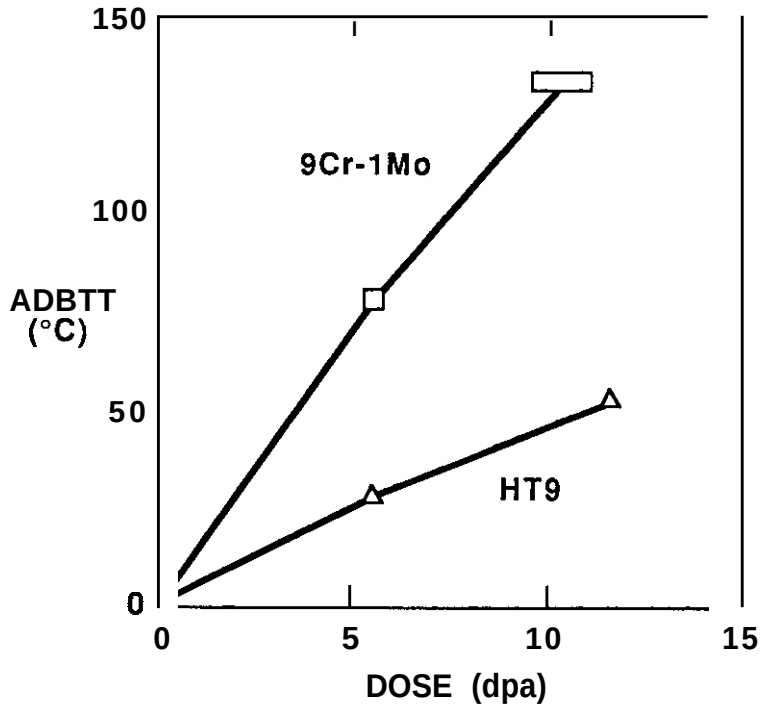


Fig. 2. Shift in DBTT as a function of dose for HT-9 and 9Cr-1Mo base metal specimens irradiated in HFIR-MFE-RB1 and -RB2.

CONCLUSIONS

Instrumented Charpy impact testing of miniature specimens of HT-9 and 9Cr-1Mo which were irradiated in the HFIR-MFE-RB2 test shows that irradiation at 55°C results in degradation of impact properties for all conditions tested. Conditions included base metal, weld metal and for HT-9, heat affected zone material. Degradation of properties included shift in ductile-brittle transition temperature and reduction in upper shelf energy. The degradation could only be attributed to the low irradiation temperature; an effect of helium production could be ruled out.

Comparison of the RB2 results with those of RB1 irradiated to half the dose showed that the degradation was approximately linear with fluence and therefore saturation had not yet been achieved. Further tests to higher dose are recommended.

FUTURE WORK

Fractographic examinations on selected specimens will be described in the next progress report.

REFERENCES

1. D. S. Gelles, W. L. Hu, F. H. Huang and G. O. Johnson, Alloy Oevelopment for Irradiation Performance Semiannual Progress Report for the Period Ending September 30, 1983, DOE/ER-0045/11, 115.

2. J. M. Vitek and J. W. Woods, ibid, DOE/ER-0045/7, 30.

3. R. J. Puigh and R. D. Stevenson, ibid, DOE/ER-0045/5, 170.

4. L. R. Greenwood, ibid, DOE/ER-0045/15, 4.

5. M. L. Grossbeck, ibid, DOE/ER-0045/12, 159.

6. W. L. Hu and D. S. Gelles, "On the Ductile to Brittle Transition Behavior of Martensitic Alloys Neutron Irradiated to 26 dpa," in Influence of Radiation on Material Properties, ASTM STP 956, F.A. Garner, C.H. Henegar, Jr. and N. Igata, eds., ASTM, Philadelphia PA., 1987, in press.

CHARPY IMPACT TEST RESULTS FOR LOW ACTIVATION FERRITIC ALLOYS - N. S. Cannon, W. L. Hu and O. S. Gelles (Westinghouse Hanford Company)

OBJECTIVE

The objective of this work is to evaluate the shift of the ductile to brittle transition temperature (OBTT) and the reduction of the upper shelf energy (USE) due to neutron irradiation of low activation ferritic alloys.

SUMMARY

Six low activation ferritic alloys have been tested following irradiation at 365°C to 10 dpa and compared with control specimens in order to assess the effect of irradiation on Charpy impact properties. It is found that alloys of composition Fe-2Cr-1.5V, Fe-12Cr-6Mn-1V and Fe-12Cr-6Mn-1W develop unacceptably large shifts in OBTT due to irradiation, Fe-9Cr-1V develops a small shift and Fe-9Cr-1W and Fe-7.5Cr-2W develop negligible shifts. There is little effect on USE in all cases. It appears that alloy development of low activation ferritic alloys should be concentrated in the Fe-7.5 to 9Cr range.

PROGRESS AND STATUS

Introduction

It is well known that the OBTT of many alloys shifts towards higher temperatures with increasing fluence. Accordingly, the change in the OBTT with neutron irradiation is an important factor in the selection of alloys for fusion reactor applications.

A series of alloys have been identified as potential alloys for low activation structural materials for fusion reactor environments.[1] Charpy specimens fabricated from most of these alloys were irradiated in the Fast Flux Test Facility (FFTF) in a series of Materials Open Test Assembly (MOTA) experiments. This document reports the results of Charpy Impact tests on one third size specimens discharged from the MOTA-1C experiment after irradiation to a nominal fluence of 3×10^{22} n/cm^2 (E > 0.1 MeV) or 10 dpa at 365°C. Identical specimens continue to be irradiated in MOTA to provide results following irradiation to approximately 30 dpa in order to determine the fluence dependence for changes in impact properties.

Specimen preparation

Miniature Charpy impact specimens were prepared for the study of the effect of neutron irradiation on the fracture toughness of several low activation alloys. The specimens have an overall dimension of 3.33 mm x 3.33 mm x 23.6 mm and a notch depth of 0.51 mm and therefore are made to the 113 size CVN standard. Specimens were precracked to an a/W approximately equal to 0.5 where a is the notch depth plus the precrack length and W, the specimen height, is 3.33 mm.

Material stocks used in the MOTA-1C experiment on Charpy impact testing included:

1. Fe-2Cr-1.5V (Heat UC-19), identified previously as Alloy Number 3, Heat Treatment: 1050°C/10m/WQ to RT + 650°C/2h/AC, identified as the L3 series.
2. Fe-9Cr-1V (Heat V02265), identified previously as Alloy Number 6, Heat Treatment: 1000°C/20h/AC to RT + 1100°C/10m/AC to RT + 700°C/2h/AC, identified as the L5 series.
3. Fe-12Cr-6Mn-1V (Heat V02267), identified previously as Alloy Number 8, Heat Treatment: 1000°C/20h/AC to RT + 1100°C/10m/AC to RT + 700°C/2h/AC, identified as the L7 series.
4. Fe-9Cr-1W (Heat V02268), identified previously as Alloy Number 7, Heat Treatment: 1000°C/20h/AC to RT + 1100°C/10m/AC to RT + 700°C/2h/AC, identified as the La series.
5. Fe-12Cr-6Mn-1W (Heat V02269), identified previously as Alloy Number 9, Heat Treatment: 1000°C/20h/AC to RT + 1100°C/10m/AC to RT + 700°C/2h/AC, identified as the L9 series.
6. Fe-7.5Cr-2W (Heat GA-3X), Heat Treatment: 1000°C/1h/AC to RT + 700°C/1h/AC, identified as the LO series.

Material for the L3 series was produced for N. Ghoniem of UCLA by the Foote Mineral Company, Exton, PA and provided by Prof. Ghoniem and the material for the LO series was produced and provided by T. A. Lechtenberg of GA Technologies, San Oiego, CA. The remaining materials were produced by Carpenter Technology Corporation, Reading, PA. Production and processing procedures have been previously described.[1,2]

Specimens were manufactured by West Richland Machine Works, W. Richland WA, engraved, heat-treated as defined above and precracked using standard procedures.3

Twelve specimens of each condition were irradiated in the below core canisters of MOTA starting in Cycle 5. The temperature of the below core canister is 365°C. Six specimens of each condition were removed from reactor at the end of Cycle 6 after an accumulated fluence of 3×10^{22} n/cm^2 or approximately 10 dpa. The remaining six specimens of each condition are expected to be removed from reactor at the end of Cycle 9 after a further fluence of 6×10^{22} n/cm^2 for a total dose of approximately 30 dpa.

Experimental procedures

The tests were conducted on a drop tower installed in a hot cell. The heating andlor cooling, specimen transport and testing were automated to handle irradiated specimens. Both unirradiated controls and irradiated specimens were tested in the same facility. Load traces were digitized and stored on both magnetic tape and disk. Computer software integrated the load data to calculated the fracture energy. The details of the test system were described in Reference 4.

The specimen temperature was indicated by a spring loaded thermocouple, calibrated previously versus a thermocouple spot welded on a dummy specimen. During the test period, the load cell and the impact velocity were checked weekly; these values were found to be relatively steady, and minor changes were compensated in the test software. The load cell calibration was conducted dynamically by comparing the maximum load obtained during a impact test of a calibrated 113 size CVN specimen with the predetermined maximum load from a three point bending test. The calibration specimens were made of loading rate insensitive 6061 Aluminum alloy in the T651 heat treated condition. The impact velocity was calculated from the time interval obtained when a flag with a known gap width on the crosshead was passed through a stationary infrared sensor during a free fall.

The total energy absorbed in the impact test can be calculated from the area under the load time record and the initial impact velocity following Newton's second law,

$$E = E_a (1 - E_a/4E_0)$$

where $E_a = V_0 \int P dt$ is the apparent energy absorbed by the specimen during the impact, V_0 is the initial impact velocity, P is the load and t is the time. $E_0 = mV_0^2/2$ is the total available energy at the impact where m is the mass of the crosshead.

Results

The instrumented Chdrpy test results on low activation alloys irradiated in MOTA-IC are included in Table 1. Table 1 also includes results for unirradiated controls. (The values for condition LO control specimens of Alloy GA-3X were previously documented in Reference 5.) The normalized energy total (NET) and normalized energy to maximum (NEM) load given in Table 1 were calculated by multiplying the appropriate energy by a factor of $L/B(W-a)^2$ where E = W = 3.33 mm, and L = 4W. This normalization factor has been described in Reference 6 and is intended to compensate the impact energy results for differences in specimen geometry such as crack length and specimen size. Although total energy is usually used to determine DBTT, some test results were incomplete, in which case the NEM was a generally more consistent determining parameter. Figs. 1 to 6 contain plots of both NET and NEM versus test temperature for all six alloys.

Curves were fitted to the data shown in Figs. 1 to 6 based on the equation

$$\text{NET (or NEM)} = A + B * \tanh [(T-TO)/CO]$$

where T is the test temperature, and A, E, TO and CO were fitting parameters. The fitting parameters for each alloy condition are listed in Table 2. The inflection point, TO. was used *to* define the DBTT; USE = A + B as taken from the NET values. Table 3 summarizes the DBTT (obtained from the NET except as noted), USE, and changes in these parameters with irradiation. Although these values are presented precisely as calculated from the curve fitting process, it should be noted that the process was subjective and the data base small.

Fig. 1 provides a comparison of the unirradiated and irradiated conditions of Fe-2Cr-1.5V (Heat UC-19). As a function of temperature, the normalized maximum energy and normalized total energy are shown in Figs. la and lb, respectively. Fig. la indicates that the DBTT for the unirradiated condition is 169°C whereas following irradiation at 365°C to 11 dpa, the DETT is above 250°C, the maximum temperature for the test apparatus. Fig. 2 provides results for Fe-9Cr-1V and shows that the DBTT for the unirradiated condition is -44°C whereas following irradiation at 365°C to 12 dpa, the DETT has shifted to 18°C. The USE is altered only slightly as shown in Fig. 2b, from 280 J/cm^2 to 240 J/cm^2. Fig. 3 shows results for Fe-12Cr-6Mn-1V. The unirradiated condition has a DETT of 10°C whereas following irradiation at 365°C to 12 dpa the DBTT has been shifted *to* 200°C. However, the results indicate only a small change in USE. Fig. 4 provides results for Fe-9Cr-1W. The DETT for the unirradiated condition is 12°C whereas following

Table 1. Charpy specimen conditions of low activation ferritic alloys irradiated in the MOTA-IC experiment at 365°C

Alloy	Dose (dpa)	Test Temp. (°C)	Max. Load (K nt)	Energy to Max. Load (J)	Normalized Energy to Max. Load (J/cm^2)	Fracture Energy (J)	Normalized Fracture Energy (J/cm2)
2Cr-1.5V	----	200	0.686	0.305	49.0	1.810	290
L3 series	----	150	0.565	0.116	17.8	0.803	124
	----	110	0.416	0.027	4.2	0.651	100
	----	20	0.431	0.018	2.3	0.149	18.8
	11.3	250	0.641	0.049	7.1	0.540	77.6
	11.3	200	0.497	0.028	4.3	0.231	36.0
	11.3	150	0.829	0.080	12.2	0.515	79.0
9Cr-1V	----	50	0.603	0.170	29.8	1.574	276
L5 series	----	23	0.634	0.136	27.8	1.332	272
	----	-10	0.617	0.141	26.7	1.367	259
	----	-40	0.584	0.127	22.4	0.963	169
	----	-80	0.490	0.025	5.0	0.324	64.5
	----	-112	0.503	0.044	7.9	0.438	78.4
	12.0	131	0.559	0.144	26.3	1.205	220
	12.0	101	1.016	0.250	44.3	2.404	426
	12.0	92	0.674	0.151	26.0	1.467	253
	12.0	65	0.664	0.141	25.3	1.372	246
	12.0	22	0.508	0.042	7.5	0.795	142
	12.0	-8	0.605	0.044	7.9	0.528	95.0
12Cr-6Mn-1V	----	100	0.650	0.163	28.7	1.031	182
L7 series	----	80	1.197	0.606	95.5	2.510	396
	----	65	0.727	0.165	27.6	1.236	207
	----	45	0.656	0.122	20.1	0.858	141
	----	25	0.616	0.073	13.6	0.631	118
	----	-20	0.591	0.047	8.0	0.415	70.8
	12.0	250	0.639	0.138	23.9	1.240	214
	12.0	210	0.610	0.045	7.4	0.675	111
	12.0	150	0.543	0.043	7.4	0.236	40.4
	12.0	25	0.336	0.013	2.2	0.042	7.3
9Cr-1W	----	100	0.482	0.218	40.5	1.935	359
L8 series	----	60	0.685	0.315	50.2	2.394	382
	----	20	0.670	0.155	26.2	1.556	262
	----	-20	0.611	0.077	11.4	0.837	125
	----	-50	0.554	0.048	7.5	0.447	70.4
	----	-80	0.342	0.025	4.5	0.175	30.8
	12.0	150	0.485	0.132	23.1	1.811	318
	12.0	100	0.651	0.177	29.7	1.418	238
	12.0	50	0.436	0.117	21.8	0.875	163
	12.0	21	0.337	0.023	4.1	0.260	46.0
12Cr-6Mn-1W	----	50	0.782	0.172	31.3	1.188	216
L9 series	----	22	0.885	0.223	37.8	1.219	207
	----	-30	0.668	0.089	17.0	0.707	135
	----	-50	0.844	0.211	40.8	0.854	165
	----	-60	0.680	0.074	13.5	0.600	110
	----	-80	0.656	0.036	6.0	0.140	23.1
	12.0	240	0.726	0.190	32.8	1.245	215
	12.0	200	0.687	0.144	27.2	0.808	153
	12.0	150	0.610	0.111	18.0	0.512	83.1

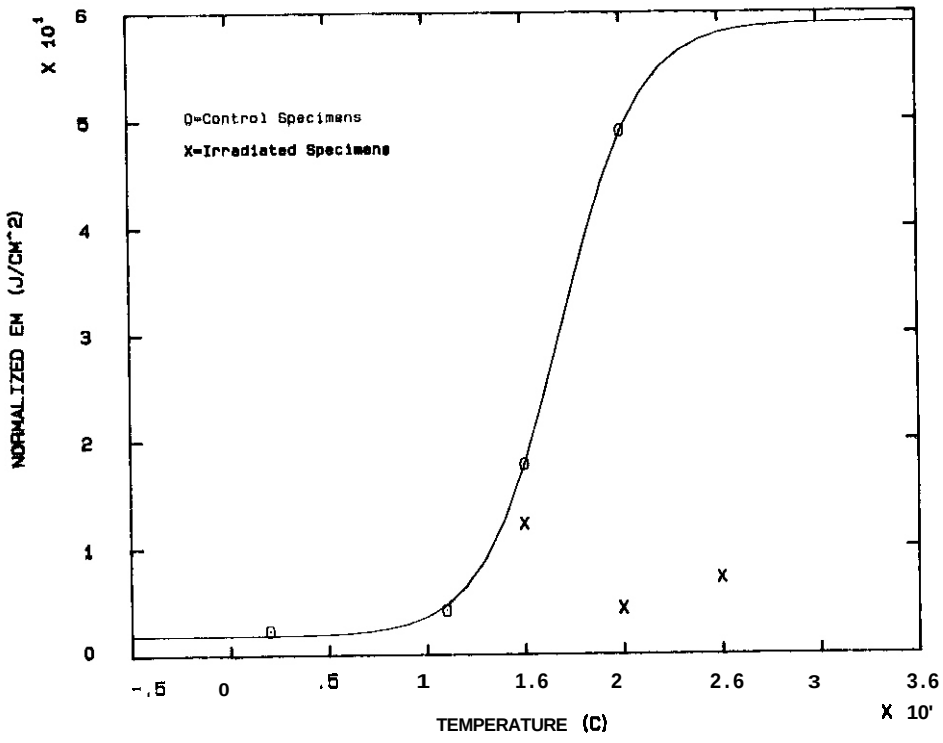
Table 1. Charpy specimen conditions of low activation ferritic alloys irradiated in the MOTA-1C experiment at 365°C (continued]

Alloy	Dose (dpa)	Test Temp. (°C)	Max. Load (K nt)	Energy to Max. Load (J)	Normalized Energy to Max. Load (J/cm^2)	Fracture Energy (J)	Normalized Fracture Energy (J/cm^2)
7.5Cr-2W LO series	----	100	0.645	0.232	44.2	2.199	418
	----	50	0.733	0.253	39.5	2.497	391
	----	21	0.693	0.225	38.2	2.264	384
	----	0	0.726	0.248	40.4	2.169	354
	----	-10	0.648	0.225	40.3	1.641	294
	----	-25	0.574	0.068	11.4	1.096	185
	----	-50	0.571	0.063	10.9	0.613	106
	----	-80	0.536	0.037	7.1	0.130	25.2
	10.5	140	0.687	0.168	28.4	1.887	319
	10.5	100	0.685	0.159	29.1	1.981	363
	10.5	21	0.792	0.251	38.1	1.260	191
	10.5	-20	0.576	0.064	10.2	1.019	161
	10.5	-60	0.559	0.029	5.1	0.336	58.9

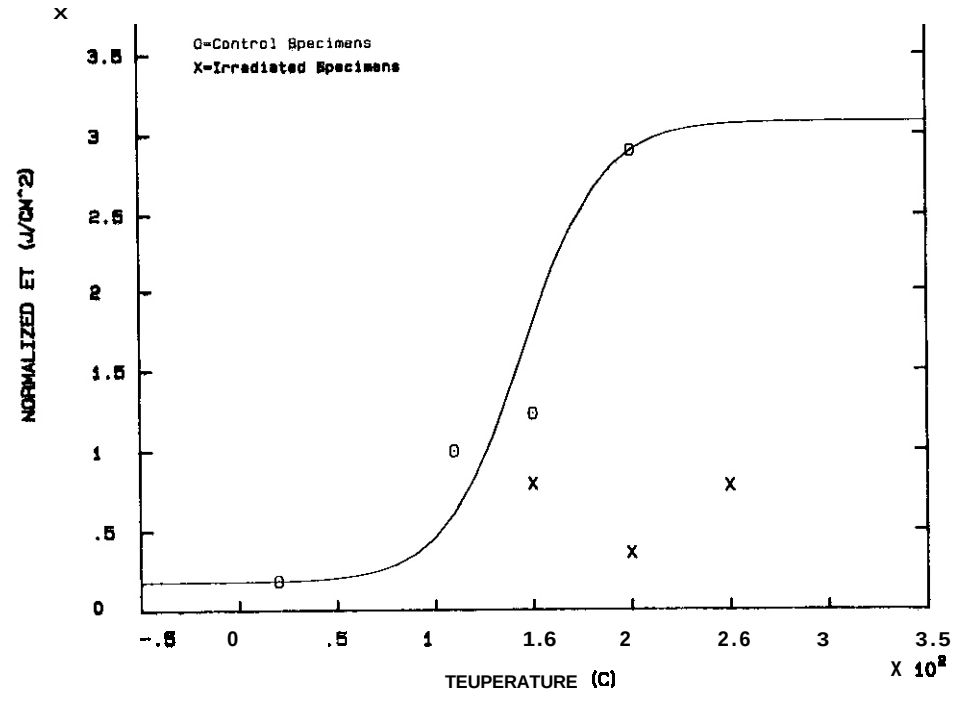
Table 2. Data fit parameters using NET (or NEM) = A + B Tanh $[\frac{T-T\phi}{C\phi}]$

Alloy	Series	Irrddiated Status*	Energy Type	A	B	Tφ	Cφ
2Cr-1.5V	L3	C	NET	163	145	145	40
		I	NET	?	?	?	40
		C	NEM	30.4	28.6	159	
		I	NEM	?	?	?	40
9Cr-1V	L5	C	NET	165	115	-44	
		I	NET	144	95	18	40
		C	NEM	16.7	12.2	-55	35
		I	NEM	15.6	11.1	36	30
12Cr-6Mn-1V	L7	C	NET	108	93	10	60
		I	NET	108	93	200	60
		C	NEH	17.0	13.6	30	50
		I	NEM	17.0	13.6	220	50
9Cr-1W	L8	C	NET	200	170	-2	40
		I	NET	180	150	70	50
		C	NEM	25.3	20.8	12	40
		I	NEM	17	12.5	44	20
12Cr-6Mn-1W	L9	C	NET	113	106	-52	45
		I	NET	113	106	165	45
		C	NEM	20	16	-30	45
		I	NEM	20	16	165	70
7.5Cr-2W			NET	215	190	-24	30
			NET	185	160	0	40
		C	NEH	24.5	19.1	-20	30
		I	NEM	19	13.6	5	30

*C: Control, I: Irradiated.

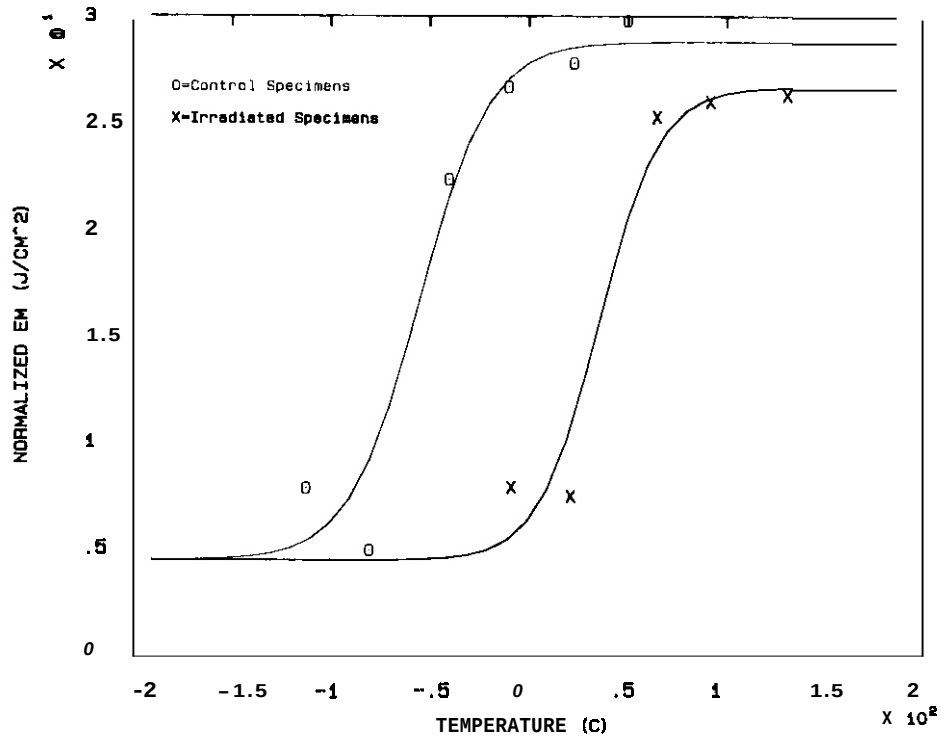


(a)



(b)

Fig. 1. Charpy impact test results as a function of test temperature for Fe-2Cr-1.5V (Series L3) plotted as a function of normalized maximum energy (a) and normalized total energy (b).



(a)

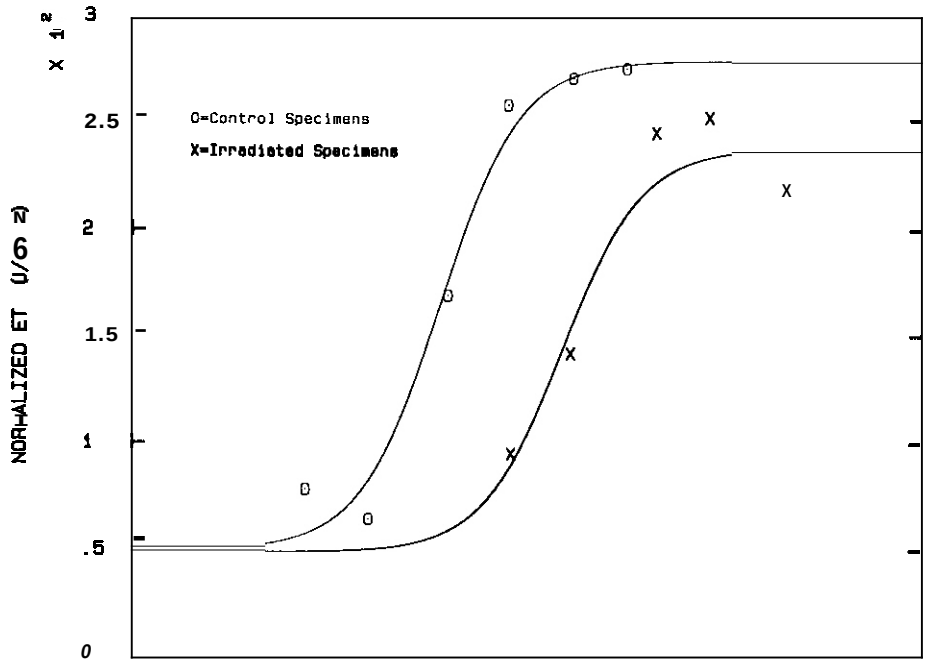
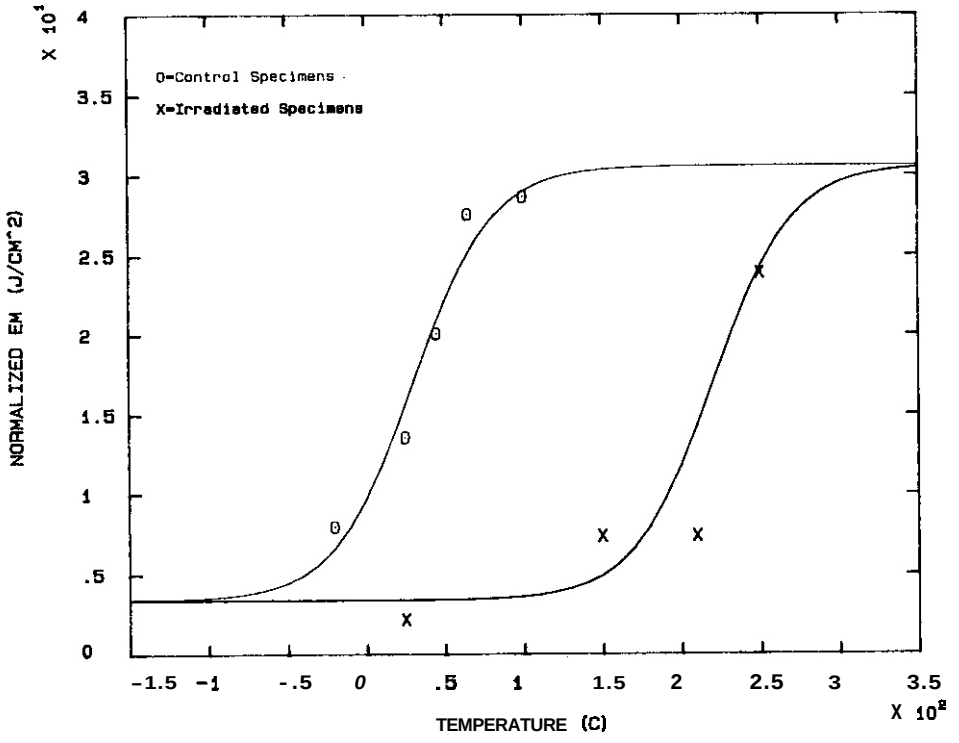
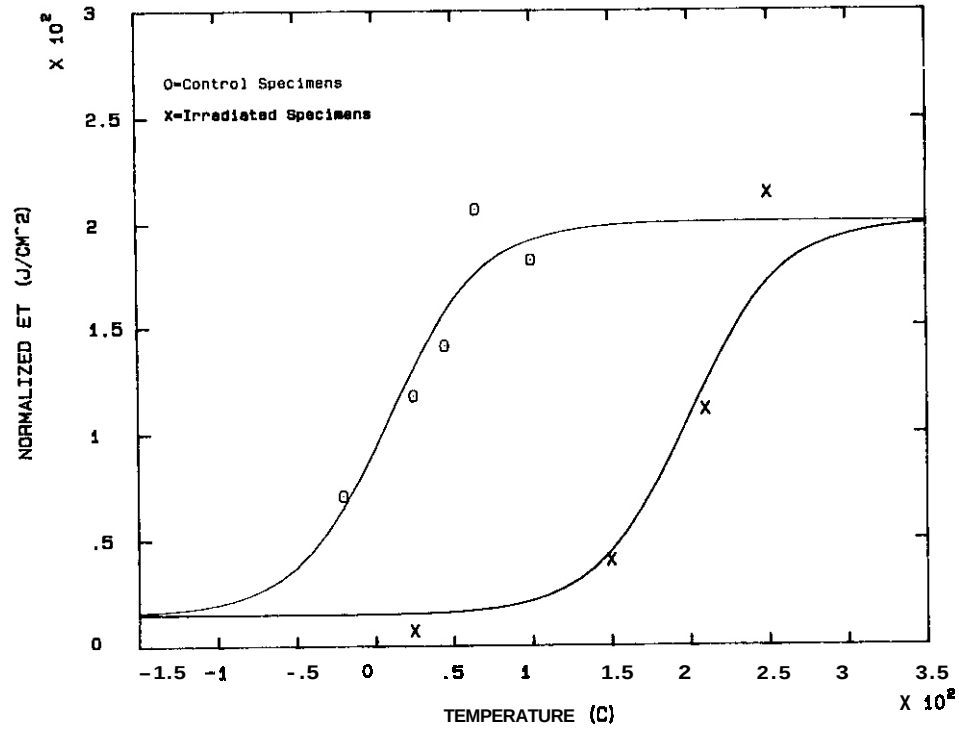


Fig. 2. Charpy impact test results as a function of test temperature for Fe-9Cr-1V (Series L5) plotted as a function of normalized maximum energy [a) and normalized total energy **(b).**

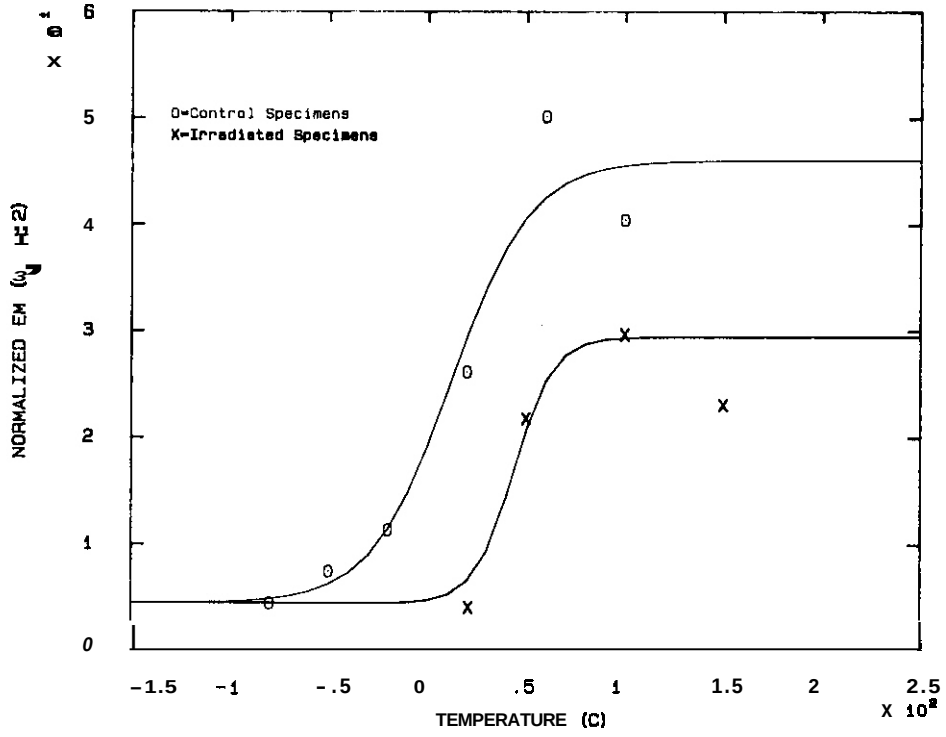


(a)

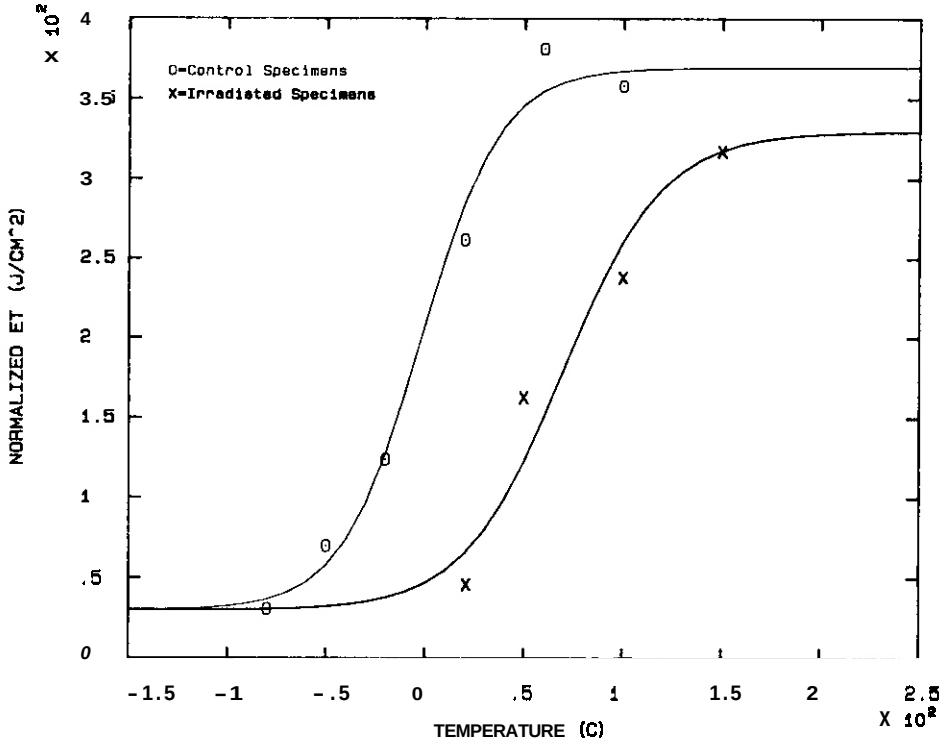


(b)

Fig. 3. Charpy impact test results as a function of test temperature for Fe-12Cr-6Mn-1V (Series L7) plotted as a function of normalized maximum energy (a) and normalized total energy (b).

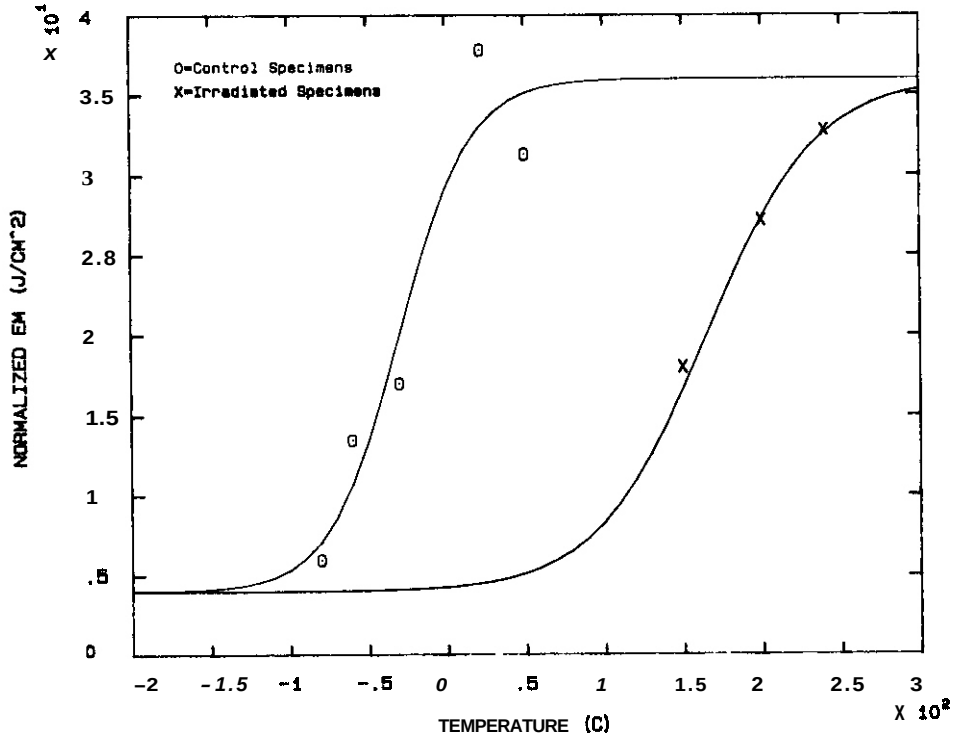


(a)

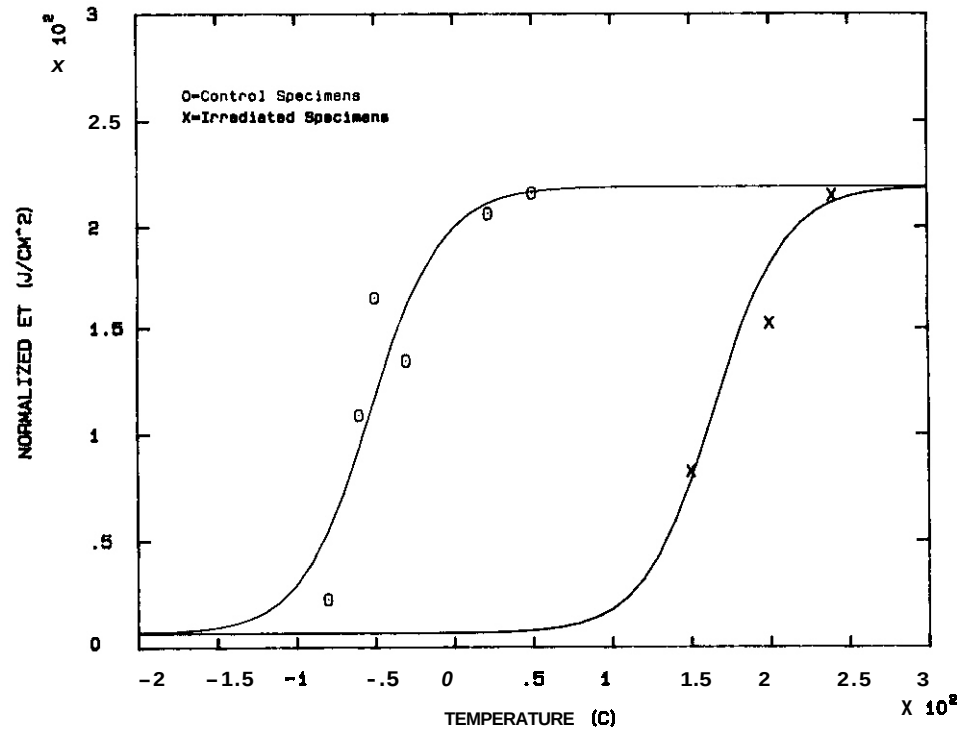


(b)

Fig. 4. Charpy impact test results as a function of test temperature for Fe-9Cr-1W (Series L8) plotted as a function of normalized maximum energy (a) and normalized total energy (b).

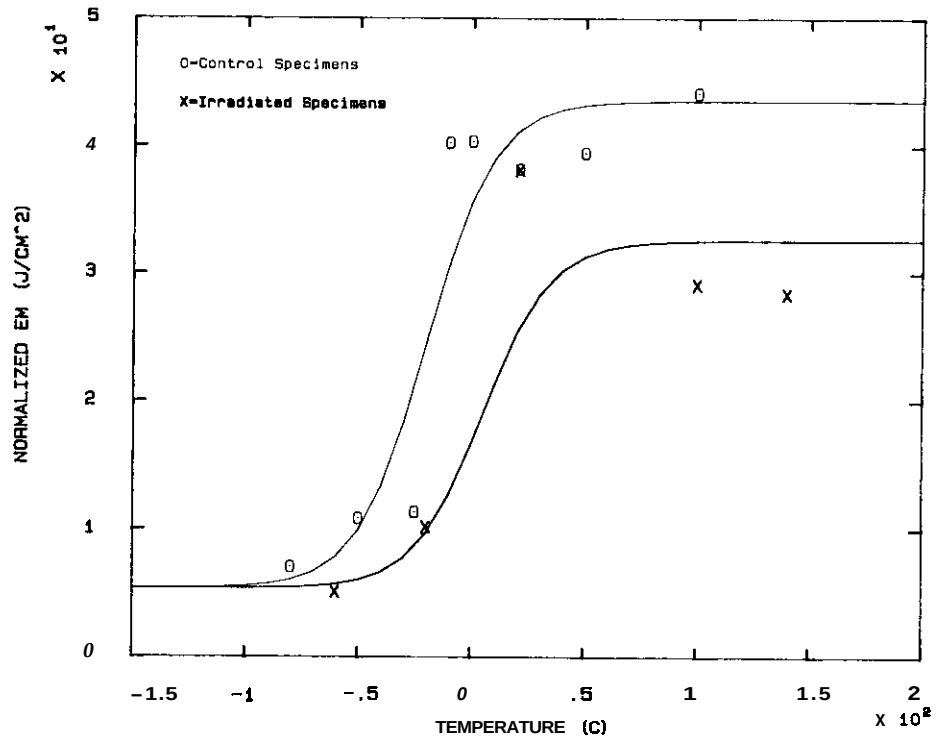


(a)

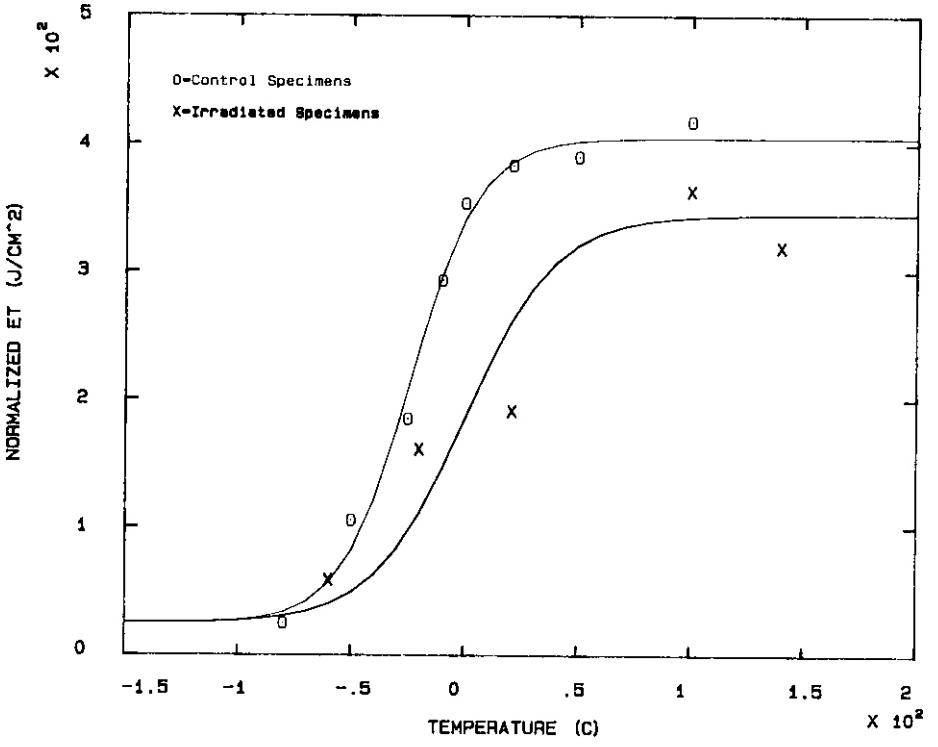


(b)

Fig. 5. Charpy impact test results as a function of test temperature for Fe-12Cr-6Mn-1W (Series L9) plotted as a function of normalized maximum energy (a) and normalized total energy (b).



(a)



(b)

Fig. 6. Charpy impact test results as a function of test temperature far Fe-7.5Cr-2W (Series LO) platted as a function of normalized maximum energy (a) and normalized total energy **(b)**.

Table 3. Summary of OBTT behavior in low activation ferritic alloys following irradiation in MOTA-1C

Alloy	Series	Control OBTT (°C)	Irrad. OBTT (°C)	Shift in OBTT (°C)	Control USE (J/cm²)	Irrad. USE (J/cm²)	Approx. Shift in USE (J/cm²)
2Cr-1.5V	L3	169*	>250	?	308	?	?
9Cr-1V	L5	44	18	62	280	239	-40
12Cr-6Mn-1V	L7	10	200	190	201	201	0
9Cr-1W	L8	12*	44*	32	370	330	-40
12Cr-6Mn-1W	L9	-52	165	217	219	219	0
7.5Cr-2W	LO	-24	0	24	405	345	-60

*Because of an improper scope setting, entire energy curve was not captured during a transition test; thus the NEM values are more appropriate for determining OBTT.

irradiation at 365°C to 12 dpa the OBTT was 44°C. The USE was reduced by irradiation from 370 J/cm² to 330 J/cm². The results for Fe-12Cr-6Mn-1W are given in Fig. 5, which indicates that the unirradiated condition has a OBTT of -52°C whereas following irradiation at 365°C to 12 dpa has resulted in a large shift in OBTT to 165°C. No change in USE due to irradiation is indicated. Finally, in Fig. 6, results are shown for Fe-7.5Cr-2W. The unirradiated condition is found to have a OBTT of -24°C whereas following irradiation at 365°C to 10.5 dpa, the OBTT is shifted to 0°C. A small drop in USE due to irradiation is indicated, from 410 J/cm² to 350 J/cm².

The OBTT and USE results of the charpy impact test series on low activation alloys were summarized in Table 3. Table 3 shows that the alloy in the Fe-2Cr range has a high DBTT and a low USE prior to irradiation and the OBTT shifts beyond 250°C following irradiation. Alloys in the Fe-12Cr range develop large shifts in OBTT on the order of 200°C. The Fe-7.5 to Fe-9Cr alloy range shows much greater promise. The OBTT values prior to irradiation are low and shifts in DBTT due to irradiation are small. Therefore, on the basis of these results, the optimum composition range for low activation ferritic alloy development appears to be Fe-7.5 to 9Cr. Tungsten additions provide somewhat higher USE behavior and smaller shifts in OBTT due to irradiation than do vanadium additions and there appears to be no penalty in increasing the tungsten level to 2%. at least for fluence levels on the order of 10 dpa.

Discussion

It is possible to explain the observed Charpy impact response of low activation ferritic alloys due to irradiation as follows. The general behavior observed was that Fe-2Cr and Fe-12Cr alloys did not perform as well as Fe-7.5 to 9Cr alloys. It has been shown that Fe-2Cr alloys develop large increases in strength, both yield and ultimate tensile strength, due to irradiation at 420°C.[1,7] This effect of irradiation is attributed to precipitation, possibly of V_4C_3 or M_7C_3 type phases.7 Therefore, a large shift in DBTT due to irradiation for Fe-2Cr-V alloys was anticipated. Unfortunately, the OBTT found prior to irradiation in heat UC-19 is probably due to the V_4C_3 which was found in the as heat treated structure. Improved heat treatment procedures should be possible but it is unlikely that such procedures would avoid the precipitation which occurs during irradiation.

Charpy impact testing to determine the effect of irradiation on a Fe-12Cr-6Mn-1Mo alloy gave results very similar to those found for the Fe-12Cr-6Mn alloys tested in the present experiment. The molybdenum containing alloy showed a 150°C shift following irradiation at 365°C to 5.4 dpa and a 220°C shift following irradiation at 365°C to 11.3 dpa.[8] Fractographic examination showed a change in fracture mode to precipitation controlled prior austenite grain boundary embrittlement and microstructural examination revealed precipitation of an Fe-Cr-Mn Chi phase.[9] Similar response should be expected in Fe-12Cr-6Mn alloys containing tungsten or vanadium. Therefore, additions of manganese for austenite stability at levels of 12 percent chromium cause unexpected embrittlement and should be avoided.

The explanation for improved properties in tungsten containing 7.5 to 9Cr alloys in comparison to vanadium containing 9Cr alloys is not yet clear. It may be associated with the tendency for V_4C_3 which has been identified in Fe-2Cr-V alloys. However, there is corroborating evidence for good OBTT response in Fe-7.5Cr-2W alloy GA-3X from work in progress. Microstructural examinations of this alloy following irradiation at 365, 420, 520 and 600°C to approximately 30 dpa shows no evidence of excessive precipitation. Therefore, additions of tungsten in the two percent level does not appear to lead to degradation of impact properties in irradiation environments.

CONCLUSIONS

The effect of irradiation on Charpy impact properties for a series of low activation ferritic alloys has been determined. Irradiation at 365°C to 10 dpa results in significant shifts in DBTT for alloys in the composition ranges Fe-2Cr-1.5V and Fe-12Cr-6.5Mn-1W or -IV whereas the shift is smaller in Fe-9Cr-1V and is almost negligible in Fe-9Cr-1W and Fe-7.5Cr-2W. Changes in USE due to irradiation appear to be unimportant in all alloys. The optimum composition for development appears to be Fe-7.5 to 9Cr and additions of tungsten are preferred over those of vanadium.

FUTURE WORK

Fractography will be performed on selected specimens in the next reporting period.

REFERENCES

1. O. S. Gelles and M. L. Hamilton, J. Nucl. Matls., (1987), also in AOIP Semiannu. Prog. Rep. Sept. 30, 1984, DOE/ER-0045/13, Office of Fusion Energy, p. 128.

2. T. A. Lechtenberg, in ADIP Semiannu. Prog. Rep. March 31, 1985, DOE/ER-0045/14, Office of Fusion Energy, p. 117.

3. R. J. Puigh and N. F. Panayotou, ibid, DOE/ER-0045/3, p. 261.

4. W. L. Hu, ibid, DOE/ER-0045/9, p. 255.

5. C. Y. Hsu and T. A. Lechtenberg, ibid, DOE/ER-0045/15, p. 137.

6. W. L. Hu, ibid, DOE/ER-0045/13, p. 106.

7. O. S. Gelles and M. L. Hamilton, ibid, DOE/ER-0045/16, p. 131.

8. W. L. Hu and D. S. Gelles, ibid, p. 140.

9. D. S. Gelles and W. L. Hu, "Radiation Embrittlement of Manganese-Stabillzed Martensitic Stainless Steel," in Fusion Matls. Prog. Rep. Sept. 30, 1986.

TEMPERING EFFECTS ON A 12 CR LOW ACTIVATION STEEL - R.D. Griffin, R.A. Dodd and G.L. Kulcinski (University of Wisconsin)

OBJECTIVE

The objective of this work is to characterize tempering effects on a low activation 12 Cr martensitic steel.

SUMMARY

A martensitic steel similar to HT-9 has been designed to reduce activation levels following irradiation. Hardness tests, optical metallography and transmission electron microscopy are being used to determine the response of the steel to tempering.

PROGRESS AND STATUS

Introduction

The martensitic steel used in this study was provided by Hanford Engineering Developmental Laboratory. It was patterned after HT-9 with vanadiun and tungsten substituted for molybdenum for strengthening, and with a low r carbon content. To compensate for the decreased carbon, The manganese level has been increased.' The composition of the steel is shown in Table 1.

Table 1

Cr	C	V	W	Mn	Si	N	P	S
11.81	0.097	0.28	0.89	6.47	0.11	0.003	< 0.005	0.005

This study is intended to provide information on the effects of heat treatment on microstructure and to provide information for comparison with irradiation results.

Experimental Procedure

The alloy was rolled and then austenitized for 20 hours at 1000 C followed by an air cool to room temperature, and then austenitized for 10 minutes at 1100 C followed again by an air cool to room temperature. Samples of the steel were then tempered at 400 C, 500 C, 600 C, 700 C, 800 C, and 900 C for two hours and at 500 C and 700 C for twenty-four hours. Optical metallography, microhardness tests, and some TEM were conducted on the samples.

Experimental Results

The results from the hardness tests are shown in Figure 1. At the higher tempering temperatures (800 C and 900 C), the hardness begins to increase sharply. This is similar to results obtained by Klueh for 12Cr-2WV-Mn steels.[2] As the manganese content is increased, the temperature at which austenite forms is lowered. At the higher tempering temperatures, austenite reforms and on cooling transforms to untempered martensite, thus explaining the hardness increase. Measurements of prior austenite grain size Were done on all the samples and the average size was 130 microns. Unexpectedly, the 800 C and 900 C tempers, which showed the hardness increases, did not differ in their austenite grain size from the lower temperature heat treatments. The results from the optical metallography are shown in Figure 2. The as-rolled and untempered samples are included to show that the normalizing treatment was successful. The microstructure of all the samples was martensitic and all samples contained large precipitates lying along the former austenite grain boundaries. The 800 C and 900 C heat treatments showed regions which were different from the tempered martensite which they both also contained. These regions contained substantial concentrations of large precipitates.

Transmission electron microscopy (TEM), is being conducted on the samples to identify the precipitates which Form. To eliminate background effects, extraction replicas are being used. Initial work has been done on the 400 C and 500 C, two hour samples. The major precipitate in both samples is $M_{23}C_6$ which is found both on the prior austenite boundaries and within the martensite laths. Figure 3 shows typical results from the extraction replicas. In Figure 3-a, large $M_{23}C_6$ carbides are shown lying along a prior austenite grain boundary. The smaller $M_{23}C_6$ carbides in Figure 3-a found in the martensite laths are also elongated precipitates. The boundary carbide average size is 0.8 µm long and 0.2 µm wide, while the lath carbide average size is 0.2 µm long and 3.0 nm wide.

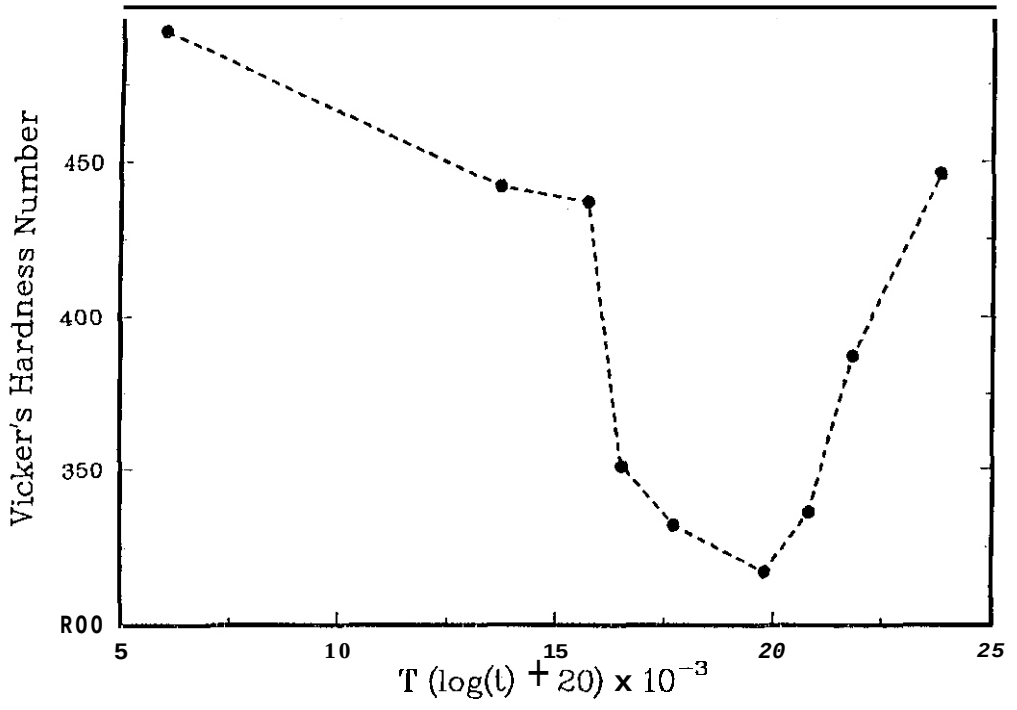


Figure 1. Vickers hardness number versus tempering parameters.

In Figure 3-h, an example of a very large austenite grain boundary $M_{23}C_6$ carbide is pictured which contains many twins. The twins were often seen in these precipitates. In Figure 3-c and 3-d a typical diffraction pattern and x-ray spectrum from these precipitates is shown. The precipitate is fcc with a_o = 1.06 nm. The metal composition in the carbides is found to be close to 49% Fe, 49% Cr, 1%V, and 1%Si.

Discussion

The high temperature tempering of this alloy results in a hardness increase which is probably due to the formation of new, untempered martensite. Additional precipitation may also be a factor in this hardness increase. Electron microscopy reveals that at 400 C and 500 C the major precipitate which is forming is the $M_{23}C_6$ carbide. This carbide is essentially half Cr and half Fe with small amounts of vanadium and silicon also present.

FUTURE WORK

The tempering study will be concluded by identifying all precipitates at each of the tempering temperatures. In addition, precipitate number densities and dislocation densities will he measured.

REFERENCES

1. O.S. Gelles and M.L. Hamilton, "Effects of Irradiation on Low Activation Ferritic Alloys," DOE/ER-0045/13, p. 128.

2. R.L. Klueh, "The Development of Ferritic Steels for Fast Induced-Radioactive Decay," DOE/ER-0045/15 p. 116.

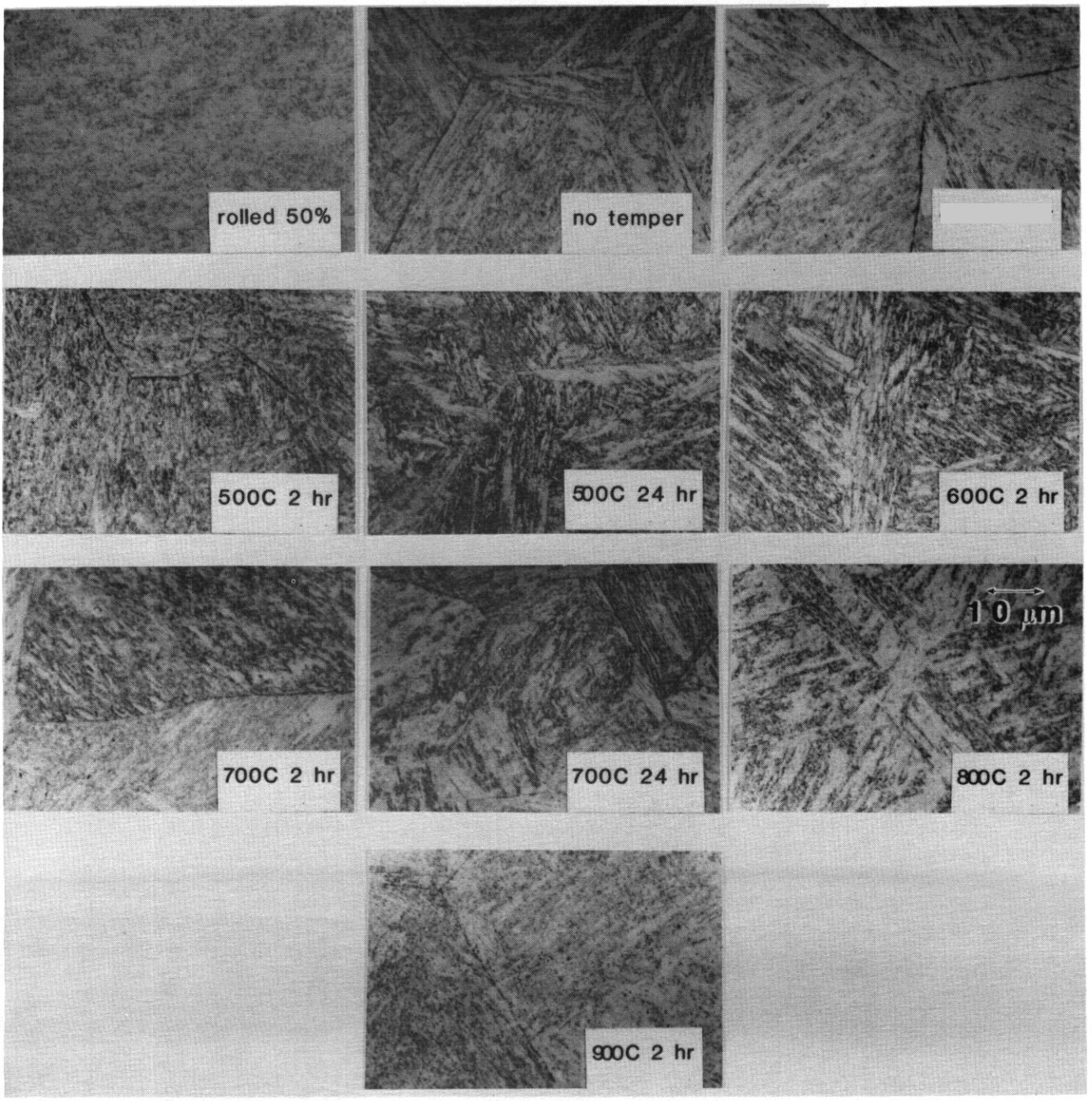


Figure 2. Optical micrographs showing the effect of tempering.

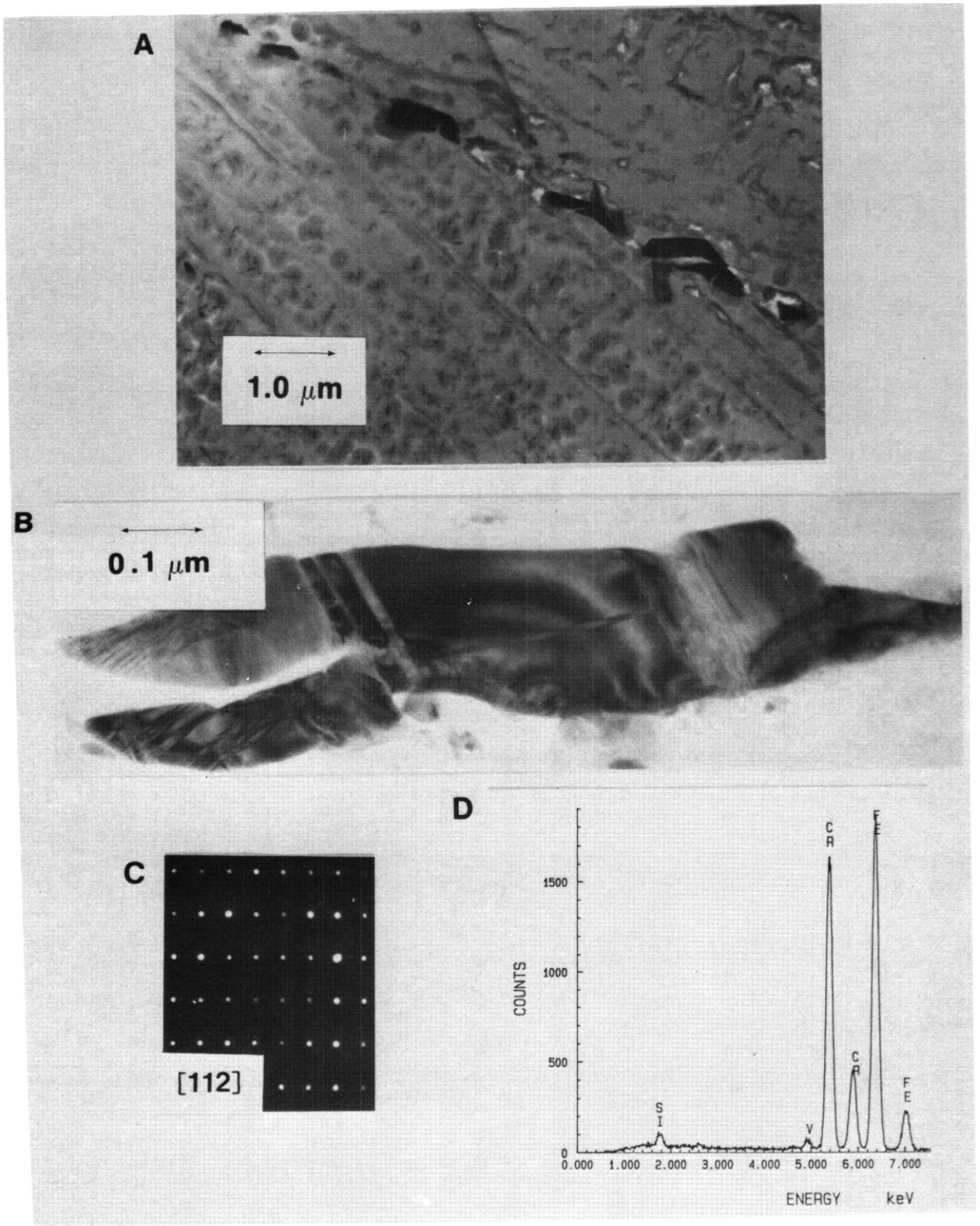


Figure 3. Results from TEM on extraction replicas.
a) TEM micrograph of austenite grain boundary and lath martensite $M_{23}C_6$.
b) Large austenite grain boundary $M_{23}C_6$ containing numerous twins.
c) Characteristic diffraction pattern from extracted $M_{23}C_6$ precipitates.
d) Characteristic EDS spectra of extracted $M_{23}C_6$ precipitates.

PROPERTIES OF WELDED LOW ACTIVATION FERRITIC ALLOYS - H. T. Lin and B. A. Chin (Auburn University)

ADIP TASK

ADIP Task I.A.5, Perform Fabrication Analysis, and I.C.1, Microstructure Stability.

OBJECTIVE

To characterize the microstructures and mechanical properties of welded low activation ferritic alloys.

SUMMARY

Sound autogeneous welds can be produced readily in thin sheets of the low activation ferritic alloys patterned on 2-1/4 Cr-1Mo, 9 Cr-1 Mo and 12 Cr-1Mo steels. The as-welded 2-1/4 Cr and 9 Cr alloys show typical microstructures of banite and martensite respectively, while 12 Cr alloys show the duplex ferrite-martensite. Observations indicate that there is a tendency to form delta ferrite in both fusion and heat-affected zones if the concentration of vanadium is greater than 1 wt%. In addition, the strengthening effect caused by the addition of tungsten and tantalum is not significant. The mechanical results suggest that a post-weld heat treatment is recommended for both 9 Cr and 12 Cr low activation alloys to enhance impact properties.

PROGRESS AND STATUS

Introduction

Ferritic alloys, composed principally of Cr and Mo, have been chosen for investigation as candidates for the structural components of fusion reactors. However, these alloys, to be used for the first wall and blanket components, will become highly radioactive from activation by high-energy fusion neutrons during service. This activity makes for difficult disposal of these materials after service. The need of devolping low activation materials was then proposed by Department of Energy in 1982 [1]. This has led to the development of low activation ferritic alloys with banitic (similar to 2-1/4 Cr-1 Mo) and martensitic (similar to 9-Cr-1Mo and HT-9) structures by Hanford Engineering Development Laboratory (HEDL) [2].

An important step in the development of these alloys is the determination of weldability because joining by conventional welding processes is an important means of fabricating engineering alloys into structural components. The typically banitic steels are known to exhibit good weldability, while martensitic steels are suspected to have inadequate toughness in the heat-affected zone (HAZ). At present, there are little data on characterization of weld structures and mechanical properties of low activation ferritic alloys. The objective of this study is to Characterize the microstructures and mechanical properties of low activation alloys encountered in both fusion zone and HAZ. This will provide baseline data for further chemical modification to improve the performance of low activation ferritic alloys.

Experimental Procedures

Eleven heats of low activation ferritic alloys patterned on 2-1/4 Cr-1 Mo, 9 Cr-1Mo and 12 Cr-1 Mo steels were fabricated by HEDL. The nominal chemical composition of low activation alloys studied is shown in Table 1 [2]. All heats were hot-rolled with an intermediate heat treatment of 700°C for 30 minutes to a final thickness of 2.54 mm. All sheets were homogenized for 20 hours at 1000°C followed by air-cooling. The materials were then solution annealed for one bur at 1150°C, air-cooled then given a tempering heat treatment of 700°C for two burs followed by air-cooling.

Autogeneous bead-on-plate welds were made using gas tungsten arc welding (GTAW) process. The welding was performed at 32 VDC, 100 A at a travel speed of 4.5 in/min to produce full penetration welds in the 2.54 mm thick material.

Metallographic sections transverse to the welding direction were prepared for optical microstructure examinations using standard technique and etched with a solution of 1 gram potassium bisulfite, 2 grams ammonium bifluoride, 83% H_2O and 17% HCl. Microhardness traverses were conducted across the weld regions to assess microstructure-property relationships. To further scope the mechanical properties of welds, mechanical tests including weld bend, charpy impact and tensile tests were performed at room temperature.

Table 1. Chemical composition of low activation ferritic alloys.

Heat No.	Composition (w/o) Cr	V	W	C	Mn	Ta
V02262	2-1/4	0.5		0.1		
V02263	2-1/4	1.0		0.1		
V02264	9.0	0.5		0.1		
V02265	9.0	1.3		0.2	1.0	
V02266	9.0	0.5		0.1	2.0	
V02268	9.0	0.3	1.0	0.1	2.5	
V02267	12.0	1.0		0.1	6.5	
V02269	12.0	0.3	1.0	0.1	6.5	
V02702	12.0	0.3	1.0	0.1	6.5	0.1
V02734	12.0	0.3	1.0	0.1	6.5	0.25
V02735	12.0	1.0	0.3	0.1	8.0	0.25

Table 2. Results of mechanical tests at room temperature for low activation alloys.

Heat No.	Ultimate Strength (Mpa)	Yield Strength (Mpa)	Total Elongation (%)	Impact Strength (in-lb)	Weld Bend Test
V02262	95.7	82.7	8.0	124.5	satisfactory
V02263	79.4	64.0	7.8	114.5	satisfactory
V02264	81.2	72.0	7.2	58.0	satisfactory
V02265	96.3	75.8	10.3	69.0	satisfactory
V02266	108.1	103.5	4.1	72.5	satisfactory
V02268	111.4	105.0	4.4	62.6	satisfactory
V02267	121.3	109.5	5.3	34.0	failed at F. Z.
V02269	127.1	120.0	3.8	25.0	failed at F. Z.
V02702	137.8	130.5	4.2	20.0	failed at F. Z.
V02734	133.6	124.5	4.2	33.0	failed at F. Z.
V02735	143.0	122.0	3.9	29.0	failed at F. Z.

Results and analysis

2-1/4 Cr Alloys

Weld Microstructure. The GTAW welds of 2-1/4 Cr low activation alloys showed no signs of cracking. Optical micrographs of the welds of heats V02262 and V02263 heats, which consist of three distinct zones: fusion zone, the coarse-grained, fine-grained and over-tempered regions of HAZ and base metal are showing in Figures 1 and 2. The fusion zone of both welds is composed principally of banite. In the HAZ, the structure consists of a mixture of banite and ferrite, the amount of ferrite increasing with distance from the fusion zone. The observations also indicate that the alloys with higher vanadium concentrations exhibit more ferrite formation in HAZ than alloys with lower vanadium concentrations. The base netal of both materials is a the tempered banitic structure.

Mechanical Properties. Figures 1 and 2 show the microhardness traverses of the as-welded 2-1/4 Cr alloys. The results show only minor variations in hardness in both the fusion zone and coarse-grained region of the HAZ. The fine-grained and over-tempered regions, however, which exhibit the greatest amount of ferrite show a corresponding decrease in microhardness. The results also reveal that materials with higher vanadium concentrations have higher hardness than those of lower vanadium concentrations. The results of mechanical tests are given in Table 2. The weld tend tests showed no failure of both welds. Both tensile specimens failed at the interface of HAZ and base metal where a minimum in the microhardness was found. Observatiions, as expected, show there is only a little uniform tensile elongation but great percentage of reduction in area. This is caused by the region of minimum microhardness being restricted to only a small region of the test speimens.

9 Cr Alloys

Weld Microstructure. The GTAW welds of 9 Cr alloys were produced with no visible signs of cracking or other defects. The microstructures of as-welded 9 Cr low activation alloys are shown in Figures 3-6. Generally, the heats with rmnganese additions show the typically martensitic structure in a lath-like morphology. The heat with higher carbon and vanadium exhibits the tendency to form ferrite at both fusion boundary and in the over-tempered region. Metallographic observations also indicate that the heat with no addition of manganese exhibits ferrite formation throughout the weld regions. In addition, the microstructure in the fusion zone of all 9 Cr heats shows a relatively coarse lath martensite morphology interspersed with carbides. These carbides were observed both along lath boundaries and within the individual laths. Generally, the over-tempered region in the HAZ of the 9 Cr low activation alloys shows a tendency to form the ferrite. This portion of the HAZ is hyposithesized to be heated to a temperature just below the A_C. Some prior-austenitic grain boundaries are visible in the base metal.

Mechanical Properties. The microhardness traverses of the 9 Cr low activation alloys are given in Figures 3-6. The heats are similar in chemical composition except for the addition of tungsten. Heats V02266 and V02268 show similar microhardness and hardenability. The fusion zone of heat V02264 exhibits scatter in the microhardness measurements as a result of the existance of delta ferrite. Also, the weld with higher vanadium and carbon concentrations has higher hardness than those with lower vanadium and carbon additions. The observations indicate that the heats with higher manganese content have less scatter in the hardness profile than those without or with lower manganese content. In addition, the alloys with similar carbon and vanadium concentration exhibit similar hardness behavior in both fusion zone and HAZ except in the over-tempered and base metal region. Table 2 lists the results of mechanical tests performed on 9 Cr alloys. All weld bend tests were satisfactory. The results show there is only minor deviation in charpy impact strength. Tensile test results reveal that all tensile specimens of 9 Cr failed in the base metal.

12 Cr Alloys

Weld Microstructure. No signs of cracks or any defects were observed on all welds of the 12 Cr low activation alloys. Figures 7-11 are optical micrographs of as-welded 12 Cr alloys. The

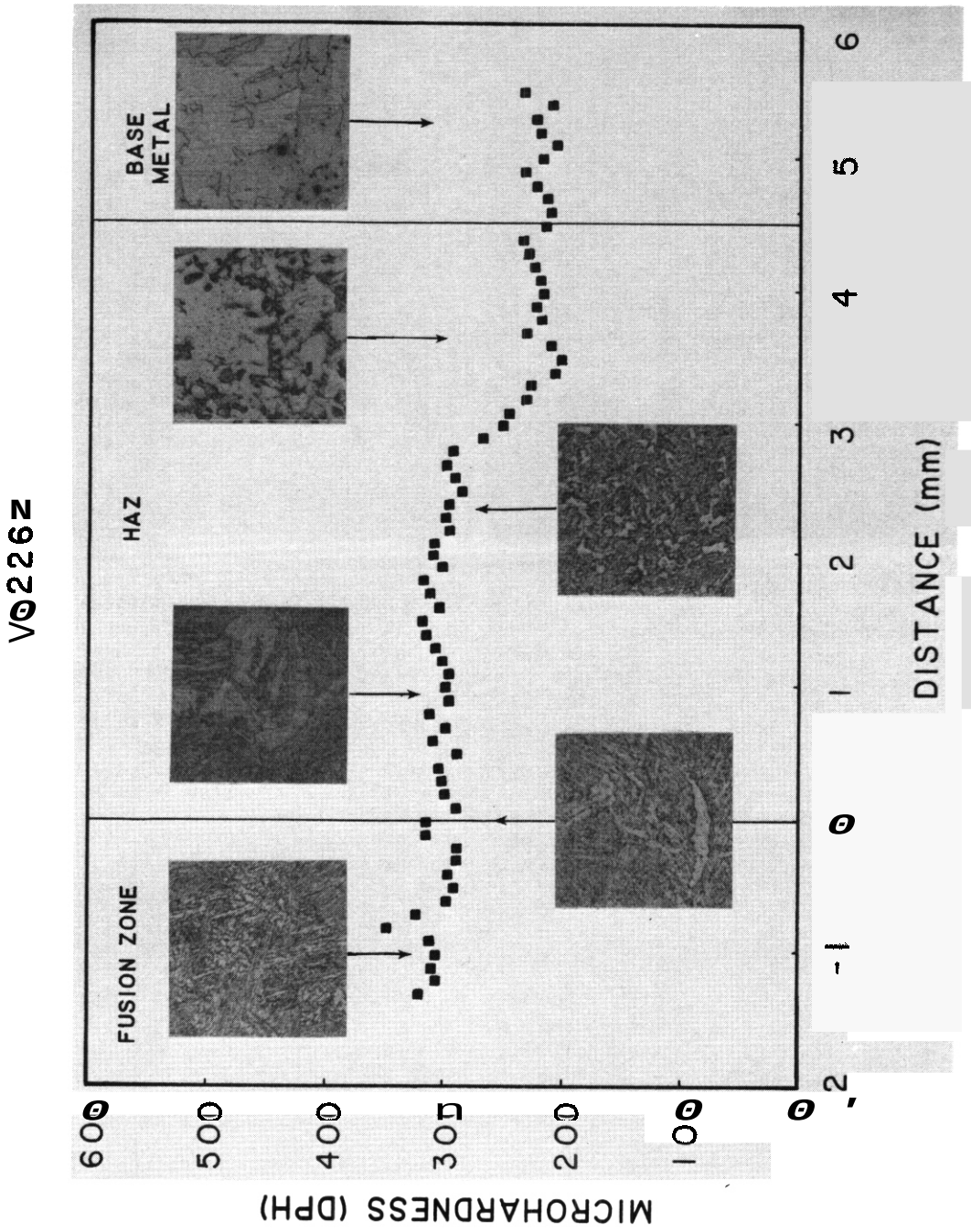


Figure 1 Microstructure and Microhardness Traverses Across the Weld Region of V02262 Alloy.

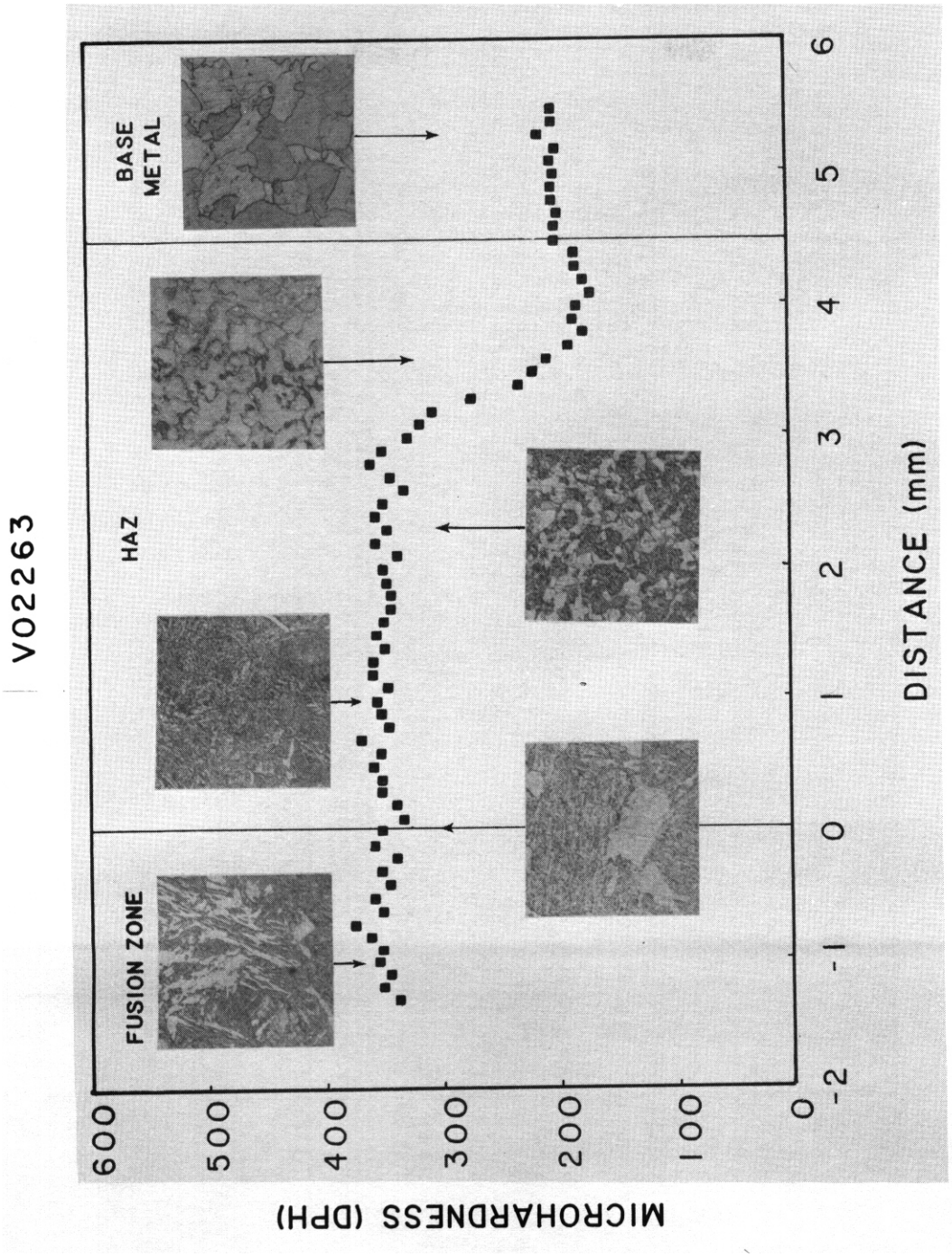


Figure 2 Microstructure and Microhardness Traverses Across the Weld Region of V02263 Alloy.

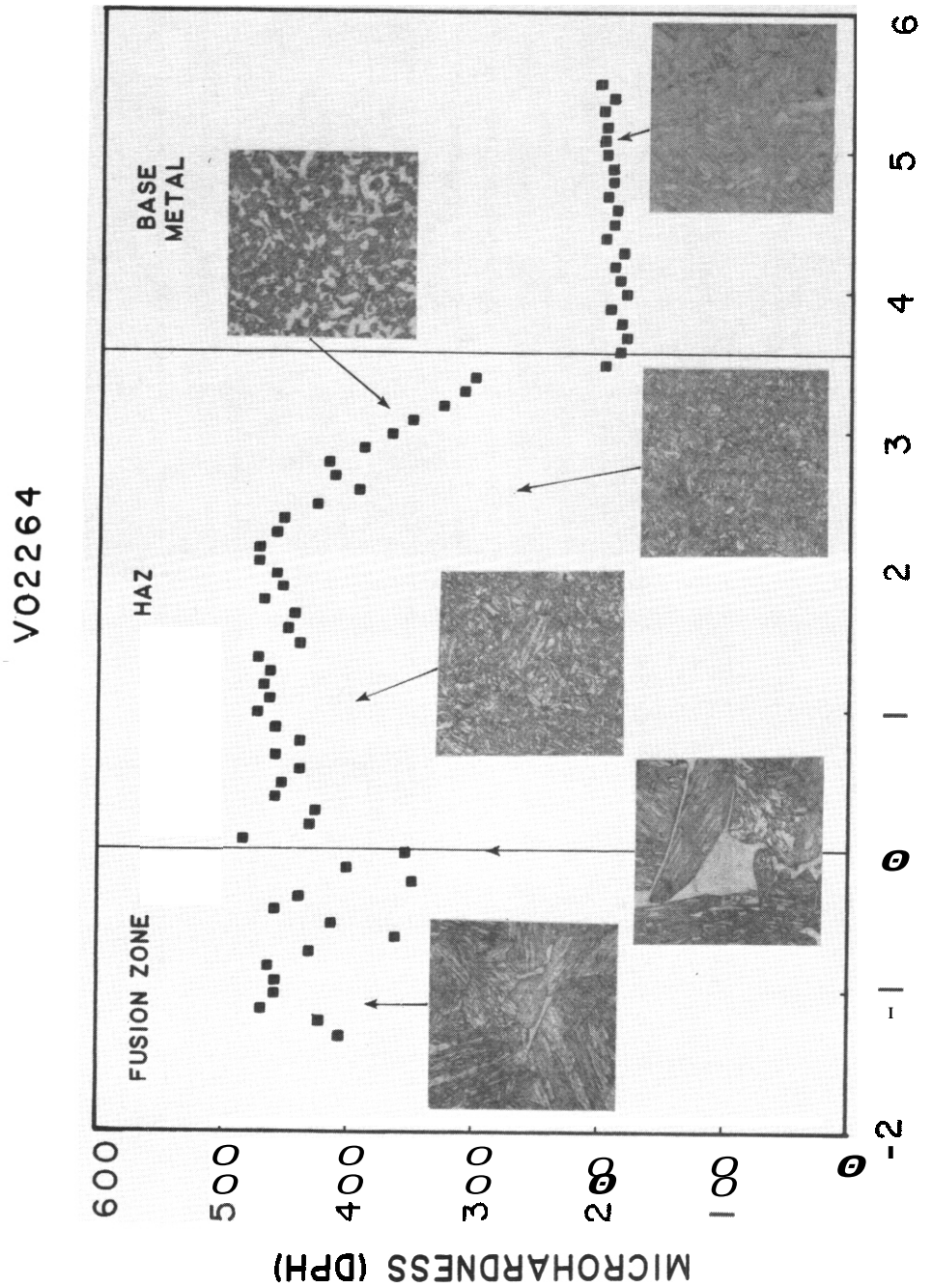


Figure 3. Microstructure and Microhardness Traverses Across the Weld Region of V02264 Alloy

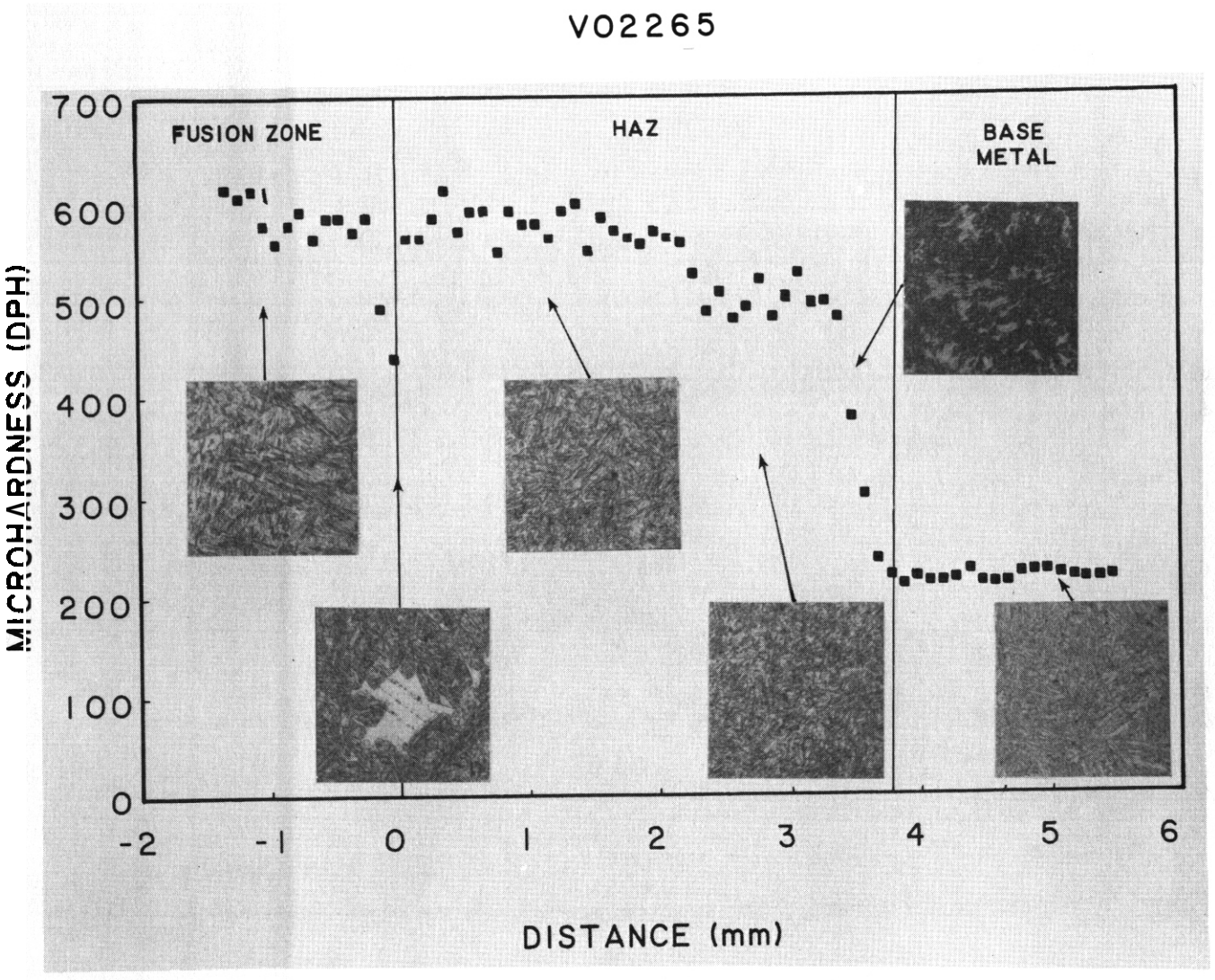


Figure 4. Microstructure and Microhardness Traverses Across the Weld Region of V02265 Alloy.

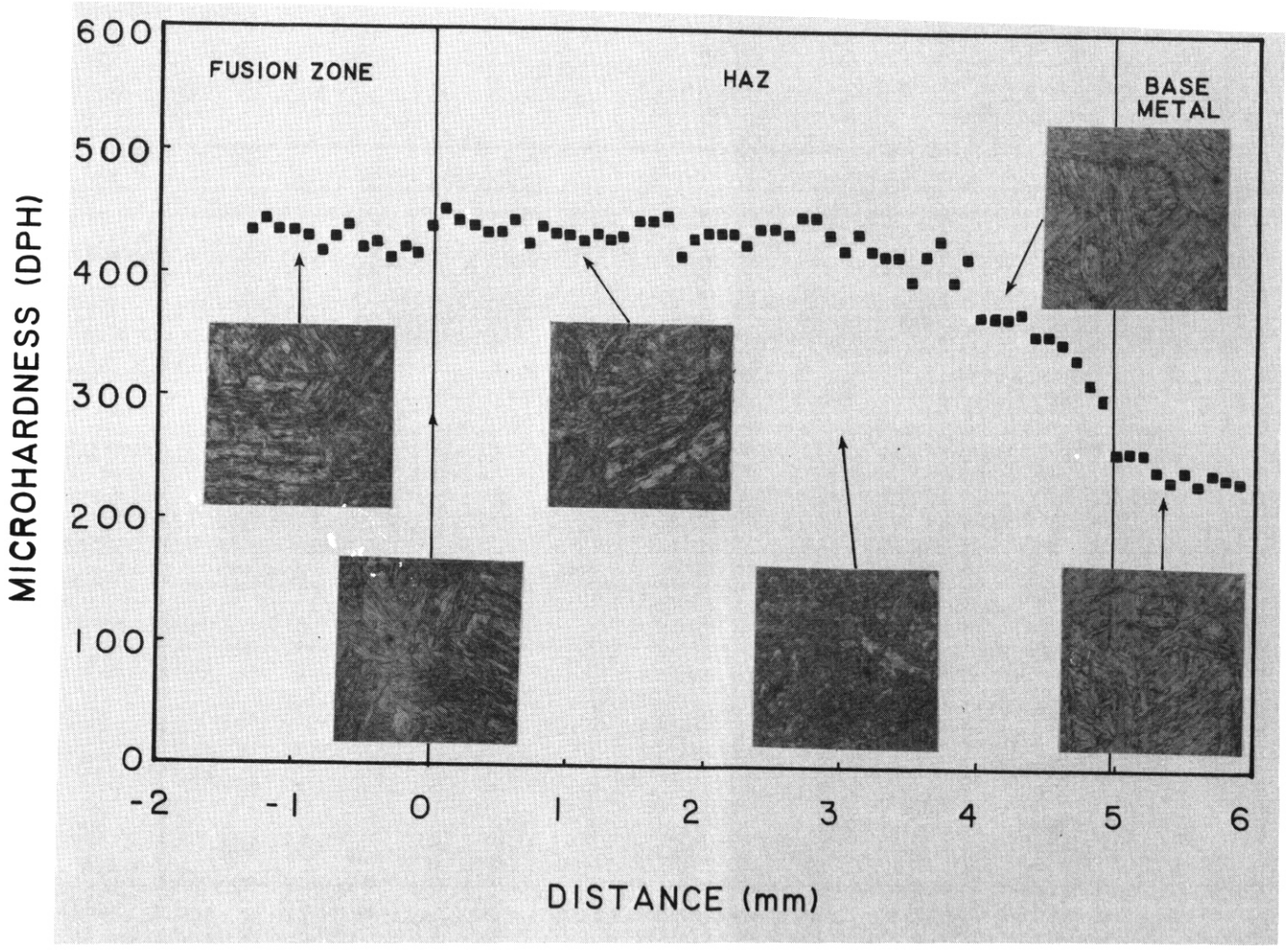


Figure 5. Microstructure and Microhardness Traverses Across the Weld Region of V0Z266 Alloy.

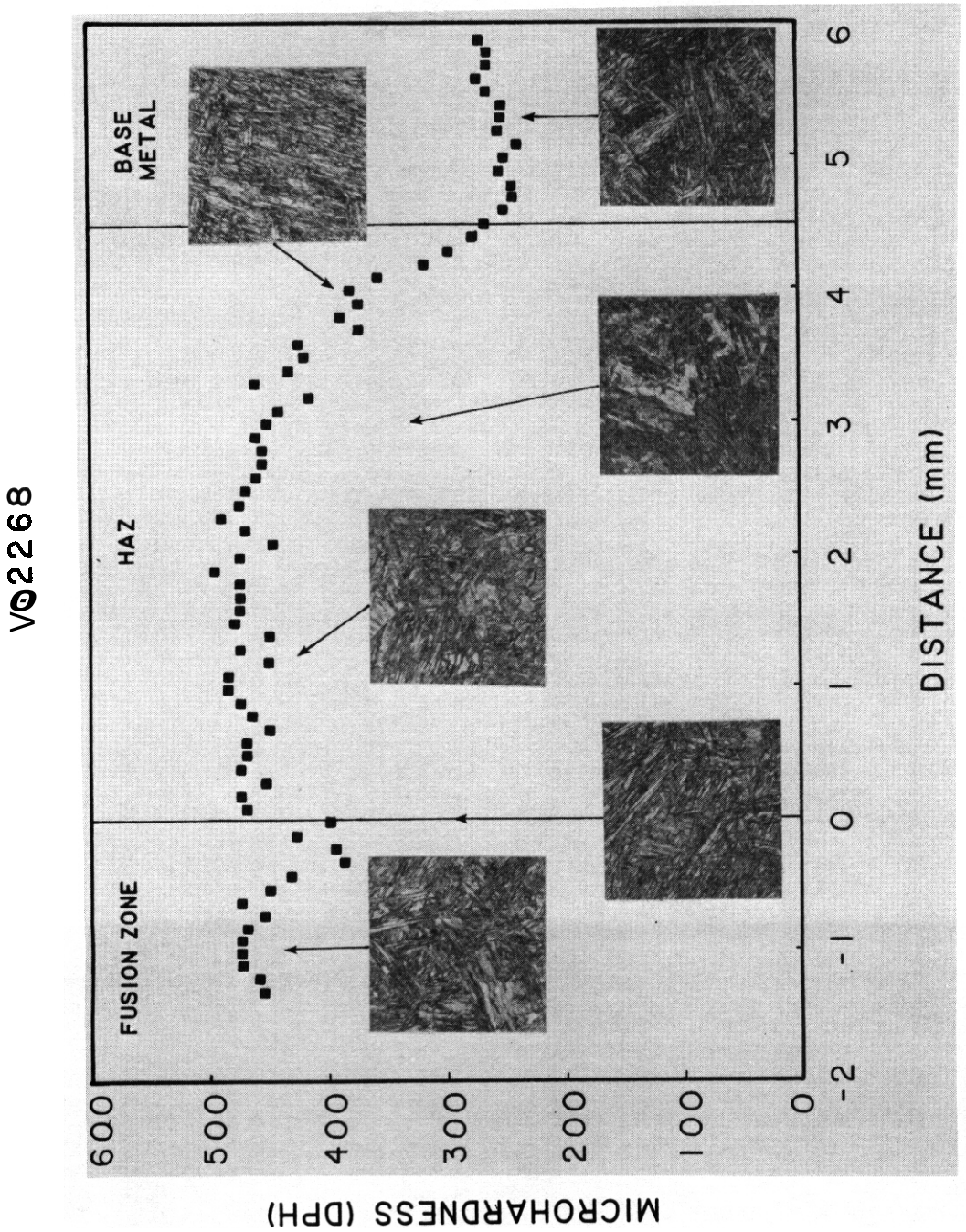


Figure 6. Microstructure and Microhardness Traverses Across the Weld Region of V02268 Alloy.

metallography indicates that microstructures of 12 Cr alloys consist of a mixture of martensite and delta ferrite. In the HAZ and base metal regions the ferrite was observed along prior-austenite grain boundaries. The observations also reveal that the amount of ferrite formation increases with increasing the vanadium concentration. Alloys, V02269, V02702 and V02734 (variable tantalum content) show that the addition of tantalum tends to reduce the formation of ferrite.

Mechanical Roperties. Microhardness results for the 12 Cr alloys are also given in Figures 7-11. kats, V02269, V02702 and V02734, with similar chemical composition exihibit similar microhardness traverses and strength. The alloys containing higher vanadium concentration show same scatter in the microhardness traverses as a result of delta ferrite. The hardness in both fusion zone and HAZ increases with increasing concentrations of tungsten. In addition, the base metals of all tempered 12 Cr heats show the same hardness. The results of mechanical tests are shown in Table 2. All weld bend specimens of the 12 Cr alloys failed at the fusion zone upon loading. Also, impact tests show no significant difference in impact strength of all 12 Cr heats. Failure in the base metal was observed for all 12 Cr tensile specimens.

Discussion

The results of this study reveal that no signs of cracks or any defects were observed in all as-welded low activation ferritic alloys. This suggests that the newly developed alloys are capable of being joined by conventional fusion processes. Generally, the welds of all low activation alloys patterned on Cr-Mo steels consists of three distinct zones: fusion zone, HAZ and base metal. The microstructure in the HAZ can be further identified into three different regions: coarse-grained, fine-grained and over-tempered regions as a result of thermal gradients developed during welding process. Each has its own character and corresponding microstructure.

The only difference between two 2-1/4 Cr alloys is the vanadium concentration which serves as strengthener. The difference in chemical composition is refected in the difference in both microstructure and microhardness traverse of the welds. The higher the concentration of vanadium, the more vanadium carbide will be produced resulting in a higher hardness measurement. Metallographic observations indicate that the alloy with higher vanadium concentration exhibits more ferrite formation in the HAZ. This observed feature suggests that the more vanadium carbide formed, the less carbon will be available to stabalize the austenitic phase and more ferrite will be produced during trnsformation. In addition, the variations in ferrite present in the HAZ are mainly due to the vanadium carbide which does not completely dissolve as the material is subjected to the welding thermal gradient. The lower the amount of dissolved carbon the more ferrite formation and hence lower hardenability. This is consistent with the observations that the amount of ferrite increases with distance from the fusion zone.

The effect of vanadium on both microstructure and microhardness of as-welded 9 Cr low activation alloys is the same as that of the 2-1/4 Cr alloys. The vanadium tends to enhance the formation of ferrite in both fusion zone and over-tempered region. However, the addition of 0.8 wt% vanadium, with an increased carbon content, increases the hardness in both fusion zone and HAZ by approximately 25 %. This is due to the formation of more vanadium carbides in both zones. The austenite formers such as manganese stabalize the austenitic phase, and tend to smooth the microhardness traverses of the 9 Cr low activation alloys. To investigate the effect of tungsten on hardenability, heat V02268 was produced with an addition of 1 wt% tungsten. Hardness measurements indicates that tungsten does not enhance the hardenability of the 9 Cr alloys significantly. This reflects the fact that solid solution hardening effects are usually small compared with those obtained by carbide precipitation. In the 9 Cr alloys studied, the hardening effect by adding tungsten is not significant.

The appearence of delta ferrite in all 12 Cr heats indicates that insufficient amount of austenite stabalizers such as manganese and carbon were present to form 100% austenite. Accordingly, more manganese or carbon needs to be added to all 12 Cr low activation alloys. The kats with more vanadium show scatter in the microhardness traverses as a result of the existance of ferrite. An examination of the microhardness of the 12 Cr alloys indicates that both increased amount of tungsten and tantalum does not strengthen the alloys significantly.

This study indicates that the addition of vanadium has the same effect on all the alloys investigated. The amount of ferrite increases with increasing additions of vanadium. However, the vanadium tends to enhance the strength of alloys as a result of vanadium carbide fromation. This suggests that the proper amount of vanadium addition needs to be controlled to achieve optimization of both strength and structural stability. The results of impact tests indicate that the 2-1/4 Cr welds have better impact strength than either 9 Cr or 12 Cr welds. This is

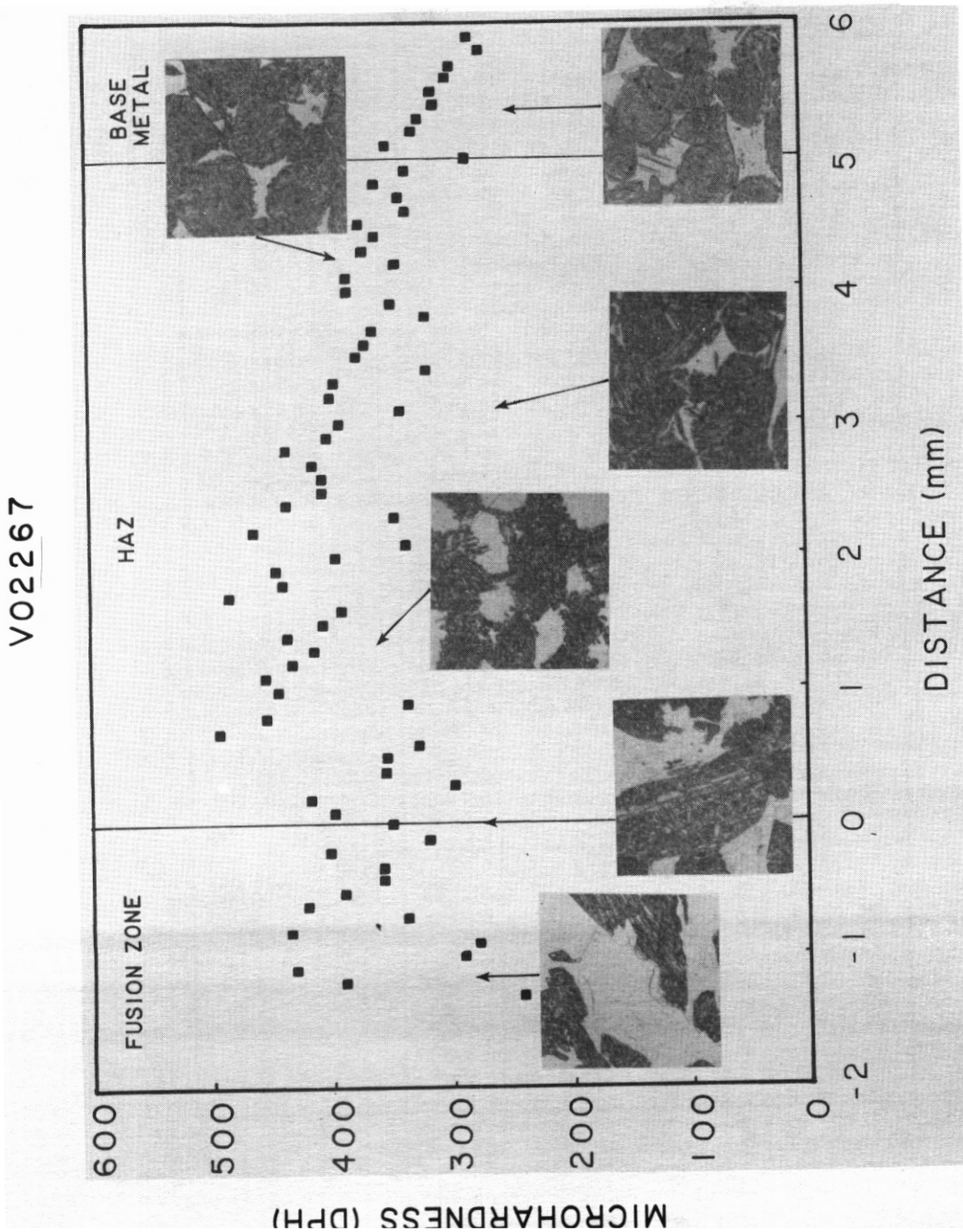


Figure 7 Microstructure and Microhardness Traverses Across the Weld Region of V02267 Alloy.

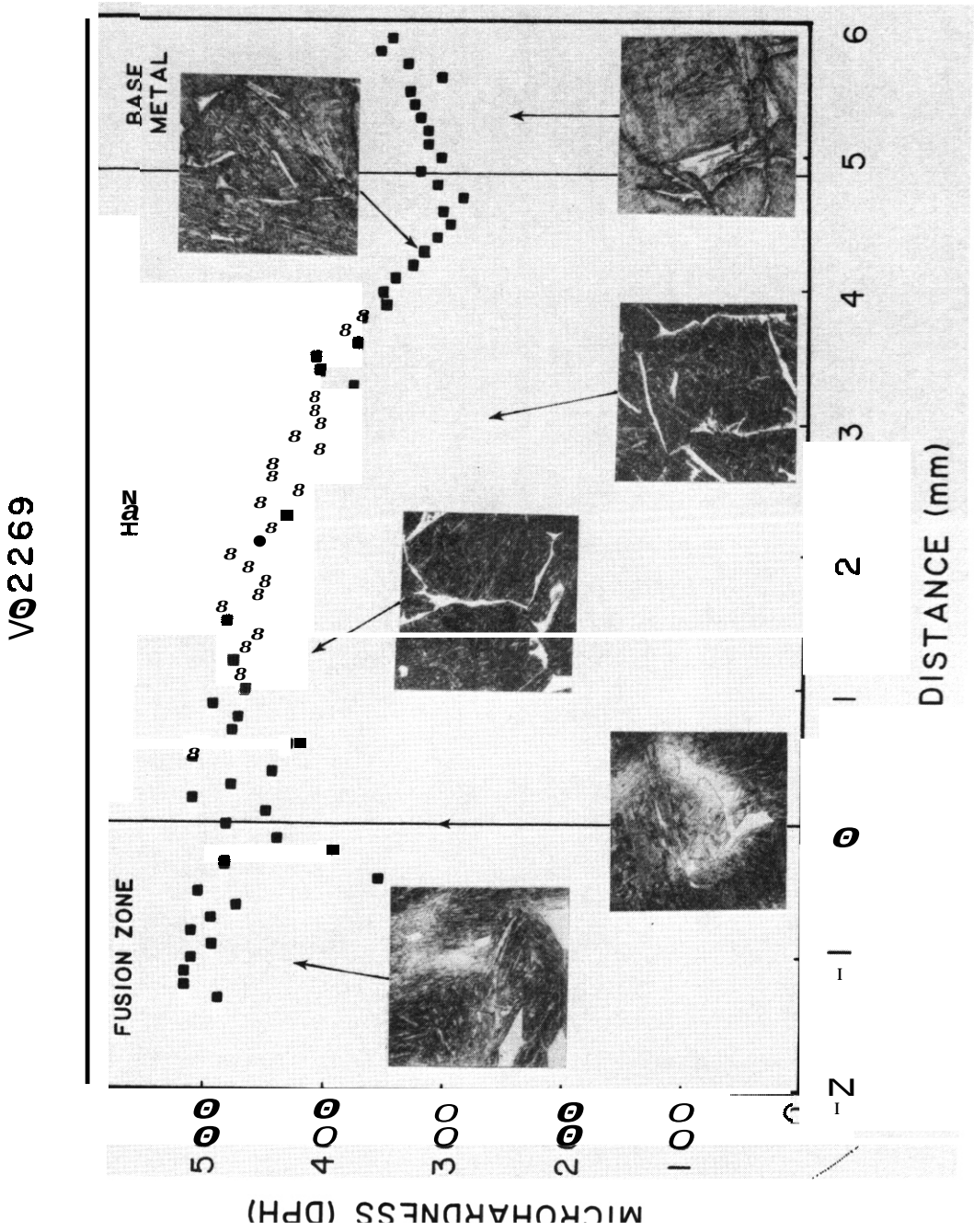


Figure 8. Microstructure and Microhardness Traverses Across the Weld Region of V02269 Alloy.

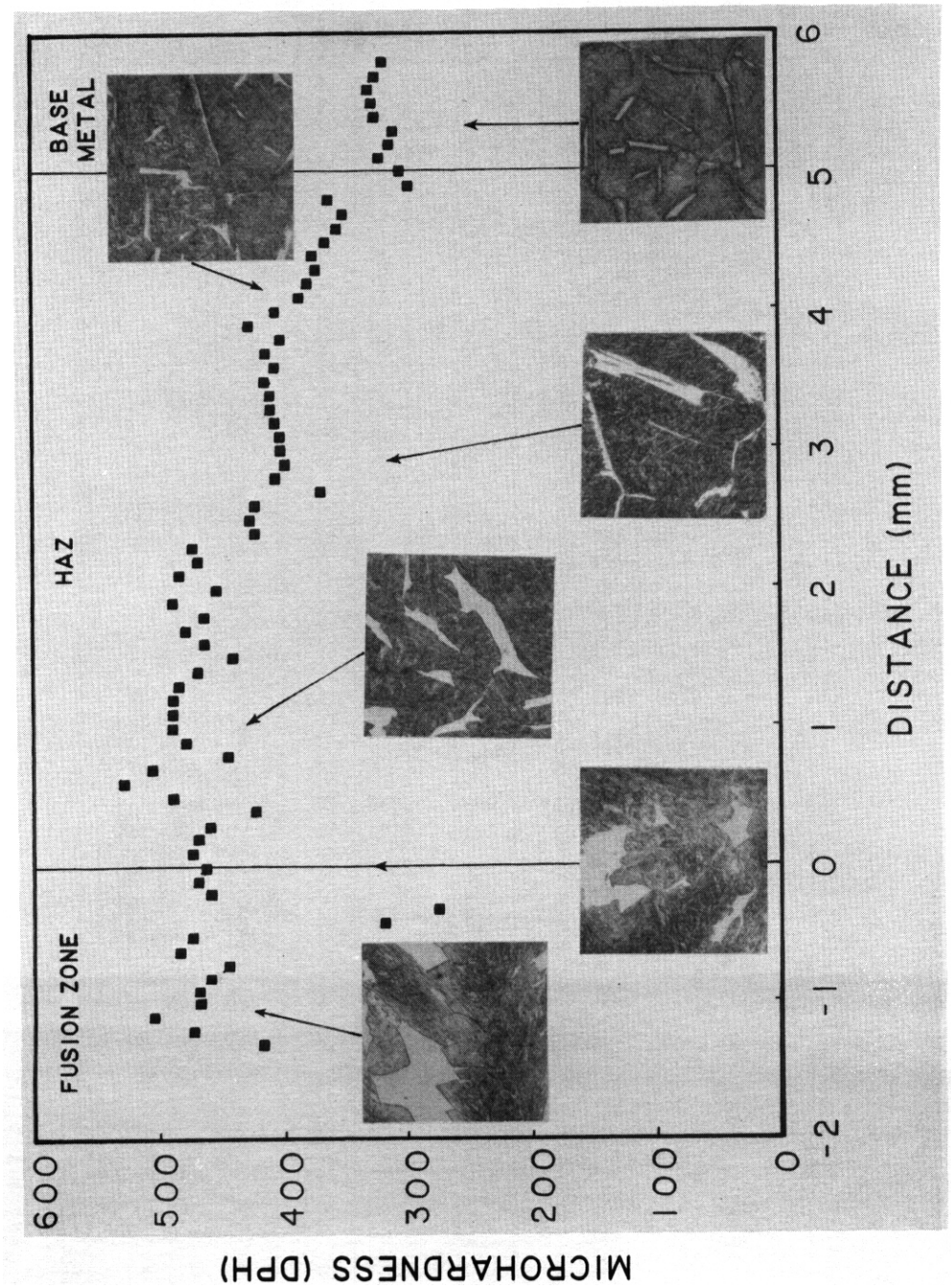


Figure 9. Microstructure and Microhardness Traverses Across the Weld Region of V02702 Alloy.

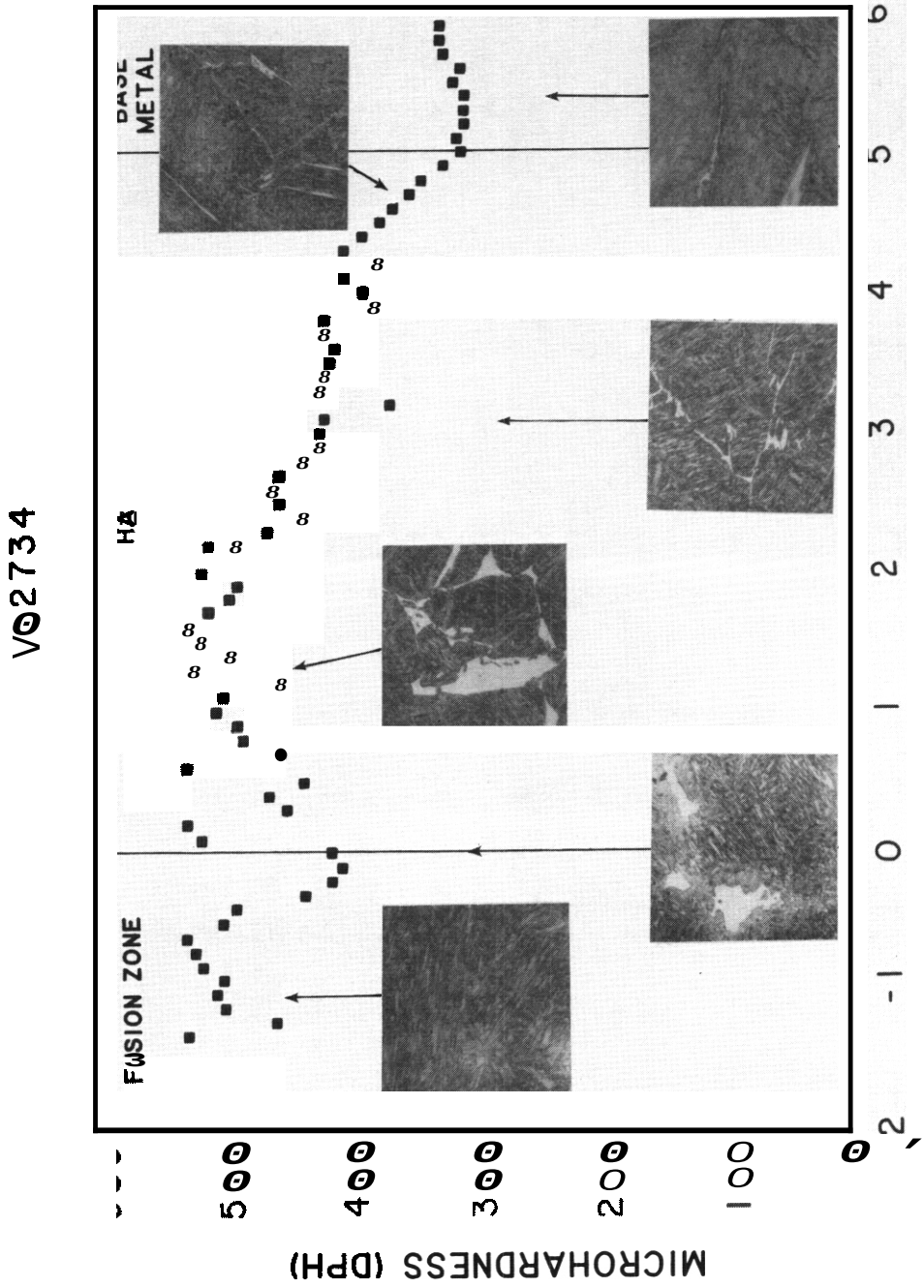


Figure 10. Microstructure and Microhardness Traverses Across the Weld Region of V02734 Alloy.

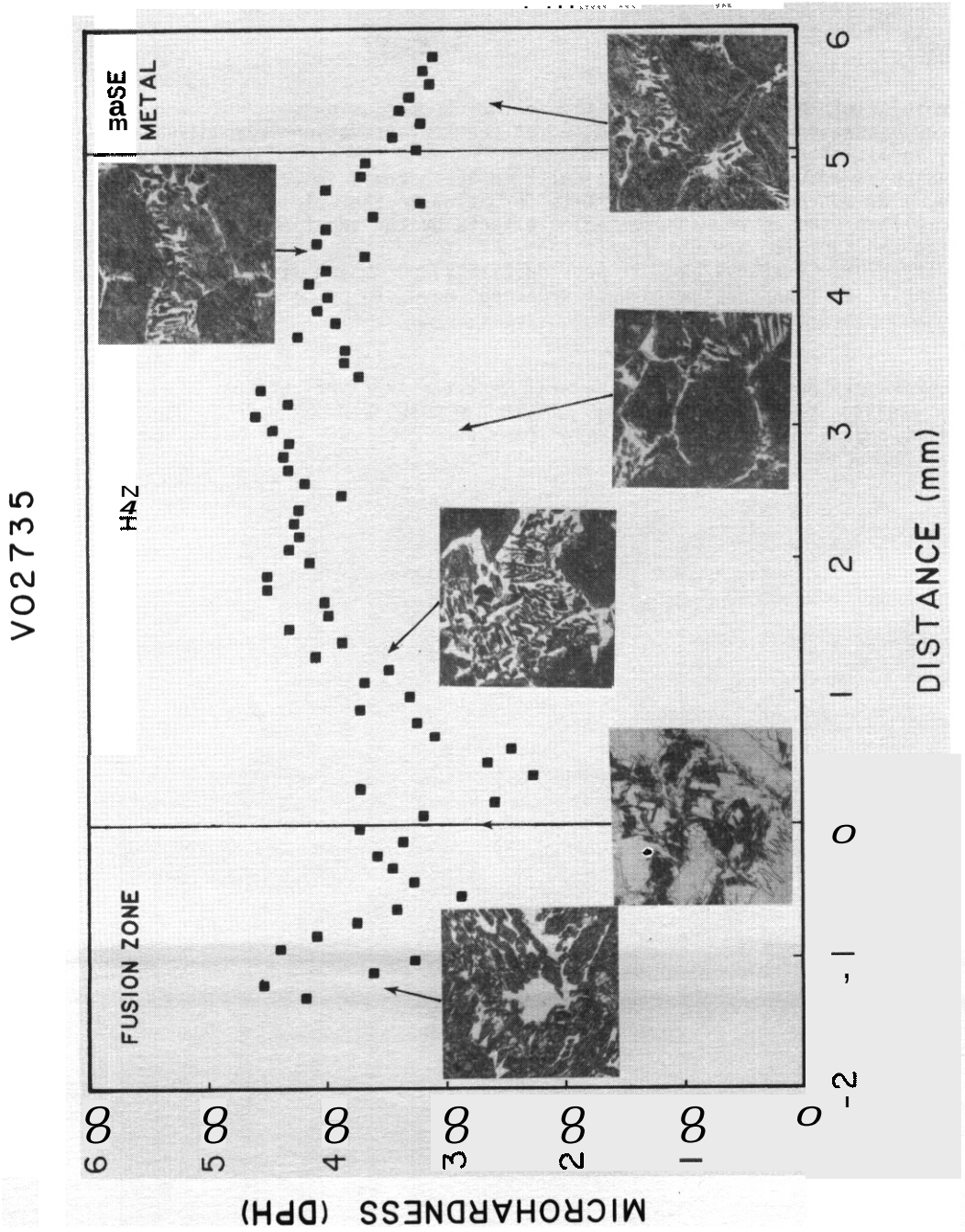


Figure 11. Microstructure and Microhardness Traverses Across the Weld Region of V02735 Alloy.

consistent with the behavior of the as-welded martensitic structure which is generally brittle with poor impact strength. Accordingly, a proper postweld heat treatment of both 9 Cr and 12 Cr welds needs to be recommended to ensure cracking will not initiate in the fusion zone. This study suggests that the developed low activation ferritic alloys show promise to be readily welded by conventional welding processes.

CONCLUSIONS

The results of this study lead to the following conclusions:

1. Sound autogeneous welds can be produced on the low activation ferritic alloys investigated.
2. Increasing vanadium concentration results in an increase in the hardness of the weld, but promotes delta ferrite formation in the welds.
3. In the alloys studied the strengthening effects by the addition of tungsten and tantalum are not significant.
4. The welds of 12 Cr alloys exhibit poor ductility and impact strength. Accordingly, a proper post-weld heat treatment needs to be developed.

REFERENCES

[1]. Nuclear Regulatory Commision, US Federal Register 41 (1982) 51446.
[2]. D. S. Gelles and M. L. Hamiton, p. 128 in AOIP Semiannu. Prog. Rep., Sep. 30. 1984, DOE/ER-0045/13, U. S. DOE, Office of Fusion Energy.

THE DEVELOPMENT OF FERRITIC STEELS FOR FAST INDUCED-RADIOACTIVITY DECAY — R. L. Klueh

OBJECTIVE

Induced radioactivity in the first-wall and blanket-structure materials will make these components highly radioactive after their service lifetime, leading to difficult radioactive waste-management problems. One way to minimize the disposal problem is to use structural materials in which radioactive isotooes induced by irradiation decay quickly to levels that allow simplified disposal techniques. We are assessing the feasibility of developing such ferritic steels.

SUMMARY

Tensile studies were made on eight heats of normalized-and-tempered chromium-tungsten steel that contained various levels of chromium, tungsten, vanadium, and tantalum. The strength and ductility of these steels were found to compare favorably with the properties of analogous chromium-molybdenum steels that are presently being considered as candidate structural materials for fusion reactor applications.

PROGRESS AND STATUS

Introduction

We have continued the studies to characterize eight heats of ferritic steel designed for fast induced-radioactivity decay (FIRD). These steels were patterned on the chromium-molybdenum steels that are of interest for fusion-reactor applications — namely, 2 1/4Cr-1Mo, 9Cr-1MoVNb, and 12Cr-1MoVW steels. The major changes for the chromium-molybdenum steels involve the replacement of molybdenum with tungsten, the use of vanadium in a 2 114% Cr steel, and the replacement of niobium in the 9% Cr steel with tantalum. (Although tantalum can be used in a FIRD steel, the decay of its transmutation products immediately after irradiation in a fast- or mixed-spectrum reactor makes such a steel difficult to study. Therefore, few, if any, irradiated transmission electron microscopy studies will be performed on steels containing tantalum.) The composition of the eight steels is given in Table 1.

Table 1. Chemical composition of fast induced-radioactivity decay (FIRO) ferritic steels

	Chemical composition,[a] (wt %)						
Alloy	Cr	W	V	Ta	C	Mn	Si
2 1/4 CrV	2.36		0.25		0.11	0.40	0.17
2 1/4 Cr-1WV	2.30	0.93	0.25		0.10	0.34	0.13
2 114 Cr-2W	2.48	1.99	0.009		0.11	0.39	0.15
2 1/4 Cr-2WV	2.42	1.98	0.24		0.11	0.42	0.20
5 Cr-2WV	5.00	2.07	0.25		0.13	0.47	0.25
9 Cr-2WV	8.73	2.09	0.24		0.12	0.51	0.25
9 Cr-2WVTa	8.72	2.09	0.23	0.075	0.10	0.43	0.23
12 Cr-2WV	11.49	2.12	0.23		0.10	0.46	0.24

[a] P = 0.014–0.016, S = 0.005–0.006, Ni < 0.01, Mo < 0.01, Nb < 0.01, Ti < 0.01, Co = 0.005–0.008, Cu = 0.02–0.03, Al = 0.02–0.03, B < 0.001, bal Fe.

We previously presented preliminary tensile data on these steels. In this report these data are presented and analyzed in more detail.

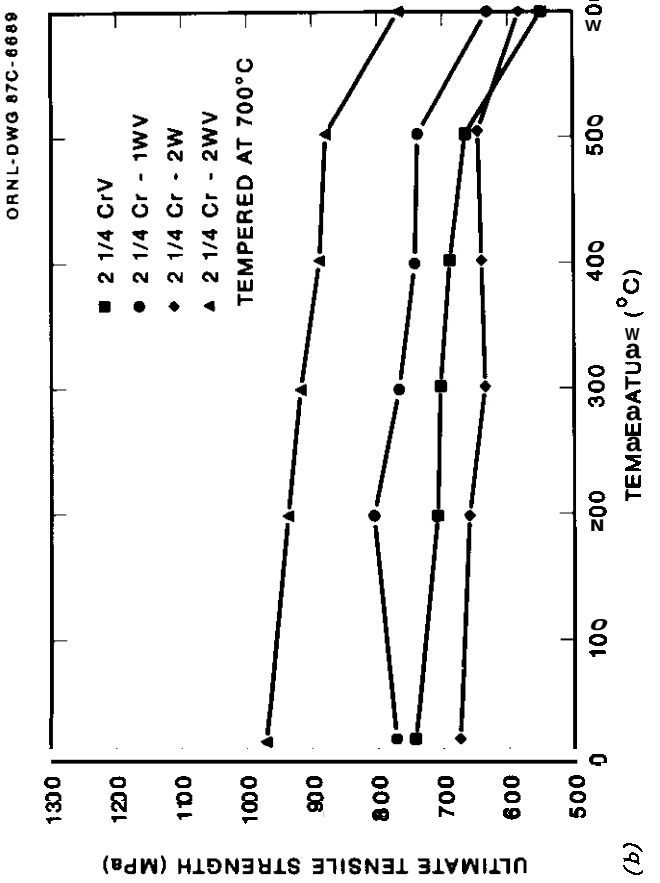
Experimental procedures

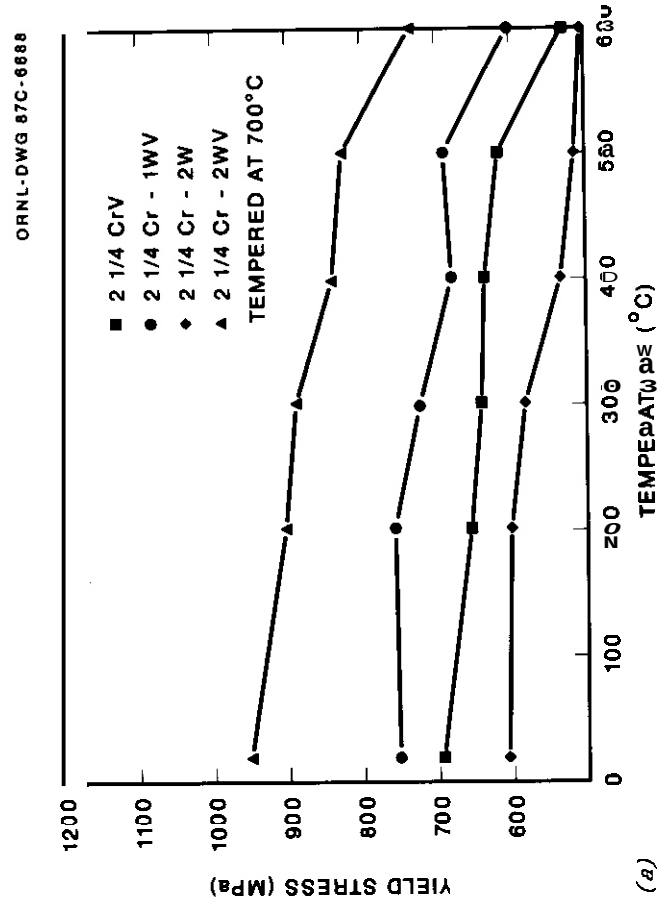
Details were provided previously on the eight heats of material. the heat treatment of the steeis, and the tensile testing procedure used.','

Results

The steels were tested in the normalized-and-tempered condition. All but the 2 1/4Cr-2W steel were normalized by annealing 0.5 h at 1050°C and cooling in flowing helium; the 2 1/4Cr-2W was annealed 0.5 h at 900°C and cooled in the flowing helium. They were tested in two tempered conditions: 1 h at 700°C and 1 h at 750°C. Tensile tests were made over the temperature range from room temperature to 600°C.

The tensile data were previously given in tabular form.[2,3] The data for the low-chromium steels tempered at 700 and 750°C are plotted in Figs. 1 and 2, respectively, and the data for the high-chromium steels are plotted in Figs. 3 and 4, respectively. For all of the steels, the strength is substantially lower after tempering at 750°C than after tempering at 700°C. In general, the relative strengths of the different steels are the same after the two different heat treatments.





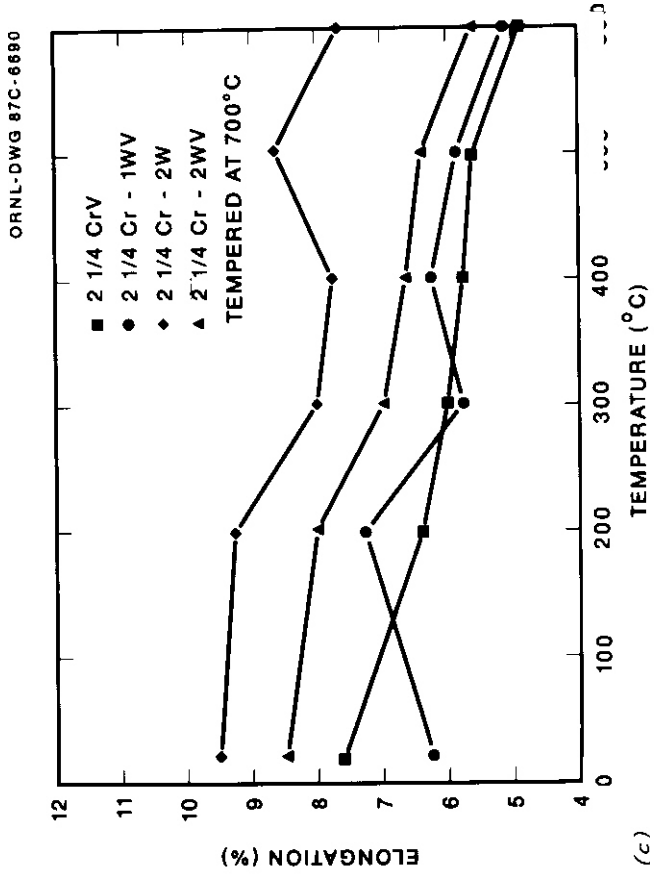
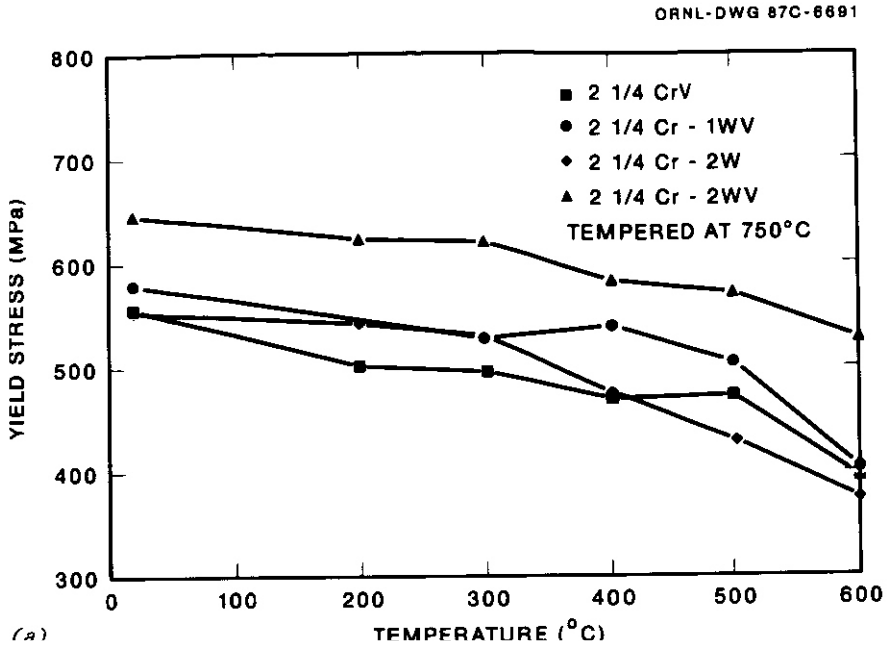
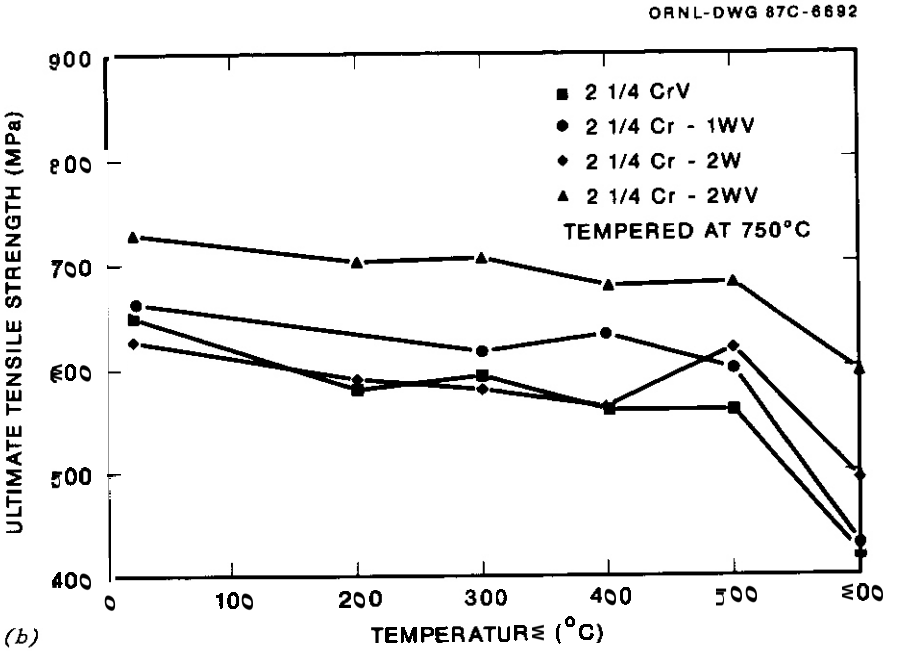


Fig. 1. Tensile properties as a function of temperature for the low-chromium steels tempered at 700°C: *(a)* 0.2% yield stress, *(b)* ultimate tensile strength, and *(c)* uniform and total elongation.





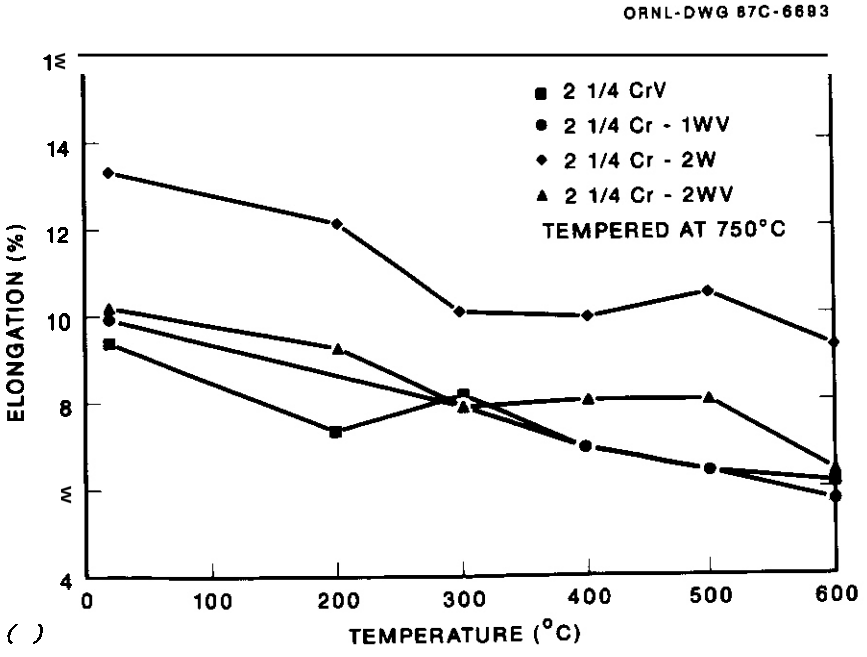
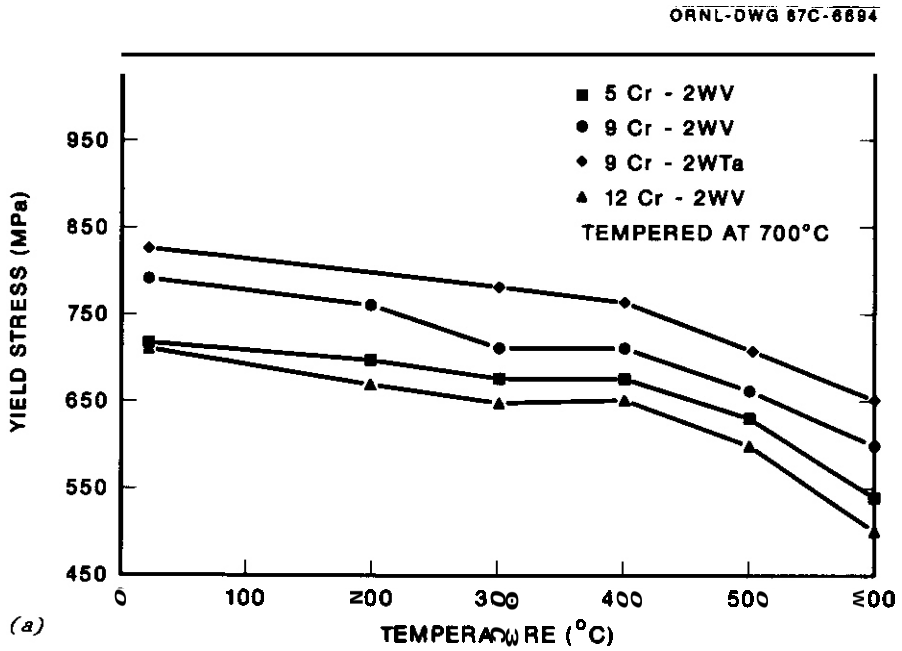
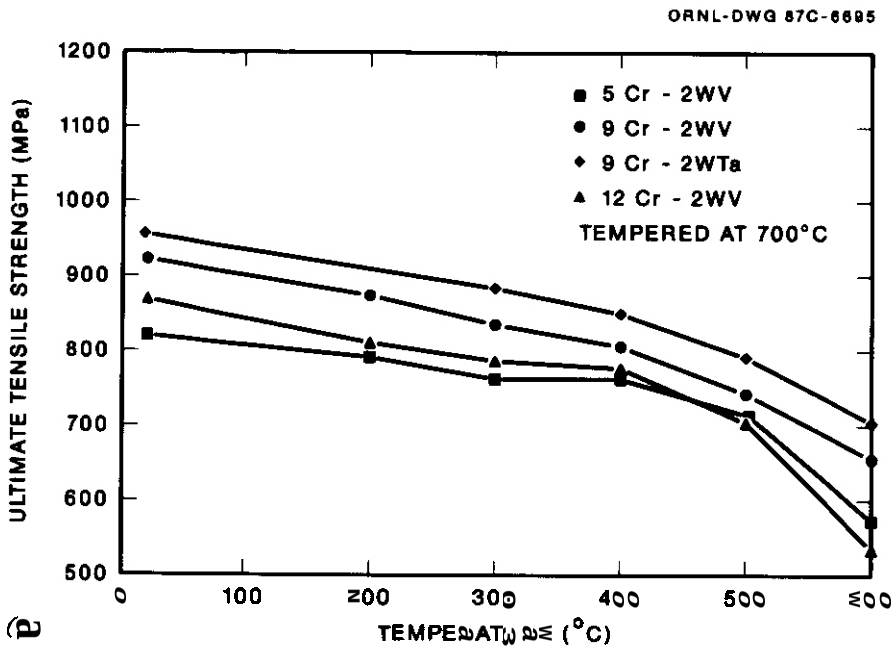


Fig. 2. Tensile properties as a function of temperature for the low-chromium steels tempered at 750°C: *(a)* 0.2% yield stress, *(b)* ultimate tensile strength, and *(c)* uniform and total elongation.





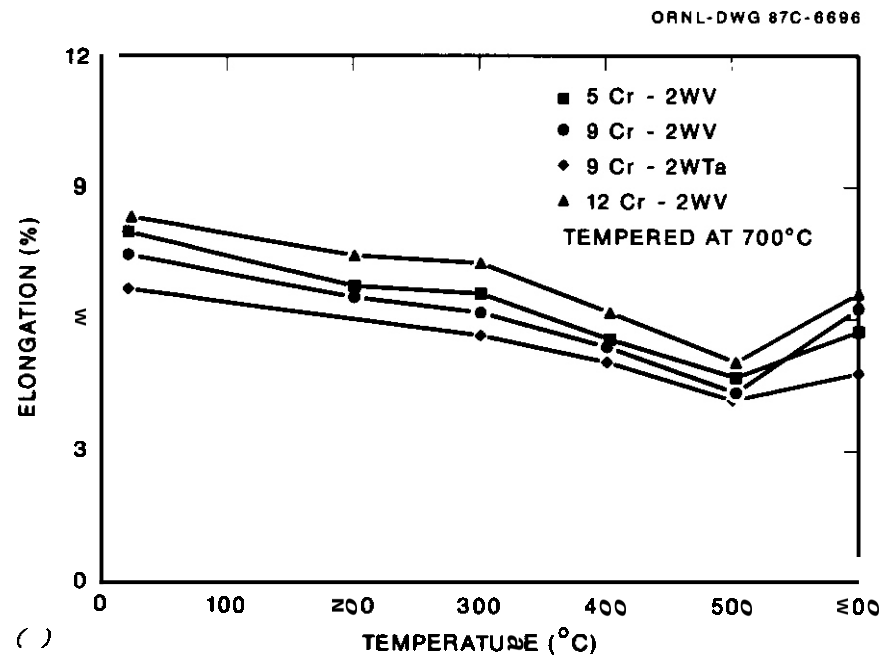
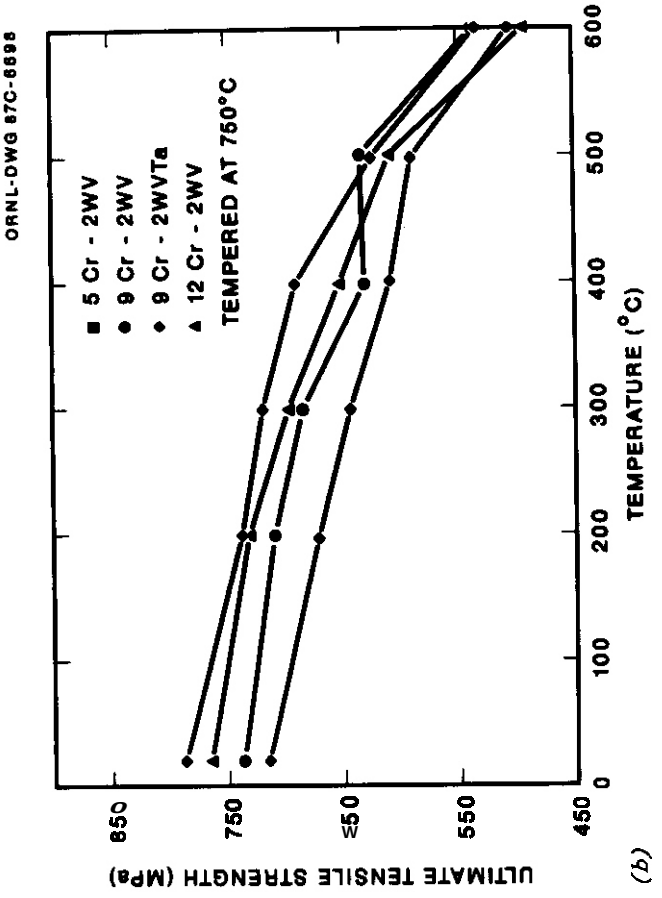
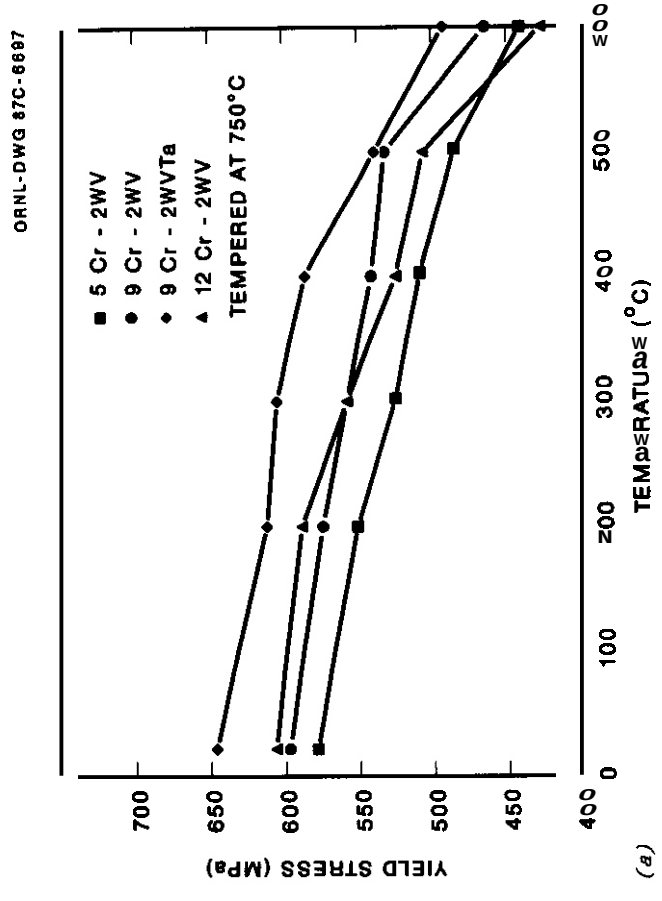


Fig. 3. Tensile properties as a function of temperature for the high-chromium steels tempered at 700°C: *(a)* 0.2% yield stress, *(b)* ultimate tensile strength, and *(c)* uniform and total elongation.





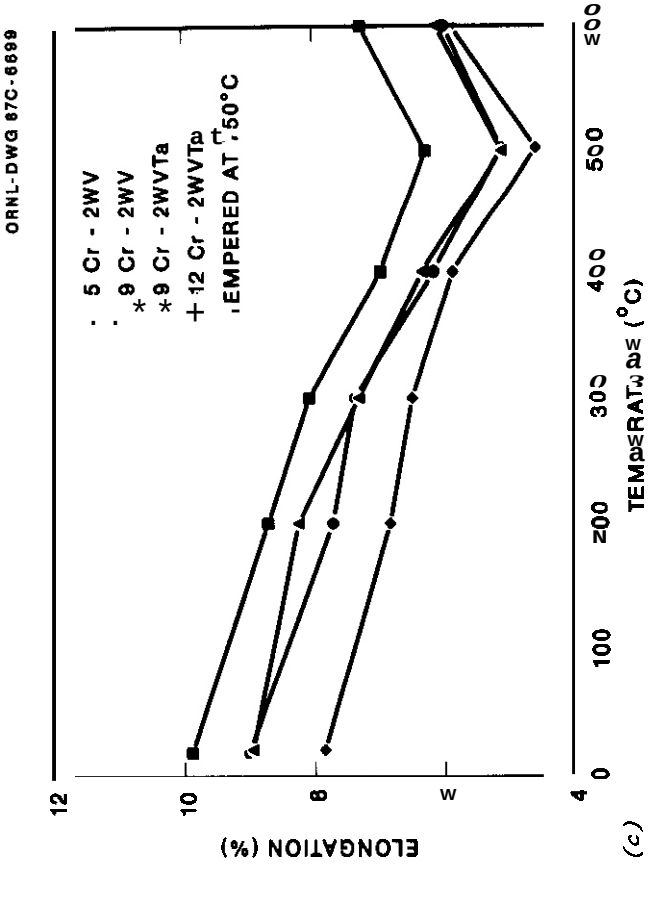


Fig. 4. Tensile properties as a function of temperature for the high-chromium steels tempered at 750°C: *(a)* 0.2% yield stress, *(b)* ultimate tensile strength, and *(c)* uniform and total elongation.

For the low-chromium steels, the general effect of tungsten and vanadium can be established (Figs. 1 and 2). After tempering at 700°C, the effect of vanadium on the 0.2% yield stress (YS) and ultimate tensile strength (UTS) is quite evident [(Figs. 1(a) and 1(b)]. The 2 1/4 CrV steel is stronger than the 2 1/4Cr-2W steel at all but the highest test temperature (600°C). The effect of tungsten is also evident for these test conditions: The 2 1/4 Cr-2WV steel is substantially stronger than the 2 1/4 Cr-1WV steel. A similar relationship applies to these steels after tempering at 750°C [Figs. 2(a) and 2(b)], although the difference in strengths of the 2 1/4 CrV, 2 1/4 Cr-2W, and 2 1/4 Cr-1WV steels is much smaller. The 2 1/4 Cr-2WV steel still remains substantially stronger than the other steels.

The total elongation results [Figs. 1(c) and 2(c)] demonstrate a favorable effect of tungsten on ductility. The 2 1/4 Cr-2W steel, which is often the weakest, has the highest elongation. However, the 2 1/4 Cr-2WV steel, which is always the strongest, has a total elongation that is as great or greater than the values for the weaker 2 1/4 CrV and 2 1/4 Cr-1WV steels. The strength behavior of the high-chromium (5-12% Cr) steels demonstrated a superiority for the 9-Cr steels [Figs. 3(a), 3(b), 4(a) and 4(b)]. The small tantalum addition to the 9 Cr-2WV steel gave the 9Cr-2WVTa steel the best YS and UTS behavior; the only exception to this was for the steel tempered at 750°C, where the UTS of the 9Cr-2WV steel was similar to the 9 Cr-2WVTa steel for the 500 and 600°C tests. From the tempering behavior observations," the 5Cr-2WV steel would have been expected to be one of the strongest. It turned out to be the weakest steel for most conditions (Figs. 3 and 4). Based on the tempering curves and the large amount of delta-ferrite in the microstructure of the 12Cr-2WV steel,[4] it was expected to be one of the weakest steels. This turned out to be the case for the steel when tempered at 700°C. It had somewhat better relative strength when tempered at 750°C, although the strength deteriorated substantially for the highest test temperature [Figs. 3(b) and 4(b)], where it again became the weakest steel. The ductilities of these steels reflect the strength behavior, with the strongest material having the lowest total elongation [Figs. 3(c) and 4(c)].

To compare the behavior of the strongest steels, Figs. 5 and 6 show the properties of the 2 1/4 Cr-2WV, 9Cr-2WV, and 9Cr-2WVTa steels after being tempered at 700 and 750°C, respectively. Under most test conditions, the 2 1/4 Cr-2WV steel not only has the best strength properties, but also the best ductility. The only exception in strength was the UTS behavior after the 750°C tempering treatment. In this case, the 9 Cr-2WVTa steel was strongest up to a 400°C test temperature, after which the 2 1/4 Cr-2WV was again strongest. The only instance where the ductility of the 2 1/4 Cr-2WV steel was not the greatest was for the steel tempered at 700°C and tested at 600°C. Here the total elongation of the 9Cr-2WV steel was slightly larger.

The tensile properties of the 2 1/4% Cr, CAVV steels tempered at 700°C were compared with 2 1/4 Cr-1Mo steel normalized by austenitizing 0.5 h at 900°C, cooling in flowing helium, and then tempering 1 h at 700°C (Fig. 7). The YS [Fig. 7(a)] and total elongation [Fig. 7(c)] of the 2 1/4 Cr-1Mo steel is similar to that of the 2 1/4 Cr-2W steel, after which the latter steel was patterned. The UTS of the 2 1/4 Cr-1 Mo is somewhat greater than that for the 2 1/4 Cr-2W steel. In all cases, the strength of the 2 1/4Cr-2WV steel is substantially better than the 2 1/4 Cr-1Mo steel.

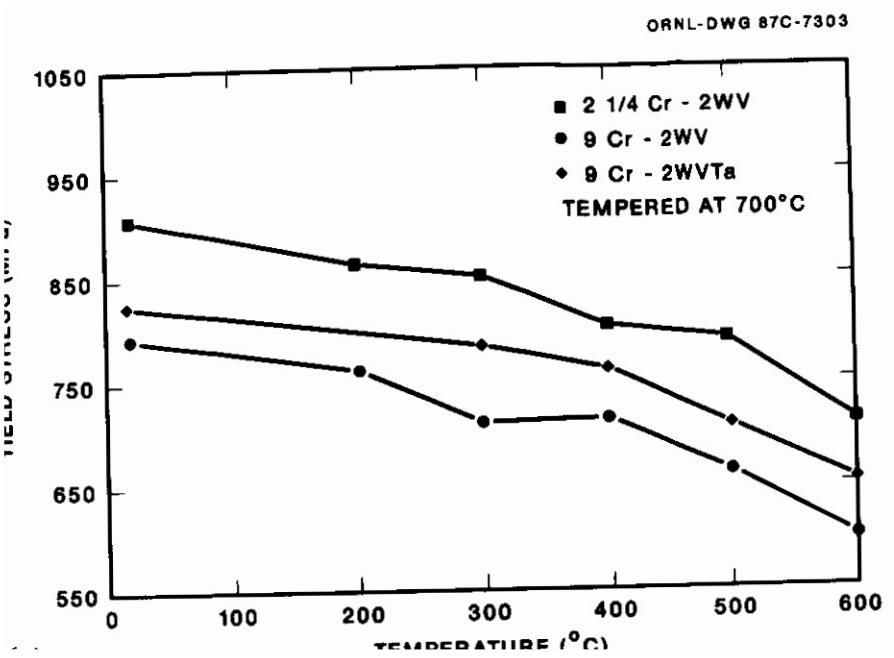
A comparison of the properties of the two strongest heats of FIRD steels with the 9 Cr-2MoVNb and 12 Cr-1MoVW steels that are presently being investigated in the fusion-reactor materials program is shown in Fig. 8. The comparison shows that the reduced-activation Cr-W steels compare favorably with 9 Cr-1MoVNb and 12Cr-1MoVW steels. Although the room-temperature YS and UTS values for the Cr-Mo steels are slightly greater than those for the Cr-W steels, at the elevated temperatures, the strengths of the 2 1/4 Cr-2WV and the 9Cr-2WVTa steels have comparable strengths with the Cr-Mo steels.

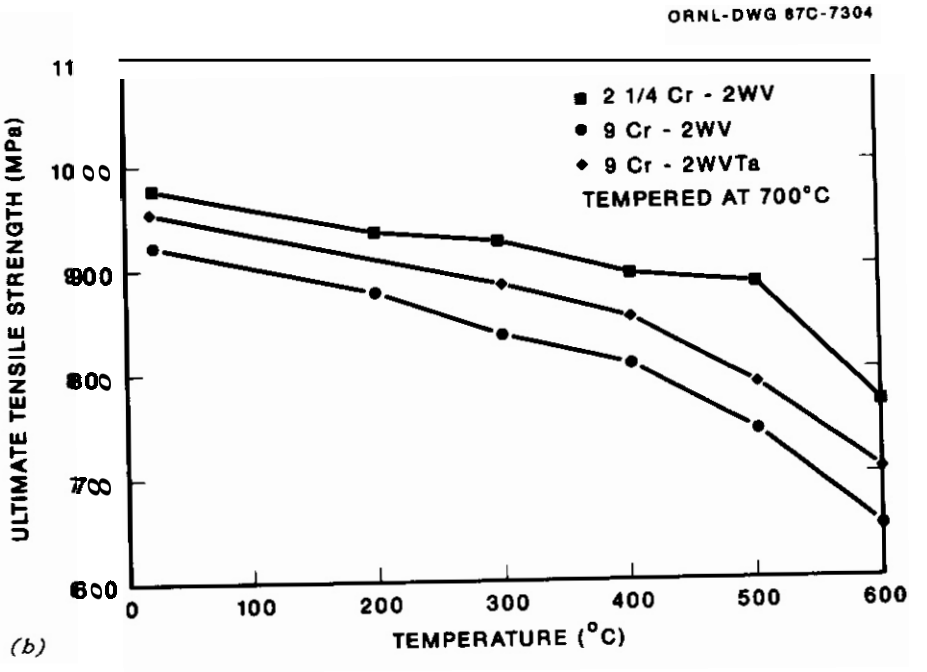
In general, the ductility behavior as measured by total elongation of the Cr-W steels exceeded that of the two Cr-Mo steels [Fig. 8(c)]. The 9Cr-1MoVNb steel had the lowest total elongation at all test temperatures. The 12Cr-1MoVW steel had the highest total elongation, after which it decreased to values as low or lower than for most of the Cr-W steels. The 2 1/4 Cr-2WV steel had the highest total elongation at all temperatures but room temperature.

Discussion

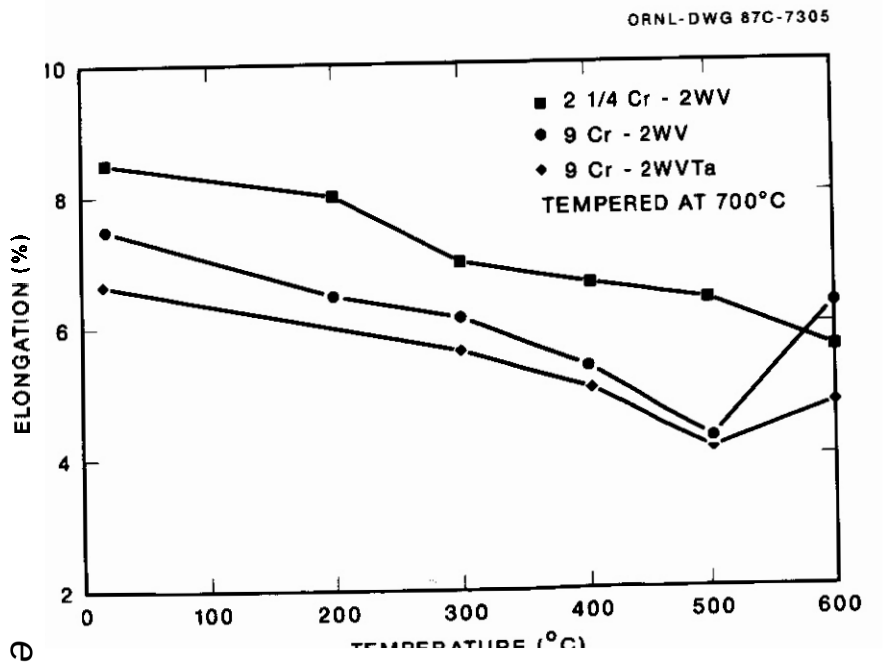
The results of the tests to determine the effect of the tungsten and vanadium content in the 2 1/4-Cr steels demonstrated the effect of these elements. The steel with 0.25% V and no tungsten had strength properties similar to the steel with 2% W and no vanadium. The steel with 2% W had excellent ductility. With the combination of tungsten and vanadium, an additive effect occurred to produce a steel with excellent strength and ductility.

When the tensile data for the steels with 2 1/4, 5, and 9% Cr containing 0.25% V and 2% W are compared, there appears to be an effect of chromium on the strength: The strength apparently goes through a minimum between 2 1/4% Cr and 9% Cr; the 5Cr-2WV steel is considerably weaker than either the 2 1/4Cr-2WV and the 9Cr-2WV steels. Except for the YS of the steels tempered at 700°C, the strength of the 5Cr-2WV is less than that for 12Cr-2WV, which contained 26% delta ferrite. A large delta-ferrite content is expected to result in lower strength. The results of the tensile studies on the high-chromium steels (Figs. 3 and 4) demonstrated the effect of the addition of the tantalum to the 9Cr-2WV steel. It appears that tantalum, like niobium in the 9Cr-1MoVNb steel, can be used to improve the strength of these steels.



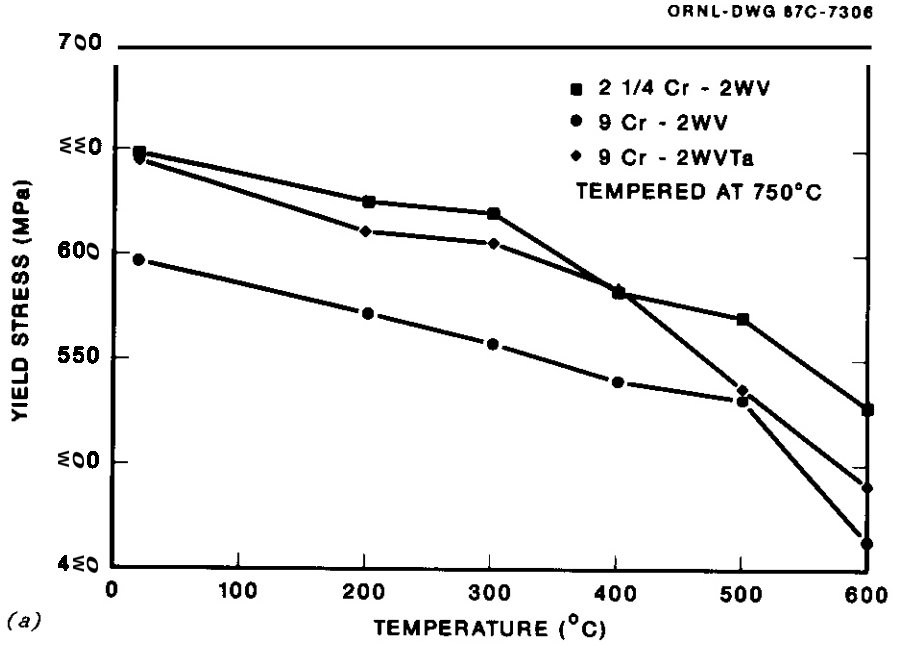


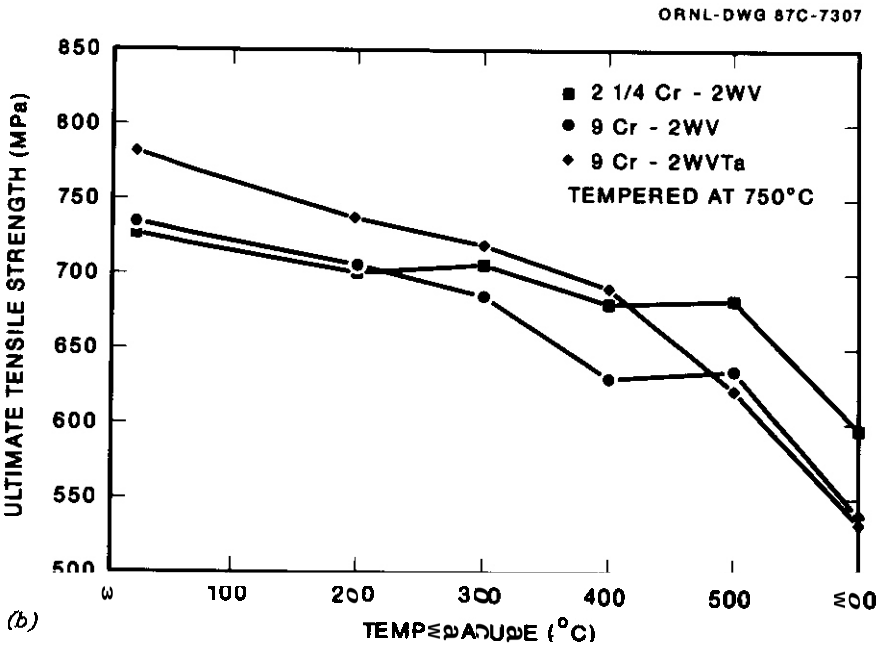
(b)



(c)

Fig. 5. Tensile properties as a function of temperature for the 2 1/4 Cr-2WV, 9Cr-2WV, and 9Cr-2WVTa steels tempered at 700°C: *(a)* 0.2% yield stress, *(b)* ultimate tensile strength, and *(c)* uniform and total elongation.





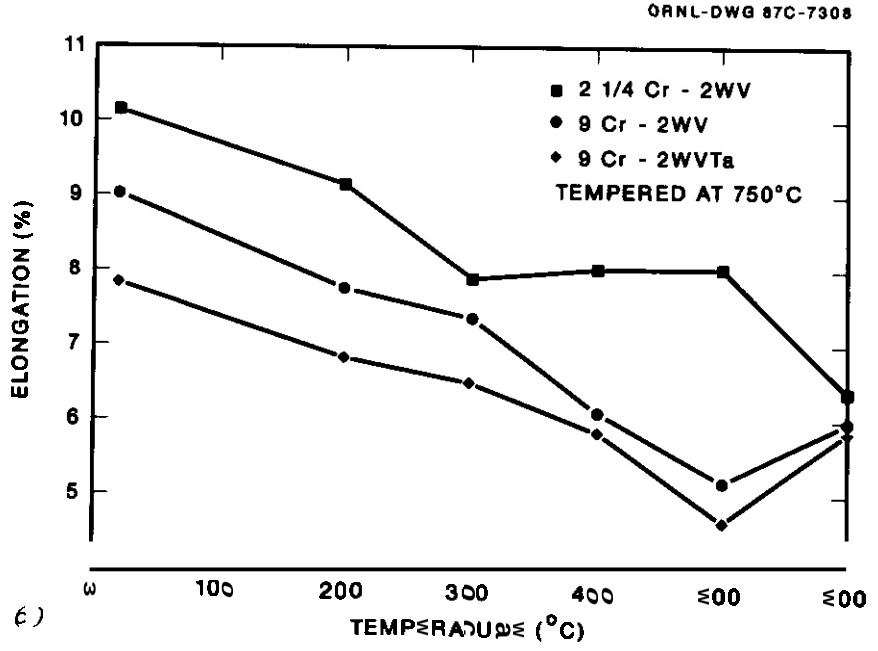


Fig. 6. Tensile properties as a function of temperature for the 2 1/4 Cr-2WV, 9 Cr2WV, and 9Cr-2WVTa steels tempered at 750°C: *(a)* 0.2% yield stress, *(b)* ultimate tensile strength, and *(c)* uniform and total elongation.

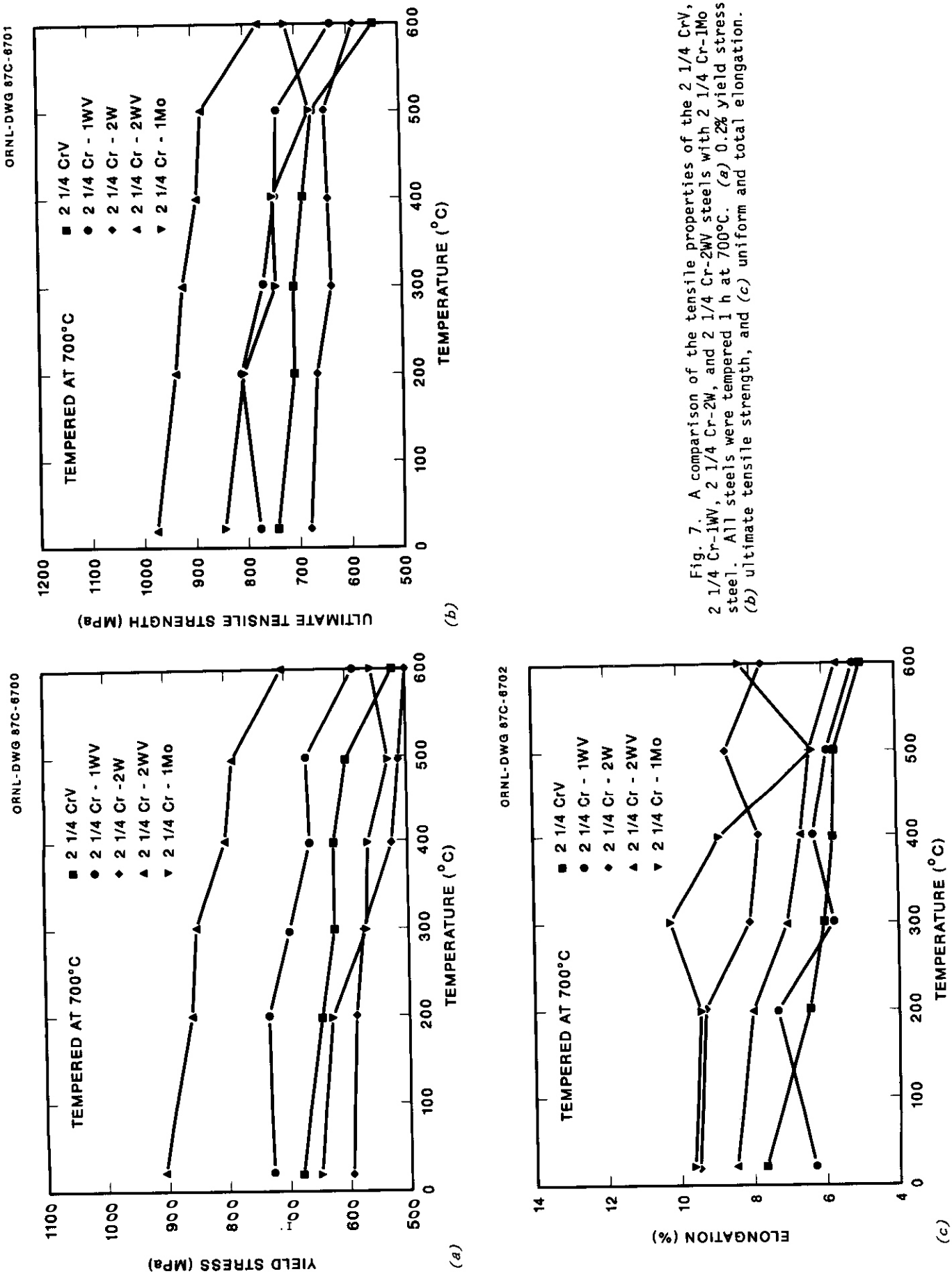
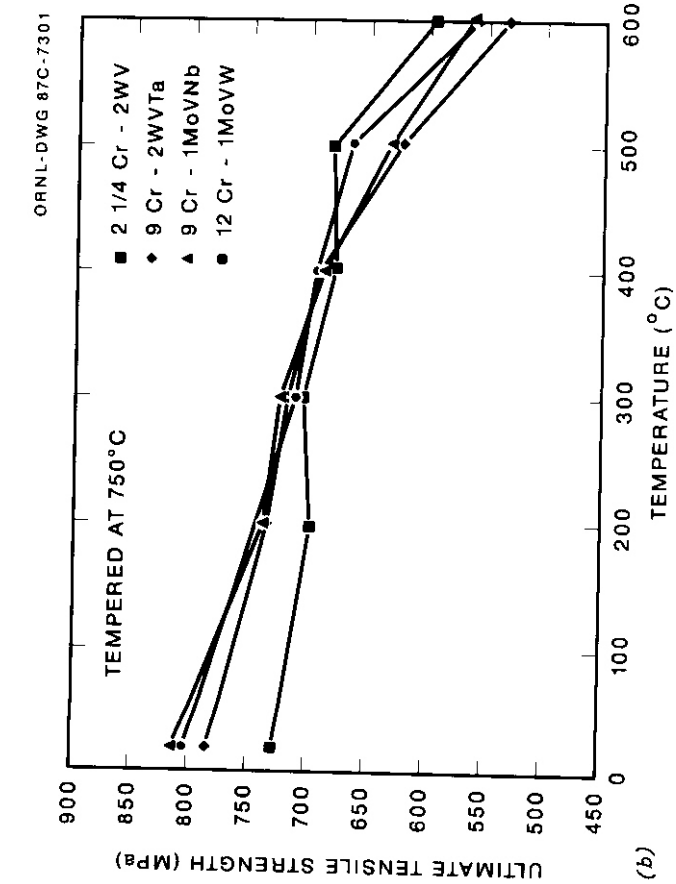
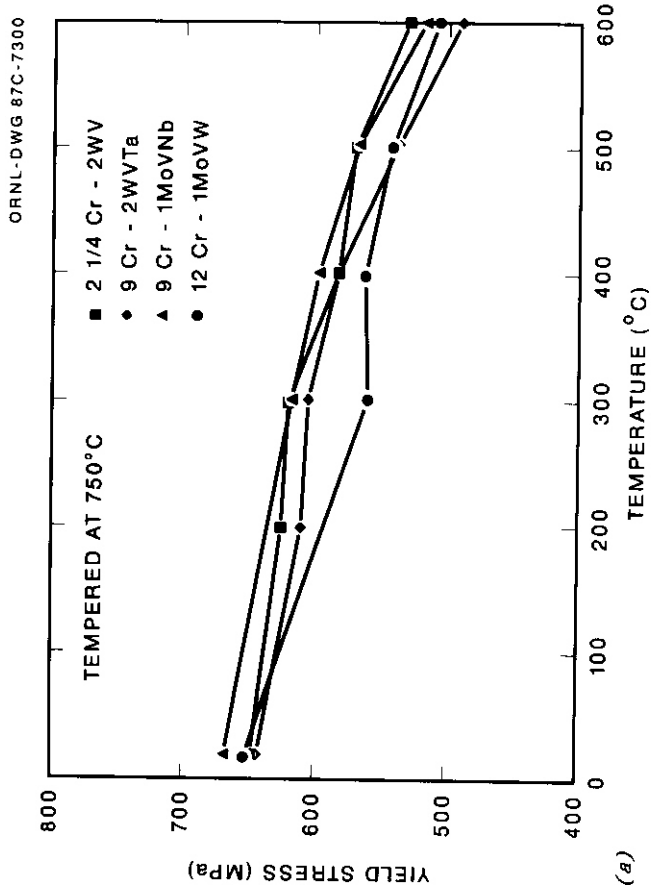


Fig. 7. A comparison of the tensile properties of the 2 1/4 CrV, 2 1/4 Cr-1WV, 2 1/4 Cr-2W, and 2 1/4 Cr-2WV steels with 2 1/4 Cr-1Mo steel. All steels were tempered 1 h at 700°C. *(a)* 0.2% yield stress, *(b)* ultimate tensile strength, and *(c)* uniform and total elongation.





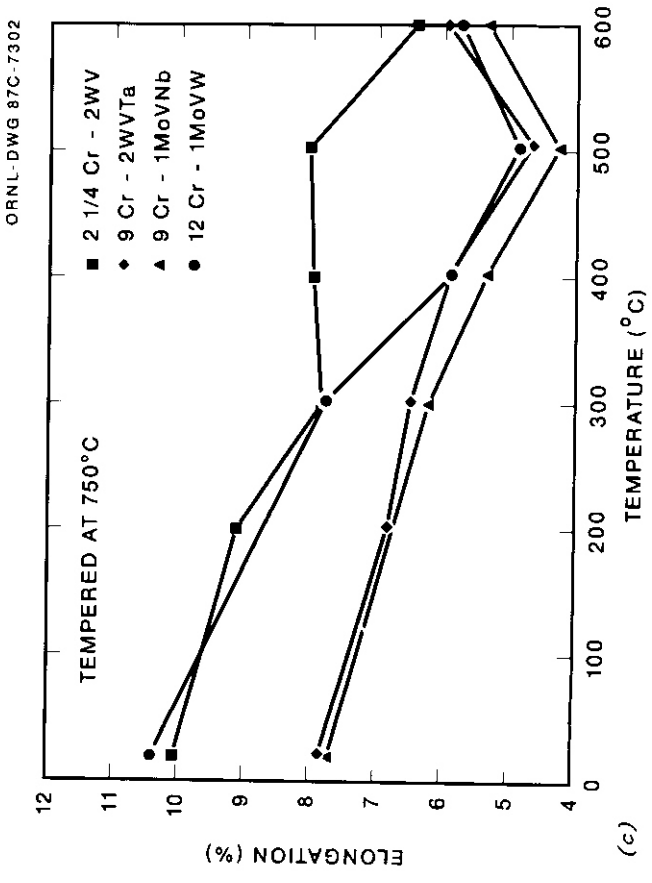


Fig. 8. A comparison of the tensile properties of the 2 1/4 Cr-2WV, and 9Cr-2WVTa steels -- the strongest Cr-W steels -- with the properties for the 9Cr-1MoVNb and 12Cr-1MoVW steels. All steels were tempered at 750°C. *(a)* 0.2% yield stress, *(b)* ultimate tensile strength, and *(c)* uniform and total elongation.

The observation that the 2 1/4 Cr-2WV steel generally has the highest strength of the eight steels investigated is not unexpected, if we accept the assumption that 2% W will play the same role as 1% Mo in the Cr-Mo steels. It is known that the only effect of chromium above 2 1/4% is to increase the hardenability and corrosion resistance; a minimum in strength near 5% Cr has also been observed for Cr-Mo steels with chromium compositions between 2 1/4 and 9%.[5] This assumes that appropriate microstructures are compared (i.e. bainite in the 2 1/4-Cr is compared to martensite in the high-chromium steel; such results would not be expected if the 2 1/4-Cr steel contained large amounts of ferrite).

The strength properties of 9Cr-1MoVNb and 12Cr-1MoVW steels have often been compared to the strength of 2 1/4 Cr-1Mo steel and found to be superior.[6] Such a comparison ignores the role of the strong carbide-forming elements vanadium and niobium and their effect on strength. It was previously pointed out that the addition of a strong carbide former to 2 1/4 Cr-1Mo should result in comparable properties, regardless of the chromium composition.[7] The present results appear to confirm this. The use of a lower-chromium ferritic steel for first walls of future fusion reactors would have some advantages.[7]

The objective for the alloy-development program for the FIRD steels was reduced-activation steels that have properties comparable to the Cr-Mo steels presently in the fusion-reactor program; the FIRD steels were patterned after these Cr-Mo steels.[1] For the 2 1/4-Cr steels, this requires that the 2 1/4Cr-2W steel have properties comparable to the analogous 2 1/4 Cr-1Mo. This was the case (Fig. 7) and appears to indicate that the replacement of molybdenum by tungsten can result in steels with comparable tensile properties. The addition of the vanadium then gives steels with improved properties over those without vanadium.

For the 2 1/4-Cr steels, the alloy-development objective would be met if the 2 1/4Cr-2W steel has properties comparable to the analogous 2 1/4 Cr-1Mo steel. According to the comparison given in Fig. 7, this was the case. Likewise, the 9Cr-2WVTa steel has tensile properties comparable to those for 9Cr-1MoVNb, after which it was patterned (Fig. 8). The strength properties of the 12Cr-2WV steel are not equivalent to those of the 12Cr-1MoVW steel, but this is because of the large amount of delta ferrite in the microstructure of the latter steel. Of course, when tempered at 700°C, the tensile properties of the 2 1/4 Cr-2WV steel surpass those for all three of the Cr-Mo steels presently in the fusion reactor materials program.

CONCLUSIONS

The results of tensile tests on eight experimental heats of Cr-W steel with chromium composition varying between 2 1/4 and 12% indicate that these steels can have properties similar to the Cr-Mo steels (2 1/4 Cr-1Mo, 9Cr-1MoVNb, and 12Cr-1MoVW) presently being considered for fusion-reactor applications. The 2 1/4 Cr-2W and 9Cr-2WVTa steels had properties comparable to those of the analogous 2 1/4 Cr-1Mo and 9Cr-1MoVNb steels, respectively. Because the 12Cr-2WV steel contained about 25% delta-ferrite, the strength of this steel was less than that of the 12Cr-1MoVW steel. The 2 1/4 Cr-2WV and 9Cr-2WVTa steels had the best properties of the steels studied, with those for the 2 1/4 Cr-2WV being slightly better for the test conditions used.

REFERENCES

1. R. L. Klueh and E. E. Bloom, "The Development of Ferritic Steels for Fast Induced-Radioactivity Decay for Fusion Reactor Applications," Nucl. Eng. Design/Fusion 2, 383-389 (1985).

2. R. L. Klueh, "The Development of Ferritic Steels for Fast Induced-Radioactivity Decay," pp. 117-123 in ADIP Semiannu. Prog. Rep., Sept. 30, 1985, DOE/ER-0045/15, U.S. DOE, Office of Fusion Energy.

3. R. L. Klueh, "The Development of Ferritic Steels for Fast Induced-Radioactivity Decay," pp. 109-113 in ADIP Semiannu. Prog. Rep., Mar. 31, 1986, DOE/ER-0045/16, U.S. DOE, Office of Fusion Energy.

4. R. L. Klueh and J. M. Vitek, "The Development of Ferritic Steels for Fast Induced-Radioactivity Decay," pp. 141-145 in ADIP Semiannu. Prog. Rep., Sept. 30, 1984 DOE/ER-0045/13, U.S. DOE, Office of Fusion Energy.

5. Babcock and Wilcox Company, Intermediate Croloy Steels, Babcock and Wilcox Company, Tubular Products Division, Beaver Falls, Pennsylvania, 1971.

6. M. K. Booker, V. K. Sikka, and B.L.P. Booker, "Comparison of Mechanical Strength Properties of Several High-Chromium Ferritic Steels," In: Ferritic Steels for High-Temperature Applications, American Society for Metals, Metals Park, Ohio, 1983.

7. R. L. Klueh, "Chromium-Molybdenum Steels for Fusion Reactor First Walls --a Review," Nucl. Eng. Design/Fusion 72, 329-344 (1982).

POSTIRRAOIATION TENSILE BEHAVIOR OF NICKEL-DOPED FERRITIC STEELS — R. L. Klueh (Oak Ridge National Laboratory)

OBJECTIVE

The goal of this study is to evaluate the properties of irradiated ferritic steels. Irradiation in the High Flux Isotope Reactor (HFIR) is used to produce both displacement damage and transmutation helium at levels relevant to fusion reactor service.

SUMMARY

Tensile specimens of normalized-and-tempered 9Cr-1MoVNb, 9Cr-1MoVNb-2Ni, 12Cr-1MoVW, 12Cr-1MoVW-1Ni, and 12Cr-1MoVW-2Ni steels were irradiated in the HFIR at 300, 400, and 500°C to displacement-damage levels of up to ~11 dpa. The nickel was added to the ferritic steels to produce helium during irradiation in this mixed-spectrum reactor. Up to 103 appm He was produced in the steels with 2% Ni. Irradiation at 300 and 400°C caused an increase in strength of all the steels relative to the strength in both the normalized-and-tempered condition and after aging the normalized-and-tempered steel for a time period similar to that in the reactor. The strength increases were accompanied by a loss of ductility. At 500°C, there was little change in the strength properties of the steels. The results at 300 and 400°C indicate an effect of helium on the strength increases; no helium effect was apparent for the specimens irradiated at 500°C.

PROGRESS AND STATUS

Introduction

For alloys that contain nickel, it is possible to simulate simultaneous helium and displacement-damage effects in mixed-spectrum fission reactors. In such reactors, the fast neutrons produce displacement damage. while helium is produced by a two-step reaction of ^{58}Ni with thermal neutrons. This technique has been widely used to study helium effects in austenitic stainless steels, which contain high-nickel concentrations. Because the 9Cr-1MoVNb and 12Cr-1MoVW steels being considered for fusion applications normally contain less than 0.5% Ni, irradiation in a mixed-spectrum reactor results in much less helium than would be formed in a fusion reactor. However, if the nickel content is raised to 2%, these steels can be irradiated in the HFIR to produce approximately the same ratio of helium to displacement damage that would be attained for the original, unmodified alloys in a tokamak-type fusion reactor first wall.

Irradiation-damage studies are in progress to investigate the effect of transmutation helium and displacement damage of 9Cr-1MoVNb and 12Cr-1MoVW steels by raising the nickel content up to 2% and irradiating in HFIR. We previously reported on the tensile properties of the nickel-doped steels after low-temperature irradiation in HFIR.[1] The tensile properties of the steels have been reported following irradiation in EBR-II at elevated temperatures (390, 450, 500, and 550°C), where no substantial helium generation occurred.[2,3] In this report we will discuss the tensile properties of these steels after irradiation in HFIR to ~10 dpa at 300, 400, and 500°C.

Experimental procedure

Electroslag remelted heats of 9Cr-1MoVNb (0.1% Ni) and 12Cr-1MoVW (0.5% Ni) ferritic steels were prepared by Combustion Engineering, Inc., Chattanooga, Tennessee. These compositions were also prepared with 1 and 2% Ni, designated 9Cr-1MoVNb-2Ni, 12Cr-1MoVW-1Ni, and 12Cr-1MoVW-2Ni. Chemical compositions of the alloys are given in Table 1.

Cylindrical tensile specimens were machined from 6.35-mm-diam rods. The rods were normalized-and-tempered prior to machining the specimens. The normalizing treatment for the 9-Cr steels was 0.5 h at 1040°C and for the 12-Cr steels 0.5 h at 1050°C, after which they were cooled in flowing helium. The 9Cr-1MoVNb was tempered 1 h at 760°C; the 12Cr-1MoVW and 12Cr-1MoVW-1Ni steels were tempered 2.5 h at 780°C. The 9Cr-1MoVNb-2Ni and 12Cr-1MoVW-2Ni steels were tempered 5 h at 700°C. Tempered martensite microstructures were obtained by these heat treatments. Details on heat treatment and microstructure have been published.[1,2]

The tensile specimens, which had a reduced section of 2-mm diam by 18.3-mm long, were irradiated in three irradiation experiments: HFIR-CTR-39, -40, and -41. For each experiment. eleven specimens were arranged along the capsule axis with each specimen surrounded by an aluminum holder. Each holder was sized to maintain a gas gap around the specimen gage section. The specified temperature was achieved by adjusting the thickness of the helium-filled gap between the specimen and holder in order to provide resistance to the

Table 1. Composition of 9Cr-1MoVNb and 12Cr-1MoVW Heats of Steel

Element	Concentration,[a] wt %					Element	Concentration,[a] wt %				
	9Cr-1MoVNb		12Cr-1MoVW				9Cr-1MoVNb		12Cr-1MoVW		
	0% Ni	2% Ni	0% Ni	1% Ni	2% Ni		0% Ni	2% Ni	0% Ni	1% Ni	2% Ni
C	0.09	0.064	0.21	0.20	0.20	Ti	0.002	0.002	0.003	0.003	0.003
Mn	0.36	0.36	0.50	0.47	0.49	co	0.013	0.015	0.017	0.015	0.021
P	0.008	0.008	0.011	0.010	0.011	cu	0.03	0.04	0.05	0.05	0.05
S	0.004	0.004	0.004	0.004	0.004	Al	0.013	0.015	0.030	0.017	0.028
Si	0.08	0.08	0.18	0.13	0.18	B	<0.001	<0.00	<0.001	<0.001	<0.001
Ni	0.11	2.17	0.43	1.14	2.27	Was	0.01	0.01	0.54	0.53	0.54
Cr	8.62	8.57	11.99	11.97	11.71		<0.001	<0.001	<0.001	0.002	<0.002
Mo	0.98	0.98	0.93	1.04	1.02	Sn	0.003	0.003	0.002	0.001	0.002
V	0.209	0.222	0.27	0.31	0.31	Zr	<0.001	<0.001	<0.001	<0.001	(0.001
Nb	0.063	0.066	0.018	0.015	0.015	N	0.050	0.053	0.020	0.016	0.017
						0	0.007	0.006	0.005	0.007	0.007

[a]Balance iron.

radial flow of heat produced in the specimen by nuclear heating. The specimen holders were contained in a 0.62-m-long aluminum tube that was surrounded by a shroud to provide a high coolant velocity. The details of the design of this holder have been published.[1]

The capsules were irradiated in a HFIR peripheral-target position with a peak thermal-neutron fluence (<0.5 eV) of ~2.5 × 10^{26} neutrons/m^2. Only the specimens at the center of the capsule were irradiated to the peak fluence. Depending on the position of the specimen relative to the center of the capsule, the displacement damage of the specimens varied from ~7.8 to 11.4 dpa. The helium concentration varied from 5 to 103 appm depending on the specimen position in the capsule and the nickel concentration. Irradiation temperatures were calculated to be approximately 300, 400, and 500°C.

Tensile tests were conducted in a vacuum chamber on a 44 kN capacity Instron universal testing machine using a nominal strain rate of 4.6 × 10^{-4}/s. Specimens were tested in three conditions. In addition to testing materials in the normalized-and-tempered condition and after irradiation, normalized-and-tempered specimens that were thermally aged for ~2500 h (the approximate time in the reactor) at 300, 400, and 500°C were also tested. Tests on the irradiated or aged specimens were at the irradiation or aging temperatures, respectively.

Results

The tensile property results for all alloys are given in Table 2. Displacement-damage levels and helium contents for each irradiated specimen are also given in this table. The data for the yield stress (YS) and ultimate tensile strength (UTS) for the 9Cr-1MoVNb and 9Cr-1MoVNb-2Ni are shown in Fig. 1; the uniform and total elongation for these steels are given in Fig. 2. Figures 3 and 4 show similar data for the 12Cr-1MoVW and 12Cr-1MoVW-2Ni. Data are shown for the steels in the normalized-and-tempered (NT) condition, after thermal aging for 2500 h (A), and after irradiation up to ~11 dpa and ~100 appm He (I). To keep the figure from being too cluttered with data, the results for the 12Cr-1MoVW-1Ni steel are not shown in Figs. 3 and 4.

In the normalized-and-tempered condition, the steels with 2% Ni were stronger than those with no nickel added (Figs. 1 and 3). Although not shown in the figures, the strength of the normalized-and-tempered 12Cr-1MoVW-1Ni steel was similar to 12Cr-1MoVW steel in this condition. The higher YS and UTS of the normalized-and-tempered steels with 2% Ni was due to the different tempering treatments used for these steels. The steels with 2% Ni were tempered at 700°C, where tempering was significantly slower than at the higher temperatures used for the standard steels and the one with 1%Ni. It was not possible to temper the 2% Ni steels at the higher temperatures because those temperatures are above the A_{c_1} temperature.[2]

Thermal aging at 300, 400, and 500°C for 2500 h had little effect on the strength or ductility of any of the normalized-and-tempered steels. The only noticeable effect was a slight decrease in YS and UTS after the 500°C aging treatment; the largest effect was for the 9Cr-1MoVNb-2Ni steel, but the overall decrease was minor.

Major changes occurred during irradiation. All of the steels showed an increase in YS and UTS when irradiated at 300 and 400°C (Figs. 1 and 3). After irradiation at 500°C, the YS and UTS of the 9Cr-1MoVNb with 0 and 2% Ni approached the properties for 9Cr-1MoVNb in the aged and normalized-and-tempered conditions. This means that the strength of the 9Cr-1MoVNb-2Ni decreased relatively more than the strength of the 9Cr-1MoVNb, and the strength of the 9Cr-1MoVNb-2Ni in the irradiated condition was significantly

Table 2. Tensile Properties of Normalized-and-Tempered, Aged and Irradiated Ferritic Steels

Alloy	Experimental Conditions[a]	Irradiation dpa	Irradiation appm	Test Temperature (°C)	Strength, MPa Yield	Strength, MPa Tensile	Elongation, % Uniform	Elongation, % Total
12Cr-1MoVW	NT			300	569	754	5.7	11.3
	NT			400	569	734	5.0	10.5
	NT			500	560	717	4.5	10.0
	A 300°C			300	590	775	6.3	12.1
	A 400°C			400	570	743	5.0	9.7
	A 500°C			500	531	683	3.6	8.6
	I 300°C	8	11	300	988	1036	2.9	7.6
	I 400°C	9.5	15	400	929	970	0.8	3.6
	I 500°C	11.4	19	500	570	625	1.1	6.0
12Cr-1MoVW-1Ni	NT			300	614	788	4.4	9.3
	NT			400	588	748	4.0	8.9
	NT			500	578	745	4.0	9.0
	A 300°C			300	641	811	4.6	9.6
	A 400°C			400	593	752	4.0	8.5
	I 300°C	8	32	300	1124	1193	2.7	5.3
	I 400°C	9.5	41	400	958	1000	0.9	3.0
12Cr-1MoVW-2Ni	NT			300	761	921	3.2	7.5
	NT			400	744	878	2.6	6.9
	NT			500	742	859	2.2	5.7
	A 300°C			300	800	952	3.3	7.4
	A 400°C			400	793	924	3.0	6.2
	A 500°C			500	703	816	2.5	6.0
	I 300°C	8	61	300	1338	1414	3.3	5.2
	I 400°C	9.6	80	400	1056	1095	0.8	3.1
	I 500°C	11.4	103	500	667	764	2.8	6.5
9Cr-1MoVNb	NT			300	587	687	3.5	9.7
	NT			400	596	681	2.8	9.0
	NT			500	569	633	2.1	7.9
	A 300°C			300	583	676	2.9	8.9
	A 400°C			400	607	695	3.0	9.2
	A 500°C			500	556	638	2.6	8.5
	I 300°C	7.9	5	300	1000	1004	0.4	5.7
	I 400°C	9.4	7	400	881	913	0.6	4.9
	I 500°C	11.2	8	500	570	629	2.6	9.0
12Cr-1MoVNb-2Ni	NT			300	751	864	2.8	8.8
	NT			400	725	826	2.4	8.1
	NT			500	710	795	1.9	7.5
	A 300°C			300	729	838	2.8	8.2
	A 400°C			400	728	800	2.8	8.0
	A 500°C			500	648	710	1.9	7.2
	I 300°C	8	58	300	1290	1325	0.6	3.3
	I 400°C	9.6	77	400	1098	1110	0.4	4.5
	I 500°C	11.3	98	500	581	642	2.7	9.0

[a]NT is a normalized-and-tempered specimen.
A is a thermally aged specimen, aged at the temperature given.
I is an irradiated specimen, irradiated at the temperature given.

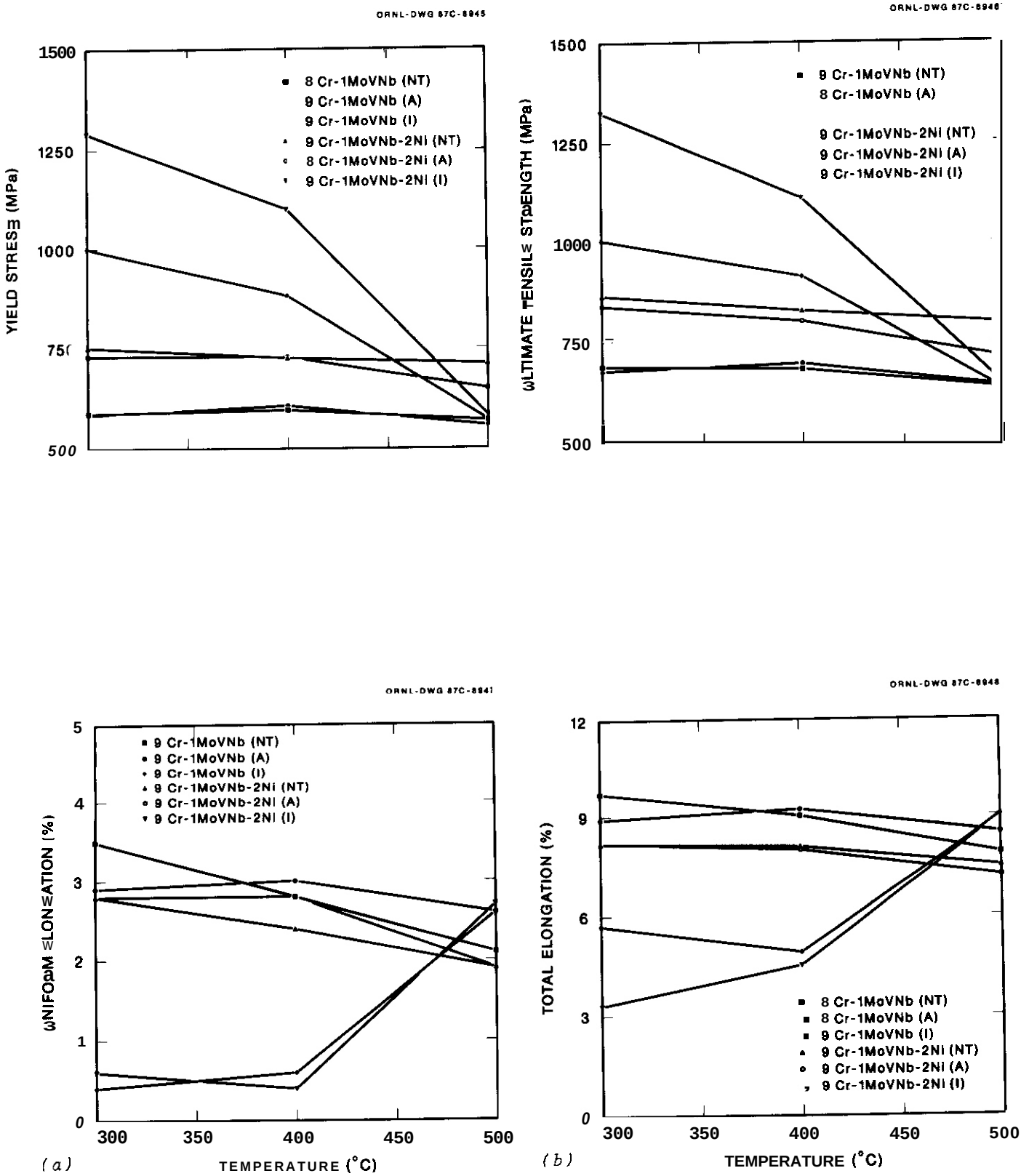


Fig. 2. Ductility properties of normalized-and-tempered (NT), thermally aged (A), and irradiated (I) 9Cr-1MoVNb and 9Cr-1MoVNb-2Ni steels; (a) uniform elongation and (b) total elongation.

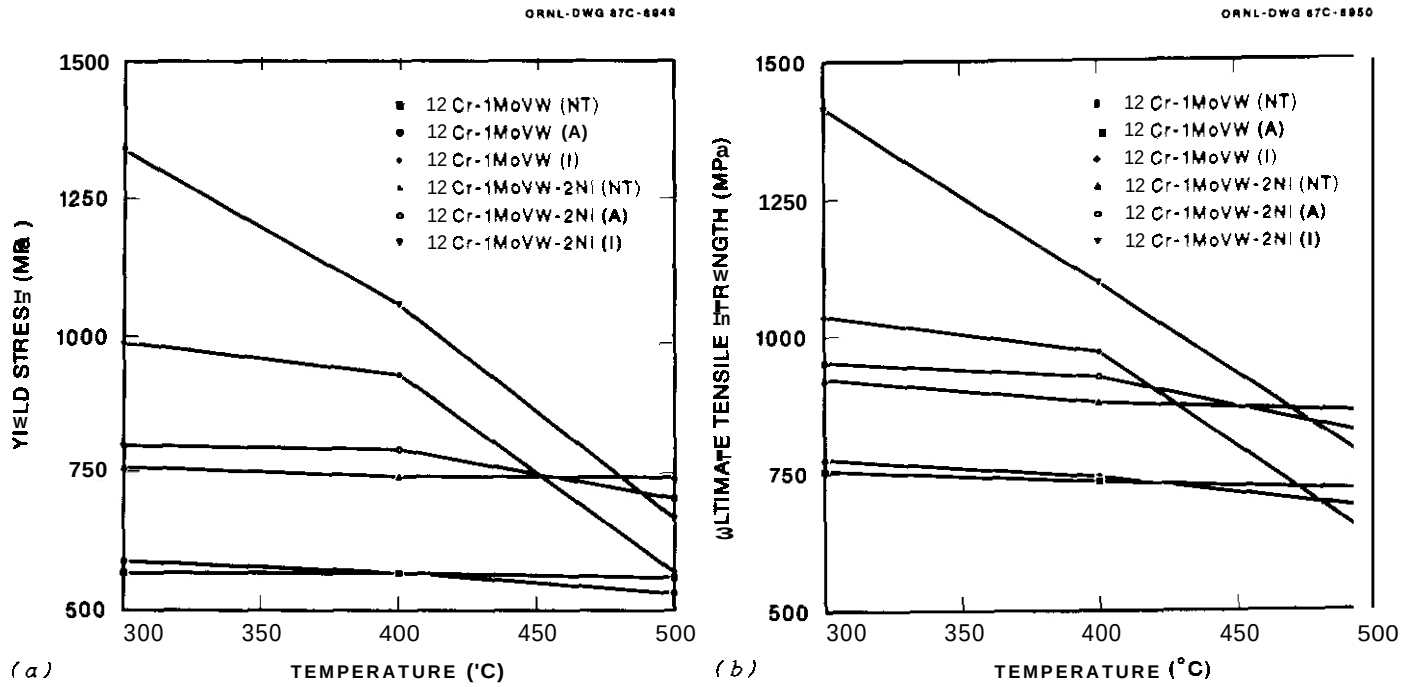


Fig. 3. Strength properties of normalized-and-tempered (NT), thermally aged (A), and irradiated (I) 12Cr-1MoVW and 12Cr-1MoVW-2Ni steels; (a) yield stress, and (b) ultimate tensile strength.

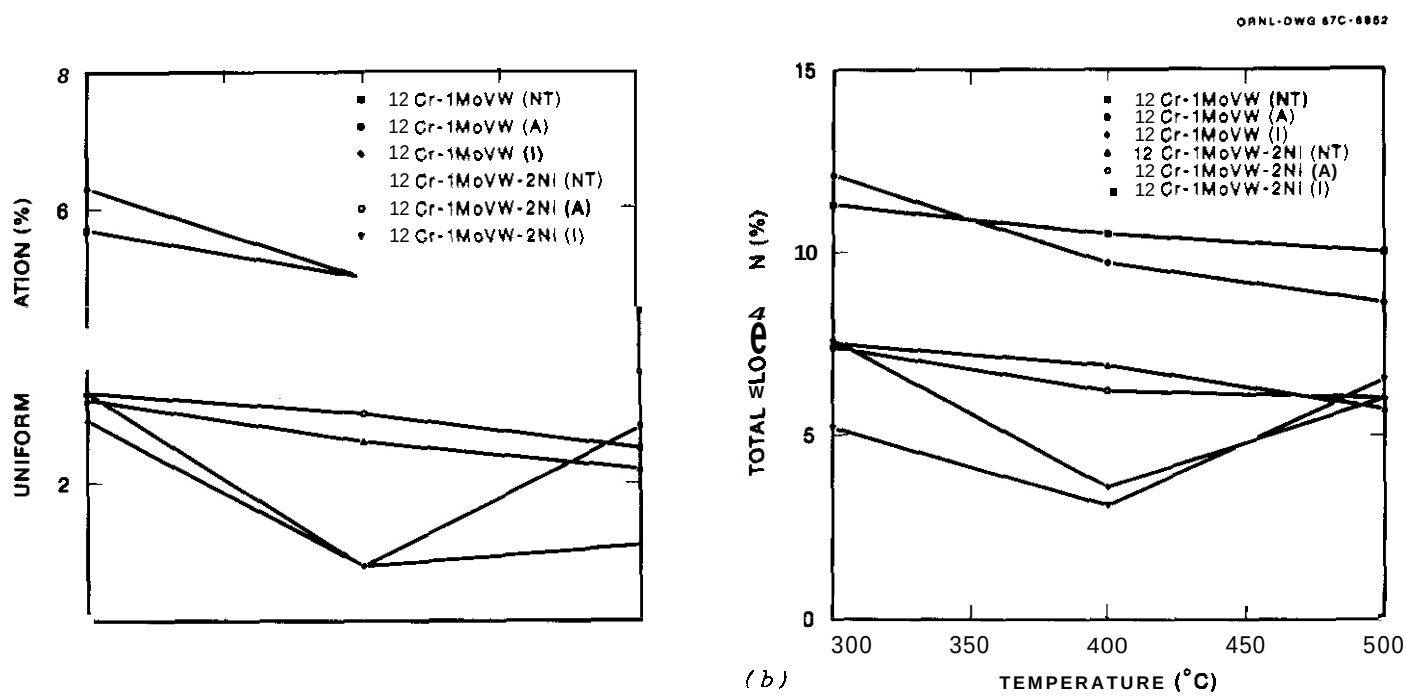


Fig. 4. Ductility properties of normalized-and-tempered (NT), thermally aged (A), and irradiated (I) 12Cr-1MoVW and 12Cr-1MoVW-2Ni steels; (a) uniform elongation and (b) total elongation.

below the normalized-and-tempered and the aged values for this steel at 500°C. The YS of the 12Cr-1MoVW and the 12Cr-1MoVW-2Ni steels after the 500°C irradiation approached the respective values for those same steels in the aged and normalized-and-tempered condition. The UTS values of these 12-Cr steels after irradiation at 500°C fell slightly below the values for the aged steels.

After irradiation at 300 and 400°C, the ductility of the 9Cr-1MoVNb and the 9Cr-1MoVNb-2Ni (Fig. 2) was slightly different from that of the 12Cr-1MoVW and the 12Cr-1MoVW-2Ni (Fig. 4). The 9Cr-1MoVNb and the 9Cr-1MoVNb-2Ni steels had quite low uniform elongations (as low as 0.4%). The uniform elongations of the 12Cr-1MoVW and the 12Cr-1MoVW-2Ni steels were close to 3%. For the total elongations of both the 9-Cr and 12-Cr steels, the steel without nickel had the largest value. The difference was quite large at 300°C, but relatively minor at 400°C. The total elongations for the two 12-Cr steels were larger for all three conditions at 300°C than at 400°C; this was also true, but to a much lesser degree, for the irradiated 9Cr-1MoVNb, but not for the irradiated 9Cr1MoVNb-2Ni, which had larger elongations at 400°C.

For the 9-Cr steels, the uniform and total elongations were higher after irradiation at 500°C than after irradiation at the two lower temperatures. This was not the case for the 12-Cr steels, where the values at 500°C were similar to the values at 300°C. The uniform elongation of the 12Cr-1MoVW and the total elongation of both the 12Cr-1MoVW and the 12Cr-1MoVW-2Ni after the 500°C irradiation approached the unirradiated values for the 12Cr-1MoVW-2Ni, which is somewhat below the values for 12Cr-1MoVW. Both the uniform and total elongation values of the two 9-Cr steels after irradiation at 500°C were somewhat above the values for unirradiated 9Cr-1MoVNb steel.

The data for the 12Cr-1MoVW-1Ni steel are not shown in Figs. 3 and 4. At 300 and 400°C, the general behavior of this steel was similar to that of the 12Cr-1MoVW and 12Cr-1MoVW-2Ni steels: The aged and the normalized-and-tempered steels had similar properties; irradiation at 300 and 400°C caused an increase in strength and a decrease in ductility. Space was unavailable in the irradiation capsule to irradiate this steel at 500°C.

Figures 5 and 6 show the change in YS and UTS, respectively, that was caused by irradiation. These changes were determined relative to the aged specimens for the respective steels. It is seen that at 300°C the relative change for both YS and UTS increases with nickel content. At 400°C. the effect of nickel is no longer obvious: the 12Cr-1MoVW-2Ni steel does not show as large an increase as the 12Cr-1MoVW and 12Cr-1MoVW-1Ni steels. The relative change of the 9Cr-1MoVNb-2Ni steel at 400°C is still greater than that for the 9Cr-1MoVNb steel. At 500°C, the relative change is quite small; negative changes occur for the steels containing 2% Ni.

Discussion

The observations on the effect of irradiation temperature on the strength of the nickel-doped and undoped steels are generally similar to previous observations on these steels.[1-3,5,6] Previous irradiations were in HFIR at 55°C and in EBR-II at 390, 450, 500, and 550°C.

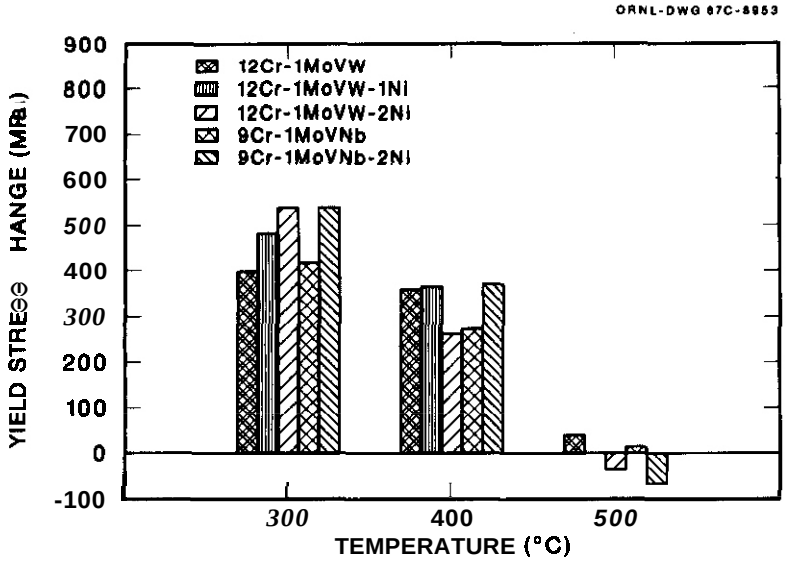


Fig. 5. Change in yield stress caused by irradiation; the change is measured relative to the thermally aged steels.

Irradiation hardening occurred for all steels irradiated to ~10 dpa at 55°C.[1,2] For the steels irradiated at elevated temperatures to ~16 dpa in EBR-II, there were some differences between the steels with 2% Ni and those with 0 and 1%Ni.[3] When irradiated at 390°C, the 9Cr-1MoVNb, 12Cr-1MoVW, and 12Cr-1MoVW-1Ni steels hardened relative to the aged steels. For the 9Cr-1MoVNb-2Ni and the 12Cr-1MoVW-2Ni steels irradiated at 390°C, there was little or no hardening (relative to thermally aged specimens). After irradiation at 450°C, the YS and UTS of the undoped steels and the one with 1%Ni were similar to those of the thermally aged (5000 h) steels. At 500 and 550°C, the strengths of these three irradiated steels were less than the aged values, indicating that there had been irradiation-enhanced softening, probably caused by the coarsening of the microstructure.[3] For the two steels with 2% Ni irradiated at 450, 500, and 550°C, there was considerable softening relative to the aged materials, and the strengths of the steels with 2% Ni approached

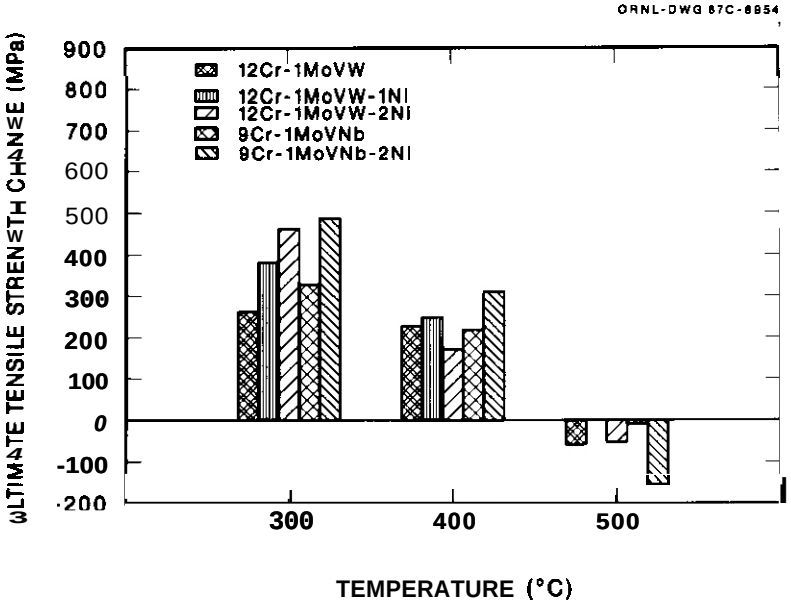


Fig. 6. Change in ultimate tensile strength of steels caused by irradiation; the change is measured relative to the thermally aged steels.

the values for those with 0 and 1% Ni. This was a considerable decrease in strength, because the 2%-Ni steels were significantly stronger than the other steels prior to irradiation.

This difference in the relative strength changes for the steels with 2% Ni and those with 0 or 1% Ni was attributed to the difference in microstructure caused by the difference in tempering treatment.[3] The large increase in strength of the undoped steels irradiated at 390°C agreed with previous work.[5,6] Strengthening by irradiation at 390°C has been attributed to the formation of irradiation-induced dislocation loops and precipitates.[5-7] The lack of a significant strength change for the steels with 2% Ni was taken to mean that, in these steels, strengthening caused by the formation of an irradiation-induced dislocation structure is offset by an irradiation-aided tempering that advances the process started at 700°C.[3]

The previous high-temperature irradiations on the nickel-doped steels were conducted in EBR-II, where very little helium was generated.[3] Although the results of the present study are in general agreement with the previous tests, there are some differences that may be caused by helium. The relative change in strength at 300°C (Figs. 5 and 6) increases with nickel -- and therefore helium -- concentration. This was true for both the 9-Cr and the 12-Cr steels. At 400°C, all of the steels showed a relative increase in strength, whereas after 15 to 16 dpa in EBR-II, the steels with 2% Ni showed little change.3 The increase in strength observed in the present tests for alloys with 0 and 1% Ni was greater than that found after irradiation in EBR-II.

To explain the observations at 300°C and the differences between the specimens irradiated at 400°C in EBR-II and those irradiated at approximately the same temperature in HFIR in the present experiments, we must examine the possible role of helium. In the present experiments, the maximum amount of helium produced -- even in the nickel-doped steels -- was close to the amounts obtained in the undoped steels irradiated in HFIR to 36 to 39 dpa.[8,9] In those experiments, only a very few, very small voids or bubbles were visible after irradiation at 300°C.[10] Even when the steel contained 2% Ni and over 400 appm He, the bubbles were extremely small at 300°C. Therefore, for the specimens irradiated at 300°C in the present study, where irradiation was to only about 10 dpa, we would not expect a significant number of voids. Essentially all the helium generated would be expected to be incorporated in extremely small bubbles or to remain in solution. Because the amount of precipitation at 300°C under the conditions of the present experiments is expected to be slight, the increase in strength after irradiation is expected to be caused primarily by the formation of dislocation loops. The observation that there is an additional increment of strength increase for the higher helium-containing alloys (higher nickel content) (Figs. 5 and 6) could be explained by hardening caused by the irradiation-produced helium -- either by small helium bubbles or helium in solution.

After irradiation in HFIR to 36 to 39 dpa at 400 and 500°C, voids were observed in both the nickel-doped and undoped steels.[8-10] Void formation was higher at 400°C. Again, because of the much lower helium concentration and displacement damage levels in the present experiment, void formation was not expected to be readily observable by transmission electron microscopy (TEM), and no TEM was conducted.

The principal cause of the increase in strength at 400°C is a combination of precipitate formation and dislocation-loop generation.[1-3] However, the increase in strength of the irradiated steels relative to the aged materials was significantly greater for the present HFIR-irradiated steels than for these same steels irradiated to 16 dpa in EBR-II.[3] This difference is shown in Table 3. The larger strength increase is most pronounced in the 2% Ni alloy, which produced the greatest amount of helium. This again could be an indication that helium in the form of fine bubbles is causing a hardening effect.

In comparing the results at 400°C from the different reactors, the difference in fluence needs to be considered. Although the higher fluence for the EBR-II irradiations could result in more irradiation-enhanced tempering for the 12Cr-1MoVW-2Ni steel, previous work gave no indication of a peak in the strengthening of the undoped steels.[11] However, there were indications that for damage levels between ~12 and 23 dpa, a saturation in strength increase occurs. A strength increase due to helium for the HFIR-irradiated steels thus seems to be an explanation for the observations at both 300 and 400°C.

Table 3. Strength Change of Irradiated Steels Relative to Thermally Aged Steels for Irradiation in HFIR and EBR-II at 400°C

	12Cr-1MoVW		12Cr-1MoVW-1Ni		12Cr-1MoVW-2Ni		9Cr-1MoVNb[a]	
	YS	UTS	YS	UTS	YS	UTS	YS	UTS
HFIR	359	227	365	248	263	171	274	218
EBR-II	249	138	215	107	38	−18	93	43

[a]No 9Cr-1MoVNb-2Ni steel was irradiated at 400°C in EBR-II.

The fact that the 12Cr-1MoVW-2Ni steel did not show a relative strength increase at 400°C as large as the other steels could again be attributed to irradiation-aided tempering,[3] which advances the process started -- but not finished -- in this steel at 700°C. That is, part of the strength increase caused by precipitation, dislocation loops, and helium is offset by the tempering. However, the 9Cr-1MoVNb-2Ni steel did not show this same behavior; in fact, it showed the highest relative strength increase (Figs. 5 and 6). No reason for this difference is immediately obvious, although the 9Cr-1MoVNb-2Ni contains niobium, and this could affect the tempering behavior of this steel.

The relative strength changes observed in the 500°C tests were negative in the EBR-II experiment on these steels,' which agrees with the observations in the present experiment. In the previous tests, the 9Cr-1MoVNb and 9Cr1MoVNb-2Ni had similar YS and UTS values after irradiation at 500°C; the same was found in the present experiment. For the 12Cr-1MoVW and the 12Cr-1MoVW-2Ni steels, the latter steel had the higher strength after irradiation in EBR-II, as was observed in the present experiment. At 500°C, therefore, there appears to be little effect of the helium on strength. This could be the result of the formation of larger, but fewer, bubbles or voids.

CONCLUSIONS

Tensile specimens of standard 9Cr-1MoVNb and 12Cr-1MoVW steels and these steels doped with up to 2% Ni were irradiated in HFIR to produce up to 11 dpa and 103 appm He at 300, 400, and 500°C. Specimens were tested at the irradiation temperature, and the results were compared with as-heat-treated (normalized-and-tempered) specimens and thermally aged specimens.

When irradiated at 300 and 400°C, all of the steels showed an increase in strength relative to the thermally aged steels; the relative increase was greater for the higher nickel-containing (helium-containing) steels, indicating that part of the strength increase may have been caused by the helium produced during irradiation. The strength increase due to helium is in addition to that due to dislocation loops generated during irradiation and any precipitate that may have formed. At 500°C, there was little or no change in strength relative to the thermally aged strength. The change in the ductility of the steels reflected the strength changes.

REFERENCES

1. R. L. Klueh and J. M. Vitek, "Effect of Low-Temperature Irradiation with (n,α) Helium Production on Tensile Properties of 12Cr-1MoVW-Type Steels," J. Nucl. Mater. 103&104, 887–892 (1981).
2. R. L. Klueh, J. M. Vitek, and M. L. Grossbeck, "Nickel-Doped Ferritic (Martensitic) Steels for Fusion Reactor Irradiation Studies: Tempering Behavior and Unirradiated and Irradiated Tensile Properties," p. 648 in Effects of Irradiation on Materials, Eleventh Conf., ASTM STP 782, H. R. Brager and J. S. Perrin, Eds. (American Society for Testing and Materials, Philadelphia, 1982).
3. R. L. Klueh, P. J. Maziasz, and J. M. Vitek, "Postirradiation Tensile Behavior of Nickel-Doped Ferritic Steels," J. Nucl. Mater. 141&143, pp. 960–65 (1986).
4. F. W. Wiffen, The Effects of CTR Irradiation on the Mechanical Properties of Structural Materials, ORNL/TM-5624 (1976).
5. R. L. Klueh and J. M. Vitek, "Elevated Temperature Tensile Properties of Irradiated 9Cr-1MoVNb Steel," J. Nucl. Mater. 132, 27 (1985).
6. R. L. Klueh and J. M. Vitek, "Tensile Behavior of 12Cr-1MoVW Steel," J. Nucl. Mater. 137, 44 (1985).
7. O. S. Gelles and L. E. Thomas, "Effects of Neutron Irradiation on Microstructure in Experimental and Commercial Ferritic Alloys," p. 559 in Ferritic Alloys for Use in Nuclear Energy Technologies, Eds., J. W. Davis and O. J. Michel (The Metallurgical Society of AIME, Warrendale, PA, 1984).
8. J. M. Vitek and R. L. Klueh, "Microstructure of HFIR-Irradiated 12Cr-1MoVW Ferritic Steel," p. 551 in Ferritic Alloys for Use in Nuclear Energy Technologies, Eds., J. W. Davis and D. J. Michel (The Metallurgical Society of AIME, Warrendale, PA, 1984).
9. J. M. Vitek and R. L. Klueh, "Microstructure of 9Cr-1MoVNb Steel Irradiated to 36 dpa at Elevated Temperatures in HFIR," J. Nucl. Mater. 122&123, 254 (1984).
10. P. J. Maziasz, R. L. Klueh and J. M. Vitek, "Helium Effects on Void Formation in 9Cr-1MoVNb and 12Cr-1MoVW Irradiated in HFIR," J. Nucl. Mater. 141&143, 929 (1986).
11. R. L. Klueh, unpublished research.

6.2 Austenitic Stainless Steels

THE DEVELOPMENT OF AUSTENITIC STAINLESS STEELS FOR FAST INDUCED-RADIOACTIVITY DECAY

R. L. Klueh and P. J. Maziasz (Oak Ridge National Laboratory)

OBJECTIVE

Induced radioactivity in the first-wall and blanket-structure materials will make these components highly radioactive after their service lifetime, leading to difficult radioactive waste-management problems. One way to minimize the disposal problem is to use structural materials in which radioactive isotopes induced by irradiation decay quickly to levels that allow simplified disposal techniques. We are assessing the feasibility of developing such austenitic stainless steels.

SUMMARY

As part of an alloy-development program for a nickel-free stainless steel, five Fe-Mn, thirteen Fe-Cr-Mn, and fifteen Fe-Cr-Mn-C alloys were examined to determine the austenite-stable region in the Fe-Cr-Mn-C system. After various heat treatments, optical and electron microscopy studies and magnetic measurements were used to assess the microstructural constituents present. The results indicate that the Schaeffler diagram, which was developed to predict the phases present in Fe-Cr-Ni-C stainless steels, cannot be directly applied to Fe-Cr-Mn-C steels. Manganese has a lower austenite-stabilizing capability against δ-ferrite formation than the Schaeffler diagram predicts by simply considering it half as effective as nickel. However, its stabilizing capability against martensite formation is higher than predicted by the diagram on the same basis. The new results can be used to empirically establish the austenite-stable composition region that should be suitable for alloying to develop a manganese-stabilized stainless Steel.

PROGRESS AND STATUS

Introduction

The various elements that make up the alloys proposed for the first wall and blanket structure of a fusion reactor undergo transmutation reactions caused by irradiation from high-energy neutrons created by the fusion reaction. After the service lifetime of the reactor, these radioactive components must be properly disposed of. The complexity of this waste disposal procedure depends on the time required for the induced radioactivity to decay to levels that are no longer hazardous to people and the environment. The more rapid the decay, the simpler is the disposal task. The common alloying elements that result in radioactive isotopes that decay over a long period of time are nickel, molybdenum, nitrogen, copper, and niobium.

An alloy-development program was proposed for fast induced-radioactivity decay (FIRD) versions of present first-wall and blanket structural candidate alloys.[1] The present standard candidate alloys include Cr-Mo ferritic steels and Cr-Ni-Mo austenitic stainless steels. For the conceptual FIRD austenitic alloys, manganese was proposed as a replacement for nickel, although it was recognized that this may prove difficult because manganese is not as strong an austenite stabilizer as nickel and because their behavior in the alloy may not otherwise be entirely equivalent. Hence, it is not possible to simply replace nickel with equal amounts of manganese. Other alloy adjustments will probably be required. It was proposed that an effort be made to first determine Fe-Cr-Mn-C compositions that produced austenite. This base could then be further modified with minor element additions to at least obtain the strength and irradiation resistance found in current candidate fusion-reactor structural materials.[1]

As a first attempt to determine alloy compositions to use as a base composition, the available phase diagrams and the Schaeffler diagram (Fig. 1) were consulted.[2] For the Schaeffler diagram, the nickel and chromium equivalents were calculated according to the following relationships:[1]

$$\text{Ni Equiv} = (\text{Ni}) + (\text{Co}) + 0.5(\text{Mn}) + 0.3(\text{Cu}) + 25(\text{N}) + 30(\text{C}) \quad ; \tag{1}$$

$$\text{Cr Equiv} = (\text{Cr}) + 2(\text{Si}) + 1.5(\text{Mo}) + 5(\text{V}) + 5.5(\text{Al}) + 1.75(\text{Nb}) + 1.5(\text{Ti}) + 0.75(\text{W}) \quad , \tag{2}$$

where the concentration of the respective elements given in parentheses is in weight percent.

As discussed in a later section, there has been considerable discussion on how to assign values to the multiplying factor for manganese for the Schaeffler diagram, and various values besides the 0.5 of Eq. (1) have been proposed.[3-5] Although the objective of the present work is the development of a nickel-free stainless steel, the initial microstructural studies gave new and direct information on the effect of manganese as an austenite stabilizer. That portion of the work is the focus of this report.

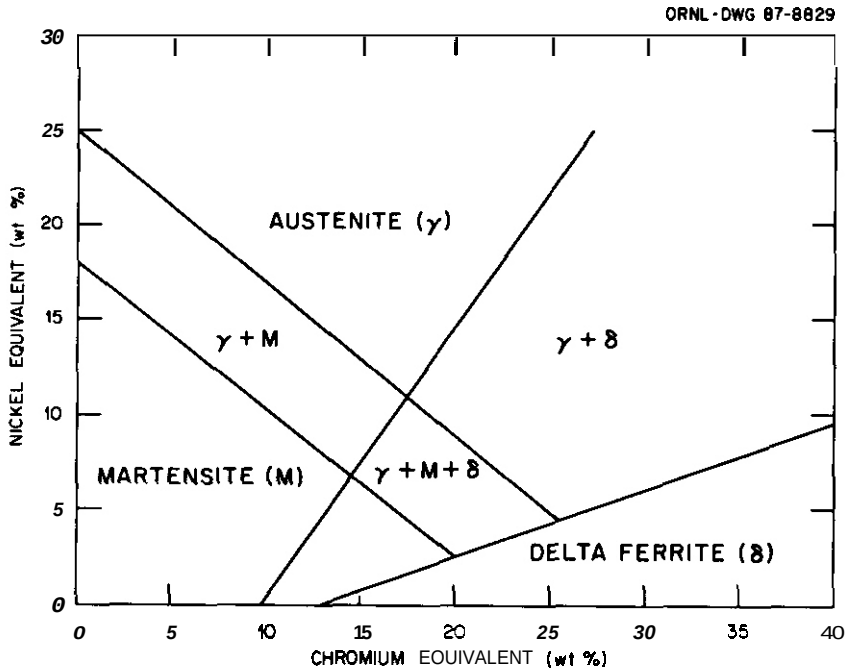


Fig. 1. The Schaeffler diagram.

Experimental procedures

Fifteen 600-g button heats of Fe-Cr-Mn-C were melted and cast (designated as PCMA-0 through PCMA-14) with the compositions given in Table 1. For the first five heats, the actual compositions obtained were often different from the nominal compositions, because manganese, and, in some cases, carbon were lost during the vacuum-arc melting process. In the later alloys, extra carbon and manganese were added to compensate for these melting losses. The nominal compositions were chosen to locate boundaries of the other phase or constituent regions as well as to find the stable austenite region of the Schaeffler diagram.

Table 1. Chemical compositions of the Fe-Mn-Cr-C steel button heats

	Chemical composition,[a] (wt %)								
Alloy	C	Mn	Si	Ni	Cr	Mo	V	cu	N
PCMA-0	0.069	13.4	0.04	0.01	15.0	0.01	0.01	0.03	0.001
-1	0.014	14.2	0.02	0.01	14.8	0.01	0.01	0.03	0.001
-2	0.056	17.1	0.04	0.01	15.2	0.01	<0.01	0.03	0.001
-3	0.089	13.9	0.02	0.01	10.0	0.01	(0.01	0.03	0.002
-4	0.093	18.9	0.02	0.01	9.9	<0.01	(0.01	0.02	0.002
-5	0.18	13.9	0.02	0.01	15.3	0.01	(0.01	0.04	0.002
-6	0.18	14.3	0.02	0.01	16.0	0.01	<0.01	0.03	0.003
-7	0.38	19.1	0.02	0.01	14.8	0.01	<0.01	0.05	0.005
-8	0.13	17.7	0.02	(0.01	20.1	0.01	(0.01	0.03	0.003
-9	0.26	17.6	0.03	0.01	20.2	0.01	(0.01	0.03	0.006
-10	0.061	19.9	0.04	0.01	10.0	0.01	0.01	0.02	0.005
-11	0.084	19.9	0.03	0.01	11.9	0.01	0.01	0.02	0.009
-12	0.18	20.0	0.02	0.01	12.0	0.01	0.01	0.02	0.008
-13	0.088	19.2	0.04	0.01	14.0	0.01	0.01	0.04	0.013
-14	0.17	19.9	0.05	0.01	15.9	0.01	0.01	0.02	0.001

[a]Balance iron.

Alloys were produced in two stages: PCMA-0 through PCMA-9 were examined before PCMA-IO through PCMA-14 were melted and processed. All of the alloys were cast into a rectangular cross section of 12.7 by 25.4 by 152 mm. The first ten alloy ingots were cold rolled to 6.4 mm in 30 to 50% increments of reduction, with homogenization treatments of 24 h at 1275°C applied after cold-rolling reduction. (Several of the steels were much more difficult to cold work than normal nickel-stabilized stainless steels because they transformed to martensite after rolling and cracked badly.) Because of the difficulties in cold rolling the first ten alloys, the last five alloys were hot rolled at 1050°C to a 6.4-mm thickness, after which they were homogenized 5 h at 1200°C.

The final step in the rolling process consisted of cold rolling from 6.4-mm plate to 0.76- and 0.25-mm sheet. The reductions from 6.4-mm were made by successively reducing the cross section 50% and then annealing for 1 h at 1150°C. The final sheet was in the 20% cold-worked condition. All of the heats except PCMA-3 were rolled to 0.76- and 0.25-mm-thick sheet; PCMA-3 cracked extensively when rolled. Difficulties with rolling were also experienced with PCMA-5.

Metallography and magnetic measurements were conducted on pieces of homogenized material, pieces of the 20% cold-worked material, and on pieces of the cold-worked material that were annealed for 1 h at 1150°C and for 8 h at 1050°C. Magnetic measurements were made with a "Ferritescope" to obtain a qualitative measure of the ferromagnetic permeability of each alloy. All specimens were examined by optical microscopy, and selected specimens were examined by transmission electron microscopy (TEM).

In addition to the button melts, we obtained small amounts of 0.25-mm-thick sheet from a series of Fe-Mn and Fe-Mn-Cr steels from the Hanford Engineering Development Laboratory (HEDL), Richland, Washington. These had been produced as small button melts with the nominal compositions given in Table 2 (ref. 6). Four of the specimens for which sufficient material was available were analyzed and found to have compositions sufficiently near the nominal Fe-Cr-Mn composition (but with some amounts of silicon and nitrogen) so that there is little difference when the nominal composition is assumed for calculating chromium and nickel equivalents. The small pieces of sheet were annealed 8 h at 1050°C before examination.

Table 2. Nominal compositions of the Fe-Mn and Fe-Cr-Mn Alloys

Fe–25Mn	Fe–5Cr–15Mn	Fe–10Cr–10Mn
Fe–30Mn	Fe–15Cr–15Mn	Fe–20Cr–20Mn
Fe–35Mn	Fe–10Cr–20Mn	Fe–20Cr–30Mn
Fe–40Mn	Fe–15Cr–20Mn	Fe–10Cr–40Mn
Fe–50Mn	Fe–5Cr–30Mn	Fe–5Cr–25Mn
	Fe–10Cr–30Mn	Fe–5Cr–35Mn
		Fe–10Cr–15Mn

Selected chemical analysis

Alloy	Chemical composition (wt %)								
	C	Mn	Si	Ni	Cr	Mo	V	cu	N
Fe–5Cr–15Mn	0.012	14.97	0.43	0.02	4.98	0.01	<0.01	0.03	0.008
Fe–10Cr–10Mn	0.013	11.28	0.19	0.01	9.75	0.01	<0.01	0.03	0.04
Fe–20Cr–30Mn	0.007	30.12	0.09	0.01	19.59	0.01	<0.01	0.03	0.00
Fe–10Cr–40Mn	0.021	39.35	0.38	0.02	9.81	0.01	<0.01	0.02	0.02

Results

The microstructures of the Fe-Cr-Mn-C alloys were examined by optical microscopy after the homogenization treatment (24 h at 1275°C) and after the solution-anneal treatments of 1 h at 1150°C and 8 h at 1050°C; selected specimens were also examined by TEM. Based on these observations, together with the chemical compositions (Tables 1 and 2), magnetic measurements (Table 3), phase diagrams, and the Schaeffler diagram, the microstructural constituents were identified (Table 4). For a complete and accurate identification of all precipitate phases, more detailed TEM study would be required on each specimen. For now, the more qualitative examinations described here will suffice for evaluations that were concerned with delineating a suitable austenitic base composition.

The magnetic measurements were used to indicate the presence of magnetic constituents (6-ferrite or a'-martensite) in the microstructure and roughly estimate their amounts. These measurements were used as an aid in identifying the constituents present. Results from the Ferritescope measurements are given in Table 3. Ferritescope measurements are routinely used to determine the amount of magnetic a-ferrite present in nonmagnetic austenitic stainless steel weld metals, where austenite and ferrite are the primary constituents.

Table 3. Ferrite number[a] of Fe-Mn-Cr-C steels

Alloy	Ferrite number[b]			
	Cold Worked	Homogenized[c]	1150°C/1h	1050°C/8 h
PCMA-0	30+	30+	30+	30+
-1	30+	30+	30+	30+
-2	30+	23.0	30+	30+
-3	30+	2.8	4.0	3.5
-4	11.0	0.2	0.2	2.0
-5	30+	1.5	5.8	3.6
-6	5.5	0.7	6.3	8.5
-7	0.5	0	0	0
-8	30+	30+	30+	30+
-9	6.0	2.4	19.0	12.0
-10	3	0	0.4	0.2
-11	5	0	0.6	0.6
-12	2	0	0.4	0.2
-13	9	7.5	16	6.2
-14	5	2	20	18

[a]Measurements made by a Ferritescope.
[b]Maximum number measured with a Ferritescope is 30.
[c]PCMA-0 through -9 were homogenized 24 h at 1275°C; PCMR-10 through -14 were homogenized at 1200°C.

Table 4. Phases and constituents[a] predicted by Schaeffler diagram and those observed

Alloy	Phases and Constituents[b,c]	
	Predicted	Observed
PCMA-0	γ + M	γ + δ + M
-1	γ + M	γ + δ + M
-2	γ + M	γ + δ + M
-3	M	γ + M
-4	γ + M	γ + M
-5	γ + M	γ + δ
-6	γ	γ + δ
-7	γ	γ
-8	γ + δ	γ + δ
-9	γ	γ + δ
-10	γ + M	γ + M
-11	γ + M	γ
-12	γ	γ
-13	γ + M	γ + δ
-14	γ	γ + δ

[a]Identified by optical and transmission electron microscopy on steels annealed 1 h at 1150°C.
[b]γ = austenite, δ = δ-ferrite, and M = martensite.
[c]Precipitate phases are not listed because these are not given on Schaeffler diagram. Precipitate phases were observed by optical microscopy in PCMA-5, -6, -8, -9, and -10.

Such measurements are used to determine a "ferrite number," which is approximately equal to the percent of δ-ferrite in the austenitic weld metal for low ferrite contents. The Ferritescope has a maximum reading of 30, so that 30+ in Table 3 indicates that the maximum reading was obtained. The ferrite numbers are used in this work to indicate the relative amount of magnetic constituent present. Better identification of the particular magnetic constituent was obtained by metallographic examination.

The observed microstructures along with those predicted by the Schaeffler diagram are given in Table 4. Figures 2 through 6 show examples of the microstructures obtained after 1 h at 1150°C for the first series of steels produced (PCMA-0 through PCMA-9). Except for the relative amount of a given phase or constituent present, the microstructures after homogenization and after 8 at 1050°C were generally similar to those observed after 1 h at 1150°C (Table 4). The delta-ferrite (δ), austenite (γ), and martensite (M) are identified as constituents (Table 4). No precipitate phases are identified in Table 4 beyond stating that precipitates were observed, meaning that they were obvious by optical microscopy and distinguishable from γ, δ, or M. Possible precipitates could include carbides or Laves, sigma, and chi phases.

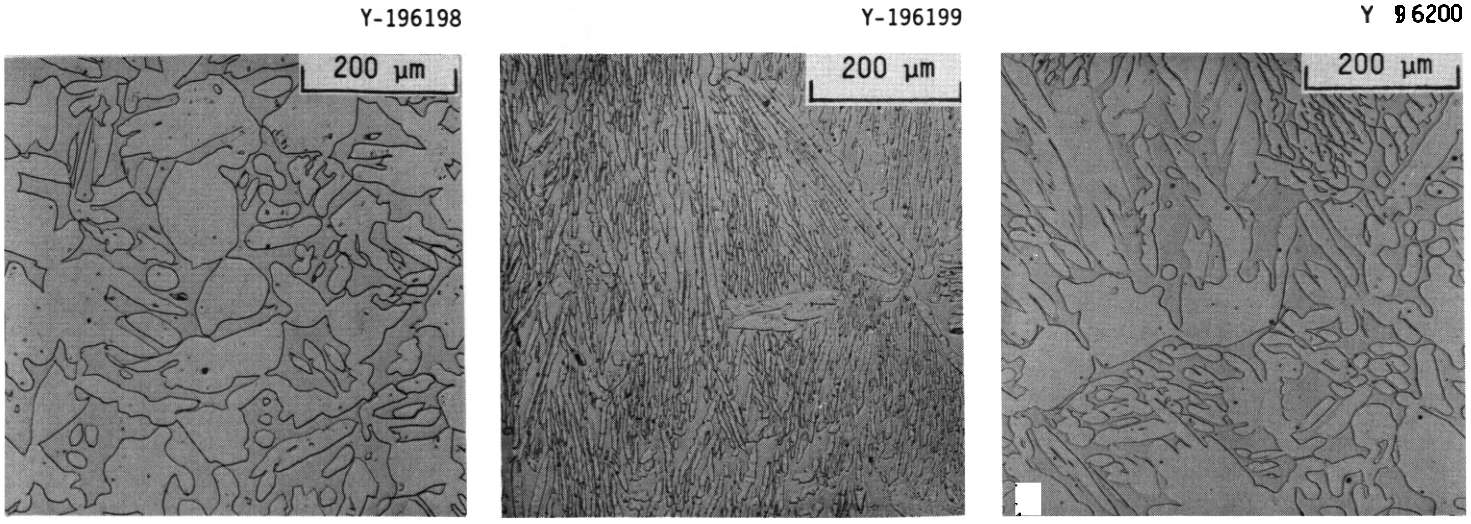


Fig. 2. Microstructure of (a) Fe-15Cr-15Mn-0.1C (PCMA-0), (b) Fe-5Cr-15Mn-0.05C (PCMA-1), and (c) Fe-15Cr-20Mn-0.1C (PCMA-2) steels solution annealed 1 h at 1150°C.

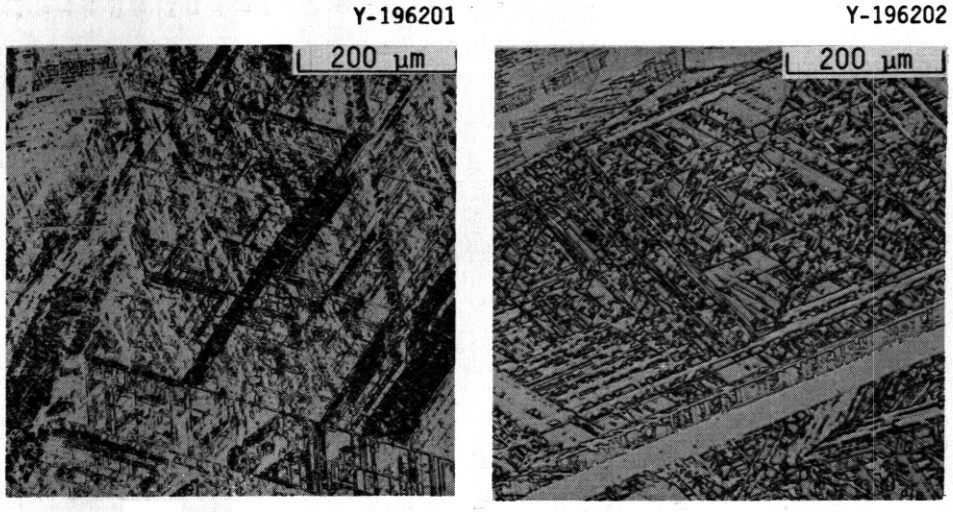


Fig. 3. Microstructure of (a) Fe-10Cr-15Mn-0.1C (PCMA-3) and (b) Fe-10Cr-20Mn-0.1C (PCMA-4) steels solution annealed 1 h at 1150°C.

Y-196203 Y-196204

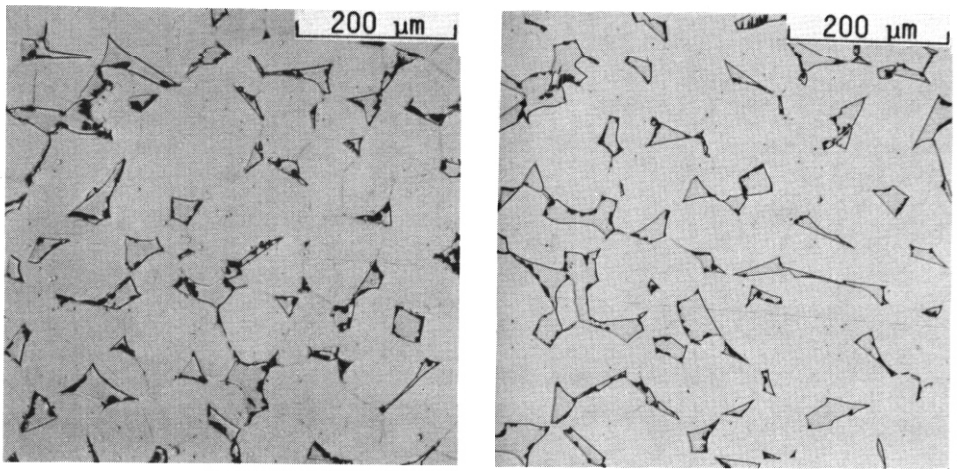


Fig. 4. Microstructure of (a) Fe–15Cr–15Mn–0.2C (PCMA-5) and (b) Fe–20Cr–16Mn–0.2C (PCMA-6) steels solution annealed 1 h at 1150°C.

Y-136205

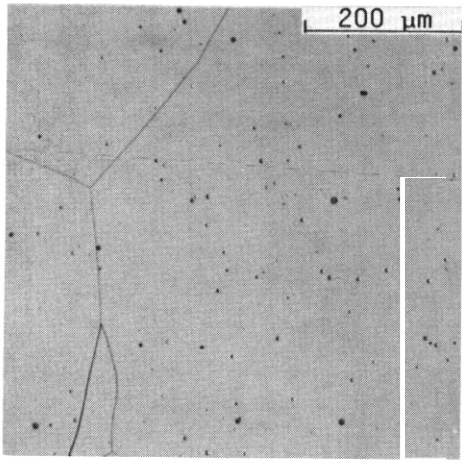


Fig. 5. Microstructure of Fe–15Cr–20Mn–0.4C (PCMA-7) steel solution annealed 1 h at 1150°C.

The first three alloys (PCMA-0 to -2) were high-chromium, low-carbon alloys, and optical microscopy indicated that they were basically duplex structures of austenite and δ-ferrite (Fig. 2). The only difference for the homogenized and solution-annealed steels appeared to be a somewhat finer δ-ferrite structure, the lower the heat-treatment temperature. Transmission electron microscopy indicated that PCMA-0, -1, and -2 contained some ε-martensite. The magnetic measurements on PCMA-2 gave a slightly lower reading in the homogenized condition than in the solution-annealed condition, suggesting that the higher temperature had produced less δ-ferrite. High magnetic readings were obtained for all alloys in the cold-worked condition. Although cold working will not change the amount of δ-ferrite present in the homogenized structure, the rolling strain can produce magnetic α′-martensite from the austenite.

The PCMA-3 and -4 alloys, which are low-chromium, low-carbon steels, had microstructures indicative of martensite and austenite (Fig. 3). From these microstructures it was not possible to separate the two constituents to estimate their relative amounts, although it appeared that substantial amounts of martensite were present. The magnetic measurements indicated that only a small amount of a magnetic constituent was present after annealing, but more magnetic material was present after cold working. These observations suggested the interpretation that the martensite observed in the homogenized and solution-annealed conditions was nonmagnetic hexagonal-close-packed ε-martensite, which can transform to magnetic body-centered-tetragonal α′-martensite when deformed.

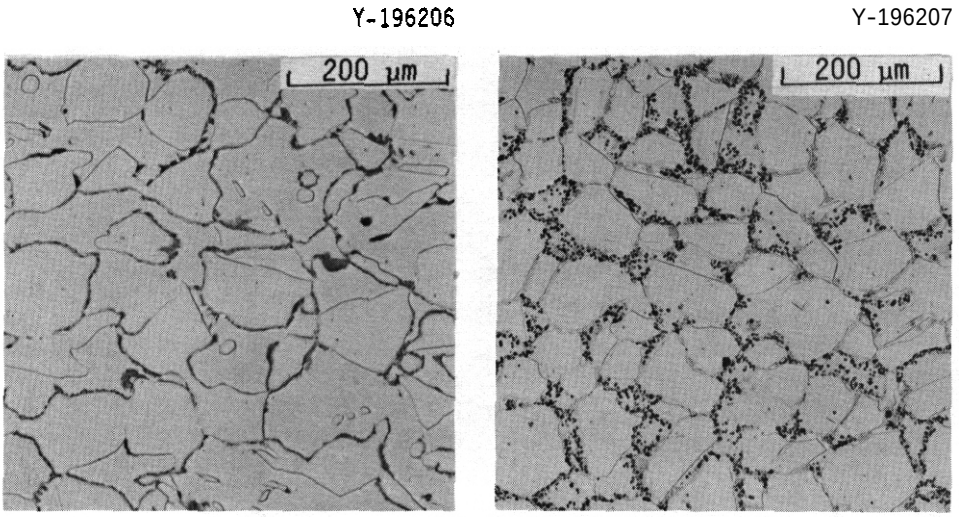


Fig. 6. Microstructure of (a) Fe-20Cr-20Mn-0.2C (PCMA-8) and (b) Fe-20Cr-20Mn-0.4C (PCMA-9) steels solution annealed 1 h at 1150°C.

The PCMA-0 through -4 steels contained 0.1% C or less. The remaining alloys contained medium (~0.2%) or high (~0.4%) carbon contents. Although carbon is an austenite stabilizer, only one of the higher-chromium alloys (PCMA-7) was 100% austenite (Fig. 5). This alloy contained both high-carbon and high-manganese contents. The PCMA-5 and -6 steels, which contained high-chromium and medium-carbon levels, both had austenitic structures (Fig. 4) with small amounts of δ-ferrite and possibly precipitates at the δ-ferrite/austenite boundaries. The amount of precipitate appeared to increase as the heat-treatment temperature decreased. The PCMA-8 and -9 steels were both high-chromium, high-manganese alloys, the first with medium carbon and the other with high carbon. Duplex microstructures containing austenite and δ-ferrite were observed, with indications that precipitates were present on the δ-ferrite/austenite boundaries (Fig. 6); the amount of precipitate appeared to increase with increasing carbon content and decreasing annealing temperature.

The most notable differences between the observed and predicted phases involved PCMA-0, -1, -5, -6, and -9. The major predicted constituents should have been either γ or γ + M, but the observations indicated that the major constituents were γ and δ.

The second series of alloys (PCMA-10 through -14) was produced after the observations on the first series demonstrated that the Schaeffler diagram did not accurately predict the microstructures of the Fe-Cr-Mn-C steels. These five steels contained about 20% Mn and varying amounts of chromium and carbon.

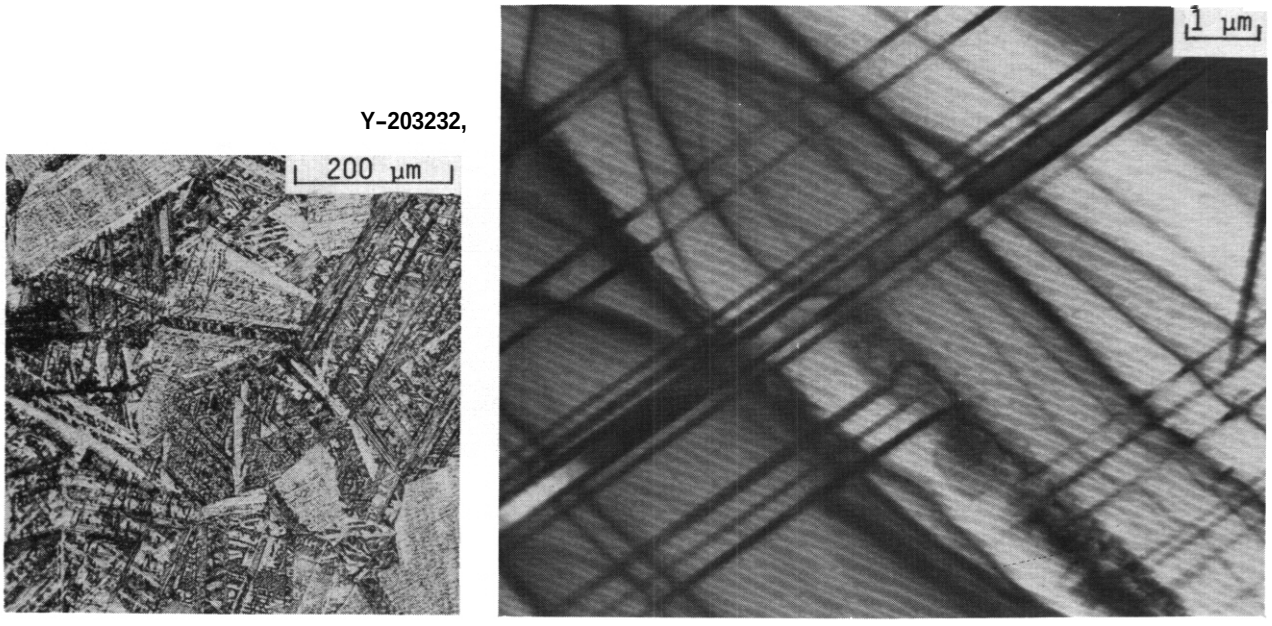
There appeared to be similarities in the microstructures of the two low-chromium. low-carbon alloys (PCMA-10 and -11). The 10% Cr-0.1% C steel (PCMA-10) contained considerable amounts of an acicular-appearing constituent [Fig. 7(a)], which was initially assumed to be ε-martensite, because the magnetic readings for the annealed steel were extremely low. The 12% Cr-0.1%C steel (PCMA-11) had a finer structure than the 10%Cr steel. With optical microscopy it was not possible to determine if the microstructure contained martensite or a high density of annealing twins [Fig. 7(c)], although it was assumed to be martensite. When these steels were examined by TEM, it appeared that only the 10% Cr steel contained martensite [Fig. 7(b)]. The 12%Cr steel contained a high density of stacking faults in austenite [Fig. 7(d)].

The 12% Cr-0.2% C steel (PCMA-12) solution annealed 1 h at 1150°C was entirely austenitic. Optical microscopy showed the steel to have a propensity for twin formation [Fig. 8(a)]; TEM revealed a matrix devoid of other phases, stacking faults, or dislocations [Fig. 8(b)].

The two high-chromium steels (PCMA-13 and -14) contained δ-ferrite (Fig. 9). Based on the optical microscopy and the magnetic measurements, the nominally 16% Cr-0.2% C steel (PCMA-14) contained the most δ-ferrite. Figure 9(c) shows a TEM micrograph of a δ-ferrite particle in the austenite matrix of PCMA-14. Note the high dislocation density in the ferrite compared to the austenite. These dislocations could be either the result of transformation stresses or of differential contractions between the phases during cooling.

The compositions of two δ-ferrite particles and three austenite grains of PCMA-14 were analyzed by XEDS (x-ray energy dispersive spectroscopy) (Table 5). For the primary alloying components -- iron, chromium, and manganese -- only the chromium showed a large amount of partitioning between the ferrite and austenite (average concentrations of 23.1 vs. 17.9%) (Fig. 10), with the concentration being higher in the ferrite.

E-49164



Y-203232,

E-49174



Y-203233'

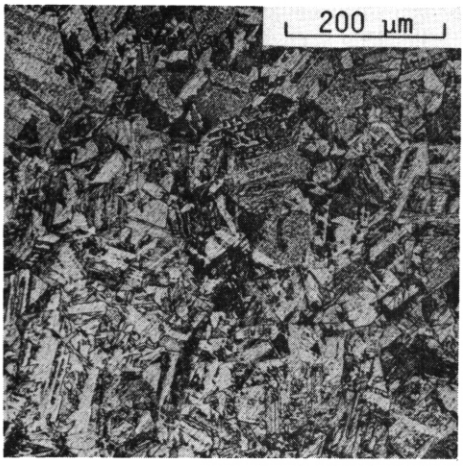


Fig. 7. Microstructures of *(a)* Fe-10Cr-20Mn-0.1C (PCMA-IO) and *(b)* Fe-12Cr-20Mn-0.1C (PCMA-11) steels solution annealed 1 h at 1150°C. The TEM examination indicated that *(a)* contains martensite needles and *(b)* contains a high density of stacking faults.

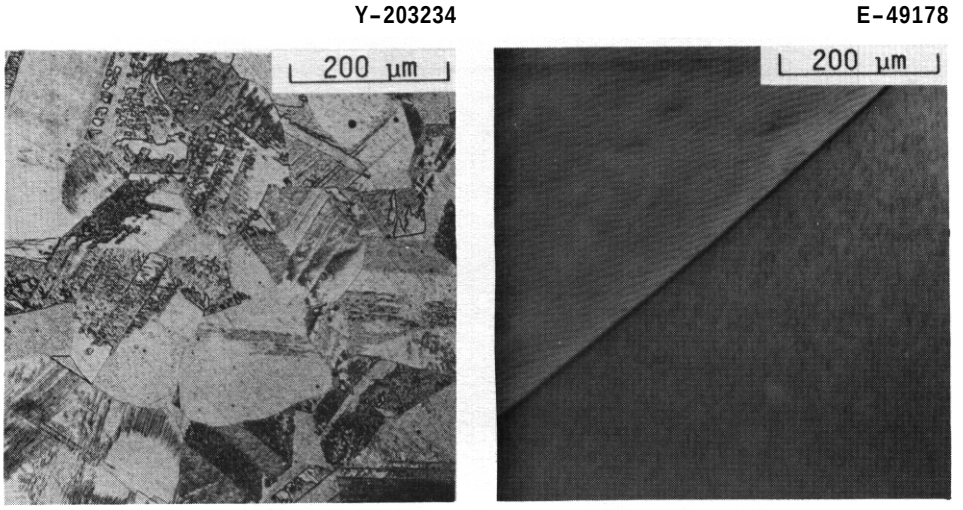


Fig. 8. Microstructure of Fe–12Cr–20Mn–0.2C (PCMA-12) solution annealed 1 h at 1150°C as observed by *(a)* optical and *(b)* electron microscopy.

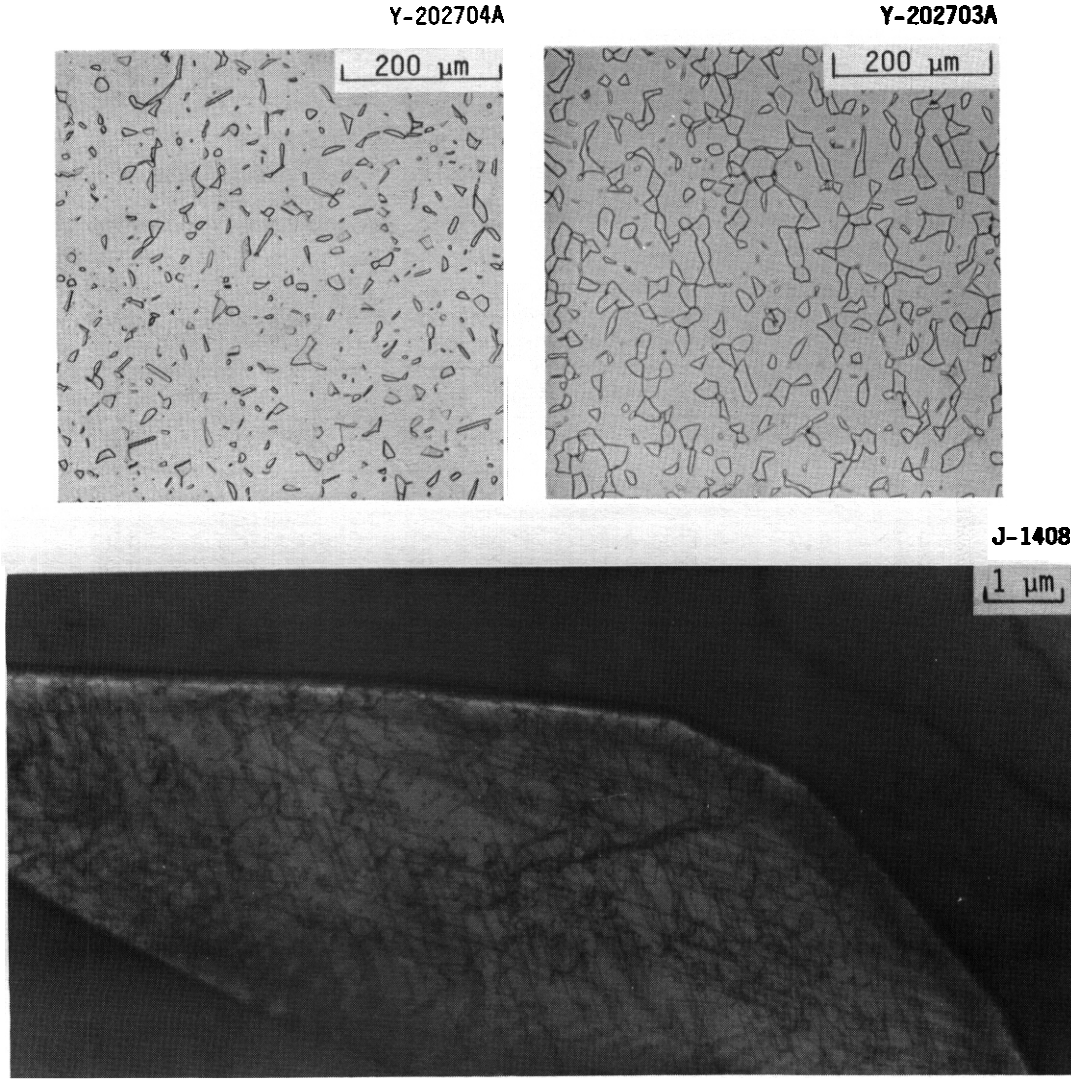


Fig. 9. Optical microstructure of *(a)* Fe–14Cr–20Mn–0.1C (PCMA-13) and *(b)* Fe–16Cr–20Mn–0.2C (PCMA-14) steels solution annealed 1 h at 1150°C. *(c)* TEM of *(b)* that shows a 6-ferrite grain in the austenite matrix.

ORNL-DWG 85C-18356

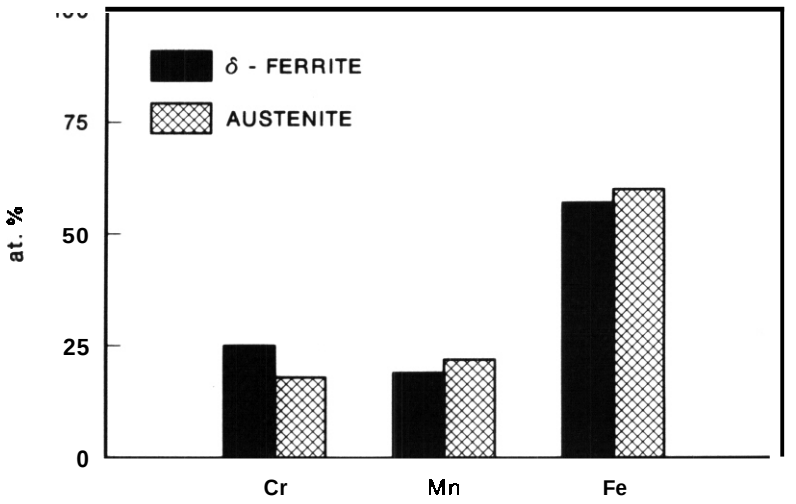


Fig. 10. Chemical composition of chromium, manganese, and iron in 6-ferrite and austenite phases as determined by XEDS on the Fe-16Cr-20Mn-0.2C steel solution annealed 1 h at 1150°C.

The manganese and iron concentrations were slightly different in the two phases -- both were higher in the austenite. The average concentrations for the manganese in the austenite and ferrite were 21.1 and 19.68, respectively.

Figure 11 shows the Schaeffler diagram with the compositions and constituents for the fifteen Fe-Cr-Mn-C alloys plotted on the diagram, using Eqs. (1) and (2) to calculate the chromium and nickel equivalents. It is clear that the diagram does not adequately describe the behavior of the Fe-Cr-Mn-C

Table 5. XEDS phase compositional measurements in Fe-20Mn-16Cr-0.2C steel (PCMA-14) solution annealed 1 h at 1150°C

Composition,[a] (at. %)[a,b]								
Si	P	Ti	V	Cr	Mn	Fe	Ni	Mo
				γ-austenite matrix				
0.7	1.0	0.1	0.3	17.9	21.5	58.4	0.0	0.1
0.7	1.0	0.1	0.1	17.8	20.6	59.6	0.0	0.05
				6-ferrite particles				
0.0	0.0	0.0	0.0	23.2	20.0	56.4	0.0	0.1
0.1	0.0	0.0	0.2	23.1	19.5	57.0	0.0	0.1
0.0	0.0	0.2	0.2	23.1	19.4	56.8	0.0	0.1

[a]Metallic elements with Z greater than Al.
[b]Each line of compositional numbers represents one individual measurement.

steels. In particular, the observed γ + 6 field has been widened considerably from that of the Schaeffler diagram.[2] Therefore, manganese does not appear to be as strong an austenite stabilizer against 6-ferrite formation as it would be if it were simply half as effective as nickel. The appearance of austenite and martensite also occurs at different compositions from those predicted by the Schaeffler diagram. In this case, manganese is a more potent austenite stabilizer against martensite than is accounted for by the simple nickel equivalency relationship.

To further delineate the differences between the Schaeffler diagram boundaries and the constituents in Fe-Cr-Mn-C alloys, we examined the eighteen Fe-Mn and Fe-Cr-Mn steels listed in Table 2. Again, optical and electron microscopy observations were made. Figure 12 shows the Schaeffler diagram with the constituents of

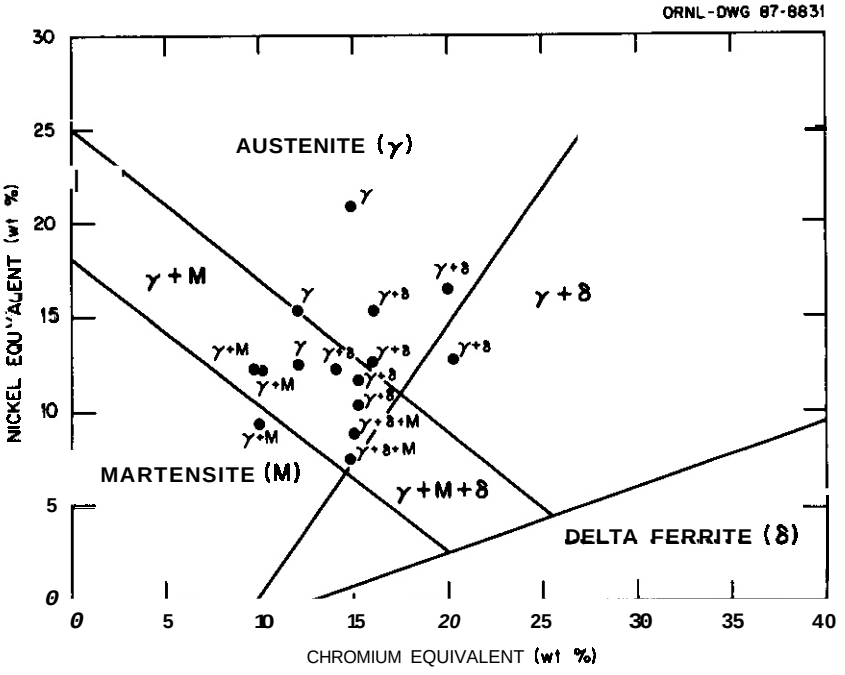


Fig. 11. The Schaeffler diagram with the fifteen Fe-Cr-Mn-C alloys indicated. The phases observed for each alloy are given.

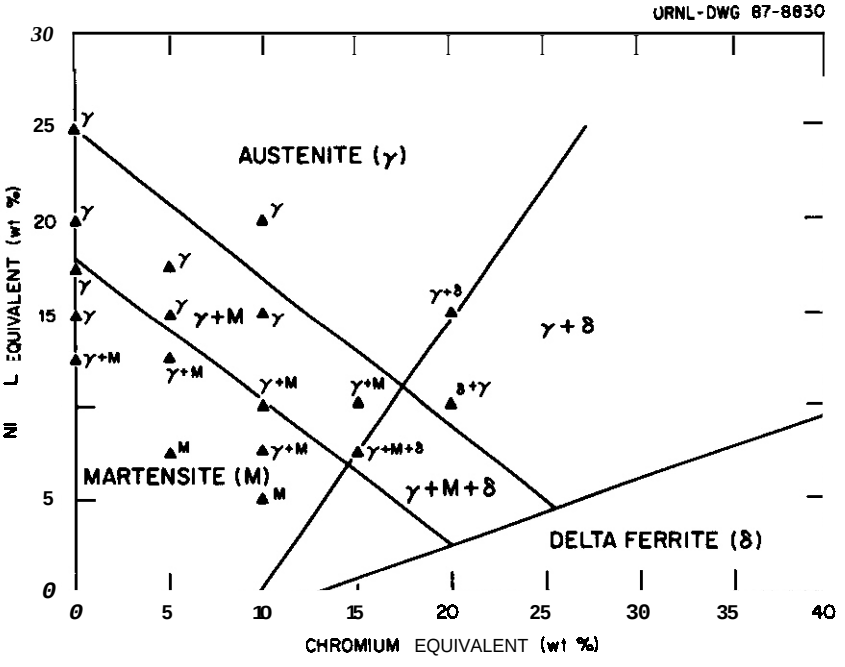


Fig. 12. The Schaeffler diagram with the eighteen Fe-Mn and Fe-Cr-Mn alloys indicated. The phases observed for each alloy are given.

the alloys superimposed. It is again obvious that many of these alloys do not behave as predicted by the diagram. The differences agree with the observations made on the Fe-Cr-Mn-C alloys.

Figure 13 shows a Schaeffler diagram with all of the 33 alloys examined. In Fig. 14. a new, modified diagram is shown with boundaries redrawn so as to accommodate the microstructural observations. Most of the observations agree with the various regions as drawn, although a few of the microstructural observations near boundaries were not in agreement with the redrawn constituent fields.

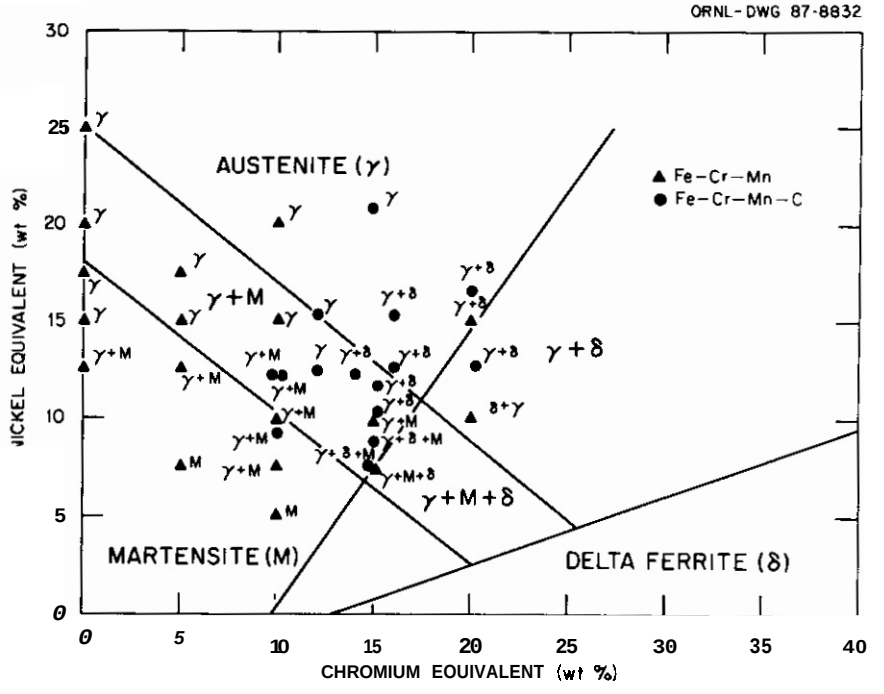


Fig. 13. The Schaeffler diagram with the 33 experimental alloys indicated. The phases observed for each alloy are given.

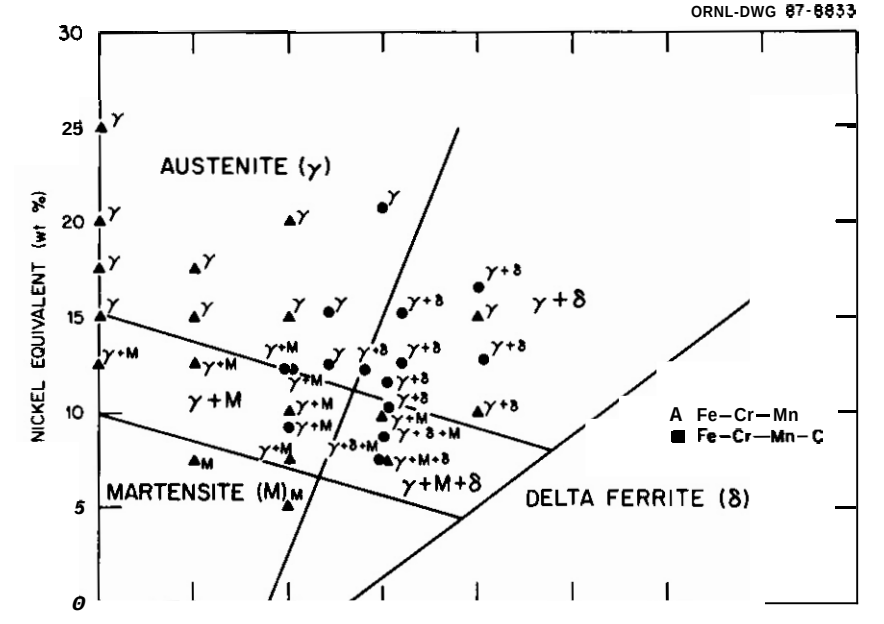


Fig. 14. A "modified Schaeffler diagram" with the phase boundaries redrawn in accordance with the observations for the high-manganese experimental alloys.

Discussion

Over the years, the use of manganese as a replacement for nickel in austenitic stainless steels has been studied by several investigators.[7] However, most of these steels, such as the 200 series stainless steels, also contain nickel and nitrogen to help stabilize the austenite. Neither of these alloying elements should be used in the FIRD steels being developed for fusion-reactor applications.

The present study shows that manganese is not as strong an austenite stabilizer relative to δ-ferrite as predicted by the Schaeffler diagram. Further, it is a stronger stabilizer of the austenite against the martensite transformation than predicted by the diagram. These results indicate that either the Schaeffler-diagram boundaries need to be altered for high-manganese alloys, or, alternatively, that the multiplying factor for manganese in Eq. (1) is not simply a constant of 0.5. Both approaches have been suggested.[3-5,8]

Schaeffler-type diagrams were developed for the high-nickel austenitic stainless steels that usually contained only small amounts of manganese.[2] Olson[8] has reviewed the large number of diagrams that have been developed to predict the phases in Cr-Ni austenitic stainless steels; the first diagram appeared in 1906.[9] Schaeffler published his first diagram in 1947;[10] he subsequently revised this diagram several times. Numerous other investigators have also proposed modifications.0

The difficulty with the use of such diagrams when large amounts of manganese are substituted for nickel has been discussed.[3-5,8] Several studies have indicated that the 0.5 multiplier for manganese in Eq. (1) may be an overestimate of manganese's austenite-stabilizing capability relative to δ-ferrite.[3-5] A recent study concluded that the effect of manganese is independent of concentration, and a constant with a value of 0.35 was proposed.3

The present work confirmed that the 0.5 multiplier for manganese in Eq. (1) is an overestimate of the austenite-stabilizing capability of manganese relative to the formation of 6-ferrite. The observation on partitioning of the elements in PCMA-14 between the 6-ferrite and austenite phases is in agreement with this observation when compared with the partitioning of nickel between these same phases in a nickel-stabilized stainless steel. For the iron, chromium, and manganese -- the primary components -- only the chromium showed a significant partitioning between the ferrite and austenite (Fig. 10), with the chromium concentration being greater in the δ-ferrite. The manganese and iron concentrations were just slightly higher in the austenite than the ferrite. For type 308 stainless steel, which nominally contains 20.5% Cr and 10.5% Ni, Vitek and David found that nickel partitioned strongly to the austenite, while chromium partitioned to the 6-ferrite.[11] After the weld metal was annealed 1 h at 900°C, the concentrations of the nickel in austenite and ferrite were 10.2 and 4.8%, respectively; the chromium concentrations in austenite and ferrite were 21.9 and 31.8%, respectively. The iron was slightly higher in the austenite than the ferrite (67.9 versus 63.5%).

The results indicate that the effect of manganese on austenite stabilization is more complicated than can be accounted for by a simple constant value of the multiplying factor for the manganese term in Eq. (1). As the present results indicate, the effect of manganese as a stabilizer against δ-ferrite formation is different from its effect as a stabilizer against martensite. In fact, the present results indicate that manganese is a stronger stabilizer against martensite than the Schaeffler diagram predicts, which would indicate that it is a stronger stabilizer than nickel in this regard, since the diagram was mainly determined for high-nickel steels. Olson[8] discussed various equations that have been proposed to predict the austenite stability relative to martensite. In several of the empirical equations, manganese is established to be twice as effective as nickel in stabilizing austenite relative to martensite, just the opposite of the Schaeffler equations. However, most of these equations were developed by studying steels that contained more nickel than manganese.

Self et al.[12] found that the effect of manganese on martensite formation depended on the chromium content. Their studies were also conducted on alloys with varying amounts of nickel, although the relative amounts of nickel and manganese covered a wide range of compositions. Self et al.[12] found that for less than 1% Cr, manganese was twice as effective as nickel in stabilizing the austenite relative to martensite. At about 9% Cr, the nickel and manganese had equivalent effects. Eichelmann and Hull[13] had previously established that for high-chromium contents (greater than 16%), the relative effects of nickel and manganese approached those predicted by Schaeffler.

These observations were taken by Self et al.[12] to mean that the effect of nickel on stabilizing austenite relative to martensite is enhanced by chromium and/or the effect of manganese is retarded by chromium. The former effect was chosen,[12] based on previous work that showed a synergistic effect of chromium and nickel in stabilizing austenite in stainless steels.[14] However, that conclusion does not appear to apply to the present results, since there was no nickel present in the alloys investigated. Thus, all that can be said in the present case is that manganese has a greater austenite-stabilizing capacity against martensite formation than nickel, as determined by the Schaeffler diagram.

The past studies thus illustrate the complicated behavior of steels containing manganese. Rather than search for an empirical relationship or relationships that will describe the behavior of manganese-stabilized stainless steels of the type being developed for fusion-reactor applications, we redrew the boundaries for austenite stability with chromium and nickel equivalents calculated by Eqs (1) and (2). These boundaries delineate the compositional region in which it should be possible to make austenite-stable alloys. Of course, these boundaries are very rough estimates to the actual boundaries. Much more data would be required to firmly establish such boundaries. In Fig. 14, the boundaries are presented as straight lines, although there is no reason that they should not be curved.8

Razikov et al.[15] developed a diagram for manganese-rich steels similar to the one given in Fig. 14. Their work, like that of Schaeffler, was carried out on cast (weld) metal. They also found that the diagram for high-manganese alloys was different from the Schaeffler diagram obtained for nickel-rich steels. However, the diagram they obtained was also different from the diagram obtained in the present work (Fig. 14). Although the boundaries between the austenite and austenite plus martensite fields and the martensite and austenite plus martensite fields were similar, there was considerable difference in the boundary line that separates the austenite from the austenite plus δ-ferrite region. The γ + δ region of the diagram of Razikov et al. was not as wide as that in the present work would indicate. The reason for this is not clear, but may be due to the more limited number of samples used to determine the latter boundary.[15] Razikov et al. used a total of only 12 specimens to determine the entire diagram, and only one of them fell in the austenite plus δ-ferrite region. Most samples had compositions that were in the martensite and martensite plus austenite regions. The difference between wrought and cast metal may also play a role, but that difference is expected to be small.

Basically, the diagram given in Fig. 14 shows that, to develop a manganese-stabilized austenitic stainless steel, it will be necessary to work with compositions that contain at least 20 to 25% Mn, 12 to 14% Cr, and 0.1 to 0.25% C. Alloys in this composition range that are alloyed with additional solid-solution and precipitate-strengthening elements are presently being investigated as possible FIRD stainless steels for the fusion-materials program.

CONCLUSIONS

A total of 33 alloys with varying compositions of iron, chromium, manganese, and carbon were examined by optical and electron microscopy and by magnetic measurements to determine the constituents present in the microstructure. The observations were compared with the results predicted using the Schaeffler diagram, which was developed for Cr-Ni stainless steels with only small amounts of manganese.

The results indicated that the Schaeffler diagram cannot be used in its present form to predict the constituents expected for high-manganese steels. For the region of the diagram where δ-ferrite forms, it was found that manganese is not as strong an austenite stabilizer as is predicted by the diagram. In the region of the Schaeffler diagram where martensite forms, it was found that manganese is a stronger austenite stabilizer than predicted by the diagram. The austenite-stable region for manganese-stabilized stainless steels is therefore moved to lower chromium and relatively high combinations of manganese and carbon. It was concluded that the development of a manganese-stabilized stainless steel should be possible in the composition range of 20 to 25% Mn, 12 to 14% Cr, and 0.1 to 0.25% C.

FUTURE WORK

In the future we will seek to alloy selected base compositions for irradiation resistance and strength.

REFERENCES

1. R. L. Klueh and E. E. Bloom, "The Development of Austenitic Steels for Fast Induced-Radioactivity Decay for Fusion Reactor Applications," Optimizing Materials for Nuclear Applications, p. 73, The Metallurgical Society, Inc., Warrendale, Pennsylvania, 1985.

2. H. Schneider. "Investment Casting of High-Hot-Strength 12-Percent Chrome Steel," Foundry Trade J., 108, 563–4 (1960).

3. E. R. Szumachowski and D. J. Kotecki, "Manganese Effect on Stainless Steel Weld Metal Ferrite," Welding J. 63, 156s-163s (1984).

4. F. C. Hull, "Delta Ferrite and Martensite Formation in Stainless Steels," Welding J. 52, 193–202 (1973).

5. R. H. Espy, "Weldability of Nitrogen-Strengthened Stainless Steels," Welding J. 61, 149s-156s (1982).

6. H. R. Brager, F. A. Garner, D. S. Gelles, and M. L. Hamilton, "Development of Reduced Activation Alloys for Fusion Service," J. Nucl. Mater. 133&134, 907-911 (1987).

7. J.H.G. Monypenny, Stainless Iron and Steel, vol. 2, p. 261, Chapman & Hall, London, 1954.

8. D. L. Olson, "Prediction of Austenitic Weld Metal Microstructure and Properties," Welding J. 65, 281s-295s (1985).

9. L. Guillet, "Nickel-Chrome Steels," Rev. Metal 3, part 1, 332 (1906).

10. A. L. Schaeffler, "Selection of Austenitic Electrodes for Welding Dissimilar Metals," Welding J. 26, 1-20 (1947).

11. J. M. Vitek and S. A. David, "Analytical Electron Microscopy Evaluation of Laser Welded 308 Stainless Steel," Scanning Electron Microscopy/1981/I, pp. 169-175, SEM, Inc., AMF O'Hare, Chicago, 1981.

12. J. A. Self, D. K. Matlock, and D. L. Olson, "An Evaluation of Austenitic Fe-Mn-Ni Metal for Dissimilar Metal Welding," Welding J. 63, 282s-288s (1984).

13. G. H. Eichelmann and F. C. Hull, "Effect of Composition on the Temperature of Spontaneous Transformation of Austenitic to Martensitic in 18-8 Stainless Steel," Trans. ASM 45, 77-104 (1953).

14. J. W. Pugh and J. D. Nisbet, "A Study of the Iron-Chromium-Nickel Ternary System," Trans. AIME 188 268-276 (1950).

15. M. I. Razikov, G. N. Kocheva, and L. G. Tolstykh, " Equilibrium Diagrams for Weld Metals in Chromium-Manganese Steels," Avt. Svarka 21, No. 4, 1-5 (1968).

SOME EFFECTS OF THERMAL-MECHANICAL PRETREATMENT AND ALLOY COMPOSITIONAL VARIATION ON SWELLING OF AUSTENITIC STAINLESS STEELS IRRADIATED IN HFIR - P. J. Maziasz, J. L. Scott, L. J. Turner (Oak Ridge National Laboratory), S. Hamada and M. P. Tanaka (Japan Atomic Energy Research Institute, assigned to ORNL)

OBJECTIVE

The objective of U.S. experiments is to develop swelling-resistant advanced austenitics based on compositional variation of the U.S.-PCA, and to test them in HFIR. One objective of the Japanese experiments is to evaluate pretreatment effects on J316 and JPCA and several compositional variation effects on JPCA and test these in HFIR. A joint objective has been to compare U.S. and Japanese results.

SUMMARY

A precision densitometer has recently been installed at ORNL for remote measurement of immersion density of irradiated transmission electron microscopy (TEM) disks. Some disks have been measured from the HFIR-JP1 and -JP3 experiments, irradiated at 300 and 400°C, respectively, to 34 dpa. and nearly all the disks have been measured from HFIR-JP7 and -JP8, irradiated at 500°C to 34 and 57 dpa, respectively. Very little swelling was measured in any of the disks irradiated at 300 and 400°C, but swelling was variable, and in many cases quite large, at 500°C. Only a few alloys appear to be swelling resistant. Of the Japanese alloys, the JPCA was the best, particularly when irradiated in the 20% cold worked (CW) condition. Swelling of the USPCA in the 25% CW (83) condition was less than the 20% CW JPCA after 57 dpa at 500°C. An unusual decrease in swelling occurred with increased dose from 34 to 57 dpa. The U.S. alloys included many modifications of the PCA composition, but the most swelling-resistant alloys contained 0.03 to 0.07 wt % P.

PROGRESS AND STATUS

Introduction

The collaborative HFIR-JP1 through -JP8 experiments have provided an important irradiation vehicle for researchers at both the Japanese Atomic Energy Research Institute (JAERI) and the Oak Ridge National Laboratory (ORNL). While only a portion of the overall collaborative program, these experiments play a key role in alloy development efforts for both programs.[1,2] Irradiation temperatures cover the range 300 to 600°C; neutron fluences produce up to 57 dpa and about 4400 appm He. Other experiments are in progress to better control the helium to dpa ratio through spectral tailoring[3,4] or isotopic tailoring,[5] or both, but these will not reach the higher fluences required to test swelling-resistant materials for several years. The Japanese portion of the HFIR-JP series of experiments includes many thermal-mechanical pretreatment variations of the JPCA as well as J316 and several compositional variants of JPCA. The U.S. program extensively investigated thermal-mechanical pretreatment variation effects on the swelling resistance of the USPCA in a previous set of experiments, HFIR-CTR-30 through -32, at up to 44 dpa.[6-8] The current focus for the U.S. program is the effect of compositional variation on the swelling resistance of 20 to 25% CW material. The U.S. alloys include several heats of type 316, many compositional variants of the USPCA, developed at ORNL,[9,10] as well as several heats of the 09 type alloy developed on the U.S. Fast Breeder Reactor (FBR) Materials Program.[11]

While TEM provides important insight into the mechanisms responsible for void swelling behavior, it is time consuming as a quantitative technique for measuring cavity swelling. The TEM technique cannot, of course, account for voids larger than the foil thickness; neither can it assess changes in density due to precipitation. Immersion density is the preferred method of measuring the total volume change that has occurred in the irradiated material.[12] The focus of this report is a survey of the swelling resistance of a large number of materials rather than the detailed examination of microstructural behavior.

Experimental

The compositions of the various Japanese steels irradiated in the HFIR-JP1 through -JP8 series of experiments can be found in Table 1, while the compositions of the U. S. steels included in these experiments are found in Table 2. Specification and identification codes for different thermomechanical treatments given either U.S. or Japanese alloys prior to irradiation are listed in Table 3.

The description of capsule design and test matrices for the HFIR-JP series of experiments can be found elsewhere.[1,2,13] Standard TEM disks (~3 mm in diam, 0.254 mm thick) were irradiated in tubes located at the reactor midplane positions of the various HFIR peripheral target position (PTP) subassemblies. Disks from HFIR-JP1 and -JP3 were irradiated at temperatures of 300 and 400°C, respectively, and to neutron fluences producing 34 dpa and up to 2500 appm He (for USPCA/JPCA with 16 wt % Ni), as verified by dosimetry.[14] HFIR-JP7 was irradiated at 500°C to a similar fluence, while HFIR-JP8 was irradiated at 500°C to a higher fluence estimated to produce 57 dpa and up to 4300 appm He.

Table 1. Alloy chemistries for Japanese disk specimens in capsules HFIR-JP-1 through -JP-8

Alloy	Content, wt %												
	C	Si	Mn	P	S	Ni	Cr	Mo	Ti	Nb	E	N	co
JPCA	0.06	0.50	1.77	0.027	0.0005	15.60	14.22	2.28	0.24		0.0031	0.0039	0.002
JPCA (QS)	0.06	0.53	1.79	0.027	0.009	16.22	14.51	2.37	0.20		0.0035	0.009	0.025
JPCA-C	0.02	0.51	1.56	0.017	0.007	15.6	15.4	2.4	0.25	0.08		0.0018	
JPCA-K	0.02	0.48	1.46	0.015	0.005	17.56	17.99	26				0.004	
Type 316	0.058	0.61	1.80	0.028	0.003	13.52	16.75	2.46	0.005	<0.1			<0.1
Ferritic steel[a]	0.056	0.74	0.70	0.008	0.0059	1.37	8.86	2.46		0.06		0.0069	

[a]Also Al, 0.04; V, 0.11; Cu, 0.02; W, 0.01.

Table 2. Alloy chemistries for U.S. disk specimens irradiated in capsules HFIR-JP-1 through -JP-8

Alloy	Content,[a] wt %														
	Cr	Ni	Mo	Mn	Si	Ti	Nb	V	C	N	P	co	Cu	E	S
JPCA	14.0	16.2	2.3	1.8	0.4	0.24			0.05	0.01	0.01			0.001	0.003
PCA-1	14.0	16.0	2.5	2.1	<0.01	0.13	0.12	<0.01	0.04	0.003	<0.001	<0.01	0.02	<0.001	0.008
PCA-3	14.3	15.8	2.5	2.0	0.4	0.13	0.11	(0.01	0.056	0.005	(0.001	(0.01	0.02	<0.001	0.007
PCA-6	14.0	16.0	2.4	1.9	0.4	0.23	0.01	<0.01	0.083	0.004	<0.001	<0.01	0.02	<0.001	0.007
PCA-8	13.9	16.0	2.7	2.1	<0.01	0.17	0.14	<0.01	0.081	0.007	<0.001	<0.01	0.02	<0.001	0.008
PCA-3	13.8	16.0	2.5	2.0	0.4	0.25	<0.01	<0.01	0.073	0.005	0.03	<0.01	0.02	(0.001	0.007
PCA-10	13.8	15.9	2.5	1.9	0.4	0.3	0.1	0.02	0.04	0.002	0.002	<0.01	0.02	(0.001	0.009
PCA-11	13.8	16.0	2.5	1.9	0.4	0.3	0.1	0.5	0.04	0.002	0.002	<0.01	0.03	(0.001	0.008
PCA-12	13.8	15.9	2.4	1.9	0.4	(0.01	0.47	0.01	0.044	0.004	0.002	0.01	0.02	(0.001	0.008
PCA-13	13.8	15.9	2.5	1.9	0.4	0.3	0.1	0.5	0.063	0.002	0.002	(0.01	0.02	(0.001	0.009
PCA-16	15.9	14.1	2.5	1.9	0.4	0.27	(0.01	0.02	0.051	0.002	0.002	(0.01	0.02	<0.001	0.009
PCA-17	15.8	16.0	2.5	1.9	0.4	0.3	<0.01	0.03	0.047	0.002	0.002	<0.01	0.02	(0.001	0.009
PCA-18	17.6	16.1	2.5	1.9	0.4	0.27	(0.01	0.02	0.044	0.002	0.002	(0.01	0.02	(0.001	0.009
PCA-00	14.0	16.0	2.46	2.0	0.4	0.24	<0.0	0.02	0.056	0.001	0.002	0.01	0.02	<0.001	0.008
PCA-19	13.8	19.9	2.44	2.1	0.44	0.28	0.1	0.5	0.076	0.002	0.030	0.01	0.01	<0.001	0.006
PCA-20	13.8	16.1	2.5	2.1	0.42	0.28	0.1	0.5	0.083	0.006	0.07	0.01	0.01	0.001	0.007
PCA-21	15.8	15.8	2.44	3.4	0.4	0.27	0.1	0.5	0.077	0.006	0.06	<0.01	0.05	0.001	0.007
PCA-22	13.8	15.9	2.3	2.5	0.4	0.28	0.1	0.5	0.078	0.004	0.03	<0.01	0.05	0.003	0.007
EP-838	11–13	4.4–4.8	0.3–0.6	12–14	0.6				0.02	0.05–0.09	0.4			0.0005	0.4
N-lot 316	16.5	13.5	2.5	1.6	0.5				0.05	0.006	0.013			0.0008	0.006
Ref. 316	17.3	12.4	2.1	1.7	0.7		0.08		0.05		0.04	0.35		0.0004	0.015
DO-316	18.0	13.0	2.6	1.9	0.8	0.05			0.05	0.05	0.01	0.004		0.0005	0.016
D9-699	14.2	15.2	1.95	2.1	0.5	0.23	0.01	0.02	0.033	0.004	0.005	0.02	0.02	<0.001	0.001
D9-697	14.4	16.2	1.5	1.9	0.5	0.25	<0.01	0.02	0.035	0.009	0.003	0.03	0.02	0.0001	0.002
09-A7	13.7	16.3	2.5	2.0	1.42	0.18	0.01	0.023	0.045	0.011	0.075	0.06	0.03	0.0005	0.017
D9-F	14.3	14.3	2.2	2.1	1.0	0.3			0.05	0.002					

[a]Balance iron.
[b]This alloy also contains approximately 1% Al.

Code	Alloy	Final alloy condition
PS-1	JPCA	Solution annealed (1175°C/1 h)
PS-2	JPCA	Solution annealed (1100°C/1 h)
PS-3	JPCA	Solution annealed (1050°C/1 h)
PC-1	JPCA	Solution annealed (1100°C/1 h) + 10% cold worked
PC-2	JPCA	Solution annealed (1100°C/1 h) + 15% cold worked
PC-3	JPCA	Solution annealed (1100°C/1 h) + 20% cold worked
A0	U.S. 316	Solution annealed (1050°C/1 h)
A1	U.S. PCA	Solution annealed (1100°C/0.5 h)
A3	U.S. PCA	A1 treatment + 25% cold worked
E3	U.S. PCA	A1 treatment + 800°C/8 h + 25% cold worked
20% CW	U.S. 316	A0 treatment + 20% cold worked

Details of the design and operating procedure for the precision densitometer are presented elsewhere.[12] The weight cell containment module is installed outside and behind a hot cell that contains the initial portion of the specimen transfer system, Fig. 1. The density is determined from the Archimedean method of comparing wet and dry weights of the TEM disks. The apparatus contains an ultrasensitive balance that is isolated from both vibrations and outside air currents, and immersed in a constant temperature bath. Specimen transfer is accomplished by an intricately designed set of valves and tubes utilizing pressured air or fluid during various stages of the circuit out of and back into the hot cell. The densitometer is controlled by a Hewlett Packard 9828T desk-top computer, which also acquires and stores the data. Disks are cleaned before and after density measurements in a sequence of ethyl alcohol, acetone and Freon 113 baths in the cell. A number of disks are rerun to establish the precision of their density measurements. Density changes of irradiated disks are determined by comparing with density measurements of unirradiated controls. These controls serve as standards that are intermittently rerun to check the accuracy of the machine. The densitometer processes about 10 disks per hour. The experimental precision (standard deviation, $\pm 1\sigma$) determined from repeated measurements on a single unirradiated control specimen is 0.005 g/cm^3.

The precision determined for multiple unirradiated control disks, each with repeated density measurements, varied from 0.004 to 0.01 g/cm^3 for several heats of type 316 and the USPCA. The precision for a single irradiated disk varied from 0.001 to 0.007 g/cm^3, with many disks falling nearer the upper value at 500°C. The precision for a given alloy irradiated at 500°C, determined by measuring multiple disks, ranged from 0.002 to a worst case of 0.06 g/cm^3, with most numbers falling between 0.01 and the lower limit. TEM was performed on a large number of Japanese disks, many of which were duplicates of those whose density was measured in this work, and these results are reported elsewhere.[15,16] Some TEM observations of US disks whose densities had been measured beforehand are included in this report.

ORNL-PHOTO-1367-86

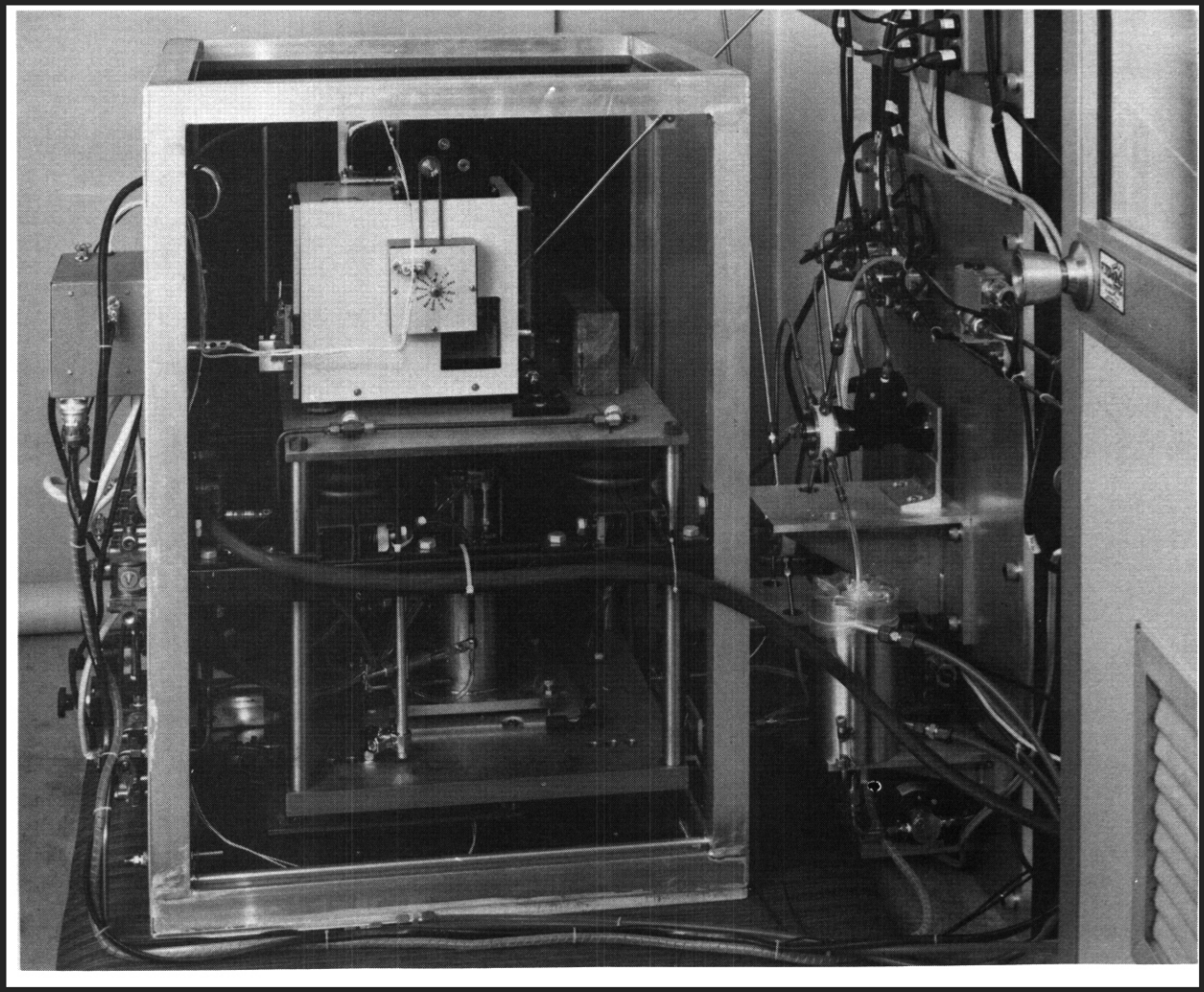


Fig. 1. The weight cell containment module of the precision densitometer, in position behind a hot cell.

Results and Discussion

1. Japanese Steels

Very little change in density could be detected after irradiation at 300 and 400°C to 34 dpa (and up to 2500 appm He). Immersion density and swelling data are given in Table 4, along with control density data, and swelling is plotted as a function of irradiation temperature for JPCA in the solution annealed (SA) and 20% cold worked (CW) conditions in Fig. 2. In this lower temperature range, swelling remains below about 0.2% regardless of alloy composition or pretreatment condition, with the exception of 20% CW J316, which shows 0.52% swelling at 300°C. There is also fairly good agreement between TEM and density determinations of volume swelling at 300 to 400°C. However, at 500°C for most alloys, swelling is generally higher and becomes quite sensitive to both alloy composition and pretreatment condition.

At 500°C, swelling increases by a factor of about 2 for 20% CW JPCA, and by nearly an order of magnitude for SA JPCA, relative to 400°C after 34 dpa. Swelling of SA JPCA is about 2.8% at 500°C, and swelling of SA 5316 is 5%. The dose dependence of JPCA and J316 in the 20% CW condition at 500°C is shown in Fig. 3, and density and swelling data for all alloys irradiated to 57 dpa at 500°C is given in Table 5. Swelling of the 20% CW JPCA at 500°C increases at the modest rate of about 0.02%/dpa to 1.26% after 51 dpa. Swelling increases more rapidly in 20% CW J316, at a rate of 0.05%/dpa, and is nearly 2% after 57 dpa. At 500°C, there is also a larger discrepancy between density and TEM determinations of swelling, as shown in Fig. 4 for SA, 20% CW 5316, and JPCA. While the relative swelling differences among alloys remain similar, TEM measurements of cavity volume fraction consistently underestimate the swelling. This is understandable, however, given the typical cavity microstructure in an analyzed area of SA JPCA, for example, irradiated at 500°C to 34 dpa in Fig. 5. In the thin areas necessary to resolve the very fine bubble structures present in these titanium-modified steels, it is easy for the large voids, which contribute most of the swelling, to be etched out by the polishing, and missed. To view these voids, one must observe areas where the foil is quite thick, and fine microstructural features are difficult to resolve.

Examination of the various thermomechanical pretreatments given to the JPCA showed that the 20% CW condition produces the best swelling resistance at 500°C, as illustrated in Fig. 6. The 20% CW and aged materials show about the same swelling behavior, and 15% CW shows slightly more swelling. There is a definite advantage of cold working relative to solution annealed material at 500°C. The SA JPCA shows a surprising sensitivity of swelling to annealing temperature, with swelling resistance becoming much worse as the annealing temperature increases. This is surprising, because higher annealing temperatures are usually recommended for titanium-modified steels, to ensure dissolution of MC and homogenization.[6]

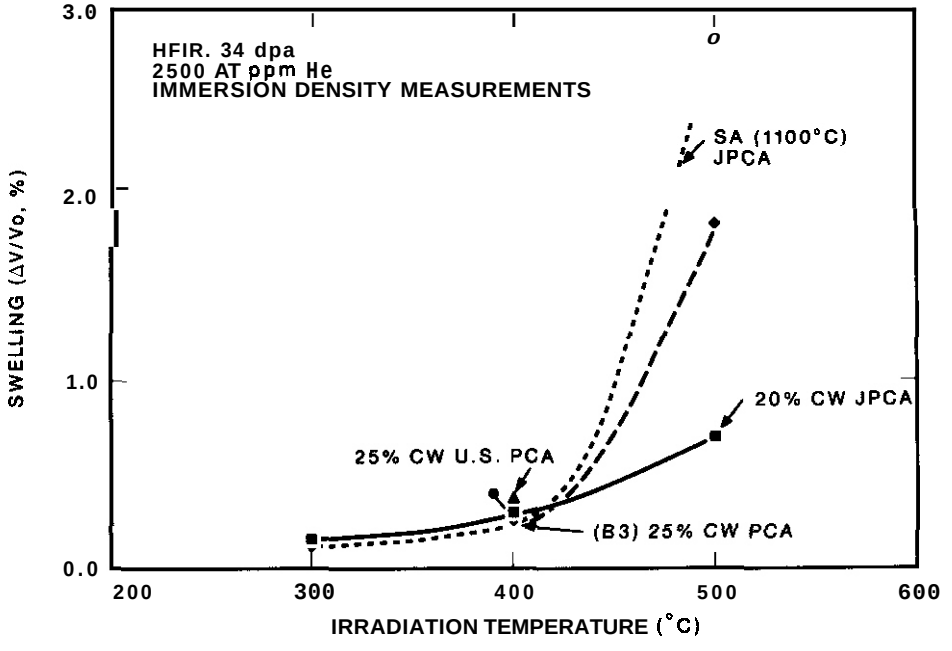


Fig. 2. A plot of immersion density determined swelling as a function of irradiation temperature for USPCA and JPCA irradiated to 34 dpa and about 2500 appm He in HFIR.

Table 4. Immersion density swelling measurements of austenitic stainless steel disks irradiated in HFIR to 34 dpa and up to 2500 appm He

Alloy	Pretreatment	Unirradiated Control Specimens		Irradiated Specimens		Swelling (%)
		Specimen ID	Density (g/cm^3)	Specimen ID	Density (g/cm^3)	
Japanese Alloys, HFIR-JP1, 300°C, 34 dpa						
J316	SA (1050°C)	SS1	7.8950	K1	7.8870	0.10
	20% CW	SC1	7.9100	L2	7.8700	0.52
JPCA	SA (1100°C)	PS2	7.9250	81	7.9140	0.14
	20% CW	PC3	7.9200	F2	7.9070	0.16
JPCA-C	SA (1100°C)	CS1	7.9114	G1	7.9010	0.13
JPCA-K	SA (1100°C)	KS1	*1.8820*	T1	7.9020	−0.25
Japanese Alloys. HFIR-JP3, 400°C, 34 dpa						
J316	SA (1050°C)	SS1	7.8950	K10	7.8810	0.18
	201 CW	SC1	7.9100	L10	7.8960	0.18
JPCA	SA (1100°C)	PS2	7.9250	B10	7.9050	0.25
	20% CW	PC3	7.9200	F10	7.8970	0.29
	20% CW + aged[a]	PA1	7.9040	M10	7.8960	0.10
JPCA-C	SA (1100°C)	CS1	7.9114	G10	7.9050	0.08
JPCA-K	SA (1100°C)	KSL	*1.8820*	T10	7.9020	−0.25
U.S. Alloys, HFIR-JP3, 400°C, 34 dpa						
00316	20% CW	AL63	7.8392	AL79	7.8590	−0.25
PCA	25% CW	EC151	7.9292	EC65	7.8990	0.38
	SA + aged[b] + 25% CW (B3)	EL-AVC	7.9274	EL83	7.9010	0.31
EP838	20% CW	EP99	7.6804	EP96	7.6420	0.50
JPCA-C	SA (1100°C)	CS1	7.9114	G1	7.9010	0.11
Japanere Alloyr, HFIR-JP7, 500°C, 34 dpa						
J316	SA (1050°C)	SS1	7.8950	K22	7.5158	5.05
	20% CW	SC1	7.9100	L22	7.8353	0.87
JPCA	SA (1175°C)	PS2	7.9250	A11	7.6855	3.07
	SA (1100°C)	PS2	7.9250	B22	7.7060	2.84
	SA (1050°C)	PS2	7.9250	C14	7.6609	3.44
JPCA	15% CW	PC3	7.9200	*022*	7.8160	1.32
	20% CW	PC3	7.9200	F22	7.8648	0.70
	20% CY + aged[a]	PA1	7.9043	M23	7.8131	1.17
	20% CW + aged[b]	PA1	7.9041	N19	7.8160	1.13
JPCA-C	SA (1100°C)	CS1	7.9114	G22	6.7920	16.48
	20% CW	CS1	7.9114	H12	7.6945	2.82
JPCA-K	SA (1100°C)	KS1	7.8820	T22	7.2854	8.19
U.S. Alloys, HFIR-JP7, 500°C, 34 dpa						
MFE ref. 316	20% CW	AC-AV3[c]	7.8954	AC11?	7.8181	0.61
PCA	SA + aged[b] + 25% CW (B3)	EL-AVC	7.9274	EL125	7.7844	1.84
D9-F	25% CW	GE-51	7.8772	GF43	7.1188	1.27
D9-J697	25% CW	GH28	1.9227	GH30	7.7126	2.72
				GH37	7.6784	3.18
D9-A7	25% CW	BA29	7.8250	BA24	7.8048	0.26
				BA25	7.7919	0.43
PCA-1	25% CW	FC65	7.9654	FC73	7.5534	5.45
				FC80	7.5269	5.81
PCA-3	25% CY	FG119	7.9518	FG116	7.8292	1.57
				FG118	7.8526	1.26
PCA-6	25% CW	FN105	7.9310	FN106	7.7957	1.76
				FN112	1.7858	1.89
PCA-8	25% CW	FS126	7.9648	FS101	7.7316	*3.02*
				FS103	7.7688	2.52
PCA-9	25% CW	FV136	7.9262	FV106	7.8747	0.65
				FW118	7.8891	0.47
PCA-00	25% CW	HH52	*1.9236*	HH36	7.7517	2.22
				HH46	7.7671	2.01
PCA-10	25% CY	FX105	7.9351	FX62	7.6706	1.45
				FX64	7.6668	3.50
PCA-11	25% CW	FY129	7.9159	FY106	7.7238	2.49
				FY95	7.1238	2.49
PCA-12	25% CW	FZ65	7.9593	FZ42	7.8210	1.17
				FZ50	7.8298	1.65
PCA-13	25% CW	HA95	7.9375	HA100	7.7839	1.97
				HA121	7.7923	1.86
PCA-16	25% CW	HD99	7.9059	HD86	7.1054	2.60
PCA-17	25% CW	HE96	7.9190	HE70	7.6423	3.62
PCA-18	*251* CW	HF109	7.9021	HF79	1.5446	4.75
PCA-19	25% CW	HT75	7.9182	HT54	7.8403	0.99
				HT61	7.8791	0.49
PCA-20	25% CW	HV58	7.9126	HV61	1.8739	*0.15*
				HV57	7.8651	0.86
PCA-21	25% CW	HW35	7.9042	HW54	7.8611	0.55
				HW59	7.8551	0.61
PCA-22	25% CW	HX57	7.9260	HX52	7.8944	0.40
				HX55	7.8827	0.55

[a]Aged 2 h at 800°C.
[b]Aged 8 h at 800°C.
[c]AV means the average of density measurements on several duplicate specimens.

Table 5. Immersion density swelling measurements of austenitic stainless steel disks irradiated in HFIR to 57 dpa and UP to about 2500 appm He

Alloy	Pretreatment	Unirradiated Control Specimens		Irradiated Specimens		Swelling (%)
		Specimen ID	Density (g/cm^3)	Specimen ID	Density (g/cm^3)	
Japanese Alloys. HFIR-JP8, 500°C. -57 dpa						
J316	SA (1050°C)	SS1	7.8950	K26	7.3809	6.97
	20% CW	SC1	7.9100	L26	7.7499	1.98
JPCA	SA (1175°C)	PS2	7.9250	A16	7.2066	9.96
	SA (1100°C)	PS2	7.9250	B26	7.3651	7.60
	SA (1050°C)	PS2	7.9250	C15	7.5009	5.65
	15% CW	PC3	7.9200	D28	7.7864	1.71
	20% CW	PC3	7.9200	F26	7.8212	1.26
	20% CW + aged[a]	PA1	7.9043	M25	7.7892	1.48
	20% CW + aged[b]	PA7	7.9043	N22	7.7822	1.57
JPCA-C	SA (1100°C)	KS1	7.9114	G24	6.4847	22.01
	20% CW	CS1	7.9114	H14	7.5979	4.13
JPCA-K	SA (1100°C)	KS1	7.8820	T24	7.0915	11.15
	20% CW	KS1	7.8820	J13	7.6411	3.15
U.S. Alloys, HFIR-JP8, 500°C, 57 dpa						
D0316	20% CW	AL-AV3[c]	7.8511	AL70	7.7708	1.03
				AL82	7.7663	1.09
MFE ref. 316	20% CW	AC-AV3[c]	7.8654	AC101	7.8271	0.49
				AC104	7.8003	0.83
EP838	20% CW	EP99	7.6760	EP4	7.5634	1.49
				EP91	7.5515	1.65
PCA	25% CW	EC151	7.9292	EC126	7.8415	1.12
	SA + aged[b]	EL-AVC	7.9274	EL110	7.8739	0.68
	t 25% CW (83)			EL126	7.8794	0.61
09-F	25% CW	GE-51	7.8772	GF49	7.8117	0.84
				GF53	7.7584	1.53
D9-J697	25% CW	GH28	7.9727	GH17	7.7075	2.79
				GH21	7.6911	3.01
D9-A7	25% CW	BA29	7.8250	BA14	7.7913	0.43
				BA22	7.7836	0.53
PCA-1	25% CW	FC65	7.9654	FC60	7.6340	4.34
				FC76	7.5861	5.00
PCA-3	25% CW	FG119	7.9518	FG105	7.8267	1.60
				FG109	7.8137	1.77
PCA-6	25% CW	FN105	7.9330	FN107	7.8150	1.51
				FN113	7.7948	1.77
PCA-8	25% CW	FS126	7.9648	FS105	7.7243	3.24
				FS120	7.7195	3.30
PCA-9	25% CW	FV136	7.9262	FV110	7.8594	0.85
				FV112	7.8645	0.78
PCA-00	25% CW	HH52	7.9236	HH39	7.7321	2.89
				HH49	7.7241	2.99
PCA-10	25% CW	FX105	7.9351	FX69	7.5197	5.51
				FX89	7.5993	4.41
PCA-11	25% CW	FY129	7.9159	FY101	7.6368	3.75
				FY102	7.6310	3.83
PCA-12	25% CW	F265	7.9593	FZ41	7.7584	2.61
				F258	7.6989	3.40
PCA-13	25% CW	HA95	7.9375	HA101	7.6989	3.10
				HA114	7.7138	2.90
PCA-16	25% CW	H099	7.9059	HD68	7.5714	4.42
				HD81	7.6408	3.47
PCA-17	25% CW	HE96	7.9190	HE77	7.5873	4.44
				HE85	7.5819	4.52
PCA-18	25% CW	HF109	7.9027	HF74	7.4662	5.85
				HF80	7.4305	6.36
PCA-19	25% CW	HT75	7.9182	HT55	7.8377	0.62
				HT51	7.8523	0.44
PCA-20	25% CW	HV58	7.9326	HV44	7.8657	0.64
				HV47	7.8698	0.59
PCA-21	25% CW	HW35	7.9042	HW47	7.8411	0.67
				HW55	7.8485	0.57
PCA-22	25% CW	HX57	7.9260	HX43	7.8803	0.61
				HX53	7.8835	0.57

[a]Aged 2 h at 800°C.
[b]Aged 8 h at 800°C.
[c]AV means the average of density measurements on several duplicate specimens.

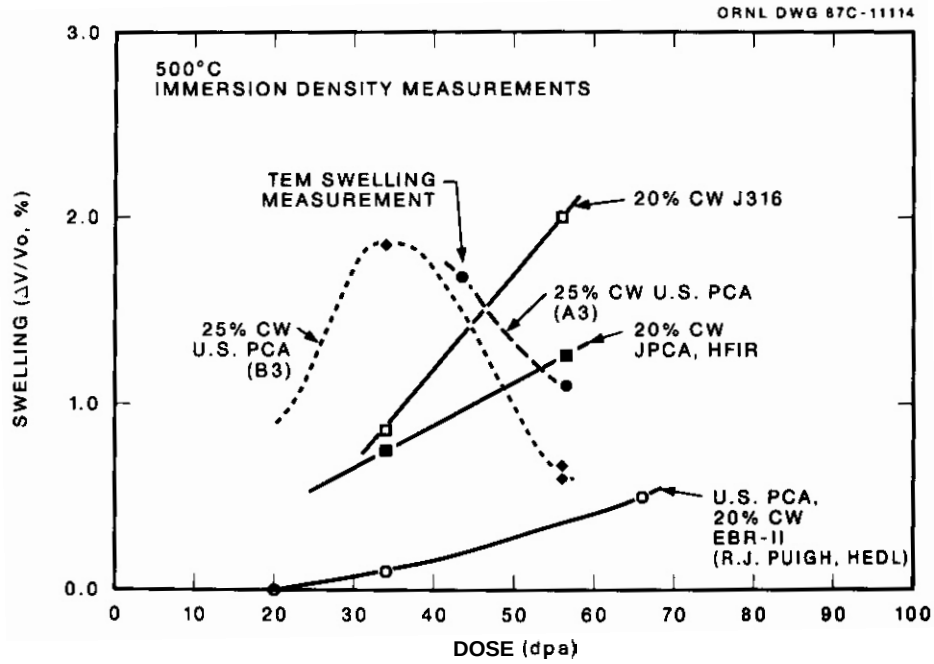


Fig. 3. A plot of immersion density swelling as a function of dose for several alloys irradiated in HFIR at 500°C. A TEM determination of swelling on 25% CW USPCA is included at 44 dpa from ref. 7. The swelling behavior of 20% CW USPCA irradiated at 495°C in EBR-II by Puigh[17] is included as a low helium (10-35 appm He) base line for comparison.

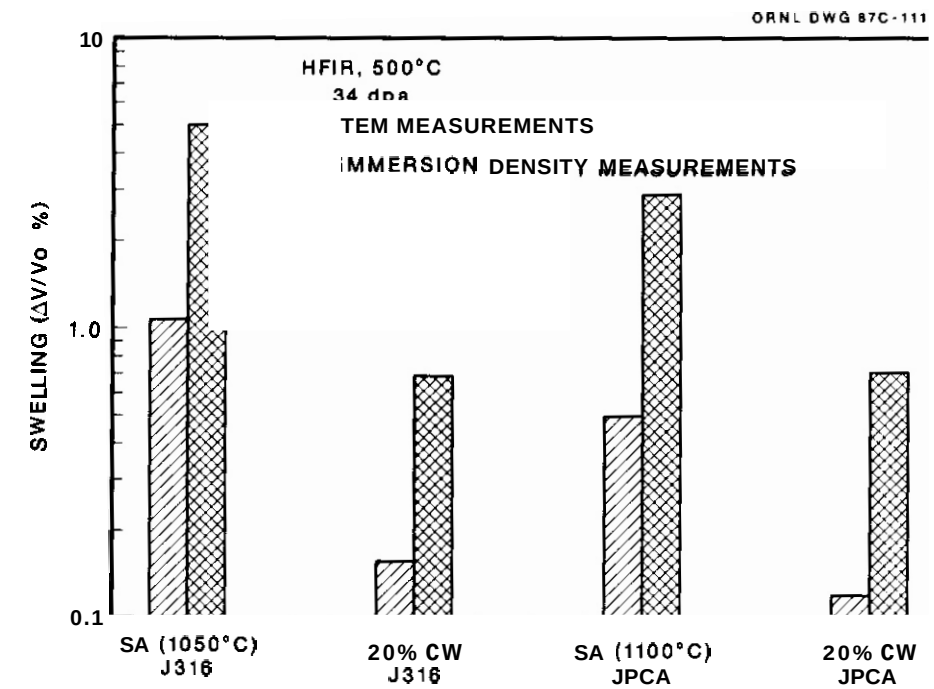


Fig. 4. A comparison of swelling measured by TEM and by immersion density change for SA and 20% CW 5316 and JPCA irradiated at 500°C to 34 dpa in HFIR.

ORNL PHOTO 4134-87

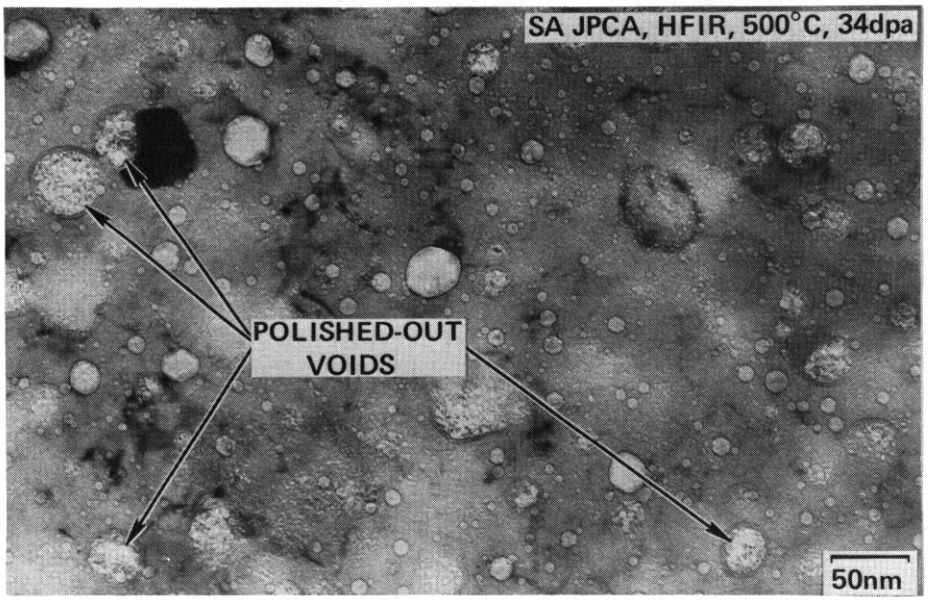


Fig. 5. TEM of SA (1100°C) JPCA irradiated at 500 C to 34 dpa in HFIR to illustrate the intersection and polishing distortion of large voids in areas that are thin enough to resolve fine helium bubbles and MC particles.

ORNL DWG 87C-11116

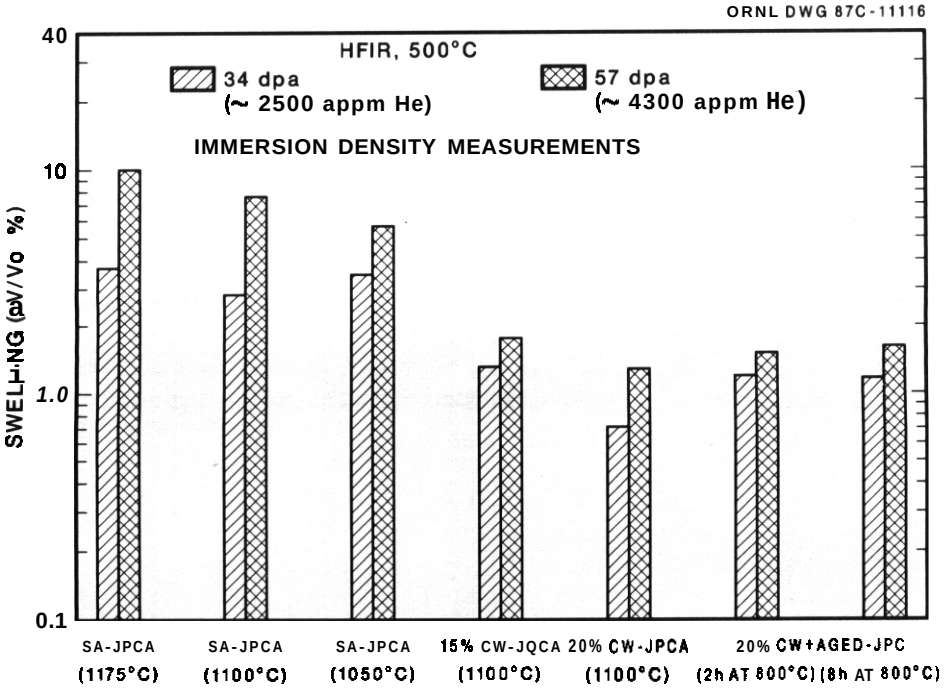


Fig. 6. Comparison of the effects of different thennomechanical heat treatments of the swelling of the JPCA irradiated at 500°C in HFIR.

Finally, reducing the carbon content (JPCA-K), or simultaneously reducing the carbon content and increasing the niobium content (JPCA-C), result in increased swelling at 500°C compared to JPCA, in both the SA and 20% CW conditions (Fig. 7). SA JPCA-C shows the highest swelling observed in the HFIR-JP series of experiments thus far, 22% after 57 dpa.

2. U.S. Steels

The temperature dependence of swelling for the USPCA is similar to that of the JPCA after irradiation to 34 dpa, with swelling being quite low at 400°C, but then increasing substantially at 500°C (see Fig. 2). After 34 dpa, swelling of the USPCA in the B3 condition (SA + aged 8 h @ 800°C + 25% CW) is about twice that of the 20% CW JPCA. However, the USPCA exhibits an unusual dose dependence of swelling, as it decreases substantially for both USPCA-B3 and -A3 (25% CW) from 34 to 57 dpa (Fig. 3). Therefore, after 57 dpa at 500°C, the 25% CW USPCA shows slightly less swelling than the 20% CW JPCA, and B 3 USPCA shows the lowest swelling of the three alloys. The B3 pretreatment was developed to provide the optimum combination of resistance to both void swelling and helium embrittlement for the PCA type alloy.[10,17] Swelling differences between USPCA-A3 (25% CW) and -B3 may be related to differences in their grain boundary microstructures. The B3 material has stable MC carbides developed prior to irradiation while no carbides form in the A3 material during irradiation. Densification due to the carbides would result in less net swelling in the B3 material. Furthermore, the difference in grain boundary precipitate microstructure could also cause differences in void formation in the immediate vicinity of the grain boundaries between the two alloys. It has been noted that the 25% CW material has necklaces of large voids near the grain boundaries that may be due to their instability and migration during irradiation.[17] By contrast, the grain boundaries of the B3 material appear to be stable due to the carbides along them, and no large voids are observed. The low swelling value for USPCA-B3 at 57 dpa is confirmed by consistent measurements from two duplicate disks.

The swelling behavior of USPCA in either the 25% CW or B3 conditions at 500°C is unusual because, by comparison, most alloys show a monotonic increase in swelling with increasing dose. This "regular" behavior is seen in Fig. 3 at 500°C for both the 20% CW JPCA irradiated in HFIR and the 20% CW USPCA irradiated in EBR-II.[18] TEM observations of the microstructural evolution of 25% USPCA CW from 34 to 44 dpa suggest insight as to why the void swelling decreases with dose (Fig. 8). While voids are present in both

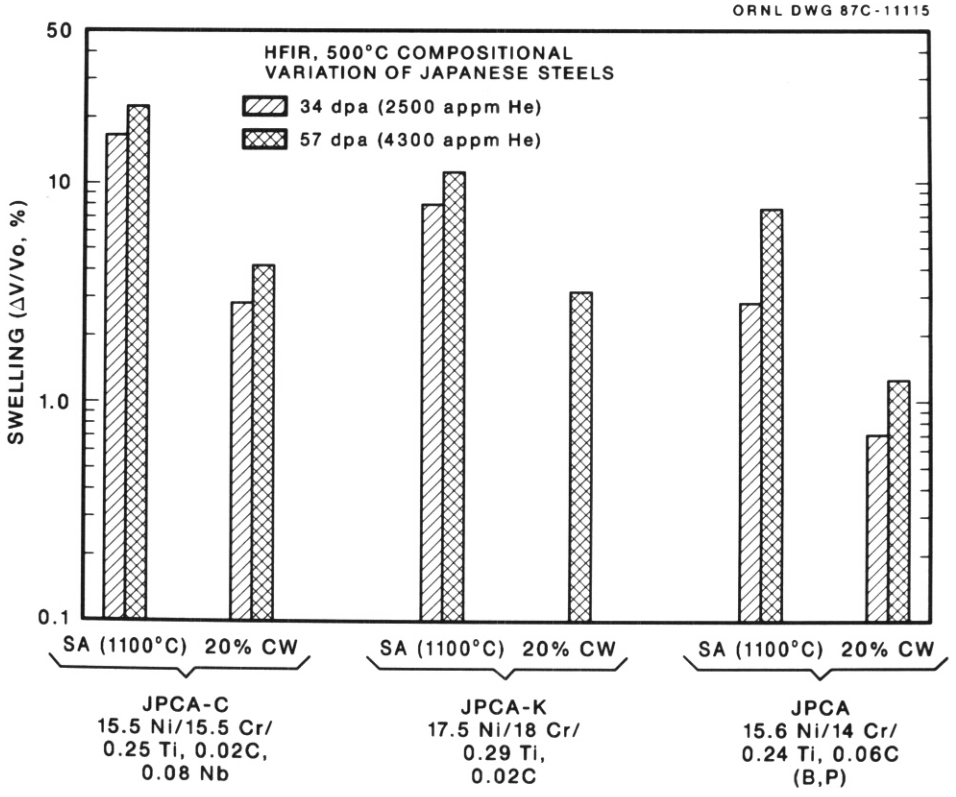


Fig. 7. Comparison of the effects of compositional variation of JPCA on swelling behavior during HFIR irradition at 500°C.

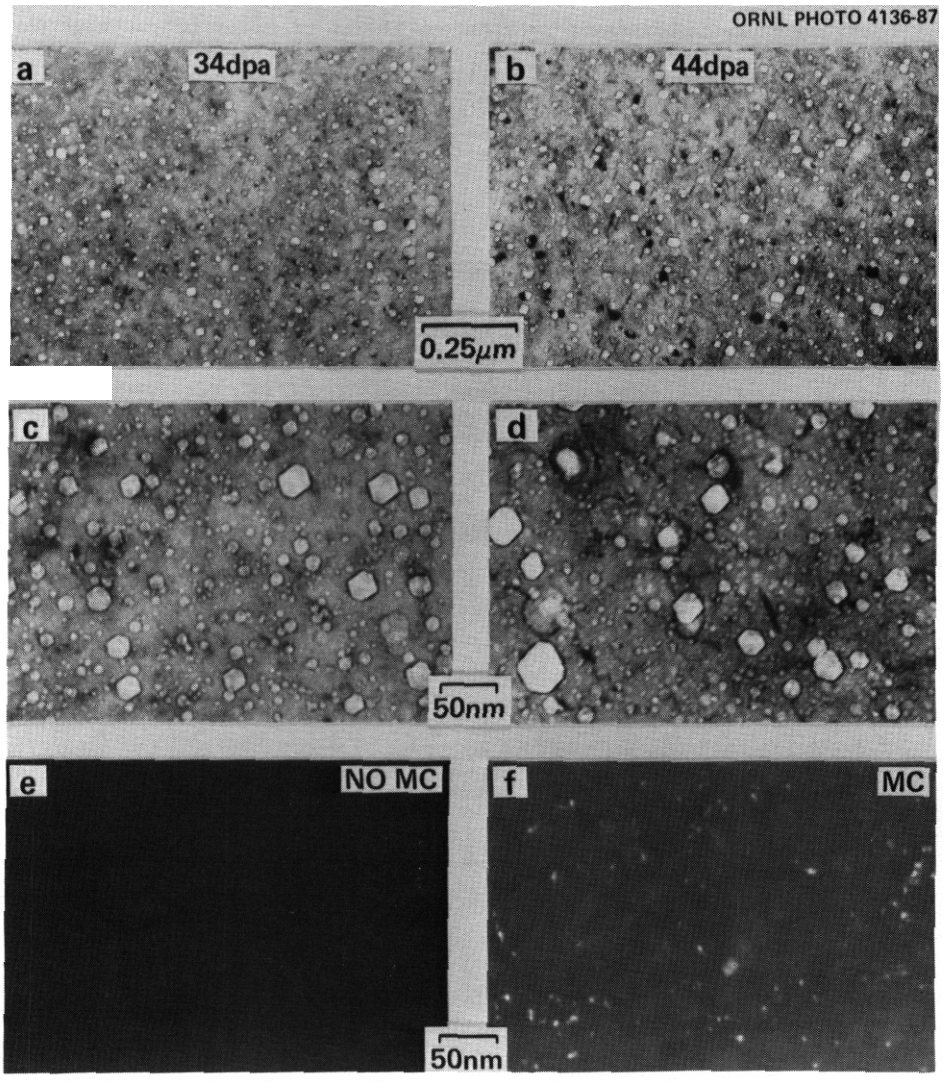


Fig. 8. A comparison of void, fine bubble and MC evolution with dose in 25% CW USPCA irradiated at 500°C in HFIR. (a) and (b) are lower magnifications of voids, (c) and (d) are higher magnifications of voids and fine bubbles in the matrix. and (e) and (f) are dark-field images to show fine MC precipitation.

microstructures. there appears to be a slight increase in the population of fine subcritical bubbles in the matrix and a decrease in the number of intermediate sized voids at 44 dpa. The largest voids appear similar in both microstructures. but only a few or the largest voids appear to be stabilized by coarser, attached precipitate particles. With regard to MC precipitation. there is an obvious increase in the population of fine particles with increasing dose [Fig. 8(e,f)]. Together. these observations suggest that an increasingly cavity-sink dominated microstructure is developing, which could lead to void shrinkage at still higher dose. While more TEM work is needed to confirm these ideas, MC is well known to have this type of strong effect on bubble and void evolution.[19] Void shrinkage is theoretically feasible if a sudden change in microstructure occurs. causing a large increase in the critical cavity size for bias-driven void growth.[20,21] A sufficiently cavity-sink dominated microstructure could reduce the net bias and cause the critical size to become very large. Voids in the microstructure could then find themselves smaller than the new critical size, and begin to shrink. Several TEM observations of void shrinkage have been noted previously in the USPCA and in 20% CW type 316 (DO-heat) irradiated in HFIR.[22,23] In each case, void shrinkage was found to coincide with large changes in either the loop or precipitate components of the microstructure with increasing dose.

Most of the U.S. data in these experiments relates to effects of alloy composition on the swelling of 20 to 25% CW material. Figure 9 shows the swelling behavior of two heats of type 316 examined in the U.S. program, DO-heat and the MFE reference heat. Both swell less than 20% CW 5316 and about the same or slightly less than 20% CW JPCA or 25% CW USPCA after 57 dpa. Both U.S. 316s are noted for their swelling resistance. Another U.S. heat of steel, N-lot 316, was not included in these experiments, because it was found to swell substantially in the 20% CW condition after only 44 dpa in HFIR.'

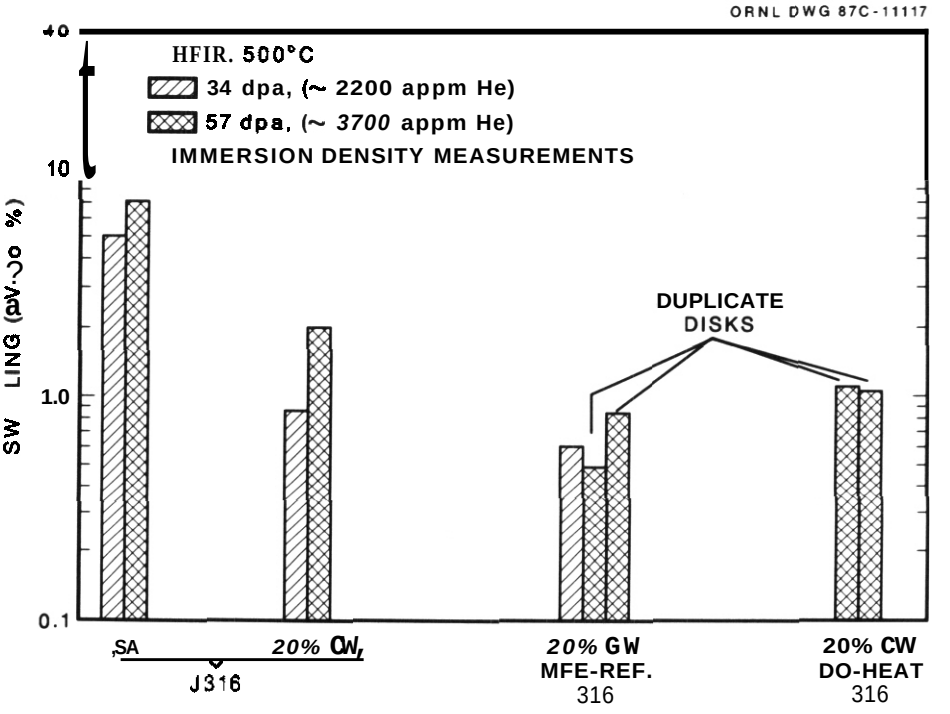


Fig. 9. A comparison of the swelling of two U S. heats of type 316 with that of 5316 irradiated in HFIR at 500°C.

Compositional effects on swelling for the USPCA were evaluated by comparing that alloy to several heats of the D9 type alloy as well as to a number of small experimental heats in which the PCA composition was modified with various combinations of minor alloying additions. Swelling data after irradiation at 500°C are included in Tables 4 and 5, and shown graphically in Fig. 10. The two heats of 09 steel showed either similar or more swelling than the USPCA after 57 dpa. However, it should be noted that the dose dependence of the D9 alloys is almost negligible between 34 and 57 dpa, suggesting that precipitate effects may also be influencing their swelling behavior. A heat of D9 modified with phosphorus (D9-A7) was included, and developed only about 0.5% swelling after 57 dpa. Figure 10 shows minor alloying element modifications (various combinations of titanium, niobium and vanadium), while varying silicon and carbon contents (PCA-00 and -1 through -13) produced no improvement in swelling resistance relative to the original USPCA. A survey of the results in Fig. 10 suggests that reductions of silicon and/or carbon levels are particularly detrimental to swelling resistance, consistent with the Japanese results presented above.

Without exception, the most effective alloying addition for swelling resistance is phosphorus. The PCA/D9 type alloys with 0.03 wt. % P or more have less than 1% swelling after 57 dpa (D9A7, PCA-9 and -19 through -22) (see Fig. 10 and Table 2). The MFE-reference heat of 316 with 0.5-0.8% swelling also has 0.03 wt % P and more than a trace level of niobium (4.08 wt %). A comparison of cavity microstructural evolution among the USPCA, D9(F) and PCA-20 after irradiation to 34 dpa shows a lack of larger voids and an abundance of very fine bubbles in the latter alloy in contrast to the former two alloys in Fig. 11. Figure 12 shows the extremely fine dispersion of MC precipitate particles that has formed among the fine bubbles of PCA-20. Neither the USPCA [Fig. 8(b)] nor D9 has much fine MC. None of the phosphorus-modified steels show any evidence of phosphide formation, as might be expected from the work of others on these and similar alloys irradiated either in an FBR or with heavy ions.[24,25] Interestingly, swelling either remains nearly unchanged or decreases slightly with increasing dose for PCA-19 through -22 (Fig. 10).

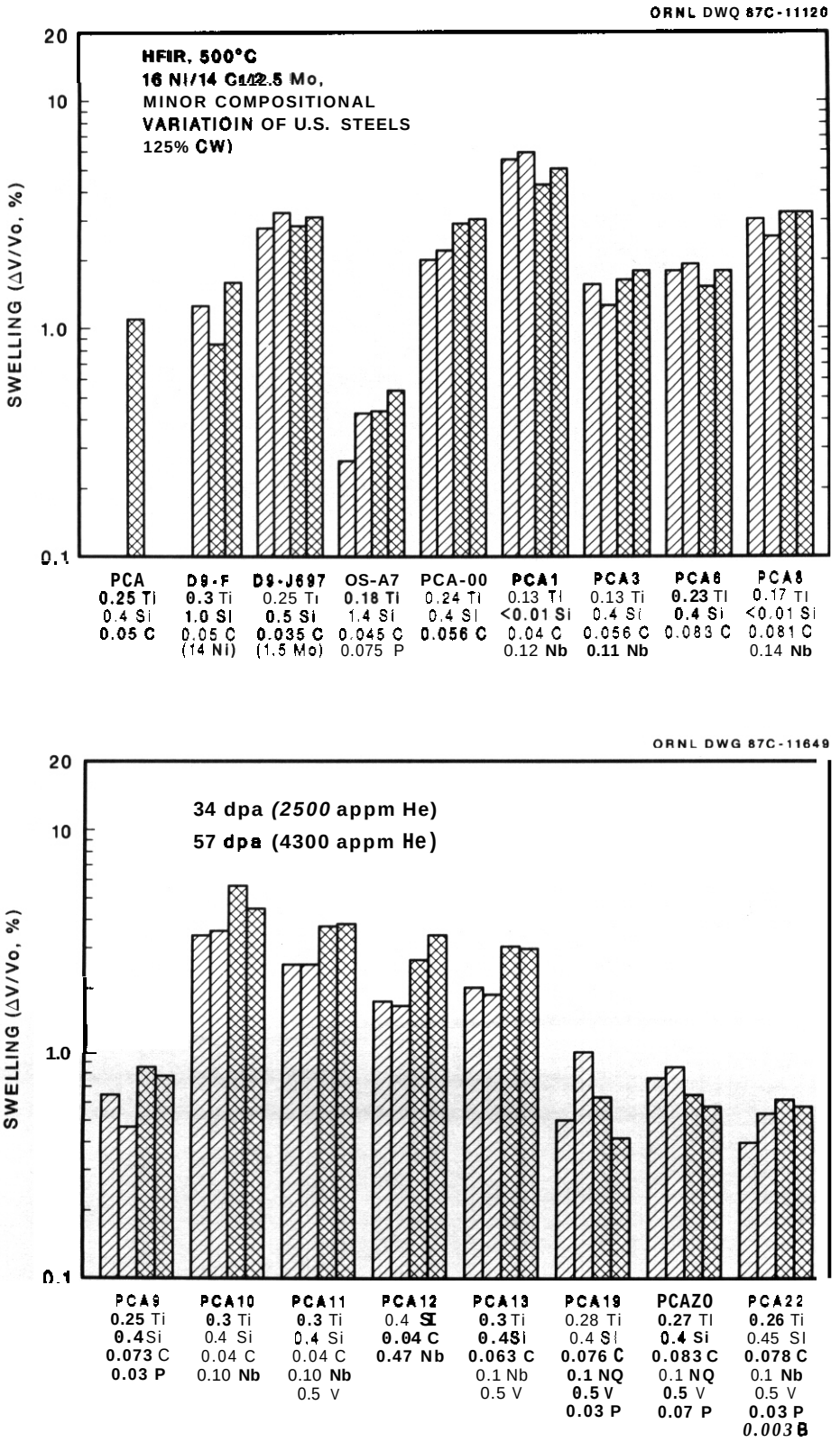


Fig. 10. A comparison of swelling for USPCA, several heats of D9, and various minor compositional variants of the USPCA, all irradiated in the 25% CW condition in HFIR at 500°C.

ORNL-PHOTO-2474-87

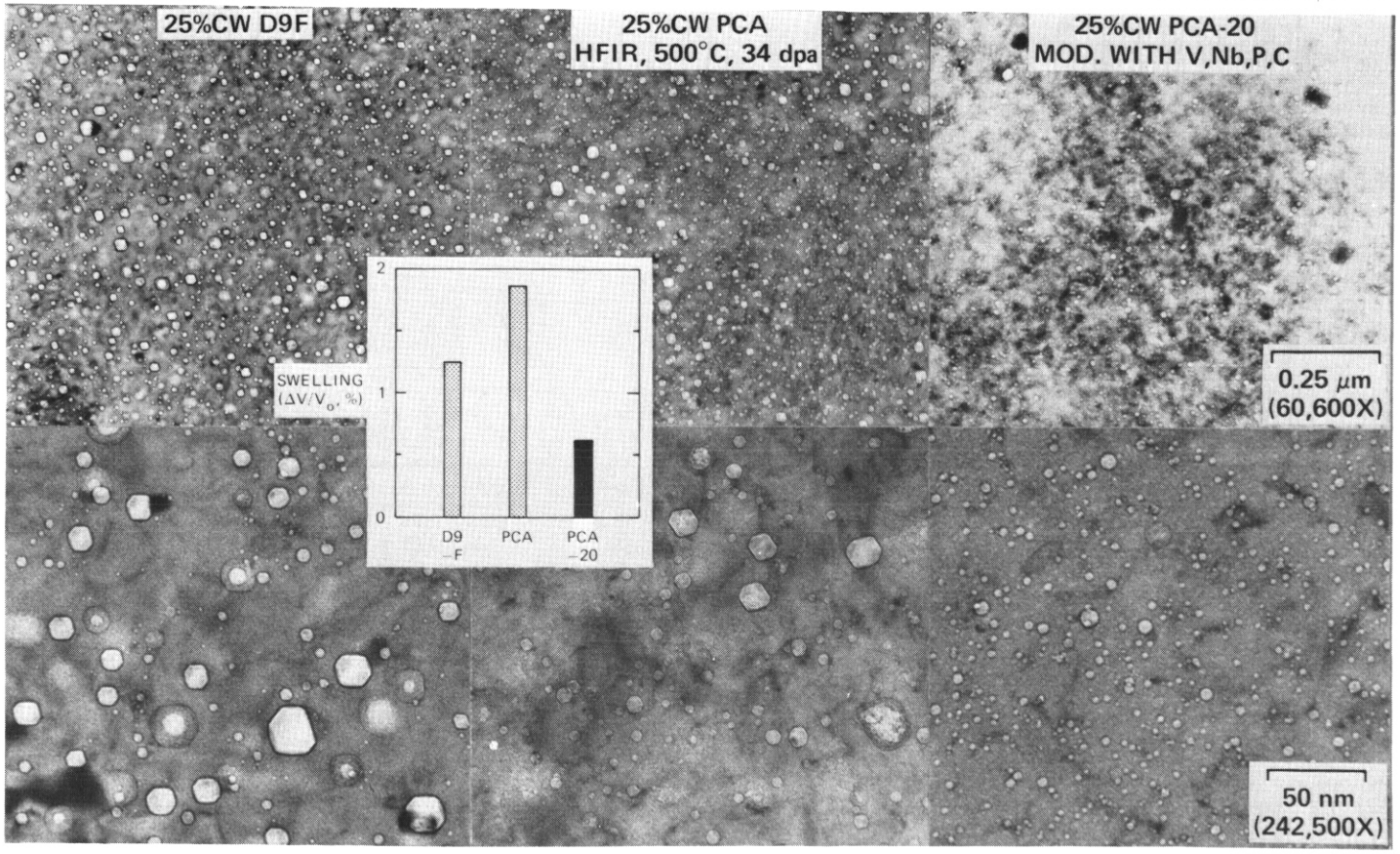


Fig. 11. A comparison of void and fine bubble microstructures for 25% CW D9(F), USPCA, and PCA-20. Note the abundance of fine bubbles and lack of voids in the phosphorus modified PCA-20.

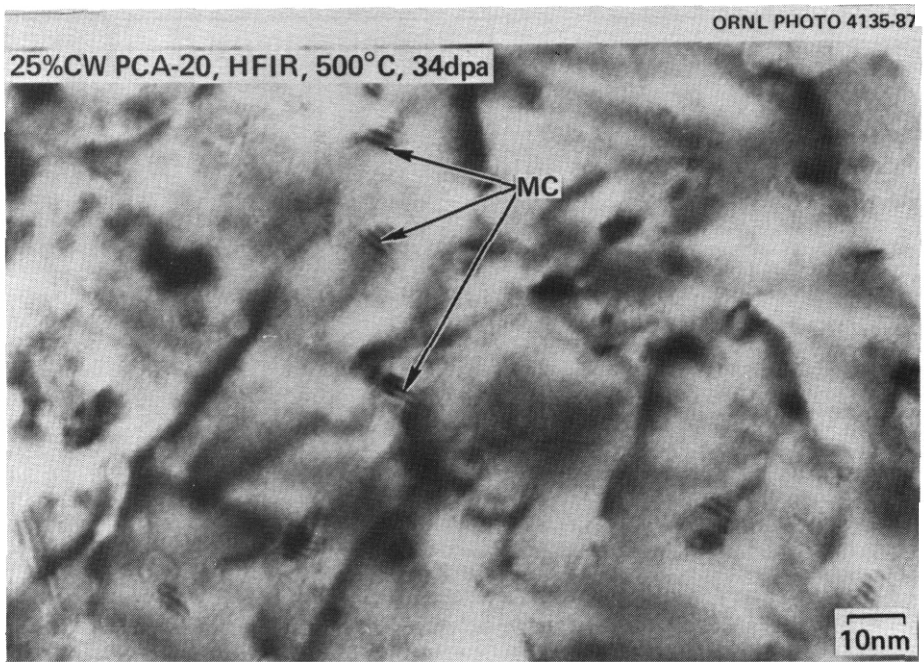


Fig. 12. Fine MC particles exhibiting Moire' fringes when imaged with g_{200} in dynamical (s = 0) contrast conditions in 25% CW PCA-20 irradiated in HFIR at 500°C to 34 dpa.

Some experimental alloys were also included with small variations in nickel and chromium relative to the base 16 Ni/14 Cr composition of the USPCA (PCA-16 through -18), as shown in Fig. 13. PCA-00 was intended to be a duplication of the original PCA (which was a large, commercially melted heat of steel), made on the same laboratory scale as the other experimental small heats of steel. The Cr-Ni variations suggest that the 16 Ni/14 Cr matrix composition of the USPCA is nearly optimum. Swelling resistance is not improved by increasing either Ni or Cr. Comparison of PCA-00 with the original USPCA suggests that impurities like nitrogen or other residual elements are also important to swelling resistance (see Table 2).

Finally, chromium content was also varied slightly in the phosphorus-modified series of alloys (PCA-20 and -21), but had little effect on swelling. In fact, the swelling results of D9-A7, PCA-9 and PCA-19 through -22 together indicate that phosphorus addition minimizes the sensitivity of swelling to variations in composition from heat to heat of steel. This factor alone is very significant for the development of swelling-resistant alloys for fusion reactors.

This work marks an end to the initial phases of alloy development of Path A alloys for the U.S. program. The B3 pretreatment appears to be the optimum preirradiation microstructural condition to impart both void swelling and helium embrittlement resistance to the original PCA alloy. An advanced austenitic with composition near the PCA-20 composition, but with additions of boron and nitrogen (0.003-0.008 and 0.01-0.03 wt %, respectively) is recommended as a candidate second generation PCA. An alloy with this composition has been melted commercially and has been shown to have outstanding high temperature thermal creep resistance at 700°C on the basis of the fine and stable dispersions of phosphide and MC precipitates that develop in annealed material.[24] The second generation PCA therefore currently has a spinoff application as a candidate superheater-reheater material for advanced steam cycle fossil power plants, and is currently the focus of Phase 2 of the Advanced Research and Technology Development (AR&TD) Fossil Energy Materials Program of the U.S. Oepartment of Energy.[10] The second generation PCA may have the potential for void swelling resistance in the solution annealed condition, whereas the current PCA/D9 alloys do not.

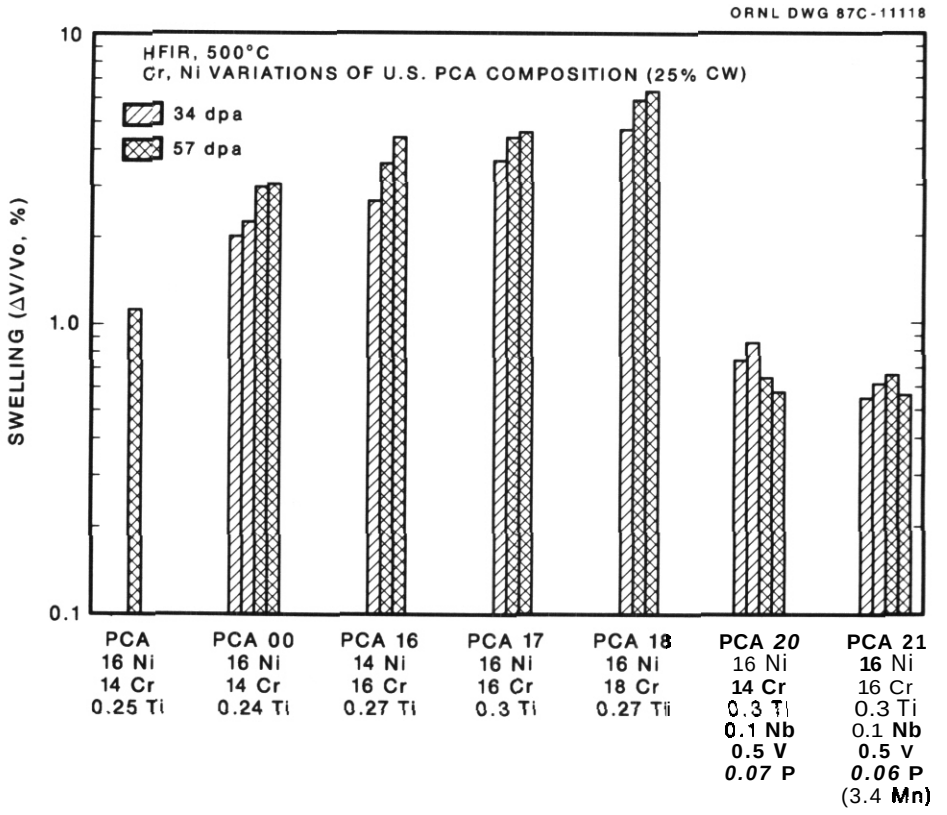


Fig. 13. Comparison of the effect of variations in chromium and nickel composition on the swelling of several PCA type alloys irradiated in HFIR at 500°C.

CONCLUSIONS

1. Density changes have been measured for Japanese TEM disks irradiated in HFIR-JPI (300°C), -JP3 (400°C), and -JP7 (500°C) to 34 dpa and in -JP8 (500°C) to 57 dpa. None of the alloys irradiated at 300 or 400°C showed much swelling, but at 500°C, their swelling was appreciable and sensitive to alloy pretreatment and composition. The JPCA showed the best swelling resistance in the 20% CW condition at 500°C (1.2% swelling after 57 dpa). Low carbon compositional variants of the JPCA had poor swelling resistance.

2. Density changes have also been measured for U.S. TEM disks irradiated in HFIR-JP3, -JP7 and -JP8. Swelling of type 316 or USPCA was low at 400°C and increased at 500°C. After 57 dpa at 500°C, 25% CW USPCA showed swelling similar to the 20% JPCA, about 1.0-1.2%, while USPCA in the B3 condition showed somewhat less swelling. The USPCA showed an unusual dose dependence of swelling at 500°C, with a substantial decrease in swelling from 34 to 57 dpa. This appears related to the latent development of fine MC precipitation and fine bubbles in that fluence range.

3. Swelling resistance of both JPCA and USPCA is better than that found in J316 at 500°C, but about the same as found in two U. S. heats of 316.

4. The same U.S. alloys included many modifications to the major and minor alloying element composition of the PCA. Several D9 alloys were included from the U.S. Fast Breeder Reactor Materials Program; they swell slightly to significantly more than the USPCA at 500°C in HIFIR. Additions of Ti, Nb, V and C alone do not improve the swelling resistance of the USPCA, and reductions of either Si or C levels make swelling much worse. By contrast, the addition of 0.03 to 0.07 phosphorus dramatically improves the void swelling resistance of the PCA/D9 type alloys. The phosphorus additions also seem to reduce the heat to heat variability of swelling resistance. Microstructurally, the void swelling resistance of PCA-20 (0.07 P) is related to the dense populations of fine bubbles and MC precipitates found after 34 dpa, whereas few fine bubbles or MC particles are found in either D9 or USPCA.

5. It is recommended that the U. S. program focus on an advanced austenitic of about the composition of PCA-20, but with more boron and nitrogen, as an alternative to the original USPCA. and acquire a larger heat of that steel.

FUTURE WORK

Future work will include continued immersion density and TEM investigation of these alloys in the remaining experiments of the HFIR-JP series. Work should begin on an advanced alternative to the USPCA. Swelling resistance of this alloy and the other compositional variants needs to be tested nearer the correct He/dpa ratio, however, before we can be confident that we can anticipate similar swelling behavior resistance in a fusion environment. Testing should include isotopic as well as spectral tailorfng. These alloys have been included in the sequential HFIR/FFTF experiments as well. A larger heat will be required for mechanical properties investigations of the advance austenitic. Further alloy development aimed toward optimization in Path A will depend on how well the current alloys continue to resist swelling, and probably must be balanced against progress made with reduced activation austenitics and the ferritic/martensitic steels of Path E.

PATENTS

An application for a patent encompassing a composition range that includes PCA-19 through -22 has been filed with the U.S. Patent Office by the U.S. Department of Energy entitled "Alloy Exhibiting Improved Radiation Resistance. Creep Resistance and Swelling Resistance." by P. J. Maziasz, D. N Braski and A. F. Rowcliffe in December of 1986 (DOE case no. S-63,612).

REFERENCES

1. J. L. Scott et al., First Annual Progress Report on United States-Japan Collaborative Testing in the High Flux Isotope Reactor and the Oak Ridge Research Reactor for the Period Ending September 30, 1984, Oak Ridge National Laboratory Report, ORNL/TM-9768, October 1985.

2. J. L. Scott et al., Second Annual Progress Report on United States-Japan Collaborative Testing in the High Flux Isotope Reactor and the Oak Ridge Research Reactor for the Period tnding September 30, 1985, Oak Ridge National Laboratory Report, ORNL/TM-10102, August 1986.

3. R. L. Klueh and E. E. Bloom, Nucl. Engin. & Design, 13 (1982) 101.

4. G. R. Hicks et al., J. Nucl. Mater. 141-143 (1986) 1018.

5. L. K. Mansur et al., J. Nucl. Mater. 139 (1986) 228.

6. P. J. Maziasz and T. K. Roche, J. Nucl. Mater. 103&104 (1981) 797.

7. P. J. Maziasz and D. N. Braski, J. Nucl. Mater. 122&123 (1984) 311.

8. P. J. Maziasz and D. N. Braski, J. Nucl. Mater. 122&123 (1984) 305.

9. P. J. Maziasz and S. Jitsukawa. p. 37 in ADIP Semiannu. Prog. Rept.. March 31, 1985. DOE/ER-0045/14, U.S. DOE, Office of Fusion Energy.

10. P. J. Maziasz, "Microstructural Stability and Control for Improved Irradiation Resistance and for High-Temperature Strength of Austenitic Stainless Steel," Proc. Conf. Microstructural Control - 86 (MiCon-86), to be published as an Amer. Soc. for Testing and Matls. - Special Technical Publication (ASTM-STP) in 1987.

11. J. J. Laidler. J. J. Holmes and J. W. Bennett, p. 41 in Conf. Proc. Radiation Effects in Breeder Reactor Materials, TMS-AIME (1977).

12. R. A. Buhl and L. J. Turner, "Remote Controlled Immersion Densitometer," Oak Ridge National Laboratory Report ORNL/TM-10378, to be published in 1987.

13. A. F. Rowcliffe. M. L. Grossbeck. and S. Jitsukawa, p. 38 in ADIP Semiannu. Prog. Rept., March 31, 1984, DOE/ER-0045/12, U.S. DOE, Office of Fusion Energy.

14. L. R. Greenwood, p. 17 in ADIP Semiannu. Prog. Rept., March 31, 1986, DOE/ER-0045/16, U.S. DOE, Office of Fusion Energy.

15. M. P. Tanaka et al.. J. Nucl. Mater. 141-143 (1986) 943.

16. S. Hamada, M. P. Tanaka, and P. J. Maziasz, p. 49 in ADIP Semiannu. Prog. Rept., March 31, 1986, DOE/ER-0045/16, U.S. DOE, Office of Fusion Energy.

17. P. J. Maziasz and D. N. Braski, J. Nucl. Mater. 141-143 (1986) 973.

18. R. J. Puigh, J. Nucl. Mater. 141-143 (1986) 954.

19. P. J. Maziasz, J. Nucl. Mater. 122&123 (1984) 472.

20. G. R. Odette and R. E. Stoller, J. Nucl. Mater. 122&123 (1984) 514.

21. L. K. Mansur and W. A. Coghlan, J. Nucl. Mater. 119 (1983) 1.

22. P. J. Maziasz and D. N. Braski, p. 28 in ADIP Semiannu. Prog. Rept., March 31, 1983, DOE/ER-0045/10, U.S. DOE, Office of Fusion Energy.

23. P. J. Maziasz and M. L. Grossbeck, p. 28 in ADIP Semiannu. Prog. Rept., March 31, 1981, DOE/ER-0045/6, U.S. DOE, Office of Fusion Energy.

24. E. H. Lee, L. K. Mansur, and A. F. Rowcliffe, J. Nucl. Mater. 122&123 (1984) 299.

25. E. H. Lee and L. K. Mansur, J. Nucl. Mater. 141-143 (1986) 695.

26. P. J. Maziasz, "Application of Analytical Electron Microscopy to Design of Creep Resistant Advanced Austenitic Stainless Steels," to be published in the Proceedings of the 45th Annual EMSA meeting, ed.. G. W. Bailey, San Francisco Press (August 1987).

IRRADIATION-PRODUCED PRECIPITATES IN AUSTENITIC STAINLESS STEELS IRRADIATED IN HFIR TO 36 dpa AT 600°C — S. Hamada and M. Suzuki (Japan Atomic Energy Research Institute, assigned to ORNL)

OBJECTIVE

The objective of this study is to evaluate the effect of titanium on the phase stability and swelling in austenitic stainless steels irradiated in HFIR to 30 dpa at 600°C.

SUMMARY

Four solution-annealed austenitic stainless steels (JPCA, low-carbon stainless steel with titanium. low carbon stainless steel with titanium and niobium. and J316) were irradiated in HFIR to 36 dpa. In JPCA. swelling was very low (0.2%) and the only phase present was MC uniformly distributed in the matrix. On the other hand, the other three alloys indicated a large amount of swelling (>1%), and coarse precipitates, (mainly G, Laves, and η-phase) were observed in low concentration throughout the matrix.

PROGRESS AND STATUS

Experimental procedures

The chemical compositions of specimens used in the experiment are given in Table 1. The low-carbon materials (alloys C and K) are being developed to increase the corrosion resistance in water-cooled fusion reactors. These materials contain titanium for swelling resistance. Alloy C also contains a small amount of niobium to form a complex Ti/Nb carbide. Solution-annealed disks were irradiated in HFIR at 600°C. Damage levels, and helium contents produced by nuclear transmutation of nickel, are presented in Table 2. Specimens were examined in a JEM 2000FX transmission electron microscope. Precipitate compositions were analyzed on particles extracted on carbon films in order to avoid extraneous γ-ray signals from the matrix.

Table 1. Chemical compositions of austenitic stainless steels

Alloy	Content,[a] wt %												
	C	Si	Mn	P	S	Ni	Cr	Mo	Ti	Nb	B	N	co
JPCA	0.06	0.50	1.77	0.027	0.005	15.60	14.22	2.28	0.24		0.0031	0.0039	0.002
Type 316	0.058	0.61	1.80	0.028	0.003	13.52	16.75	2.46	0.005	<0.1			<0.1
C	0.02	0.51	1.56	0.017	0.007	15.6	15.4	24	0.25	0.08		0.0018	
K	0.02	0.48	1.46	0.015	0.005	17.56	17.99	26	0.29			0.004	

[a]Balance iron.

Table 2. Damage levels and helium contents in austenitic stainless steels irradiated in HFIR to ~36 dpa at 600°C

Capsule	Irradiation Temperature (°C)	Neutron Dose. dpa				Helium Content, appm			
		JPCA	J316	K	C	JPCA	J316	K	C
JP6	600	36.7	36.1	37.2	36.7	2714	2355	2989	2673

Results and discussion

Cavities observed in austenitic stainless steels irradiated in HFIR to ~36 dpa at 600°C are shown in Fig. 1. Small cavities are uniformly distributed in high concentration throughout the matrix in JPCA. Swelling is very low (<0.2%). In 316, large voids, converted from helium bubbles, were observed in low concentration in the matrix. In steels C and K, large voids were present in very high number density in the matrix. Data on cavities are given in Table 3. The phase stability — thatis, the precipitation behavior under irradiation — strongly influences swelling behavior. Figure 2 shows the precipitation

ORNL-Photo 4106-87

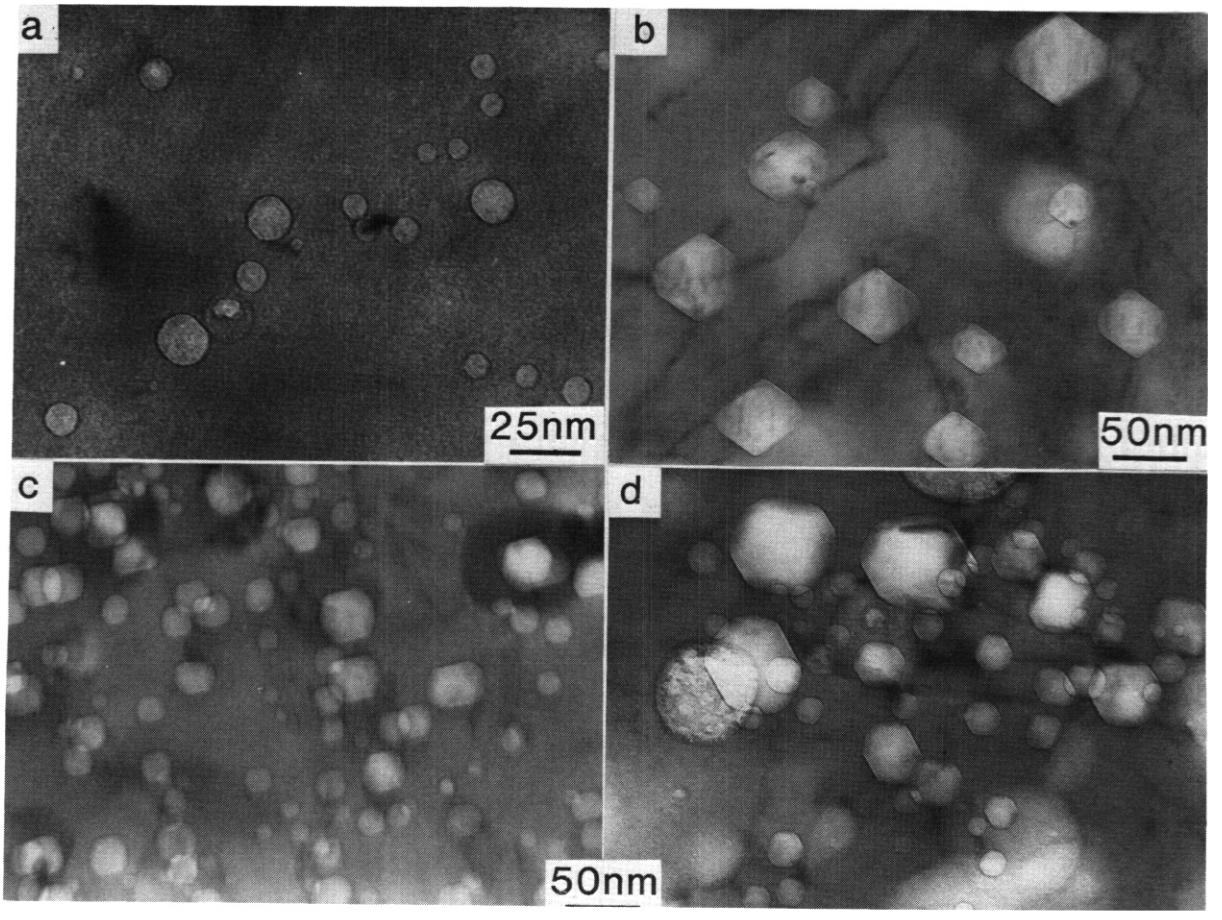


Fig. 1. Cavities observed in SA austenitic stainless steels irradiated in HFIR to ~36 dpa at 600°C. (a) JPCA, (b) 316, (c) alloy C, and (d) alloy K.

Table 3. Cavity data on austenitic stainless steels irradiated in HFIR to ~36 dpa at 600°C

	Diameter (nm)	Concentration (m^{-3})	Swelling[a] (%)
JPCA	6.3	1.7×10^{22}	0.22
J316	33.9	4.8×10^{20}	1.00
C	17.1	2.8×10^{20}	1.16
K	24.0	2.2×10^{20}	1.20

[a]Swelling calculated from cavity-volume fraction.

behavior in these alloys. In JPCA, interstitial loops produced by irradiation grow and intersect to form line dislocations. Small precipitates with Moire´ fringes nucleate and grow on these dislocation lines in high concentration. These precipitates trap helium and small cavities develop on the interface. In 316, coarse precipitates were dispersively observed in the matrix. Cavities with intermediate size were associated with the interface of precipitates and fine cavities were often observed inside the same precipitate. Alloy C contained a higher density of coarse precipitates than J316. Most of these precipitates were associated with voids. Alloy K also contained large precipitates which are similar to those in 316. These precipitates were associated with huge voids. Precipitates observed in these alloys were extracted by carbon replica film and the chemical compositions were analyzed by EDX. Figure 3 shows small precipitates with Moire´ fringes observed in JPCA that were titanium-enriched MC type. The coarse precipitates in 316 contained internal cavities. These particles were enriched in Ni, Cr, and Si, and were identified as η-phase (M_6C) (ref. 1). Precipitates present in alloy C were classified in three types. First are the ones with relatively simple or regular shapes. Most of them were identified as nickel and silicon-rich η-phase, as shown in Fig. 4. The second type is shown in Fig. 5. Figure 5(a) and (b) shows the underfocused and overfocused image, respectively. These pictures demonstrate the presence of small bubbles inside the precipitates. The irregular surface of these precipitates indicates traces of large voids associated with the interface inside the thin foil. Figure 5(c) and (d) shows dark field images of this

ORNL-Photo 4107-87

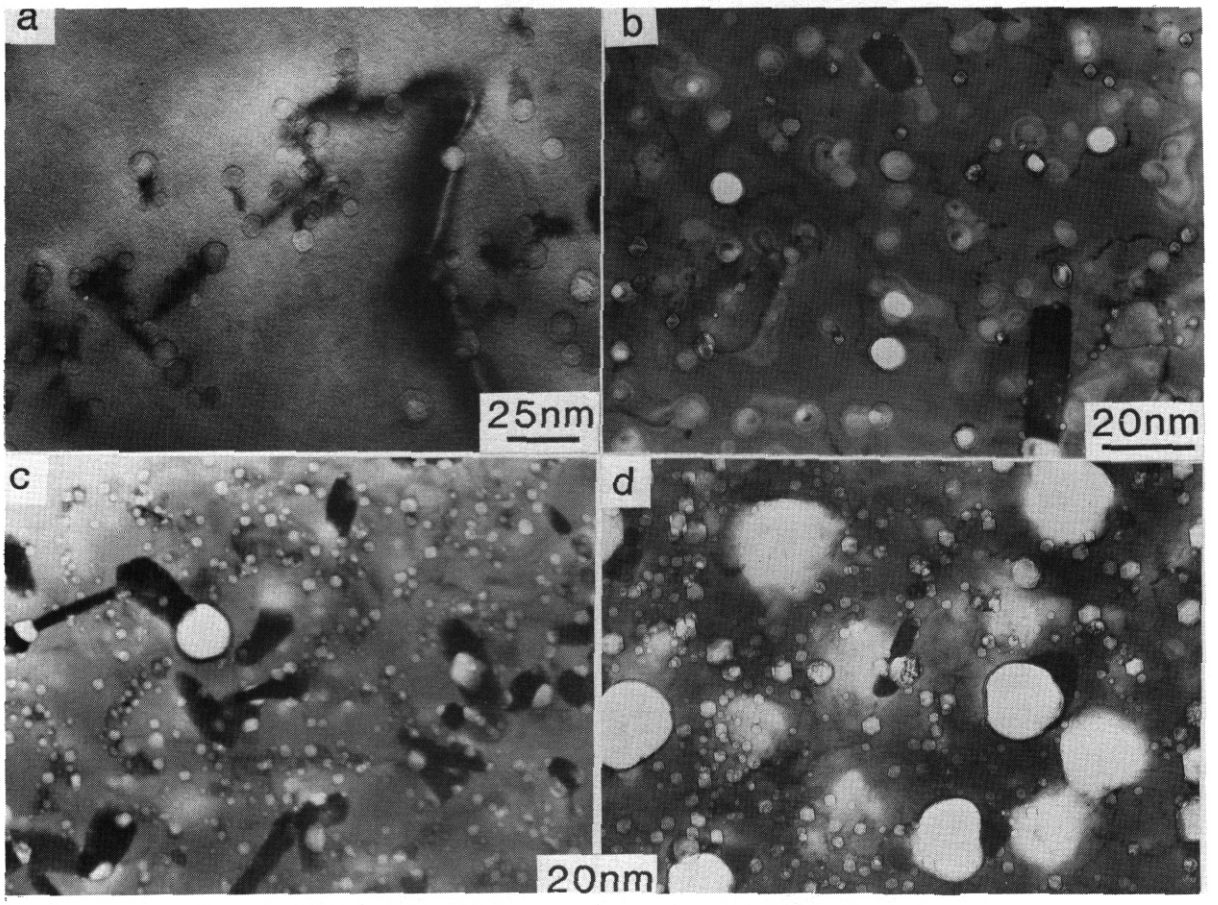


Fig. 2. Precipitates observed in SA austenitic stainless steels irradiated in HFIR to ~36 dpa at 600°C. (a) JPCA, (b) 316, (c) alloy C, and (d) alloy K.

precipitate. These pictures indicate that this precipitate is composed of two crystal structures — thatis, two phases or one phase in two orientations. The two outer parts of the sandwich are of similar structure and composition; the central region has a different structure and composition (Fig. 6). The sandwiched region, as shown in Fig. 6, is highly enriched in nickel and silicon (positions A,C,E,F). This phase was identified as G-phase (depleted in chromium) from the chemical composition and diffraction pattern (lattice parameter a_0 = 1.12 nm). On the other hand, a phase containing significantly higher concentrations of molybdenum and chromium formed the outer regions of the sandwich, as shown in Fig. 6. The identification of this phase is in progress. The third particle type is the irregularly shaped precipitate given in Fig. 7. This particle is composed of several regions like the one described above. Each region of the particle, however, indicates the same chemical composition, unlike the precipitate shown in Fig. 5. Figure 8 shows the analyzed portions and chemical compositions in the particle. The phase is considered to be Laves, enriched in nickel and silicon. Lee et al.[2] reported the existence of sympathetically nucleated phases in CW 316 aged at 600°C for 10,000 h. The MC phase was not observed in this alloy,

The analysis for precipitates observed in alloy K is in progress. Figure 9 shows data of the chemical composition of phases. Most of the precipitates are enriched in Ni, Cr. Si, and Mo except only one [precipitate marked 'D' in Fig. 9(b)]. The precipitate marked 'D' was identified as type MC.

ORNL-Photo 4108-87

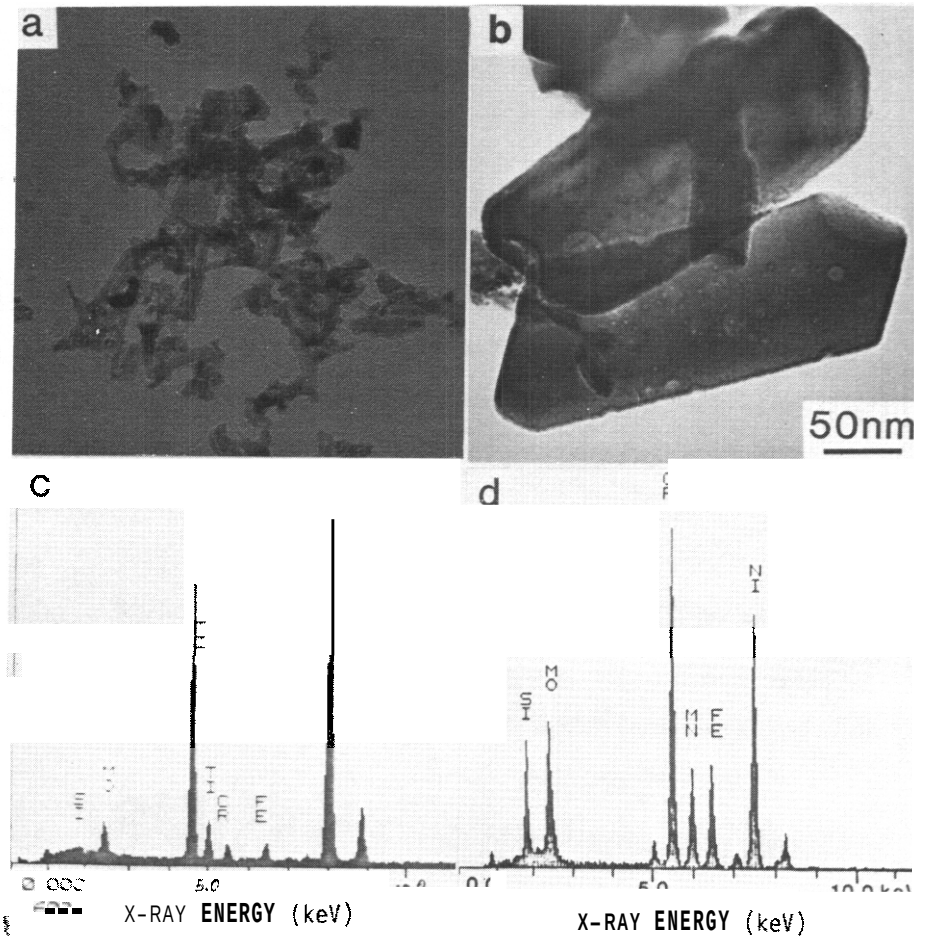


Fig. 3. Phases observed in SA JPCA and 316 irradiated in HFIR to ~36 dpa at 600°C and spectrum. (a,c) MC precipitate in JPCA; (b,d) η phase in J316.

ORNL-Photo 4109-87

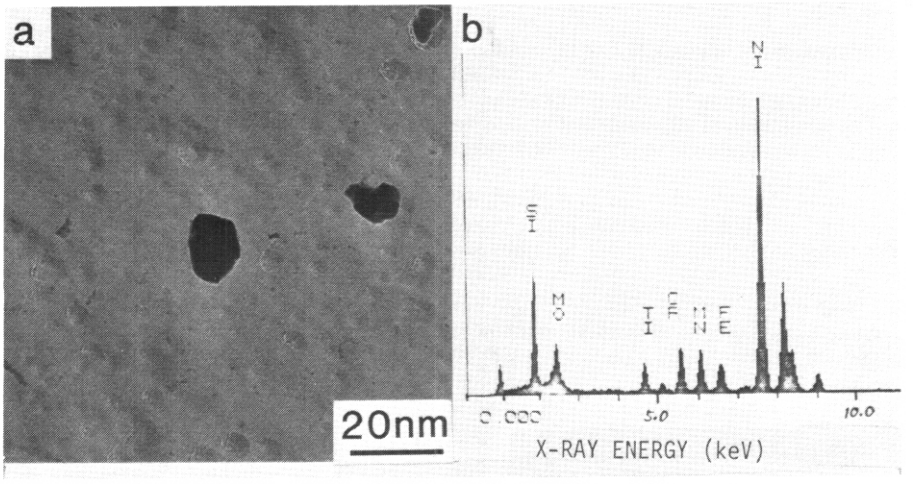


Fig. 4. Regularly shaped blocky G phase in SA alloy C irradiated in HFIR to ~37 dpa at 600°C and x-ray spectrum from extracted particle.

ORNL-Photo 4110-87

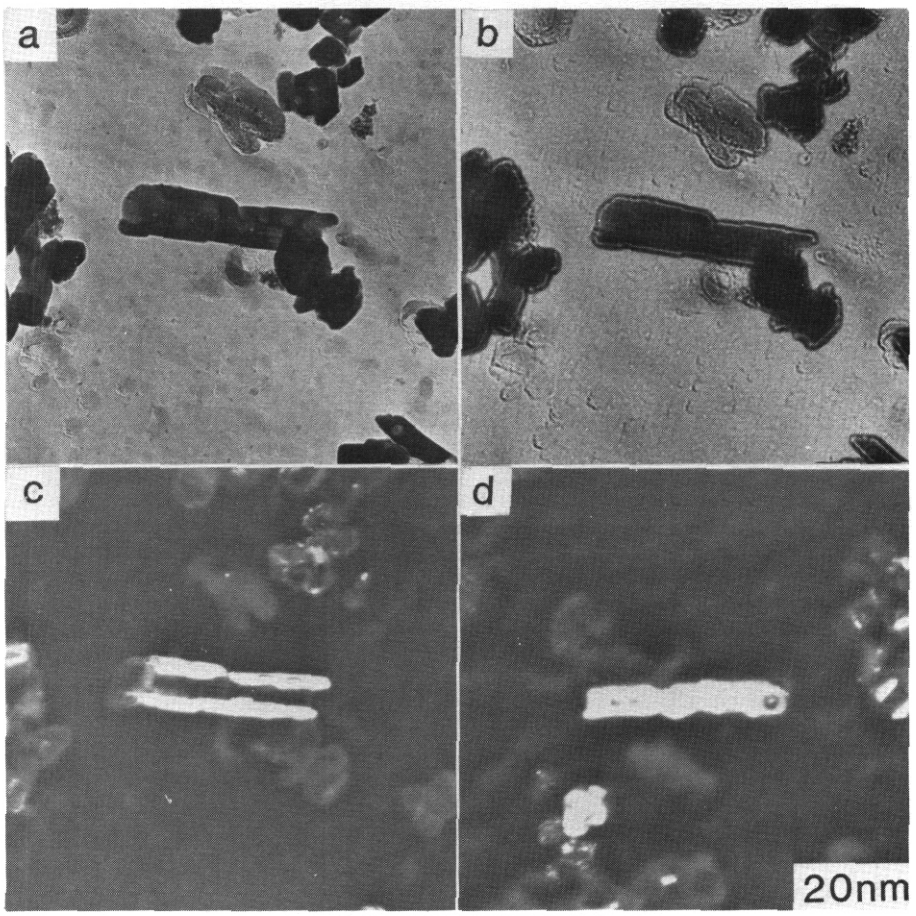


Fig. 5. Sandwiched particle extracted from SA alloy C irradiated in HFIR to 37 dpa at 600°C. (a) Underfocus, (b) overfocus, (c) and (d) dark field.

The data obtained in this experiment shows JPCA possesses superior swelling resistance and phase stability compared with the other three alloys. The low carbon stainless steels seem to indicate worse swelling resistance and phase stability than 316 stainless steel in spite of the addition of ~0.25 Ti to increase the swelling resistance. The atomic ratios of C:Ti are 1 and 0.3 in JPCA and the two low carbon stainless steels (C and K), respectively. The microstructure of solution-annealed LSIA after EBR-II irradiation to ~3 × 10^{22} n/cm^2 (~15 dpa) at 593°C has been described by Thomas.[3] LSIA contains carbon and titanium of 0.08 and 0.15 wt %, respectively — namely, the atomic ratio C:Ti is ≈ 0.5. Both the precipitate volume fraction and the void swelling reached a maximum at ~593°C, the majority of voids occurring at precipitate-matrix interfaces.[4] From the results on the swelling in the present experiment, it would be desirable for the C:Ti ratio to become unity for resistance to void swelling. In the low carbon stainless steels, however, the effectiveness of altering the C:Ti ratio to approach unity for swelling resistance remains to be demonstrated.

SUMMARY AND CONCLUSIONS

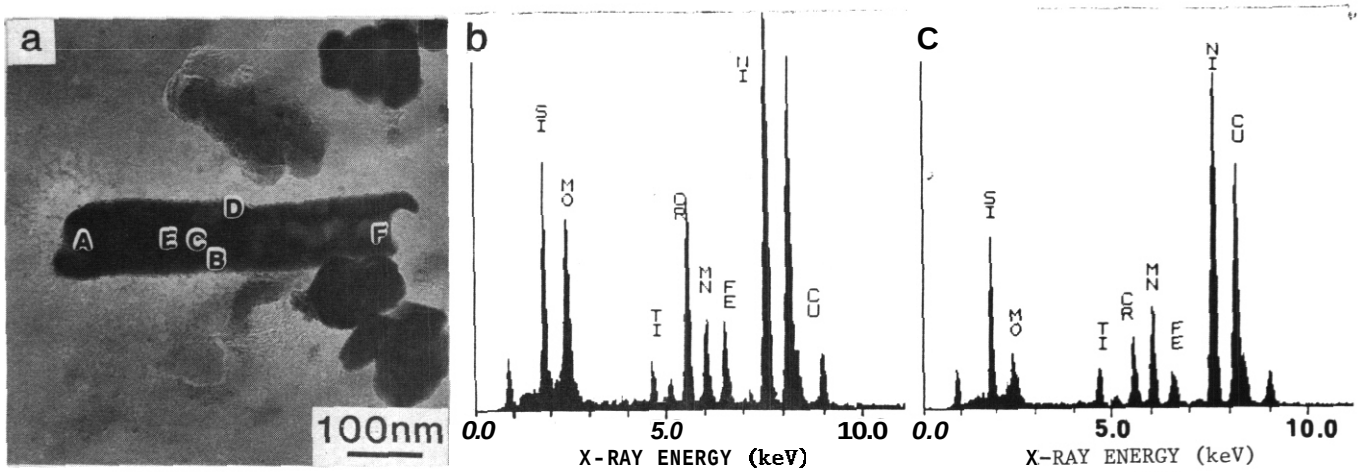
1. Solution-annealed JPCA, 316, and two low carbon stainless steels have been irradiated up to ~36 dpa and ~2500 appm He at 600°C in HFIR. Swelling was 0.2% in JPCA and more than 1% in the other three alloys.

2. The JPCA contained small MC precipitates with Moire- fringes uniformly distributed in the matrix, which were associated with small cavities.

3. Coarse η-phase (M_6C type) particles were observed in low concentration in the matrix of 316. These precipitates contain micro-cavities inside and small cavities attached on the surface.

4. Coarse G and Laves phases were found in high concentration in alloy C. Some of the particles possessed an irregular shape and were composed of several small precipitates. MC precipitates were not observed in this alloy.

ORNL-Photo 4111-87



Position Analyzed	Composition, wt %								
	Fe	Ni	Cr	Mn	Ti	Si	P	Mo	V
A	5.13	55.21	6.02	257	4.81	16.33	1.51	7.36	0.47
B	5.99	39.05	14.28	1.51	2.48	12.38	1.26	21.25	1.37
C	4.01	57.16	5.42	4.33	5.41	14.44	1.50	6.80	0.42
D	5.64	43.73	11.15	2.09	3.04	12.52	1.35	18.75	1.20
E	4.23	55.13	6.06	3.61	4.79	13.91	1.29	9.82	0.54
F	3.98	54.57	6.48	3.68	4.59	14.90	1.22	9.04	0.49

Fig. 6. Chemical compositions and x-ray spectrum of sandwich particle (a) analyzed positions, (b) x-ray spectrum from position B, (c) x-ray spectrum from position F.

ORNL-Photo 4112-87

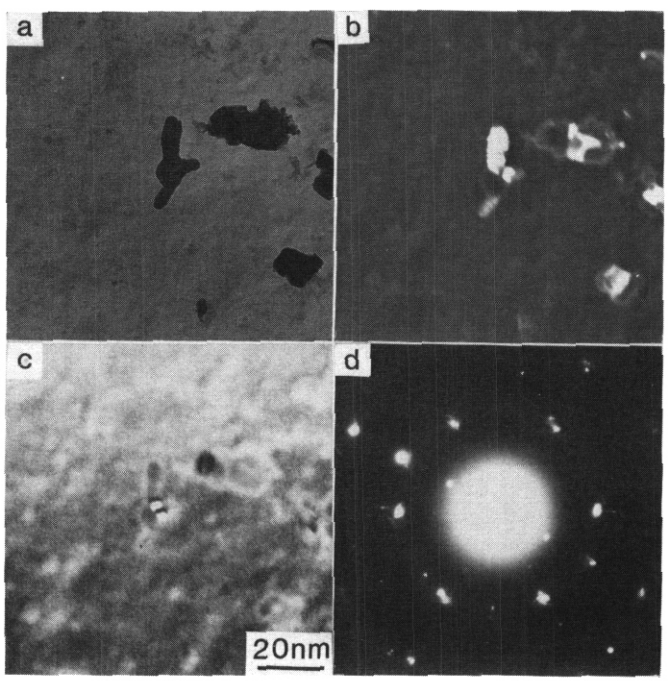
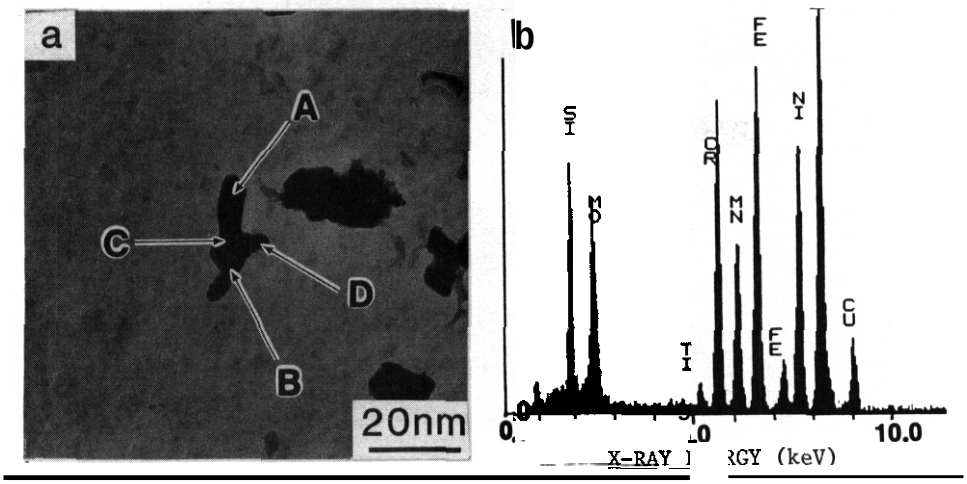


Fig. 7. Irregularly shaped particle extracted from SA alloy C irradiated in HFIR to ~37 dpa at 600°C. (a) Bright field, (b) and (c) dark fields, and (d) diffraction pattern.

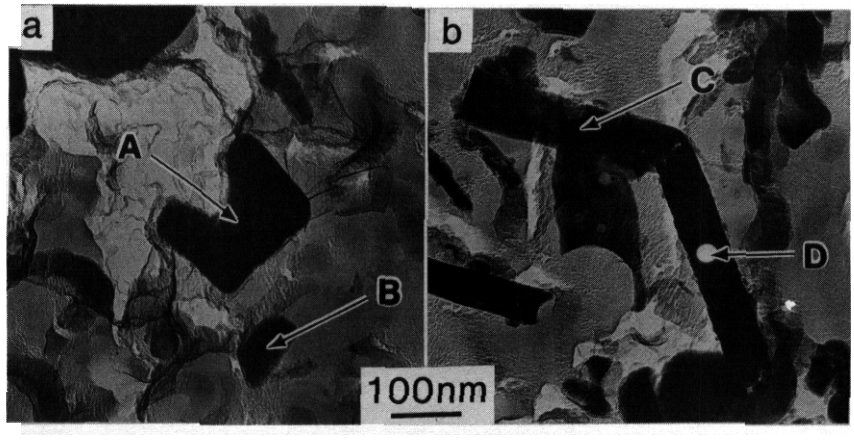
ORNL-Photo 4113-87



Position Analyzed	Composition. wt %								
	Fe	Ni	Cr	Mn	Ti	Si	P	Mo	V
A	23.63	21.79	17.05	1.23	0.30	11.23	1.16	21.47	1.33
B	11.08	20.86	22.31	0.17	0.54	10.02	1.45	30.98	1.89
C	20.53	22.47	17.33	3.47	0.13	11.64	1.61	21.84	1.29
D	21.76	22.35	16.19	1.32	0.35	11.60	1.49	21.39	1.21

Fig. 8. Chemical compositions and x-ray spectrum of irregular shaped particle extracted from SA alloy C irradiated in HFIR to ~37 dpa at 600°C. (a) Analyzed positions and (b) x-ray spectrum from region A.

ORNL-Photo 4114-87



Position Analyzed	Composition. wt %								
	Fe	Ni	Cr	Mn	Ti	Si	P	Mo	V
A	9.04	31.07	30.86	0.66	1.16	9.65	1.14	14.18	1.87
B	9.33	28.36	29.98	0.97	0.75	9.68	1.36	17.14	1.89
C	14.32	40.49	16.90	1.93	0.86	13.18	0.59	10.68	0.95
D	2.23	2.25	2.13	0.00	88.96	0.59	0.07	3.78	0.00

Fig. 9. Precipitates observed in SA alloy K irradiated in HFIR to ~37 dpa at 600°C and chemical compositions by EDX from extracted particles.

5. Irregularly shaped blocky and elongated precipitates developed in alloy K. Most of the particles were enriched in Ni, Cr, Si, and Mo. Large precipitates were associated with huge voids.

6. To increase the swelling resistance by addition of titanium, it seems desirable to maintain the atomic ratio of C:Ti at unity.

FUTURE WORK

Further study of these steels will be conducted following irradiation to ~50 dpa.

REFERENCES

1. S. Hamada, M. P. Tanaka, and P. J. Maziasz, "Irradiation-Enhanced Precipitates in Type 316 Stainless Steel Irradiated in HFIR," Fusion Reactor Materials Semiannu. Prog. Rep. Sept. 30, 1986, DOE/ER-0313/1.

2. E. H. Lee, P. J. Maziasz, and A. F. Rowcliffe, "The Structure and Composition of Phases Occurring in Austenitic Stainless Steels in Thermal and Irradiation Environments," pp. 191–218 in Phase Stability During Irradiation, TMS-AIME, Pittsburgh, PA, 1981.

3. L. E. Thomas, "Phase Instabilities and Swelling Behavior in Fuel Cladding Alloys," Trans. ANS 28, 151 (1978).

4. E. H. Lee, A. F. Rowcliffe, and E. A. Kenik, "Effects of Si and Ti on the Phase Stability and Swelling Behavior of AISI 316 Stainless Steel," J. Nucl. Mater. 83, 79–89 (1979).

MICROSTRUCTURAL CHANGE OF JPCA IRRADIATED TO 58 dpa AT 300°C IN HFIR — M. Suzuki, S. Hamada. and M. P. Tanaka (Japan Atomic Energy Research Institute, assigned to ORNL)

OBJECTIVE

The objective of this work is to determine the microstructural development and swelling behavior of JPCA irradiated in HFIR at temperatures from 300 to 600°C.

SUMMARY

Characteristic microstructural features observed in JPCA irradiated at 300°C in HFIR are the formation of many fine bubbles and dislocation loops. Radiation produced MC-type precipitates were found after only 34 dpa irradiation. The present work revealed that bubbles and dislocation loops do not show noticeable change during the irradiation from 34 (helium content: 2470 appm) to 58 dpa (helium content: 4260 appm). On the other hand, the number density of MC-type precipitates decreased during the irradiation. The microchemical examination of the precipitates showed that the chromium content decreased and the nickel and silicon were enriched during irradiation.

PROGRESS AND STATUS

Experimental procedures

The material used in the present experiment was JPCA. solution annealed, which was irradiated to 58 dpa (helium content estimated to be produced was 4260 appm) in HFIR. Chemical compositions and heat treatments are shown in Table 1. Microstructural data were obtained from thin foils and carbon replicas using a JEM 2000FX electron microscope with an energy dispersive x-ray analysis (EOS) system.'

Table 1. Chemical Compositions and Heat Treatments of JPCA Used (Heat Treatment: Solution Annealed at 1100°C)

Alloy	Content, wt %												
	C	Si	Mn	P	S	Ni	Cr	Mo	Ti	Nb	6	N	co
JPCA	0.06	0.50	1.77	0.027	0.005	15.60	14.22	2.28	0.24		0.0031	0.0039	0.002

Results and Discussion

The microstructure of JPCA irradiated to 58 dpa at 300°C was entirely covered with many fine bubbles and dislocation loops. Figures 1 and 2 show the helium bubbles and dislocation loops, which were imaged in the underfocused kinematical condition and in the dark field image using <200> streaks, respectively. Most bubbles were less than ~3 nm in diameter. Numerical data are given in Table 2. The average size and density of the bubbles were similar to the measurements made for the 34 dpa irradiated specimens. The swelling is calculated to be 0.18% at 58 dpa and 0.22% at 34 dpa. Thus, within the experimental uncertainties of the TEM method. there was no change in swelling over the range 34 to 58 dpa. As for the dislocation loops, both number density and average size decreased slightly as compared to the 34 dpa specimen.

On the other hand, the MC-type precipitate, which was the only precipitate produced by the irradiation at 300°C, exhibited some difference between 34 and 58 dpa specimens, Table 3. In the 10 dpa irradiated specimen, no MC-type precipitates were found. After 34 dpa irradiation, however, many fine MC-type precipitates were observed by the Moire' technique.2 After 58 dpa irradiation, the number density observed by the Moire' fringe was less than in the 34 dpa irradiated specimens.

The compositions of MC-type precipitates were determined using the carbon extraction replica technique. As reported previously,[3] both thermally produced and radiation produced MC-type precipitates have a size dependence on the chemical compositions. Smaller particles have a lower titanium content and a larger chromium content. Particles produced during irradiation have lower titanium contents than particles produced during thermal aging for 2 h at 800°C after 20% cold working. Figure 3 shows the titanium and chromium content of the precipitate as a function of the precipitate diameter. In the irradiated steel, reduction of titanium content in the MC-type precipitate was compensated by the increase of chromium, nickel, and silicon. It was found that the nickel and silicon concentrations in the MC particles tended to increase with increasing fluence whereas the chromium concentration tended to decrease, Fig. 4.

ORNL-PHOTO-4115-87

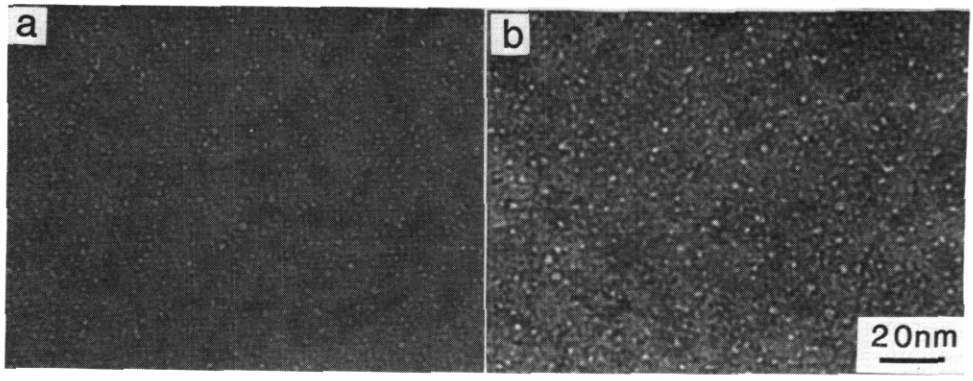


Fig. 1. Bubbles Observed in JPCA Irradiated at 300°C in HFIR to (a) 34 dpa and (b) 58 dpa.

ORNL-PHOTO-4116-87

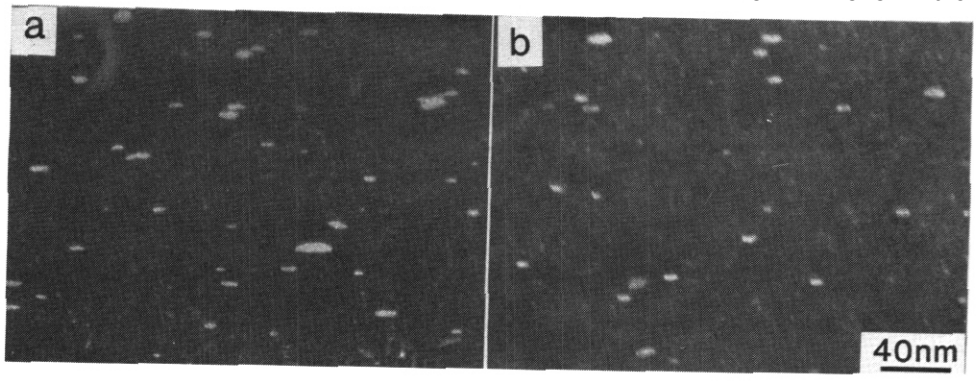


Fig. 2. Dislocation Loops in JPCA Irradiated at 300°C in HFIR to (a) 34 dpa and (b) 58 dpa.

Table 2. Microstructural Data of JPCA Irradiated at 300°C in HFIR

		33.6 dpa	50 dpa
Bubble	Density (m^{-3})	2.4×10^{23}	2.1×10^{23}
	Average Diameter (nm)	2.7	2.5
	Swelling (%)	0.22	0.18
Loop	Density (m^{-3})	4.7×10^{27}	1×10^{22}
	Average Diameter (nm)	11.5	9.9

Table 3. Concentration of MC Particles (m^{-3})

	10 dpa	33.6 dpa	50 dpa
300°C	N.D.	19×10^{22}	S
400°C	--	19×10^{22}	--

N.D. = none detected.
S = small ($< 2 \times 10^{21}$ m^{-3}).

The reasons for the size-dependence of composition is not clear at the present time. However, it should be noted that the radiation-induced changes in compositions increase in magnitude as the particle size decreases. One possibility is that the composition changes during irradiation as a result of solute segregation and recoil mixing across the interface.

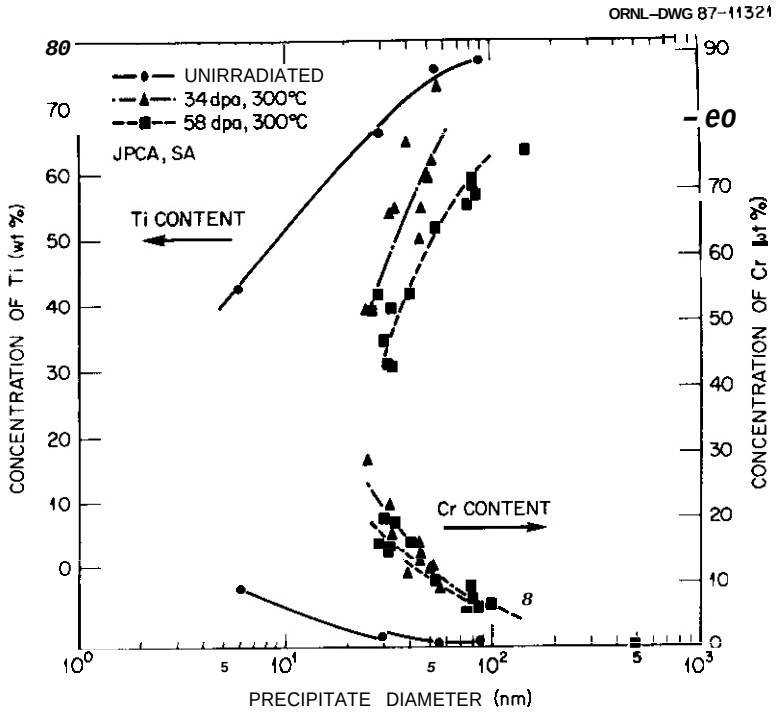


Fig. 3. Concentration of titanium and chromium content in MC-type precipitate as a function of precipitate diameter.

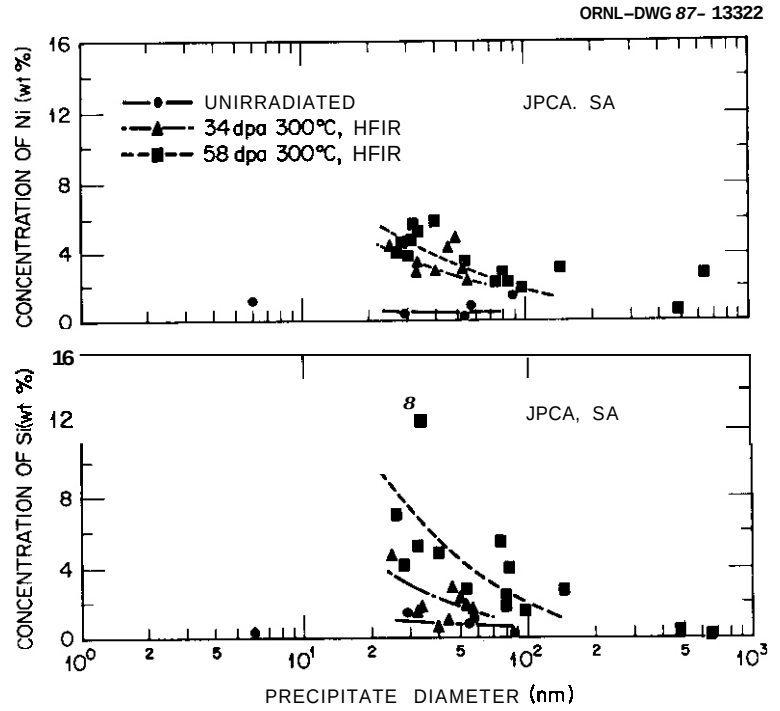


Fig. 4. Concentration of nickel and silicon content in MC-type precipitate as a function of precipitate diameter.

CONCLUSIONS

Observation of JPCA irradiated to 58 dpa at 300°C in HFIR revealed the following results:

1. At the irradiation temperature of 300°C, characteristic features of the microstructures are the formation of many fine bubbles (~3 nm) and dislocation loops. Average bubble size did not grow during the irradiation from 34 to 58 dpa, and hence swelling was almost the same at 34 and 58 dpa. Both density and average size decreased slightly.

2. A titanium-rich MC-type precipitate was the only precipitate in the 300°C irradiation; the precipitate number density decreased slightly between 34 and 58 dpa.

3. Titanium and chromium contents in a radiation produced MC-type precipitate were larger than those in a thermally produced one. Chromium content decreased with irradiation from 34 to 58 dpa, while nickel and silicon contents increased.

FUTURE WORK

Further measurements will be made on specimens irradiated at higher temperatures (400°C — capsules JP-5; 500°C — capsule JP-8).

REFERENCES

1. M. P. Tanaka, P. J. Maziasz, A. Hishinuma, and S. Hamada; to appear in Journal of Nuclear Materials.

2. W. Kesternich, Phil. Mag. A 52(4), 533 (1985).

3. M. P. Tanaka, S. Hamada, K. Fukai, and P. J. Maziasz, in ADIP Semiannu. Prog. Rep. March 31, 1986, DOE/ER-0045/16, U.S. DOE, Office of Fusion Energy.

MECHANICAL PROPERTIES AND FRACTURE BEHAVIOR OF 20% COLD-WORKED 316 STAINLESS STEEL IRRADIATED TO VERY HIGH NEUTRON EXPOSURES - M. L. Hamilton, F. H. Huang, and F. A. Garner (Hanford Engineering Development Laboratory); W. J. S. Yang (General Electric Company)

OBJECTIVE

The object of this effort is to define the mechanisms by which irradiated alloys fail during service or after removal from service.

SUMMARY

Stainless steels irradiated in EBR-II at temperatures in the range 380 to 500°C tend to exhibit saturation of mechanical properties at relatively low fluence levels. At fluences on the order of 13 to 15 x 10^{22} n/cm^2 (E > 0.1), however, there is a rapid increase in hardness just after the onset of void swelling. The hardness increase is not attributed just to the voids themselves but rather to an indirect effect of voids on nickel depletion in the alloy matrix. The strong dependence of stacking fault energy on nickel and chromium content and particularly on deformation temperature combine to promote extensive stress-induced formation of ε-martensite at room temperature. This leads to a very brittle failure mode characterized as quasi-cleavage. At higher deformation temperatures it leads to a failure mode designated channel fracture.

PROGRESS AND STATUS

Introduction

In earlier studies conducted in the Experimental Breeder Reactor EBR-II to moderate levels of neutron fluence it was shown that irradiation-induced changes in the tensile properties of AISI 316 stainless steel and some other austenitic steels could be related to concurrent changes in the microstructure.[1-5] Since the various microstructural components tend to saturate in density with continued exposure it was expected that the tensile properties would also reach saturation levels that would persist to relatively large neutron fluences. Data on a relatively low swelling heat of 316 stainless steel confirmed the validity of this assumption at neutron fluence levels approaching 13 x 10^{22} n/cm^2 (E > 0.1 MeV).[6] Other related studies demonstrated that predictive correlations of post-irradiation fracture toughness could be developed from the more easily obtained tensile properties, presumably because the microstructural origins of radiation-induced toughness degradation should be identical to those responsible for changes in tensile properties.[7,8]

When other heats of steel exhibiting an earlier onset of swelling were evaluated it was obvious that significant changes in fracture mode were occurring at high neutron exposure.[9,10] These changes were most pronounced for deformation at low temperatures. At higher test temperatures the fracture mode resembled the channel fracture that was observed earlier both in annealed 304, 308 and 316 stainless steels[11,12] and to a limited extent in 20% cold-worked 316, all at fluences less than or equal to 10 x 10^{22} n/cm^2 (E > 0.1 MeV).** The channels observed in these studies appeared as narrow bands in which the local deformation was often several hundred percent or higher, as evidenced by the elongation of voids within the band. This flow localization is thought to be a consequence of dislocation sweeping that significantly reduced the hardness within the channel.

The unanticipated change in behavior at higher fluence was first observed during disassembly and evaluation of a fueled experiment designated the P-53 test which had been irradiated in EBR-II. Both the fuel cladding and duct assembly were constructed from 20% cold-worked AISI 316 stainless steel. When 1.9 cm diameter circular specimens were punched for density measurements from the duct which housed the fuel assembly, several cracks developed between adjacent holes. Small pieces of this duct were also easily broken off while using a manipulator in the hot cell. In addition, the fuel pins, which had run at low power to very high fluences (~18 x 10^{22} n/cm^2, E > 0.1 MeV), had survived irradiation with no breaches but sustained numerous breaches during handling of the pins in the hot cell.

It was therefore decided to conduct mechanical property tests, fractography, and microstructural analyses on the duct material over a range of test temperatures. Several 3.0 mm diameter microscopy specimens of AISI 316 and three titanium-modified 316 stainless steels that were irradiated in other experiments were also broken at room temperature and their fracture behavior examined. Table 1 contains the alloy compositions and initial thermal-mechanical conditions.

Table 1. Alloy compositions (wt.%)

Alloy	Ni	Cr	Mo	Si	Mn	Ti	C	P	B	Zr	W	Fe
AISI 316*	13.5	17.5	2.5	0.6	1.75	--	0.05	0.002	0.0005	--	--	Bal
LS-1**	13.0	16.0	1.8	0.9	1.0	0.10	0.05	0.001	--	0.05	0.05	Bal
LS-2**	19.5	8.7	2.3	1.0	1.9	0.27	0.04	--	--	--	--	Bal
D-18**	15.0	12.0	2.5	1.0	2.0	0.25	0.04	--	--	--	--	Bal

*1050°C/5 min/air cool + 20% cold work.
**1150°C/15 minlair cool + 25% cold work.

EXPERIMENTAL OETAILS

Specimen Preparation

The hexagonal P53 duct was constructed from FFTF First Core steel with the individual flats measuring 3.2 cm in width and 1.02 mm in thickness.* Tensile specimens were obtained from rectangular strips having their long dimension parallel to the axis of the duct. The obvious embrittlement of the duct made it imperative to utilize a specimen with the largest possible gage width, gage length and filet radius. The dimensions previously utilized for flat tensile specimens in the U.S. Breeder Reactor or Fusion Materials programs were judged to be unacceptable. Additional constraints on specimen fabrication arose from the limited amount of material remaining between the holes punched in the duct and the necessity for remote fabrication. Conforming as much as possible to the guidance provided by ASTM Procedure E8, a new tensile specimen was designed and is shown in Fig. 1.

Most of the tensile blanks were obtained from regions adjacent to the corners of the duct and thus had the potential for being somewhat stronger than the central regions of the duct face. To check for this possibility, hardness measurements were made on sections of unirradiated duct and it was found that the duct corners were worked only slightly more (3-6%) than were the duct flats. Even this small variation in hardness and dislocation density is expected to be relaxed during irradiation',** and thus no significant variations in strength are expected to arise due to the location on the duct face from which the specimens were obtained.

Seven tensile specimens from the duct and a number of unirradiated control specimens were machined remotely in the hot cell and photographed at a magnification of ~2.8x. The gage dimensions were determined from the photographs. A small amount of variability was observed between specimens but was judged to be insignificant with respect to the test results.

Compact tension specimens were fabricated from the 1.9 cm diameter disks punched from the center of the duct faces. Oensity measurements were performed prior to fabrication of the specimens using an immersion technique. The configuration of the circular compact tension specimen is shown in Fig. 2. Since the strength of the irradiated material was extremely high, it was very difficult to cut a sharp notch in the specimen and to induce a crack by fatigue prior to testing (precrack). The first few specimens failed during precracking because of the lack of prior knowledge of the material's fracture properties. Successful precracking required careful optical examination of crack extension and careful monitoring of cyclic load reduction.

Fractographic and microstructural analyses were performed on the broken tensile and compact tension specimens as well as on irradiated microscopy disks that were fractured manually. Since the radioactivity of the original tensile and compact tension specimens was substantial, fractographic specimens of smaller volume were prepared by slicing off a thin section containing the fracture surface. The fractographic analysis of microscopy disks was preceded by submerging them in pure ethyl alcohol and breaking them remotely by bending with pliers. The fracture surfaces were examined in a JSM 35C scanning electron microscope. Microscopy foils were prepared from tensile specimens by slicing perpendicularly to the tensile axis. Microstructural studies were performed in either a JEM 100CX or a JEM 1200EX transmission electron microscope.

*FFTF is the acronym for Fast Flux Test Facility, located in Richland, WA.

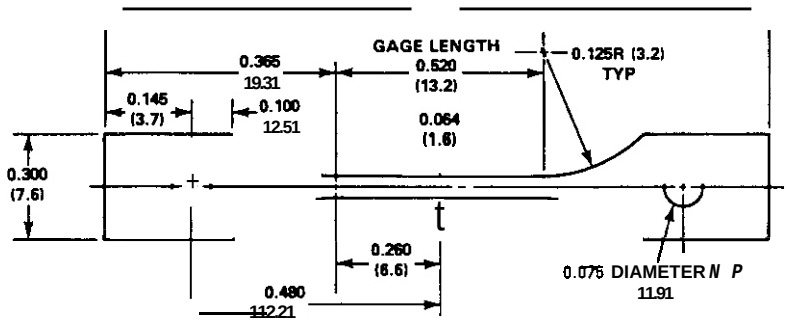


Fig. 1. Tensile specimen dimensions.

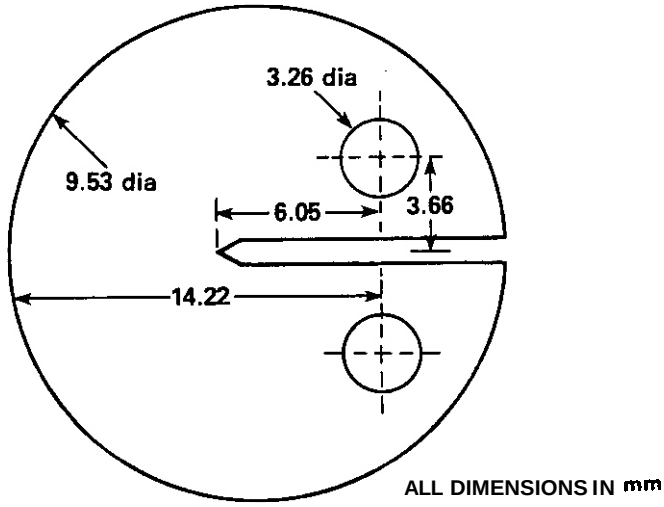


Fig. 2. Compact tension specimen dimensions.

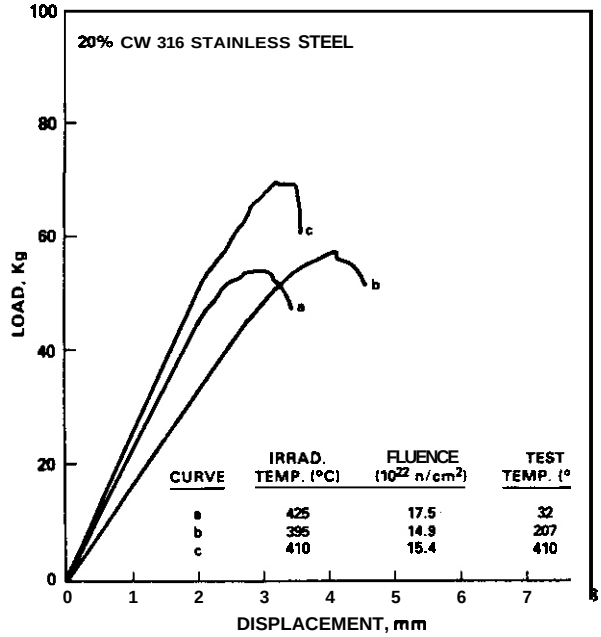


Fig. 3. Load versus displacement curves for specimens tested at elevated temperatures.

Test Procedures

Tensile tests were conducted in air at three different temperatures: room temperature, the fuel handling temperature of 205°C and the irradiation temperature, which varied from 385 to 488°C. All tests were performed at a strain rate of 6.4 x 10^{-4} sec^{-1}. Specimens were tested in a shielded testing facility using the Modular Test Unit (MTU). The MTU is a hydraulically actuated test frame designed to remotely perform tensile, fatigue and compression type mechanical testing. Tensile specimens were carefully positioned in the load train. A thermocouple in contact with the specimen was used to monitor its temperature. To prevent undesirable specimen straining during heat up to the test temperature, the load was continuously monitored and the position of the actuator was adjusted to maintain loads well below the load required for yielding. Load versus deflection data were obtained using a load cell in series with the load train and a linear variable differential transformer extensometer attached to the load train actuator. Yield strength was determined by the 0.2 percent offset method.

Details of the compact tension test procedure are described in references 13 and 15. Fracture toughness tests were conducted in air at 32°C, 205°C and at the irradiation temperature (395-425°C). The specimen was unloaded after reaching the maximum load, heat tinted at 500°C for about one hour, and broken at room temperature to allow optical measurement of the corresponding crack extension. The results were analyzed by a J-integral approach. A list of the specimens tested is included in Table 2. Note that void swelling in these specimens ranged from 3.4 to 8%.

Test Results

The tensile test results are given in Table 3. Since there were small gradients in neutron flux and temperature along the specimen axis, the irradiation parameters listed were determined for the specimen midpoint. Fluences were based on HIST computer code calculations, while irradiation temperatures were interpolated between the temperature estimated for the bottom of the fuel column (370°C) and the beginning-of-life subchannel outlet temperature adjacent to the relevant duct face. The temperatures of the duct faces at the top of the core were assumed to be the same as the subchannel outlet temperatures, which were calculated with the COBRA computer code. COBRA is a standard thermal-hydraulic code in wide use in the nuclear industry. HIST is a fuel performance predictive code developed by Westinghouse Hanford Company and is a version of the SIEX code.

Typical load-displacement curves of the compact tension specimens are shown in Fig. 3. The material displayed little plasticity prior to reaching the maximum load, at which point a sudden load-drop was observed for all specimens. Since well-defined crack extension was not observed, the maximum load was taken as the onset point of crack extension, where the critical value of J, J_{1c}, was calculated.

The compact tension test results are given in Table 4. Only 11 valid tests were performed. Several Specimens failed during precracking, and several others were tested before a fatigue crack was produced while precracking methods for these specimens were still being established.

The plane strain fracture toughness K_c can be estimated from the values of J_{1c} through the following equation:

$$K_c = \left[\frac{E\ J_{1c}}{1-\nu^2}\right]^{1/2} \qquad (1)$$

where ν is Poisson's ratio and E is Young's modulus. The calculated values of K_c are also listed in Table 4.

Discussion of Test Results

Examination of Figs. 4 through 6 shows that the post-irradiation strength of the P53 First Core duct was significantly higher than was observed for this steel at lower fluences. This was an unexpected result, since the strength and ductility of 20% cold worked 316 were both believed to saturate with fluence at about 5 x 10^{22} n/cm^2 (E > 0.1 MeV). As shown in Figs. 7 and 8 the ductility of this steel depends not only on the fluence and irradiation temperature but also on the test temperature, particularly at lower test temperatures. With one exception (specimen 4a tested at room temperature) the P53 specimens exhibited ductilities greater than 4.5%. The ductilities found in the P53 tests conducted at room temperature, however, fell substantially under the trend line established at lower fluence.

There was another very pronounced difference in the behavior of First Core steel with respect to the test temperature. As shown in Fig. 9 the fracture surfaces of the specimens tested at room temperature were oriented 90 degrees to the tensile axis, suggesting a brittle mode of failure, while the fracture surfaces of specimens tested at higher temperatures were inclined at angles of 30-60 degrees to the tensile axis, a behavior typical of plastic deformation in a ductile material. Faceted regions were also evident on the surface of specimens tested at the higher temperatures.

Table 2. Density specimens used for compact tension tests

Specimen Identity	Fluence 10^{22} n/cm^2, E > 0.1 MeV	Irradiation Temperature °C	Swelling % ΔV/V
F1C	14.0	395	4.6
F2C	14.2	395	4.3
F3C	14.9	395	4.6
F4C	15.5	395	4.7
F5C	15.3	395	N.D.
F6C	14.5	395	3.4
F1D	15.3	410	5.6
F2D	15.4	410	5.4
F3D	16.2	410	5.5
F4D	16.9	410	6.0
F5D	16.7	410	4.9
F6D	15.9	410	4.6
F1E	15.9	425	6.7
F2E	16.0	425	7.3
F3E	16.8	425	7.1
F4E	17.5	425	8.0
F5E	17.4	425	6.2
F6E	16.4	425	5.9

Table 3. Tensile data on P53 specimens+

Specimen	Irradiation Exposure Temperature °C	Irradiation Exposure Fluence 10^{22} n/cm^2	Test Temperature °C	Yield Strength MPa	Ultimate Tensile Strength MPa	Uniform Elongation %	Total Elongation %
4a	460	15.5	20	1293	1432	1.9*	1.9
5	474	14.5	20	1238	1505	6.5*	6.5
7	487	11.3	20	1140	1393	4.6*	4.6
3	442	16.2	205	1350	1492	4.6	6.3
2	385	12.8	205	1627	1703	1.a	5.2
4	460	15.5	460	1127	1223	5.6	7.2
6	488	12.8	488	917	1067	5.8	7.7

+ $\varepsilon = 6.4 \times 10^{-4}$ sec^{-1}
* Failure occurred at the maximum load.

It was observed after the tensile tests were completed that all seven specimens were strongly attracted to a magnet. Examination of other pieces of duct material showed a variable degree of magnetism, which was particularly strong in areas deformed during punching. It appears that while the duct specimens may have exhibited some degree of magnetization prior to fabrication, they were strongly magnetized along their

Table 4. Fracture toughness of P53 duct
loading rate = 2.1 x 10^{-3} mm/sec

Test Temperature °C	Irradiation Temperature °C	Fluence 10^{22} n/cm^2 E > 0.1 MeV	J_{Ic} kJ/m^2	K_C MPa$\sqrt{m}$
207	395	14.9	38.6	88.8
395	395	15.5	42.9	90.2
32	410	15.3	35.6	87.0
30	410	16.2	39.7	91.0
205	410	16.9	34.0	83.8*
205	410	16.7	46.5	97.5
410	410	15.4	34.0	80.1
32	425	17.5	24.3	71.9
206	425	16.4	37.8	87.8
205	425	16.8	27.4	74.8
425	425	17.4	29.6	74.4

*Loading rate = 2.1 mm/sec

For the 11 tests: Average K_C = 84.3 MPa$\sqrt{m}$
Standard Deviation = 8.2 MPa$\sqrt{m}$
Range = 71.9 to 91.9 MPa$\sqrt{m}$

entire length during tensile testing. This suggested that a martensitic transformation had occurred during deformation.

Figs. 10 and 11 show the temperature dependence of J_{Ic} and K_C for various irradiation conditions. Previous results" for another duct designated P14A and irradiated to lower fluence are also plotted for comparison. The dependence of fracture toughness on irradiation temperature is shown in Fig. 12 where the values of J_{Ic} are plotted for specimens with the same test and fluence conditions. Earlier studies have shown that the fracture toughness of 20% CW 316 decreases by a factor of 2 after irradiation to a fluence of 11 x 10^{22} n/cm^2 (E > 0.1 MeV). No further degradation was observed in this study with increasing fluence up to 17.5 x 10^{22} n/cm^2. Fig. 13 shows the absence of any strong effect of fluence on the fracture toughness of the P53 duct material.

The most significant change in fracture behavior following high fluence exposure of 316 is the drastic reduction in resistance to crack propagation. The tearing modulus of the P53 specimens tested at elevated temperatures was estimated to be about 2, compared with a value of 15 observed for the material irradiated to a fluence of 11 x 10^{22} n/cm^2.[1] For P53 tests conducted at room temperature the tearing modulus approached zero.

As shown in Fig. 10, test temperature did not have a strong effect on the fracture toughness for irradiation temperatures up to 425°C. The toughness decreased somewhat with increasing irradiation temperature in the range of 395-425°C, but the trend for higher irradiation temperatures is not known.

FRACTOGRAPHIC AND MICROSTRUCTURAL ANALYSES

Tensile Specimens

Specimens 4a and 5 from the P53 duct, irradiated to 16 x 10^{22} n/cm^2 (E > 0.1 MeV), fractured transgranularly at room temperature, exhibiting features on the fracture surface similar to chevron patterns. These specimens had elongations of 1.9% and 6.5%, respectively. As shown in Fig. 14, the fracture was initiated at one corner of specimen 4a, presumably from a pre-existing flaw, and propagated across the specimen diagonally. Small regions having a typical shear fracture morphology appeared on the edges of the specimen at the end of the crack path. The fracture surface was flat and perpendicular to the tensile axis. Faint river patterns were visible along the diagonal crack path. High magnification pictures of local regions revealed a high density of cavities with a definite crystallographic shape. The size and density of these cavities correspond well with that of the void swelling found in the matrix during examination of a TEY specimen cut from this tensile specimen. The cavities in the fracture surface are therefore believed to be voids. The crystallographic shape of the voids remains intact without any sign of smearing, indicating brittle behavior in the surrounding matrix. The room temperature fracture mode was therfore designated "quasi-cleavage".

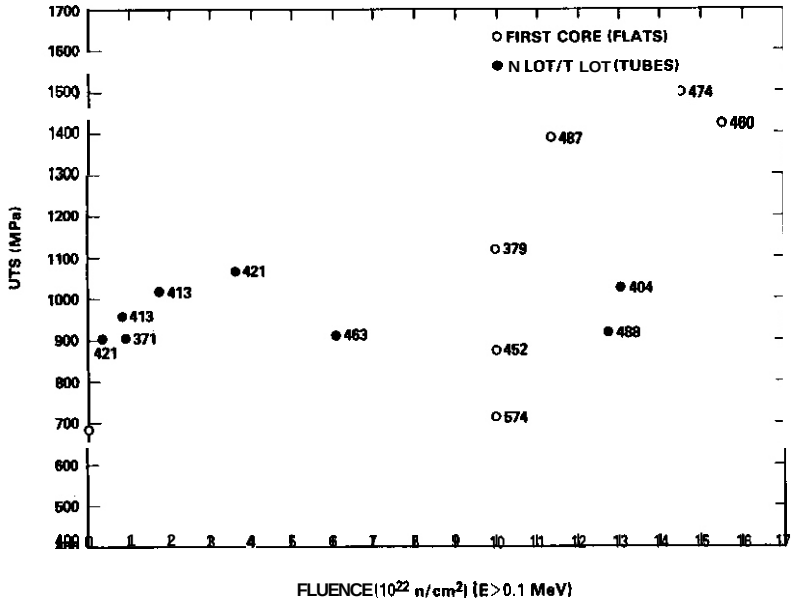


Fig. 4. Ultimate strength of First Core and N-lot AISI 316 steels tested at room temperature. The irradiation temperatures are shown beside each datum. The N-lot heat does not begin to swell as soon as First Core and does not exhibit an increase in ultimate strength.

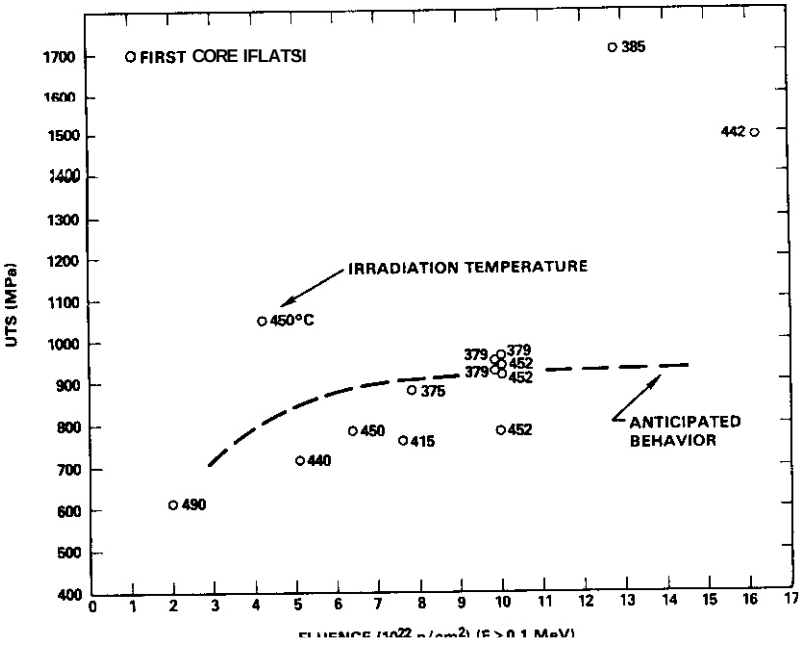


Fig. 5. Ultimate strength of First Core steel tested at 205-232°C. Irradiation temperatures are shown beside each datum.

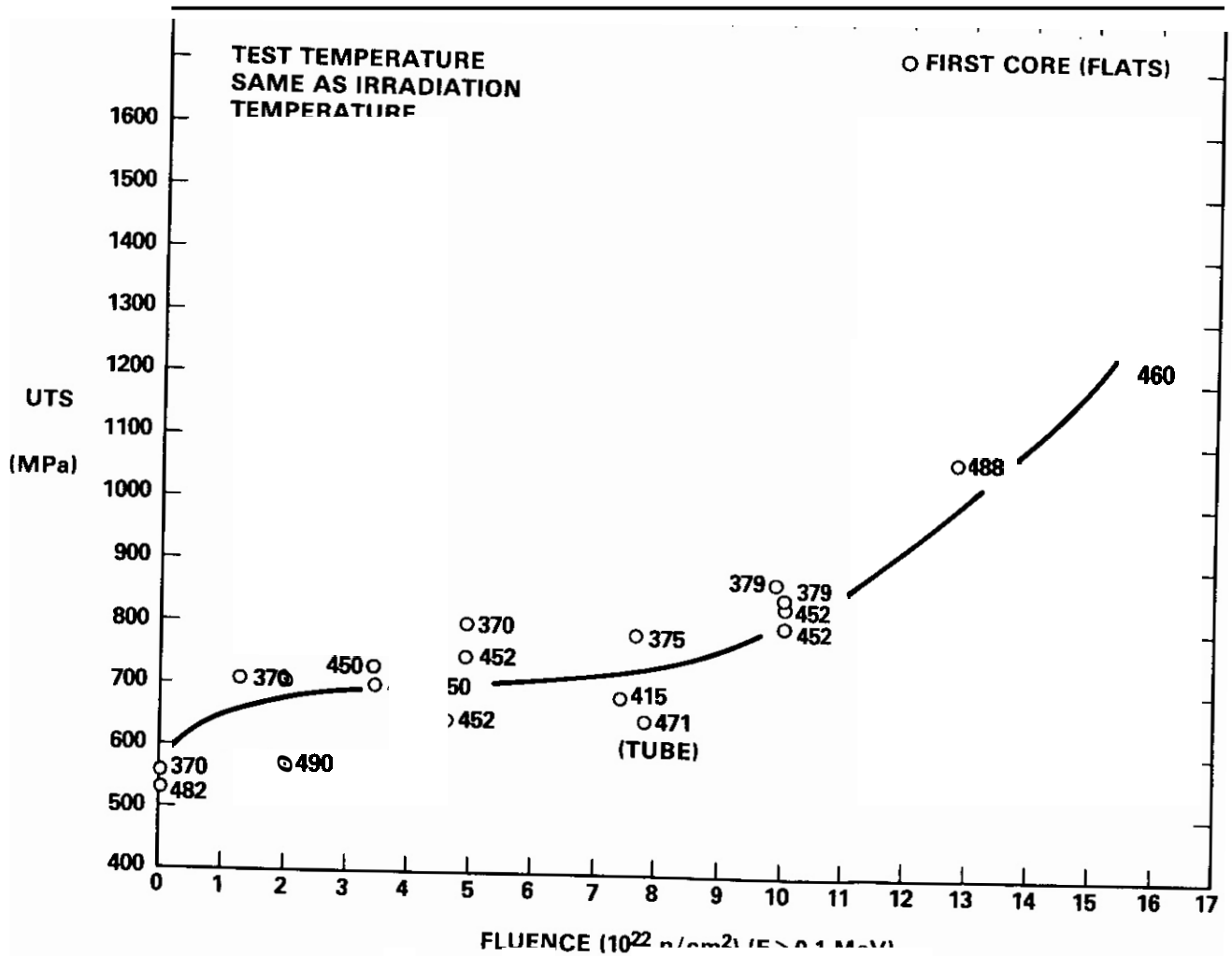


Fig. 6. Ultimate strength of First Core teel t at the emperature. Irradiation emperatures are shown beside each datum.

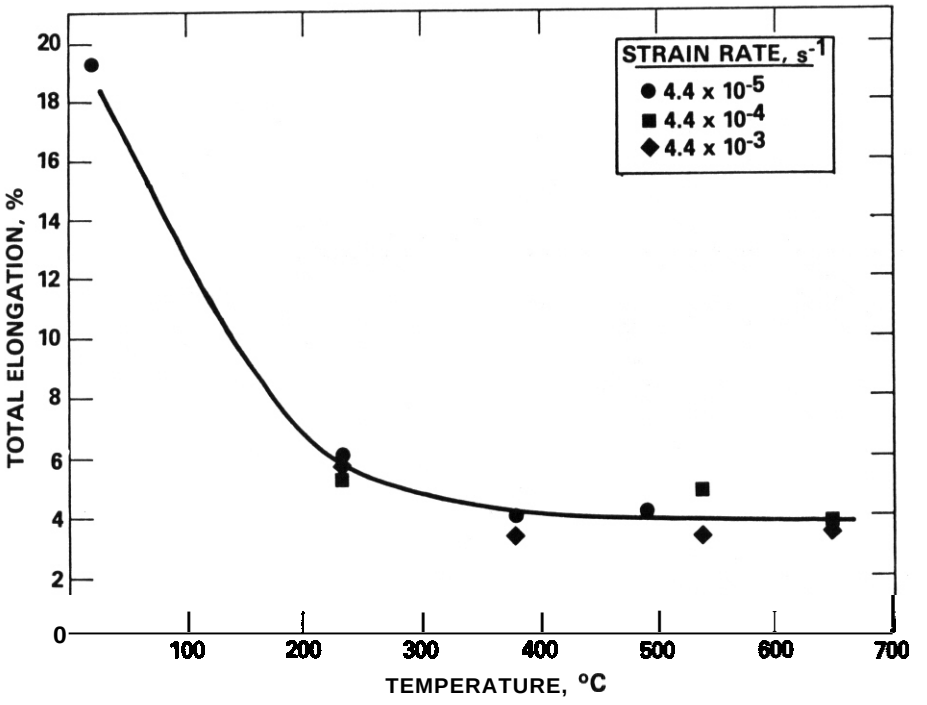


Fig. 7. Ductility of 20% cold worked 316 (First Core) irradiated to 1.3 x 10^{23} n/cm^2 (E > 0.1 MeV) at 380°C.

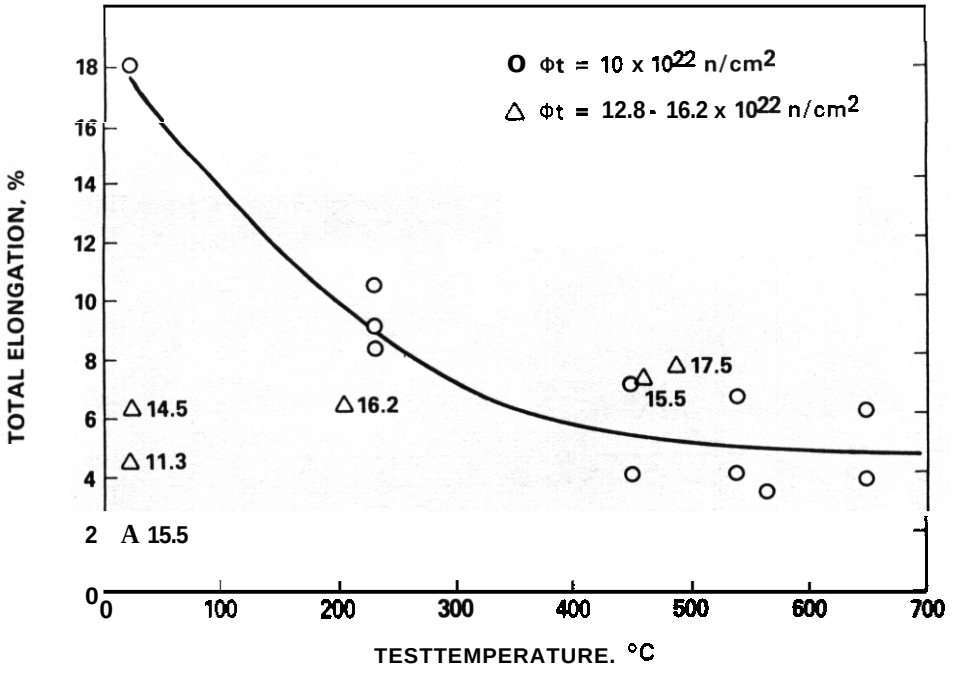


Fig. 8. Ductility of 20% cold worked 316 (First Core) irradiated at 450-490°C. Neutron fluences are given beside each P-53 datum.

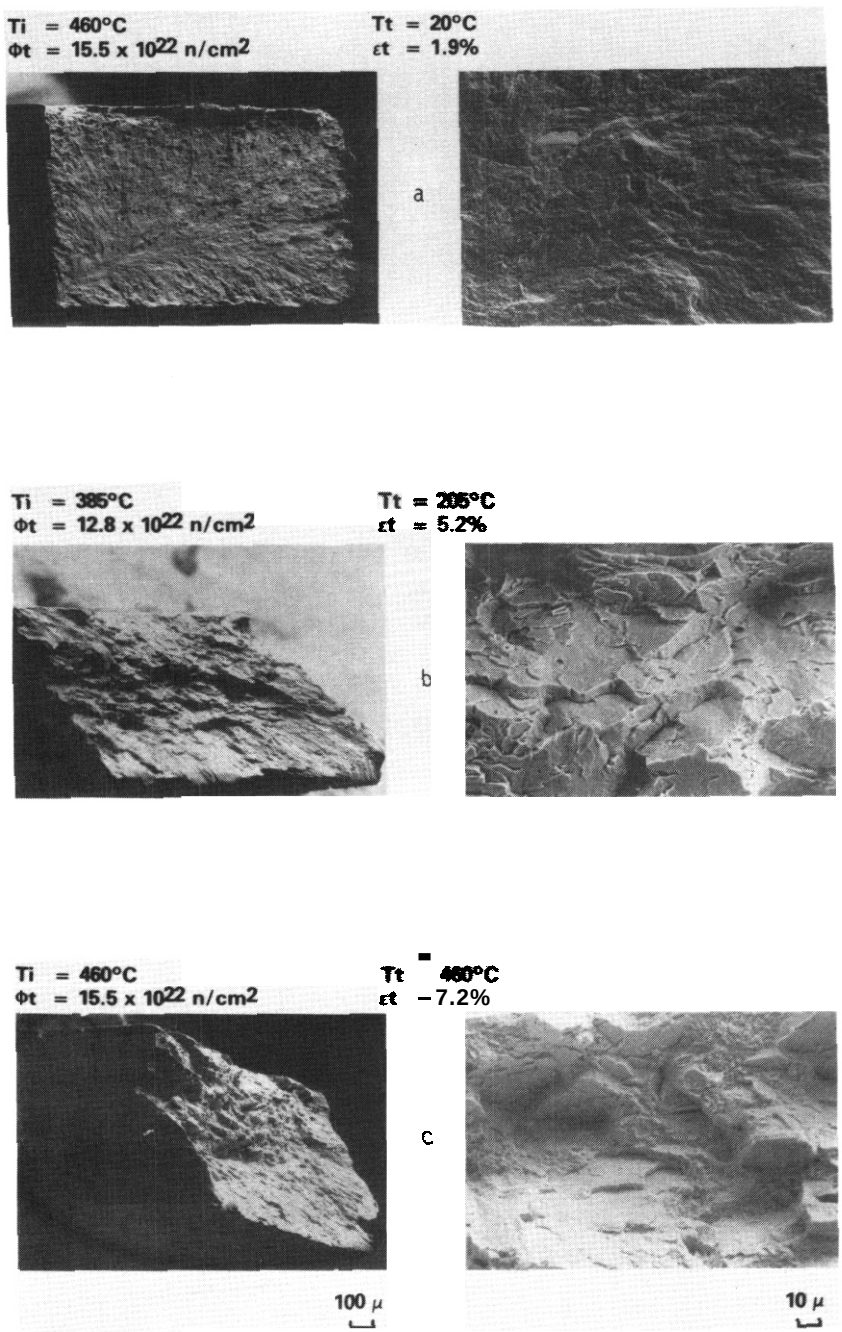


Fig. 9. Fractography of tensile specimens from P53. a) Brittle fracture at room temperature (Specimen 4a). b) Channel fracture at 205°C (Specimen 2). c) Channel fracture at 460°C (Specimen 4) The total elongation and irradiation/test conditions are shown for each specimen.

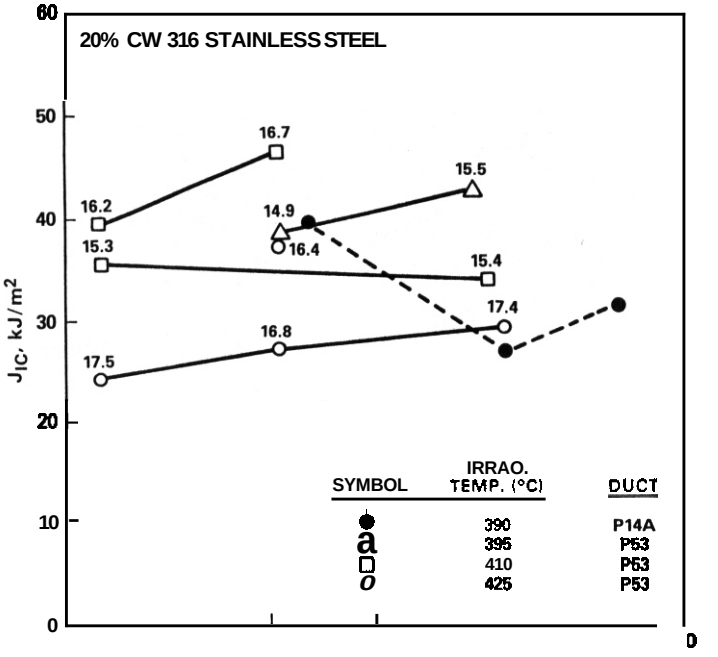


Fig. 10. Effect of test temperature on J_{IC} of irradiated 20% cold worked type 316 stainless steel

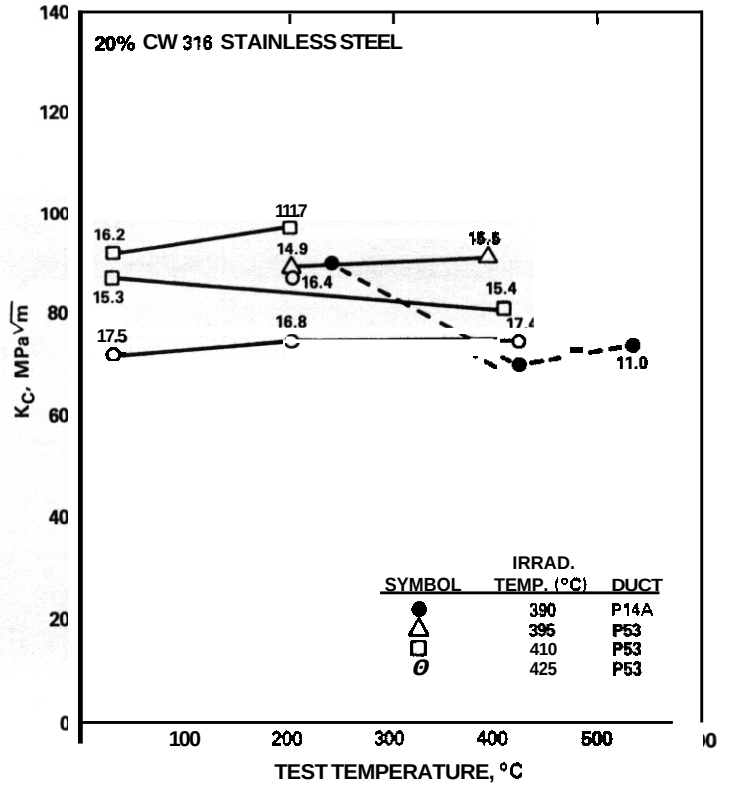


Fig. 11. Effect of test temperature on K_C of irradiated 20% cold worked type 316 stainless steel.

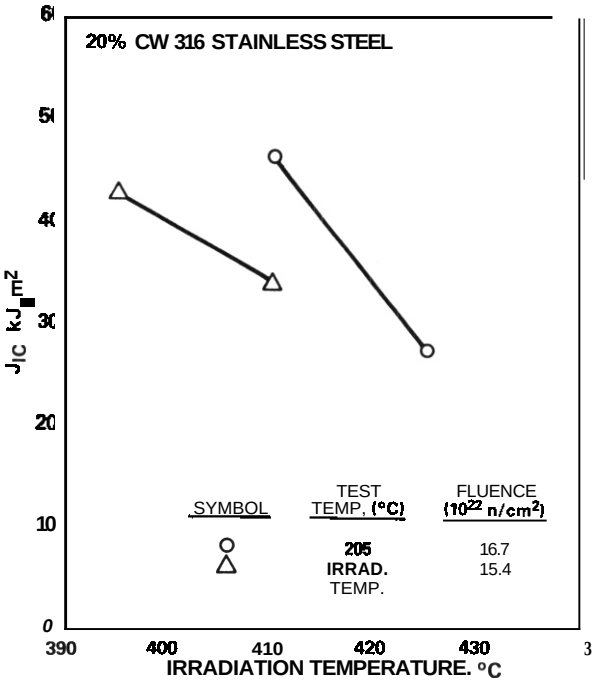


Fig. 12. Effect of irradiation temperature on the fracture toughness of irradiated 20% cold worked type 316 stainless steel.

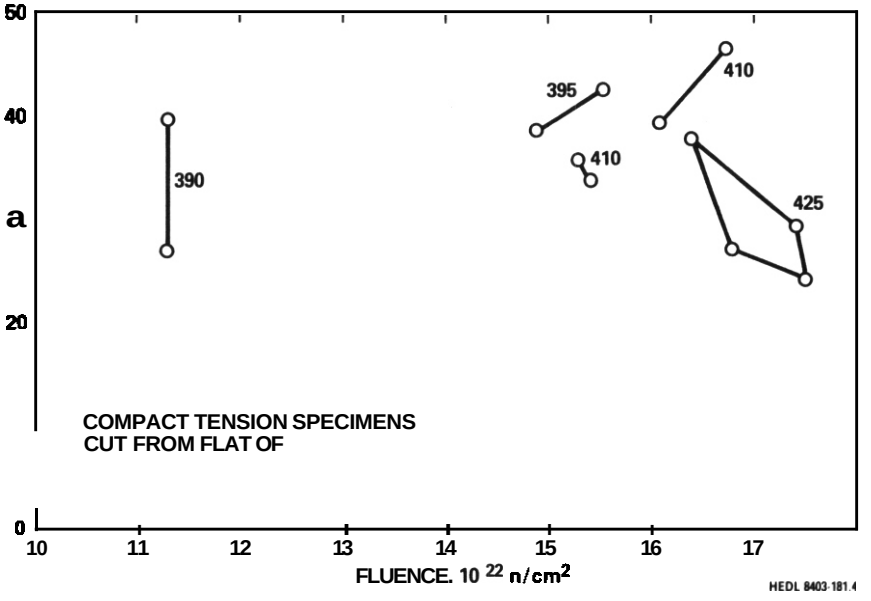


Fig. 13. Effect of neutron fluence on the fracture toughness of specimens obtained from the P53 duct. connected data points are obtained from specimens irradiated at the temperature shown (°C) but tested at different temperatures.

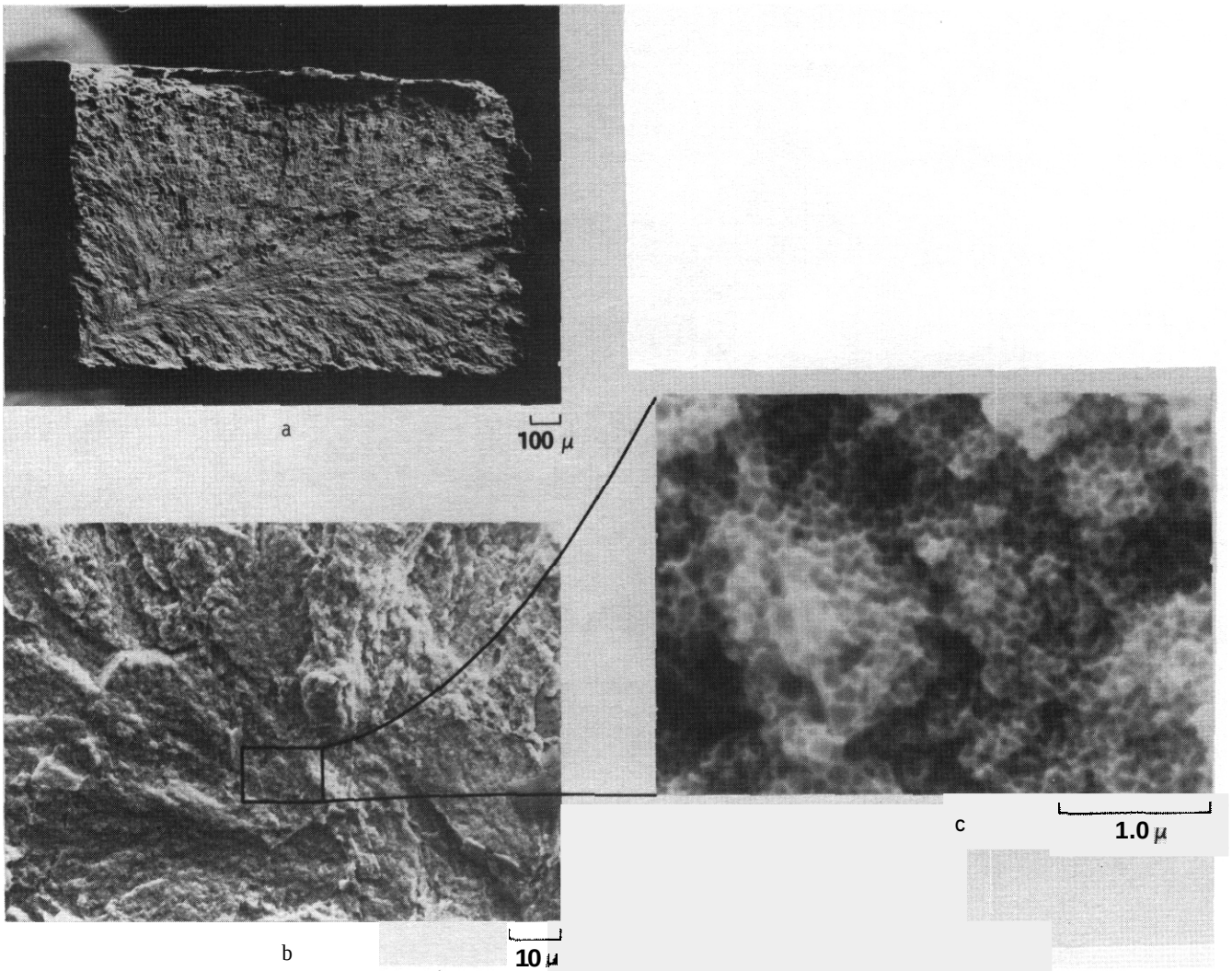


Fig. 14. a,b) Quasi-cleavage fracture of P53 tensile specimen 4a. c) voids with their crystallographic shape intact in a high-magnification picture of a local region.

The microstructure of the specimen prepared from the section adjacent to the fracture surface exhibited little evidence of plastic deformation. There were no obvious deformation channels in this specimen. Occasionally, however, fine slip bands were found, as illustrated in the bright field micrograph shown in Fig. 15a. In dark field, however, a very high density of thin stacking fault plates or precipitates were observed throughout the specimen, as can be seen in Fig. 15b. Note that only one-fourth of these faults are imaged under the conditions employed to produce this micrograph. The streaks shown in the selected area diffraction pattern (inset, lower left) are without intensity maxima, indicating that these microstructural features are on the order of monolayers in thickness.

Two other P53 tensile specimens, designated numbers 2 and 4, tested at 205 and 460°C respectively, fractured transgranularly by a shear mode. Smeared voids resulting from dislocation shearing were revealed at high magnifications of the facet surfaces, Providing direct evidence of channel fracture. Fig. 16 shows examples of the facets and smeared voids found on the fracture surface and also shows sheared voids found in deformation bands below the fracture surface.

Burgers vector analyses were performed for the three deformed specimens shown in Fig. 9. No slip systems were detected other than the {111} <110>, the {111} <112> partials and the {111} <112> twins normally operating in fcc systems. Analysis of the various precipitates (M_6C, $M_{23}C_6$, γ', G-phase, etc.) were conducted for a variety of specimens from the high fluence P53 test and a lower fluence test designated P14. No dramatic changes were observed in precipitation behavior with increased fluence. Thus the large increase in hardening observed at high fluence cannot be attributed either to irradiation-induced precipitation or changes in dislocation substructure.

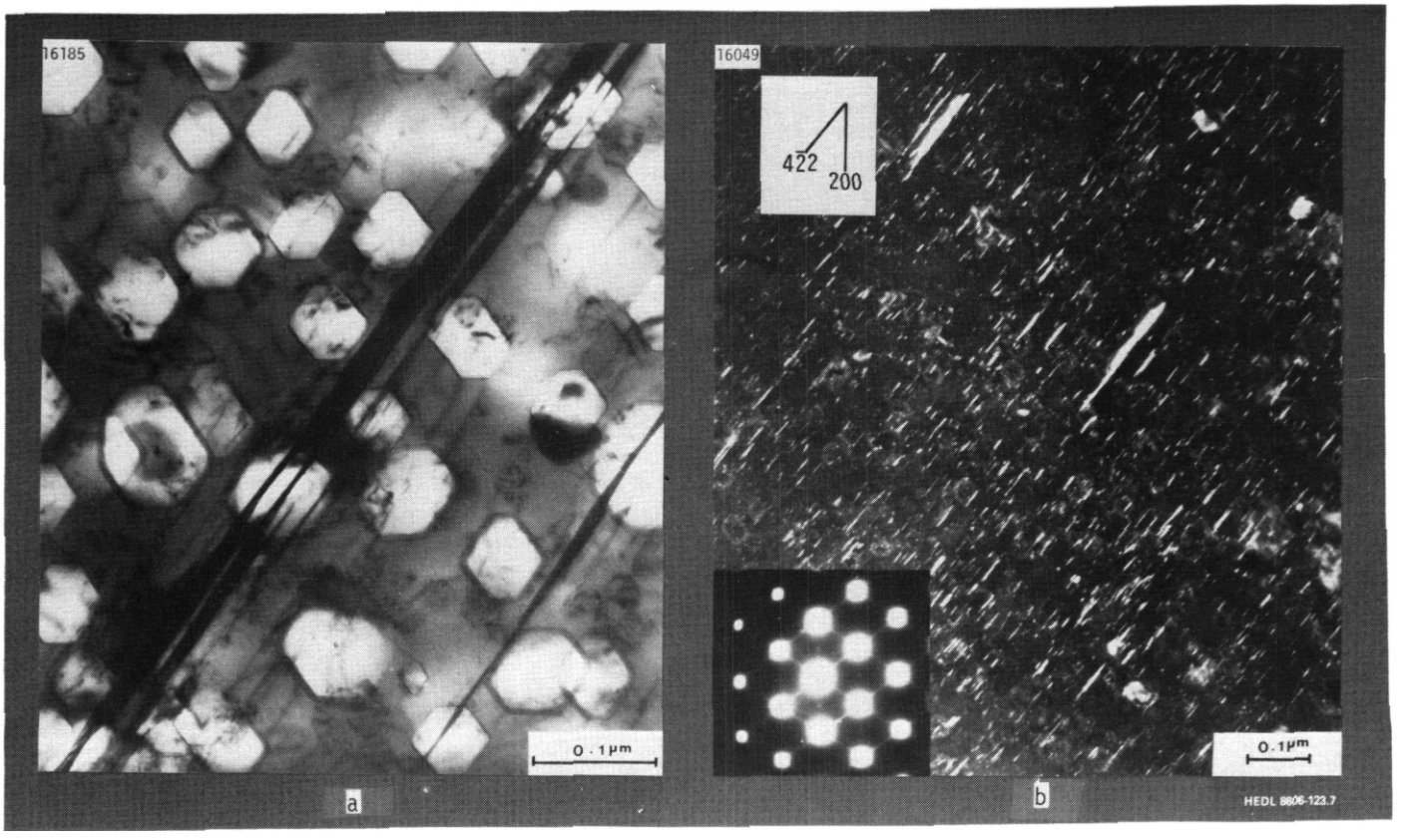


Fig. 15. (a) Deformation bands in the gage section of P53 specimen 4A. (b) Thin stacking fault plates on one set of {111} planes in P53 specimen 4a. The inserted limited area diffraction pattern reveals streaks without maxima arising from the thin stacking fault plates.

Compact Tension Specimens

Examination of the fracture surfaces of the compact tension specimens from the P53 duct revealed that the precrack induced by room temperature fatigue exhibited cleavage-type growth. The fracture surface of this specimen exhibited quasi-cleavage fracture when tested at room temperature and 205°C. The specimen tested at the irradiation temperature, however, showed channel fracture. Fractographs of the precracked region and the tested zone are given in Figs. 17, 18 and 19 for specimens tested at room temperature, 205°C and 410°C, respectively. Since the fracture surfaces were oxidized during heat tinting, high magnification examination of the channeling patterns on the fracture surface was not conducted.

Microscopy Disks

Table 5 sumnarizes the failure modes observed in manually deformed microscopy disks for a variety of titanium-modified stainless steels irradiated to high fluence. Since First Core steel was used as a reference for the evaluation of room temperature embrittlement, a few additional specimens of First Core were also evaluated. These were an electropolished disk designated 46M7 from the AA1 experiment and an unpolished fragment of the P53 duct. The two specimens received a similar neutron fluence, 16×10^{22} n/cm^2 ($E > 0.1$ MeV). and both were irradiated at ~400°C. The measured void swelling was 3.5% for the 46M7 specimen and 3.9% for the P53 specimen.

The polished TEM disk, 46M7, was examined by microscopy and then purposely cracked by impact, i.e., the fine point of a sharp pair of tweezers was dropped on the foil surface. Cracks opened from the perforated foil edge in a brittle zig-zag fashion as shown in Fig. 20. Each sawtooth of the crack edge was aligned with a twin plate in the matrix as demonstrated in Fig. 21. Careful examination of the thin region along the crack path revealed diffraction patterns corresponding to a bcc structure. The lattice parameter of the bcc structure deduced from the diffraction patterns was a_o = 0.29 nm, which is close to the lattice parameter of a-ferrite (0.286 nm). Dark-field pictures using the bcc diffraction spots revealed a thin layer of bcc material along the crack path, 20 to 40 nm in width. Examples are given in Fig. 22. Finding a thin bcc layer along the crack path suggests that a stress-induced martensitic transformation ($\gamma \rightarrow \varepsilon \rightarrow \alpha$) may have occurred along the crack path. EDX analysis indicated that the matrix Ni content varied

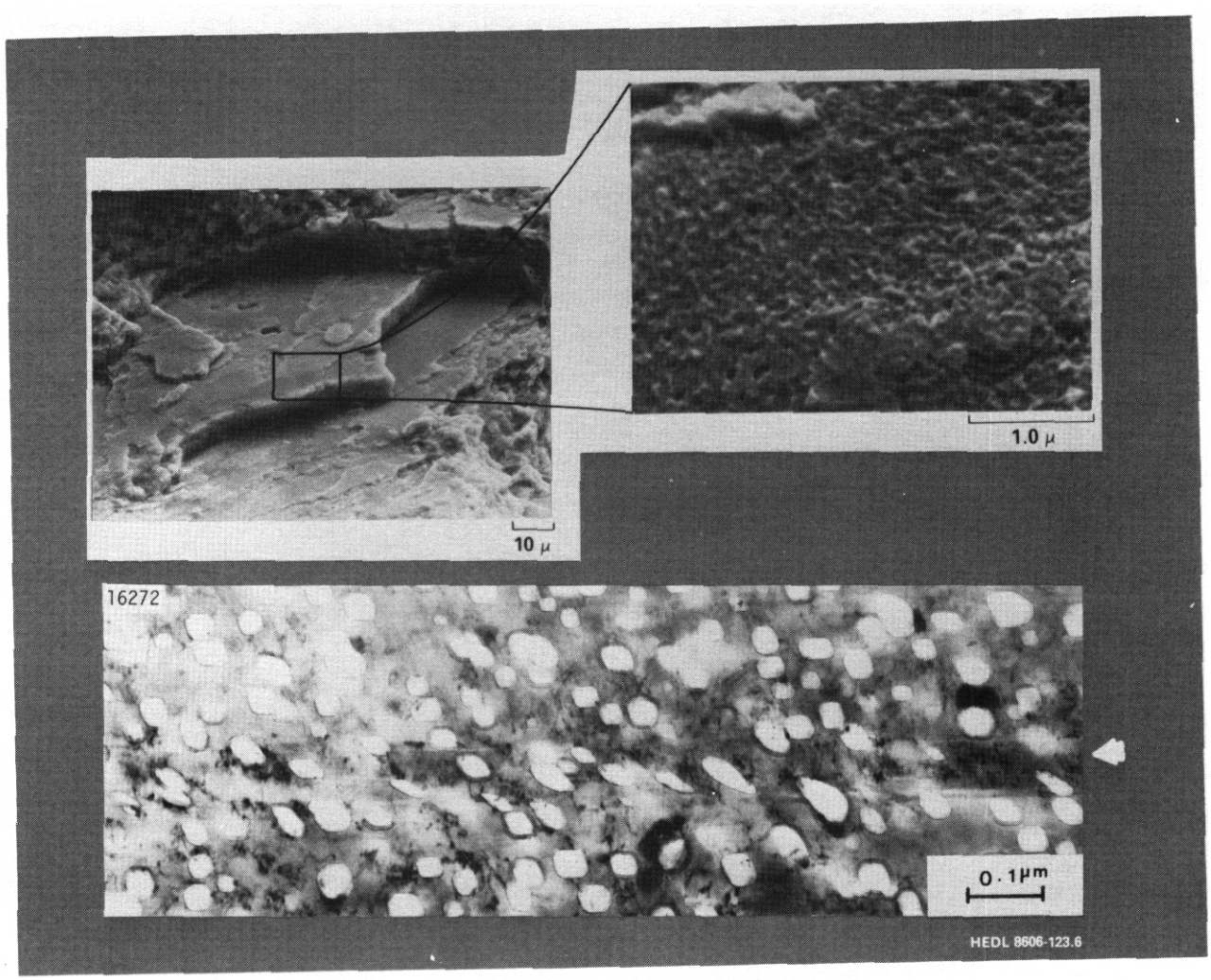


Fig. 16. High Magnification SEM Pictures of the Channel Faceted Surface and a TEM Picture of Deformation Bands Revealing Sheared Voids in **P53** Specimen 4 Tested at **460°C.**

from 9 to 12 **wt%,** which is not low enough for the γ matrix to thermally transform into ferrite. Furthermore, no **bcc** phase was detected in the thin foil before **it** was damaged.

The same TEM disk was then broken in half by bending and its fracture surface examined in the scanning electron microscope. This revealed that failure in thin regions of the foil, where the material is essentially a single crystal, was quasi-cleavage in nature. occurring along twin boundaries. The fracture mode changed to channel fracture imnediately after the crack met a grain boundary on its way into a thicker region of the foil.

A fragment of the P53 duct specimen was broken by bending to verify the fracture mode observed in specimen **46M7.** The fragment was clamped at one end in a small vise to form a cantilever and then a small piece of material was broken from the free end by pushing and striking **it** with the manipulator. The fracture surface showed channel fracture, consistent with the results obtained on specimen **46M7.** Microscopy conducted **on** a thin foil prepared from this fragment revealed a martensitic transformation in some of the grains as shown in Fig. 23. No **bcc** phase was found in thin foils prepared from the gage section of tensile specimens tested at room temperature. Deformation twins found in some of the grains shown in Fig. 24 had the same appearance as the ϵ phase earlier reported to form in the absence of radiation in deformed 304 stainless **steel.**[16]

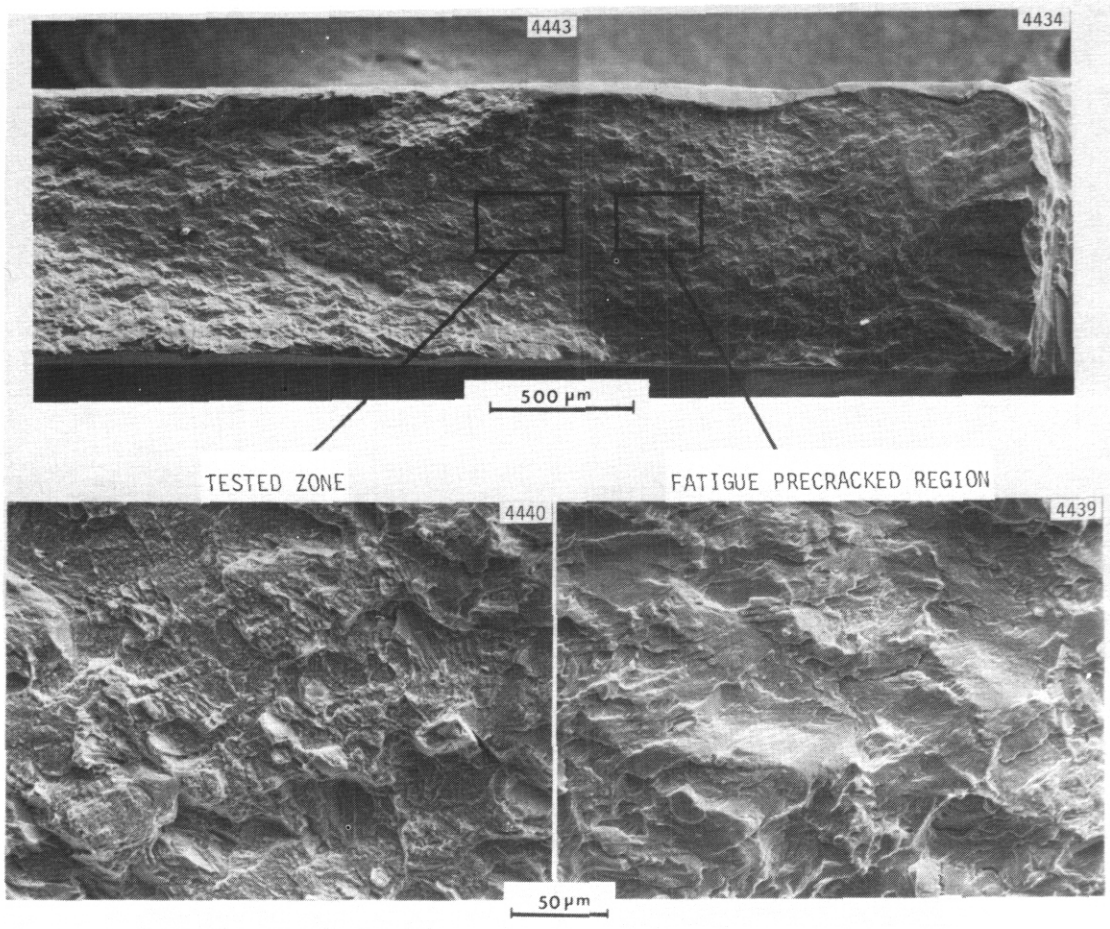


Fig. 17. Cleavage fracture in fatigue precrack region and quasi-cleavage fracture in tested zone of P53 compact tension specimen tested at room temperature.

Table 5. SEM fractography study of TEM disks fractured at room temperature

Alloy	Specimen	Irradiation Experiment	Fluence 10^{22} n/cm^2, E > 0.1 MeV	Irradiation Temperature °C	Density Change %	Fracture Mode
First Core	C75	RS-1	10.3	370	0.41	Transgranular ductile dimple
First Core	46M7	AA-I	15.6	400	3.09	Transgranular channel
Titanium-Modified Stainless Steels	LS-1	AA-VII	15.1	400	1.32	Transgranular channel
	LS-2	AA-VII	18.5	427	0.08	Transgranular ductile dimple plus small amount of channeling
	D18	AA-VII	18.5	427	2.08	Transgranular fracture with poorly defined dimples and some channeling

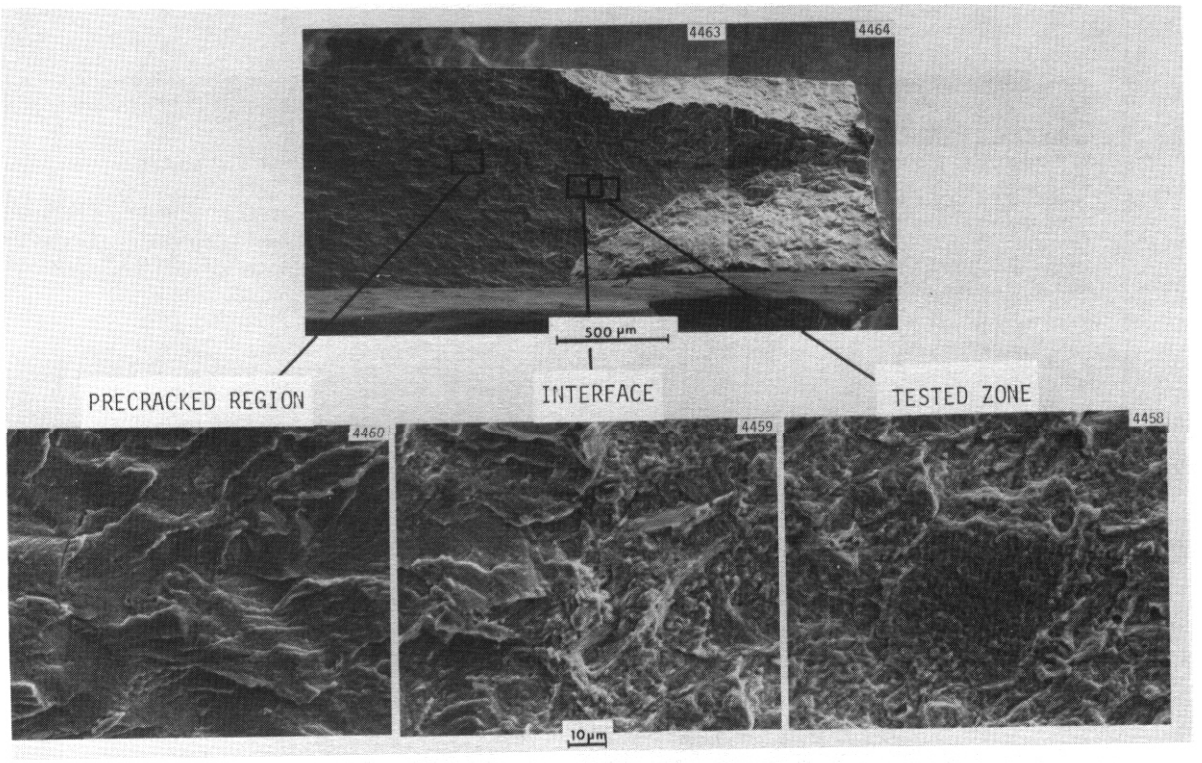


Fig. 18. Cleavage fracture in fatigue precrack region and quasi-cleavage fracture in tested zone of a P53 compact tension specimen tested at 205°C.

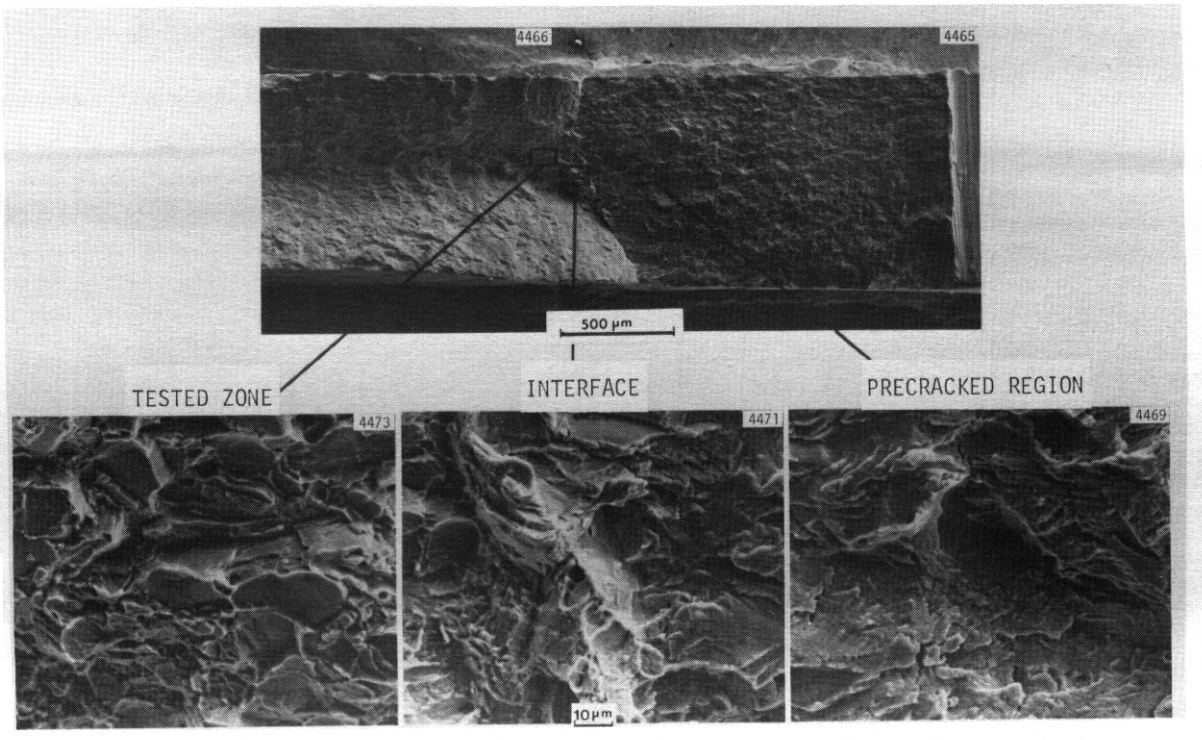


Fig. 19. Cleavage fracture in fatigue precrack region and channel fracture in tested zone of a P53 compact tension specimen tested at 395°C.

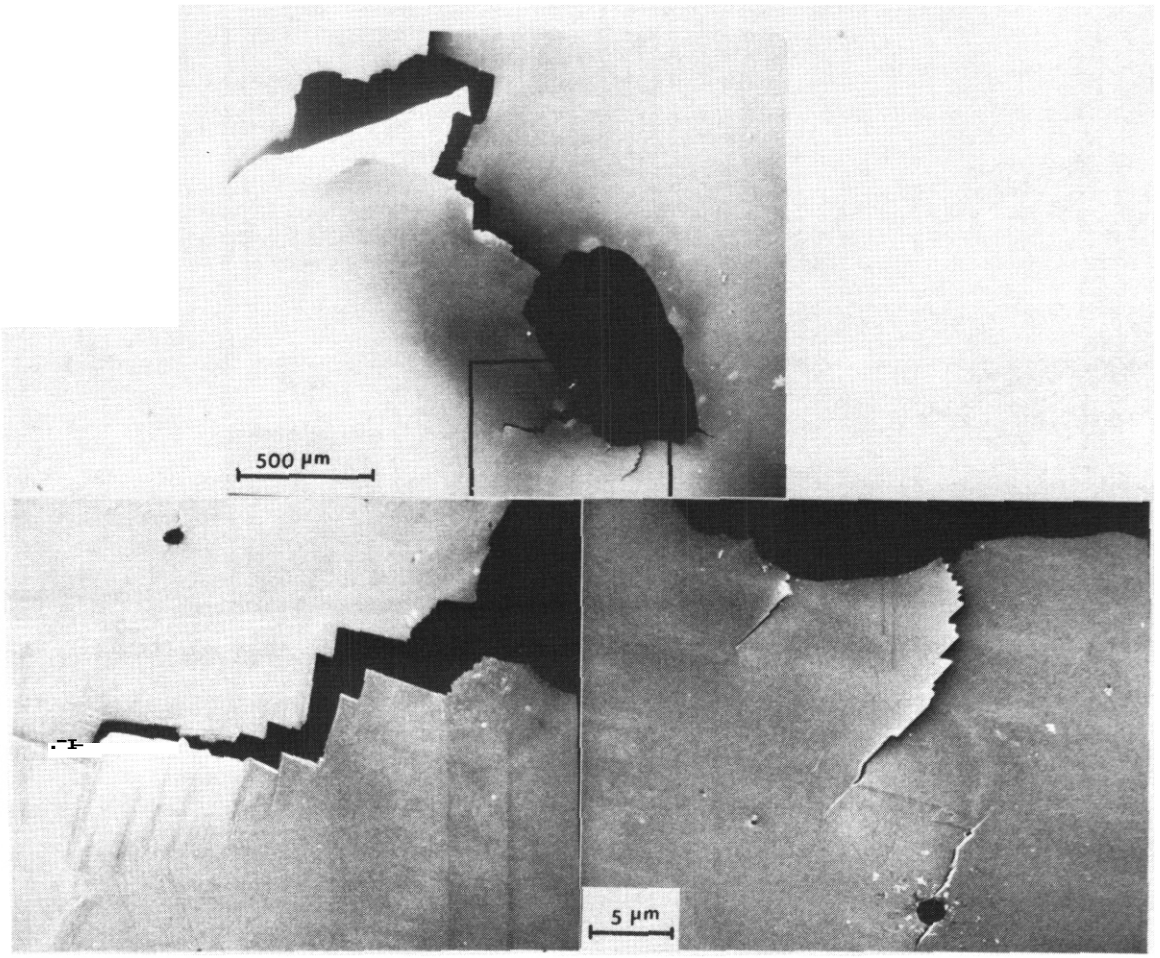


Fig. 20. Brittle cracks produced at room temperature in a prethinned First Core TEM disk designated 46M7.

Summary of Failure Modes

Whereas the tensile data seemed to indicate an abrupt change from channel failure to quasi-cleavage failure when the test temperature fell to room temperature, the results of the compact tension and microscopy disk studies show that the situation is somewhat more complex. The First Core steel not only changes its fracture mode as a function of neutron fluence and test temperature, but also as a function of the stress state and the nature of the constraints imposed on the deforming volume.

Consider the various failure modes observed at room temperature. Failure occurred by cleavage at low threshold stress in the precracked zones and by quasi-cleavage in the tested zone of compact tension specimens. Quasi-cleavage was also observed in tensile tests and in the thinned region adjacent to the hole of a microscopy disk. In the latter case the failure mode changed to channel fracture as the crack point encountered different constraints in crossing a grain boundary. Bending of disks, on the other hand, caused only channel fracture to occur.

Channel fracture also occurred in the titanium-modified steels, even though the phase evolution of these steels is somewhat more complex than that of unmodified steels and swelling is delayed by this difference in evolution.

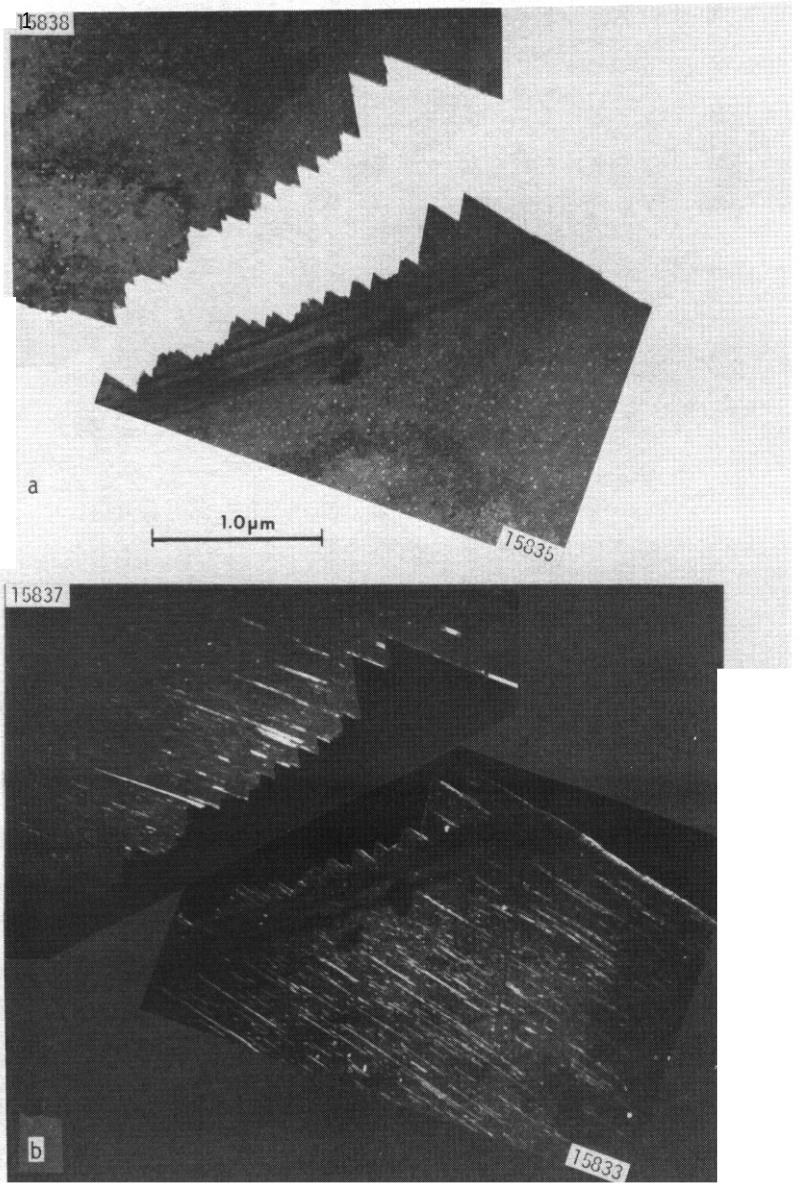


Fig. 21. Crack teeth aligned with twins in the matrix in specimen 46M7 (a) bright-field, (b) dark-field.

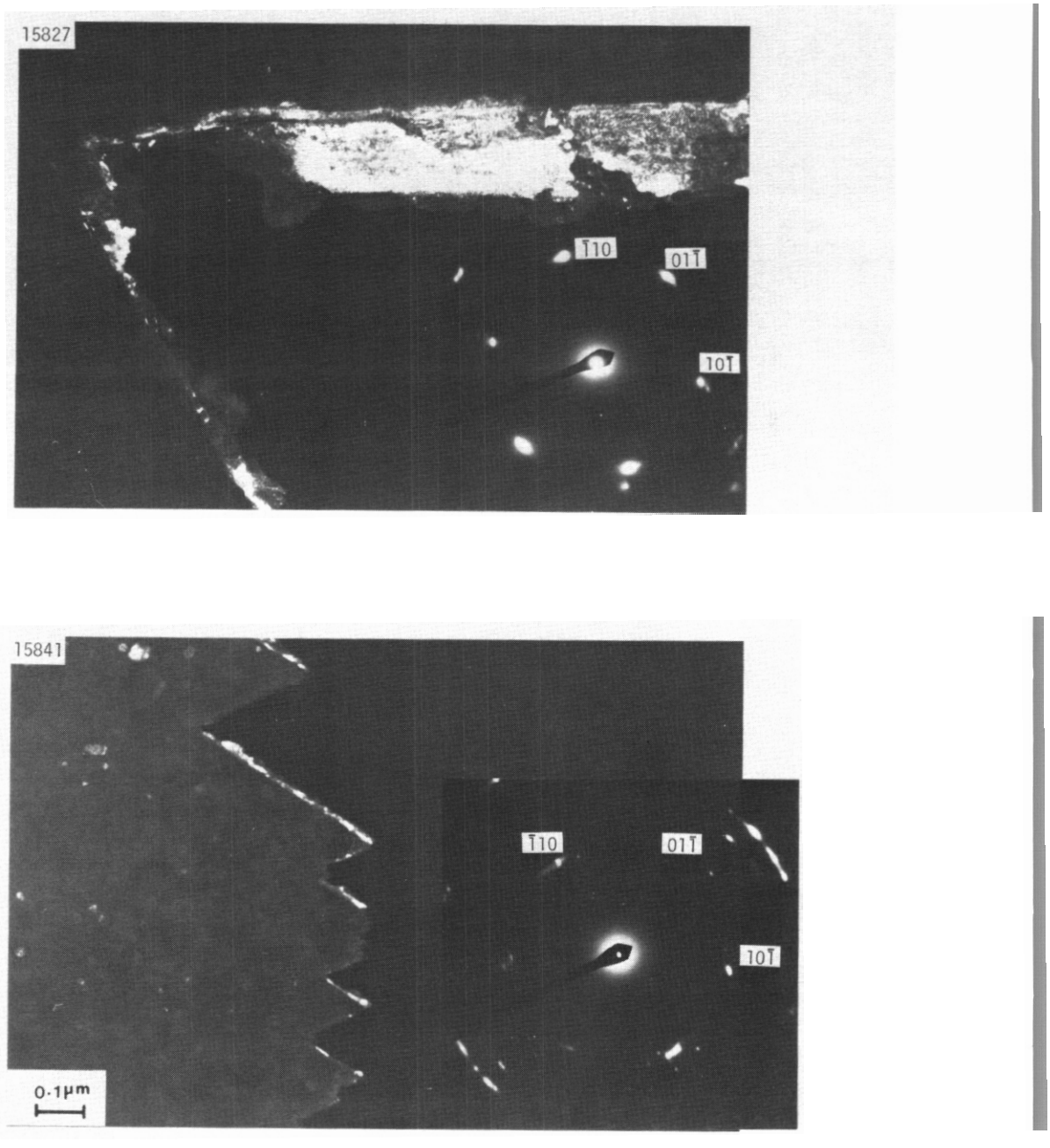


Fig. 22. a–Martensite layer observed along the crack path in 46117. The inserted diffraction patterns are <111> patterns of a bcc lattice.

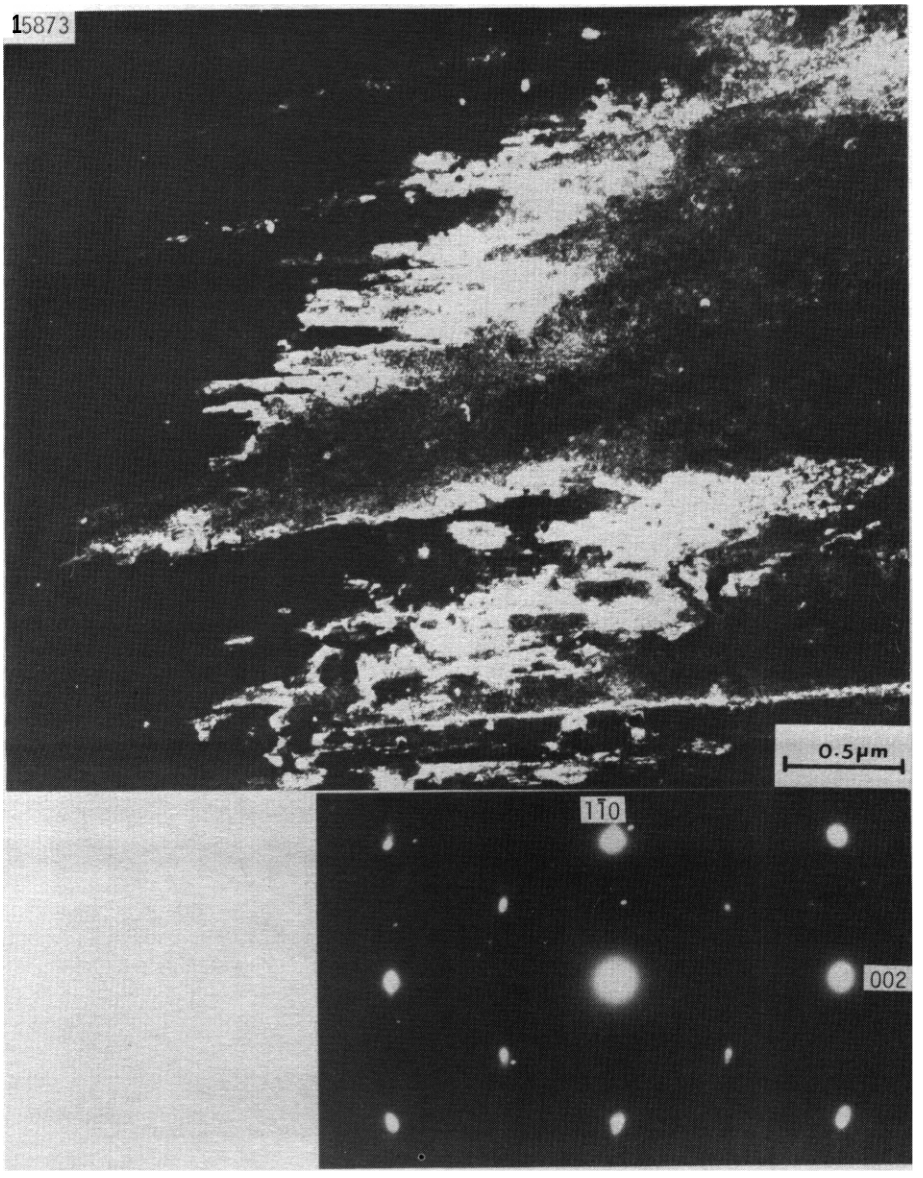


Fig. 23. Martensitic material and its associated diffraction pattern observed in a P53 duct fragment deformed at room temperature.

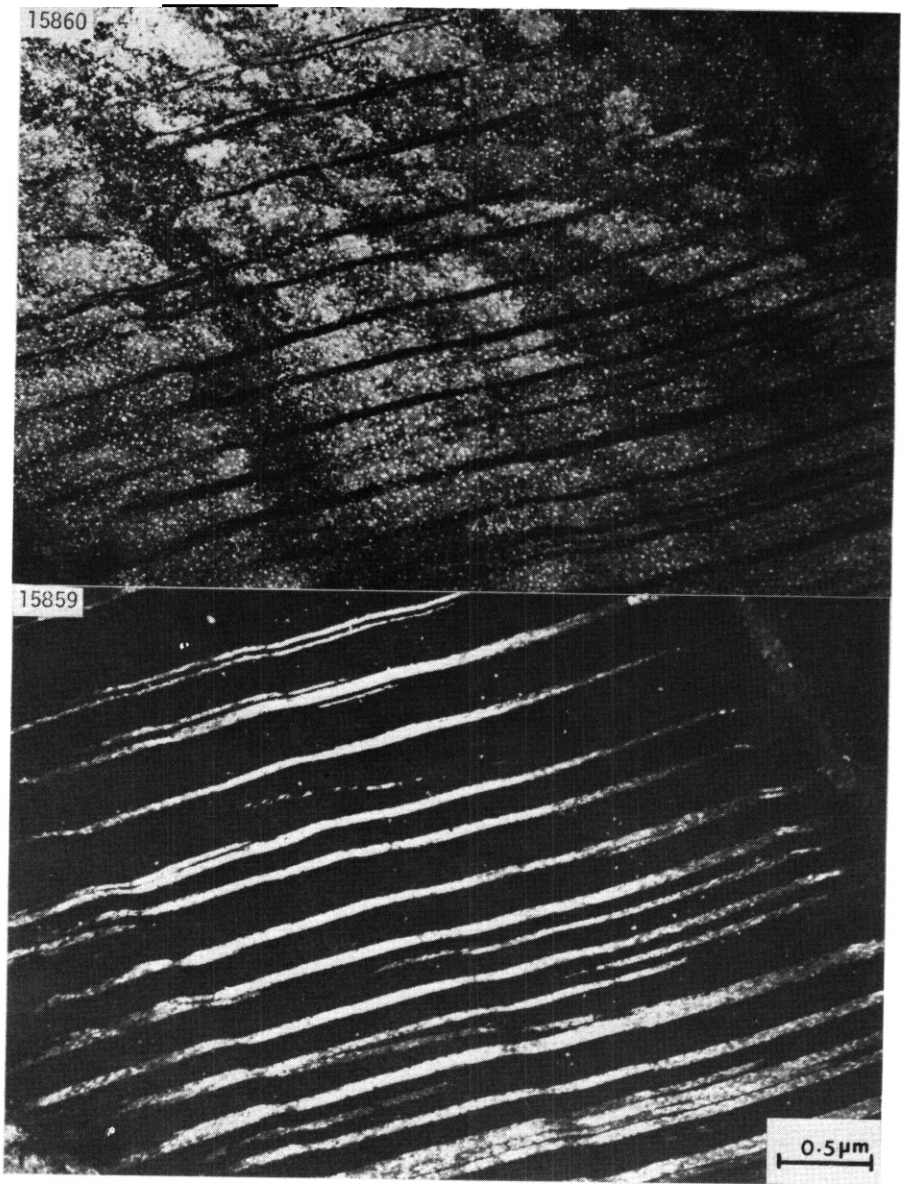


Fig. 24. Deformation twins observed in the P53 duct that appear to be e-Martensite. (top) bright-field, (bottom) dark-field picture of the same area.

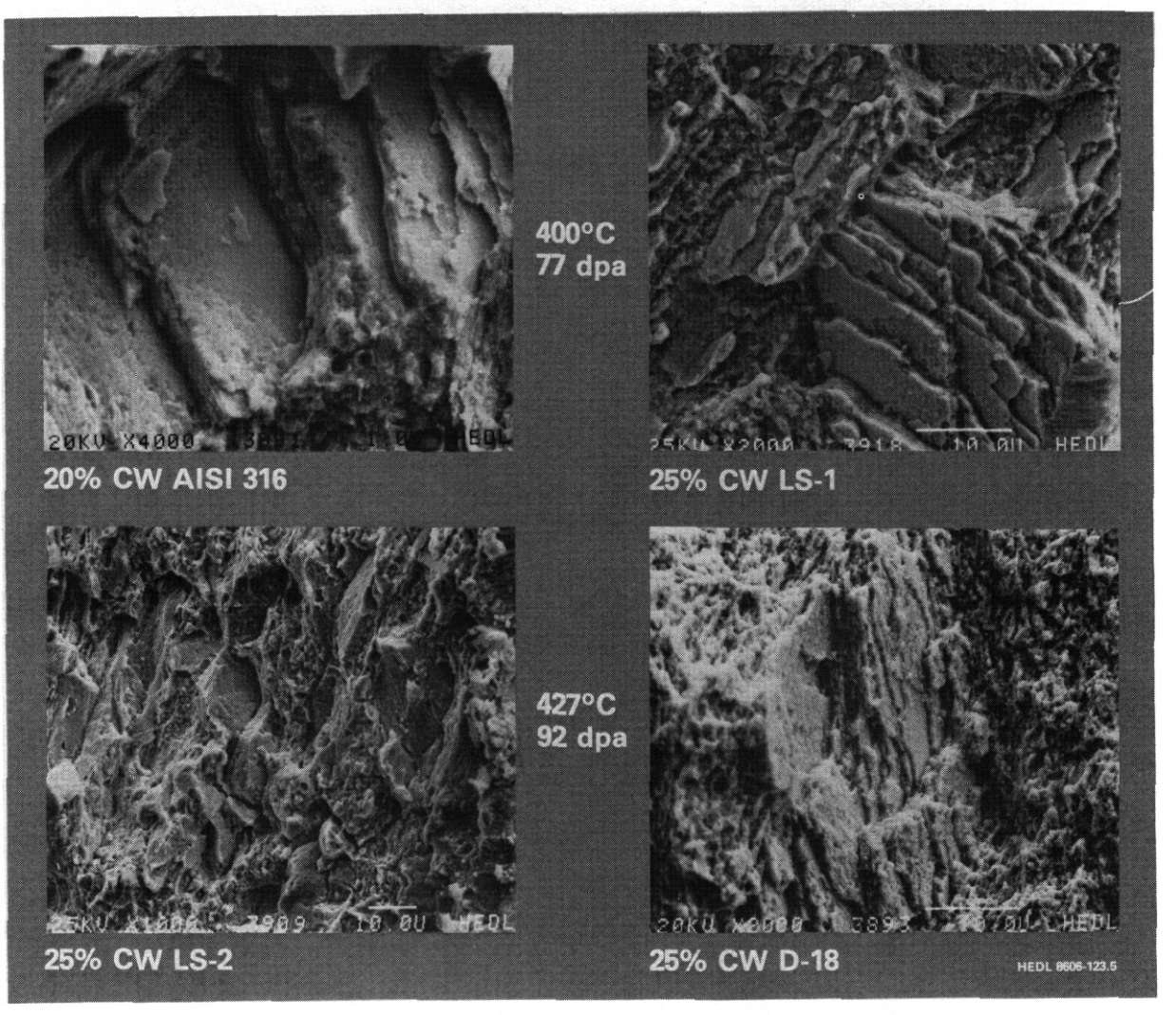


Fig. 25. Channel fracture observed on microscopy disks of various austenitic alloys irradiated in EBR-II. These disks were broken manually at room temperature.

The amount of channel fracture appears to be related to the amount of swelling. Note in Fig. 25 that comparable levels of faceting on the fracture surface require higher fluences for the LS2 and D18 steels which swell later than the 316 and LS1 steels. It also appears that the amounts of swelling and faceting each correlate with the nickel level of the steel.

A Proposed Model for the Changes in Fracture Mode

The results of these and other studies[11-13] show that the development of both channel fracture and quasi-cleavage is associated with the concurrent development of significant levels of swelling. Both swelling and the changes in failure mode are retarded by cold-work, increases in nickel content (304 vs 316 stainless, D18 vs LS2) and the addition of solutes (316 vs LS1). The current study also indicates that a deformation-induced martensite transformation plays a large role in hardening the alloy and thus contributing to its precipitous decrease in tearing resistance.

It appears that it is possible to link these two factors in a model that will explain the results of this study. Such a model will have its most severe test in providing an explanation for the shift from channel fracture to quasi-cleavage as the temperature is lowered.

The link between martensite formation and the onset of rapid void swelling is proposed to lie in the radiation-induced changes in composition that occur on a microscopic scale. This microchemical evolution

results in the progressive removal of a large fraction of the nickel and most of the silicon from the alloy matrix into a variety of precipitates such as γ' (Ni_3Si) and G-phase.[17-19] Nickel and silicon have a large effect on vacancy diffusivity and their removal from solution increases the supersaturation of vacancies, thus promoting void nucleation.[19-24] It has been shown that irradiation of 316 stainless steel in a variety of conditions always leads to a reduction in the matrix nickel content to ~9%.[25] Similar behavior has been observed in titanium and phosphorus-modified steels, where the onset of rapid swelling has also been correlated with the drop in nickel content.[,]

Once formed, however, voids strongly segregate nickel at their surface via the inverse Kirkendall effect, in which the slowest diffusing elements segregate by default at the bottom of vacancy gradients.[28,29] Thus, as voids become the dominant feature of the microstructure, the spaces between them become increasingly depleted in nickel and enriched in chromium. In several irradiation experiments involving low nickel levels and larger than average silicon levels, the matrix depletion has been so strong as to cause the region between voids to transform to massive ferrite, leaving only the voids coated with austenite.[28-30]

The fault structure that occurs on (111) planes in fcc alloys is identical to that of the hcp ε-phase involved in the $\gamma \rightarrow \varepsilon \rightarrow \alpha$ transformation of austenite to ferrite. A drop in stacking fault energy thus predisposes the alloy toward this transformation. While silicon and other solutes influence somewhat the stacking fault energy (SFE) of austenitic alloys,[,] chromium and particularly nickel have a very large influence.

As shown in Table 6, Latanison and Ruff[] have demonstrated that the stacking fault energy at room temperature of Fe-18Cr-XNi alloys drops 31% when X decreases from 15.9 to 10.7%. Lecroisey and Thomas[34] noted that in simple ternary alloys the SFE at room temperature fell from 45 ergs/cm^2 in Fe-14.1Ni-17.8Cr to 24 ergs/cm^2 in Fe-12.5Ni-15.9Cr. Bampton and coworkers[] and Rhodes and Thompson[] confirm the influence of nickel and chromium on SFE, with the latter stating that SFE in mJ/m^2 = 17.0 + 2.29 (Ni) -0.9 (Cr) for alloys with relatively low chromium levels.

Table 6. Stacking fault energy (SFE) of Fe-Cr-Ni alloys as function of temperature and composition[*]

T, °C	Ni, wt %	Cr, wt %	SFE, mJ/m^2	
25	10.7	18.3	16.4	44% difference
25	15.9	18.7	23.6	
325	10.7	18.3	30.4	5% difference
325	15.9	18.7	31.8	

Table 6 shows one other very important factor that must be taken into consideration. As noted by Latanison and Ruff[] as well as Lecroisey and Thomas,[] the stacking fault energy increases with temperature but not at the same rate in each alloy. Table 6 shows that the increase in SFE at 325°C is only 5% when the nickel level increases from 10.7 to 15.9%, while at room temperature a comparable increase in nickel yields an increase of 44%.

This provides a possible explanation of why the formation of ε microplatelets such as shown in Fig. 15 is so much more pronounced in the tensile tests conducted at room temperature. Not only is the yield strength larger at the lower temperature but the impact of the reduced matrix nickel levels is much larger at room temperature. At higher temperatures the stacking fault energy is higher and the impact of nickel segregation is not so pronounced. Thus more localized deformation (channels) is permitted before martensite formation and its associated embrittlement occurs.

If this model is correct, the effect of voids on hardening is more indirect than direct. The incremental hardening attributable to the voids themselves is overshadowed by their influence on matrix composition and the subsequent formation of martensite. Whereas voids, dislocations and Frank loops represent pre-existing hardening obstacles, the martensite barriers are probably formed within the 0.2% offset used to define the yield strength. As the martensite barriers develop, the local hardening probably shifts the

deformation to other areas. When the entire gage length is hardened, failure follows virtually immediately thereafter and the extensive γ/ε boundaries provide low energy paths for crack propagation. This explains how the tearing modulus can decrease so strongly with neutron fluence while the fracture toughness does not decline.

Conclusions

An important conclusion of this study is that the tensile strength, ductility and fracture toughness of 20% cold-worked AISI 316 at fluences on the order of 15-18 x 10^{22} n/cm^2 (E > 0.1 MeV) are sufficient to permit typical in-reactor operations. However, careful handling must be employed in post-irradiation handling operations conducted out of reactor at much lower temperatures.

The severe embrittlement observed at low temperatures is thought to be an indirect consequence of the onset of rapid void swelling. The nickel that segregates to void surfaces via the inverse Kirkendall effect further depletes a matrix already reduced by extensive radiation-induced coprecipitation of nickel and silicon. The loss of nickel and the increase in chromium in the region between voids leads to a substantial decrease in stacking fault energy and causes extensive formation of ε-martensite microplatelets. These harden the matrix so as to increase the strength substantially above the "saturation levels" attained at much lower fluence. The γ/ε boundaries also provide a low energy path for crack propagation, reducing the tearing modulus to near zero and producing a very brittle failure mode referred to as quasi-cleavage.

At higher deformation temperatures the influence of nickel segregation on stacking fault energy is much less pronounced and large levels of flow localization are required before failure occurs. In this case failure occurs along the flow localization paths, commonly refered to as channels. These channels survive as facets on the fracture surface.

FUTURE WORK

This effort will continue, concentrating next on bcc alloys.

REFERENCES

1. G. D. Johnson, F. A. Garner, H. R. Brager and R. L. Fish, pp. 393-412 in ***Effects of Radiation on Materials: Tenth Conference,*** ASTM STP 725, D. Kramer and J. S. Perrin, Eds.; American Society for Testing and Materials, 1981.

2. F. A. Garner, M. L. Hamilton, N. F. Panayotou and G. D. Johnson, ***Journal of Nuclear Materials,*** Vols. 103 & 104, pp. 803-807, 1981.

3. H. R. Brager, L. D. Blackburn and D. L. Greenslade, ***Journal of Nuclear Materials,*** Vols. 122 & 123, pp. 332-337, 1984.

4. H. R. Brager, F. A. Garner and M. L. Hamilton, ***Journal of Nuclear Materials,*** Vols. 133 & 134, pp. 594-598, 1985.

5. R. L. Simons and L. A. Hulbert, pp. 820-839 in ***Effects of Radiation on Materials: Twelfth International symposium,*** ASTM STP 870, F. A. Garner and J. S. Perrin, Eds.; American Society for Testing and Materials, Philadelphia, 1985.

6. M. L. Hamilton, N. S. Cannon and G. D. Johnson, pp. 636-647 in ***Effects of Radiation on Materials: Eleventh Conference,*** ASTM STP 782, H. R. Brager and J. S. Perrin, Eds.; American Society for Testing and Materials, 1982.

7. M. L. Hamilton, F. A. Garner and W. G. Wolfer, ***Journal of Nuclear Materials,*** Vols. 122 & 123, pp. 106-110, 1984.

8. M. L. Hamilton, F. A. Garner and W. J. S. Vang, ***Fusion Technology,*** Vol. ***10,*** pp. 405-410, 1986.

9. F. A. Garner, ***Journal of Nuclear Materials,*** Vols. 133 & 134, pp. 113-118, 1985.

10. F. A. Garner, H. R. Brager, M. L. Hamilton, R. A. Dodd and D. L. Porter, ***Radiation Effects,*** Vol. 101, pp. 37-53, 1986.

11. R. L. Fish, J. L. Straalsund, C. W. Hunter, and J. J. Holmes, pp. 149-164 in ***Effects of Radiation on Substructure and Mechanical Properties of Metals and alloys,*** ASTM STP 529, American Society for Testing and Materials, 1973.

12. W. J. Mills, ***Fracture Toughness of Irradiated Stainless steel Alloys,*** HEDL-SA-3471, Hanford Engineering Laboratory Report, January 1986.

13. F. H. Huang, ***International*** *Journal* of ***Fracture,*** Vol. 25, pp. 181-193, 1984.

14. H. R. Brager, F. A. Garner, E. R. Gilbert, J. E. Flinn and W. G. Wolfer, pp. 479-507 in ***Radiation Effects*** in ***Breeder Reactor Structural Materials,*** M. L. Bleiberg and J. W. Bennet, Eds.; TMS-AIME, New York, 1977.

15. F. H. Huang and G. L. Wire, Journal of ***Engineering Materials and Technology,*** Vol. 101, p. 403, 1978.

16. P. L. Magonon, Jr. and G. Thomas, ***Metallurgical Transactions,*** Vol. 1, p. 1571, 1970.

17. F. A. Garner, pp. 165-189 in ***Phase Stability During Radiation,*** J. R. Holland, L. K. Mansur and D. I. Potter, Eds.; TMS-AIME, Warrendale, PA, 1981.

18. F. A. Garner, Journal ***of Nuclear Materials,*** Vols. 122 & 123, pp. 459-471, 1984.

19. F. A. Garner and W. G. Wolfer, **ibid**, pp. 201-206.

20. F. A. Garner and W. G. Wolfer, *Journal* ***of Nuclear Materials,*** Vol. 102, pp. 142-150, 1981.

21. 6. Esmailradeh and A. S. Kumar, pp. 468-480 in ***Effects*** of ***Radiation*** *on* ***Materials: Twelfth*** *International* ***Symposium,*** ASTM STP 870, F. A. Garner and J. S. Perrin, Eds.; American Society for Testing and Materials, Philadelphia, PA, 1985.

22. 6. Esmailzadeh, A. S. Kumar and F. A. Garner, *Journal* of ***Nuclear Materials,*** Vols. 133 & 134, pp. 590-593, 1985.

23. F. A. Garner and A. S. Kumar, in ***Radiation-Induced Changes in Microstructure,*** ASTM STP ***955,*** F. A. Garner, N. H. Packan and A. S. Kumar, **Eds.**; American Society for Testing and Materials, Philadelphia, PA, 1987, in press.

24. W. A. Coghlan and F. A. Garner, ibid.

25. H. R. Brager and F. A. Garner, *Journal* of ***Nuclear Materials,*** Vol. 117, pp. 159-176, 1983.

26. L. E. Thomas, p.597 in ***Proceedings,*** *40th Annual* ***Meeting of the Electron Microscopy Society of*** *America*, G. W. Bailey, Ed.; Washington, DC, 1982.

27. M. Itoh, S. Onose and S. Yuhara, in ref. *23.*

28. H. R. Brager and F. A. Garner, pp. 219-235 in ref. 17.

29. D. L. Porter and E. L. Wood, *Journal* ***of Nuclear Materials,*** Vol. 83, pp. 90-97, 1979.

30. 0. J. Mazey, D. R. Harries and J. A. Hudson, pp. 61-67 in ***Proceedings, Irradiation Behavior of Metallic Materials for Fast Reactor Core Components,*** Ajaccio, Corsica, 1979.

31. D. Dulieu and J. Nutting, pp. 140-145 in ***proceedings, Metallurgical Developments in*** *High* ***Alloy Steels,*** Scarborough, England, June 1964.

32. 8. Thomas and G. Henry, *Memoires Scientifique,* ***Revue Metallurgique,*** Vol. LXIV, pp. 625-636, 1967.

33. R. M. Latanison and A. W. Ruff, Jr., ***Metallurgical Transactions,*** Vol. 2, pp. 505-509, 1971.

34. F. Lecroisey and B. Thomas, *Physica* ***status Solidi A,*** Vol. 2, pp. K217-K219, 1970.

35. C. C. Bampton, I. P. Jones and M. H. Loretto, ***Acta Metallurgica,*** Vol. 26, pp. 39-51, 1978.

36. C. G. Rhodes and A. W. Thompson, ***Metallurgical Transactions,*** Vol. 8A, pp. 1901-1906, 1977.

6.3 Vanadium Alloys

CHARPY IMPACT PROPERTIES OF V-15Cr-5Ti - N. S. Cannon, M. L. Hamilton and A. M. Ermi (Westinghouse Hanford Company)

OBJECTIVE

The object of this effort is to determine the influence of composition, heat treatment and irradiation conditions on the impact properties of vandium-based low activation alloys.

SUMMARY

Impact tests have been completed on unirradiated one-third size Charpy specimens of V-15Cr-5Ti. The ductile-to brittle transition temperature was unexpectedly high, on the order of 130°C. Irradiation of this alloy in FFTF-MOTA in lithium-filled TZM subcapsules has also been completed at 385, 420, 520, and 600°C, with damage levels ranging from 10 to 30 dpa. Impact tests on these specimens are now being planned.

PROGRESS AND STATUS

Introduction

Vanadium alloys are currently being considered for use in fusion reactors for first wall and blanket applications on the basis of both low activation considerations and the increase in operating temperature achievable over that available with the use of ferritic steels.[1]

V-15Cr-5Ti in the annealed condition (1200°C/1.0 hrlair cool) was irradiated in FFTF-MOTA to doses ranging from 10 to 30 dpa. The specimens were maintained in lithium-filled TZM subcapsules at 385, 420, 520, and 600°C. Both TEM disks and one-third size Charpy specimens were employed.

The specimens were removed from the subcapsule, cleaned at Argonne National Laboratory, and are now ready for density measurements and impact testing in air at HEDL. Details of the test procedure are presented elsewhere.[2]

Results

The impact tests on the unirradiated specimens are complete. As shown in Fig. 1, the ductile-to-brittle transition temperature was unexpectedly high, on the order of 130°C. It is anticipated that irradiation will lead to a higher transition temperature, and impact tests on these specimens must he very carefully conducted to prevent accidental breakage and to avoid damaging the temperature-limited drop tower.

Future Work

Impact tests and density measurements on the irradiated material will commence shortly.

REFERENCES

1. D. L. Smith, Journal of Nuclear Materials, 122/123, (1984) 51-65.

2. W. L. Hu and D. S. Gelles, pp. 631-645 in Proceedings of Topical Conference on Ferritic Alloys for Use in Nuclear Energy Technologies, J. W. Davis and D. J. Michel, Eds.; Snowbird, Utah, June 19-23, 1983.

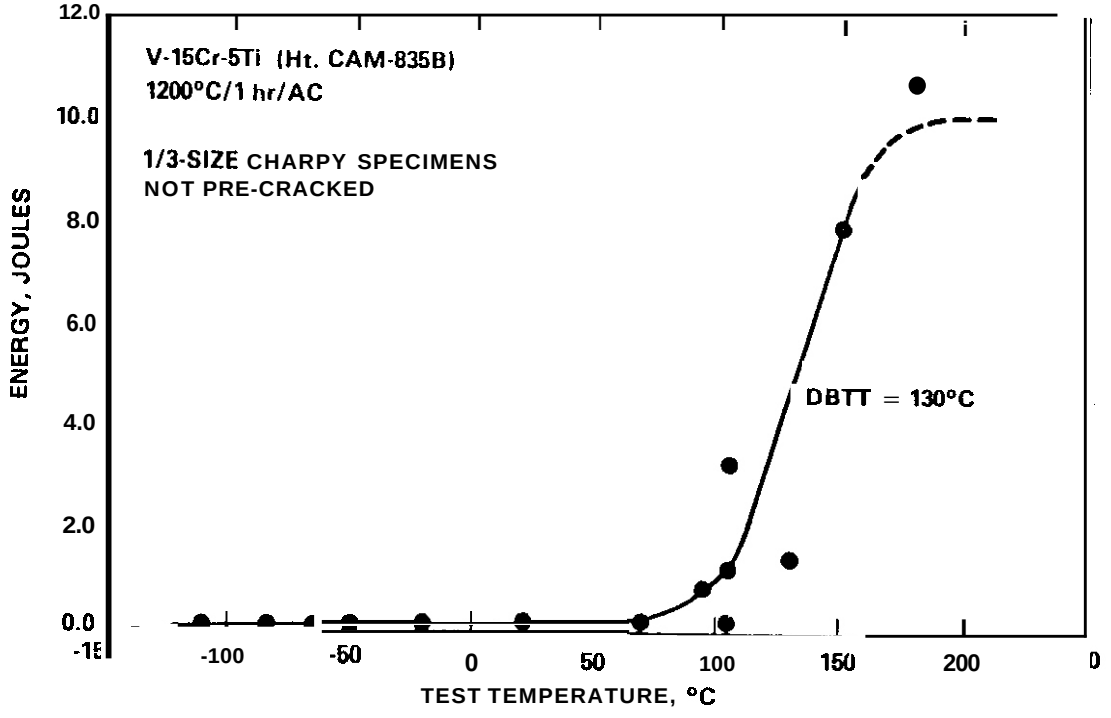


Fig. 1. Charpy test results on V-15Cr-5Ti in the annealed and unirradiated condition

PREPARATION AND FABRICATION OF VANAOIUM BASE ALLOYS - A. G. Hins and H. R. Thresh (Argonne National Laboratory)

OBJECTIVE

Two objectives are focused upon during execution of the vanadium alloy materials fabrication task. They are: (i) to supply fabricated vanadium alloy sheet and bar stock for material properties testing by experimenters active in other tasks of the development program and (ii) to evaluate the influence of process variables on the mechanical properties of selected vanadium alloys. Both objectives are met by fabricating various alloy materials with continually upgraded process operations, which are revised through feedback from the results obtained on previous fabrication runs. Work on the second objective is augmented by an extensive review of fabrication histories on prior vanadium alloy production done for the LMFBR program. Influence of interstitial content on fabricability of the various alloys is being studied and is used as a screening tool in support of the materials testing program. Efforts to date have been focused on the V-15Cr-5Ti and V-10Cr-5Ti alloys. Work has begun on other alloys of the V-Cr-Ti, V-Ti and V-Ti-Si alloy systems. The work also provides for the continuation of complementary activity ongoing at Teledyne Wah Chang Albany.

SUMMARY

Past reports detailed the design and startup of a fabrication process flowsheet. The planned fahrication methods were used to process a 13 Kg quantity of V-15Cr-5Ti alloy. Adopting the same approach, a 2.6 Kg dual lot of V-10Cr-5Ti alloy was consolidated, consumable arc melted, extruded and final rolled to customer specified shapes and sizes during this reporting period. The primary products were 0.035" and 0.020" sheet for tensile tests and 0.140" stock for charpy bar tests, Additional sheet and bar material has been fabricated from previously cast alloys of V-20Ti, V-7.5Cr-15Ti and V-3Ti-1Si.

In addition, this effort provides for correlation of complementary fabrication work on V-12Cr-5Ti and V-10Cr-10Ti alloys at Teledyne Wah Chang Alhany.

PROGRESS AND STATUS

Introduction

The processing steps outlined in the ANL revised flowsheet[1] for the fabrication of V-15Cr-5Ti alloy. have been used to produce two billets, dual lot, of V-10Cr-5Ti alloy. However, the extrusion flowsheet was revised to allow production of small, 1.3 Kg, billets on a 350 ton vertical extrusion press. In this case a much higher extrusion ratio, 12:1 vs the previous 4:1, was employed to effect a high primary breakdown working operation.

Alloy Processing

In attempting to optimize the number of alloy compositions synthesized with the amount of material produced in each alloy cycle, heat size is being reduced to increase the breadth of compositional variables that can be studied. Hence the extrusion part of the process flow has been moved from the 1250 ton Lake Erie Press to the 350 ton Lombard Press.

A total of eleven 4-1/2" long consolidation bars were made by D.C. plasma arc melting. A 3-melt cycle was used to optimize homogeneity of major constituents. The finished bars were joined by TIG welding in an inert atmosphere to produce a 49" long consumable melting electrode. This was vacuum arc melted into a 2" water cooled copper mold. The resultant 11-1/2" ingot was cut in half and the pieces machined to 1.74" diameter for extrusion stock. Seven-inch long stainless steel cans were loaded with the billets and sealed by arc welding. A 2-hour soak at 1125°C preceded the extrusion run and the extrusion press container was heated to 475°C. Extrusion AM205 was made through a 1" x 1/4" bar die, which provided a calculated extrusion ratio of 11.8:1. Extrusion AM206 was made through a 5/16" x 3/4" die.

An attempt was made to hot straighten the bowed extrusion bars. However, extreme material toughness at the extruded bar temperature left a minimal result. After cooling, the stainless steel clad was stripped from the vanadium alloy bars using mechanical peeling techniques. A "wash" parting compound, applied to the billet before assembly, aided the stripping operation.

After a vacuum anneal of one hour at 850°C, final rolling operations on the V-10Cr-5Ti alloy were conducted at room temperature. During sheet rolling. intermediate vacuum anneals were used in a sequence that led to a final product cold work of 50%. Finished material hardness was in the range of R_A 60-64. This particular alloy did not exhibit the "alligator" cracking problems during rolling that were experienced with the V-15Cr-5Ti alloy. The breakdown of the cast structure at the hot working stage,

which inherently used the compressive mode of the extrusion process, contributed to this situation. Ultrasonic examinations were run on all product sheets and no internal laminations or other flaws were found. Although this alloy fabrication sequence involved a larger breakdown extrusion ratio and a thinner feed bar for final rolling, a conclusion was made that the V-10Cr-5Ti permits a higher level of fahrication management to be attained when compared to the V-15Cr-5Ti material.

Material Characterization

Analytical chemistry work has not been completed on the V-10Cr-5Ti alloy product to date. However, such analyses are planned for the next report.

Metallographic examination of samples from the two extrusions, AM205 and AM206, and final sheet products have been carried out in the longitudinal and transverse modes. In the extruded state, a recrystallized equiax single phase alloy dispersed with occasional elongated grains resembling a stringer formation is observed. It is known that such stringers are not due to constitutional inhomogeneities within the structure. A typical structure of a longitudinal section from extrusion AM206 is recorded in Figure 1. Although the general structure is similar to V-15Cr-5Ti, the V-10Cr-5Ti displays an almost complete absence of a dark round precipitate found in the high Cr alloy in a zoned distribution pattern. The microstructure from 50% cold worked alloy from extrusion AM205 is shown in Figure 2. This structure is typical of a heavily deformed single phase equiax grain alloy.

FUTURE WORK

Further characterization work on the V-10Cr-5Ti alloy will be pursued especially to define the overall chemistry of this material. Property measurements of previously fabricated alloys will be reviewed to permit the next alloy candidate to be identified. This alloy selection will allow initial fabrication efforts to commence.

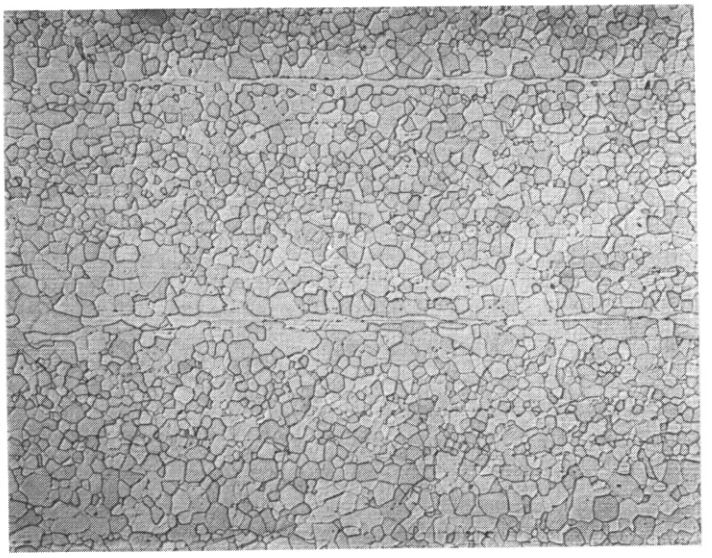


Figure 1. Microstructure of Extruded V-10Cr-5Ti Alloy Bar (AM206), Magnification X100, Longitudinal Section

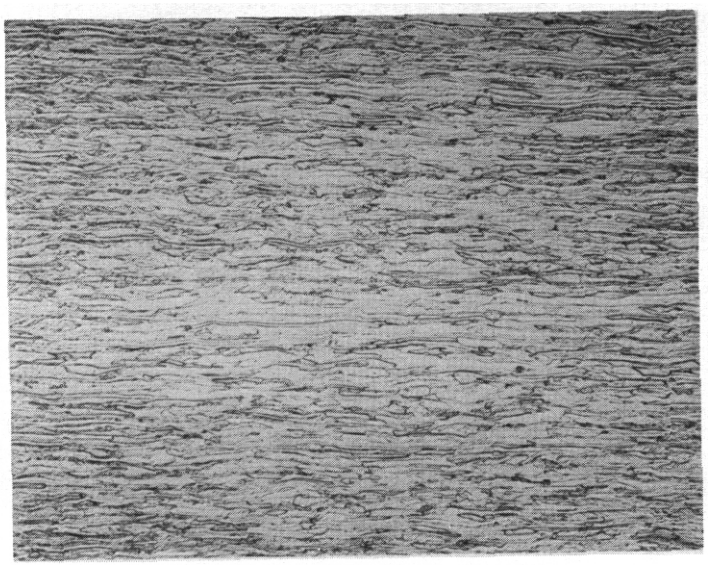


Figure 2. Microstructure of Cold Rolled (50% C.W.) V-10Cr-5Ti Alloy Sheet, Magnification X200, Longitudinal Section.

REFERENCES

1. A. G. Hins and H. R. Thresh, "Preparation and Fabrication of Vanadium Base Alloys," pp. 73-71 in Alloy Development for Irradiation Performance: Semiannual Progress Report for Period Ending March 31, 1986, DOE/ER-0045, Oak Ridge National Lahoratory, Oak Ridge, TN, Sept. 1986.

EFFECT OF HEAT TREATMENT AND IMPURITY CONCENTRATION ON THE TENSILE DEFORMATION OF UNIRRADIATEO AND IRRADIATED VANADIUM ALLOYS - B.A. Loomis, R. H. Lee, and D. L. Smith (Argonne National Laboratory)

OBJECTIVE

The objective of this research is to provide guidance on the applicability of vanadium-base alloys for structural components in a fusion reactor.

SUMMARY

The effect of heat treatment and oxygen, nitrogen, carbon, and hydrogen impurities on the yield strength, ultimate tensile strength, ductility, and fracture mode for the V-15Cr-5Ti, V-12Cr-5Ti, V-15Ti-7.5Cr, V-20Ti, and V-3Ti-1Si alloys was determined from tensile tests at 20°C. In the case of the V-Cr-Ti alloys in the fully recrystallized condition, the results showed that for the alloys to exhibit ductile fracture on tensile deformation at 20°C, they must be annealed in vacuum (rather than in argon-filled capsules) and contain 800-900 ppm oxygen. The V-20Ti and V-3Ti-1Si alloys, which contain 800-900 ppm oxygen, exhibited ductile fracture after a recrystallization anneal in vacuum as well as in argon-filled capsules. These results were interpreted as evidence that vanadiun alloys containing chromiun solute are more susceptible to hydrogen embrittlement. The yield strength of vanadiun alloys, which were similarly annealed in vacuun and contained comparable oxygen concentration 1800-900 ppm), increased with an increase of the combined titaniun and chromium concentration. The total elongation of these alloys was not significantly altered by the change in alloy composition. On the basis of microstructures obtained fran ion-irradiated alloys, it was concluded that the V-3Ti-1Si and V-20Ti alloys were not intrinsically more resistant to hardening and embrittlement on neutron irradiation than the V-15Cr-5Ti alloy.

PROGRESS AND STATUS

Introduction

The vanadiun-base alloys are considered to be potentially useful materials for structural components in a magnetic fusion reactor. However, substantial developnent work is required to determine the effects that composition, thermo-mechanical treatment, processing variables, impurity concentration, irradiation, and chemical environment have on the properties of candidate alloys. In this report, we present the results of an investigation on the effect of heat treatment and impurity concentration on the yield stress, ultimate tensile strength, and ductility of several candidate vanadium-base alloys at 20°C. These tensile results and the microstructures of the ion-irradiated alloys provide insight into the anomalous embrittlement of the V-15Cr-5Ti alloy in canparison to the ductility exhibited by the V-20Ti and V-3Ti-1Si alloys after neutron irradiation.[1]

Materinls and procedure

Tensile specimens of vanadiun alloys with the compositions listed in Table 1 were obtained from sheet stock that had undergone a 50% reduction in thickness. The tensile specimens were 1/3 ASTM standard size with a thickness of 0.76 mm. The as-fabricated tensile specimens received one of the following heat treatments:

A - 1 h at 1125°C in vacuum (2×10^{-5} Pa);
B - 1 h at 1125°C in argon-filled capsule + 10 min at 1125°C in vacuum;
C - 1 h at 1125°C in argon-filled capsule;
D - 1 h at 1200°C in argon-filled capsule t 10 min at 1125°C in vacuum;
E - 1 h at 950°C in argon-filled capsule + 10 min at 1125°C in vacuum;
F - 1 h at 1050°C in vacuum;
G - 1 h at 1100°C in argon-filled capsule;
H - 1 h at 1200°C in argon-filled capsule.

After lieat treatment, the surfaces of the sheet tensile specimens were polished to a 0.003-mm finish.

The optical microstructures for the unirradiated, annealed alloys are shown in Figs. 1 and 2. The annealing temperatures and time shown in these figures resulted in a recrystallized grain size of ~0.020 mm. The microstructures of these alloys obtained by transmission electron microscopy (TEM) showed the presence of precipitates with diameters ranging from 0.002 to 0.005 mm and a precipitate nunber density ranging fran 0.4 $\times 10^{10}$ mm^{-3} to 2 $\times 10^{10}$ mm^{-3}. The higher number density of precipitates was characteristic for the alloys with 800-900 ppm oxygen, whereas the lower nunber density of precipitates was more characteristic for the other alloys in Table 1. The annealed, unirradiated material had a dislocation density of ~10^{7} mm^{-2}.

Table 1. Alloy compositions

Alloy Number	Alloy	Source	Melt Number	Concentration wt. ppm)			
				O	N	C	H
EL-23	V-15Cr-5Ti	ORNL Fusion	CAM 834-6	310	**460**	320	-
BL-24	V-15Cr-5Ti	ANL Inventory	ANL 101	810	138	230	50
BL-41	V-15Cr-5Ti	ANL Fusion	ANL 204	350	95	100	5
BL-40	V-12Cr-5Ti	Wah Chang	TWC 040	180	42	70	-
BL-10	V-15Ti-7.5Cr	ANL Inventory	ANL 94	936	375	340	50
BL-15	V-20Ti	ORNL Fusion	CAM 832	830	830	130	-
EL-27	V-3Ti-1Si	ORNL-PETTEN	ORNL 10831	910	260	450	-

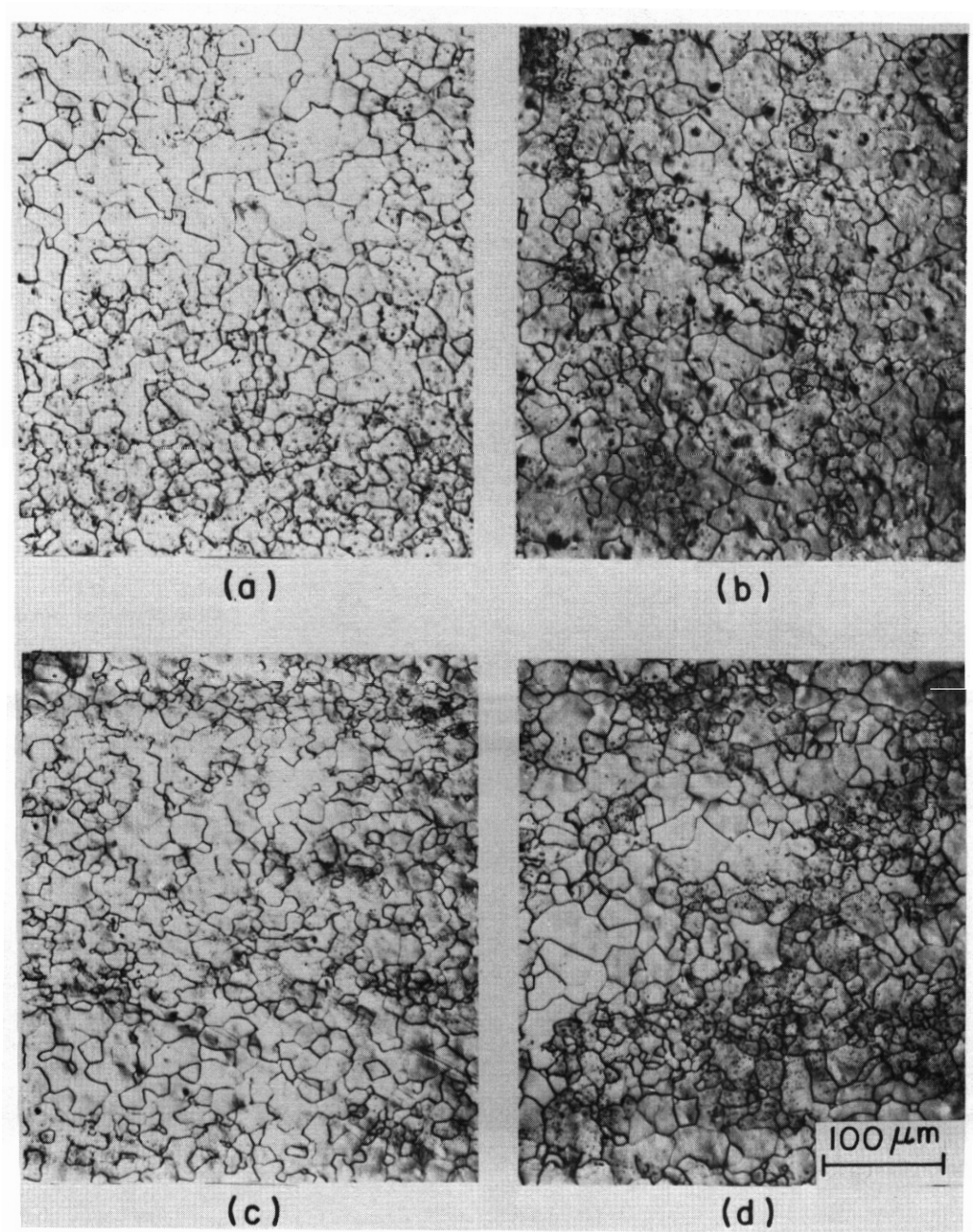


Fig. 1. Optical microstructures after 1-h anneal for (a) CAM 832 V-20Ti, 1100°C; (b) ANL 101 V-15Cr-5Ti, 1200°C; (c) ANL 204 V-15Cr-5Ti, 1125°C, and (d) TWC 040 V-12Cr-5Ti, 1125°C.

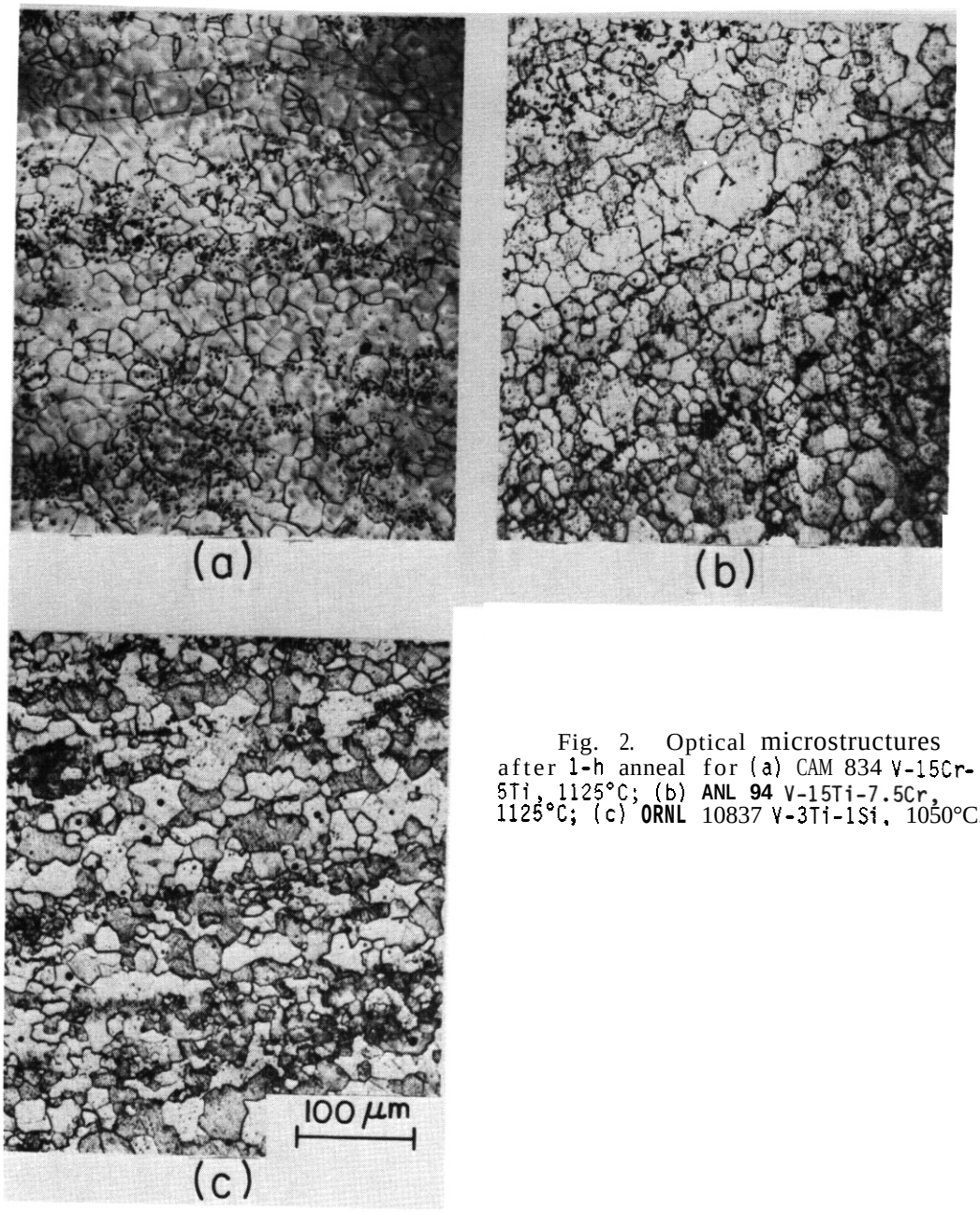


Fig. 2. Optical microstructures after 1-h anneal for (a) CAM 834 V-15Cr-5Ti, 1125°C; (b) ANL 94 V-15Ti-7.5Cr, 1125°C; (c) ORNL 10837 V-3Ti-1Si, 1050°C.

Tensile specimens of the vanadiun alloys were tested at a tensile strain rate of 0.0011 mm/mm/s for a cross-head speed of 0.008 mm/s. The fractured tensile specimens were examined by scanning electron microscopy (SEM) and energy dispersive x-ray spectroscopy (EDXS) in a JEOL 100 CX electron microscope.

Microstructure specimens of the vanadiun alloys were irradiated at 650°C with 4.0-MeV $^{51}V^{2+}$ ions to an irradiation damage level of 50 atom displacements per atom (dpa). The 650°C irradiations of the specimens were conducted in a cryogenically pumped chamber evacuated to 1.3×10^{-6} Pa. The chamber was connected by a cryogenically pumped ion-beam transport tube to the 2-MeV Tandem accelerator at Argonne National Laboratory. The specimens were irradiated at a displacement damage production rate of 5×10^{-3} dpa·s^{-1}. Following irradiation, the specimens were sectioned from the irradiated surface to a depth of 1.05×10^{-3} mm and then sectioned from the opposite surface to perforation in an 80%CH_3OH-20% H_2SO_4 solution at 5°C. The microstructures of the irradiated alloys were observed by TEM in a Philips 400T electron microscope operated at 120 keV.

Experimental results

Tensile test data. The yield strength, ultimate tensile strength, uniform elongation, total elongation, and fracture mode of the alloy tensile specimens are listed in Table 2 for several different heat treatment conditions. The load-elongation curves for the tensile specimens are shown in Fig. 3.

Table 2. Tensile test data for alloy specimens

Specimen	Alloy	Heat Treatment	Yield Strength (MPa)	Ultimate Tensile Strength (MPa)	Elongation (%) Uniform	Elongation (%) Total	Fracture	Figure No.
BL-23L-1	V-15Cr-5Ti	A	591	692[a]	24.5	24.5	Brittle	3a
BL-41L-1	V-15Cr-5Ti	A	570	674	25.8	32.3	10% Ductile	3c
BL-41L-7	V-15Cr-5Ti	B	636	701[a]	14.9	14.9	Brittle	3c
BL-41L-8	V-15Cr-5Ti	C	405[b]	-	4.6	4.6	Brittle	3c
BL-24L-14	V-15Cr-5Ti	A	514	599	20.7	29.4	Ductile	3d
BL-24L-10	V-15Cr-5Ti	B	485	594	19.7	28.4	75% Ductile	3d
BL-24L-16	V-15Cr-5Ti	C	317[b]	-	3.7	3.7	Brittle	3d
BL-24L-18	V-15Cr-5Ti	0	545	634	23.1	32.0	Ductile	3e
BL-24L-1	V-15Cr-5Ti	E	520	631	23.6	32.2	75% Ductile	3e
BL-27L-1	V-3Ti-1Si	F	337	427	23.9	33.0	Ductile	3a
BL-27L-9	V-3Ti-1Si	G	446	518	24.9	34.7	Ductile	3f
BL-15L-1	V-20Ti	H	588	692	21.9	32.1	Ductile	3a
BL-15L-16	V-20Ti	I	712	759	20.2	26.2	50% Ductile	3f
BL-40L-1	V-12Cr-5Ti	A	519	613	26.4	31.1	10% Ductile	3a
BL-1OL-1	V-15Ti-7.5Cr	A	643	718	21.0	29.7	50% Ductile	3b
BL-1OL-20	V-15Ti-7.5Cr	I	291[b]	-	2.9	2.9	Brittle	3b

[a]Specimen broke before undergoing a reduction in cross-sectional area.
[b]Specimen broke before the Stress exceeded the elastic stress limit.

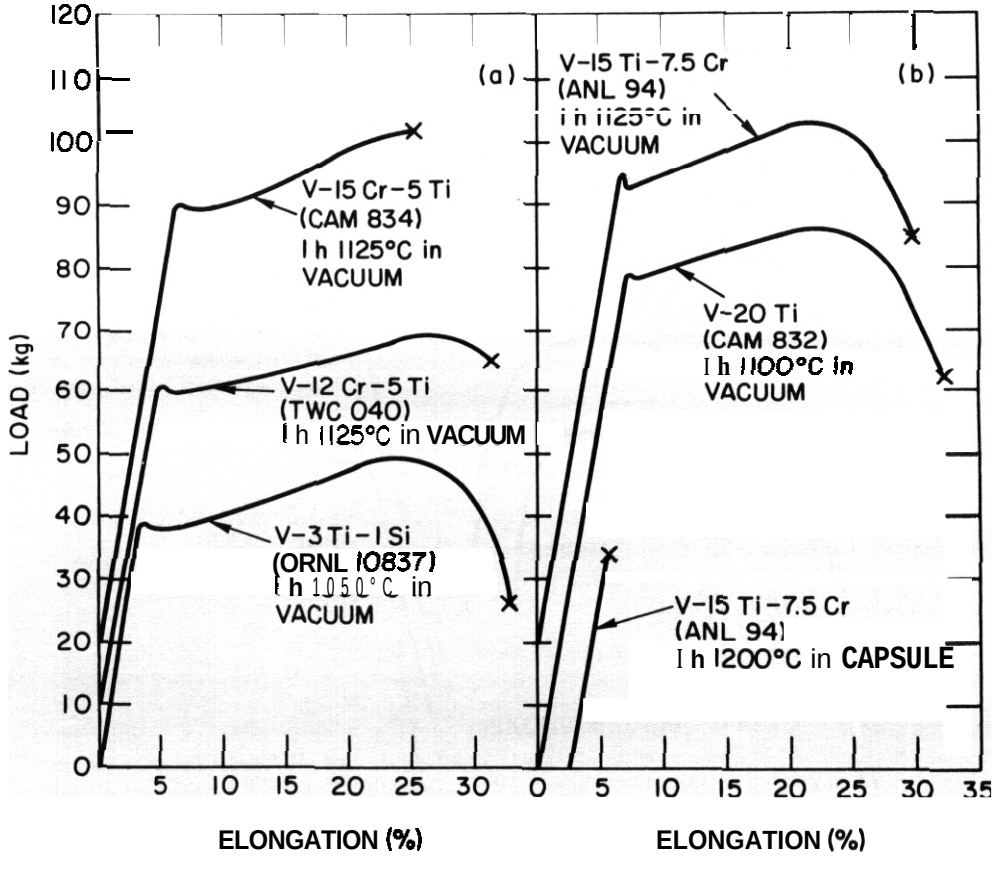


Fig. 3. Load-elongation curves for vanadium-base alloys.

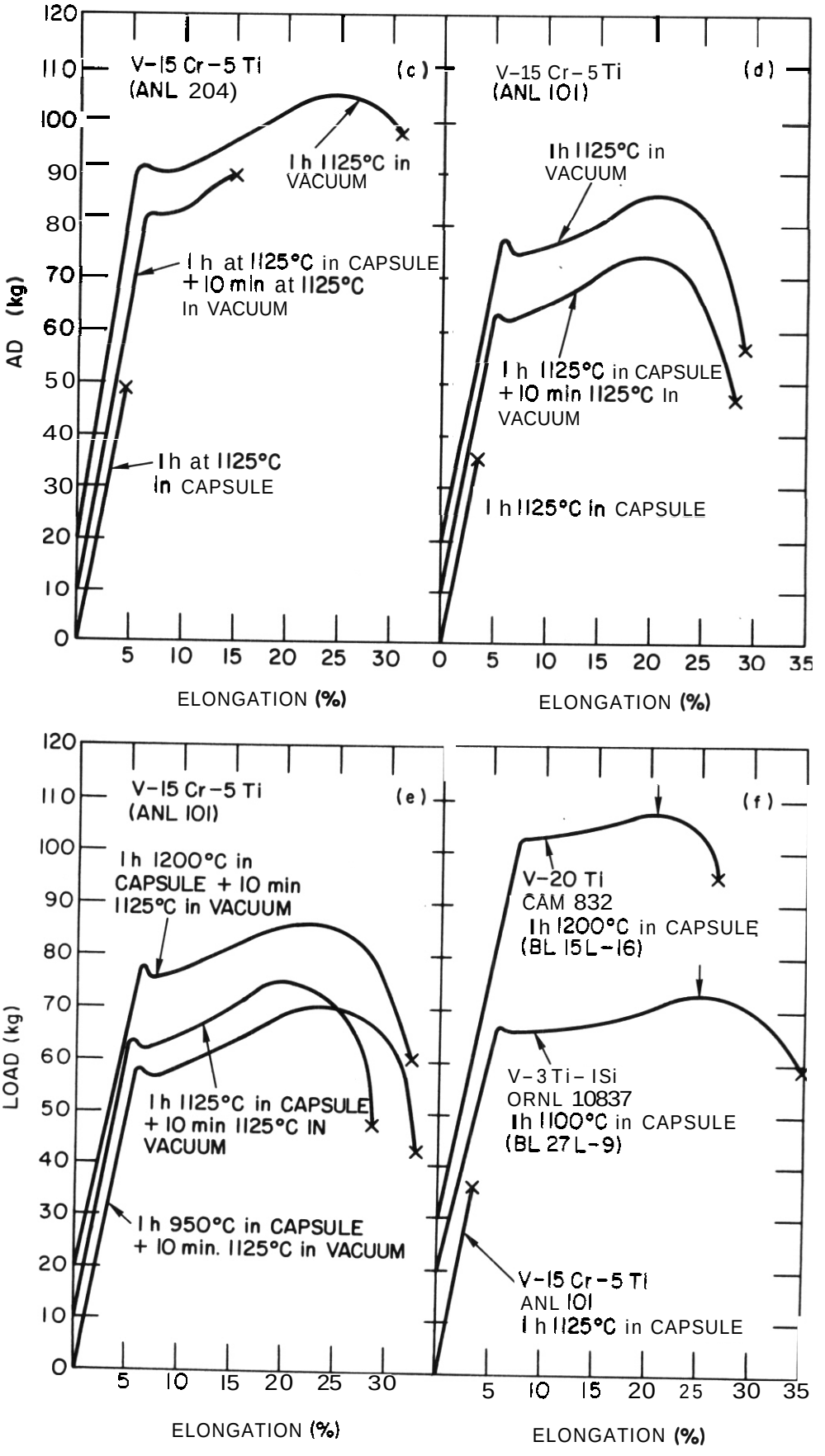

V-15 Cr-5 Ti
(ANL 204)
(c)
1 h 1125°C in VACUUM
1 h at 1125°C in CAPSULE + 10 min at 1125°C In VACUUM
1 h at 1125°C in CAPSULE
AD (kg)
ELONGATION (%)
V-15 Cr-5 Ti
(ANL 101)
(d)
1 h 1125°C in VACUUM
1 h 1125°C in CAPSULE + 10 min 1125°C In VACUUM
1 h 1125°C in CAPSULE
ELONGATION (%)
V-15 Cr-5 Ti
(ANL 101)
(e)
1 h 1200°C in CAPSULE + 10 min 1125°C in VACUUM
1 h 1125°C in CAPSULE + 10 min 1125°C IN VACUUM
1 h 950°C in CAPSULE + 10 min. 1125°C in VACUUM
LOAD (kg)
ELONGATION (%)
(f)
V-20 Ti
CAM 832
1 h 1200°C in CAPSULE
(BL 15L-16)
V-3 Ti-1Si
ORNL 10837
1 h 1100°C in CAPSULE
(BL 27L-9)
V-15 Cr-5 Ti
ANL 101
1 h 1125°C in CAPSULE
ELONGATION (%)

Fig. 3. (Contd.)

The results presented in Table 2 indicate that the method of heat treatment has a major effect on the tensile properties of the alloys, particularly the V-Cr-Ti alloys. In the case of the V-15Cr-5Ti alloys, the anneals in capsules at 950-1200°C resulted in brittle fracture of the tensile specimens. An anneal of the V-15Cr-5Ti specimens at 1125°C in vacuun for 10 min after an anneal in an argon-filled capsule resulted in a substantial increase of the percentage of ductile fracture (75%) for the EL-24 V-15Cr-5Ti alloy and little significant increase in the ductile fracture for the EL-41 V-15Cr-5Ti alloy. An increase of the annealing time to 1 h in vacuum resulted in 100% ductile fracture for the EL-24 V-15Cr-5Ti alloy and 10% ductile fracture for the EL-41 V-15Cr-5Ti alloy specimen. In the process of increasing the temperature of the tensile specimens during an anneal in vacuum, it was observed that a substantial evolution of gas occurred at 300-400°C. The composition of the gas has not been determined, but we are reasonably certain that the gas was hydrogen. The response of the V-20Ti and V-3Ti-1Si alloy tensile specimens to tensile deformation after annealing in a capsule and after annealing in vacuum showed that these alloys were much less susceptible to "gaseous (hydrogen) embrittlement," as evidenced by the difference between the uniform and the total elongation (6-10%).

Tensile specimens that contained 800-900 ppm oxygen and which were annealed in vacuum exhibited an 8-10% difference between the uniform elongation and the total elongation. These specimens tended to exhibit a high percentage of ductile fracture (Table 2). Tensile specimens exhibiting this behavior were obtained fran the EL-24 V-15Cr-5Ti, EL-27 V-3Ti-1Si, EL-15 V-20Ti, and EL-10 V-15Ti-7.5Cr alloys. Tensile specimens that contained less than 350 ppm oxygen and which were annealed in vacuum exhibited a 0-6% difference between the uniform elongation and total elongation. These specimens tended to exhibit a high percentage of brittle fracture. Tensile specimens exhibiting this behavior were obtained from the EL-23 V-15Cr-5Ti, EL-41 V-15Cr-5Ti, and EL-40 V-12Cr-5Ti alloys.

The fracture surface and the chemical analysis (EDXS) for the BL-41L-7 and BL-24L-18 V-15Cr-5Ti tensile specimens that were annealed for 1 h at 1125°C in a capsule + 10 min at 1125°C in vacuun are shown in Fig. 4. The deformation markings on the BL-24 alloy specimen (Fig. 4b) and the absence of these markings on the EL-41 alloy specimen (Fig. 4a) are consistent with their load-elongation curves in Figs. 3c and 3d, respectively.

Ion irradiations. The TEM microstructures for EL-23 V-15Cr-5Ti, EL-15 V-20Ti, and EL-27 V-3Ti-1Si alloys after ion irradiation at 650°C to 50 dpa are shown in Fig. 5. A V-5Ti specimen, which was not tensile tested, is also shown. The TEM microstructure for the EL-24 V-15Cr-5Ti alloy after ion irradiation at 650°C to 50 dpa is shown in Fig. 6. The microstructures for the BL-23 V-15Cr-5Ti and V-5Ti alloys are remarkably similar, but they are substantially different from microstructures for the V-20Ti and V-3Ti-1Si alloys. However, the TEM microstructure for the ion-irradiated EL-24 V-15Cr-5Ti alloy (Fig. 6) appears very similar to the microstructures for the ion-irradiated V-20Ti and V-3Ti-1Si alloys (Figs. 5c and 5a, respectively).

The microstructures of the ion-irradiated V-5Ti (Fig. 5b) and EL-23 V-15Cr-5Ti (Fig. 5d) alloys contained a high density (~5 x 10^{23} m^{-3}) of disc-shape precipitates with a diameter of ~6 nm. In the case of these alloys, the precipitates with a {100} habit plane appeared to be associated with the dislocation structure. The microstructures for the EL-24 V-15Cr-5Ti (Fig. 6), EL-27 V-3Ti-1Si (Fig. 5a), and EL-15 V-20Ti (Fig. 5c) alloys also contained a high density of disc-shape precipitates (~10^{23} m^{-3}), but the diameter of these precipitates was ~60 nm. In the case of these alloys, the precipitates with a {100} habit plane formed a "raft-like" structure.

The presence of strain field contrast in the vicinity of the precipitates in the V-5Ti and BL-23 V-15Cr-5Ti alloy microstructures suggested that these precipitates were coherent with the matrix. Strain field contrast was clearly absent around the precipitates in the microstructure of the V-20Ti alloy. In the case of the V-3Ti-1Si alloy and the BL-24 V-15Cr-5Ti alloy, sane of the precipitates appeared to have strain field contrast, i.e., a partially coherent precipitate structure.

Discussion of results

The addition of either chromiun, titaniun, oxygen, nitrogen, or carbon to pure vanadium results in solid solution strengthening, i.e., an increase in yield stress and a decrease in ductility.[2-4] In the present study, the vanadium alloys contained a high density of precipitates and, therefore, the strength of the alloys was due to the combined effects of solid solution strengthening and precipitate strengthening. Comparison of the yield strength for the BL-10L-1 V-15Ti-7.5Cr, EL-15-1 V-20Ti, BL-24L-14 V-15Cr-5Ti, and BL-27L-1 V-3Ti-1Si alloys (Table 2), which contained canparable amounts of oxygen impurity and were similarly annealed in vacuum, shows that the yield strength increased with an increase of the combined titanium and chromnium concentration. However, the total elongation of these alloys was not significantly altered by the change in alloy composition.

The increase in the percentage of ductile fracture for the V-15Cr-5Ti alloy on increasing the oxygen concentration from 300 ppm to 800 ppm (e.g., compare specimen numbers BL-23L-1 and BL-24L-14 in Table 2) is attributed to "solution softening" of the alloy matrix, which resulted from a decrease of the titanium and oxygen concentration in solution on formation of a higher number density of TiO precipitates. The yield strength, tensile strength, and ductility for the EL-23L-1 and BL-24L-14 alloys are consistent with this interpretation of the experimental results. At the present stage of our investigation, the titanium and

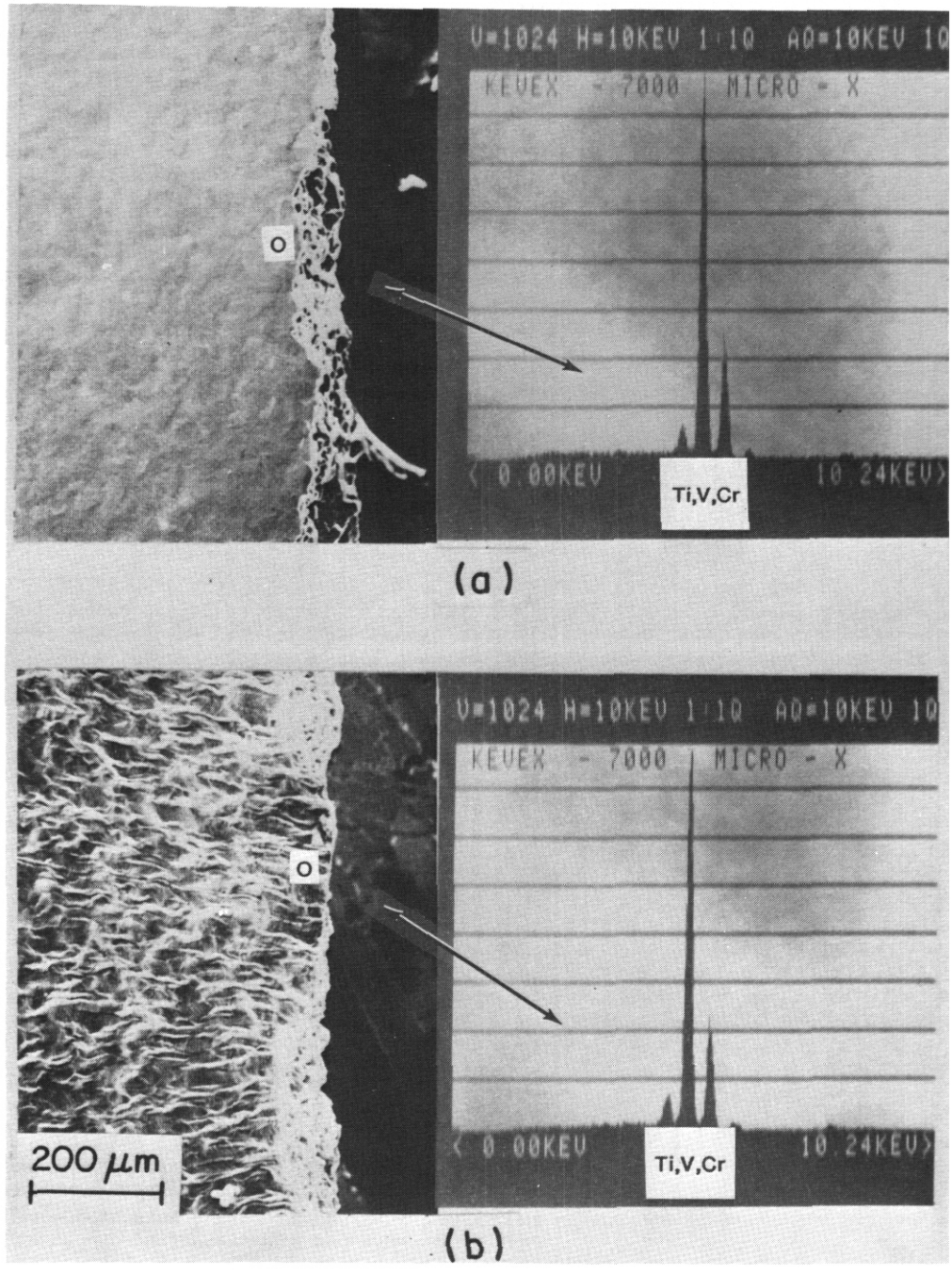


Fig. 4. Fracture surface and chemical analysis for the (a) BL-41L-7 and (b) BL-24L-18 V-15Cr-5Ti tensile specimens.

oxygen solutes are considered to be the principal constituents responsible for the "solution softening" effect because precipitates with the TiO composition have only been identified in unirradiated V-Ti alloy? and precipitates with the Ti_3O composition have only been identified in ion-irradiated V-15Cr-5Ti alloys.[6]

The results of the tensile tests on the vanadium-base alloys at 20°C suggest that the V-15Cr-5Ti alloy is more susceptible to hydrogen embrittlement that the V-20Ti and V-3Ti-1Si alloys. Calculations on the elastic interaction of hydrogen with substitutional solutes in vanadium have shown that titanium solute in vanadium traps hydrogen impurity whereas chromium solute in vanadium does not trap hydrogen.[7] The addition of titanium solute to vanadium has been previously shown to result in an appreciable increase of resistance of vanadium to hydrogen embrittlement.[8] Therefore, it might be expected that the substitution of chromium solute for titanium solute in a V-20Ti alloy to give a V-15Cr-5Ti alloy would result in greater susceptibility of the alloy to hydrogen embrittlement.

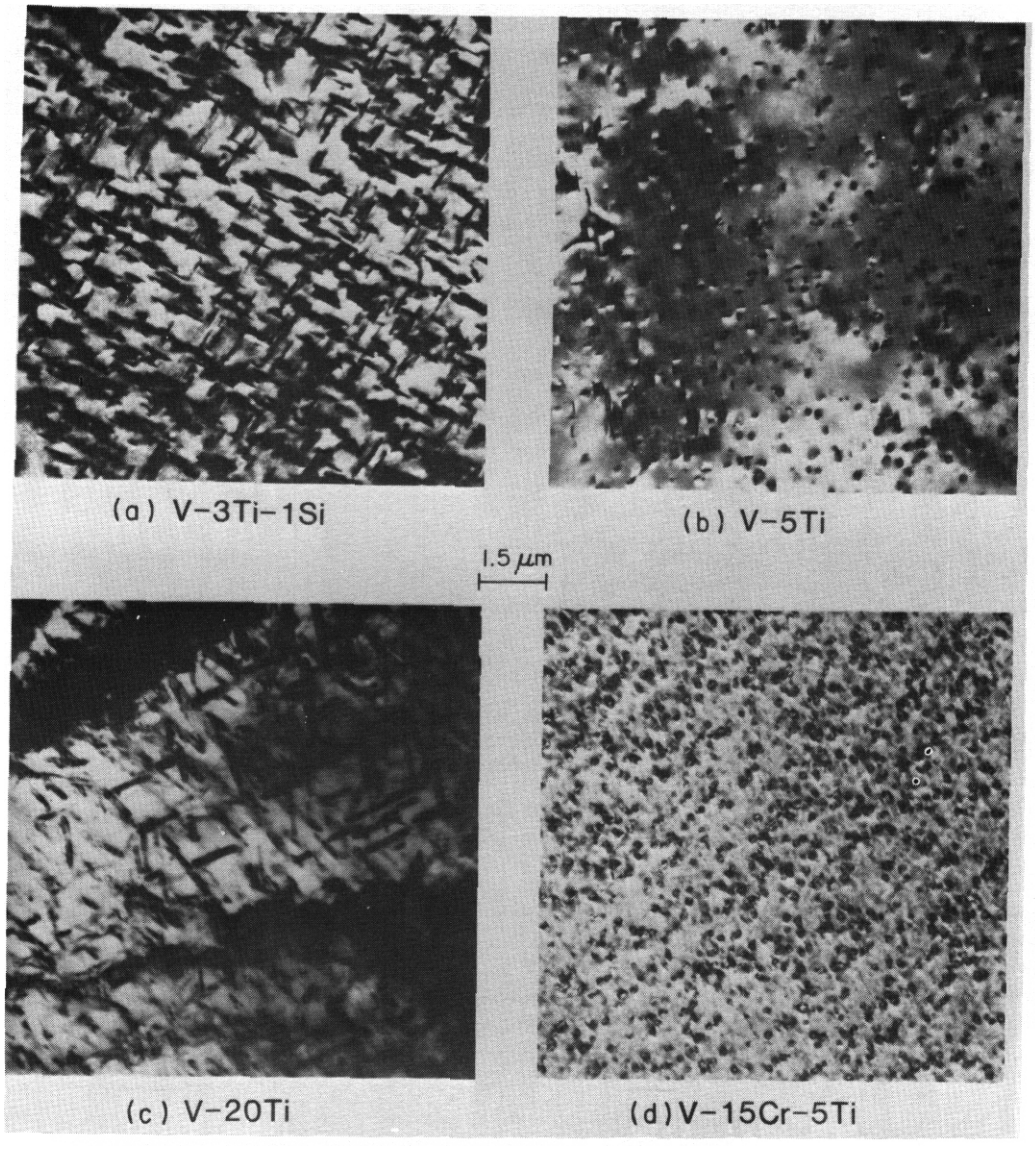


Fig. 5. TEM microstructures of four vanadim-base alloys after 4-MeV V ion irradiation at 650°C to 50 dpa.

The results of tensile tests on V-15Cr-5Ti, V-3Ti-1Si, and V-20Ti alloys after neutron irradiation at 420, 520, and 600°C to 40 dpa have shown that the V-15Cr-5Ti alloy is more susceptible to irradiation hardening and embrittlement than the V-3Ti-1Si and V-20Ti alloys.[1,9] In the case of the neutron-irradiated V-15Cr-5Ti alloy, the tensile specimens were obtained fran the CAM 834 heat of alloy, which contained ~300 ppm of oxygen.[9] The results of tensile tests at 20°C on specimens prepared from the CAM 834 heat of alloy for the present study (Table 2) show that this heat of V-15Cr-5Ti alloy is intrinsically more susceptible to brittle fracture than the V-20Ti and V-3Ti-1Si alloys on tensile deformation. However, if the V-15Cr-5Ti alloy contains 800-900 ppm oxygen (BL-24, ANL 101 heat of alloy), the tensile specimens exhibit ductile fracture; this is the case for the V-20Ti and V-3Ti-1Si alloys on tensile deformation at 20°C. This latter result is obtained only if the V-15Cr-5Ti alloy is annealed in vacuum before tensile testing.

It is assuned that the microstructure developed in neutron-irradiated V-20Ti and V-3Ti-1Si alloys is necessary for resistance of these vanadiun alloys to irradiation embrittlement. Likewise, it is assmed that the microstructure in the neutron-irradiated CAM 834 V-15Cr-5Ti alloy does not confer acceptable resistance to neutron-induced irradiation hardening. Therefore, we suggest that the vacuum-annealed, BL-24 V-15Cr-5Ti alloy will have acceptable resistance to neutron-induced irradiation hardening because of the similarity of the microstructure of this material on ion irradiation to the microstructures in the V-20Ti and V-3Ti-1Si alloys on ion irradiation. Furthermore, we suggest that the greater resistance of the V-20Ti and V-3Ti-1Si alloys to irradiation hardening in canparison to the CAM 834 V-15Cr-5Ti alloy is due to a relatively low concentration of oxygen (300 ppm) in the latter alloy rather than an intrinsic difference in the alloy canposition.

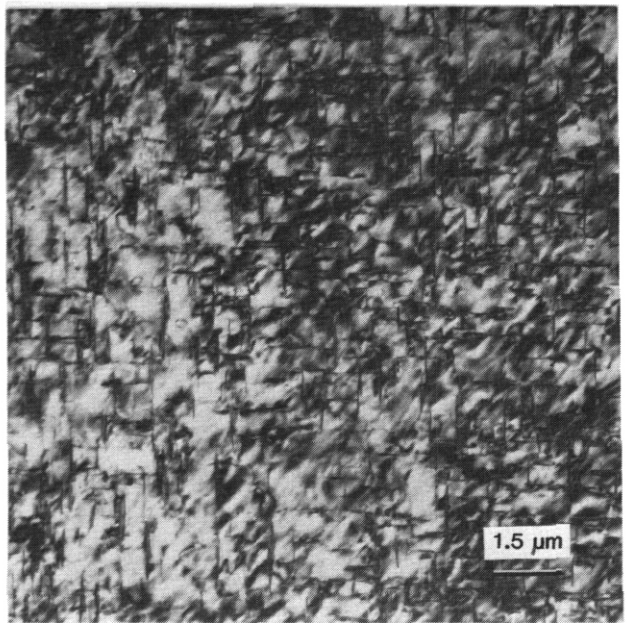


Fig. 6. TEM microstructure of the BL-24 V-15Cr-5Ti alloy after 4-MeV $^{51}V^{2+}$ ion irradiation at 650°C to 50 dpa.

CONCLUSIONS

1. Anneals of the V-Cr-Ti alloys for the purpose of recrystallization must be conducted in a vacuum environment rather than in an argon-filled capsule environment for these alloys to exhibit ductile fracture on tensile deformation at 20°C.
2. The presence of 800-900 ppm oxygen in a recrystallized V-15Cr-5Ti alloy may be necessary for this alloy to exhibit ductile fracture on tensile deformation at 20°C.
3. The V-Cr-Ti alloys may be more susceptible to hydrogen embrittlement than the V-20Ti and V-3Ti-1Si alloys.
4. The V-3Ti-1Si and V-20Ti alloys are not intrinsically more resistant to hardening and embrittlement on neutron irradiation than the V-15Cr-5Ti alloy.
5. The yield strength of vanadiun alloys, which are similarly annealed in vacuum and contain conparable oxygen concentration (800-900 ppm), increases with an increase of the conbined titaniun and chromium concentration. The total elongation of these alloys is not significantly altered by the change in alloy composition.

FUTURE WORK

Tensile specimens of the V-15Cr-5Ti, V-12Cr-5Ti, V-15Ti-7.5Cr, V-20Ti, and V-3Ti-1Si alloys will be tested at temperatures ranging up to 700°C.

REFERENCES

1. D. N. Braski, "The Effect of Neutron Irradiation on Vanadium Alloys," J. Nucl. Mater. 141-143, 1125 (1986).
2. N. Iwao, T. Kainuna, T. Suzuki, and R. Watanabe, "Mechanical Properties of High Strength Vanadium-Base Ternary Alloys," J. Less-Common Met. 83, 205 (1982).
3. O. L. Harrod and R. E. Gold, "Mechanical Properties of Vanadiun and Vanadiun-Base Alloys," Int. Met. Rev. 4, 163 (1980).
4. T. Kainuna, N. Iwao, T. Suzuki, and R. Watanabe, "Effects of Oxygen, Nitrogen, and Carbon Additions on the Mechanical Properties of Vanadium and V/Mo Alloys," J. Nucl. Mater. 80, 339 (1979).
5. K. H. Kramer, "Ausscheidungsvorgange in Rein-Vanadin und Vanadin-Titan Legierungen," J. Less-Common Met. 21, 365 (1970).
6. B. A. Loomis, B. J. Kestel, S. B. Gerber, and G. Ayrault, "Effect of Heliun on Swelling and Microstructural Evolution in Ion-Irradiated V-15Cr-5Ti Alloy," J. Nucl. Mater. 141-143, 705 (1986).
7. A. J. Shirley and C. K. Hall, "Trapping of Hydrogen by Metallic Substitutional Impurities in Niobium, Vanadium. and Tantalum." Acta. Metall. 32, 49 (1984).
8. S. Tanaka and H. Kimura, Supplement, "Hydrogen Embrittlement of Vanadium-Titanium Alloys," Trans. Jpn. Inst. Met. 21, 513 (1980).
9. D. N. Braski. "The Tensile Properties and Swelling of Several Vanadium Alloys after Irradiation to 40 dpa in FFTF," pp. 60-64 in Alloy Development for Irradiation Performance: Semiannual Progress Report for Period Ending March 31, 1986, DOE/ER-0045/16, Oak Ridge National Laboratory, Oak Ridge, TN., September 1986.

THE FORMATION OF TITANIUM TRITIOE IN V-20Ti — D. N. Braski (Oak Ridge National Laboratory)

OBJECTIVE

The goal of this work is to simulate the production of helium in vanadium alloys so that they may be evaluated under neutron irradiation conditions for possible future use as a first wall structural material for a fusion reactor.

SUMMARY

More than expected amounts of ^3He were measured in V-20Ti because of what appeared to be the formation of titanium tritide during the tritium trick procedure. Slightly more 3He was also measured in warm-worked V-20Ti and other vanadium alloy specimens compared to annealed ones - probably because the diffusion of tritium was assisted by the presence of dislocations. The high-helium contents caused substantial losses in ductility in annealed V-20Ti specimens but had little effect in warm-worked specimens. The formation of titanium tritide in high-titanium-content vanadium alloys should be investigated further.

PROGRESS AND STATUS

Introduction

The 14 MeV neutrons streaming from the plasma of a fusion reactor would produce substantial quantities of helium (~5 appm/dpa) in a vanadium alloy first wall. Since these amounts of helium will not be produced in vanadium alloys irradiated in fission reactors that are used to evaluate candidate materials, it has been necessary to devise other ways of adding helium to the microstructure. One method that has been used successfully is the preimplantation of 3He using the "tritium trick."[1] This report shows some unusual bubble distributions observed in the V-20Ti alloy after a rather long tritium trick run aimed at producing relatively high helium levels. The effect of the helium on the tensile properties of both annealed and warm-worked V-20Ti is discussed.

Procedure

The V-20Ti used in this experiment was obtained from heat CAM 833-7 of the Fusion Program stock made by Westinghouse Corporation. Both annealed material (1 h at 1100°C) and material warm-rolled at 500°C from 1.52 to 0.76 mm (50% reduction) were investigated. Small 3-mm-diam by 0.25-mm-thick disks and miniature tensile Specimens of the SS-3 type,[2] of each condition, Were wrapped in tantalum foil and placed in the tritium charging apparatus.[1] After an initial bakeout at 700°C for 24 h under vacuum, the temperature was lowered to 400°C and the tritium was valved in and maintained at a pressure of 53 kPa (400 torr) for 792 h. The charging was terminated by raising the temperature back to 700°C and reducing the retort pressure to approximately 10^{-6} Pa. Residual tritium on the specimen surfaces was removed ultrasonically in a solution consisting of one part HNO_3, one part HF, and one part H_2O, by volume.

The amounts of ^3He in the vanadium alloys Were determined by Dr. Brian Oliver, of Rockwell International. Canoga Park, California. using a vacuum fusion technique. TEM specimens were prepared by dual-jet polishing in a solution of 12½ vol % H_2SO_4 in methanol, at 0C. Tensile specimens were tested under a vacuum of 10^{-5} Pa (10^{-7} torr) or better with a crosshead speed of 0.5 mm/min (strain rate $\approx 10^{-3}$ s^{-1}).

Results

Figure 1 shows the helium charging curves for annealed V-20Ti as well as those for pure vanadium and several other annealed vanadium alloys that were included in the same charging run. The charging curves show the 3He level in the metal as a function of decay time and reflect the solubility of tritium in each alloy. In past experiments. the curves for vanadium alloys always fell below those for pure vanadium and in the case of V-3Ti-1Si, V-15Cr-5Ti, and VANSTAR-7, this was still true. However, the amounts of helium found in the V-20Ti greatly exceeded those measured in pure vanadium. For a decay time of 792 h, the V-20Ti contained 2647 appm of ^3He compared to about 1150 appm (extrapolated from data for a shorter decay time) for pure vanadium. This large increase in helium content compared to the pure material suggested that another mechanism for tritium uptake was operating in the V-20Ti.

Table 1 lists the helium concentrations measured in annealed and warm-worked specimens of a number of vanadium alloys that were present in the same tritium trick experiment. In every case, the warm-worked material was found to contain slightly more helium. It was presumed that these increases were due to the presence of high dislocation densities which enhanced the diffusion of tritium in those materials.

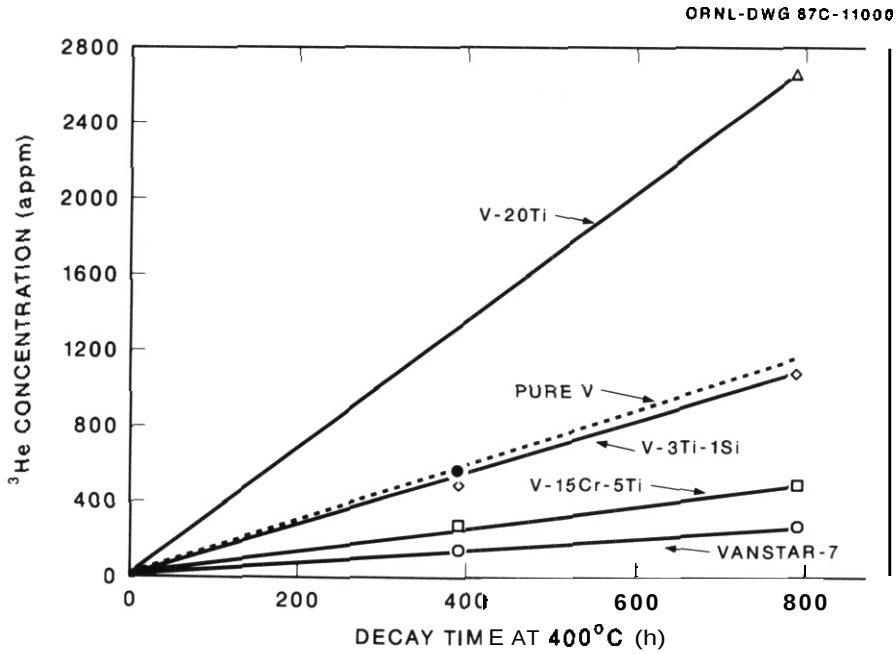


Fig. 1. ^{3}He level in pure vanadium and vanadium alloys as a function of decay time at 400°C.

Table 1. Helium content of various vanadium alloys

Alloy	Condition	Helium Concentration,[a] appm	
		Measured	Average
V–20Ti	Annealed	2651 2642	2647
V–20Ti	Warm-worked	2740 2737	2739
VANSTAR-7	Annealed	256.0 255.9	256.0
VANSTAR-7	Warm-worked	265.5 264.7	265.1
V–15Cr–5Ti	Annealed	483.3 472.5	477.9
V–15Cr–5Ti	Warm-worked	532.5 530.0	531.3
V–3Ti–1Si	Annealed	1088 1067	1078
V–3Ti–1Si	Warm-worked	1096 1104	1100

[a]Helium concentrations measured by Dr. B. M. Oliver, Rockwell International, Canoga Park, CA 91304.

An examination of the V–20Ti disks with 2647 appm He using TEM showed that the microstructure contained a large number of helium bubbles, both in the grain matrices and on grain boundaries (Figs. 2 and 4). Bubbles in the matrices were arranged in a disk-like morphology as shown in Fig. 2. Those disks lying with their long dimension parallel to the plane of the foil appear circular in shape while those at higher angles take on more linear shapes. It is seen that the disks are made of smaller bubbles (see Fig. 2, disk "A") that are able to coalesce into one continuous disk (disk "B"). A reasonable way to interpret these observations is that the bubbles collected on a tritide phase that formed during the tritium charging procedure and later decomposed during the 700°C vacuum outgassing treatment, leaving the bubbles behind. It is likely that the tritide is a titanium tritide. not vanadium tritide, because the bubble "disk" mrphology has not been observed in pure vanadium under similar conditions. It also appears that the amount of titanium needed to form the tritide is greater than 5% because the disks have never been observed in the V-15Cr-5Ti alloy. However, the formation of the tritide may not only depend on titanium content but also on the distribution of titanium in the alloy (i.e., the degree of segregation of the titanium in the alloy). In any case, the formation of titanium tritide and the creation of excess ^{4}He in V-20Ti are not desirable from the standpoint of simulating helium production for an irradiation experiment. It may be possible to avoid tritide formation in V–20Ti if tritium charging is conducted at higher temperatures. From another point of view, the formation of tritide in high-titanium-content alloys could be a very important tritium effect relating to a vanadium alloy first wall and it should be investigated further.

ORNL-PHOTO-J04243

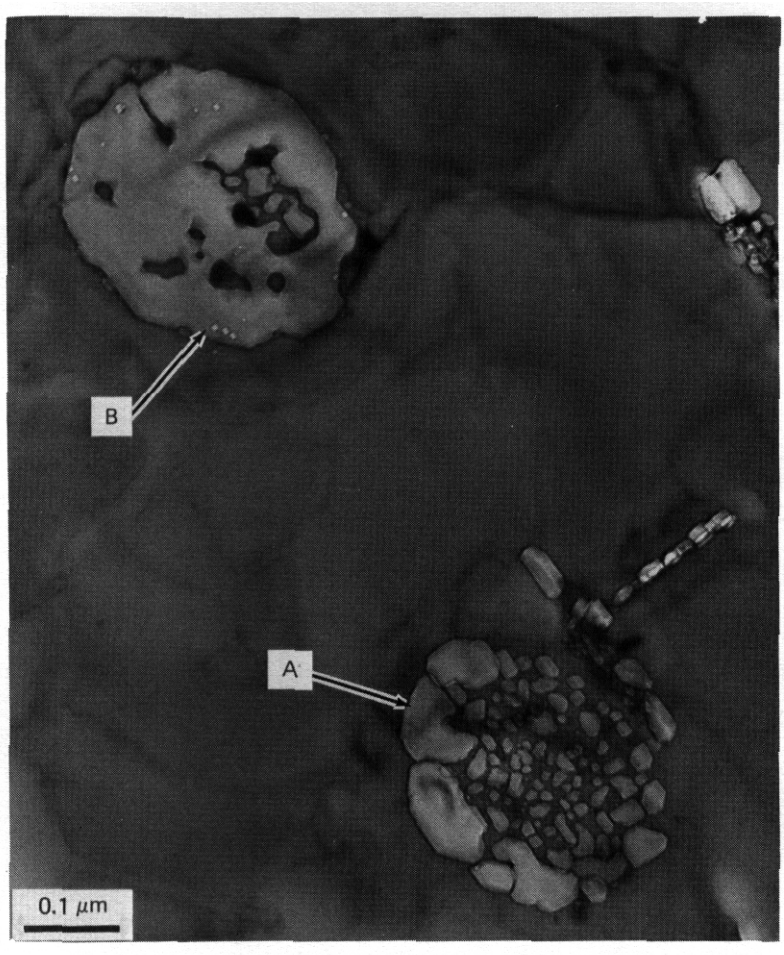


Fig. 2 Disk-like helium bubbles found in V-20Ti after the tritium trick procedure using a decay time of 792 h. Smaller bubbles in disk "A" are believed to coalesce into continuous bubble disks similar to disk "B"

ORNL-DWG 87C-11001

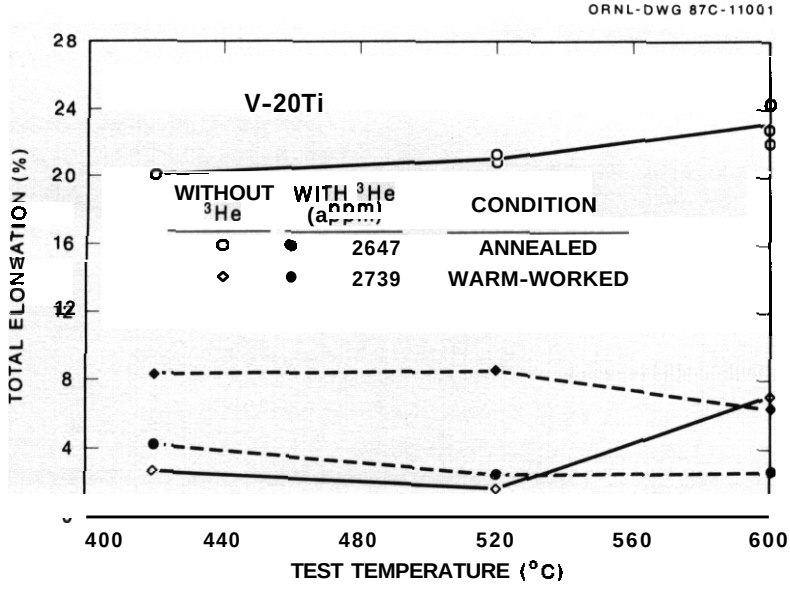


Fig. 3. Total elongation of annealed and warm-worked V-20Ti specimens as a function of test temperature. Open points denote specimens without helium while the solid points represent those containing 2647 appm 3He.

The effect of the high helium content on the tensile properties of V-20Ti is given in Table 2. The properties of both annealed and 50% warm-worked V-20Ti containing 2647 appm ^{3}He can be compared directly to the same respective materials before doping with helium. Helium in the annealed material lowered both the strength and ductility of the specimens. A plot of total elongation as a function of test temperature is given in Fig. 3 which illustrates the substantial losses in total elongation. These losses were probably due to the large number of helium bubbles in the grain boundaries (see Fig 4). The warm-worked specimens behaved differently. Before doping, they exhibited very high yield and ultimate tensile strengths (due to their high dislocation densities induced by the warm-working) which were accompanied by the usual losses in ductility. After the tritium trick, their strengths were reduced at every test temperature, but their uniform and total elongations increased. It is likely that these changes in strength and ductility were due to recovery at the elevated temperatures experienced during the tritium trick procedure. Helium probably had little effect on the ductility of the warm-worked specimens because the dense dislocation networks effectively distributed the bubbles more uniformly. This effect was demonstrated previously in the V-15Cr-5Ti alloy. [3]

CONCLUSIONS

1. The V-20Ti alloy absorbed much more tritium and subsequently contained more ^{3}He than pure vanadium or other vanadium alloys with less titanium. This result was probably due to the formation of titanium tritide in the microstructure.

2. Warm-worked vanadium specimens absorbed more tritium and contained more ^{3}He than annealed specimens of the same alloy because of the dislocation-aided diffusion of tritium in the warm-worked specimens.

3. Bubbles of ^{3}He formed in the matrix on tritide particles and coalesced into large bubble disks. There were also a large number of bubbles in the grain boundaries of the annealed specimens.

4. Annealed V-20Ti specimens doped with ^{3}He suffered slight decreases in yield and ultimate strengths and large decreases in elongation. Warm-worked specimens did not appear to be affected by the helium.

5. Titanium tritide formation in V-20Ti at 400°C may have important implications in the development of vanadium alloys for a first wall and should be investigated further.

REFERENCES

1. D. N. Braski and D. W. Ramey, "Effects of Radiation on Materials: Twelfth International Symposium", ASTM STP 870, F. A. Garner and J. S. Perrin, Eds., American Society for Testing and Materials, Philadelphia, 1985, pp. 1211–1224.

2. D. N. Braski, p. 64 in ADIP Semiannu. Prog. Rep. Sept. 30, 1984, DOE/ER-0045/13, U.S. DOE, Office of Fusion Energy.

3. D. N. Braski, pp. 83–86 in ADIP Semiannu. Prog. Rep. Sept. 30, 1985, DOE/ER-0045/15, U.S. DOE, Office of Fusion Energy.

Table 2 Tensile properties of V–20Ti

Specimen Number	Condition	Helium Content (appm)	Test Temperature (°C)	Strength, MPa		Elongation, %	
				Yield	Ultimate Tensile	Uniform	Total
WA53	Annealed	0	420	466	630	14.0	20.7
WA32	Annealed	0	520	459	641	13.8	21.3
WA66	Annealed	0	520	442	632	11.3	20.3
WA14	Annealed	0	600	474	662	16.2	22.8
WA62	Annealed	0	600	423	664	17.0	24.3
WA37	Annealed	0	600	447	666	14.7	22.0
WA70	Annealed	2649	420	417	526	3.8	4.3
WA57	Annealed	2649	520	312	382	2.6	2.6
WA33	Annealed	2649	600	412	500	2.8	2.8
WE11	Warm-worked	0	420	932	1033	1.3	2.7
WE9	Warm-worked	0	520	968	1007	1.3	1.7
WE10	Warm-worked	0	600	881	1057	3.3	7.0
WE1	Warm-worked	2649	420	605	719	6.8	8.3
WE2	Warm-worked	2649	520	614	737	6.4	8.6
WE3	Warm-worked	2649	600	581	721	6.1	6.5

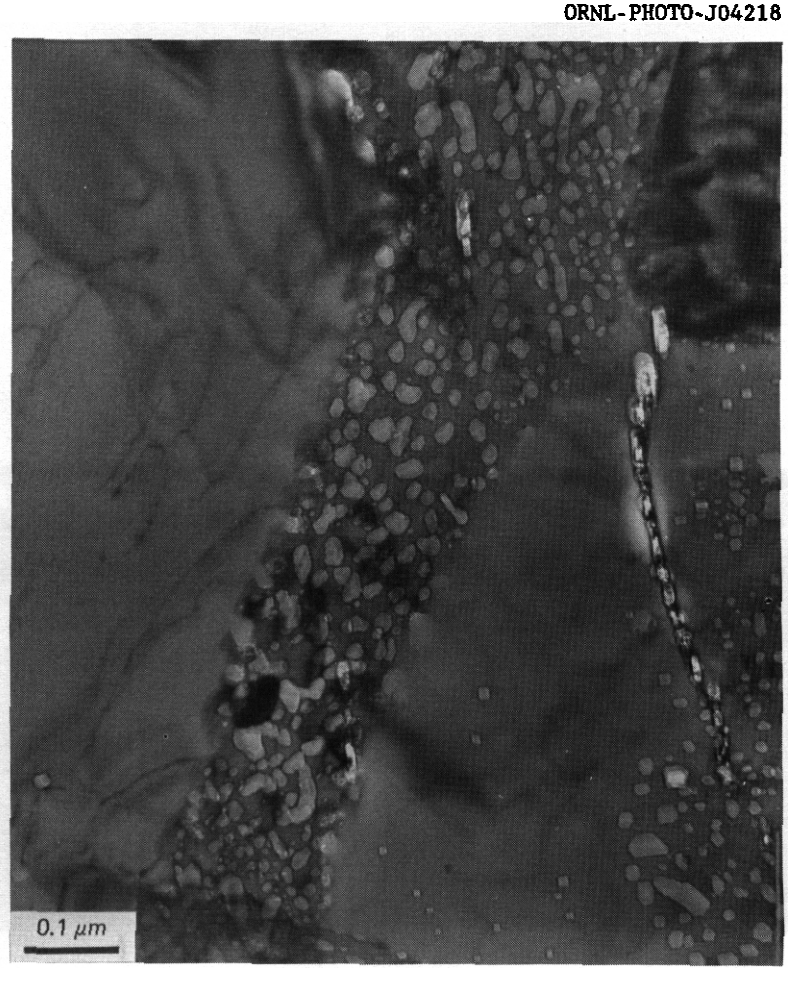


Fig. 4. 3He bubbles *in* V-20Ti grain boundary after tritium trick using 792 h decay time. Alloy contains 2647 appm He.

6.4 Copper Alloys

No contributions received this period.

6.5 Environmental Effects on Structural Alloys

CORROSION OF VANADIUM ALLOYS IN FLOWING LITHIUM - 0. K. Chopra and D. L. Smith (Argonne National Laboratory)

OBJECTIVE

The objective of this program is to investigate the influence of a flowing lithium environment on the corrosion behavior and mechanical properties of structural alloys under conditions of interest for fusion reactors. Corrosion rates are determined by measuring the weight change and depth of internal corrosive penetration as a function of time and temperature. These measuraoents, coupled with metallographic evaluation of the alloy surface, are used to establish the mechanism and rate-controlling processes for the corrosion reactions. Initial effort on mechanical properties is focused on fatigue and tensile tests in flowing lithium environment of controlled purity.

SUMMARY

Corrosion data are presented for several vanadium alloys exposed to flowing lithium at 482 and 427°C Metallographic evaluation of the exposed specimens is also presented. The influence of alloy composition and exposure conditions on the corrosion behavior of vanadium alloys is discussed.

PROGRESS AND STATUS

The corrosion behavior of several vanadium alloys is being investigated in a flowing lithium environment. A detailed description of the lithium loop and the test procedure has been presented earlier.[1,2] The corrosion d ta for V-15Cr-5Ti alloy exposed to lithium at 538, 482, 427, and 372°C have been reported previously.' The results indicate that chemical interactions between alloy elements and nitrogen or carbon in lithium play a dominant role in the corrosion behavior of this alloy. At temperatures >450°C, the dissolution rates of V-15Cr-5Ti are an order of magnitude greater than for the ferritic HT-9 alloy. For these tests, the concentration of N and C in lithium was 50-100 and 6-12 wppm, respectively. The nitrides of V and Ti and carbides of V, Ti, and Cr are expected to be stable under these conditions. Consequently, the chemical interactions to form these compounds will have a strong effect on the corrosion behavior of vanadium alloys. Ouring this reporting period, corrosion tests were conducted on several vanadium alloys at 482 and 427°C, in lithium containing ~20 wppm nitrogen, to assess the influence of nitrogen on corrosion.

The weight losses of several vanadium alloys exposed to flowing lithium at 482 and 427°C (run 8) are shown in Fig. 1. The tests were conducted in two separate isothermal test vessels and the lithium flow was from the high-temperature to the low-temperature test vessel. The results indicate that, at both temperatures, the weight losses of all alloys increase linearly with time after an incubation period ranging up to

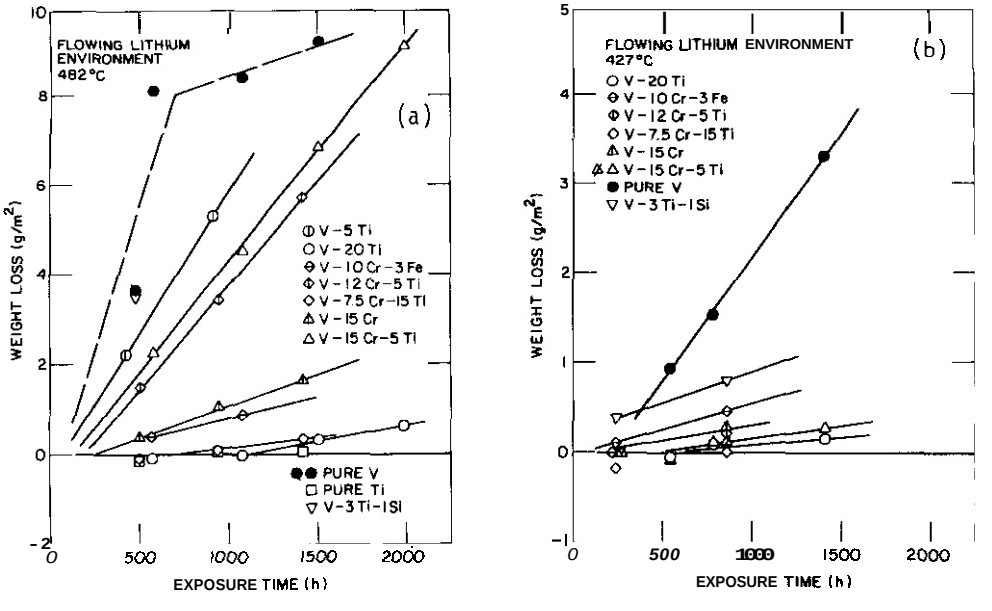


Fig. 1. Weight loss versus exposure time for vanadim alloys exposed to flowing lithium at (a) 482°C and (b) 427°C. Each symbol type represents weight loss for a single specimen after various exposure times.

700 h. The incubation period increases with an increase in the Ti content of the alloy. Alloys containing 15 or *20* wt. % Ti, in fact, show a weight gain during the initial 700-h exposure to lithium. The dissolution rates for the various alloys exposed during run 8 are given in Table 1. The results from previous test runs,[3] i.e., runs 5 and 6, are also included in the table. Pure vanadium shows the highest dissolution rates and the alloys containing 15% Ti have the lowest rates. At 482°C, the dissolution rates decrease in the following order: Pure V, V-3Ti-1Si, V-5Ti-(10 to 15Cr), V-12 to 15 Cr-(3Fe-1Zr), and V-15 to 20Ti-17.5 Cr). A similar trend is also seen at 427°C; however, all alloys that contain Ti show low dissolution rates. The data also indicate that for the present lithium-exposure conditions, the dissolution rates of all vanadium alloys are greater than those for the ferritic steels. For example, dissolution rates for ferritic HT-9 and Fe-9Cr-1Mo steel at 482 and 427°C are *–0.2* and 0.07 mg/m3·h, respectively.3

Table 1. Dissolution rates for vanadiun alloys exposed to flowing lithium

	Dissolution rate (mg/m^2·h)[a]					
	Run *6* (–50 wppm N)[b]		Run 8 (~20 wppm N)[b]		Run 5 (~100 wppm N)[b]	
	538°C	482°C	482°C	427°C	427°C	372°C
Pure V	-	-	c	2.76	-	-
V-10Cr-3Fe-1Zr	-	-	0.86	0.73	-	-
V-15Cr	-	-	1.38	0.47	-	
V-5Ti	-	-	6.34	-	-	
V-12Cr-5Ti	-	-	4.64	0.17	-	
V-15Cr-5Ti	2.66	**2.95**	4.97	0.27	0.54	**0.036**
V-20Ti	-	0.22	0.72	0.24	-	
V-7.5Cr-15Ti	-	-	0.48	d	-	
V-3Ti-1Si	-	-	7.15[e]	0.75	-	-

[a]Dissolution rates based on net weight loss. The values are not corrected for weight change due to nonmetallic element transfer.
[b]Represents the average nitrogen content in lithium during the different test runs.
[c]Dissolution rates change with time, i.e., the rates are –13 mg/m2·h during the initial 500-h exposure and decrease to –2 mg/m^2·h for longer times.
[d]The specimen showed weight gain for times up to ~800 h.
[e]Calculated from a single exposure time.

The weight losses for the V-15Cr-5Ti alloy exposed to lithium at 538, 482, 427, and 372°C are shown in Fig. *2.* During exposure, the concentration of nitrogen in lithium was –100, 50, and 20 wppn for test runs 5, 6, and 8, respectively. The results indicate that the dissolution rates for V-15Cr-5Ti alloy increase with an increase in temperature; however, the rates at 482 and 538°C are approximately the same. A minor change in the nitrogen content in lithium does not have a significant effect on the dissolution rates, since the metal nitrides are expected to form at these concentrations of N.

Figure 3 shows the temperature dependence of the equilibriun values of nitrogen and carbon concentrations in lithium for which metal nitrides and carbides are stable. The equilibrium values of nitrogen concentration in lithiun for the fonation of Li_9CrN_5 are also plotted.[4] The results indicate that for the exposure conditions during test runs 5, *6,* and *8,* the nitride of V and Ti, ternary nitride of Cr, and carbides of Ti, V, and Cr are expected to be stable. Consequently, the chemical interactions to form these compounds will have a dominant role in the corrosion behavior of vanadium alloys in lithium.

Micrographs of the surfaces of the various vanadiun alloys exposed to lithium at 482°C are shown in Figs. 4 and 5. The surface features of these alloys may be classified into three general categories based on the Ti content in the alloy, viz., alloys containing no Ti, 5% Ti, and >15% Ti. The pure vanadium specimen has an etched appearance with heavily corroded regions; however, it is relatively free of reaction products. The V-10Cr-3Fe-1Zr and V-15Cr alloys also have an etched appearance, but the surfaces contain some reaction products. The surfaces of the alloys containing 5% Ti show patches of reaction products. The patches are diffuse and ill-defined in the Cr-containing alloys. The alloys containing 15 or 20% Ti develop a uniform scale of reaction products (Fig. 5). The appearance of the surface scale is not significantly different for alloys with and without Cr. Electron microprobe X-ray analyses of the V-5Ti-(12 to 15Cr) and V-15 to 20 Ti-(7.5Cr) alloy surfaces showed that nitrogen was present and that the concentrations of Cr and Ti were not significantly different from those in the bulk alloy.

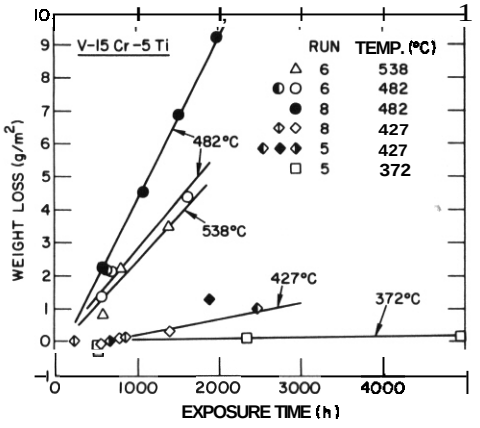


Fig. 2. Weight loss versus exposure time for V-15Cr-5Ti alloy exposed to flowing lithiun at various temperatures. Each symbol type represents weight loss'for a single specimen after various exposure times.

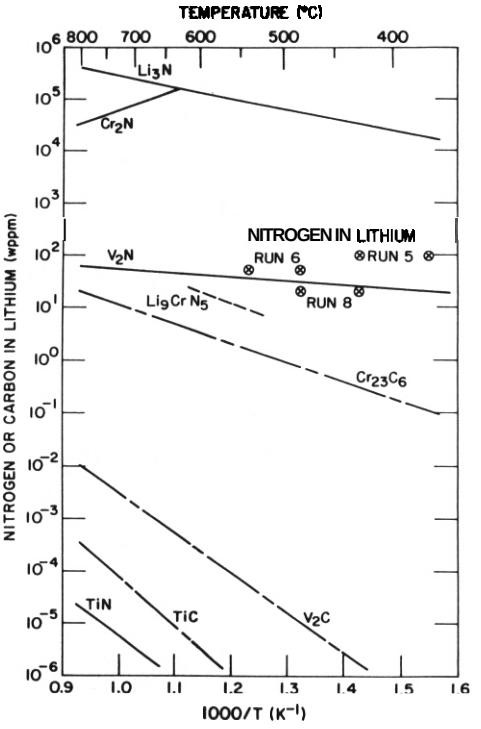


Fig. 3. Temperature dependence of the nitrogen and carbon concentrations in lithim at which selected structural metal nitrides and carbides are stable.

Metallographic examination of cross sections of the various lithiun-exposed specimens revealed a similar behavior. Alloys containing >15% Ti develop a unifonn reaction scale after exposure to lithium. The surface scale is well defined for the V-20Ti alloys. Micrographs of the cross sections of V-20Ti specimens exposed to lithiun at 538, 482, and 427°C are shown in Fig. 6. The results indicate that the V-20Ti specimens develop a uniform surface scale during the initial ~700 h of exposure and the thickness of the scale increases with an increase in temperature, e.g., ~1.5, 2.5, and 6.0 μm at 427, 482, and 538°C, respectively. However, the scale thickness does not change significantly with time, i.e., the rate of movement of the alloylscale interface is approximately the same as recession of the specimen surface. The formation of the reaction scale accounts for the weight gain for the V-20Ti specimens during the initial ~700-h exposure.

Another Si)nificant feature of the V-20Ti alloys is their etching behavior. The grain boundaries and small regions wJthin the grains are attacked preferentially by the etch. The etching behavior is different for specimens exposed at different temperatures. For example. the specimen exposed at 538°C shows very deep grooves, whereas the Specimen exposed at 427°C shows strings of cavities along the boundaries. For the same etching conditions, the unexposed V-20Ti alloy showed no macrostructure. These results indicate microstructural changes in the alloy after exposure to lithium. The specimens are being analyzed chemically to determine the changes in nonmetallic elements in the alloy after exposure to lithium.

The cross section of the V-15Cr-5Ti specimen exposed at 538°C is shown in Fig. 7. Sections of a thin surface layer (~2 μm thick) appear to be breaking off from the specimen. These results suggest significant compositional and microstructural modification of the specimen surface and account for the 1arge Height losses for V-15Cr-5Ti alloy after exposure to lithium. The pure vanadium specimen also showed a very corroded surface but little or no reaction product. The specimens of V-15Cr and V-10Cr-3Fe-1Zr alloys showed little corrosion (Fig. 7).

All the Cr-containing alloys, with the exception of V-7.5Cr-15Ti alloy, were very brittle after exposure to lithium. The V-10Cr-3Fe-1Zr alloy, in particular, cracked very easily during handling. Micrographs of the V-10Cr-3Fe-1Zr specimen (Fig. 7) show the presence of an additional phase.

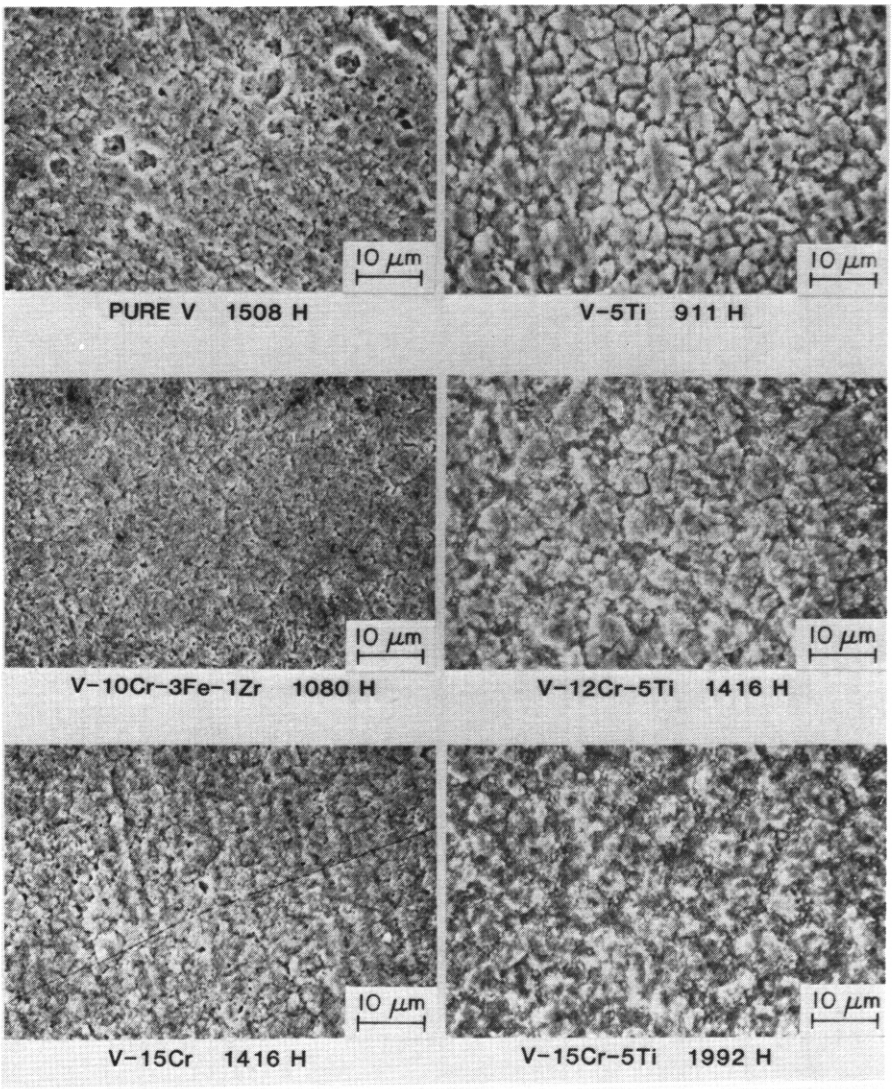


Fig. 4. Micrographs of the surfaces of vanadium alloys exposed to flowing lithium at 482°C for various times.

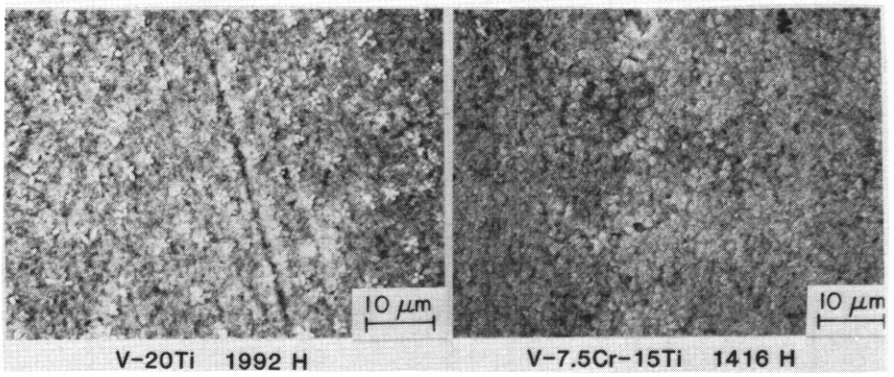


Fig. 5. Micrographs of the surfaces of vanadium alloys containing >15% Ti exposed to flowing lithium at 482°C for various times.

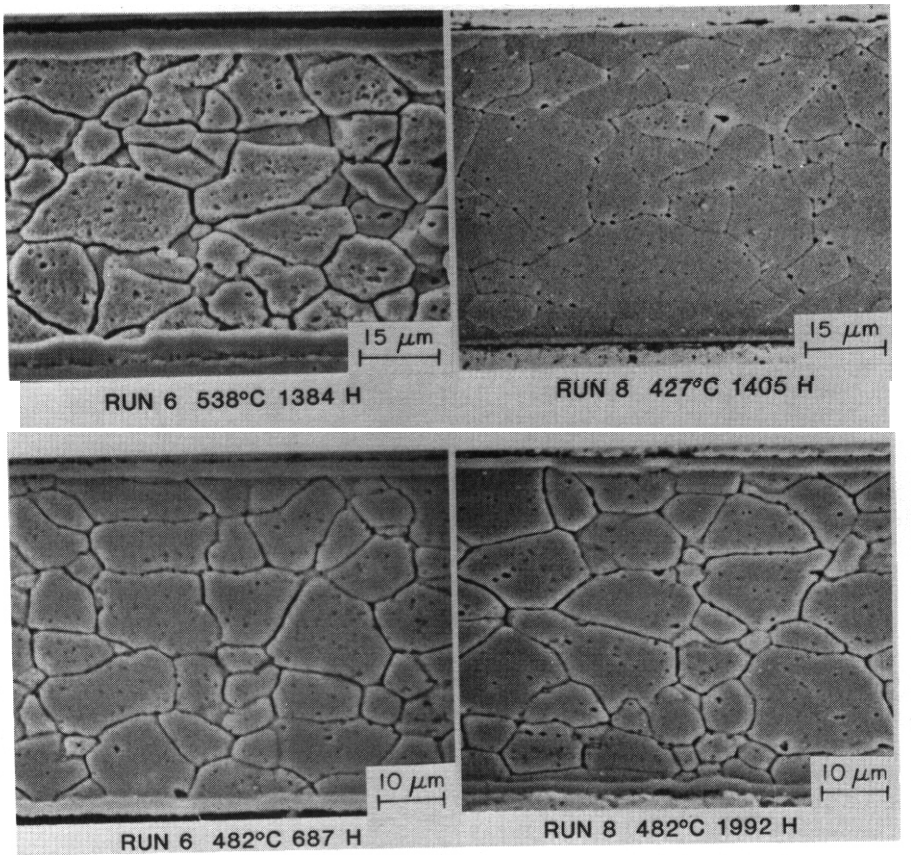


Fig. 6. Micrographs of cross sections of V-20Ti specimens exposed to lithim at different temperatures.

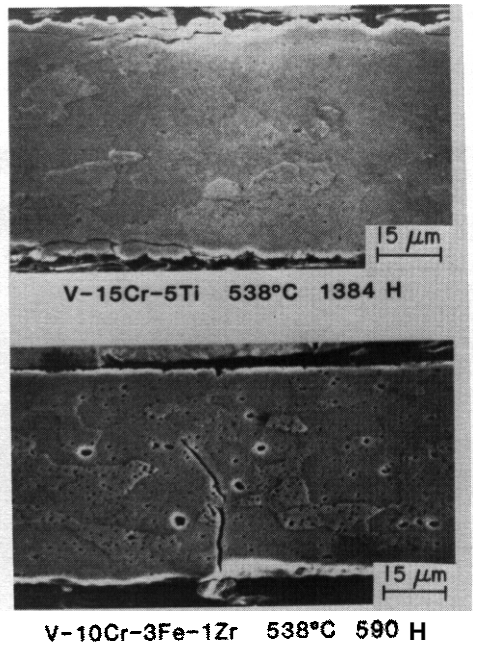


Fig. 7. Micrographs of cross sections of V-15Cr-5Ti and V-10Cr-3Fe-1Zr specimens exposed to lithim at 538°C.

The results of the metallographic examination of the lithium-exposed specimens indicate that low dissolution rates for the V-20Ti and V-7.5Cr-15Ti alloys are due to the formation of a protective nitride layer on the alloy surface. However, this nitride layer is quite brittle and can spall when exposed to thermal stresses. Alloys containing 5% Ti or less do not develop a uniform nitride layer. The chemical products easily break off from the alloy surfaces, resulting in high dissolution rates. Similar behavior is observed for pure V, i.e., high dissolution rates due to chemical interactions between V and nonnetallic elements such as N andlor C. The addition of Cr to vanadium seems to influence the chemical interactions and reduce dissolution rates. However, the Cr-containing alloys embrittle after exposure to lithium. The embrittlement is most likely due to the pickup of hydrogen. During exposure, the hydrogen content in lithiun was estimated to be –100 wppm.

SUMMARY

The corrosion data for several vanadiun alloys indicate that for the present tests, the concentrations of N and/or C in lithiun are above acceptable limits, and chemical interactions between alloy elements and N or C in lithiun play an important role in the corrosion behavior of these alloys. When exposed at 482°C to lithiun containing >20 wppn N and 8 to 12 wppn C, the dissolution rates of the various vanadiun alloys decrease in the following order: pure vanadiun, V-3Ti-1Si, V-5Ti-(12 to 15 Cr), V–10 to 15Cr-(3Fe-1Zr), and V–15 to 20Ti-(7.5Cr). The alloys containing 15 to 20% Ti develop a uniform nitride layer. All chromium-containing alloys embrittle after exposure to lithim containing 100 wppm hydrogen.

FUTURE WORK

The lithiun-exposed specimens are being analyzed chemically to determine the changes in nonmetallic elenents after exposure to lithium. Microhardness measurements are also being performed to determine the depth of these compositional changes. X–ray diffraction and electron microprobe analyses will be performed to evaluate the nature of the reaction products on the alloy surfaces. Corrosion tests are also planned in lithiun containing –1 wppm N to evaluate the dissolution behavior of vanadiun alloys under conditions where vanadiun nitride does not form.

REFERENCES

1. O. K. Chopra and D. L. Smith, "Environmental Effects on Properties of Structural Alloys in Flowing Lithium," pp. 200–204 in Alloy Development for Irradiation Performance: Semiannual Progress Report for Period Ending September 30, 1984, DOE/ER-00 5/13, Oak Ridge National Laboratory, Oak Ridge, Tenn., March 1985.

2. O. K. Chopra and D. L. Smith, "Corrosion of Ferrous Alloys in a Flowing Lithium Environment," J. Nucl. Mater. 133 & 134, 861-866 (1985).

3. O. K. Chopra and D. L. Smith, "Corrosion of Ferritic Steels and V-15Cr-5Ti Alloy in Flowing Lithium." to be published in Fusion Structural Materials Semiannual Progress Report for the Period Ending September 30, 1986, Oak Ridge National Laboratory, Oak Ridge, Tenn.

4. M. G. Barker, J. A. Lees, and I. E. Schreinlechner, "The Corrosion of Type 316 Stainless Steels in Static and Dynamic Liquid Lithim," to be published in Proc. 14th Symp. on Fusion Technology, Avignon, France, September 1986.

THERMAL CONVECTION LOOP STUDIES IN SUPPORT OF MASS TRANSPORT MODELING OF LITHIUM/12Cr-1MoVW STEEL SYSTEMS - G. E. Bell and M. A. Abdou (University of California, Los Angeles) and P. F. Tortorelli (Oak Ridge National Laboratory)

OBJECTIVE

The objective of this research is to provide experimental data and information for development of, and comparison with, an analytical model of the mass transport processes of 12Cr-1MoVW steel over the range of 350 to 650°C in the presence of thermally convective lithium. Chemical and metallurgical changes in the system will be closely monitored throughout the test period with particular emphasis placed on the initial 500 h to provide data on the transient chemical and weight loss mechanism kinetics. The analytical model will include chemical and transport mechanisms not previously investigated for liquid lithium mass transport in ferrous alloy systems including chemical and particle dynamics and initial system transient modeling.

SUMMARY

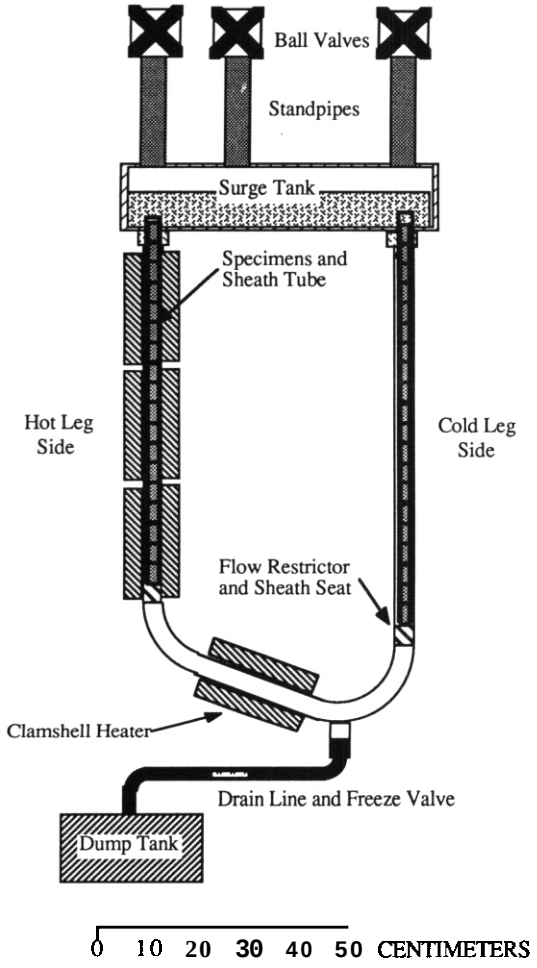
The 12Cr-1MoVW material was obtained from GA Technologies fusion alloy stockpile in January 1987. The standard ORNL thermal convection loop and specimen string were substantially redesigned to minimize some of the uncertainties typically associated with mass transfer model development in liquid metal corrosion loop systems and to simplify loop fabrication. The experimental systems and specimens were then fabricated, installed, and tested during the current reporting period. Experimental operation is expected to begin in April 1987.

PROGRESS AND STATUS

In order to develop an analytical model of the mass transport process in lithium systems and to test such a model using experimental data, a cooperative effort between the ADIP Program at Oak Ridge National Laboratory and the FINESSE[1] Project at The University of California, Los Angeles was initiated. The details of the modeling effort can be found elsewhere.[1] To facilitate modeling of the experiments, material homogeneity and geometric simplicity have been stressed during the design and fabrication of these thermal convection loop (TCL) experiments. These requirements have necessitated changes in the design and fabrication of the ORNL TCL systems.

Relative to the standard ORNL TCL experiments, a different style of mass transport specimen is being utilized. The standard ORNL design uses small (0.79 × 1.90 × 0.09 cm), flat, discrete specimens wired to flexible thin rods and these are inserted into the hot and cold leg tubes (1.57 cm ID) of the loop. The standard ORNL TCL has two surge tanks which provide expansion volumes and sample withdraw1 pathes for the flat specimens. Details of the standard ORNL design and operating procedures can be found elsewhere.[2] A schematic of the the new TCL design is shown in Fig. 1 and a photograph of one of the fabricated loops is shown in Fig. 2. The main body of the loop is formed by 3.175 cm ID tubing. The mass transport specimens for the subject investigations are short tubular pieces (1.90 cm OD × 1.57 cm IO × –3.81 cm long) shown in Fig. 3. Each loop will have 42 specimens (20 and 22 in the hot and cold legs, respectively). The specimens were normalized and tempered (30 min at 1050°C, 2.5 h at 780°C in argon atmosphere) and mechanically polished to 600 grit and 0.3 μm finishes on the outside and inside surfaces, respectively, to provide the starting microstructure and surface characteristics. The specimens are stacked one-on-top-of-the-otherto form a continuous tube. The stack is axially supported by a specimen sheath (2.54 cm OD × 0.065 cm wall) tube which forms a close-fitting annular specimen containment. Lithium flow is produced by imposing a temperature gradient between the hot and cold legs of the loop and is directed through the inside diameter of the specimens by flow reducers at the bottom of both the hot and cold legs on which the specimen sheath tube rests after insertion. Threaded retraction rods allow insertion and removal of the specimens and sheath tube. This provides a flow rate control orifice at the top of the hot and cold legs. The retraction rod, specimen stack, and specimen sheath tube are shown in Fig. 4. The specimens themselves and the specimen insertion/removal system are much larger and less flexible than the ORNL standard design which necessitated an increase in loop size (tubing diameter and tank volume) and stricter alignment tolerances for the fabrication of the loops. The two hot and cold leg surge tanks have been joined to form a single surge volume tank. The hot leg crossover tube has been eliminated to provide greater mechanical stability, stiffness, and alignment for the system and to accommodate the more rigid specimen insertion and removal system.

All loop construction material in intimate contact with the lithium was taken from the plate, bar and tube stock provided from GA Technologies. The only exception was the retractor rod ends for specimen insertion and withdrawal, which were made from 9Cr-1Mo material due to a shortage of 12Cr-1MoVW bar stock. The surface area of this 9Cr-1Mo piece is less than 0.1% of the total loop and specimen surface area and the composition and microstructure are similar to that of the host material. The presence of this modest chemical inhomogeneity should not significantly affect the overall mass transport process because of the small surface area of the 9Cr-1Mo material. The composition of the 12Cr-1MoVW plate, bar and tube stock was determined by Combustion Engineering. The analysis is given in Table 1.



Fiu. 1. Schematic of new thermal convection loop design.



Fig. 2. Photograph of as-built TCL.

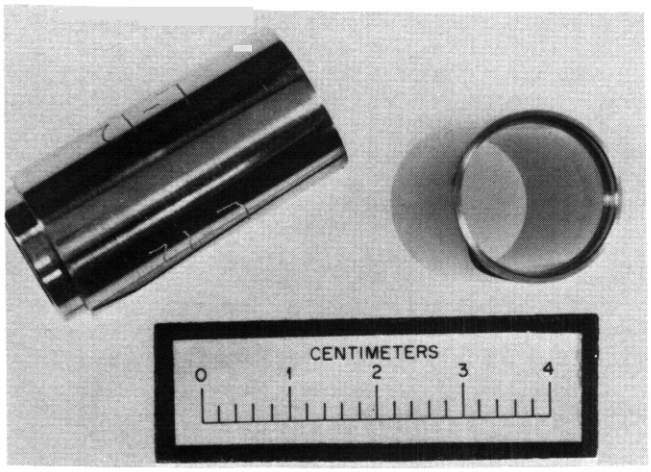


Fig. 3. Mass transfer specimen.

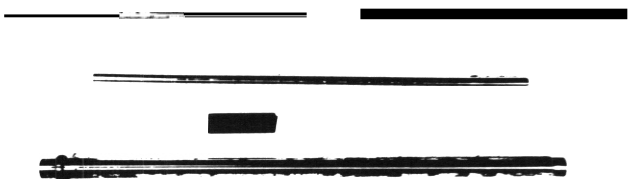


Fig. 4. Top: Retractor/flow control rod. Middle: Stacked mass transfer specimens. Bottom: Specimen sheath tube.

Table 1. Composition of materials used in TCL fabrication

Material description	1.5-in.-OD tube loop body (wt %)	1.0-in.-OD tube sheath (wt %)	0.75-in.-OD tube specimens (wt %)	0.38-in. plate surge tank (wt %)
C	0.20	0.20	0.19	0.19
Mn	0.70	0.73	0.67	0.68
P	0.020	0.020	0.017	0.017
S	0.002	0.004	0.004	0.007
Si	0.14	0.16	0.13	0.20
Ni	0.42	0.42	0.42	0.41
Cr	11.91	12.00	12.00	11.95
Mo	1.04	1.04	1.03	1.04
V	0.24	0.24	0.24	0.24
Nb	0.005	0.009	0.003	0.004
Ti	0.002	0.002	0.001	0.002
co	0.073	0.074	0.071	0.071
cu	0.09	0.08	0.07	0.07
Al	0.010	0.008	0.002	0.001
6	<0.001	<0.001	<0.001	<0.001
W	0.39	0.40	0.40	0.40
As	0.011	0.015	0.006	0.007
Sn	0.004	0.005	0.002	0.003
Zr	<0.001	(0.001	(0.001	<0.001
N	0.040	0.043	0.042	0.045
Fe	Balance	Balance	Balance	Balance

Two TCLs will be operated to cover the desired temperature range. Loops GEB-1 and GEB-2 will operate from approximately 350 to 500°C and 500 to 650°C, respectively. The larger tubing and the removal of the crossover tube between the hot and cold leg side of the loop reduces the flow resistance and thus increases the flow rate at a given temperature differential. Flow velocities of 2 to 3 cm/s at 150°C are normally estimated in the ORNL standard design. Lithium velocities between 5 and 10 cm/s have been observed in the new larger system at temperature differentials of less than 150°C. The absolute and differential temperatures and flow velocity in the loop can be adjusted by (1) variation of heater inputs on the surge tank and the hot and cold legs, (2) adjustment of the flow restriction at the top of the hot leg specimen sheath tube, and/or (3) addition/removal of insulation around the loop. A comparison between the-design parameters of the new system and standard ORNL system is given in Table 2.

Table 2. Comparison of standard ORNL and new TCL designs

	Standard ORNL design	New TCL design
Specimen geometry	Rectangular and flat	Tubular specimens
Surge tanks	Two, hot and cold leg	One
Main Body Tubing	1.90-cm OD × 0.165-cm wall	3.81-cm OD x 0.318-cm wall
Estimated lithium velocity	2–3 cm/s at $\delta T \approx 150°C$	5–10 cm/s at $\delta T < 150°C$
Flow Reynolds number	500–700 at 500°C	1200–2300 at 500°C
Total volume of lithium	25 liters	5.3 liters
Total surface area to lithium volume ratio	71.2 m^{-1}	144.7 m^{-1}
Specimen surface area to lithium volume ratio	17 m^{-1}	34.9 m^{-1}

The TCLs will be filled with a flush charge of lithium and operated at nearly isothermal conditions near the mean loop temperature to remove any contamination which may have adhered to the walls during fabrication (weld oxide layer, residual machine oil, etc.). The flush charge will be discarded into the dump tank and each loop refilled with a fresh operational charge of lithium. Both the flush and operational charges are cold trapped for more than 300 h at 195°C and hot-gettered for more than 100 h at 815°C to remove oxygen and nitrogen impurities, respectively, prior to being put in the loops. Typical chemical analyses of the lithium for these impurities are given in Table 3.

Table 3. Chemical analyses of lithium for GEB-1

	Oxygen (wppm)	Nitrogen (wppm)
Flush charge	200	61
Operational charge	410	25

The specimens will be weighed and inspected at 100, 300, 500, 700, 1000, 1500, 2000, 2500 and 3000 h of coupon exposure. Samples of the lithium will be taken each time the specimens are removed and analyzed to provide a chemical history of the lithium environment.

REFERENCES

1. M. A. Abdou et al., "Modeling, Analysis, and Experiments for Fusion Nuclear Technology," *FNT Progress Report: Modeling & FINESSE,* UCLA-ENG-86-44, UCLA, Los Angeles, Calif., January 1987.

2. J. H. DeVan and J. R. DiStefano, "Thermal-Convection Loop Tests of Type 316 Stainless Steel in Lithium," pp. 200-208 in *ADIP Quarterly Progress Report, March 31,* 1978, DOE/ET-0058/1, U.S. DOE, Office of Fusion Energy.

THERMAL GRADIENT MASS TRANSFER IN FERROUS ALLOY Pb-17 at. % Li SYSTEMS - P. F. Tortorelli (Oak Ridge National Laboratory)

OBJECTIVE

The purpose of this work is to determine the corrosion resistance of candidate first-wall materials to slowly flowing Pb-17 at. % Li in the presence of a temperature gradient. Dissolution and deposition rates are measured as functions of time, temperature, and additions of minor elements to the lead-lithium. These measurements are combined with chemical and metallographic examinations of specimen surfaces to establish the mechanisms and rate-controlling processes for the dissolution and deposition reactions.

SUMMARY

Scanning electron microscopy and associated energy dispersive x-ray analysis of type 316 stainless and 12Cr-1MoVW steels exposed to thermally convective Pb-17 at. % Li yielded quantitative information about changes in surface morphology and composition as a result of mass transfer reactions. In the case of type 316 stainless steel, substantial preferential dissolution of nickel and chromium occurred at 500°C and led to the formation of a deep corrosion zone of irregular penetration. The extent and morphology of this corrosion zone was found to be sensitive to the starting microstructure of the steel. The 12Cr-1MoVW steel corroded uniformly with no change in its surface concentration. Mass transfer deposits in the type 316 stainless steel system differed depending on their position in the cold leg, where the temperature varied from 400 to 460°C. Depending on the temperature, the majority of the deposits were principally composed of iron. iron-nickel, or chromium.

PROGRESS AND STATUS

In the preceding progress report,[1] weight change and initial surface structure and composition data from long-term (10,000 h) baseline thermal convection loop (TCL) experiments with austenitic and ferritic steels showed the aggressiveness of the Pb-17 at. % Li environment, particularly with respect to the type 316 stainless steel. Extensive microstructural analyses of these exposed materials have now been completed so as to better characterize and understand both the dissolution and deposition processes in the lead-lithium systems.

As described earlier,[1] type 316 stainless steel and 9Cr-1Mo steel TCLs were used to expose specimens of type 316 stainless and 12Cr-1MoVW steels, respectively, to molten Pb-17 at. % Li. In each loop, those specimens located at the maximum loop temperature of 500°C were exposed for varying periods of time up to about 10,000 h, while the remainder of the coupons positioned around the loop accumulated approximately 10,000 h of exposure to the circulating lead-lithium. During the current reporting period, polished cross sections of selected specimens exposed at the maximum loop temperature (500°C) were examined by use of scanning electron microscopy in conjunction with energy dispersive x-ray analysis (EDX). Representative micrographs of type 316 stainless steel specimens exposed for 3886 and 7007 h are shown in Fig. 1.

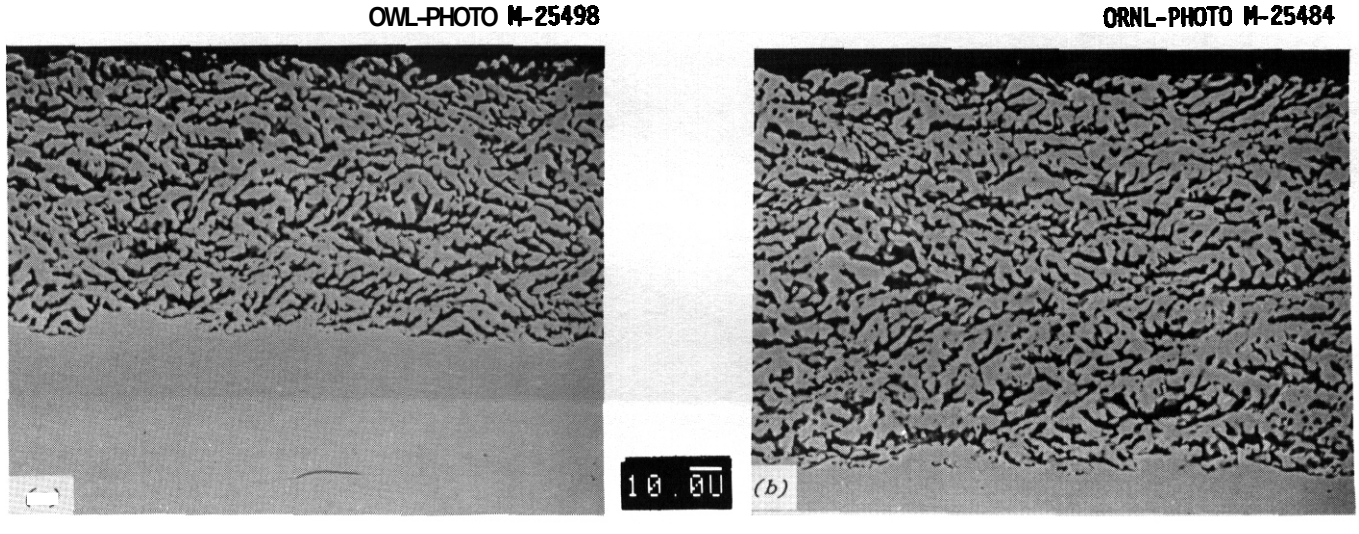


Fig. 1. Scanning electron micrographs of polished cross sections of type 316 stainless steel exposed to thermally convective Pb-17 at. % Li at 500°C. *(a)* 3886 h. *(b)* 7007 h.

As noted previously,[1,2] the exposure of this steel to molten Pb-17 at. % Li results in the development of a very irregular, penetrated surface zone. Such zones are depleted in nickel and chromium relative to the starting concentrations of these elements in the type 316 stainless steel. This preferential dissolution is clearly shown by the the EDX data obtained from polished cross sections (see, for example, Fig. 2). The amount of depletion remains approximately constant throughout the depth of the affected zone. In contrast to the type 316 stainless steel, the exposed surfaces of the 12Cr-1MoVW steel remained planar during the corrosion process: as shown by the micrographs of polished cross sections in Fig. 3, this steel corroded uniformly. Compositional analyses revealed no preferential depletion of any of the constituents of the 12Cr-1MoVW steel after long-term exposure to the lead-lithium. These results for the type 316 stainless and 12Cr-1MoVW steels are in agreement with previous limited (and less quantitative) observations based on analyses of the outermost corroded surface.[1]

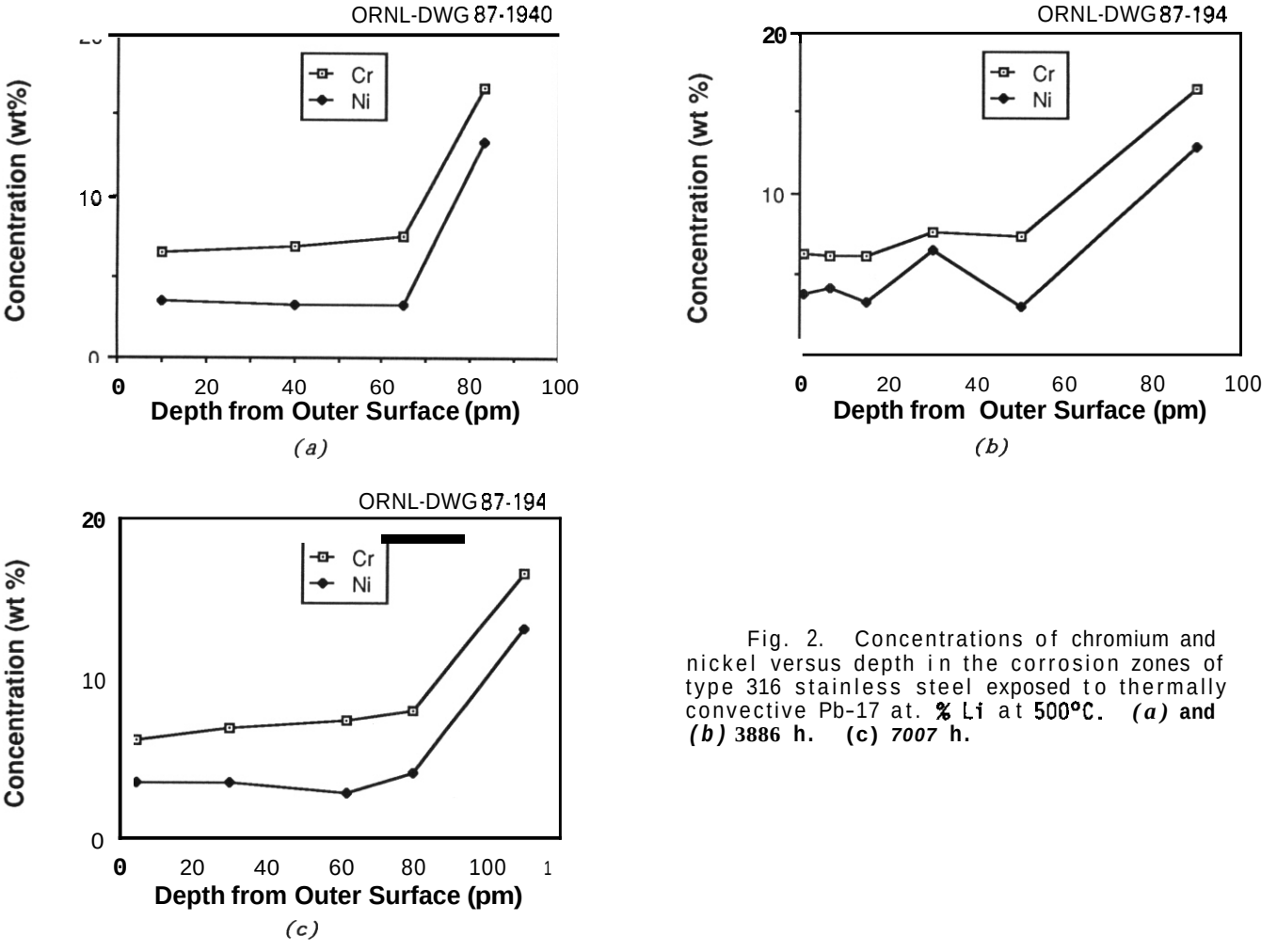


Fig. 2. Concentrations of chromium and nickel versus depth in the corrosion zones of type 316 stainless steel exposed to thermally convective Pb-17 at. % Li at 500°C. *(a)* and *(b)* 3886 h. (c) *7007* h.

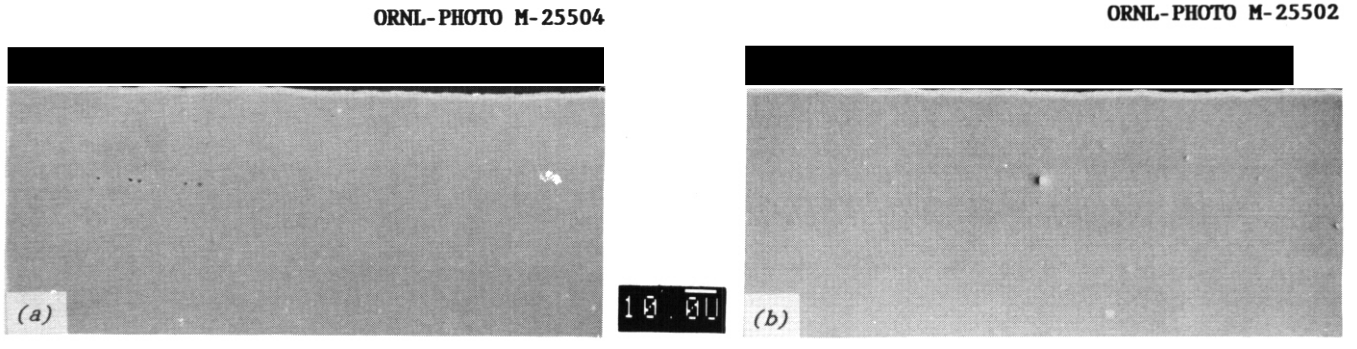


Fig. 3. Scanning electron micrographs of polished cross sections of 12Cr-1MoVW steel exposed to thermally convective Pb-17 at. % Li at 500°C. *(a)* 7027 h. *(b)* 10,076 h.

The microstructural results summarized above are consistent with a surface destabilization model that can explain the differences in surface recession behavior between the austenitic (type 316 stainless steel) and ferritic (12Cr-1MoVW steel) alloys.[2] In this model, which is based on the original work of Harrison and Wagner,[3] a surface that undergoes preferential dissolution develops a very nonuniform, rugged corrosion front, while an initially planar surface should recede uniformly in the absence of such selective leaching. Such a treatment fits the present results quite well. The development of a very irregular solid-liquid interface on the type 316 stainless steel accompanies the preferential dissolution of nickel and chromium (see Fig. 2), while the 12Cr-1MoVW steel, whose surface composition does not change appreciably during the corrosion process, maintains a planar solid-liquid interface throughout the extended exposure. However, the recent examination of the polished cross sections of the exposed type 316 stainless steel has revealed morphological differences between different sides of a specimen coupon that must also be considered in the application of such a model. These differences can be seen in the lower magnification micrographs of Fig. 4. Note that, for all three specimens, the corrosion zone is thicker on the "short" side than on the longer faces. Furthermore, the main branch penetrations appear perpendicular to the original surface on the "short" side and parallel to the "long" sides (see Fig. 5 also).

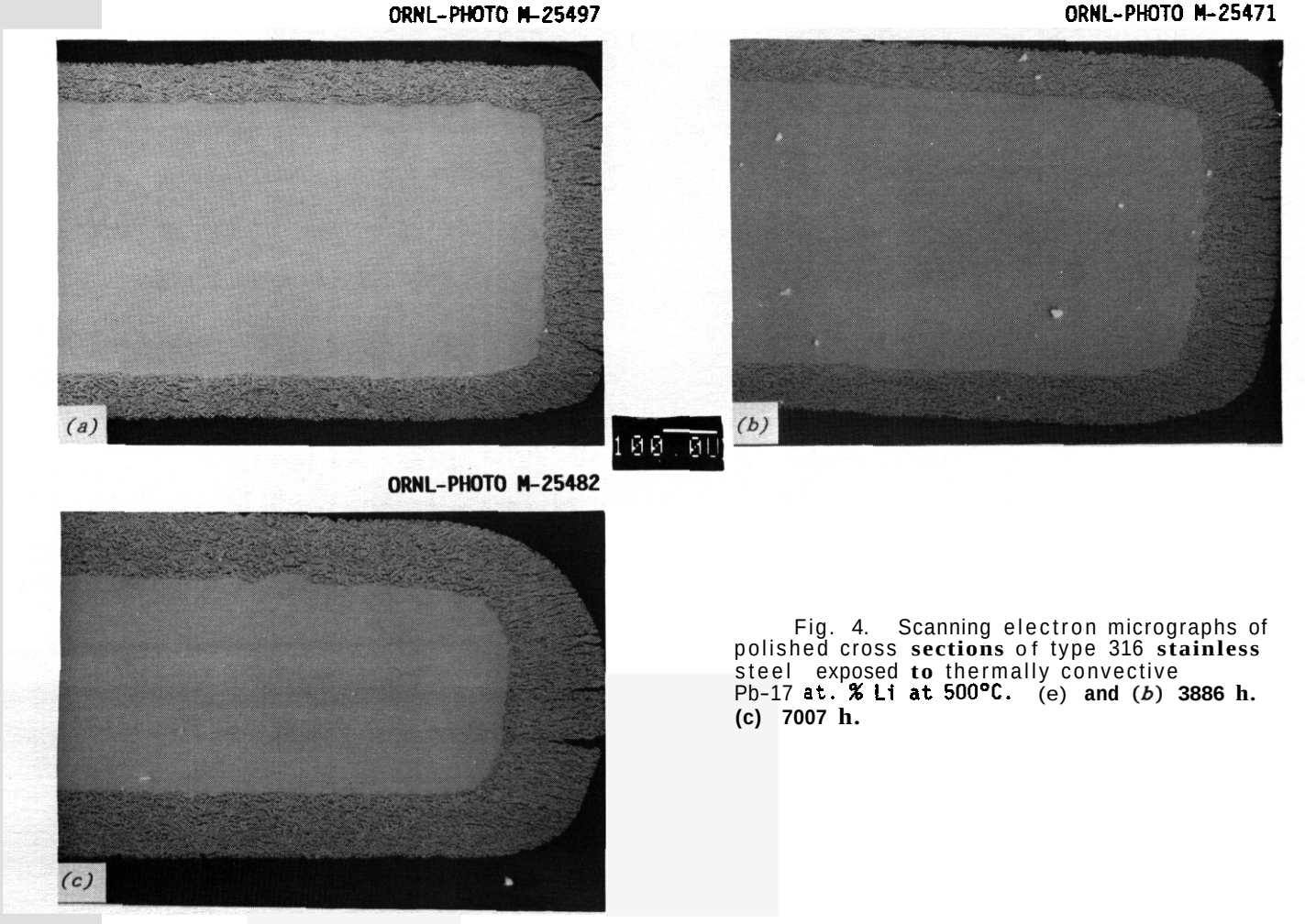


Fig. 4. Scanning electron micrographs of polished cross sections of type 316 stainless steel exposed to thermally convective Pb-17 at. % Li at 500°C. (a) and (b) 3886 h. (c) 7007 h.

The difference in corrosion between the long and short faces of a coupon cannot be explained by any nonuniformity in temperature across the specimen: the specimens were cut in half along an isothermal section perpendicular to the lead-lithium flow direction (see Fig. 5) and, in addition, the thicker corrosion zones were observed on both "short" ends of each specimen. It thus appears that the variation in thickness of the corrosion zone must be related to hydrodynamic effects and/or microstructural influences. The change in flow conditions created by the presence of the coupon "edges" will cause more turbulence on the short faces and can lead to accelerated dissolution if the corrosion process depends on conditions in the liquid. However, such a variation in flow dynamics would not alone explain the observed morphological differences in the mode of attack; the difference in penetration morphology between the corrosion zones on the long and short faces strongly suggests that the process leading to such irregular attack must be sensitive to the steel's microstructure. Indeed, when selected specimen cross sections were etched to reveal the grain structure, definite grain elongation parallel to the direction of main branch penetration was

observed (see, for example, Fig. 6). The effect of cold work was to "bias" the penetration by the lead-lithium such that the influence of microstructure on corrosion in this environment was revealed. The observation of this type of dependency has important implications for the measurement of corrosion losses (particularly in terms of sound metal loss and corrosion zone thickness) and the comparison of such measurements from different experiments and/or from specimens prepared in different ways. Chopra and Smith[4] and Fauvet et a1.5 have previously found that corrosion of cold worked austenitic stainless steel by Pb–17 at. % Li (as measured by weight losses[4,5] and thickness of the corrosion zones) was greater than that of such steels in the annealed condition.

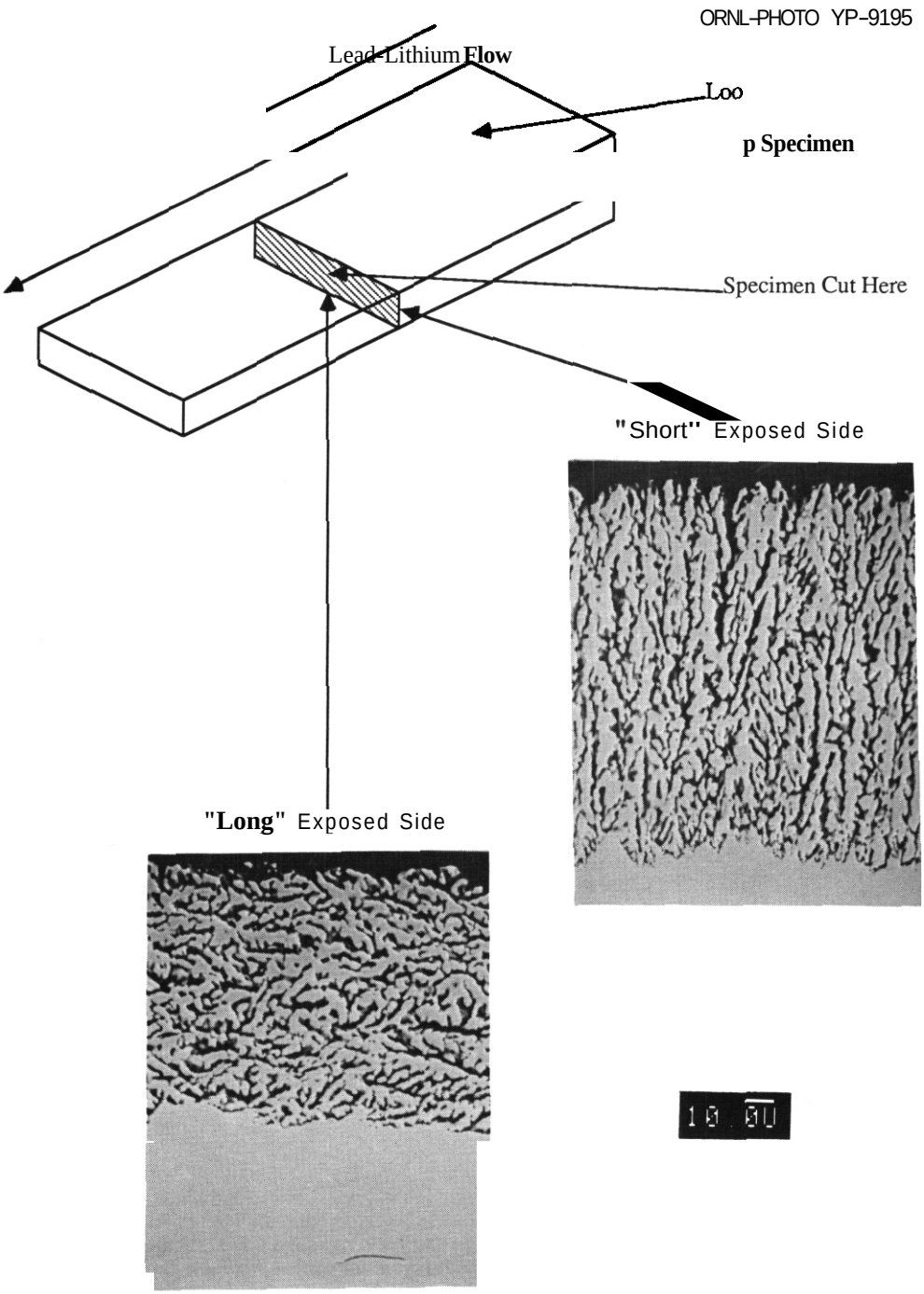


Fig. 5 Schematic drawing of a typical loop coupon indicating how it was cut for polishing and illustrating the different corrosion zone morphologies observed on a polished cross section of type 316 stainless steel exposed to thermally convective Pb-17 at. % Li at 500°C for 3886 h.

ORNL-PHOTO Y-208470

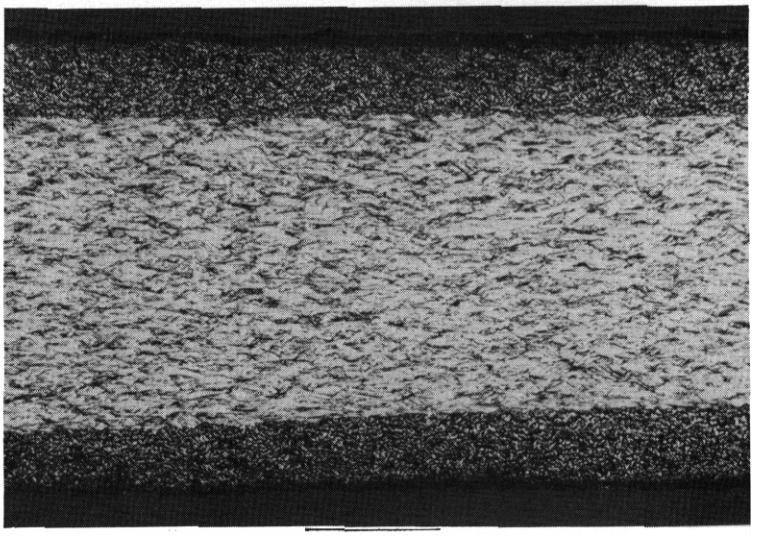


Fig. 6. Optical micrograph of the polished and etched cross section of type 316 stainless steel exposed to thermally convective Pb-17 at. % Li at 500°C for 7007 h.

The observed microstructural influence on the attack of the type 316 stainless steel can be accommodated by the surface destabilization mdel described above and elsewhere.[2,3] The subject model requires initial perturbation of the starting planar surface to trigger the destabilization and subsequent growth of an irregular interface, and grain boundaries or slip lines can nicely serve as such perturbation sites.[3] Therefore, in the context of this model, the biasing provided by the presence of slip lines and the elongation of grain boundaries in the rolling direction can lead to the morphological differences between corrosion zones that develop on long and short faces of the same coupon. Indeed. Fauvet et al. attributed their observation that cold working increased the attack of type 316L stainless steel by Pb-17 at. % Li to the presence of slip lines in the worked material.[5] Furthermore, because the observed depth of corrosive attack is based on a two dimensional analysis of a process that occurs in three dimensions, the "thicker" corrosion zones on the short sides may actually be due to a less tortuous penetration path provided by the availibility of more grain boundaries and/or slip lines in the direction perpendicular to the original surface. It is thus possible that the actual three dimensional penetration distances are about the same regardless of the particular surface in contact with the liquid metal. However, the anisotropy in corrosiveness still exists in terms of the amount of sound metal remaining.

In nonisothermal liquid metal systems. the deposition of dissolved species in the cold zone can be as important as the actual dissolution processes in the hotter parts of the circuit. It is therefore instructive to examine the deposits that formed in the cold leg of the Pb-17 at. % Li TCLs as a result of mass transfer. Weight change data presented in the previous progress report' shared that the maximum weight gain in the type 316 stainless steel TCL was not at the coldest coupon position in the loop. Subsequently, both the exposed surfaces and polished cross sections of the cold leg coupons from the type 316 stainless steel loop experiment were analyzed by scanning electron microscopy and EDX. Selected micrographs are shown in Fig. 7. On any one particular coupon, variations in deposit density were noted and. on some coupons, there were rather large areas free of deposits. One of the reasons for such variability in deposit coverage appeared to be related to the adhesion of the deposits, particularly for the lower temperature coupons [for example see the left-hand side of Fig. 7(c)]. Such loss of deposits may have occurred during exposure to the liquid metal, during cooling after removal from the liquid stream, and/or during the standard specimen cleaning process with lithium that has been described in detail previously.[1,2] In addition, the lack of deposits on certain areas of a specimen may be related to preferential nucleation. The observations of small deposits in definite patterns on some some of the surfaces [such as the left-hand side of Fig. 7(d)] may support such a mechanism, particularly in view of the variability of deposit coverage from one specimen position to another and the accompanying change in deposit composition (see below). The growth of deposits requires registry with the underlying surface and, given that the starting compositions of all the cold leg specimens were the same (type 316 stainless steel), the accommodation and sticking of deposits of differing composition may vary considerably. In any case, the appearance of substantial deposit-free areas on the surfaces at the two coldest loop positions may help to explain why the maximum weight gain was not at the coldest loop position.

The compositions of mass transfer deposits on each type 316 stainless steel cold leg specimen were determined by EDX from deposits observed on the surface and in cross section. The measured compositions from these two viewpoints were consistent with each other. Table 1 summarizes the principal composition results; it contains the average elemental concentrations determined from a number of deposits of a particular type in either the normal or cross sectional view. Note the marked dependence of deposit composition on loop position. At the higher temperature positions in the deposition zone (460 and 445°C), the

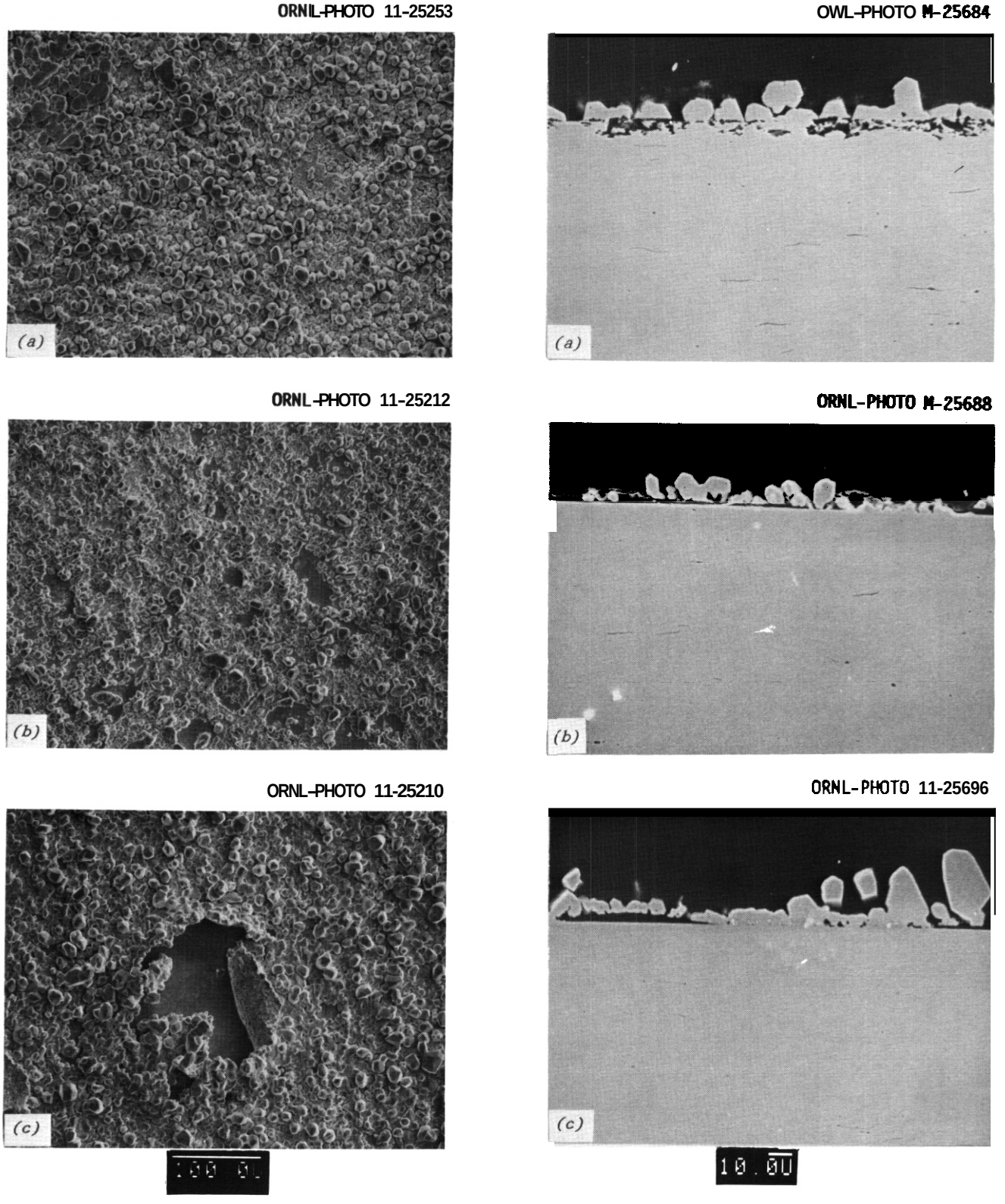


Fig. 7. Scanning electron micrographs showing the normal and cross sectional (polished) views of type 316 stainless steel specimens exposed in the cold leg of a thermal convection loop that circulated Pb-17 at. % Li at a maximum temperature of 500°C. *(a)* 460°C. *(b)* 455°C. *(c)* 430°C. *(d)* (next page) 415°C. (e) 400°C.

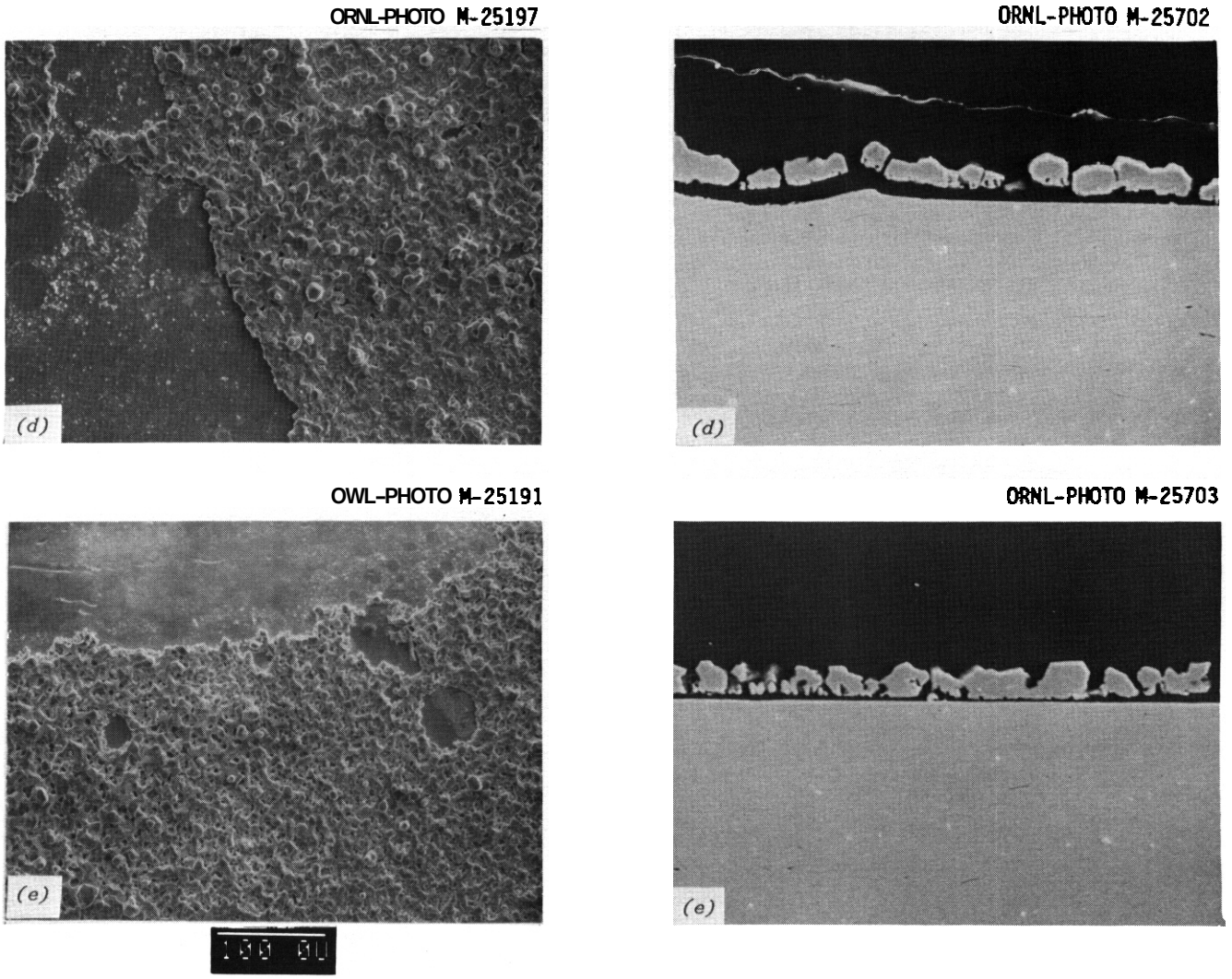


Fig. 7. (cont'd).

Table 1. Compositions of mass transfer deposits on type 316 stainless steel coupons in cold leg of Pb-17 at. % Li thermal convection loop after 10,008 h of exposure

Cold leg temperature (°C)	Deposit concentration (wt %)[a]									
	Normal					Cross section				
	Fe	Cr	Ni	Si	Mo	Fe	Cr	Nf	Si	Mo
460	90	7	3	0.4	0.4	91	5	3	0.4	0.1
445	90	7	2	0.2	0.1	90	7	3	0.4	0.0
430	51	12	36	0.3	0.1	50	12	38	0.7	0.1
	29	68	4	0.0	0.0	37	53	10	0.4	0.2
415	34	64	2	0.2	0.5	27	70	2	0.3	0.0
	45	13	41	0.4	0.7	42	14	44	0.5	0.1
400	25	70	4	0.2	0.6	27	71	1	0.4	0.1
						42	25	32	0.7	0.1

[a]Determined by energy dispersive x-ray analysis.

mass transfer deposits were principally iron, while at lower temperatures, they were either iron-nickel or chromium-rich, thereby necessitating two different average compositions in Table 1. At 430°C, many of the deposits were iron-nickel and a few were enriched in chromium. At 415°C, chromium-rich deposits dominated, although there were some lower in chromium, but more concentrated in nickel. In some cases, two-phase deposits were noted with one phase enriched in chromium and the other in nickel. At the coldest loop coupon position (400°C), most deposits were chromium-rich, although some were of this two-phase mixture (see Fig. 8). Such variation in overall deposit composition as a function of temperature can be attributed to one or more factors: elemental solubilities, differing elemental deposition kinetics and/or sticking coefficients, various chemical reactions in the liquid or at the interface, and hydrodynamics. The present data cannot be used to distinguish the relative importance of these factors, although it is apparent that the variation of deposit composition cannot be explained strictly on the basis of solubilities; the transition from iron to iron-nickel to chromium-rich deposits as the temperature decreases is not consistent with the solubilites of these elements in lead-lithium.

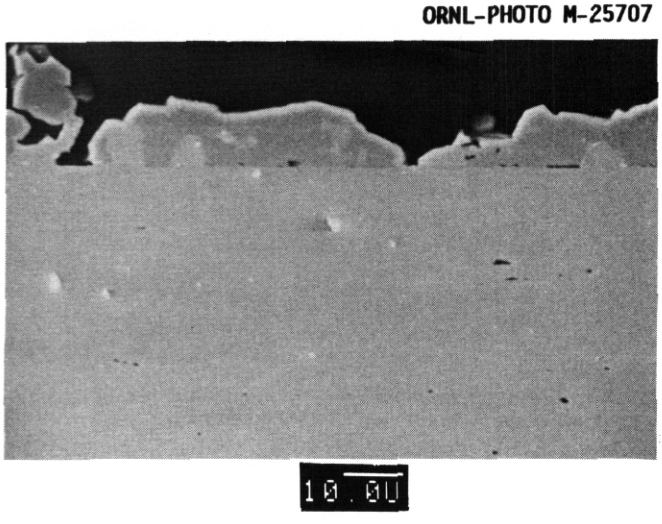


Fig. 8. Scanning electron micrograph of a polished cross section of type 316 stainless steel exposed at 400°C in the cold leg of a thermal convection loop that circulated Pb-17 at. % Li at a maximum temperature of 500°C.

CONCLUSIONS

1. Extensive analysis of type 316 stainless and 12Cr-1MoVW steels exposed to Pb-17 at.% Li at 500°C for extended periods of time confirmed preferential dissolution of nickel and chromium from the former steel and the constancy of the starting surface composition of the ferritic alloy through about 10,000 h of exposure. On the basis of a surface destabilization model, such a preferential dissolution process leads to the development of the irregular surface of exposed type 316 stainless steel.

2. Cold work had a definite effect on the extent and morphlogy of the corrosive attack of type 316 stainless steel exposed to Pb-17 at. % Li at 500°C. The cold work appeared to provide the necessary pertubation sites for the initiation of surface destabilization caused by preferential dissolution and therefore controlled the directionality of the attack and the apparent depth of corrosion.

3. The composition and surface coverage of mass transfer deposits in the type 316 stainless steel Pb-17 at. % Li TCL varied with position in the cold leg and exhibited a complex dependence on temperature.

FUTURE WORK

The surface analyses of the cold leg specimens from the 12Cr-1MoVW steel TCL experiment with Pb-17 at. % Li will be completed during the next reporting period. Microstructural influences on the corrosion process in lead-lithium will be further investigated by examination of other exposed type 316 stainless steel specimens. Initial experiments on corrosion inhibition in lead-lithium will be completed. Evaluation of the corrosion susceptibilities of low activation alloys to molten lithium will be continued using the lithium TCLs.

REFERENCES

1. P. F. Tortorelli, "Long-Term Corrosion of Type 316 Stainless Steel and 12Cr-1MoVW Steels in Thermally Convective Pb-17 at. % Li," pp. 322-27 in *Fusion Reactor Materials Semiannu. Prog. Rep. Sept. 30, 1986,* DOE-ER-0313/1, U.S. DOE, Office of Fusion Energy.

2. P. F. Tortorelli and J. H. DeVan, "Corrosion of Ferrous Alloys Exposed to Thermally Convective Pb-17 at. % Li," *J. Nucl. Mater.* 141-143, 592-98 (1986).

3. J. D. Harrison and C. Wagner, "The Attack of Solid Alloys by Liquid Metals and Salt Melts," *Acta. Metall.* 7, 722-35 (1959).

4. O. K. Chopra and O. L. Smith, "Compatibility of Ferrous Alloys in a Forced Circulation Pb-17-Li System," *J. Nucl. Mater.* 141-143, 566-70 (1986).

5. P. Fauvet, J. Sannier, and G. Santarini, "Corrosion of 316L Stainless Steel in Flowing 17Li83Pb Alloy," pp. 1003-09 in *Proc. 13th Symp.* on Fusion *Technology,* Vol. 2, Commission of the European Communities, Pergamon Press, 1984.

7. SOLID BREEDING MATERIALS

MODEL OF TRITIUM TRANSPORT IN CERAMIC BKEEUER MATERIALS - J. P Kopasz and C. E. Johnson (Argonne National Laboratory)

OBJECTIVE

The objective of this work is to develop **a** computer model that will describe tritium behavior in ceramic breeder materials. The model will enable one to compare the relative contributions of diffusion in the solid. desorption from the solid surface, and permeation through **a** porous medium to the overall tritium inventory.

SUMMARY

A computer model of tritium transport and release is being developed. The model considers diffusion through the solid and desorption from the solid surface. The mode: is based on **a** differential equation that predicts heat transfer in a solid sphere at constant heat generation and heat radiation at the surface. The tritium release over time calculated with our model **was** compared with the measured release for samples of Li_2SiO_3 from the LISA-1 experiment. Overall agreement between the model and experiment **was** good. Improvements in the model to enable handling of samples with large distribution of grain sizes **are** now being considered. It is also envisaged that the diffusion-desorption model will be combined with programs which calculate the effective rate constants at different oxygen potentials.

PROGRESS AND STATUS

A computer program is being developed to describe tritium behavior in ceramic breeder materials. AS presently constructed the program focuses on modeling diffusion in the solid and desorption from the surface. The program is based on the solution of the differential equation

$$\frac{1}{D}\frac{\partial C}{\partial t} = \frac{1}{r^2}\frac{\partial}{\partial r}\left(r^2\frac{\partial C}{\partial r}\right) + \frac{G}{D}$$

where

D is the diffusivity
C is the tritium concentration
r is the grain radius
G is the tritium generation rate

This equation is also applicable to heat transfer in **a** solid sphere with heat produced at **a** constant rate per unit time per unit volume. Carslaw and Jaeger have solved this equation for Several boundary conditions. The conditions one wishes to model determine the boundary conditions for the equation. The heat transfer for a solid sphere with heat generated at a constant rate, zero initial temperature, and radiation into a medium at Zero temperature is considered to be analogous to tritium breeder blanket with constant tritium generation and tritium desorption into a purge flow gas stream at low (zero) tritium Concentration. The boundary conditions for these tWO cases are described by the equations:

$$K\frac{\partial v}{\partial n} + Hv = 0 \qquad \textbf{and} \qquad D\frac{\partial c}{\partial n} + K_{des}\,c_s = 0$$

where

cs is the surface concentration
K_{des} is the desorption rate constant
K is the thermal conductivity
v is the temperature of the medium
H is a constant = hK

Since the surface concentration is not in the same units as the bulk (volume) concentration, a new parameter. K_d, is defined **as** the effective desorption rate constant, where K_d times the tritium concentration evaluated at the surface is equal to the desorption rate ($K_{des}C_s$). The constant K_d is related to the desorption rate constant K_{des} by a factor describing the thickness of the surface. It may be argued that these boundary conditions do not apply to an operating breeder blanket, since the tritium concentration in the purge gas will not necessarily be zero. However, since the tritium concentration in the purge gas is likely to be an order of magnitude or more lower than that in the blanket surface, and that the tritium is quickly carried away by the purge gas, the assumption of zero concentration in the purge gas appears to be valid.

The Solution provided by Carslaw and Jaeger[1] to the heat transfer problem is

$$V = \frac{}{6h\kappa}\{h(a^2-r^2)+2a\} - \frac{2Ha2A_o}{r\kappa}\sum_{n=1}^{\infty}\frac{\sin r\alpha_n \exp(-\kappa\alpha_n^2 t)}{a^2[a^2\alpha^2 + ah(ah-1)]\sin a\alpha_n}$$

V = temperature
A_o = heat generation rate
K = ρc_p
κ = thermal conductivity
h = H/K
H = heat transfer coefficient
r = distance along radius
a = radius

Further, α_n represents the roots of $a\alpha \cot a\alpha = 1 - ah$

t = time

Making the following assumptions

C = V
G/D = A_o/K
κ = D
R_t = $K_d C_a$ = dC/dt

and allowing for a temperature change (remembering D and K_d ire dependent on temperature) leads to the equation for tritium release given below

$$R_t = \left(1 - \frac{3K_d}{Ga} C_1\right)\left[\frac{Ga}{3} - 2h^2 aG \sum_{n=1}^{\infty}\frac{\exp(-D\alpha_n^2 t)}{\alpha_n^2[a^2\alpha_n^2 + ah(ah-1)]}\right] + Kd\ C_1$$

where

K_d = effective first-order desorption rate constant
C_1 = tritium Concentration evaluated at r=a prior to a temperature change
h = K_d/D
R_t = tritium release rate

The release rate was calculated using the diffusion-desorption model and compared to the observed tritium release rate for a sample of Li_2SiO_3 from the LISA-1 experiment. A typical plot is shown in Fig. 1. The model predicts the initial rise in release rate and the release rate after 100,000 Seconds quite well but does a poorer job of predicting the release rate between 10,000 and 75,000 seconds. The calculated tritium release profile is also in good agreement with the observed data for time periods after a large temperature decrease (-250,000, 450,000, and 675,000 sec) or increase (-350,000 sec). One shortcoming of the current model is that it uses a characteristic radius of the sample to calculate the release rate. The samples used in the LISA-1 experiments have a large distribution of grain sizes. and it is difficult to assign a characteristic grain size to the sample. Since the tritium release is dependent on the grain size, this could have a substantial effect on the release profile. To correct this shortcoming. the model is being altered to allow for a distribution of grain sizes as input.

FUTURE WORK

A model is being developed which will describe tritium behavior in ceramic breeder materials. This model will be used to interpret tritium release data from in-pile experiments and to evaluate the diffusion constants obtained assuming pure diffusional release. The dependence of tritium release and desorption rate on the oxygen activity of the purge gas will be investigated. Additional complexity due to grain size distribution, grain boundary diffusion, surface effects, and gas phase transport will be added to the model. To solve these more complex systems of equations DISPL, a Software package for solving Second order nonlinear systems of partial differential equations, will be used.

REFERENCES

1. H. S. Carslaw and J. C. Jaeger, Conduction of Heat Solids, 2nd Edition. p. 245.

2. R. C. Clemmer, P. A. Finn, R. F. Malecha, B. Misra, M. C. Billone, D. L. Bowers, A. K. Fischer, L. R. Greenwood, R. F. Mattas, S. W. Tam, R. B. Poeppel, G. T. Reedy, I. T. Dudley. F. F. Dyer, E. D. Clemmer, J. S. Watson, P. W. Fischer, J. R. Conlin, R. L. Childs, J. L. Scott, R. M. Arons, and A. E. Scandora, "The TRIO Experiment."

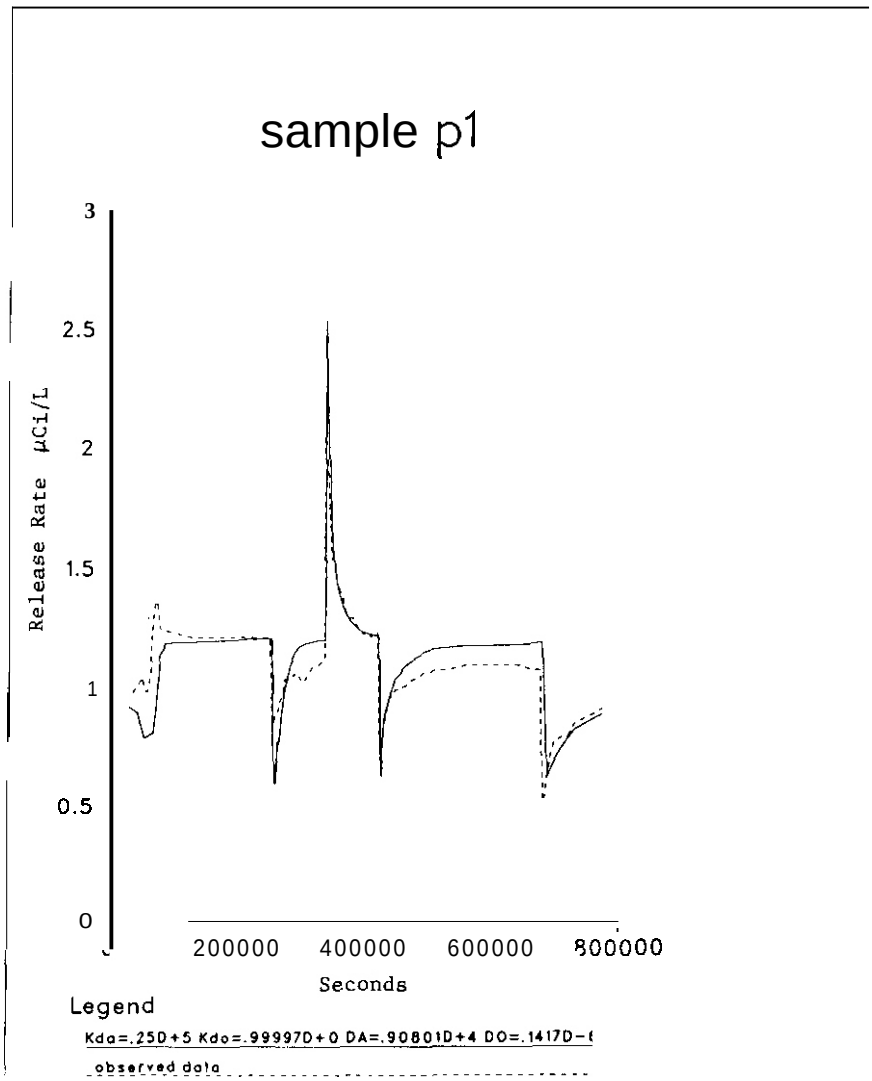


Fig. 1. Calculated and Observed Tritium Release from Li_2SiO_3.

ADSORPTION, SOLUTION, AND DESORPTION CHARACTERISTICS OF THE $LiAlO_2$-H_2O SYSTEM - Albert K. Fischer and Carl E. Johnson (Argonne National Laboratory)

OBJECTIVE

The objective of this work is to provide measured thermodynamic and kinetic data related to tritium retention and release from ceramic tritium breeders. Adsorption, dissolution, desorption, and H_2O evolution are being measured for the $LiAlO_2$-H_2O-H_2 system. This information, together with similar information for other ceramic breeders will (1) enable comparison among candidate materials, and (2) enable blanket operating conditions to be more rigorously defined. An additional objective is to elucidate the principles underlying the behavior of tritium in breeders as well as other interactions of breeders with reactor components.

SUMMARY

Isotherms are reported for adsorption of H_2O on $LiAlO_2$ at 500°C and for solubility of OH- in $LiAlO_2$ also at 500°C. The kinetics of the water evolution process appears to be second order in hydroxide content. Calculations have indicated that for the solid phase there is a critical oxygen activity below which tritide is the dominant tritium species rather than tritons which prevail above the critical oxygen activity. These relationships have important implications for the design, performance. and interpretation of tritium release experiments.

INTRODUCTION

Adsorption, dissolution, desorption, and H_2O evolution are being measured for the $LiAlO_2$-H_2O-H_2 system to provide thermodynamic and kinetic information for the breeder, $LiAlO_2$. The first isotherm for this system, for 500°C, is now available.

Frontal analysis gas chromatography (the breakthrough technique1 is being used for the measurements of adsorption. Post-adsorption uptake of water vapor is being measured to determine the solubility of hydroxide in $LiAlO_2$. Such data will yield adsorption isotherms to describe the thermodynamics of adsorption of water vapor and solubility isotherms for the solubility of protons (i.e., hydroxide) as a Solute. The reverse processes, desorption and evolution of water vapor, are being measured to describe the kinetics of the release process. Determination of the dependence of these quantities on oxygen activity is also included in the experimental program.

ADSORPTION-DISSOLUTION MEASUREMENTS

The experimental effort is directed to obtaining heats of adsorption of which three types are mentioned in the literature. namely, Langmuir, Tempkin, and Freundlich. These literature treatments differ in their assumptions about the dependence of the heat of adsorption on the degree of surface coverage. The Langmuir approach assumes that the heat of adsorption Is constant and independent of θ, the fraction of surface coverage. The Tempkin approach treats the heat of adsorption as a linear function of E and requires a linear plot of E versus $\ln(p)$ where p is the partial pressure of water vapor. The Freundlich approach is based on logrithmic dependence of the heat of adsorption on θ and is tested by a linear plot of $\ln(\theta)$ versus $\ln(p)$. Adsorption data at 500°C are plotted in Fig. 1 as $\ln(\theta)$ vs $\ln(p)$; linear dependence is observed, suggesting Freundlich behavior. Freundlich behavior is usually taken to indicate surface heterogeneity, i.e., the availability of more than one kind of surface site for adsorption. This is understandable, in part, in terms of surface dislocations, ledges, etc. In the present case, there are the additional possibilities for O^{-2}, Li^{+}, and Al^{+3} sites to participate in adsorption with different energies depending on the species and the exposed crystal plane. It is possible that different kinds of sites dominate in different measurements involving different ranges of coverage. For measurements in a range of smaller fractional surface coverages, it is more likely that a single kind of site will be reflected in the data.

The second phase of an experimental run yields data on the solubility of OH- in $LiAlO_2$. The data points and the regression line for the series at 500°C are shown in Fig. 2. Solubility is reported in units of mol fraction, x_{OH}. These data (and the adsorption data presented above) are still subject to correction for baseline adsorbed and dissolved hydroxide. Necessarily, the measurements are differential rather than integral. A correction factor will be derived requiring overall thermodynamic consistency of all data at all measured temperatures. Earlier, such a procedure was applied to the data for the solubility of hydroxide in Li_2O. If tritoxide behaves as hydroxide, then the solubility of hydroxide in units of mol fraction may be converted to solubility of tritons in parts per million by weight with the relationship, wppm (T in $LiAlO_2$) = $4.5 \times 10^4 x_{OH}$.

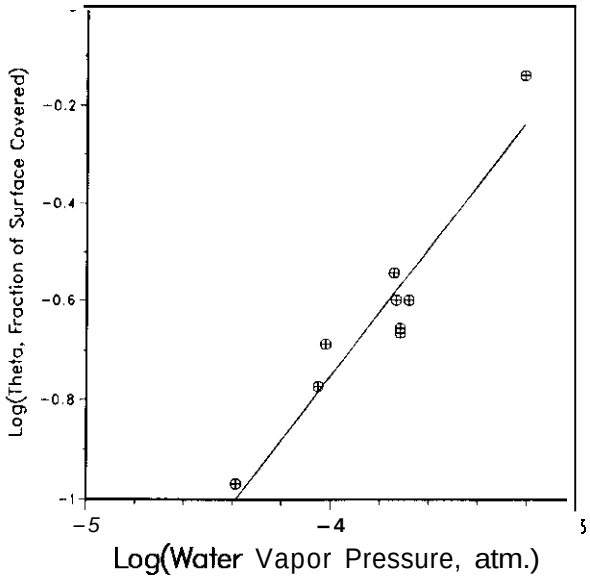


Fig. 1. Surface adsorption isotherms *for* adsorption of H_2O on $LiAlO_2$ at 500°C (Freundlich isotherm) as a function of water vapor pressure. $\log \pm = 1.81+0.693\log(p,atm)$.

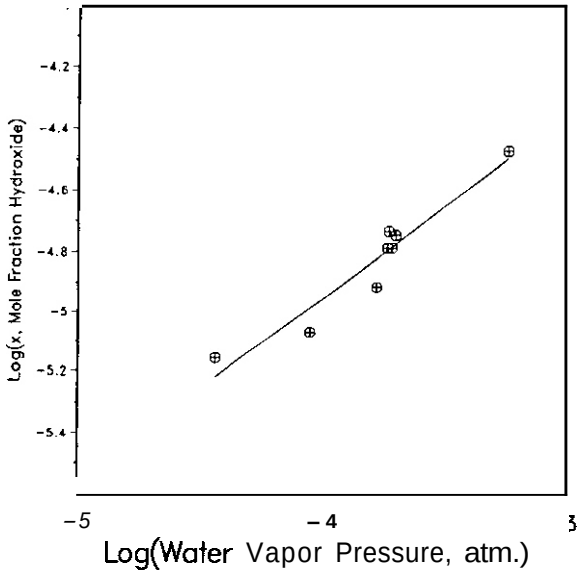


Fig. 2. Solubility of hydroxide in $LiAlO_2$ at 500°C as function of water vapor pressure. $\log x_{OH} = -1.76+0.604\log(p,atm)$.

The slope of the curve in Fig. 2 is of interest as it will provide an indication of whether $LiAl_5O_8$ acts as a solute in $LiAlO_2$ or as a separate phase according to the reaction:

$$5LiAlO_2 + 2H_2O = 4LiOH + LiAl_5O_8 \quad (1)$$

If $LiAl_5O_8$ forms a separate phase, the slope will be 0.5; if $LiAl_5O_8$ is a solute in $LiAlO_2$, the slope will be 0.4. The uncorrected value of 0.6 is reminiscent of the Tetenbaum measurements on the solubility of

hydroxide in Li_2O where 0.6 was also observed for the raw data. In that case. corrections for baseline dissolved hydroxide and for non-ideality eventually gave a value close to 0.5.

In order to show the relationship between surface adsorbed hydroxide (θ) and dissolved hydroxide (x_{OH}) Fig. 3 is presented showing the ratio of E: x_{OH} at 500°C as a function of partial pressure of water vapor.

KINETICS OF EVOLUTION OF WATER VAPOR

After completion of the adsorption-dissolution part of a run, the Pate of evolution of water into a flowing helium stream is measured. Data for an earlier run were reported as showing first order or second order kinetics depending on temperature. With the much larger data base that is now available, a more detailed examination of kinetic behavior is possible. It now appears that for reproducibility of reaction order data a helium flow rate of approximately 45 to 65 cc/min is required. At this higher flow rate the water evolution process appears to be second order.

Second order kinetics for the H_2O evolution process is consistent with a rate controlling bimolecular surface process. The bimolecularity results from surface diffusion of protons to form adjacent OH groups which combine to split out an H_2O molecule. In a situation with a small amount of tritium and with a dominance of protium, such as is likely to exist in a reactor. the bimolecular process will be reflected by a rate equation that is pseudo-first order in tritium.

CONCEPTUAL DEVELOPMENTS

In this period, effort was also given to clarification of the nature of the dissolved and diffusing tritium species in ceramic tritium breeders. Review of experimental and theoretical work indicates a correspondence between the interstitial proton in oxides with the hydroxide ion. For tritium, the correspondence is between the triton and the tritoxide ion. Transport of protons (or tritons) is thought to proceed by a hopping process from oxide to oxide in the oxygen sublattice and is assisted by vacancies in the cation sublattice. However, our calculations[1] indicate that there is a critical oxygen activity at which the concentration of hydroxide (protons) in the solid phase is equal to the Concentration of hydride. Below this critical oxygen activity, hydride (or tritide) is the dominant species. At these oxygen activities the oxide vacancy concentration is also greater and the tritium diffusion process is Seen as that of tritide diffusion through oxide vacancies. The possible occurrence of regions of low Oxygen activity is plausible on the bas's of observations of elemental lithium formed during neutron bombardment of lithium-containing materials.' It follows that the diffusion of tritium from such a region in a ceramic particle proceeds from a region of low oxygen activity to a region of high oxygen activity at the surface. In the process, tritium changes from a tritide ion to a triton ion, and the diffusion process changes from tritide movement into oxide vacancies to triton hopping among oxide ions.

This involvement of the tritide ion is a new aspect of the tritium transport process which needs to be considered in the design, performance, and interpretation of tritium release experiments. For deductions of diffusion constants from an overall tritium release rate it is necessary to consider two diffusion constants, one for tritide movement by diffusion through oxide vacancies, and one for triton movement for diffusion by hopping among oxide ions. Also, the physical thicknesses of the two kinds of diffusion regions need to be determined to assign the correct boundary conditions. There may also be an intermediate transition zone in which the triton and tritide concentrations are nearly equal and in which the possibility exists for formation of HT and T_2 which can migrate into helium bubbles.

CONCLUSIONS

Measurements of adsorption of H_2O, dissolution of hydroxide, and evolution of H_2O from $LiAlO_2$ are providing important data for the thermodynamics of adsorption. for hydroxide Solubility, and for the kinetics of water vapor evolution. The progress in conceptual developments is providing new insights into important processes involved in understanding tritium behavior in ceramic tritium breeders.

FUTURE WORK

The present work will involve gathering sufficient additional data to construct adsorption isotherms for different temperatures, to determine solubility of hydroxide as a function of temperature and partial pressure of H_2O, and to determine activation energies of H_2O evolution. The effect of H_2 in the gas phase on these quantities will be measured. Subsequently, the breeder material, Li_4SiO_4, will be the probable candidate for study in the same way so that ultimate programmatic comparison of the two will be possible. Further background will be developed regarding the consequences of H_2 and O_2 adsorption.

REFERENCES

1. A. K. Fischer and C. E. Johnson, Proceedings of the American Ceramic Society, April 1986 Meeting in Pittsburgh, PA.

2. K. Noda et al., J. Nucl. Mater., 91, 1980, Radiation Damage in Sintered Li_2O Pellets-ESR Study.

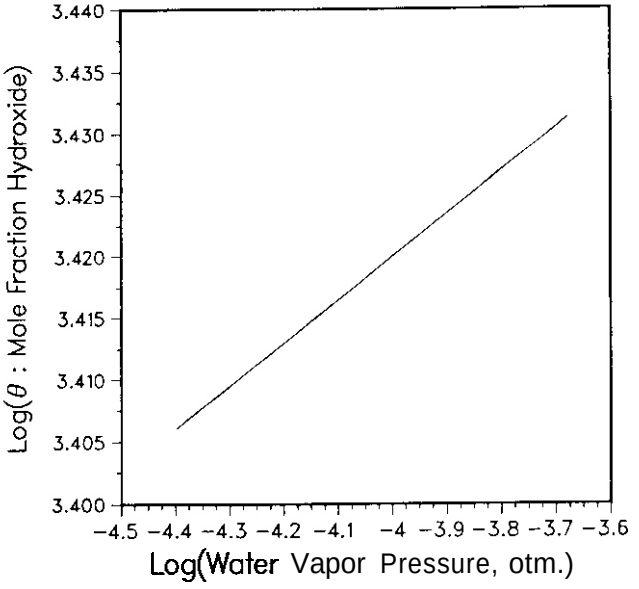


Fig. 3. Relationship between degrees of surface adsorption and hydroxide solubility at 500°C as function of water vapor pressure. $\log(f/H_{OH}) = 3.56+0.3551\log(p,atm)$.

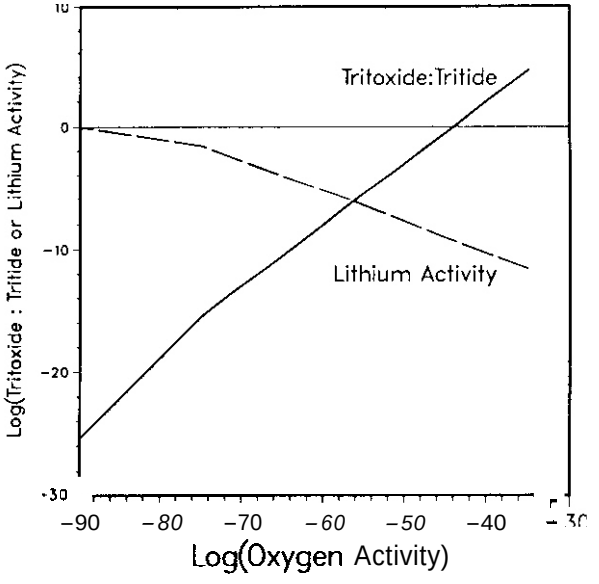


Fig. 4. Calculated relationships among lithium activity, tritide: triton ratio, and oxygen activity in $LiAlO_2$ at 800 K.

SOLID BREEDER MATERIALS FABRICATION AND MECHANICAL PROPERTIES - R. B. Poeppel (Argonne National Laboratory)

OBJECTIVE

The objectives of this program are to synthesize ceramic powders and/or fabricate samples of candidate solid breeder materials for various international cooperative irradiation test programs and to characterize the mechanical properties of selected lithiun ceramics.

SUMMARY

The fabrication of lithiun oxide rings for the CRITIC-I experiment was completed and the rings transferred to Chalk River. Lithium zirconate, lithiun aluminate and lithium silicate ceramic powders were sent to Hanford Engineering and Developnent Laboratory to be fabricated for FUBR-1B replacement capsules. Three papers[1-3] were prepared for the American Ceramic Society Special Symposium on "Fabrication and Properties of Lithium Ceramics." Initial materials have been synthesized to fabricate test specimens for the measurement of mechanical properties of lithium orthosilicate. The paper describing the mechanical properties of lithiun oxide was published in the Journal of Nuclear Materials.[4]

PROGRESS AND STATUS

A 10-cm-high stack of depleted lithiun oxide rings was fabricated for the CRITIC-I experiment (Chalk River Instrumented Tritium Irradiation Capsule). The rings are ~4 cm OD, ~3 cm ID and ~0.7 cm high, ~90% of theoretical density, and with a 30-60 μm grain size. Fine-grained, sinterable lithium oxide powder was prepared by high-temperature, vacuum calcination of molten lithium carbonate. The product was ball-milled, cold-pressed, and fired in an oxygen atmosphere. Final dimensions were achieved by diamond grinding. A paper fully describing the fabrication and material characteristics is in preparation.

The Li_2ZrO_3 was synthesized from hafnium-free zirconyl nitrate obtained from Teledyne Wah Chang and depleted lithium carbonate from Oak Ridge Y12. The zirconyl nitrate was first converted to fine-grained zirconia by precipitation with ammonium hydroxide from aqueous solution. The precipitate was washed three times with water and once with ethyl alcohol. The powder was separated by centrifuge after each rinse. After the final rinse the powder was heated in a laboratory furnace and held at 440°C for three days. The product was then ball-milled with lithium carbonate, spray dried, and calcined at 650°C for 75 h. Two hundred fifty grams of powder was sent to Hanford. Lithium aluminate fabrication has been reported previously. Briefly, fine DeGussa alumina was wet ball-milled with depleted lithium carbonate, spray dried, and calcined for several days at 650°C in air. One hundred grams was sent to Hanford.

Lithium orthosilicate was made by a procedure not previously reported. The powder was synthesized from Cabot Corporation Cab-O-si1 amorphous silica and depleted lithiun carbonate. The silica was first dried to obtain accurate weights of reactants. Weight loss after vacuum oven heating to ~150°C was ~1.5% while weight loss was ~2% after heating in air to 650°C. The dried silica was ball-milled for ~3 days with depleted lithium carbonate and Carbowax 3350 polyethylene glycol in isopropyl alcohol. The charge contained 171 g silica, 429 g lithiun carbonate, 11 g PEG, and 4.2 L alcohol. When the mixture was spray dried, 623 grams of product was recovered. This was divided and placed into three alumina crucibles, heated to 650°C for 72 h, and cooled to room temperature. Lumps were broken up and the powder screened through 140 mesh. Two hundred fifty grams was sent to Hanford.

FUTURE WORK

Additional lithium orthosilicate ceramic powder will be prepared. Compression test samples will be pressed and sintered. Stoichiometry will be checked by atomic absorption spectroscopy. Microstructure will be characterized by SEM. The samples will be tested in compression at temperatures between 700 and 950°C with strain rates ranging from 10^{-6} to 10^{-4} s^{-1}.

REFERENCES

1. D. S. Applegate and R. B. Poeppel, "CRITIC-I Instrumented lithium Oxide Irradiation Part 1 - Lithium Oxide Fabrication and Characteristics," to be published in Proc. Symp. on Fabrication and Properties of Lithiun Ceramics, 89th Ann. Mtg. of Am. Ceram. Soc., Pittsburgh, Pa., April 26-30, 1987.

2. R. B. Poeppel, J. L. Routbort, E. Buchmann, B. Londschien, D. S. Applegate, and M. C. Billone, "Steady-State Deformation of Some Lithium Ceramics," ibid.

3. R. B. Poeppel and R. F. Mattas, "Fabrication of Li_2CO_3 Bricks for Fusion Breeder Neutronics Experiments," ibid.

4. K. C. Goretta, D. S. Applegate, R. B. Poeppel, M. C. Billone, and J. L. Routbort, "Deformation of polycrystalline Li_2O," J. Nucl. Mater. 141-143, 282-288 119861.

8. CERAMICS

No contributions received this period.

9. SUPERCONDUCTING MAGNET MATERIALS

IRRADIATION EFFECTS ON ORGANIC INSULATORS - M. B. Kasen (National Bureau of Standards)

OBJECTIVE

The overall objective of this work is to develop functional organic-matrix composite insulators for use in the superconducting magnets of magnetic fusion energy systems. The immediate objective is to develop a method for efficient screening of the significant parameters influencing degradation of such materials under neutron irradiation at 4 K.

SUMMARY

An integrated approach has been developed for rapid screening of the influence of component variables on the performance of electrical insulators required for superconducting magnets in magnetic fusion energy systems. It incorporates an efficient method for specimen production in the form of 3.2-mm (0.125-in) diameter rods. Test methods include short-beam shear, fracture strength (G_{Ic}), and strain-controlled torsion. Unreinforced (neat resin) and glass-fiber reinforced specimens having three types of epoxy matrices and one type of basmaleimide matrix have been produced and submitted to ORNL for irradiation in the LTNIF facility. However, the irradiation was not performed during the present reporting period due to startup delays on the LTNIF facility. Furthermore, NBS has been informed by ORNL personnel that the required irradiation cannot be performed on the type E glass-reinforced specimens due to the interaction between the high thermal neutron flux in the reactor and the boron element in this type of glass.

PROGRESS AND STATUS

One hundred ninety-six specimens have been awaiting irradiation in the LTNIF facility for a period in excess of one year. The irradiation program, consisting of exposure of equal batches of specimens to three increasing radiation levels, was to be performed during March of 1987. However, NBS has been informed by ORNL personnel that new calculations have indicated that interaction of the high thermal neutron flux in the reactor with the boron content of the type E glass used in the composite specimens will result in a level of damage precluding a meaningful experiment. The E-glass type of reinforcement had been used in previous cryogenic experiments using gamma irradiation, and was therefore selected to provide a comparison of gamma versus neutron irradiation. Since this type of glass is most commonly used in magnet insulation, it was also intended to provide baseline performance data under neutron irradiation against which the performance of other types of fiber reinforcement could be directly compared.

This unfortunate development will reduce the present program to the irradiation and subsequent cryogenic mechanical property testing of only the unreinforced resin specimens.

FUTURE WORK

Subsequent to cryogenic irradiation, the unreinforced specimens will be warmed to room temperature and returned to NBS for cryogenic mechanical testing. Due to termination of funding, this activity will conclude the NBS participation in the overall program to develop radiation-resistant organic-matrix insulators for magnetic fusion energy systems.

DOE/ER-0313/2
Distribution
Categories
UC-20 and 20c

DISTRIBUTION

1–13. Argonne National Laboratory, 9700 South Cass Avenue, Argonne, IL 60439

M. C. Billone
O. K. Chopra
R. G. Clemmer
D. R. Diercks
P. A. Finn
A. K. Fischer
Y. Y. Liu
B. A. Loomis
R. F. Mattas
L. A. Niemark
S. W. Tam
E. R. Van Deventer
H. Wiedersich

14. Argonne National Laboratory, EBR-II Division, Reactor Materials Section, P.O. Box 2528, Idaho Falls, IO 83403-2528

D. L. Porter

15. Arizona State University, Department of Mechanical and Aerospace Engineering, Tempe, AZ 85281

W. A. Coghlan

16. Auburn University, Department of Mechanical Engineering, Auburn, AL 36849

B. A. Chin

17–30. Battelle-Pacific Northwest Laboratory, P.O. Box 999, Richland, WA 99352

J. L. Brimhall
D. G. Doran (5)
M. D. Freshley
F. A. Garner
D. S. Gelles
M. L. Hamilton
H. L. Heinisch
G. W. Hollenberg
B. O. Shipp
O. O. Slagle

31–32. Carnegie Institute of Technology. Carnegie-Mellon University, Schenley Park, Pittsburgh, PA 15213

W. M. Garrison, Jr.
J. C. Williams

33–36. GA Technologies, Inc., P.O. Box 85608, San Diego, CA 92138

J. Bauer
G. R. Hopkins
T. A. Lechtenberg
D. I. Roberts

37–38. General Dynamics Corporation, 5001 Kearny Villa Road, San Diego, CA 92138

T. L. Cookson
V. Stegar

39. General Electric, Advanced Nuclear Technology Operation, 310 Oeguine Drive, Sunnyvale, CA 94088

S. Valdyanathan

40. Georgia Institute of Technology, School of Textile Engineering, Atlanta, GA 30332

D. S. Tucker

41. Grumman Aerospace Corporation, c/o TFTR Project, Princeton Plasma Physics Laboratory, Princeton University, A. Site, Building I-E, Princeton, NJ 08540

R. G. Micich

42–44. Lawrence Livermore National Laboratory, P.O. Box 808, Livermore, CA 94550

E.N.C. Dalder
M. Guinan
J. Perkins

45–53. Los Alamos National Laboratory, P.O. Box 1663, Los Alamos, NM 87545

J. L. Andersen
L. Caudel
D. J. Dudziak
H. M. Frost
G. Hurley
C. D. Kise
R. Liepens
R. J. Livak
T. Zocco

54. Manlabs, Inc., 231 Erie Street, Cambridge, MA 02139

D. Tognarelli

55. Massachusetts Institute of Technology, Department of Metallurgy and Materials Science, Cambridge, MA 02139

L. W. Hobbs

56. Massachusetts Institute of Technology, 138 Albany Street, Cambridge, MA 02139

O. K. Harling

57–58. Massachusetts Institute of Technology, 77 Massachusetts Avenue, Cambridge, MA 02139

I-Wei Chen

N. J. Grant

59–60. Massachusetts Institute of Technology, Plasma Fusion Center Headquarters, Cambridge, MA 02139

H. D. Becker

D. B. Montgomery

61. McDonnell-Douglas Astronautics Company, East, P.O. Box 516, Bldg. 92, St. Louis, MO 63166

J. W. Davis

62–63. National Bureau of Standards, Boulder, CO 80302

F. R. Fickett

M. B. Kasen

64. National Materials Advisory Board, 2101 Constitution Avenue, Washington, DC 20418

K. M. Zwilsky

65. Naval Research Laboratory, Washington, DC 20375

J. A. Sprague

66–131. Oak Ridge National Laboratory, P.O. Box X, Oak Ridge, TN 37831

Central Research Library
Document Reference Section
Laboratory Records Department (2)
Laboratory Records - RC
Patent Section
J. Bentley
L. A. Berry
E. E. Bloom
D. N. Braski
W. P. Eatherly
M. L. Grossbeck
S. Hamada
R. L. Klueh
R. A. Lillie
K. C. Liu
A. W. Longest
L. K. Mansur
P. J. Maziasz
T. K. Roche
A. F. Rowcliffe (35)
R. L. Senn
I. Siman-Tov
R. E. Stoller
M. S. Suzuki
K. R. Thoms
P. T. Thornton (3)
P. F. Tortorelli
F. W. Wiffen
S. J. Zinkle

132–134. Princeton Plasma Physics Laboratory, Princeton University, P.O. Box 451, Princeton, NJ 08540

J.P.F. Conrads
H. Furth
Long-Poe Ku

135. Rensselaer Polytechnic Institute, Troy, NY 12181

D. Steiner

136. Rockwell International Corporation, NA02, Rocketdyne Division, 6633 Canoga Avenue, Canoga Park, CA 91304

D. W. Kneff

137–138. Sandia National Laboratories, P.O. Box 5800, Albuquerque, NM 87185

M. J. Davis

W. B. Gauster

139–141. Sandia National Laboratories, Livermore Division 8316, Livermore, CA 94550

W. Bauer
J. C. Lippold
W. G. Wolfer

142. University of California, Department of Chemical and Nuclear Engineering, Santa Barbara, CA 93106
G. R. Lucas

143-145. University of California, Department of Chemical, Nuclear and Thermal Engineering, Los Angeles, CA 90024
M. A. Abdou
R. W. Conn
N. M. Ghoniem

146. University of California, Los Alamos National Laboratory, P.O. Box 1663, Los Alamos, NM 87545
T. Zocco

147. University of Missouri, Department of Nuclear Engineering, Rolla, MO 65401
A. Kumar

148. University of Michigan, Department of Nuclear Engineering, Ann Arbor, MI 48109
T. Kammash

149-153. Westinghouse Hanford Company, P.O. Box 1970, Richland, WA 99352
A. M. Ermi
G. D. Johnson
F. M. Mann
R. J. Puigh
R. L. Simons

154. Department of Energy, Oak Ridge Operations Office. P.O. Box E, Oak Ridge, TN 37831
Assistant Manager for Energy Research and Development

155-158. Department of Energy, Department of Fusion Energy, Washington, DC 20545
S. E. Berk
J. F. Clarke
M. M. Cohen
T. C. Reuther

159-289. Department of Energy, Technical Information Center, Office of Information Services, P.O. Box 62, Oak Ridge, TN 37831
For distribution as shown in DOE/TIC-4500, Distribution Categories UC-20 (Magnetic Fusion Energy) and UC-20c (Reactor Materials)

☆U.S. GOVERNMENT PRINTING OFFICE: 1987-748-168/60091